eISBN 978-1-60805-448-0
ISBN 978-1-60805-507-4

Photonic Bandgap Structures

Novel Technological Platforms for Physical, Chemical and Biological Sensing

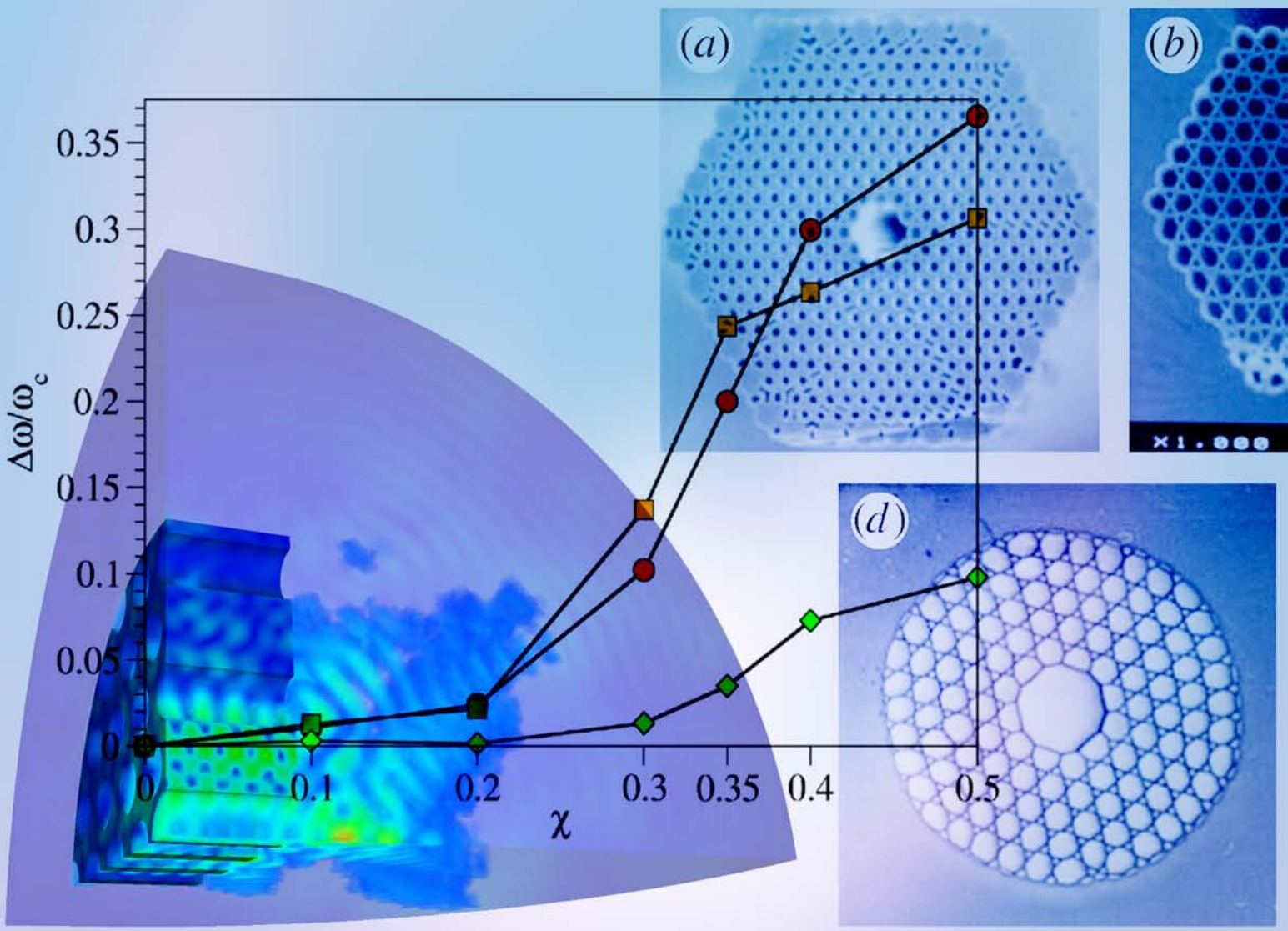

Editors
Marco Pisco, Andrea Cusano & Antonello Cutolo
University of Sannio
Italy

Bentham Books

Photonic Bandgap Structures
Novel Technological Platforms for Physical, Chemical and Biological Sensing

Editors

Marco Pisco, Andrea Cusano and Antonello Cutolo

Optoelectronic Division
Department of Engineering
University of Sannio
Italy

eBooks End User License Agreement

Please read this license agreement carefully before using this eBook. Your use of this eBook/chapter constitutes your agreement to the terms and conditions set forth in this License Agreement. Bentham Science Publishers agrees to grant the user of this eBook/chapter, a non-exclusive, nontransferable license to download and use this eBook/chapter under the following terms and conditions:

1. This eBook/chapter may be downloaded and used by one user on one computer. The user may make one back-up copy of this publication to avoid losing it. The user may not give copies of this publication to others, or make it available for others to copy or download. For a multi-user license contact permission@benthamscience.org

2. All rights reserved: All content in this publication is copyrighted and Bentham Science Publishers own the copyright. You may not copy, reproduce, modify, remove, delete, augment, add to, publish, transmit, sell, resell, create derivative works from, or in any way exploit any of this publication's content, in any form by any means, in whole or in part, without the prior written permission from Bentham Science Publishers.

3. The user may print one or more copies/pages of this eBook/chapter for their personal use. The user may not print pages from this eBook/chapter or the entire printed eBook/chapter for general distribution, for promotion, for creating new works, or for resale. Specific permission must be obtained from the publisher for such requirements. Requests must be sent to the permissions department at E-mail: permission@benthamscience.org

4. The unauthorized use or distribution of copyrighted or other proprietary content is illegal and could subject the purchaser to substantial money damages. The purchaser will be liable for any damage resulting from misuse of this publication or any violation of this License Agreement, including any infringement of copyrights or proprietary rights.

Warranty Disclaimer: The publisher does not guarantee that the information in this publication is error-free, or warrants that it will meet the users' requirements or that the operation of the publication will be uninterrupted or error-free. This publication is provided "as is" without warranty of any kind, either express or implied or statutory, including, without limitation, implied warranties of merchantability and fitness for a particular purpose. The entire risk as to the results and performance of this publication is assumed by the user. In no event will the publisher be liable for any damages, including, without limitation, incidental and consequential damages and damages for lost data or profits arising out of the use or inability to use the publication. The entire liability of the publisher shall be limited to the amount actually paid by the user for the eBook or eBook license agreement.

Limitation of Liability: Under no circumstances shall Bentham Science Publishers, its staff, editors and authors, be liable for any special or consequential damages that result from the use of, or the inability to use, the materials in this site.

eBook Product Disclaimer: No responsibility is assumed by Bentham Science Publishers, its staff or members of the editorial board for any injury and/or damage to persons or property as a matter of products liability, negligence or otherwise, or from any use or operation of any methods, products instruction, advertisements or ideas contained in the publication purchased or read by the user(s). Any dispute will be governed exclusively by the laws of the U.A.E. and will be settled exclusively by the competent Court at the city of Dubai, U.A.E.

You (the user) acknowledge that you have read this Agreement, and agree to be bound by its terms and conditions.

Permission for Use of Material and Reproduction

Photocopying Information for Users Outside the USA: Bentham Science Publishers grants authorization for individuals to photocopy copyright material for private research use, on the sole basis that requests for such use are referred directly to the requestor's local Reproduction Rights Organization (RRO). The copyright fee is US $25.00 per copy per article exclusive of any charge or fee levied. In order to contact your local RRO, please contact the International Federation of Reproduction Rights Organisations (IFRRO), Rue du Prince Royal 87, B-I050 Brussels, Belgium; Tel: +32 2 551 08 99; Fax: +32 2 551 08 95; E-mail: secretariat@ifrro.org; url: www.ifrro.org This authorization does not extend to any other kind of copying by any means, in any form, and for any purpose other than private research use.

Photocopying Information for Users in the USA: Authorization to photocopy items for internal or personal use, or the internal or personal use of specific clients, is granted by Bentham Science Publishers for libraries and other users registered with the Copyright Clearance Center (CCC) Transactional Reporting Services, provided that the appropriate fee of US $25.00 per copy per chapter is paid directly to Copyright Clearance Center, 222 Rosewood Drive, Danvers MA 01923, USA. Refer also to www.copyright.com

CONTENTS

Foreword *i*

Preface *ii*

List of Contributors *iii*

CHAPTERS

1. **Theoretical Background of Photonic Crystals: Bandgap and Dispersion Properties** **3**
   C. Ciminelli

2. **Analysis of Photonic Crystal Structures** **23**
   A. Gopinath

3. **Photonic Crystal Technologies: From Theories to Practice** **49**
   D. W. Prather, S. Shi, A. Sharkawy, J. Murakowski and G. J. Schneider

4. **Photonic Crystal Fiber: Theory and Fabrication** **84**
   A. Cucinotta

5. **Nanostructured Organic Photonics** **93**
   A. Camposeo, E. Mele, L. Persano and D. Pisignano

6. **Slow Light for Sensing** **118**
   M. A. Fiddy

7. **Circular Bragg and Photonic Crystal Resonators** **135**
   J. Scheuer, E. Benisty and O. Weiss

8. **Photonic Crystal Fiber for Chemical Sensing Using Surface-Enhanced Raman Scattering** **157**
   Y. Han and H. Du

9. **Guided Resonances in Photonic Crystal Slabs for Sensing Applications** **180**
   A. Ricciardi, M. Pisco, G. Castaldi, V. Galdi, S. Campopiano, A. Cutolo and A. Cusano

10. **Physical, Chemical and Biological Sensors Based on Photonic Crystals** **195**
    S. Zlatanovic and A. Grot

11. **Photonic Crystal Fibers for Physical, Chemical and Biological Sensing** **216**
    R. Corradini and S. Selleri

Subject Index **232**

FOREWORD

Since the first formal studies of multi-layer dielectric stacks by Lord Rayleigh in 1887 and subsequent research that lead to the term "photonic crystal" to be coined by Eli Yablonovitch and Sajeev John in 1987, the mathematics that describe the formation of photonic band gaps, low loss waveguiding, and standing wave optical resonances have included terms for the physical dimensions of the structure and the refractive indices of the structure's materials. As the menu of possible photonic crystal structures has grown to include 3-dimensional "woodpile" stacks, inverse opals, 2-dimensional slabs, guided mode resonant filters, and photonic crystal fiber, the menu of material choices has also expanded to include a cornucopia of possibilities that include silicon, compound semiconductors, dielectrics, and organic (carbon-based) media. It was perhaps inevitable that scientists would begin to manipulate the physical "constants" of these photonic crystal structures (period, thickness, refractive index) to transform photonic crystals into sensors.

In many respects, the photonic crystal is an ideal sensor system. By simply illuminating the structure with a laser, LED, or incandescent lamp, the reflected or transmitted spectrum reveals a great deal about its physical makeup. With the advent of miniature spectrometers, low-power LEDs, and semiconductor lasers, instrumentation for measuring the properties of photonic crystals has become miniature, inexpensive, and rugged. Meanwhile, the ability to inexpensively fabricate photonic crystal structures, despite their nanometer-scale features, has made remarkable advances, which now make them suitable even for sensor applications in which the device will be single-use disposable, as in point-of-care medical diagnostics. As a result, photonic crystal sensors allow high resolution and rapid measurement of structures within microfluidic channels, biomedical tubing, microtiter plates, test tubes, and flasks without the need for electrical contacts, a source of power on the device itself, or any direct physical contact to the detection instrument.

This eBook represents many of the exciting sensing applications that utilize photonic crystal structures. In it, you will find the fundamental operating principles of photonic crystals and a description of the analytical methods that are used to derive their optical properties from Maxwell's Equations. The text describes methods for creating photonic crystal structures, and in particular stresses designs that enable the structure to interact with gaseous or liquid materials. The ability for photonic crystals to generate high intensity evanescent electric fields on their surfaces allows for chemical sensing using Surface-Enhanced Raman Scattering, while the incorporation of materials into their structure that exhibit optical gain enables the creation of light emitting devices that can be used as sensors. The ability of photonic crystals to form optical standing waves results in "slow light" and associated electric field enhancements that can be used for sensing either through detection of shifts in the resonant wavelength due to biomolecule adsorption or through the enhanced excitation of fluorescent dyes that are used to "tag" biomolecules such as DNA or proteins.

I hope that you will find this text to be a useful guide and introduction to the many exciting ways that photonic crystals are being applied to a variety of problems in sensing. Photonic crystal-based sensing is an exciting multidisciplinary field that involves electromagnetics, optics, nanofabrication, material science, chemistry, biology, and (sometimes) mechanical engineering. It is the goal of the authors to welcome the enthusiasm and ideas of new students with backgrounds in these fields to join with us in the goal of extending photonic crystals into high precision sensing tools that can find applications in research and commercial products.

Brian T. Cunningham
Department of Electrical and Computer Engineering
Department of Bioengineering
University of Illinois at Urbana-Champaign
USA

PREFACE

Photonic Crystals (PhCs) have inspired a lot of interest and many research efforts have been devoted to their possible applications in communications and information fields due to the opportunity they offer to efficiently manipulate the light on wavelength and sub-wavelength scale. The outstanding potential of photonic bandgap structures encourage their employment also in sensing applications. As a matter of fact, the microstructure of the PhCs opens up for a large degree of freedom in optical waveguides design, enabling the implementation of novel and intriguing transduction principles for sensing applications, by basically exploiting the dependence of the PhCs' spectral properties on the physical and geometrical features of the crystal itself. Furthermore, the possibility to realize a PhC through holes-patterned in a dielectric would allow the integration with sensitive materials in order to improve the functionality of the final device for physical, chemical and biological sensing, either tailoring the sensing system performance or conferring selectivity capability.

On these bases, PhCs offer a new possibility of realizing effective and compact sensors and open the way for the development of 'lab-on-chip' portable devices which allow several chemical and biological analysis to be performed in parallel onto the same platform, by taking advantage of the large scale integration and wavelength multiplexing capabilities of the PhCs.

In spite of the outlined potential of the PhCs for physical, chemical and biological sensing applications, the PhCs fabrication processes, the defects introduction, as well as the integration with additional materials enabling sensing capabilities, imply several challenges of physical realization and process availability, that still prevent PhCs to be fully exploited in the sensing fields.

Up to now, great effort has been carried out by the scientific community to develop photonic devices, however, the weak integration of competencies required to address this challenge, intrinsically multidisciplinary, limits the capability to achieve high performances devices. A highly integrated approach involving continuous interactions of different backgrounds aimed to optimize each single aspect with a continuous feed-back, would enable the definition of an overall and global design concept.

In this scientific context, this eBook would sustain the research and the development of a novel generation of photonic devices for physical, chemical and biological sensing. The eBook would provide not only the basics knowledge of the PhC theory and technology and the main applications to date, but also a significant insight in crossover researches, technologies and sciences that could enable the concurrent addressing of the issues related to the different aspects of the PhC sensors' global design such as the identification, functionalization and activation of sensing materials, the development of novel optical transduction principles, the exploitation of advanced technologies and light-matter interaction's phenomena at micro and nano-scale.

In the chapters 1-4 of the eBook, a brief review of PhCs' basic concepts, numerical and technological tools useful in the design and understanding of novel PhCs configurations is provided for the readers. In the chapters 5-9, we propose a selection of crossover topics emerging in the scientific community as breaking through researches, technologies and sciences for the development of novel technological platforms for physical, chemical and biological sensing.

The eBook ends with two chapters focused on the description of the main PhCs sensors to date.

We would like to thank Prof. Brian T. Cunningham for writing the foreword and Bentham Science Publishers for their support and efforts. One of the editors (A.C.) likes to dedicate this eBook to his women: Maria Emilia, Maria Teresa, Maria Alessandra. The editor M.P. dedicates this eBook to his daughters Laura and Giulia.

Marco Pisco, Andrea Cusano, Antonello Cutolo

University of Sannio
Italy

List of Contributors

Eyal Benisty
School of Electrical Engineering, Department of Physical Electronics, Tel-Aviv University, 69978 Tel-Aviv, Israel

Stefania Campopiano
Department of Technology, University of Naples "Parthenope", Centro Direzionale di Napoli Isola C4, 80143 Napoli, Italy

Andrea Camposeo
NNL, National Nanotechnology Laboratory of CNR-Istituto Nanoscienze, Università del Salento, *via* Arnesano I-73100 Lecce, Italy

Giuseppe Castaldi
CNR-SPIN and Waves Group, Department of Engineering, University of Sannio,I-82100 Benevento, Italy

Caterina Ciminelli
Optoelectronics Laboratory, Politecnico di Bari, I-70125 Bari, Italy

Roberto Corradini
Department of Organic and Industrial Chemistry, University of Parma, I-43124, Italy

Annamaria Cucinotta
Information Technology Department, University of Parma, I-43124 Parma, Italy

Andrea Cusano
Optoelectronic Division – Engineering Department, University of Sannio, Corso Garibaldi 107, 82100 Benevento, Italy

Antonello Cutolo
Optoelectronic Division – Engineering Department, University of Sannio, Corso Garibaldi 107, 82100 Benevento, Italy

Henry Du
Department of Chemical Engineering and Materials Science, Stevens Institute of Technology, Hoboken, NJ 07030, USA

Michael A. Fiddy
Center for Optoelectronics and Optical Communications, University of North Carolina at Charlotte, Charlotte, NC 28223I, USA

Vincenzo Galdi
CNR-SPIN and Waves Group, Department of Engineering, University of Sannio, I-82100 Benevento, Italy

Anand Gopinath
Department of Electrical and Computer Engineering, University of Minnesota, Minneapolis, MN 55455, USA

Annette Grot
Pacific Biosciences, Inc., 1505 Adams Drive, Menlo Park, California 94025-1451, USA

Yun Han
Department of Chemical Engineering and Materials Science, Stevens Institute of Technology, Hoboken, NJ 07030, USA

Elisa Mele
Istituto Italiano di Tecnologia (I.I.T.), Center for Biomolecular Nanotechnologies, *via* Barsanti 1, I-73010, Arnesano (LE), Italy

Janusz Murakowski
Department of Electrical and Computer Engineering, University of Delaware, Newark, Delaware 19716, USA

Luana Persano
NNL, National Nanotechnology Laboratory of CNR-Istituto Nanoscienze, Università del Salento, *via* Arnesano I-73100 Lecce, Italy

Marco Pisco
Optoelectronic Division – Engineering Department, University of Sannio, Corso Garibaldi 107, 82100 Benevento, Italy

Dario Pisignano
NNL, National Nanotechnology Laboratory of Istituto Nanoscienze-CNR and Dipartimento di Matematica e Fisica "Ennio De Giorgi", Università del Salento, *via* Arnesano I-73100 Lecce, Italy

Dennis W. Prather
Department of Electrical and Computer Engineering, University of Delaware, Newark, Delaware 19716, USA

Armando Ricciardi
Optoelectronic Division – Engineering Department, University of Sannio, Corso Garibaldi 107, 82100, Benevento, Italy

Jacob Scheuer
School of Electrical Engineering, Department of Physical Electronics, Tel-Aviv University, 69978, Tel-Aviv, Israel

Garrett J. Schneider
Department of Electrical and Computer Engineering, University of Delaware, Newark, Delaware 19716, USA

Stefano Selleri
Department Information Engineering, University of Parma, I-43124, Italy

Ahmed Sharkawy
Department of Electrical and Computer Engineering, University of Delaware, Newark, Delaware 19716, USA

Shouyuan Shi
Department of Electrical and Computer Engineering, University of Delaware, Newark, Delaware 19716, USA

Ori Weiss
School of Electrical Engineering, Department of Physical Electronics, Tel-Aviv University, 69978, Tel-Aviv, Israel

Sanja Zlatanovic
Department of Electrical and Computer Engineering, University of California San Diego, 9500 Gilman Drive, La Jolla, CA 92093, USA

CHAPTER 1

Theoretical Background of Photonic Crystals: Bandgap and Dispersion Properties

Caterina Ciminelli*

Optoelectronics Laboratory, Politecnico di Bari, I-70125 Bari, Italy

Abstract: Photonic crystals (PhCs), able to manipulate light at a scale on the order of the wavelength or even shorter, have the potential for developing new technologies and devices for a wide range of applications. In particular, PhCs have been used to investigate, both theoretically and experimentally, photonic sensors because of their peculiar properties, such as the capability of enhancing field-matter interaction and control over the group velocity. In this chapter the basic physics of photonic crystals with specific reference to the origin of the photonic band gap and to their design for achieving specific dispersion properties, is reviewed.

Keywords: Photonic crystals, photonic band gap, photonic crystals applications.

1. INTRODUCTION

The study of the electronic properties of the crystals, starting from the principle that the electrons are subjected to a potential changing in space as a function of the periodicity, led to distinguish materials with respect to their electrical conductivity, that can be derived from the analysis of the electronic band diagrams.

A similar situation can be found in photonics, for dielectrics having periodic structures as in crystalline solids. A periodic dielectric structure can create either allowed or forbidden photonic bands,. This means that light propagation can be allowed or inhibited by the dielectric structure in a certain frequency range. The gaps in the photonic frequency spectrum are called photonic band gaps (PBGs) and the periodic dielectric structures are called photonic crystals (PhCs).

The understanding of the PhCs optical properties and the effort in designing and developing a new generation of photonic devices exploiting PhCs can be dated about two decades.

In 1987 E. Yablonovitch [1] proposed a three dimensional structure that could have the capability to completely inhibit spontaneous emission within its electromagnetic band gap. S. John [2] in the same year demonstrated the possibility of strongly localizing the light. The focus point of the above mentioned works is the idea that a periodic arrangement of either dielectric or metallic elements can exhibit photonic band gap regions depending on polarization and/or direction, where the propagation of the electromagnetic waves is forbidden. This property depends on the material, on the frequency of operation and on the crystal lattice properties.

Starting from the pioneering works in late 80s the research activity in this field has strongly advanced, due to a very large amount of theoretical and experimental results on one-dimensional (1D), two-dimensional (2D) and three-dimensional (3D) photonic crystal structures (see Fig. **1**) both in dielectric and metallic materials due to their unique properties of light confinement and localization together with the strong reduction of the device size, orders of magnitude less than the conventional photonic devices, allowing a potential very high scale of integration.

***Address correspondence to Caterina Ciminelli:** Optoelectronics Laboratory, Dipartimento di Elettrotecnica ed Elettronica, Politecnico di Bari, *Via* Re David, 200, 70125 Bari, Italy; Tel: +39-080-596.34.04; Fax: +39-080-596.36.10; E-mail: c.ciminelli@poliba.it

Marco Pisco, Andrea Cusano and Antonello Cutolo (Eds)
All rights reserved-© 2012 Bentham Science Publishers

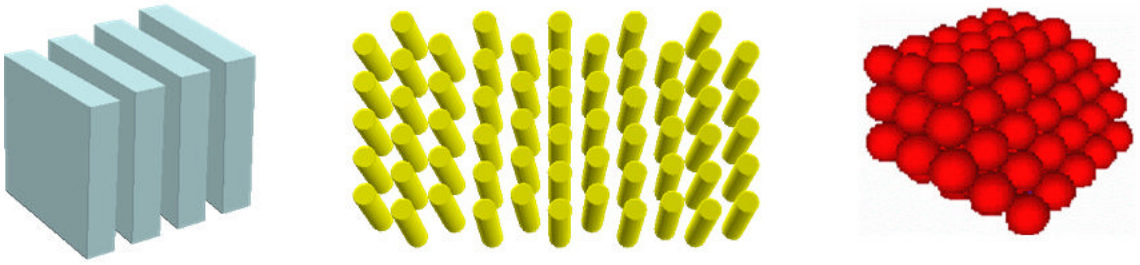

Figure 1: Photonic crystal structures. *From left to right*: 1D, 2D (hexagonal lattice of rods), 3D (opal structure).

The work on photonic crystal was firstly focused on 3D structures operating at microwave wavelengths. These PhCs were large enough to be easily fabricated because the lattice constant is proportional to the operating wavelength. The first challenges regarding the PhCs emerged when the 3D crystals became to be scaled to operate at optical wavelengths.

The simplest PhC is the well-known configuration formed by a multi-layer of two alternating materials of different refractive index. The stacking and the refractive index variation are along one axis. A simple example is a Bragg reflector that has been demonstrated in small index contrast as well as high index contrast semiconductor materials, showing stop-band regions characterized by high reflectivity.

2D photonic crystals are more difficult to be fabricated than 1D PhCs but their increased technological complexity, even if still quite less than that at 3D PhCs, is largely compensated by the potential applications in integrated photonic circuits. Two different types of structure can be considered. The first one consists of dielectric rods in air while the second one is composed by holes in a dielectric medium.

A good in-plane confinement is achieved by using this second kind of structure in a thin slab, where the propagation of the light can be fully controlled in two directions. 2D PhC slabs strongly differ from the corresponding 2D PhCs when the thickness of the slab is of the same order or even smaller than the light wavelength.

Since 2D PhCs do not have a periodic structure in the third dimension, the immediate consequence for that is still the need of preventing the light from escaping out-of-plane also in presence of a dielectric slab. However, using 2D waveguiding photonic crystal structures, light control is possible also in the third direction, allowing to use 2D structures instead of more complex 3D configurations.

This chapter is devoted to a brief summary of the concepts at the basis of the PhCs behaviour such as photonic band and band gaps. Moreover, main PhC properties and target applications are briefly discussed.

2. FUNDAMENTAL PRINCIPLES OF PHOTONIC CRYSTALS

2.1. Maxwell's Equations

The electric field $\mathbf{E}(\mathbf{r}, t)$, the magnetic field $\mathbf{H}(\mathbf{r}, t)$, the electric flux density $\mathbf{D}(\mathbf{r}, t)$, and the magnetic flux density $\mathbf{B}(\mathbf{r}, t)$, are described by the Maxwell's equations:

$$\nabla \cdot \mathbf{B}(\mathbf{r},t) = 0 \tag{1}$$

$$\nabla \cdot \left[\mathbf{D}(\mathbf{r},t)\right] = 4\,\pi\rho(\mathbf{r}) \tag{2}$$

$$\nabla \times \mathbf{E}(\mathbf{r},t) = -\frac{1}{c}\frac{\partial \mathbf{B}(\mathbf{r},t)}{\partial t} \tag{3}$$

$$\nabla \times \mathbf{H}(\mathbf{r},t) = \frac{1}{c}\frac{\partial \mathbf{D}(\mathbf{r},t)}{\partial t} + \frac{4\pi}{c}\mathbf{J}(\mathbf{r},t) \quad \textbf{(4)}$$

where ρ(**r**, t) and **J**(**r**, t) are the free electric charge and current densities, respectively, and c is the speed of light.

Maxwell's Eqs. can be simplified making some assumptions. The electric and magnetic fields can be expressed in a time-harmonic form:

$$\mathbf{H}(\mathbf{r},t) = \mathbf{H}(\mathbf{r})e^{-j\omega t} \quad \textbf{(5)}$$

$$\mathbf{E}(\mathbf{r},t) = \mathbf{E}(\mathbf{r})e^{-j\omega t} \quad \textbf{(6)}$$

where ω is the angular frequency of the electromagnetic (e.m.) wave. The constitutive Eqs. relating the fields to the flux densities in a linear, macroscopic and isotropic material are:

$$\mathbf{D}(\mathbf{r},t) = \varepsilon(\mathbf{r})\mathbf{E}(\mathbf{r},t) \quad \textbf{(7)}$$

$$\mathbf{B}(\mathbf{r},t) = \mu(\mathbf{r})\mathbf{H}(\mathbf{r},t) \quad \textbf{(8)}$$

where ε(**r**) is the dielectric constant and μ(**r**) is the magnetic permeability of the material. In a nonmagnetic medium μ(**r**) = μ_0, where μ_0 is the magnetic permeability in free space. The dielectric constant is assumed real, isotropic, perfectly periodic and independent of frequency. A further assumption is to have no free charges or currents such as: ρ = **J** = 0. Thus, the Maxwell's Eqs. can be reduced to:

$$\nabla \cdot \mathbf{B}(\mathbf{r},t) = 0 \quad \textbf{(9)}$$

$$\nabla \cdot \left[\varepsilon(\mathbf{r})\mathbf{E}(\mathbf{r},t)\right] = 0 \quad \textbf{(10)}$$

$$\nabla \times \mathbf{E}(\mathbf{r},t) + \frac{\mu_0}{c}\frac{\partial \mathbf{H}(\mathbf{r},t)}{\partial t} = 0 \quad \textbf{(11)}$$

$$\nabla \times \mathbf{H}(\mathbf{r},t) - \frac{\varepsilon(\mathbf{r})}{c}\frac{\partial \mathbf{E}(\mathbf{r},t)}{\partial t} = 0 \quad \textbf{(12)}$$

By using the constitutive relations (7-8) into the above equations, Eqs. (11-12) become

$$\nabla \times \mathbf{E}(\mathbf{r}) - j\frac{\omega}{c}\mathbf{H}(\mathbf{r}) = 0 \quad \textbf{(13)}$$

$$\nabla \times \mathbf{H}(\mathbf{r}) + j\frac{\omega}{c}\varepsilon(\mathbf{r})\mathbf{E}(\mathbf{r}) = 0 \quad \textbf{(14)}$$

The properties of the photonic crystals can be derived from these equations.

2.2. Electromagnetic Modes

Eqs. (13) and (14) are combined [3] into the master equation

$$\nabla\times\left[\frac{1}{\varepsilon(\mathbf{r})}\nabla\times\mathbf{H}(\mathbf{r})\right]=\left(\frac{\omega}{c}\right)^2\mathbf{H}(\mathbf{r}) \quad \textbf{(15)}$$

The solution of this Eq. completely determines the fields. The electric field can be obtained from (14) as:

$$\mathbf{E}(\mathbf{r})=\left[\frac{jc}{\omega\varepsilon(\mathbf{r})}\right]\nabla\times\mathbf{H}(\mathbf{r}) \quad \textbf{(16)}$$

Eq. (15) is an eigenvalue Eq. that can be rewritten in the form

$$\Theta\mathbf{H}(\mathbf{r})=\left(\frac{\omega}{c}\right)^2\mathbf{H}(\mathbf{r}) \quad \textbf{(17)}$$

where Θ is an operator applied to an eigenfunction $\mathbf{H}(\mathbf{r})$ with eigenvalue $(\omega/c)^2$.

The eigenfunctions $\mathbf{H}(\mathbf{r})$ are the fields that can exist in the structure, *i.e.*, the electromagnetic modes of the system. The operator Θ is linear and thus any linear combination of solutions of Eq. (17) is a solution itself. The operator Θ is also Hermitian and, thus, two modes with different frequencies are orthogonal.

An important feature of the electromagnetic modes is that there is no a specified length scale. Once the eigenvalues and eigenfunctions of Eq. (15) are determined, they can be scaled to any physical size or wavelength range. We can suppose a compression or an expansion of the scale by a factor s. In this case, a change of variables $\mathbf{r}' = s\mathbf{r}$, $\nabla' = \nabla/s$, and $\varepsilon'(\mathbf{r}) = \varepsilon(\mathbf{r}/s$ into Eq. (15) results in

$$s\nabla'\times\left[\frac{1}{\varepsilon(\mathbf{r}'/s)}s\nabla'\times\mathbf{H}(\mathbf{r}'/s)\right]=\left(\frac{\omega}{c}\right)^2\mathbf{H}(\mathbf{r}'/s) \quad \textbf{(18)}$$

where $\varepsilon(\mathbf{r}'/s) = \varepsilon'(\mathbf{r}')$. Thus,

$$\nabla'\times\left[\frac{1}{\varepsilon'(\mathbf{r}')}\nabla'\times\mathbf{H}(\mathbf{r}'/s)\right]=\left(\frac{\omega}{cs}\right)^2\mathbf{H}(\mathbf{r}'/s) \quad \textbf{(19)}$$

It can be seen that when the dimensions are scaled by a factor s, the electromagnetic mode is the same, but the mode and the frequency have to be rescaled as $\mathbf{H}(\mathbf{r}'/s)$ and ω/s, respectively. Due to this scalability property, photonic crystal components can be designed without specifying the size and subsequently fabricated in any scale to perform experiments in varying wavelength ranges.

2.3. Photonic Bandgap Structures

The photonic band structure is defined by the relationship between the wave vector **k** and the frequency ω of the light. In a homogeneous material the diagram (ω, **k)** is a line whose slope is proportional to the refractive index while in a periodic material the frequency as a function of the wave vector forms bands which can be separated by band gaps.

The photonic band structures are strongly related to symmetry considerations. If the system has a continuous translational symmetry the dielectric constant is invariant to any translation by an operator $\mathbf{T}_t$. This property can be expressed in the form:

$$T_t\varepsilon(r)=\varepsilon(r+t)=\varepsilon(r) \quad \textbf{(20)}$$

where **t** is a generic vector.

$\mathbf{T}_t\mathbf{H}(\mathbf{r})$ is still an eigenmode of the system $\mathbf{H}(\mathbf{r})$ at the same frequency of $\mathbf{H}(\mathbf{r})$. The eigenvalues can be expressed as $e^{j\mathbf{k}\cdot\mathbf{r}}$ where **k** is the wavevector. The above mentioned translation property leads to have:

$$\mathbf{T}_t e^{j\mathbf{k}\cdot\mathbf{r}} = \mathbf{T}_t e^{j(\mathbf{k}\cdot(\mathbf{r}+\mathbf{t}))} = e^{j\mathbf{k}\cdot\mathbf{r}} e^{j\mathbf{k}\cdot\mathbf{t}} \quad \textbf{(21)}$$

where $e^{j\mathbf{k}\cdot\mathbf{t}}$ is a constant. This means that the function $\mathbf{v} = \mathbf{u}e^{j\mathbf{k}\cdot\mathbf{r}}$, with **u** eigenvector of Θ, shows the same periodicity of the crystal and, this in turn, allows expressing **u** as a series of pseudoperiodic functions. To better understanding that the concept of reciprocal lattice has to be introduced.

2.3.1. Reciprocal Lattice

In general, a plane wave $e^{j\mathbf{k}\cdot\mathbf{r}}$ propagating within a lattice defined by **r** vectors does not have the same lattice periodicity and the wave vector **k** can assume only discrete values.

It has been already explained that only for some specific values of the wave vector the plane wave will show the same lattice periodicity. The periodicity condition for the plane wave can be expressed in the form:

$$e^{j\mathbf{k}''\cdot(\mathbf{r}+\mathbf{R})} = e^{j\mathbf{k}''\cdot\mathbf{r}} \quad \textbf{(22)}$$

where **k''** and **R** are the wavevector and the distance between two lattice points, respectively.

From Eq. (22) $e^{j\mathbf{k}''\cdot\mathbf{R}} = 1$ is derived. It can be also expressed as

$$\mathbf{R}\cdot\mathbf{k}'' = 2\pi n \quad \textbf{(23)}$$

with n an integer.

From Laue diffraction conditions it can be demonstrated that the radiation can interfere when

$$\mathbf{d}\cdot(\mathbf{k}-\mathbf{k}') = 2\pi n \quad \textbf{(24)}$$

where **d** is the distance vector between two lattice points, **k** is the wave vector of the incident wave and **k'** is the wave vector of the diffracted wave, respectively.

With the same meaning of the parameters **d** and **R**:

$$\mathbf{R}\cdot(\mathbf{k}-\mathbf{k}') = 2\pi n \quad \textbf{(25)}$$

This Eq. is equivalent to Eq. (23) if $(\mathbf{k}-\mathbf{k}') = \mathbf{k}''$.

Eqs. (23) and (25) have the following meanings:

- all **k''** vectors satisfying Eq. (23) can be associated to diffracted plane waves having the same periodicity of the lattice;

- all **k''** vectors satisfying Eq. (25) can originate constructive interference.

k'' vectors above introduced make the set of reciprocal lattice vectors **G.**

From Eq. (21) we can put $e^{j\mathbf{k}\cdot\mathbf{R}} = e^{j(\mathbf{k}+\mathbf{G})\cdot\mathbf{R}}$. Thus, the eigenfunctions are degenerate and any superposition of degenerate eigenfunctions is itself an eigenfunction for a wavevector **k** (or **k**+**G**)

$$\mathbf{H}_{\mathbf{k}}(\mathbf{r}) = \sum_{\mathbf{G}} C_{\mathbf{G}} e^{j\left[(\mathbf{k}+\mathbf{G})\cdot\mathbf{r}\right]} = e^{j(\mathbf{k}\cdot\mathbf{r})} \sum_{\mathbf{G}} C_{\mathbf{G}} e^{j(\mathbf{G}\cdot\mathbf{r})} \tag{26}$$

where $C_{\mathbf{G}}$ are constant values. This Eq. is the expression of the Bloch's theorem:

$$\mathbf{H}_{\mathbf{k}}(\mathbf{r}) = e^{j(\mathbf{k}\cdot\mathbf{r})}\mathbf{u}_{\mathbf{k}}(\mathbf{r}) \tag{27}$$

where

$$\mathbf{u}_{\mathbf{k}}(\mathbf{r}) = \mathbf{u}_{\mathbf{k}}(\mathbf{r}+\mathbf{R}) \tag{28}$$

Eqs. (27) and (28) mean that any eigenfunction can be written as a product of a plane wave and a periodic function (Fourier series). The eigenvector is also called Bloch mode.

When Eq. (27) is substituted to Eq. (15), one gets:

$$(j\mathbf{k}+\nabla)\times\left[\frac{\mathbf{1}}{\varepsilon(\mathbf{r})}(j\mathbf{k}+\nabla)\times\mathbf{u}_{\mathbf{k}}(\mathbf{r})\right] = \left[\frac{\omega(\mathbf{k})}{c}\right]^2\mathbf{u}_{\mathbf{k}}(\mathbf{r}) \tag{29}$$

In this equation, **k** is a parameter. Eq. (29) is an eigenvalue Eq. for which $\mathbf{u}_{\mathbf{k}}(\mathbf{r})$ is an eigenfunction and $(\omega(\mathbf{k})/c)^2$ the eigenvalue. When the periodic boundary condition (28) is imposed, the eigenvalues get discretized $(\omega_n(\mathbf{k})/c)^2$, where *n* denotes the index of the discrete eigenvalues. By solving Eq. (29), *n* solutions $\mathbf{u}_{\mathbf{k},n}(\mathbf{r})$ and n eigenvalues $(\omega_n(\mathbf{k})/c)^2$ are obtained. For each value of **k**, there are n solutions with frequencies $\omega_n(\mathbf{k})$. The behaviour of ω_n as a function on **k,** defines the photonic bands, *i.e.*, the photonic band structure. A band gap consists of a range of frequencies where there is no solution for any wavevector **k**.

The generic vector of the primitive lattice can be expressed as $\mathbf{R} = l\mathbf{a}_1 + m\mathbf{a}_2 + n\mathbf{a}_3$; same form can be used for the generic vector of the reciprocal lattice: $\mathbf{G} = l\mathbf{b}_1 + m\mathbf{b}_2 + n\mathbf{b}_3$. By exploiting Eq. (25) in the form $\mathbf{R}\cdot\mathbf{G} = 2\pi n$, one can calculate the basic vectors of **G** as:

$$\begin{aligned} \mathbf{b}_1 &= 2\pi\frac{a_2\times a_3}{a_1\cdot a_2\times a_3}; \quad \mathbf{b}_2 = 2\pi\frac{a_3\times a_1}{a_1\cdot a_2\times a_3}; \\ \mathbf{b}_3 &= 2\pi\frac{a_1\times a_2}{a_1\cdot a_2\times a_3} \end{aligned} \tag{30}$$

For a 2D PhC, $a_1 = a_x$ and $a_2 = a_y$, then $b_1 = (2\pi/a)y$ and $b_2 = (2\pi/a)x$.

It can be seen from Eq. (26) that Bloch states $\mathbf{u}_{\mathbf{k}}(\mathbf{r})$ and $\mathbf{u}_{\mathbf{k}}+\mathbf{G}(\mathbf{r})$ are equal, as they are the states for any summation of the wavevector and integer multiples of the reciprocal lattice vector. Thus, as an example, for a 1D PhC wavevector values in the range:

$$-\pi/a_i < k_i \le \pi/a_i, \text{ where } i = x, y, z \tag{31}$$

can be considered when solving the eigenvalue Eq. (29). Eq. (31) defines the Brillouin zone for a 1D PhC.

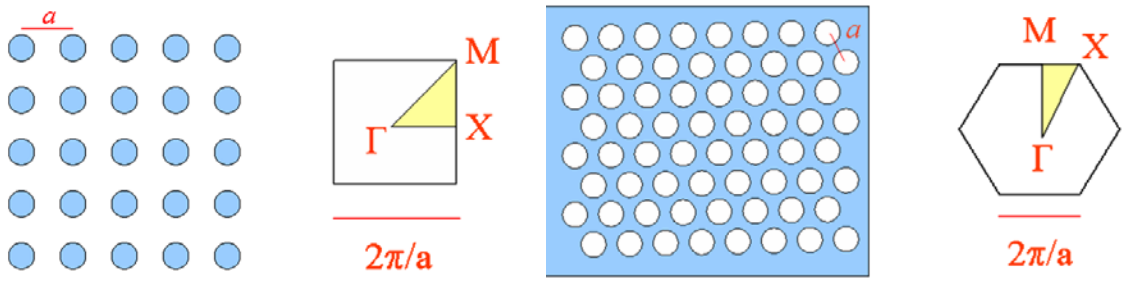

Figure 2: 2D PhC lattices and related irreducible Brilluoin zone: *on the left* square lattice of dielectric rods; *on the right* hexagonal lattice of holes in dielectric.

On the basis of the relationship $\mathbf{R} \cdot \mathbf{G} = 2\pi n$, the Brilluoin zone can be defined also for 2D PhC structures. For a square lattice having lattice constant a the reciprocal lattice is still a square one with lattice constant $2\pi/a$. In case of hexagonal lattice with lattice constant a the reciprocal lattice is again hexagonal but rotated by 30° with respect to the primitive one, and with a lattice constant $2\pi/a$.

The Brillouin zone is strictly related to the concept of redundancy in **k**. The set of the symmetry operations on the crystal allows to further reduce Brilluoin zone to a smaller region named irreducible Brillouin zone. It is a portion of the elementary cell of the reciprocal lattice where none redundancy does exist for the Bloch states. Brilluoin zones and irreducible ones are illustrated in Fig. **2** for both square and hexagonal lattices.

The introduction of the concepts of Bloch states and irreducible Brilluoin zone leads to conclude that the solution of the Maxwell's Eqs. in a periodic structure can be reduced to the calculation of the wavector **k** at the frequencies $\omega_{i,k}$ within the irreducible Brilluoin zone and of the periodic functions $\mathbf{u}_{i,k}(\mathbf{r})$, so that the Bloch states expressed by the Eq. (27) can solve the eigenvalue Eq. (17). $\mathbf{u}_{i,k}(\mathbf{r})$ can be expressed in form of Fourier series and, discretized through the coefficients of the series.

2.3.2. Simulation Methods

The algorithms used for analyzing photonic crystal structures require very long computer time and large memory, and exhibit some serious issues when a complete physical insight is desired, *e.g.* determination of band diagrams and radiation modes, as briefly described in the following.

The Plane Wave Method (PWM) [4, 5] is largely used for the computation of band diagrams. However, it cannot be used for investigating photonic crystal slabs because of the lack of periodicity along the etching direction. To solve this problem one can consider an artificial fully periodic structure obtained by periodically repeating the original photonic crystal slab along the etching direction. In this case the described algorithm is called Supercell Method (SCM) [6]. Its accuracy is a growing function of the decoupling between adjacent supercells, and so a large supercell area could be requested [7], involving a large number of plane waves in the field expansion. Therefore, also this method results to be computationally very expensive for the theoretical analysis of complex photonic crystal-based devices.

Bloch-Floquet Method (BFM) [8] is based on the Bloch waves and Floquet's theorem. It can be used for studying layered waveguiding structures formed by homogeneous regions along the direction normal to the propagation plane. It is most useful for analyzing PhCs slab with 2D periodicity where the finite size of the PhC lattice, together with the presence of both cladding and substrate, has to be taken into account. In these structures, which are 3D structures from the numerical point of view, BFM allows the evaluation of transmission and reflection spectra and out-of-plane scattered power in very short computer time with high accuracy, as demonstrated both theoretically and experimentally in [9].

Although Bloch-Floquet method presents similarities with the PWM due to the expansion in spatial harmonics of the field within the layer of the PhC slab, it offers some peculiar characteristics. Among the advantages with respect to the PWM, it have to be considered the possibility of studying structures limited

in size, overcoming the limits of the PWM that, even when using supercell method, can be applied to structures with lattice having an infinite size in the slab plane.

Moreover, Bloch-Floquet method allows calculating the modes even for complex propagation constant, *e.g.* the leaky modes and the modes at frequencies within the band gaps.

Transmission and reflection of the PhCs can be evaluated together with the out-of-plane losses.

The Finite Difference Time Domain (FDTD) [10] is a very general method useful to calculate the transmission and reflection spectra of 2D guided–wave PBG devices [11], but computation of band diagrams is rather difficult [12, 13]. A good level of accuracy requires a very small discretization step, thus involving large CPU time, in particular for the analysis of structures with a refractive index variation in three dimensions. Moreover, the high contrast discontinuities occurring in PhCs, cause large reflections and so a huge number of time steps has to be considered before the field reaches a significant steady state.

The Finite Element Method (FEM) [14, 15] requires a very dense grid of finite elements where high refractive index discontinuities are present and this produces an increase of computation time, particularly in the analysis and design of complicated photonic crystal slab devices.

In the Transfer Matrix Method (TMM) [16] the structure under analysis is approximated with a number of layers that are invariant along the propagation direction, and the Maxwell's Eqs. are used in the plane perpendicular to the propagation direction and in the **k** space. The total transfer matrix of the structure can be calculated as a product of the elementary transfer matrices, analytically determined for each layer. Either the transmission and reflection spectra or the band diagrams of a periodic structure can be obtained. TMM is not an efficient method for the design of long PC slab devices because the computational effort grows quickly with the longitudinal dimension of the structure.

The Scattering Matrix Method (SMM) [17, 18] allows the evaluation of both field distributions and transmission spectra. The structure is assumed to be formed by homogeneous medium where non overlapping optical scattering centres having arbitrary shape and size are located. When scattering centres with circular cross section are considered, the CPU time can be minimized by exploiting the Bessel-Hanken functions for the electromagnetic (e.m.) field expansion. However, the computational complexity scales with the third power of the number of holes or rods in the PBG device, and so even this method can hardly be used for the design of large photonic crystal structures.

The Bi-directional mode Expansion and Propagation (BEP) [19] method was demonstrated to be accurate and useful in analyzing structures having deep perturbation [20]. The perturbed waveguide is considered as a sequence of longitudinally invariant slices. Maxwell's Eqs. are solved in those waveguide sections and for each of them the propagation constants and mode distribution functions are derived. A large number of modes can be requested in each slice to achieve an acceptable accuracy, involving large matrix dimensions and huge computational efforts.

Green's functions [21] are a mathematical artifice which facilitates the solution of differential Eqs. when the boundary conditions are known and the excitation of the structure is made by means of point source. The Green's function is already known in many problems, since its real part is commonly used to obtain the electro-magnetic field in a certain structure. This solution is easily obtained, once the Green's function is known, by integration of the boundary conditions. The approach does not require to find such a complete set of eigenfunctions and this represents an advantage since the normalization of a complete set of eigenfunctions can be difficult and time consuming, even for relatively simple problems. The Green's function of a complicated system can be found by a matrix multiplication involving several Green's functions of a much simpler system. Such approach has been applied to the study of multilayer systems and photonic crystal slabs [22]. In [23] a new model for simulating wave propagation in 2D PhCs by means of Green's functions has been proposed. In particular, the method has been used for studying a Fabry–Peròt cavity to evaluate its response in presence of a Hankel source or a plane wave excitation.

The analysis of all physical effects occurring when a source field propagates in a multilayered structure with a periodic arrangement of scatterers, by taking into account both physical and geometrical parameters has been reported in [24]. The comparison of the Green's functions – based method with other well-known algorithms, including FDTD, showed a very good agreement and some advantages, in terms calculation time and evaluation of both in-plane and out-of-plane scattering losses.

2.3.3. Physical Origin of the Photonic Band Gap

To understand the origin of the photonic band gap, one can refer to the simplest form of photonic crystal, that is a multilayer film made of layers with alternating refractive indexes. Bragg grating is an example of such a stack layer: it consists of a periodic stack of quarter-wavelength dielectric layers. If the Bragg condition[1] is not satisfied the light reflected from each layer in the grating becomes out of phase and interfere destructively. When the Bragg condition is satisfied, the contributions of reflected light from each layer add constructively in the backward direction, forming a peak whose central wavelength depends on the grating parameters. The periodic variation in the refractive index causes the photons scattering which generates band-gaps in the in-plane photon dispersion relation.

From the variational problem for the e.m. field it can be demonstrated that the modes at lower frequency concentrate their energy within the higher refractive index regions while, on the contrary, the modes at higher frequency are concentrated within lower refractive index regions.

Thus, for each k value there will be a gap between the lower bands, named "dielectric bands", relevant to the high dielectric permittivity layers and the upper bands, named "air bands", that are less concentrated in the high dielectric permittivity layers. The dielectric/air bands are analogous to the valence/conduction bands in a semiconductor.

To obtain a band gap for any propagation direction in the plane, a structure having a 2D periodicity must be considered. A process, similar to that one described for 1D photonic crystals, occurs also in 2D PhCs when a normal wave impinges on the structure. A portion of this wave is split into forward and reverse waves and part is diffracted in different directions. This process is repeated when the forward wave encounters next set of discontinuities. Depending on the physical and geometrical characteristics of the structure, such as the refractive index, radius of holes/cylinders, and lattice periodicity, waves propagating inside the crystal may interfere each other. In such a way the reflected power increases while the transmitted one decreases, and a photonic band gap can be created. Since the radiation is reflected, the photonic band gap is created. The band gap can be defined "complete" when it exists independently of the polarisation and the angle of incidence of the light.

In 2D PhCs not only there are two main propagation directions instead of a single one, but also the wave polarization must be carefully considered.

An example of photonic band gap diagram for a structure having square lattice made by dielectric columns in air is in Fig. **3** ***left***. The dielectric constant is $\varepsilon = 12$ (silicon) and the radius is $r = 0.40a$, where a is the lattice constant. This lattice configuration gives a TM bandgap for normalized frequencies in the range 0.22 - 0.24.

A different behaviour can be observed for TE and TM polarizations. The band gaps for TM polarization are larger than those for TE polarization. Furthermore, the TM band gaps tend to extend along the three main propagation directions and, so, along any in-plane propagation direction. It can be also observed that TM band gaps occur at lower energies than the TE band gaps. The differences between TE and TM

[1] An electromagnetic wave, propagating along the periodicity direction will experience several partial reflections. By assuming Λ as the grating period along the propagation direction and λ as the operating wavelength, if the Bragg condition $\Lambda = m\lambda$, with m an integer, is verified, the phase shift among the reflected signals will be an integer multiple of 2π. Partial reflections add perfectly in phase, inhibiting the propagation of the e.m. wave and causing the total reflection of the incidence signal. This phenomenon, that is at the basis of the conventional Bragg grating, is also the origin of the new properties of the PhCs.

polarizations are due to the fact that the dielectrics rods are not connected to one other. In general, not connected regions of materials with high dielectric constant facilitate the formation of band gaps for the TM polarization, like dielectric rods in air, while connected regions with high dielectric constant facilitate the formation of band gaps for the TE polarization, like dielectric grid in air. Intermediate characteristics can provide a complete band gaps for both polarizations, like triangular dielectric lattice of holes in a dielectric material. For complementary structures the opposite situation occurs.

The triangular lattice is the 2D PhC having the highest symmetry. As for the square lattice, it is possible to design either structures formed by disconnected cylinders or structures having dielectrics regions connected to one other. The same polarization-dependent behaviour above reported can be observed: TM band gaps form in lattice made by isolated regions with high permittivity and TE band gaps in connected lattices. The connected triangular lattice is able to combine these two characteristics when the holes diameter increases approaching the lattice period, forming isolate veins of dielectric. In this case the presence of a complete photonic band gap can be observed (see Fig. **3** ***right***), *i.e.,* a frequency region in which there are neither TE nor TM polarized modes.

In designing 2D PhC structures very useful instruments are the gap maps.

In fact, they show the position of the photonic band gaps when one or more parameters among elementary cell geometry, refractive index contrast, column or hole radius, lattice constant and filling factor[2] are changed.

In 3D photonic crystals a fully three dimensional band gap can be formed, independently of the light direction. To get a complete band gap in a 3D PhC, the crystal must be made by using materials having a large refractive index difference to induce a strong enough scattering. Specific care must be also devoted to the choice of the lattice geometry. Face-centred cubic lattice is favourite for the formation of the band gaps

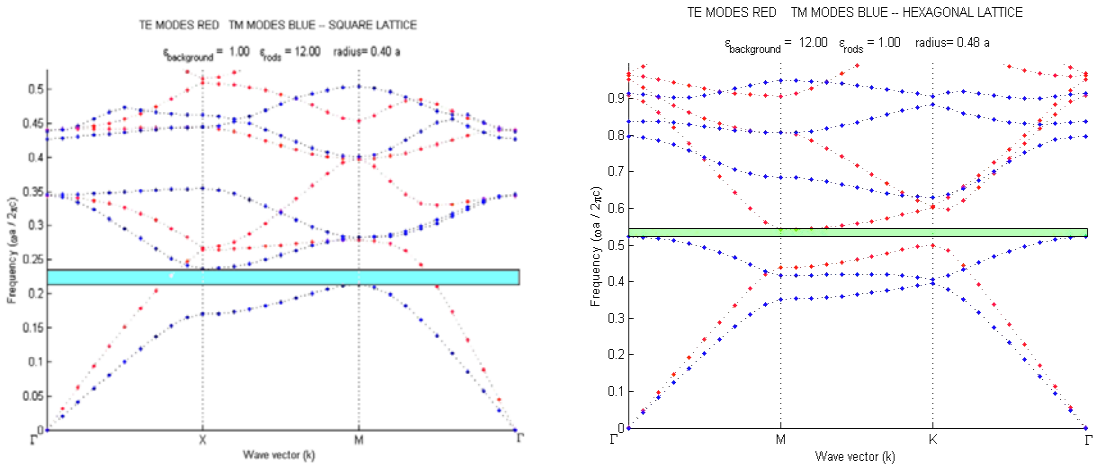

Figure 3: Photonic band diagram for: *on the left* TE modes (red lines) and TM modes (blue lines) of a 2D photonic crystal having square lattice made by air holes in silicon (ε = 12, r = 0.40a), *on the right* TE modes (red lines) and TM modes (blue lines) of a 2D photonic crystal having triangular lattice made by holes in silicon (ε = 12, r = 0.48a).

2.3.4. Defects in Photonic Crystals

Semiconductors doping is fundamental in realizing electronic devices. A sort of doping is also required for implementing specific functions in the photonic crystals. In this case doping is achieved adding or removing a certain amount of dielectric material, thus breaking the crystal periodicity. The translational

[2] Filling factor: is a measure of the e.m. energy localized in the dielectric regions with high index with respect to the energy distributed within the whole volume.

symmetry of the periodic lattice is disturbed when defects are introduced and the consequence is that Bloch mode can not still be considered a solution of the Maxwell's equations. A rigorous analysis of the influence of the defects has to be made by using specific electromagnetic models, that are the same used for the study of finite size photonic crystals.

The defect can be a material with different size or a different refractive index.

If the defect is created by adding extra dielectric material to one or more cells, the effect is similar to that one of a donor atom in a semiconductor while removing dielectric material leads to have a defect that behaves like an acceptor atom in semiconductors.

When a defect is introduced in a perfect crystal, one ore more localized evanescent mode can be created within the photonic band-gap. The parts of the crystal on both sides of the defect behave like mirrors where modes exponentially decay. Any light propagating in the space between the mirrors bounds back and forth and, thus, is trapped. Since the distance between the mirrors is of the order of the light wavelength, the modes are quantized. Therefore, due to the presence of defects corresponding to frequencies inside the photonic band gaps, localized mode can exist. In particular, states with frequencies close to the middle of the band gap can be localized more tightly than states near to the band edge.

The type and the size of the defect define the shape and the properties of the localized states, such as frequency, polarization, symmetry, field distribution. Mainly, the defects can be classified in point defects and extended defects.

Point defects are associated to disruption of the crystal periodicity strongly localized and determine the presence of e.m. modes at discrete frequencies that can be considered analogous to isolated electronic states. Point defects in a 1D PhC can be realized by modifying either the refractive index or the thickness of one layer of the stack. This defect is equivalent to a Fabry-Perot cavity. Modes can occur at discrete frequencies within the band gaps, depending on the defect characteristics. These frequencies can be associated to the resonant modes of the cavity limited by the semi-infinite Bragg reflectors. Due to the phase contribution introduced by the reflectors that changes the resonance conditions, the introduction of a point defect not always induces the presence of discrete energy levels within the photonic gap. Then, it is important to properly design the cavity length and the dielectric layers.

In 2D and 3D PhCs, point defects can be created by modifying the refractive index, by changing the size of one or some elements in the lattice, by inserting some elements with different geometry. As for 1D PhCs, a point defect can create discrete energy levels within the band gaps, but differently from them, these levels correspond to localized e.m. modes only when the band gaps are omnidirectional at a given polarization. In this case the mode is strongly localized within the defect region and is evanescent in the surrounding regions. If the band gap is not omnidirectional a fraction of the e.m. energy will leak away from the defect region along allowed propagation directions.

The phenomenon of localizing states by introducing point defects can be useful in designing cavities with high quality factor and small mode volume.

1D, 2D or 3D extended defects can be created only in PhCs of higher or equal dimension. The simplest and most studied example of 1D defect is a linear waveguide in a 2D PhC obtained by removing or modifying one or several rows of the lattice along the desired guiding direction. Extended defects result in the presence of transmission bands inside the photonic band gap of the unperturbed photonic crystal.

2.3.5. PhCs in Slab Waveguides

In Section 1 we already introduced the concept that it is possible to control the light also in the third direction reducing the technological complexity of the 3D PhC structures by realizing 2D PhCs in a slab waveguide. PBG effects allow to control the propagation into the periodicity plane while index guiding

(generalizing the total internal reflection) ensures the light confinement in the direction perpendicular to that plane.

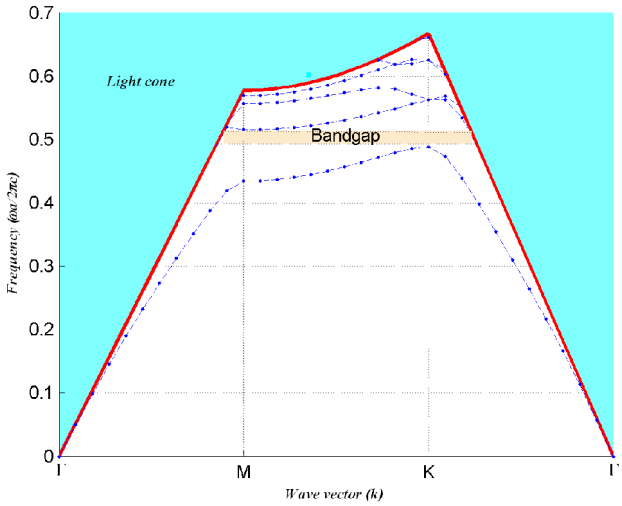

Figure 4: Band diagram for a hexagonal lattice of air holes in a polystyrene slab with thickness = 1.2a and holes radius = 0.34a (a is the lattice constant). Blue region is the light cone. A band gap is present for TE-like modes.

Free space light-line and substrate light-line are useful data when the propagation of e.m. waves in limited PhC structures is studied. The light line is the straight line passing through the origin in the (ω - k) diagram; in the free space its slope is equal to the free space light velocity while in a specific medium the slope is c/n, where n is the refractive index of the medium.

Guided Bloch modes in a slab PhC structure must have an effective index higher than the refractive index of the external media, so that they are sufficiently confined and lie between the above mentioned light-lines. This requirement is rather severe and the propagation modes of the PhC structure that are weakly confined, are intrinsically lossy even if the losses can be reduced by means of a proper design and careful fabrication.

The band structure calculated for 2D PhC corresponds to states whose wavevector do not have a vertical component perpendicular to the periodicity plane. When the structure has a finite height, the e.m. analysis has to be carried out by simulating a real three-dimensional periodicity. The calculation of the band diagram can be made in two steps. The first step is the calculation of the slab states in a periodic cell and the second one consists in determining the light cone and overlapping it to the band diagram calculated in the first step.

Light cone is a region of the band diagram versus the in-plane component of the wavevector formed by a continuous of states corresponding to all possible frequencies in the superstrate and in the substrate that can irradiate in the vertical direction. Guides modes, localized into the slab plane, are allowed to exist only in the regions of the band diagram that are outside the light cone. The states lying below the light cone can not irradiate and, thus, are guided in the plane of the slab, but they decay exponentially in the superstrate and substrate regions.

Under this new condition in the band diagram, the band gap is the range of frequencies where guided modes can not exist but radiation can be still considered in that region.

When the translation symmetry in the vertical direction is broken, the states do not have still pure TE and TM polarization. Due to the presence of a horizontal plane at the middle of the slab acting as mirror

symmetry plane, two categories having strong similarities with TE and TM states in 2D PhC will exist: even (TE-like) and odd (TM-like) modes.

Fig. **4** shows the band diagram for a PhC structure in a polystyrene slab with thickness = 1.2a and holes radius = 0.34a.

The bandgap is incomplete also because there are radiating modes at every ω. The presence of the radiating modes means that vertical radiation losses can not be avoided if translational symmetry is completely broken.

The presence of the band gap is influenced by two critical aspects. First, to consider two separate band structures for the even and odd modes, a mirror symmetry must be preserved. If the substrate is asymmetric, the mirror symmetry is broken but the asymmetry can be assumed to be weak and, thus, negligible if the index contrast is high and the modes are strongly confined within the slab. The second aspect is the proper value of the slab height. waveguide height. It must not be neither too small, in order to avoid a weak confinement, nor too high because in that case higher order mode would exist. Optimum value is about λ/2, which corresponds to an average index dependent on the polarization [3].

3. TARGET APPLICATIONS

In the generic photonic band diagram in Fig. **5**, three different frequency ranges can be identified to utilize for real applications [25].

The first one is the lowest frequency range below the first band gap. The gradient of the dispersion curve in the lowest photonic band depends on the effective refractive index of the PhC and, therefore, on the polarization. This means that, due to the dependence of the effective index for each polarization on the photonic band, the index can be artificially controlled by the PhC structure. This characteristic is called "form birefringence".

Second region is the photonic band gap. It is the main property of the PhCs used to realize light reflectors. It is applied in reflection-type devices.

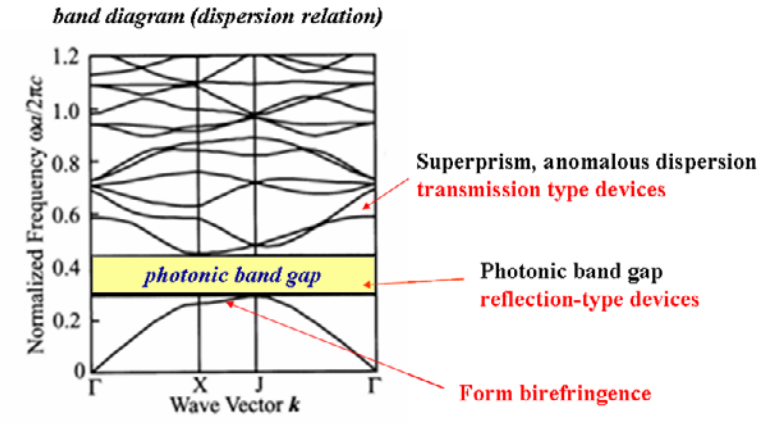

Figure 5: Band diagram and target applications of photonic crystals.

Third region is the frequency range above the photonic band gap even when multiple photonic band gap does exist.

The slope of a band is proportional to the group velocity v_g of the light. In general, there are different positions or portions of the band where the curve is flat, making v_g anomalous. At the band edge v_g could be very small, *i.e.,* slope about null, and this induces a strong localization of the light energy.

In 2D and 3D PhCs such very small or zero v_g appears not only at the edge of the first band but also in the other bands.

The existence of an anomalous group velocity regime can enhance various interactions of light with materials in the PhC. In addition, the 2D or 3D band dispersion diagram leads to the drawing of the isofrequency curves, as better explained in subsection 3.4, which provide unique characteristics of PhCs, allowing the modeling and design of a very interesting transmission-type devices, such as superprims and supercollimators.

Currently, since 2D PhCs are relatively easy to fabricate, they are the most used structures to realize functional devices.

The confinement of the light in the third direction and the efficient coupling of light to a 2D PhC are still issues to be addressed. This is the reason why the 2D PhC slab are widely studied.

3.1. Waveguides and Reflectors

By introducing defects into the crystal, localized electromagnetic modes acting as waveguides and microcavities can be created.

A line defect can be used to guide light from one location to another into the lattice.

Light propagating in the waveguide with a frequency within the band gap of the crystal is well confined, and can travel along the waveguide.

In a conventional waveguide the light can be guided by means of total internal reflection, while in PhCs the light confinement is achieved by exploiting the photonic band gap of a periodic medium. Within the band gap the reflectivity of a PhC tends to unity when increasing the number of rows. This is more verified when the index contrast is high. A wave may experience a large number of successive reflections without any significant attenuation. Due to the confinement mechanism the PhC waveguides can be fabricated even with sharp bends.

The existence of a photonic band gap allows also to realize high efficiency reflectors.

If an optical beam with a wavelength within the band gap impinges on the surface of a PhC the optical power will be fully reflected, except for some loss factor. The high index contrast makes this mechanism particularly efficient, allowing to obtain reflectivities higher than 90%.

The reflectivity of PhCs derives from their geometry and periodicity. In the frequency range of interest the materials chosen for realizing the PhC structure should be essentially lossless.

The 2D PhC must be designed to reflect all in-plane light within some specified frequency band.

3.2. Microcavities

A point defect in a photonic crystal can act as a small cavity.

In a 2D o 3D PhCs, microcavities do not suffer from light leakage because of the photonic band gap of the crystal surrounding the defect.

Even if the microcavities are realized in a PhC slab, some leakage occurs in vertical direction because the presence of the defect implies that the structure is no longer perfectly periodic. The modes can not be still considered Bloch waves and are characterized only by their frequency. A mode resonating within a microcavity at a given frequency can couple to modes of the light cone at the same frequency.

The cavity optical response can be described in terms of quality factor, Q. The e.m. field of the localized mode couples at some points to radiating modes outside the crystal. Then, the field oscillation within the cavity is damped in time. Q factor measures the decay rate of the e.m. mode energy in the cavity:

$$Q = 2\pi \frac{\tau}{T} \tag{32}$$

where τ is the decaying time and T is the optical period.

If the field is assumed to be exponentially decaying in time, Q can be also expressed in the frequency domain as:

$$Q = \frac{\omega_0}{\Delta\omega} \tag{33}$$

where ω_0 is the center frequency of the resonance and $\Delta\omega = 1/\tau$ is the spectral width of the cavity mode.

Q can be also expressed in terms of wavelength as $Q = \lambda_0/\Delta\lambda$ where λ_0 is the center wavelength and $\Delta\lambda$ is the full width at half maximum in wavelength.

Losses broaden the resonance in frequency and, then, lower Q.

A proper design of a PhC cavity can ensure very high Q factors. Q factor of the optical resonator based on the total internal reflection is limited by their modal volume V. When V is of the same order of λ, Q reduces to a very small value. This aspect can be intuitively explained. Modes with small volume have a wide distribution in k but the confinement based on total internal reflection is efficient only for those components verifying the total internal reflection condition. Thus, a wide distribution in k leads to a reduction of Q. The confinement based on photonic band gap does not impose any restriction on the k distribution. Thus, resonators with very high Q and small V can be realized. This kind of component is at the basis of a large number of applications.

When the modal volume becomes very small, an effect named Purcell effect appears [26]. It consists in an increase of the available states at the resonant frequency. The first consequence is an increase of the spontaneous emission rate by a factor $\lambda^3 Q/V$. This means that is possible to enhance the spontaneous emission at the desired wavelength, property that can be exploited in high efficiency light emitting diode.

Thus, PhCs allows to realize cavities having high-quality factor and extremely low mode volume, so providing high spectral selectivity and a large enhancement of the resonant e.m. field within the cavity.

Some strategies have been also proposed in literature to increase Q. One of these is to delocalize the resonant mode; as an example slightly reducing the radius of a number of holes around the defect. This represents a perturbation of the lattice responsible for a spreading of the modal field but, at the same time, an increase of Q.

3.3. Light Emitters

The properties of the PhC microcavities allow a strong field localization with a very high Q factor. This, in turn, ensures the possibility of realizing sources with a reduced pulse width and a high spectral purity due to the reduction of the ASE.

This is the first application discussed for the PhCs in 1987 by Yablonovitch. A defect induced into a PhC exhibits a strong localization of the light having a wavelength within the photonic band gap. As above mentioned, this microcavity can acts as an ultrasmall laser cavity. Such a cavity has the potential to control

the spontaneous emission and this property can allow the development of ultralow threshold lasers to be used as light source in a high-density photonic integrated circuit, in quantum communication and computation systems.

Dispersion curves flatness increases at the band gap edges, thus group velocity becomes very small or null vanishes. An optical mode having a frequency at the band edge is slower by the continuous partial reflections caused by the refractive index periodicity and this causes a strong interaction between light and active material. In semiconductor PhCs, the distributed reflection within the crystal gives origin to a light emitted at the band edge frequency, having with high output power and very low threshold currents. Same principle can be used for fabricating high efficiency optical amplifier.

3.4. Anomalous Group Velocity Dispersion

As above mentioned, the photonic band structure also affects the group velocity of an optical wave packet propagating in the medium. The dispersion determines also the effective refractive index and the related effects such as refraction and collimation.

A monochromatic wave propagates in a linear, isotropic and homogeneous medium according to the wave equation. The most simple solution of the wave Eq. is a plane wave having a sinusoidal distribution in space and time. The propagation speed of this kind of wave is defined phase velocity and is expressed as $v_\varphi = \omega/k_0$. In case of a wave packet, *i.e.,* a group of waves with a certain distribution of the wave vectors centred at k_0, it can be considered a frequency ω associated to each component k. If the wave packet propagates in a dispersive medium where the relationship between ω and k is non linear and the propagation of the wave packet does not occur propagate at the phase velocity $v_\varphi = \omega_0/k_0$, where ω_0 is the spectrum central wavelength. In this case, the signal and therefore the light energy propagates at group velocity defined as $v_g = (\partial\omega/\partial k)_{k=k_0}$. Phase and group velocity are linked by the Eq. $v_g = v_\varphi - \lambda(\partial v_\varphi/\partial\lambda)$. Group velocity can be either positive or negative and can be also either larger or smaller than the phase velocity.

Phase and group refractive indices can be derived from the phase and group velocity: $n_\varphi = c/v_\varphi$ and $n_g = c/n_g \cong n_\varphi - \lambda(\partial n_\varphi/\partial\lambda)$. Phase and group velocities and indices can be determined from the dispersion diagrams as it is shown in Fig. **6** for a 2D photonic crystal.

Phase velocity is defined as the ratio ω/k at the corresponding points of the dispersion diagram. Group velocity is deduced from the slope of the curve in that point. Depending on the specific point in the dispersion curve, either positive or negative values for the group velocity can be found.

In case of more complex photonic crystal structures, such as 2D and 3D ones, phase velocity can be again determined from the ratio ω/k for a given direction of the wave vector **k**. The group velocity could not be collinear with the phase velocity and can be strongly variable from zero to values slower than the vacuum speed of light, with a dependence both on frequency and propagation direction. Another important parameter is the group velocity dispersion defined as $\beta = \frac{d^2k}{d\omega^2}$, that is given by the curvature of the band structure.

To understand the operating principle of some devices exploiting the dispersion properties of the photonic crystals the concept of isofrequency curve in the **k** plane has to be introduced.

The isofrequency curve is the locus of points having the same frequency $\omega(\mathbf{k})$, that can be determined by intersecting the dispersion diagram with a plane, normal to the frequency axis at ω. The gradient of the function $\omega(\mathbf{k})$ in each point of an isofrequency curve identifies the direction, the sense and the velocity at which the e.m. energy travels inside the crystal.

In isotropic bulk materials the isofrequency curves are circles having radius changing with the frequency. The situation is totally different in the PhCs, where regions with a curve gradient constant with respect to ω and k, and regions with a propagation direction for the e.m. energy changing very rapidly can both exist. The sign of v_g can be positive or negative if v_g is directed towards the exterior or the interior of the isofrequency contour, respectively. The anisotropy of the photonic crystal often imposes different directions for the group and phase velocities.

Regions with gradient constant with respect to ω and k, can be exploited for realizing the supercollimators [27]. If an un-collimated optical beam, that can be represented as a combination of plane waves with different propagation directions, impinges on the surface of a PhC, the refracted waves, associated to different components, can propagate in parallel directions, giving an optical beam that appear to be perfectly collimated. Direction and sense of each refracted wave can be obtained by means of the procedure depicted in Fig. **6** ***left***.

It is different is the operating principle at the basis of the superprisms [28-30]. A prism is a structure able to separate the spectral components of an optical beam exploiting the variation of the refractive index as a function of the wavelength. Conventional prism have a spectral selectivity too low to be used in applications such as mux/demux in WDM systems.

PhCs allow to change the dispersion properties of the material. The crystal has to be designed so that in the spectral region of interest the isofrequency curves could show a strong sensitivity to small variations in frequency, changing in shape from concave to convex forms. Under these conditions if a polychromatic beam impinges on crystal surface, the refracted waves generated from each spectral component experience propagation directions that can be also very different even for small changes in wavelength (see Fig. **6** ***right***).

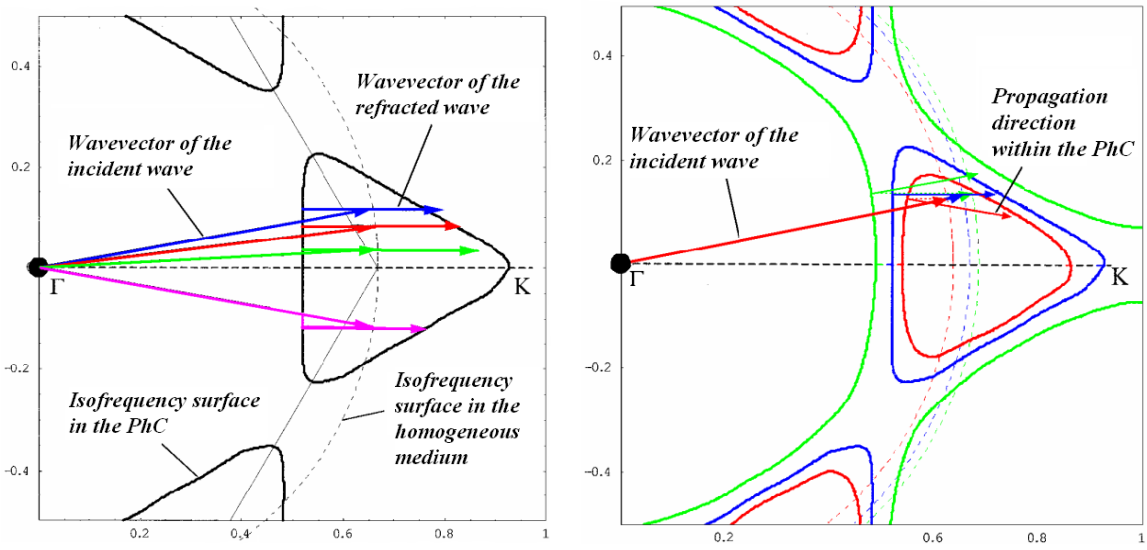

Figure 6: Operating principle of: *on the left* a supercollimator, *on the right* a superprism. A specific colour is associated to each component of the optical beam.

By fixing a proper shape for the output surface of the crystal, at distances in the order of few microns from the input section the spectral components can be spatially filtered and routed towards different output ports.

High spectral resolution demultiplexers based on superprism structure have been proposed in literature. Their main advantage when used in DWDM systems consists in the possibility of demultiplexing/multiplexing a large number of signals by using a single component having micrometric size. In addition, the high sensitivity to wavelength in a superprism is frequently accompanied by high sensitivity to refractive index change. This property can found application in sensing and nonlinear optics.

In the same PhC, both self-collimating and divergent propagation can be realized, depending on the band structure dispersion at a certain wavelength and propagation direction.

3.5. Negative Refraction

When light is launched into a dielectric medium with constant refractive index n it is refracted at an angle determined by Snell's law. Homogeneous materials generally have a positive refractive index. This property results in incident and refracted beams both lying on opposite sides of the surface normal.

In a material with $n < 0$, namely "negative index material" the direction of refraction is reversed. This material can focus the light in a specific way leading to novel optical behaviour to be exploited, as an example, in "superlenses" [31], producing three dimensional images with a sharpness below the Rayleigh resolution limit and, then, not limited by diffraction issues.

One kind of negative index materials are metallic elements having a resonant response to light, exhibiting negative refraction at microwave frequencies and known as ''metamaterials''. Nevertheless, some of these artificial materials have high optical loss at optical frequencies.

On the contrary, it has been demonstrated [32, 33], that photonic crystals can exhibit negative refraction in the optical frequency range with relatively low loss.

PhCs show refractive index anomalous dispersion near to their high-frequency band edge. The refractive index of the structure made by photonic crystal depends not only on the refractive index of composing materials but it is even determined by the photonic band structure. Based on the characteristics of the photonic band structure the photonic crystals can have an index smaller than unity without any absorption.

An example of an imaging effect induced by a negative refraction photonic crystal in shown in Fig. **7**.

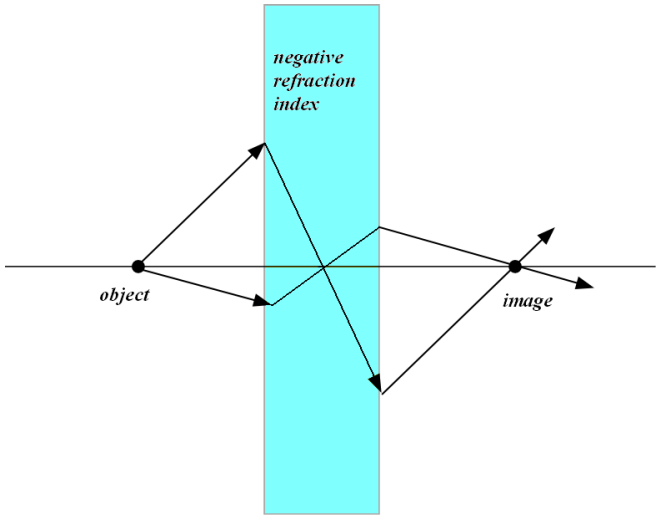

Figure 7: Operating scheme for a superlens.

A light source emits on one side of the photonic crystal structure. An optical beam that impinges on the PhC surface may split into a number of beams due to the presence of different dispersion surfaces at a given frequency. Moreover, a beam a the exit of a PhC surface may split into a number of beams due to the diffraction effect.

The image can be formed if some conditions are verified to guarantee that the negative refraction can occur at any angle. First, the constant-frequency contour of the photonic crystal is convex with a negative photonic effective mass. In addition all wavevectors at that frequency are included within the constant-

frequency contour of the PhC. Furthermore, the frequency is below $\pi c/a_s$, where a_s is the surface-parallel periodicity of the PhC.

Surface characteristics and thickness must be optimized for reducing internal reflection.

An open issue on PhCs is its finite aperture d, as for all imaging systems. In presence of aperture limitation, certain information with spatial frequency much higher than $2\pi/d$ is lost behind the aperture.

The lost information cannot be regenerated by any medium.

CONCLUSION

Photonic crystal structures have been introduced in a wide range of optoelectronic devices. In most of these devices, advantages such as small size, lower power consumption and higher performance and reliability of PhC-based devices have been demonstrated.

In the last decade, the continuous improvement in high resolution lithography and etching processes makes photonic crystal devices interesting components to be included in cost-effective VLSI systems, where they can be integrated with optical and electronic systems.

REFERENCES

[1] Yablonovitch E. Inhibited spontaneous emission in solid-state physics and electronics. Phys Rev Lett 1987; 58: 2059–2062.

[2] John S. Strong localization of photons in certain disordered dielectric superlattices. Phys Rev Lett 1987; 58: 2486.

[3] Joannopoulos JD, Meade RD, Winn JN. Photonic Crystals: Molding the Flow of Light. Princeton University Press, 1995.

[4] Johnson SG, Joannopoulos JD. Block-iterative frequency-domain methods for Maxwell's Eqs. in a planewave basis. Opt Express 2001; 8(3): 173-190.

[5] Plihal M, Maradudin AA. Photonic band structure of two-dimensional systems: The triangular lattice. Phys Rev B 1991; 44(16): 8565-8571.

[6] Ramos-Mendieta F, Halevi P. Electromagnetic surface modes of a dielectric superlattice: the supercell method. J Opt Soc Am B 1997; 14(2): 370-381.

[7] Kuchinsky S, Allan DC, Borrelli NF, Cotteverte J-C. 3D localization in a channel waveguide in a photonic crystal with 2D periodicity. Opt Commun 2000; 175(1-3): 147-152.

[8] Ciminelli C, Peluso F, Armenise MN. Modeling and design of two-dimensional guided-wave photonic band-gap devices. J Lightwave Technol 2005; 23: 886-901.

[9] Ciminelli C, Chong HM, Peluso F, De La Rue RM, Armenise MN. High-Q Guided-Wave Photonic Crystal Extended Microcavity. ECOC 2004 Proceedings, Post-deadline Paper Th. 4.2.6, Stockholm, 2004.

[10] Taflove. Computational Electrodynamics: The Finite-Difference Time-Domain Method. Norwood, MA: Artech House Inc., (1995).

[11] D'Urso B, Painter O, O'Brien J, Tombrello T, Yariv A, Scherer A. Modal reflectivity in finite-depth two-dimensional photonic-crystal microcavities. J Opt Soc Am B 1998; 15(3): 1155-1159.

[12] Boroditsky M, Coccioli R, Yablonovitch E. Analysis of photonic crystals for light emitting diodes using the finite differences time domain technique. Proceedings of SPIE 1998; 3283: 184-190.

[13] Ward AJ, Pendry JB. A program for calculating photonic band structures, Green's functions and transmission/reflection coefficients using a nonorthogonal FDTD method. Comp Phys Commun 2000; 128: 590-621.

[14] Finite Elements – Theory and Application. New York: D. L. Dwoyer, M. Y. Hussaini and R. G. Voigt Editors, Springer-Verlag, 1986.

[15] Hwang J-K, Hyum S-B, Ryu H-Y, Lee Y-H. Resonant modes of two-dimensional photonic bandgap cavities determined by the finite-element method and by use of the anisotropic perfectly matched layer boundary conditions. J Opt Soc Am B 1998; 15(8): 2316-2324.

[16] Pendry JB. Photonic band structures. J Mod Optic 1994; 41(2): 209-229.

[17] Yonekura J, Ikeda M, Baba T. Analysis of finite 2-D photonic crystals of columns and lightwave devices using the scattering matrix method. J Lightwave Technol 1999; 17 (8): 1500-1508.

[18] Centeno E, Felbacq D. Rigorous vector diffraction of electromagnetic waves by bidimensional photonic crystals. J Opt Soc Am A 2000; 17(2): 1-8.

[19] Sztefka G, Nolting HP. Bidirectional eigenmode propagation for large refractive index steps. IEEE Photonic Tech L 1993; 5(5): 554-557.

[20] Ctyroky J, Helfert S, Pregla R. Analysis of a deep waveguide Bragg grating. Opt Quant Electron 1998; 30(5/6): 343-358.

[21] Green DN, Bass SC. Representing Periodic Waveforms with Nonorthogonal Basis Functions. IEEE T Circuits Syst 1984; CAS-31(6): 518-535.

[22] Zhao L-M, Wang X-H, Gu B-Y, Yang G-Z. Green's function for photonic crystal slabs. Phys Rev E 2005; E-72: 026614 1-6.

[23] Ciminelli C, Marani R, Armenise MN. Investigation of a point-like and plane-wave excitation in 2D photonic bandgap microcavities using Green's function method. Opt Quant Electron 2009; 41 (4): 255-265.

[24] Ciminelli C, Marani R, Armenise MN. Fast and Accurate Investigation of 2D Multilayered Photonic Crystals by a 3D Model based on Green Function. IEEE J Quantum Elect 2010; 46 (11): 1549-1560.

[25] Inoue K, Ohtaka K. Photonic Crystals. Physics, Fabrication and Applications. Springer-Verlag, 2004.

[26] Purcell EM. Spontaneous emission probabilities at radio frequencies. Phys Rev 1946, 69: 681-686.

[27] Wu L, Mazilu M, Krauss TF. Beam stearing in planar-photonic crystals: from superprism to supercollimators. J Lightwave Technol 2003; 21 (2): 561-566.

[28] Lupu A, Cassan E, Laval S, El Melhaoui L, Lyan P, Fedeli JM. Experimental evidence for superprism phenomena in SOI photonic crystals. Opt Express 2004, 12 (23): 5690-5696.

[29] Baba T, Matsumoto T. Resolution of photonic crystal superprism. Appl Phys Lett 2002, 81 (13): 2325-2327

[30] Notomi M. Theory of light propagation in strongly modulated photonic crystals: Refraction-like behavior in the vicinity of the photonic band gap. Phys Rev B 2000, 62: 10696–10705.

[31] Pendry JB. Negative refraction makes a perfect lens. Phys Rev Lett 2000, 85: 3966–3969.

[32] Luo C, Johnson SG, Joannopoulos JD, Pendry JB. All-angle negative refraction without negative effective index. Phys Rev B 2002, 65: 201104.

[33] Foteinopoulou S, Economou EN, Soukoulis CM. Refraction in media with a negative refractive index. Phys Rev Lett 2003, 90: 107402.

CHAPTER 2

Analysis of Photonic Crystal Structures

Anand Gopinath*

Department of Electrical and Computer Engineering, University of Minnesota, Minneapolis, MN 55455, USA

Abstract: Photonic crystals are periodic structures with spatial variation of the dielectric, magnetic and metallic properties in one, two and three dimensions. For the present we confine this discussion to mixed dielectric structures. The propagation of electromagnetic waves through these crystals may result in pass and stop bands, depending on the structure. The wave propagation is governed by Maxwell's Eqs. and these calculations are usually performed for infinite structures and subsequently modified for finite structures. There are different approaches to solving the wave propagation problem and these range from the plane wave expansion method (PWEM) [1], the transfer matrix method [2], the finite difference time domain method (FDTD) [3] and the finite element method [4] which are among the most popular. In this chapter only the plane wave expansion and the finite difference methods are discussed.

Keywords: Analysis of photonic crystal, plane wave expansion method, finite difference time domain method.

1. INTRODUCTION

1.1. Formulation of the Wave Eq. Problem

Electromagnetic wave propagation is governed by Maxwell's equations. For charge and source free media and time variation of the form $e^{j\omega t}$, these are:

$$\nabla \times E = -j\omega B \quad \textbf{(1)}$$

$$\nabla \times H = j\omega D \quad \textbf{(2)}$$

and taking the divergence of these gives

$$\nabla \cdot D = 0 \quad \textbf{(3)}$$

$$\nabla \cdot B = 0 \quad \textbf{(4)}$$

Assuming that only nonmagnetic media are considered, then $\mu = \mu_0$ and all the dielectrics in the photonic crystals to be considered are assumed to be isotropic so that $\varepsilon = \varepsilon_0\ \varepsilon_r$. In this case the constituent relationships between B and H and B and H is given by

$$B = \mu_0\ H \quad \textbf{(5)}$$

$$D = \varepsilon_0 \varepsilon_r\ E \quad \textbf{(6)}$$

Then the above Eqs. 1 to 4 become

$$\nabla \times E = -j\omega\mu_0 H \quad \textbf{(7)}$$

$$\nabla \times H = j\omega\varepsilon_0\varepsilon_r E \quad \textbf{(8)}$$

$$\nabla \cdot D = 0 \quad \textbf{(9)}$$

$$\nabla \cdot B = 0 \quad \textbf{(10)}$$

***Address correspondence to Anand Gopinath:** Department of Electrical and Computer Engineering, University of Minnesota, 200 union Street S.E., Minneapolis, MN 55455, USA; Phone: 612-625-3054 Fax: 612-624-4578; E-mail: gopinath@umn.edu

Marco Pisco, Andrea Cusano and Antonello Cutolo (Eds)
All rights reserved-© 2012 Bentham Science Publishers

In general the propagation of waves through the mixed dielectric medium of the periodic photonic crystal is a vector wave problem and therefore the formulation needs to reflect this. To eliminate the H in Eq. 5 and E in Eq. 6, take the curl of these and substituting:

$$\nabla \times \frac{1}{\varepsilon_r} \nabla \times H = k_0^2 H \tag{11}$$

$$\nabla \times \nabla \times E = k_0^2 \varepsilon_r E \tag{12}$$

where $k_0^2 = \omega^2 \mu_0 \varepsilon_0$. Note that the velocity of light in free space is given by $c = 1/\sqrt{\mu_0 \varepsilon_0}$.

The usual solution method is to take the inner product with a testing function which is usually the either H^* or E^* which is the Galerkin method. Thus for Eq. 11

$$\int H^* \cdot \nabla \times \frac{1}{\varepsilon_r} \nabla \times H \, d\Omega = \int \frac{\omega^2}{c^2} H \cdot H^* \, d\Omega \tag{13}$$

Now let

$$L_H = \nabla \times \frac{1}{\varepsilon_r} \nabla \times \tag{14}$$

$$L_E = \nabla \times \nabla \times \tag{15}$$

and also $\lambda = (\omega / c)^2$, then Eqs. 11 and 12 become

$$L_H H = \lambda_H H \tag{16}$$

$$L_E E = \lambda_E E \tag{17}$$

It can be shown that both L_H and L_E operators are Hermitian [5], which implies that the eigenvalues of these above Eqs. are real. The usual solution method is to expand the unknown function in a set of basis functions

$$H = \sum a_i u_i \tag{18}$$

and subsequently take the inner product with a set of testing functions w_i and when this test function set is identical or the complex conjugate of the basis set, then this is the Galerkin method [6]. The span of the basis and test functions need to be identical, when they span the entire domain then this is the entire-domain method and both the functions need to satisfy the boundary conditions. Sub-domain methods include the Finite Element method (FEM) and the basis and testing functions need to satisfy the boundary conditions when the subdomain includes the boundaries. Before discussing the solutions of the wave equation, some details about the periodic structures which comprise photonic crystals are first discussed.

1.2. Periodic Structures

The present section is based on the definitions of crystals from solid state physics included in the books by Ashcroft and Mermin [7] and Kittel [8]. An ideal crystal is the periodic repetition of the basic dielectric structure or cell in space and the basic cell may be in one or two or three dimensions. The cell comprises of a set of points which form a space lattice and associated with these lattice points are dielectric objects, spheres or cubes or other geometric structures which are the basis at these points which form the cell. Alternatively, the cell may comprise of a dielectric medium with geometric voids or filled with a second dielectric or metal at these points. The periodic array in space of these cells form the crystal. In three dimensions, the cell may be defined by three fundamental translation vectors

$$R = m_1 a_1 + m_2 a_2 + m_3 a_3 \quad \textbf{(19)}$$

where the vectors a_i are the fundamental translation vectors and the arrangements of the dielectric objects should look the same from any point r in any one unit cell to r' in another unit cell and thus

$$r' = r + m_1 a_1 + m_2 a_2 + m_3 a_3 \quad \textbf{(20)}$$

$$= r + R \quad \textbf{(21)}$$

where m_i are integers. Other operations besides translation involve rotation and mirror symmetry. However, these are not discussed here and the interested reader is referred to the above books [7, 8] and others on crystallography.

In a two dimensional lattice with identical "atoms" as the basis, shown in Fig. **1**, two choice of the translational vectors are shown. Note that the lattice needs the basis of "atoms" to form the unit cell which is periodic to form the crystal.

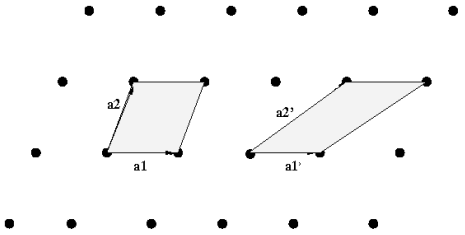

Figure 1: Schematic arrangement of a two dimensional lattice of identical "atoms".

There are many definitions of an unit cell and the corresponding translation vectors or lattice vectors in a photonic crystal. If the translation vectors satisfy the Eq. 20 then they are called *primitive translation vectors*. A two dimensional two "atom" structure is illustrated in Fig. **2**. The translational vectors a_1, a_2 constitute a set of primitive vectors and the area defined by them corresponds to the area of the unit cell. The vectors $a_{1'}, a_{2'}$ are not suitable vectors as they do not satisfy Eq. 21 and the cells do appear to be identical from the different end points.

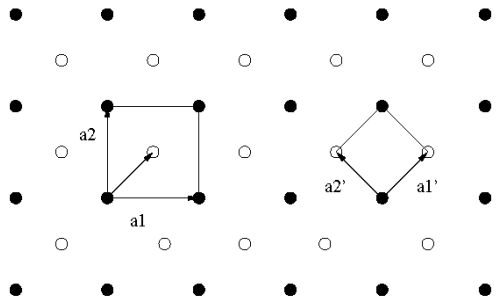

Figure 2: Schematic arrangement of a two dimensional lattice of two different "atoms". The primitive vectors are a_1, a_2 , whereas the vectors $a_{1'}, a_{2'}$ do not satisfy Eq. (21).

The lattices and the basis "atoms" form the unit cells and the primitive translation vectors also define the primitive cell. The Wigner-Seitz cell in two dimensions is formed by the area enclosed by bisecting the lattice lines connecting one "atom" to all its adjacent "atoms." For example, the square lattice results in a square Wigner-Seitz cell as shown in the lower part of Fig. **3** and the cell for the equilateral triangular lattice results in a hexagonal cell also shown in this figure. These are also called the Bravais lattices.

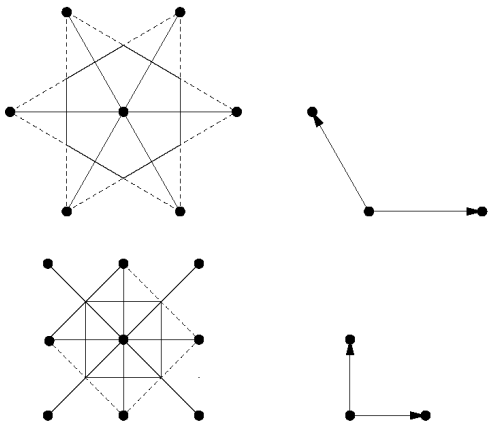

Figure 3: The Wigner-Seitz primitive cells for the equilateral triangular and square two dimensional lattices and "atoms" are shown together with their translation vectors.

There are a total of five two dimensional Bravais lattices formed with translation vectors [8] but with no rotation or mirror reflections, the two shown in the Fig. **4** are the square and hexagonal lattices. The others are the rectangular lattice, the centered rectangular lattice and the oblique lattice.

In three dimensions, there are seven lattice types as listed by Kittel [8] and these include the three cubic lattices which are the simple cubic lattice with the "atoms" at the eight vertices Fig. **5**, the body centered cubic lattice (bcc) which has an extra "atom" in the center of the cube Fig. **6** and the face centered cubic (fcc) lattice has an extra "atom" in the middle of each face of the cube Fig. **7**. The others, not shown here include the monoclinic, triclinic, orthorhombic, tetragonal, trigonal and the hexagonal.

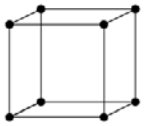

Figure 4: Cubic lattice.

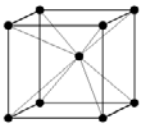

Figure 5: Body centered cubic lattice.

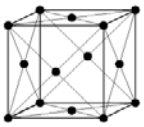

Figure 6: Face centered cubic lattice.

Only the cubic lattices are considered here and to obtain the Wigner-Seitz cells, the simple cube results in a cube centered about one "atoms" of the cube as shown in Fig. **7**. The primitive vectors for the bcc lattice centers at one corner of the cube with the vectors to central "atom" from this corner to three adjacent cubes (see Kittel [8]) and the fcc also has a similar primitive vectors from the corner of the cube to "atoms" on the faces of adjacent cells. The corresponding Wigner-Seitz cells for the bcc and the fcc structures are shown in Fig. **8**.

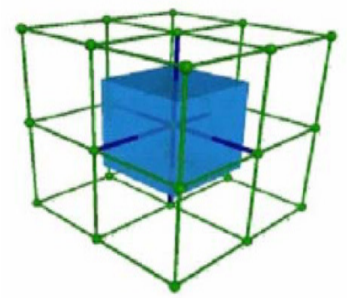

Figure 7: Wigner-Seitz cubic lattice (with permission from Dr. J. Ÿrgen Henk, Max-Planck-Institut f Ÿr Mikrostrukturphysik, Halle (Saale), Germany, from the web).

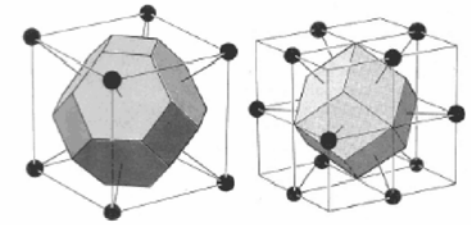

Figure 8: Body centered cubic and face centered cubic Wigner-Seitz lattices (with permission from Dr. J Ÿrgen Henk, Max-Planck-Institut f Ÿr Mikrostrukturphysik, Halle (Saale), Germany, from the web).

The concept of reciprocal lattices arises from the fact that the dielectric "atoms" are periodic, defined by the translation vector R in Eq. 20, and therefore the relative permittivity $\varepsilon_r(r)$ satisfies the following condition:

$$\varepsilon_r(r) = \varepsilon_r(r+R) \tag{22}$$

Following the treatment in [6, 8], consider the transformation of this periodic structure into the spatial Fourier domain resulting in spatial frequencies. In an one dimensional periodic dielectric structure, the fundamental spatial frequency is $2\pi/a$, where a is the period in real space and $2\pi/a$ is in the reciprocal space, the Fourier transformed spatial component in the k-space. In three dimensions, the spatial Fourier components of the dielectric crystal may be written as

$$\varepsilon_r(r) = \sum_G \varepsilon_r(G)\, e^{jG\cdot r} \tag{23}$$

where G is a set of vectors in k-space. From Eqs. 22 and 23

$$\varepsilon_r(r+R) = \sum_G \varepsilon_r(G)\, e^{jG\cdot(r+R)} = \sum_G \varepsilon_r(G)\, e^{jG\cdot r}\; e^{jG\cdot R} = \varepsilon_r(r) \tag{24}$$

which implies that $e^{jG\cdot R} = 1$ and hence $G\cdot R = 2\pi m$. Note that the translational lattice vector R is given by Eq. 19 repeated here

$$R = m_1 a_1 + m_2 a_2 + m_3 a_3 \tag{25}$$

and therefore the vector G may be defined as

$$G = n_1 g_1 + n_2 g_2 + n_3 g_3 \tag{26}$$

and the vectors g_i are defined by

$$g_i \cdot a_j = 2\pi\delta_{ij} \tag{27}$$

where δ_{ij} is the Kronecker delta function with $\delta_{ij} = 1$ when $i = j$ and $\delta_{ij} = 0$ for $i \neq j$. The usual definition of g_i which satisfies these conditions is given by

$$g_i = 2\pi \frac{a_j \times a_k}{V} \tag{28}$$

where i, j, k are cyclically $1, 2, 3$.

Note that V is the volume of the primitive cell given by

$$V = a_1 \cdot a_2 \times a_3 \tag{29}$$

The primitive vectors are defined by Eq. 25 and are not unique. In reciprocal space, k-space, the volume in $(2\pi)^3 / V$. The Wigner-Seitz cell in real space has a corresponding cell called first Brillouin zone (FBZ) in reciprocal k-space: the simple cubic Wigner-Seitz lattice in real space is a cubic lattice in k-space, the body-centered cubic Wigner-Seitz lattice in k-space is identical to the Wigner-Seitz lattice of the face centered cubic in real space and *vice versa*. For all three reciprocal lattices the origin is label the Γ point. These are also called the irreducible Brillouin zones (IBZs), since every point in the in the BZ may be mapped to the first BZ and this becomes the IBZ.

Propagation in periodic structures requires the use of the periodic boundary conditions and this is governed by the Bloch theorem. The plane wave propagating through this periodic medium is modulated by the periodic dielectric structure. Thus Eq. 22 demonstrates the periodicity of the dielectric material of the photonic crystal and in the present case the assumption is that these are non magnetic which implies that the permeability $\mu_r = 1$ throughout the crystal and has no periodicity.

Suppose the electric and magnetic fields are given by the following equations

$$E(r) = E_k(r) e^{-jk \cdot r} \tag{30}$$

$$H(r) = H_k(r) e^{-jk \cdot r} \tag{31}$$

and due to the periodicity of crystal it follows that

$$E_k(r) = E_k(r + R) \tag{32}$$

$$H_k(r) = H_k(r + R) \tag{33}$$

and from the above Eqs. and the Bloch theorem [7] suggests that

$$E_k(r + R) = E_k(r) e^{-jk \cdot R} \tag{34}$$

$$H_k(r + R) = H_k(r) e^{-jk \cdot R} \tag{35}$$

This implies that the plane waves given by $e^{-jk \cdot r}$ are modulated by the spatial periodic functions $E_k(r)$ or $H_k(r)$.

These results are used in the calculations discussed in the following sections.

2. PLANE WAVE EXPANSION METHOD

Only one of the two Eqs. need to be solved, consider the Eq. 11 in H repeated here

$$\nabla \times \frac{1}{\varepsilon_r} \nabla \times H = \frac{\omega^2}{c^2} H \tag{36}$$

The solution is by the method of weighted residuals, as discussed in in section 2. H is expanded in a basis set that satisfy the boundary conditions as described in Eq. 18 and repeated here.

$$H = \sum_{n=1}^{N} a_n u_n \tag{37}$$

Substituting in Eq. 36

$$\sum_{n=1}^{N} \nabla \times \frac{1}{\varepsilon_r} \nabla \times a_n u_n = \frac{\omega^2}{c^2} a_n u_n \tag{38}$$

Choosing a set of test functions w_m and taking the inner product leads to

$$\sum_{n=1}^{N} a_n [w_m, \nabla \times \frac{1}{\varepsilon_r} \nabla \times u_n] = a_n [w_m, \frac{\omega^2}{c^2} u_n] \tag{39}$$

and in matrix form becomes

$$A\, x = \lambda B\, x \tag{40}$$

Note that the basis and test functions may be defined over the entire domain and then this becomes the whole domain method, when they are defined over subdomains then it becomes the subdomain method. The finite element method (FEM) is a subdomain method in which the inner product over the subdomain are evaluated analytically with identical basis and test functions and then the matrix is assembled. The basis functions if defined over the unit cell need to satisfy the boundary conditions including the Bloch theorem. Sub domain basis functions need to satisfy continuity and those at the boundary of the unit cell need to satisfy the periodic boundary Bloch condition.

The choice of propagation direction has to be made and in all cases a minimum number is chosen to characterize the photonic crystal, determined by the reciprocal lattice of the structure.

An excellent review of the techniques of calculating the mode structures in photonic crystals by the plane wave method is provided by the papers [9, 10] and are the basis of this section. Prather *et al.* [6] have expanded this in considerable detail.

2.1. One Dimensional Case

Electromagnetic wave propagation through the photonic crystal cell is governed by the time harmonic Maxwell's Eqs. in Eqs. 7 to 10, and here the curl Eqs. are repeated and expanded in Cartesian coordinates. Thus, the curl Eqs. are

$$\nabla \times E = -j\omega\mu_0 H \tag{41}$$

$$\nabla \times H = j\omega\varepsilon_0\varepsilon_r E \tag{42}$$

and in Cartesian coordinates these are expanded as

$$\frac{\partial E_z}{\partial y} - \frac{\partial E_y}{\partial z} = -j\omega\mu H_x \tag{43}$$

$$\frac{\partial E_x}{\partial z} - \frac{\partial E_z}{\partial x} = -j\omega\mu H_y \tag{44}$$

$$\frac{\partial E_y}{\partial x} - \frac{\partial E_x}{\partial y} = -j\omega\mu H_z \tag{45}$$

and

$$\frac{\partial H_z}{\partial y} - \frac{\partial H_y}{\partial z} = j\omega\varepsilon_0\varepsilon_r E_x \quad \textbf{(46)}$$

$$\frac{\partial H_x}{\partial z} - \frac{\partial H_z}{\partial x} = j\omega\varepsilon_0\varepsilon_r E_y \quad \textbf{(47)}$$

$$\frac{\partial H_y}{\partial x} - \frac{\partial H_x}{\partial y} = j\omega\varepsilon_0\varepsilon_r E_z \quad \textbf{(48)}$$

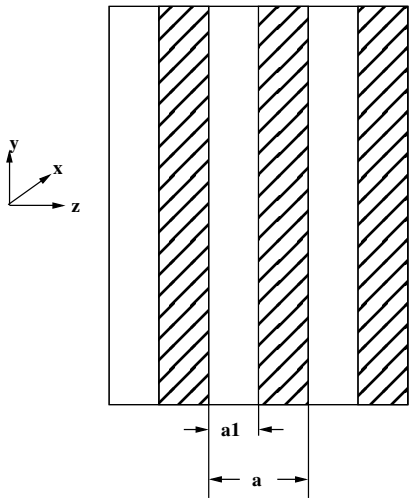

Figure 9: Schematic arrangement of a one dimensional photonic crystal.

The one dimensional case considered is shown schematically in Fig. **9** which comprise of periodic layers dielectric in the z-direction. It is also assumed that the layers are constant in the x and y directions which implies that the field variation in these directions are also zero:

$$\frac{\partial}{\partial x} = \frac{\partial}{\partial y} \Rightarrow 0 \quad \textbf{(49)}$$

Thus, the above Eqs. 43, 44, 45 and 48 become:

$$-\frac{\partial E_y}{\partial z} = -j\omega\mu H_x \quad \textbf{(50)}$$

$$\frac{\partial E_x}{\partial z} = -j\omega\mu H_y \quad \textbf{(51)}$$

$$-\frac{\partial H_y}{\partial z} = j\omega\varepsilon_0\varepsilon_r E_x \quad \textbf{(52)}$$

$$\frac{\partial H_x}{\partial z} = -j\omega\varepsilon_0\varepsilon_r E_y \quad \textbf{(53)}$$

Pairing Eqs. 51 and 53

$$\frac{\partial E_x}{\partial z} = -j\omega\mu H_y \quad \textbf{(54)}$$

$$-\frac{\partial H_y}{\partial z} = j\omega\varepsilon_0\varepsilon_r E_x \tag{55}$$

Eliminating the H_y from the first and E_x from the second:

$$\frac{1}{\varepsilon_r}\frac{\partial^2 E_x}{\partial z^2} + \frac{\omega^2}{c^2}E_x = 0 \tag{56}$$

$$\frac{\partial}{\partial z}[\frac{1}{\varepsilon_r}\frac{\partial H_y}{\partial z}] + \frac{\omega^2}{c^2}H_y = 0 \tag{57}$$

Either of these may be used for the calculation and the second Eq. is chosen for these calculations. The periodic dielectric structure is described by the Eqs. 23 to 27 and the one dimensional case considered here the primitive translation vector is defined as

$$\boldsymbol{a} = a_z\ a \tag{58}$$

and the reciprocal vector is $a_z g = a_z 2\pi/a$, the spatial Fourier analysis of $1/\varepsilon_r$ one dimensional structure with periodic boundary conditions has the form

$$\frac{1}{\varepsilon_r(z)} = \sum_{n=-\infty}^{n=\infty} X(n)e^{jngz} \tag{59}$$

where

$$X(n) = \frac{1}{a}\int_0^a \frac{1}{\varepsilon_r(z)}e^{-jpgz}dz \tag{60}$$

$$= \frac{1}{a}\int \sum_{n=-\infty}^{n=\infty} X(n)e^{j(n-p)gz}dz \tag{61}$$

For the one dimensional structure shown in Fig. **9**, the above Eq. 61 becomes

$$X(n) = \frac{1}{a}\left(\int_0^{a_1}\frac{1}{\varepsilon_{r1}}e^{j(n-p)gz}dz + \int_{a_1}^{a}\frac{1}{\varepsilon_{r2}}e^{j(n-p)gz}dz\right) \tag{62}$$

Let $(n-p) = n'$ and integrating this equation, the two cases are when $n' \neq 0$ and $n' = 0$ and these are

$$X(n') = \frac{1}{jn'g}\left(\frac{e^{jn'ga_1}-1}{\varepsilon_{r1}} + \frac{e^{jn'ga} - e^{jn'ga_1}}{\varepsilon_{r2}}\right) \quad n' \neq 0 \tag{63}$$

$$= \left(\frac{a_1}{\varepsilon_{r1}a} + \frac{a-a_1}{\varepsilon_{r2}a}\right) \quad n' = 0 \tag{64}$$

The next step is to express H_y in a basis function set and these are plane waves modulated by $1/\varepsilon_r$ of Eq. 59 periodic boundary condition, which is the Bloch condition in Eq. 35. However, the modulation is based on the reciprocal vector **G** and assuming that the wave propagates as e^{-jkz}, the magnetic field component H_y may be written as a sum of the modulation terms as:

$$H_y = \sum_{m=-\infty}^{\infty} h(m)\, e^{-j(k+mg)z} \tag{65}$$

Substituting in Eq. 57, rearranging, substituting $n = n'$ results in the following

$$\sum_n \sum_m X(n-m)(k+mg)(k+ng)h(m)\, e^{-j(k+ng)z} = \frac{\omega^2}{c^2} \sum_n h(n) e^{-j(k+ng)z} \quad \textbf{(66)}$$

The next step is to take the inner product with a set of testing functions which are usually chosen to be the same as the expansion functions from Eq. 38

$$w_{n'} = e^{j(k+n'g)z} \quad \textbf{(67)}$$

Note that the inner product is over the span of the irreducible Brillouin zone, which in this case is over a leading to the equations

$$\sum_n \sum_m X(n-m)(k+mg)(k+ng)h(m) \int_0^a e^{j(n'-n)gz} dz = \frac{\omega^2}{c^2} \sum_n h(n) \int_0^a e^{j(n'-n)gz} dz \quad \textbf{(68)}$$

Note that $n'-n$ is an integral number or zero and $(n'-n)g = (n'-n)2\pi / a$ is either an integer multiple of 2π or zero and hence

$$\int_0^a e^{j(n'-n)gz} dz = \frac{e^{j(n'-n)2\pi} - 1}{j(n'-n)} = 0 \quad n' \neq n \quad \textbf{(69)}$$

$$= a \quad n' = n \quad \textbf{(70)}$$

Therefore the n-th Eq. in Eq. (68) becomes

$$\sum_m X(n-m)(k+mg)(k+ng)h(m) = \frac{\omega^2}{c^2} h(n) \quad \textbf{(71)}$$

This leads to the standard eigenvalue matrix Eq. of the form

$$A\, h = \lambda B\, h \quad \textbf{(72)}$$

where $\lambda = \omega^2 / c^2$ and B is an identity matrix (note that λ here is not the wavelength). The matrix A is symmetric and hermitian with real eigenvalues. Since the basis are plane wave harmonic functions convergence is poor and a large number of terms need to be used for reasonable accuracy. The domain of calculation is the irreducible Brillouin zone.

To calculate the matrix components, the values of $X(n)$ need to be evaluated by the fast Fourier transform (FFT) algorithm, and then a value of k is chosen and the values of $\lambda = \omega^2 / c^2$ are obtained by solving this matrix Eq. by standard subroutines (note that λ here is not the wavelength). The procedure is repeated for all the wave vectors in the Brillouin zone to obtain all the eigenvalues over the zone. These results are then grouped together and the band structure over the entire Brillouin zone is obtained by symmetry and plotted as shown in Fig. **10** for the case of one dimensional structure in Fig. **9**.

2.2. Two Dimensional Plane Wave Expansion Method

Examples of two dimensional periodic structures are periodically placed rods, either in a square lattice (see Fig. **2** or in a triangular form (see 0). The two-dimensional photonic crystal is periodic in two dimensions and assumed to be uniform in the third, examples are periodically place rods or holes in a dielectric slab as shown in Fig. **11**. The method of calculation of the propagating modes follows [6, 11, 12].

In this two-dimensional case, the cell is be defined by primitive translation vectors $\mathbf{a_1}$ and $\mathbf{a_2}$, as in Eq. 19 and shown in Fig. **2**

$$R = m_1 a_1 + m_2 a_2 \tag{73}$$

and also satisfies Eq. 20 in its two dimensional form

$$r' = r + m_1 a_1 + m_2 a_2 = r + R \tag{74}$$

The translation vector **R** generates the two-dimensional lattice when the values of the integers m_1 and m_2 are varied and only the primitive cell needs to be considered.

The reciprocal lattice vector **G** satisfies the equation

$$e^{G \cdot R} = 1 \tag{75}$$

which implies

$$G \cdot R = 2\pi i \quad for\ i = \pm 1, \pm 2, ... \tag{76}$$

and the components of this vector are

$$G = m_1 \mathbf{g_1} + m_2 \mathbf{g_2} \tag{77}$$

where reciprocal primitive vectors are $\mathbf{g}_1$ and $\mathbf{g_2}$, which satisfy the equation

$$\mathbf{g_i} \cdot \mathbf{a_j} = 2\pi\delta_{ij} \tag{78}$$

and

$$\delta_{ij} = 0 \quad for\ i \neq j \tag{79}$$

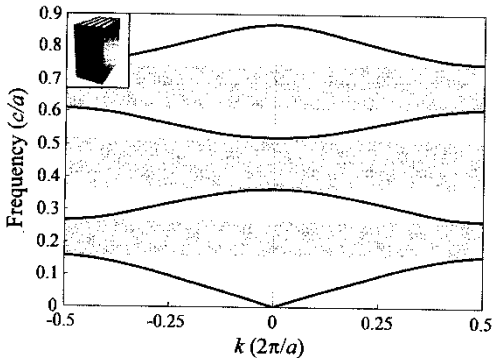

Figure 10: Band diagram of a one dimensional photonic crystal, two layers with ε_r=12.25 and 1, width of each layer 0.5a, the spacing of the unit cell. (with permission from John Wiley &Sons, from, *Photonic Crystals,* by Prather, Shi, Sharkawy, Murakowski, Schneider, 2009, John Wiley, [6]).

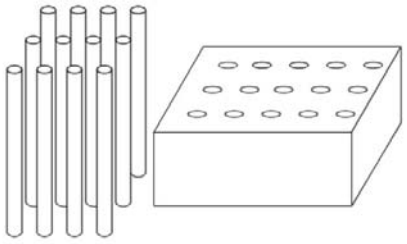

Figure 11: Schematic arrangement of two dimensional photonic crystals of rods periodically placed or holes in a dielectric block. The assumption is that the structure does not vary in the third dimension.

Two dimensional structures as shown in Fig. **11** may be arranged in square or triangular lattices. In the latter case, the equilateral triangular lattice, also known as the hexagonal lattice, provides symmetry although other triangular structures, also known as the oblique lattices are also possible. These two structures, square and equilateral triangular cases, shown in Figs. **12** and **13** are discussed in this section.

The square lattice in Fig. **12** has its primitive vectors given by $a_1 = a\,a_x$ and $a_2 = a\,a_y$ are equal and orthogonal, a is a constant. The corresponding reciprocal vectors are $g_1 = (2\pi / a)a_x$ and $g_2 = (2\pi / a)a_y$. Due to symmetry only 1/8 of the Brillouin zone surrounding the point Γ needs to be considered, given by the triangle ΓXM in the reciprocal lattice shown in Fig. **12**. The equilateral triangular lattice has it primitive vectors shown in Fig. **13** are $a_1 = a\,a_x$ and $a_2 = (a/2)(a_x + \sqrt{3}a_y)$ and the corresponding reciprocal vectors are $g_1 = (2\pi / a)(a_x - a_y / \sqrt{3})$ and $g_2 = (4\pi / a)(a_y / \sqrt{3})$.

Note that for the periodic lattice the relative dielectric permittivity satisfies the condition that $\varepsilon_r(r) = \varepsilon_r(r + R)$ and therefore the reciprocal of the relative dielectric permittivity also satisfies the periodic condition $\varepsilon_r^{-1}(r) = \varepsilon_r^{-1}(r + R)$. The reciprocal of the relative dielectric permittivity $1/\varepsilon_r(r)$ needs to be as a Fourier series in terms of the reciprocal lattice vectors *G*. Thus

$$\frac{1}{\varepsilon_r(\mathbf{r})} = \sum_{\mathbf{G}'} \boldsymbol{\kappa}(\mathbf{G}') e^{j(\mathbf{G}'.\mathbf{r})} \qquad \textbf{(80)}$$

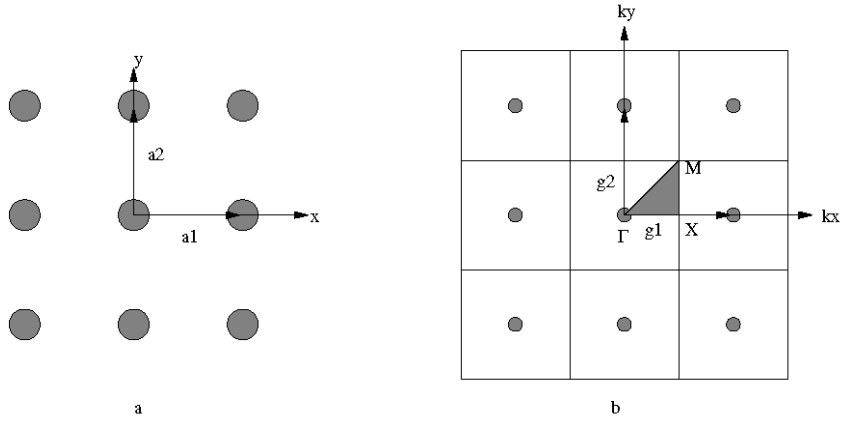

Figure 12: Schematic arrangement of two dimensional photonic crystal of "atoms" periodically placed in a square lattice with the primitive vectors shown for (a) the real space and (b) the reciprocal space. These "atoms" may be dielectric rods or holes in a dielectric block shown in the previous Fig. **11**.

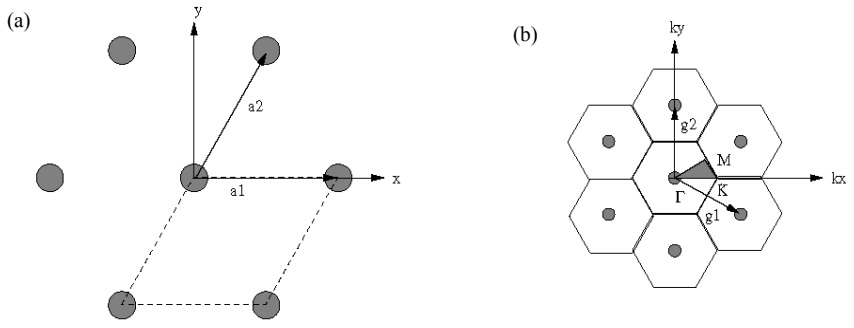

Figure 13: Schematic arrangement of two dimensional photonic crystal of "atoms" periodically placed in an equilateral triangular or hexagonal lattice with the primitive vectors shown for (a) the real space and (b) the reciprocal space. These "atoms" may be dielectric rods or holes in a dielectric block shown in the previous Fig. **11**.

where $\boldsymbol{\kappa}(\mathbf{G}')$ is the Fourier expansion term given by

$$\boldsymbol{\kappa}(\mathbf{G}') = \frac{1}{S}\int_S \frac{1}{\varepsilon_r(\mathbf{r})} e^{-j(\mathbf{G}'.\mathbf{r})} dS \tag{81}$$

integration is over the unit cell S.

For lattices with arbitrary distribution of the dielectric within the primitive cell with the primitive vectors redefined if necessary, the calculation of $\boldsymbol{\kappa}$ needs to be performed on a piecewise process numerically.

For the circular rods radius r, ε_{rb} embedded in a background ε_{ra}, an analytic derivation [6, 13] that provides the following result:

$$\boldsymbol{\kappa}(G') = \begin{cases} \dfrac{1}{\varepsilon_{ra}} f + \dfrac{1}{\varepsilon_{rb}}(1-f) & |G'| = 0 \\ \left(\dfrac{1}{\varepsilon_{ra}} - \dfrac{1}{\varepsilon_{rb}}\right) f \dfrac{J_1(|G'|R}{|G'|R} & |G'| \neq 0 \end{cases} \tag{82}$$

where the fill factor is $f = \pi r^2 / S$, S is the area of the primitive cell, either in the square or parallelogram lattice and typically given as $S = ab\sin\theta$, where a and b are the lengths of the primitive vectors and θ is the angle between them. Also $J_1(|G'|R)$ is the Bessel function of the first kind, order 1.

In the two-dimensional case, the plane wave incident on the photonic crystal may have its **H** vector normal to the plane of the crystal which implies that the components of the **E** field are in the plane of the crystal, which then becomes a Transverse Electric (TE) wave. Alternatively the **E** vector is normal to the plane, the components of the **H** field are in the plane of the photonic crystal, which becomes the Transverse Magnetic (TM) wave. The assumption that there is no variation in the z direction that implies $\partial/\partial z = 0$. For the TE case, $E_z = 0$ and Eqs. 43 to 44 show that both $H_x = H_y = 0$ and Eqs. 45 to 48 become

$$\frac{\partial H_z}{\partial y} = j\omega\varepsilon_0\varepsilon_r E_x \tag{83}$$

$$-\frac{\partial H_z}{\partial x} = j\omega\varepsilon_0\varepsilon_r E_y \tag{84}$$

$$\frac{\partial E_y}{\partial x} - \frac{\partial E_x}{\partial y} = -j\omega\mu H_z \tag{85}$$

Eliminating E_x and E_y from these Eqs. results in

$$\frac{\partial}{\partial x}\left(\frac{1}{\varepsilon_r}\frac{\partial H_z}{\partial x}\right) + \frac{\partial}{\partial y}\left(\frac{1}{\varepsilon_r}\frac{\partial H_z}{\partial y}\right) + \frac{\omega^2}{c^2} H_z = 0 \tag{86}$$

For the TM mode, $H_z = 0$ and $\partial/\partial z = 0$ and Eqs. 47 to 48 show that both $E_x = E_y = 0$. From the remaining Eqs. 43, 44 and 48 it follows

$$\frac{\partial E_z}{\partial y} = -j\omega\mu H_x \tag{87}$$

$$\frac{\partial E_z}{\partial x} = j\omega\mu H_y \tag{88}$$

$$\frac{\partial H_y}{\partial x} - \frac{\partial H_x}{\partial y} = j\omega\varepsilon_0\varepsilon_r E_z \tag{89}$$

Eliminating H_x and H_y from these equations

$$\frac{1}{\varepsilon_r}\left(\frac{\partial^2 E_z}{\partial x^2} + \frac{\partial^2 E_z}{\partial y^2}\right) + \frac{\omega^2}{c^2} E_z = 0 \tag{90}$$

The solution technique for these Eqs. is similar to the one-dimensional case: the H_z or the E_z component is a plane wave, $e^{-jk\cdot r}$ direction defined by r, modulated by a periodic function representing the photonic crystal, and this function is expanded as a Fourier series with unknown coefficients, $1/\varepsilon_r$ is also expressed in a Fourier series with known coefficents, and these terms are substituted in the appropriate wave equation. The testing functions are also plane waves and taking the inner products results in an eigenvalue matrix equation, which is solved numerically. Details are in the following sections.

2.2.1. Solution for the TE Polarization

This section discusses the TE mode case formulated in terms of H_z. Let

$$H_z = u(k,r)e^{jk\cdot r} \tag{91}$$

where $u(k, r+R) = u(k,r)$ which includes the periodicity of the crystal. Expanding this term in a Fourier series

$$u(k,r) = \sum_G h(k,G)e^{jG\cdot r} \tag{92}$$

which in turn results in

$$H_z = \sum_G h(k,G)e^{j(k+G)\cdot r} \tag{93}$$

Substituting for H_z from Eq. 93 and for $1/\varepsilon_r$ from Eq. 80 into Eq. 86, after simplification the result is

$$\sum_{G,G''} (\mathbf{k}+\mathbf{G})\cdot(\mathbf{k}+\mathbf{G}'')\kappa(\mathbf{G}''-\mathbf{G})h(k,G)e^{j(k+G'')\cdot r} = \frac{\omega^2}{c^2}\sum_{\mathbf{G}} h(k,G)e^{j(k+G)\cdot r} \tag{94}$$

where $G'' = G + G'$.

Taking the inner product of Eq. 94 with $e^{-j\mathbf{G}'.\mathbf{r}}$ and integrating over the unit cell

$$\sum_G (\mathbf{k}+\mathbf{G})\cdot(\mathbf{k}+\mathbf{G}')\kappa(\mathbf{G}'-\mathbf{G})h(k,G) = \frac{\omega^2}{c^2}h(k,G') \tag{95}$$

since

$$\int_S e^{j(G''-G').r}\,ds = \begin{cases} S & for \quad G'' = G' \\ 0 & for \quad G'' \neq G' \end{cases} \tag{96}$$

and similarly for G and G' for the right hand side of Eq. 95. This leads to the matrix equation:

$$\mathbf{Ah} = \boldsymbol{\lambda}\mathbf{h} \tag{97}$$

where $\lambda = \omega^2/c^2$. This Eq. is symmetric and hermitian and the eigenvalues are real and numerical solution is with standard subroutines.

2.2.2. Solution for the TM Polarization

The TM wave is polarized with the E_z field normal to the plane of the wafer and as discussed above $H_z = E_x = E_y = 0$ are zero, the transverse magnetic field components H_x and H_y are non zero. The E_z field is assumed to be given by the series

$$E_z = \sum_G \zeta(k,G) e^{j(k+G)\cdot r} \tag{98}$$

Substituting for E_z from Eq. 98 and for $1/\varepsilon_r$ from Eq. 80 into Eq. 90, after simplification the result is

$$\sum_{G,G''} (\mathbf{k}+\mathbf{G})^2 \kappa(\mathbf{G}''-\mathbf{G}) \zeta(k,G) e^{j(k+G'')\cdot r} = \frac{\omega^2}{c^2} \sum_{\mathbf{G}} \zeta(k,G) e^{j(k+G)\cdot r} \tag{99}$$

Again taking the inner product of Eq. 99 with $e^{-j\mathbf{G}'.\mathbf{r}}$ and integrating over the unit cell results in the following equation

$$\sum_G \kappa(\mathbf{G}'-\mathbf{G})(\mathbf{k}+\mathbf{G})^2 \zeta(k,G) = \frac{\omega^2}{c^2} \zeta(k,G') \tag{100}$$

This leads to a matrix eigenvalue Eq. which is nonsymmetric. To convert it to a symmetric version the substitution is made using the expression

$$b(k,G) = | K+G | \zeta(\mathbf{k},\mathbf{G}) \tag{101}$$

Multiplying both sides of the Eq. 100 by $|K+G|$ and substituting for $\zeta(k,G)$ results in the following equation

$$\sum_G | K+G | \kappa(\mathbf{G}'-\mathbf{G}) | K+G | b(k,G) = \frac{\omega^2}{c^2} b(k,G') \tag{102}$$

which leads to the matrix eigenvalue equation

$$\mathbf{Ab} = \boldsymbol{\lambda}\mathbf{b} \tag{103}$$

which is symmetric and hermitian.

Solutions of these matrix Eqs. have been performed for different values of k and the results from [6] are reproduced with permission. Fig. **14** shows the results for a square lattice rod array, the radius is $0.2a$, a is the lattice spacing, the rod $\varepsilon_r ra = 12.25$ in air. These calculations were with 256 plane waves and both the TE and TM modes are plotted. The TM modes show a band gap where no propagation occurs.

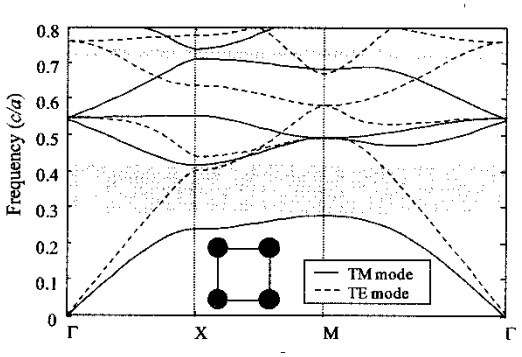

Figure 14: Band diagram for the two dimensional photonic crystal of "atoms," dielectric rods radius *a*, radius is 0.2*a*, *a* is the side of the square lattice, the rod ε_r=12.25 in air. (with permission from John Wiley &Sons, from, Photonic Crystals, by Prather, Shi, Sharkawy, Murakowski, Schneider, 2009, John Wiley, [6]).

An equilateral triangular lattice calculation with rods radius $0.4a$, again with the $\varepsilon_{ra} = 12.25$ in air is shown in Fig. **15**. The TE mode shows a bandgap but not the TM modes.

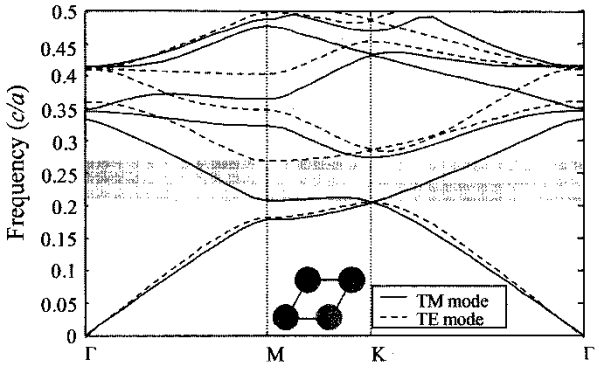

Figure 15: Band diagram for the two dimensional photonic crystal of "atoms," dielectric rods radius *a*, radius is 0.4*a*, *a* is the side of the equilateral triangular lattice, the rod ε_r=12.25 in air. (with permission from John Wiley &Sons, from Photonic Crystals, by Prather, Shi, Sharkawy, Murakowski, Schneider, 2009, John Wiley, [6]).

2.3. Three-dimensional Plane Wave Expansion Method

For three dimensional crystals, the vector wave Eq. needs to be solved, the solutions cannot be separated into the TE and TM modes. The procedure follows the earlier discussions, the expression for the $1/\varepsilon_r$ is obtained by Fourier transform and the wave Eq. in the H field in Eq. 36 is used for these calculations. The H is expressed as a series in which two polarizations are included and thus form separate series. Substituting in the wave equation, simplifying and then taking the inner product with a set of testing functions results in a matrix Eq. which is then solved for different values of the propagation vector k. This vector needs only to cover the basic Brillouin zone and often this is reduced because of symmetry considerations as seen in the two-dimensional structure solutions.

The three-dimensional structures are analyzed using the **H** formulation in Eq. 36 since it is hermitian and repeated here for clarity.

$$\nabla \times \frac{1}{\varepsilon_r} \nabla \times H = \frac{\omega^2}{c^2} H \tag{104}$$

The lattice dielectric structure is periodic and may be expressed in a Fourier series of the form

$$\frac{1}{\varepsilon_r(\mathbf{r})} = \sum_{\mathbf{G}'} \boldsymbol{\kappa}(\mathbf{G}') e^{j(\mathbf{G}'.\mathbf{r})} \tag{105}$$

where $\boldsymbol{\kappa}(\mathbf{G}')$ is the Fourier expansion term given by

$$\boldsymbol{\kappa}(\mathbf{G}') = \frac{1}{V} \int_S \frac{1}{\varepsilon_r(\mathbf{r})} e^{-j(\mathbf{G}'.\mathbf{r})} dV \tag{106}$$

integration is over the unit cell volume V, G is the reciprocal lattice vector of the form

$G = m_1 g_1 + m_2 g_2 + m_3 g_3$ where g_i are the primitive reciprocal lattice vectors and m_i are integers. The propagation vector is given as $k = a_x x + a_x y + a_x z$. As in the two-dimensional case, the plane of the form $e^{j(k+G)\cdot r}$ defines the direction of the propagation and the direction of the H vector is normal to this direction and therefore may have any one of two orthogonal components given by a_G^1 and a_G^2, furthermore

these vectors, a_G^1, a_G^2, and $(k+G)$ are mutually orthogonal to each other. Thus the Fourier components of the H field takes the form

$$H_k(r) = \sum_G \sum_{\eta=1}^{2} h_G^\eta a_G^\eta e^{j(k+G)\cdot r} \tag{107}$$

Substituting in the wave Eq. for H and $1/\varepsilon_r$ from Eqs. 107 and 105 in Eq. 107 and simplifying results in the following equation

$$-\sum_G \sum_{G''} \sum_{\eta=1}^{2} h_G^\eta \kappa(G''-G)(k+G'')\times[(k+G)\times a_G^\eta] e^{j(k+G'')\cdot r} = \frac{\omega^2}{c^2} \sum_G \sum_{\eta=1}^{2} h_G^\eta a_G^\eta e^{j(k+G)\cdot r} \tag{108}$$

where $G'' = G + G'$.

The next step is to take the inner product with the plane wave testing function $e^{-j(k+G')\cdot r}$ and subsequently include the direction vectors a_G^η. Note that as before

$$\int_V e^{j(G-G')\cdot r} dv = \begin{cases} V & for \quad G = G' \\ 0 & for \quad G \neq G' \end{cases} \tag{109}$$

Initially taking the inner product with the plane wave $e^{-j(k+G')\cdot r}$, this Eq. becomes

$$-\sum_{G'} \sum_{\eta=1}^{2} h_G^\eta \kappa(G-G')(k+G')\times[(k+G')\times a_{G'}^\eta] = \frac{\omega^2}{c^2} \sum_{\eta=1}^{2} h_G^\eta a_G^\eta \tag{110}$$

Taking the scalar product of both sides of the above Eq. 110 with a_G^1 and after further simplification

$$-\sum_{G'} \sum_{\eta=1}^{2} h_G^\eta \kappa(G-G')[(k+G')\times a_{G'}^\eta]\cdot[(k+G')\times a_G^1] = \frac{\omega^2}{c^2} h_G^1 \tag{111}$$

As stated above, $(k+G)$, a_G^1 and a_G^2 are mutually orthogonal to each other which implies that

$$(k+G')\times a_G^1 = |\, k+G' \,| \, a_G^2 \tag{112}$$

$$(k+G')\times a_G^2 = -|\, k+G' \,| \, a_G^1 \tag{113}$$

and the above Eq. 111 becomes

$$\sum_{G'} \kappa(G-G') \,|\, k+G' \,||\, k+G' \,|\, [h_{G'}^1 (a_{G'}^2 \cdot a_G^2) - h_{G'}^2 (a_{G'}^1 \cdot a_G^2)] = \frac{\omega^2}{c^2} h_G^1 \tag{114}$$

the assumption here is that the vector $a_{G'}^1$ of the left hand side of Eq. 111 and the vector a_G^2 of the testing function are not orthogonal to each other.

Similarly, taking the scalar product of both sides of Eq. 110 with a_G^2 obtains

$$-\sum_{G'} \kappa(G-G') \,|\, k+G' \,||\, k+G' \,|\, [-h_{G'}^1 (a_{G'}^2 \cdot a_G^1) + h_{G'}^2 (a_{G'}^1 \cdot a_G^1)] = \frac{\omega^2}{c^2} h_G^2 \tag{115}$$

again assuming that the vector $a_{G'}^2$ of the left hand side of Eq. 111 and the vector a_G^1 of the testing function are not orthogonal to each other.

Combining these two Eqs. 114 and 115

$$\sum_{G'}\sum_{\eta=1}^{2}\kappa(G-G')\,|\,k+G'\,||\,k+G'\,|\begin{pmatrix} a^2_{G'}\cdot a^2_G & -a^1_{G'}\cdot a^2_G \\ -a^2_{G'}\cdot a^1_G & a^1_{G'}\cdot a^1_G \end{pmatrix} h^\eta_G = \frac{\omega^2}{c^2}h^\eta_G \tag{116}$$

The solution method is to first obtain the coefficients κ, then choose the propagation vector k within the reduced Brillouin zone and after that solve the above matrix Eq. to obtain the eigenvalues and the corresponding eigenvectors of ω as a function of k.

Included is an example of a calculation of a cubic structure with spheres of air radius $0.45a$ embedded in a background of ε_r refractive index of 3.5. The dispersion diagram is shown in Fig. **16**.

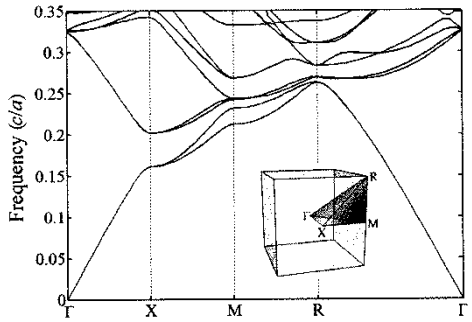

Figure 16: Band diagram for the three dimensional photonic crystal of "atoms," air spheres radius $0.45a$, refrative index of 3.5 in a cubic structure side *a.* (with permission from John Wiley &Sons, from, Photonic Crystals, by Prather, Shi, Sharkawy, Murakowski, Schneider, 2009, John Wiley, [6]).

The Joanopoulos group in MIT have published [14] code that does the plane wave calculations and available at: http://ab-initio.mit.edu/mpb/.

2.4. Photonic Crystal Slab Structures

The slab structures with periodic holes are the most widely investigated photonic crystals, a sketch of such a structure is shown in Fig. **17**. The slab is usually a semiconductor, Silicon or a III-V material, for example GaAs/AlGaAs or InP/InGaAsP, with periodic holes. The absence of holes constitutes a defect, as shown in Fig. **18** and becomes a waveguide.

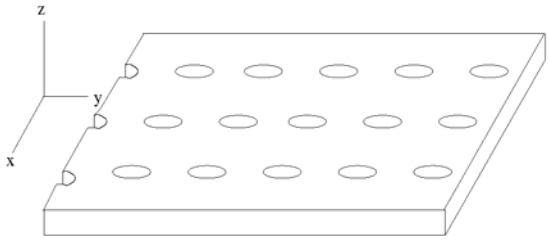

Figure 17: Slab thickness t, effective dielectric constant $\boldsymbol{\epsilon_r}$, with through holes periodically placed, either in a square or triangular lattice.

Note that a wave propagating along the slab and guided by it has its propagation vector $k_{\|}$ real and the k_z vector is now imaginary. Thus

$$k = k_{\|} + k_z \tag{117}$$

The usual $\omega - k_{\|}$ dispersion diagram has a light line as shown in Fig. **17** which defines the guided modes of the slab. The modes with velocity greater than c/n_{eff} radiate, where $n_{eff} = \sqrt{\varepsilon_{r-eff}}$ is the effective index of the slab.

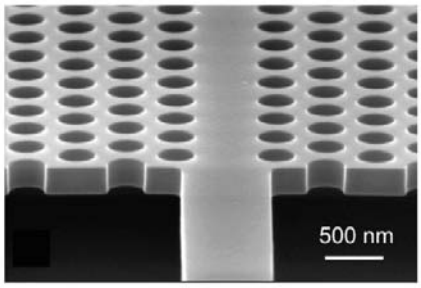

Figure 18: Slab of Silicon with holes in a triangular lattice. The waveguide defect is excited by the input tab shown in this figure. (reproduced with permission from OSA, in Optics Express, 11, 22, 2927-2939, 2007, authors S. J. McNab, N. Moll, Y. A. Vlasov).

The slab structure is strictly not a photonic crystal as it in not periodic in the plane normal to the slab, in Fig. **17** this is the z direction. The analysis of this structure may assume that similar slabs are stacked in the z direction, which then makes it periodic. Since the stacked version is similar to the three dimensional lattice structure, the analysis follows the discussion outlined earlier. However, the modes that are guided by the slab have $k_{\|}$ real and k_z imaginary, which implies that the modes decay $\pm z$ direction from the slab to its periodic boundary. Unlike the two-dimensional case, the modes cannot be separated into the TE and TM classes, however, if the slab structure is symmetric in the z direction, then even and odd modes may be calculated. An approach to the periodically stacked slab is to calculate the mode structure of the slab using the method for three dimensional crystal discussed above, confining the propagation vector k to the plane of the slab only examines the guided modes. The light line which becomes the light cone may then be superimposed on the dispersion diagram.

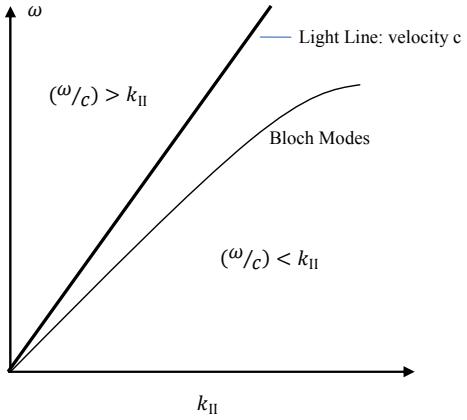

Figure 19: Dispersion diagram of the modes in a slab structure. When the phase velocity is greater than the velocity of light c, assuming that the space between the slabs is free space, the modes radiate. This boundary between guided modes and radiating modes is defined by the light line, below this light line, guided modes propagate, these are the Bloch modes.

The reciprocal vectors take the form

$$G = m_1 g_1 + m_2 g_2 + m_3 g_3 = G_{xy} + m_3 g_3 \tag{118}$$

and

$$g_3 = a_z \frac{2\pi}{\ell} = a_z g_3 \tag{119}$$

where ℓ is the periodic spacing of the slabs and $m_i, i = 1,2,3$ are integers. The H vector is given by the following summation, as above:

$$H_k(r) = \sum_G \sum_{\eta=1}^{2} h_G^\eta a_G^\eta e^{j(k+G)\cdot r} \tag{120}$$

Following [15], to calculate the even and odd modes which are with respect to the z direction, the propagation vector $(k+G)$ becomes $(k_{xy} + m_1 g_1 + m_2 g_2 + m_3 a_z g_3)$ for one plane wave and the other is defined by $(k_{xy} + m_1 g_1 + m_2 g_2 - m_3 a_z g_3)$. Note that the polarization vectors a_G^η with $\eta = 1, 2$, are orthogonal to each other and the corresponding plane wave propagation vectors $(k+G)$ as defined above. The polarization vectors are decomposed into their components parallel and perpendicular to the plane of the slab:

$$a_G^\eta = a_{G,xy}^\eta + a_{G,z}^\eta = a_{m_1 m_2 m_3, xy}^\eta + a_{m_1 m_2 m_3, z}^\eta \tag{121}$$

Since the even and odd modes relate to the z direction, the polarization vectors are of the form

$$\begin{cases} a^1_{m_1 m_2 m_3, z} &= -a^1_{m_1 m_2 (-m_3), z} \\ a^1_{m_1 m_2 m_3, xy} &= a^1_{m_1 m_2 (-m_3), xy} \end{cases}, \quad \begin{cases} a^2_{m_1 m_2 m_3, z} &= a^2_{m_1 m_2 (-m_3), z} \\ a^1_{m_1 m_2 m_3, xy} &= -a^2_{m_1 m_2 (-m_3), xy} \end{cases} \tag{122}$$

The odd and even modes with respect to the z-direction requires in one mode for one of the two polarization vectors of **H** to be even and the other becomes odd, the other mode requires the first vector to be odd and the second vector to be even as shown above in equations. Substituting in the wave Eq. and taking the inner product the two solutions are:

$$\begin{aligned} \mathbf{H_k(r)} = \sum_{m_1 m_2} e^{(G_{xy} + k_{xy})\cdot r_{xy}} \Big[& h^2_{m_1 m_2 0} a^2_{z, m_1 m_2 0} \\ & + \sum_{m_3=1}^{\infty} 2 (h^1_{m_1 m_2 m_3} a^1_{z, m_1 m_2 m_3} + h^2_{m_1 m_2 m_3} a^2_{z, m_1 m_2 m_3}) \cos(m_3 g_3 z) \\ & + \sum_{m_3=1}^{\infty} 2 (h^1_{m_1 m_2 m_3} a^1_{xy, m_1 m_2 m_3} + h^2_{m_1 m_2 m_3} a^2_{xy, m_1 m_2 m_3}) \sin(m_3 g_3 z) \Big] \end{aligned} \tag{123}$$

with $h^1_{m_1 m_2 0} = 0$. This is the even or TE like mode

and

$$\begin{aligned} \mathbf{H_k(r)} = \sum_{m_1 m_2} e^{(G_{xy} + k_{xy})\cdot r_{xy}} \Big[& h^1_{m_1 m_2 0} a^1_{z, m_1 m_2 0} \\ & + \sum_{m_3=1}^{\infty} 2 (h^1_{m_1 m_2 m_3} a^1_{z, m_1 m_2 m_3} + h^2_{m_1 m_2 m_3} a^2_{z, m_1 m_2 m_3}) \sin(m_3 g_3 z) \\ & + \sum_{m_3=1}^{\infty} 2 (h^1_{m_1 m_2 m_3} a^1_{xy, m_1 m_2 m_3} + h^2_{m_1 m_2 m_3} a^2_{xy, m_1 m_2 m_3}) \cos(m_3 g_3 z) \Big] \end{aligned} \tag{124}$$

with $h^2_{m_1 m_2 0} = 0$. This is the odd or TM like mode.

An example of this calculation is shown in the Fig. **20** from [6], slab thickness is $0.5\,a$, ε_r is 12, holes are in a triangular lattice, diameter $0.5\,a$, spacing between slabs ℓ is $4\,a$.

3. OTHER PLANE WAVE CALCULATION APPROACHES FOR THE SLAB STRUCTURE WITH HOLES

The other approach is to use perfectly matched (PML) layers, [15], above and below the slab, Sacks *et al.* [16] and Prather *et al.* [6] have discussed this approach. Interested readers should consult these references.

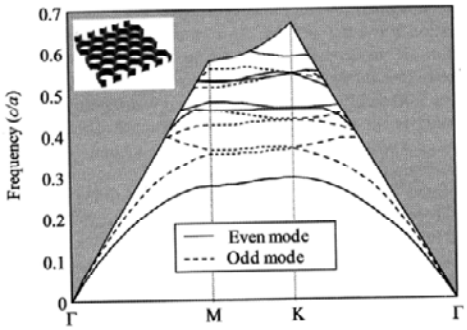

Figure 20: Calculations of the band structure of a slab with triangular holes using the stacked slab approach discussed in this section, for the even and odd modes shown with the light cone, assuming that the space between the slabs is free space, where the wave velocity is c. (with permission from Prather, Shi, Sharkawy, Murakowski, Schneider and John Wiley, [6]).

3.1. Finite Difference Time Domain Method

The finite difference time domain (FDTD) method is based on the direct solution of the Maxwell curl equations, proposed by Yee [17]. The initial formulation was in Cartesian coordinates with structured meshes and many applications have retained this format, even though unstructured meshes and formulation in other coordinates have also been developed. The advantages of the FDTD method is that it is simple to implement, a variety of media and structures may be analyzed, the algorithm is suitable for parallel computation, with the Cartesian coordinates and structured mesh there is no matrix Eq. to solve. The disadvantages are that it is computationally intensive and slow. In this section, the method is discussed in some detail and application for the analysis photonic crystal structures are outlined.

The Eqs. to be solved are, assuming no conductivity

$$\nabla \times E = -\mu \frac{\partial H}{\partial t} \quad \nabla \times H = \varepsilon \frac{\partial E}{\partial t} \tag{125}$$

and expanding in Cartesian coordinates these become

$$\frac{\partial E_z}{\partial y} - \frac{\partial E_y}{\partial z} = -\mu_0 \frac{\partial H_x}{\partial t} \tag{126}$$

$$\frac{\partial E_x}{\partial z} - \frac{\partial E_z}{\partial x} = -\mu_0 \frac{\partial H_y}{\partial t} \tag{127}$$

$$\frac{\partial E_y}{\partial x} - \frac{\partial E_x}{\partial y} = -\mu_0 \frac{\partial H_z}{\partial t} \tag{128}$$

$$\frac{\partial H_z}{\partial y} - \frac{\partial H_y}{\partial z} = \varepsilon_0 \varepsilon_r \frac{\partial E_x}{\partial t} \tag{129}$$

$$\frac{\partial H_x}{\partial z} - \frac{\partial H_z}{\partial x} = \varepsilon_0 \varepsilon_r \frac{\partial E_y}{\partial t} \tag{130}$$

$$\frac{\partial H_y}{\partial x} - \frac{\partial H_x}{\partial y} = \varepsilon_0 \varepsilon_r \frac{\partial E_z}{\partial t} \tag{131}$$

The exercise is now to solve these Eqs. simultaneously, the Yee [17] approach is to use central differences in both the spatial domain and the time domain. The spatial partial derivative is approximated by the usual Taylor's series central difference expansion for the i^{th} point.

$$\frac{\partial f}{\partial u} = \frac{f^n_{i+1/2} - f^n_{i-1/2}}{\Delta u} \tag{132}$$

where u is the spatial coordinate and n is the time coordinate. Note that $(i \pm 1/2)$ are grid points at which f^n is known so that the first order derivative in now at the i^{th} point. The question of why this is not $i+1$ and $i-1$ will become obvious in due course.

The time difference Eq. is of the form

$$\frac{\partial g^n}{\partial t} = \frac{g_i^{n-1/2} - g_i^{n-1/2}}{\Delta t} \tag{133}$$

The time step is from $n-1/2$ to $n+1/2$, again the question of why is this not $n-1$ to $n+1$ will become obvious as the discussion progresses.

Assume that a Cartesian three dimensional regular grid of points over the computational domain, the spacings in the x, y, z directions are $\Delta x, \Delta y, \Delta z$ respectively, the numbering is i, j, k corresponding to the three coordinates x, y, z, the time step parameter is Δt and defines the time as n which corresponds to $n\Delta t$ time steps. Thus

$$i, j, k \equiv i\Delta x, j\Delta y, k\Delta z \quad and \quad n \equiv n\Delta t$$

The space mesh has two interpenetrating meshes, one for the H fields and the other for the E fields and these are separated in space by $\Delta x/2, \Delta y/2, \Delta z/2$. Each H field point is surrounded by six E field points, two in in each of the coordinate directions, half mesh spacing distance from the H field point. Each of these six E field points in turn are also surrounded by six H field points, two in in each of the coordinate directions, half mesh spacing distance from the E field point. The time step Δt is also split in half, to obtain $\Delta t/2$. Each point in each of the meshes has all three components of the field H_x, H_y, H_z defined at each point in the H mesh, similarly E_x, E_y, E_z are defined at each mesh point in the E mesh. Thus the H Eqs. are solved first for the time at $(n+1/2)\Delta t$ for the value of H component terms resolved with the corresponding E terms at time $n\Delta t$. The E Eqs. are next solved at time $(n+1)\Delta t$ with the H terms at time $(n+1/2)\Delta t$. The component Eqs. 126 to 131 are solved with the finite difference form shown below.

Now consider the Eq. in 126

$$-\mu_0 \frac{\partial H_x}{\partial t} = \frac{\partial E_z}{\partial y} - \frac{\partial E_y}{\partial z} \tag{134}$$

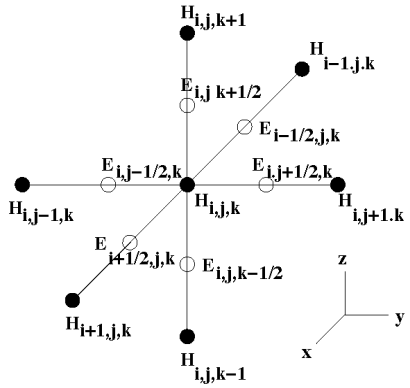

Figure 21: The three-dimensional FDTD H-mesh showing the H and E nodes and the spacings for the H component equations.

The finite difference form may be written with the time $n+1/2$ and $n-1/2$ for the H_x field at the (i,j,k) point and time of n for the E_z and E_y components defined at points midway between the regular grid points, as shown in Fig. **21**:

$$H_x\,|_{i,j,k}^{n+1/2} = H_x\,|_{i,j,k}^{n-1/2} - \frac{\Delta t}{\mu_0}\left[\frac{(E_z\,|_{i,j+1/2,k}^{n} - E_z\,|_{i,j-1/2,k}^{n})}{\Delta y} - \frac{(E_y\,|_{i,j,k+1/2}^{n} - E_y\,|_{i,j,k-1/2}^{n})}{\Delta z}\right] \tag{135}$$

In this equation, the H_x term is defined at the H-mesh grid point i,j,k but the E_y and E_z components are defined at points midway between the H grid points. The remaining difference Eqs. for the time derivative Eqs. of H_y and H_z in 127 and 128 are

$$H_y\,|_{i,j,k}^{n+1/2} = H_y\,|_{i,j,k}^{n-1/2} - \frac{\Delta t}{\mu_0}\left[\frac{(E_x\,|_{i,j,k+1/2}^{n} - E_x\,|_{i,j,k-1/2}^{n})}{\Delta z} - \frac{(E_z\,|_{i+1/2,j,k}^{n} - E_z\,|_{i-1/2,j,k}^{n})}{\Delta x}\right] \tag{136}$$

and

$$H_z\,|_{i,j,k}^{n+1/2} = H_z\,|_{i,j,k}^{n-1/2} - \frac{\Delta t}{\mu_0}\left[\frac{(E_y\,|_{i+1/2,j,k}^{n} - E_y\,|_{i-1/2,j,k}^{n})}{\Delta x} - \frac{(E_x\,|_{i,j+1/2,k}^{n} - E_x\,|_{i,j-1/2,k}^{n})}{\Delta y}\right] \tag{137}$$

The Eqs. 129, 130, and 131 for the **E** components in finite difference form for the E-mesh point i,j,k by analogy to the above **H** Eqs. are given below.

$$E_x\,|_{i,j,k}^{n+1} = E_x\,|_{i,j,k}^{n} + \frac{\Delta t}{\varepsilon_0\varepsilon_r}\left[\frac{(H_z\,|_{i,j+1/2,k}^{n+1/2} - H_z\,|_{i,j-1/2,k}^{n+1/2})}{\Delta y} - \frac{(H_y\,|_{i,j,k+1/2}^{n+1/2} - H_y\,|_{i,j,k-1/2}^{n+1/2})}{\Delta z}\right] \tag{138}$$

$$E_y\,|_{i,j,k}^{n+1} = E_y\,|_{i,j,k}^{n} + \frac{\Delta t}{\varepsilon_0\varepsilon_r}\left[\frac{(H_x\,|_{i,j,k+1/2}^{n+1/2} - H_x\,|_{i,j,k-1/2}^{n+1/2})}{\Delta z} - \frac{(H_z\,|_{i+1/2,j,k}^{n+1/2} - H_z\,|_{i-1/2,j,k}^{n+1/2})}{\Delta x}\right] \tag{139}$$

$$E_z\,|_{i,j,k}^{n+1} = E_z\,|_{i,j,k}^{n} + \frac{\Delta t}{\varepsilon_0\varepsilon_r}\left[\frac{(H_y\,|_{i+1/2,j,k}^{n} - H_z\,|_{i-1/2,j,k}^{n})}{\Delta x} - \frac{(H_x\,|_{i,j+1/2,k}^{n} - H_x\,|_{i,j-1/2,k}^{n})}{\Delta y}\right] \tag{140}$$

Thus, the H mesh is defined at the at the i,j,k points and whole number additions to these points but also at the half spacing points, and similarly the E mesh points are defined at whole numbers. With these equations, the time marches from n to $n+1/2$ and then from $n+1/2$ to $n+1$ and each field components is updated with this marching algorithm.

3.2. Stability and Numerical Dispersion

There are restrictions on the size of the mesh increments $\Delta x, \Delta y, \Delta z$ and the time increment Δt to ensure that the marching algorithm is stable and accurate, so that the field values do not oscillate with the iterations and do not become very large. To ensure stability according to Taflov [18]

$$\Delta t \le \frac{1}{c\sqrt{\frac{1}{(\Delta x)^2} + \frac{1}{(\Delta y)^2} + \frac{1}{(\Delta z)^2}}} \tag{141}$$

For a cubic grid, when $\Delta x = \Delta y = \Delta z = \Delta$, then this limit becomes

$$\Delta t \le \frac{\Delta}{c\sqrt{3}} \tag{142}$$

The discretization of the computational domain results in so called numerical dispersion. Thus the phase delay in some radial direction is determined by the propagation times the radial distance. However in this simulation method the delay is determined by the need to follow the discretized grid. Taflov [18] estimates that this numerical dispersion has the form

$$\left[\frac{1}{c\Delta t}\sin\left(\frac{\omega\Delta t/2}{2}\right)\right]^2=\left[\frac{1}{\Delta x}\sin\left(\frac{k_x\Delta x}{2}\right)\right]^2+\left[\frac{1}{\Delta y}\sin\left(\frac{k_y\Delta y}{2}\right)\right]^2+\left[\frac{1}{\Delta z}\sin\left(\frac{k_z\Delta z}{2}\right)\right]^2$$

In the limit of small $\Delta t,\Delta x,\Delta y,\Delta z$, this Eq. becomes

$$\left(\frac{\omega}{c}\right)^2=k_x^2+k_y^2+k_z^2 \qquad \textbf{(143)}$$

Thus, decreasing the spatial increment to $\lambda_{min}/20$ in general reduces the numerical dispersion significantly. However, most codes use $\lambda_{min}/10$ as the standard and this is adequate for most structures. Note that λ_{min} is the smallest value of the wavelength in the structure being analyzed.

3.3. Boundary and Excitation Conditions

The usual Diritchlet and Neumann conditions for both the E and H fields are implemented by setting the corresponding field node values to zero for the Diritchlet condition, and the Neumann condition is implemented by use of image points. Radiation boundaries requires the implementation of the absorbing boundary conditions in which none of the propagating fields leaving should return to affect the fields in the computational domain. In these absorbing boundary conditions, the computational domain is surrounded by lossy layers in which the impedance defined by the ratio of $Z=\sqrt{\mu/\varepsilon}$ with both μ and ε complex, is kept constant and equal to that within the domain. The loss terms are increased with each layer so that the energy is all absorbed by the final layer reached. The perfectly matched layer (PML) boundary proposed by Bérenger [15] is generally considered the standard to meet. A detailed discussion of these layers is in the books by Bérenger [19] and Taflov [18] and interested readers should refer to these books and related articles.

The excitation at any boundary node may be either the sinusoidal or pulsed excitation with a specific direction of propagation defined by the k vector. With sinusoidal excitation at particular nodes within the computational domain, the steady state solution is reached after some number of iterations and the magnitude and phase of the component fields is obtained. For transient simulations, the usual technique is to use a pulsed excitation in the form of a Gaussian or other shape, which is shifted in frequency so that the range of frequencies of interest are present. The narrower the pulse, the wider is range of frequencies present. The time domain response at the output nodes is then Fourier transformed to obtain the frequency response.

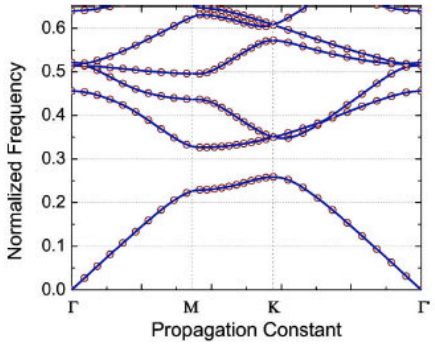

Figure 22: Calculations of the band structure of a slab with triangular holes using the non-orthogonal 2-D FDTD scheme compared to the 2-D PWE scheme. This is for the TE modes, slab effective index of 2.76 and air holes r/a of 0.3. (reproduced with permission from the IEEE, from the Journal of Lightwave Technology, 2007, 25 (9), 2612-2617, authors W. Kuang, W. J. Kim, J. D. O'Brien).

For periodic structures, the propagation through the structure is modeled by taking the output at the boundaries and using this as the excitation at the input repeatedly until steady state is reached. In photonic crystals, this is effectively the Bloch conditions which have to be satisfied. Thus, the unit cell in three dimensions is subdivided into many subcells and the propagation through this cell is calculated with specific excitation conditions, usually a pulsed excitation with a particular propagation direction defined by k. The Fourier transform of the temporal response extracts the resonances. Performing this for all the desired directions within this primitive cell obtains the band structure.

The slab structures discussed above have both rectangular and triangular hole grids. The triangular hole grids are not simply modeled in the Cartesian coordinate FDTD codes and use non-orthogonal FDTD formulation as discussed by Kuang, Kim and O'Brien [20]. An example of this calculation is shown in Fig. **22**

3.4. Propagation Calculations

The FDTD approach also allows the calculation of propagation in photonic crystals of finite size, for example the structure shown in Fig. **18**. The plane wave technique is not able to do this as it only deals with infinite structures.

4. OTHER METHODS OF CALCULATING BAND DIAGRAMS

Other methods for calculating the band diagrams of photonic crystals include the array of methods used in solid state physics for the electronic band diagrams of crytalline material and also the finite difference and finite element methods, many of these are available in the literature.

REFERENCES

[1] Ho KM, Chan CT, Soukoulis CM. Existence of a photonic band gap in periodic dielectric structures. Phys Rev Lett 1990; 65: 3152-3155.

[2] Li Z-Y, Lin L-L. Photonic band structures solved by a plane-wave-based transfer-matrix method. Phys Rev E 2003; 67: 046607.

[3] Pendry JB. Calculating photonic band structure. J Phys-Condens Mat 2003; 8: 1085-1108.

[4] Mias C, Webb JP, Ferrari RL. Finite element modeling of electromagnetic waves in doubly and triply periodic structures. IEE Proc-Optoelectron 1999; 146: 111-118.

[5] Joannopoulos JD, Mead RD, Winn JN. Photonic Crystals. Princeton. Princeton University Press, 1995.

[6] Prather DW, Shi S, Sharkawy A, Murakowski J, Schneider GJ. Photonic Crystals. John Wiley, 2009.

[7] Ashcroft NW, Mermin ND. Solid State Physics. Saunders Co., 1976.

[8] Kittel C. Introduction to Solid State Physics. 6th edition. John Wiley, 1986.

[9] Meade RD, Rappe AM, Brommer KD, Joannopoulos JD. Finite element modeling of electromagnetic waves in doubly and triply periodic structures. Phys Rev B, 1993; 48(11):8434-8437.

[10] Johnson SG, Fan S, Villeneuve PR, Joannopoulos JD. Guided modes in photonic crystal slabs. Phys Rev B 1999; 60(6): 5751-5758.

[11] Plihal M, Shambrook A, Marududin AA, Ping S. 2-dimensional photonic band structures. Opt Commun 1991; 80: 199-205.

[12] Plihal M, Marududin AA. Photonic band structure of 2-dimensional systems - the triangular lattice. Phys Rev B, 1991; 44: 8565-857

[13] Lourtioz J-M, Benisty H, Berger V, Gerad J-M, Maystre D, Tchelnokov A. Photonic Crystals. Springer, 2005.

[14] Johnson SG, Joannopoulos JD. The MIT Photonic-Bands Package Homepage, http://ab-initio.mit.edu/mpb/, version 4.2. 2009.

[15] Bérenger JP. A perfectly matched layer for the Absorption of electromagnetic waves. J Comput Phys 1994; 115:185-200.

[16] Sacks ZE, Kingsland DM, Lee R, Lee J. A perfectly matched anisotropic absorber for use as and absorbing boundary condition. IEEE Trans Antenn Propag 1995; AP-43:1460-1463.

[17] Yee KS. Numerical solution of initial boundary value problems involving Maxwell's Eqs. in isotropic media. IEEE Trans Antenn Propag, 1966, AP-14: 302- 307.

[18] Taflov A. Computational Electrodynamics: The Finite-Difference Time Domain Method. 1st edition. Artech House, Boston, Massachusetts, 1995.

[19] Bérenger JP. Perfectly Matched Layer (PML) for Computational Electromagnetics. Morgan & Claypool Publishers. San Rafael, California, 2007.

[20] Kuang W, O'Brien JD. Finite-Difference Time Domain Method for non orthogonal unit-cell two-dimensional photonic crystals. J Lightwave Technol 2007; 25(9): 2612-26-17.

CHAPTER 3

Photonic Crystal Technologies: From Theories to Practice

Dennis W. Prather*, Shouyuan Shi, Ahmed Sharkawy, Janusz Murakowski and Garrett J. Schneider

Department of Electrical and Computer Engineering, University of Delaware, Newark, Delaware 19716, USA

Abstract: Photonic Crystals (PhCs) provide significant capabilities in terms of emission control, localization, guiding, dense integration, high-speed operation, and the ability to engineer the dispersion properties of a given material. As a result, they have led the way towards true miniaturization of nanophotonic circuits, and hold the key to achieving the long-sought goal of large-scale integrated photonic systems on a chip, including integrated photonic chemical/biological sensor devices. In this chapter, we present brief discussion and summary of major achievements in theory, applications and fabrication of photonic crystals. We present applications relying on engineering the confinement properties as well as the dispersive properties and present some of the fabrication techniques for both planar and three-dimensional photonic crystal structures.

Keywords: Photonic crystals, photonic crystals fabrication, photonic crystals engineering.

1. INTRODUCTION

Sensors have become pervasive in our society and have found their way into everything from common consumer gadgets to automobiles and high-tech spacecraft. Sensors and transducers can be used to measure temperature, pressure, humidity, light, stress, acceleration, vibration, torque, flow, composition, fatigue and detect the presence of chemical and biological toxins and pollutants. The current market for sensors in the US alone is tabbed at $10 billion and is projected to grow to over $12 billion by 2010 [1]. However, the ability to quickly and accurately sense chemical and biological hazards in our environment has become especially critical in light of the past attacks on postal facilities and government offices and the ongoing threat of chemical/biological terrorism. Similarly, recent headlines concerning influenza pandemics and antibiotic-resistant bacteria further underscore the pressing need for chem/bio sensing capabilities. Therefore, research teams are attempting to design an economical, compact, low power, light weight sensor capable of accurately detecting common chemical and biological hazards in real time.

There is a growing need for miniature low-cost sensors for use in monitoring environmental conditions. Applications range from environmental pollution monitoring, industrial process control and homeland security threat detection to biomedical diagnostics. Integrated opto-chemical sensors [2] can provide the required functionality by monitoring chemistry induced changes in the refractive, absorptive, or luminescent properties of materials.

The unique dispersion properties of photonic crystals (PhCs), and their ability to manipulate light on a scale commensurate with the wavelength, make them a promising platform for such chem-bio sensing applications [3, 4]. Properly engineering the dispersion properties of the material enables the creation of multiple, dense, parallel sensors monitoring different chemical reactions in a device much smaller than a typical optical sensor. Dispersion-guiding PhC structures enable the use of lower refractive index materials because the creation of a bandgap is not necessary. This in turn improves coupling efficiency into the device.

The remainder of this section provides a brief historical introduction to PhCs as a field of research, including an overview of their fundamental electromagnetic properties and the primary methods used to

***Address correspondence to Dennis W. Prather:** Electrical and Computer Engineering Department, University of Delaware, 140 Evans Hall, Newark, Delaware 19716, USA; Email: dprather@ee.udel.edu

Marco Pisco, Andrea Cusano and Antonello Cutolo (Eds)
All rights reserved-© 2012 Bentham Science Publishers

analyze them. Section 2 provides a description of devices and applications of PhCs that are based on strong confinement due to photonic band gaps. Section 3 describes an alternative device paradigm in PhCs, namely dispersion engineering, which affords such effects as self-collimation for structureless guiding, and so-called superprism, enabling compact, broadband beam steering and wavelength-division multiplexing. Section 4 presents an overview of techniques that have been explored and developed to meet the challenges of fabricating PhC devices.

1.1. Overview and History of Photonic Crystals

The field of PhCs can be thought of as merely a generalization of the conventional one-dimensional (1D) thin-film stack, wherein layers of two or more different optical materials are arranged in a periodic fashion. In such devices, it is well known that certain frequencies are transmitted while others are not. As the index contrast between the alternating layers is increased, the selectivity of the transmitted and reflected wavelengths is also increased. When generalized to two- and three-dimensions, this selectivity gives rise to high mode confinement.

While 1D thin-film stacks have been known for over a century, their generalization to higher dimensions was not proposed until the 1970s by Bykov [5-8] as a potential means of inhibiting spontaneous emission. Bykov proposed the use of a periodic structure that served to inhibit certain electromagnetic frequencies, thereby disallowing spontaneous emission. This type of structure has recently come to be called a "photonic crystal and it can inhibit the propagation of light over a certain band of wavelengths, while allowing other bands to propagate. Such behavior may give rise to a "photonic bandgap" (PBG), analogous to the electronic bandgap in semiconductor materials. An example of a simple, easily fabricated periodic structure that may exhibit the property of a bandgap is shown in Fig. **1**.

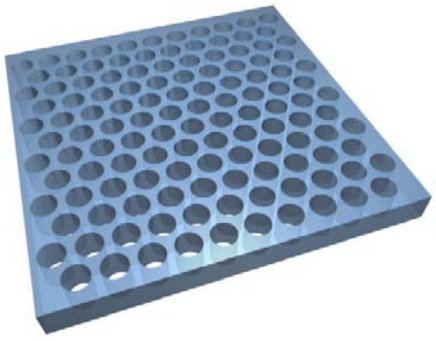

Figure 1: Periodic structure of air holes in a high-index finite-height substrate. Such a structure can prohibit propagation for a certain band of frequencies called a photonic bandgap.

These devices ultimately became known as photonic-bandgap (PBG) structures. In a similar vein, Yablonovitch [9] proposed a structure where an electronic and photonic gap overlapped in energy; such a structure would be incapable of light emission by recombination, thereby making it possible to enhance the performance of lasers, heterojunctions, bipolar transistors, and solar cells. Subsequent to this work, John [10] proposed using such structures for the localization of light in strongly scattering dielectric structures. In each of these cases, the underlying idea was to engineer the properties of photons (*i.e.,* electromagnetic modes) in a photonic crystal in a manner comparable to electrons in atomic crystals. That is to say, in the electronic case the wave functions of electrons interact with the periodic potential of the atomic lattice and, for a certain range of energies (analogous to frequencies for photons), electronic states do not exist, thus, giving rise to an electronic bandgap. For PhCs, the analogue of the electronic potential in an atomic crystal is the periodic variation of the dielectric constants arising from the various constituent materials of the PhC structure. Likewise, due to the periodic interaction, photonic bandgaps appear wherein certain modes, or frequencies, are forbidden. Futhermore, in such a structure, one can introduce one or more line or point defects, which locally disrupt the periodic lattice, wherein a localized mode may exist with a frequency inside the bandgap; such modes are confined to the region of the defect by virtue of being suppressed

within the surrounding lattice. For this reason, these devices offer extreme mode confinement as well as the ability to control and route light very compactly and efficiently.

With these advances, the field of PhCs, and in particular their realization in silicon-based materials, has been a very active field of research over the last several decades. During this time, great success has been achieved in identifying suitable periodic structures, dielectric materials and both theoretical as well as experimental demonstration and characterization of one, two, and three-dimensional PhC and bandgap structures.

1.2. Milestones of Early PhC Research

The more recent interest in PhCs can be attributed to the early papers of Yablonovitch [9] and John [10]. Following the publication of these largely theoretical papers, efforts began to experimentally demonstrate an actual bandgap device. Early experimental efforts at microwave frequencies failed to observe a complete bandgap [11]. Subsequently, theorists were motivated to investigate the problem systematically [12-16]. Initial attempts to solve Maxwell's Eqs. in 3D using the scalar-wave approximation [17] gave results contrary to experiments. Subsequent solutions incorporating the vector nature of the electromagnetic field were developed, based on the plane-wave expansion method [13, 14, 18, 19]. Eventually, it was determined that for sufficient dielectric contrast (>3.6:1), a complete bandgap could be achieved in a diamond like FCC lattice. Yablonovitch then proceeded to fabricate the diamond structure by drilling cylindrical holes into dielectric material [20]. Transmission measurements for this new structure showed a complete bandgap, in agreement with theory.

After this initial success, the field of photonic bandgap devices grew exponentially. Additional structures were found to possess bandgaps, such as the so-called "woodpile" structure shown in Fig. **2**, which also has diamond symmetry, and which can be realized in a layer-by-layer manner by stacking rods in a criss-cross fashion. Furthermore, this device was scaled down, using silicon processing technology developed for microelectronics fabrication, which extended the frequency of the gap into the terahertz [21-24] and infrared regimes [25].

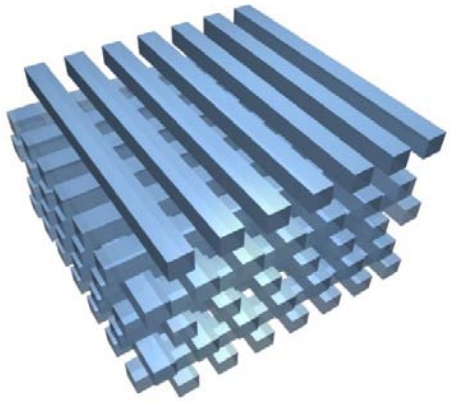

Figure 2: A three-dimensional photonic crystal structure (woodpile).

Alternatively, some researchers turned to the colloidal self-organization of monodisperese spheres [26], knowing that natural opals change color when viewed at different angles under white-light illumination. Along these lines, optical properties such as transmission, reflection, diffraction, and dispersion were measured in artificial opal structures made from monodisperse polystyrene colloids [27-36]. Transmission data showed dips corresponding to directional stop bands on a wavelength scale comparable to the spacing of the spheres.

Three-dimensional (3D) photonic crystals impose periodicity in all three dimensions. An example of a three-dimensional photonic crystal is the woodpile structure in Fig. **2**. However, a crucial drawback of full

3D PhCs in general, and self-organizing colloidal structures in particular, is that, once fabricated, the bandgap behavior cannot be easily altered or engineered for a particular function or application. In addition, the controlled introduction of defects (*i.e.,* doping) is hard to achieve, which in the end has significantly limited their usefulness.

To overcome this limitation, Joannopoulos, *et al.* [37] studied two-dimensional (2D) PhC structures, and in particular they examined defect-channel waveguides to guide optical light in air along channels of missing dielectric material, and around very tight bends in such channels, with minimal loss [38-43]. 2D PhCs can be realized using either a periodic array of dielectric rods of any shape and/or geometry, or by using perforated dielectric slab of air holes. Such structures can be further optimized to achieve either a wider, or a narrower, bandgap based on the desired application. Two-dimensional photonic crystals impose periodicity in two dimensions while the third dimension is either practically infinitely long (photonic crystal fibers) or has a finite height (photonic crystal slabs).

By introducing a point defect in a 2D PhC lattice, Villeneuve, *et al.* were able to design a high-*Q* nanocavity, which supported a single localized mode [44]. Channel-drop filters were later studied by Haus, *et al.* and Fan, *et al.* [45, 46], who used two waveguides and an optical resonator system of two single-mode cavities, and another structure with a single cavity that supports doubly degenerate hexa-pole states, to achieve wavelength filtering [47, 48]. Fan, *et al.* later analyzed the effect of waveguide branching in PhCs using two resonant cavities with equal decay rates in the branched waveguides [49]. Povinelli, *et al.* presented a study in which they constructed quasi-2D defect modes in a 3D PhC structure [50]. Such modes had a striking similarity to those found in 2D PhCs in terms of polarization, field profile, and projected band structures.

Johnson also studied the effect of cross talk in waveguide intersections [51]. He used resonant tunneling to achieve nearly 100% throughput and 0% cross talk between crossing perpendicular PhC waveguides.

Key contributions to PhC research have also come in the area of materials systems, such as III-V semiconductor materials. In this area, Scherer, *et al.* demonstrated PhC structures in perforated slabs of GaAsP [52-55]. Similar structures were later fabricated in InGaAsP, which led to a two-dimensional photonic-band-gap defect-mode laser designed for a peak emission wavelength of 1.55 μm at room temperature [56-60]. Lee, *et al.* measured the spontaneous emission power spectrum of the fabricated structure [61, 62], and theoretical studies of the were presented by Xu, *et al.* and Vuckovic, *et al.* [63, 64].

Yoshie, *et al.* later characterized different modes within two-dimensional PhC nanocavities with InAs quantum dots as an active material [65]. They observed highly localized donor-mode resonances with 3–5-nm line widths. Additionally, Loncar introduced line defects to PhC slab structures to resemble an optical wire or waveguide [66, 67]. Meanwhile, Adibi, *et al.* explored different techniques to control the positions of guided modes as well as the number of guided modes within a waveguide, eventually leading to the design of single-mode PhC waveguides in a perforated slab of air holes [68, 69].

Strong directionally dispersive optical properties in PhCs were studied and explored for so-called "superprism" applications by Kosaka, *et al.* [70-72], who demonstrated extraordinary angle-sensitivity of light propagation. In this work, a transmitted beam was swung from –70° to +70° with a slight change in the incident angle within ±7°. This phenomenon implies the presence of a negative effective refractive index, [73] and was used to demonstrate effects such as beam steering and self-collimation [74]. Device designs based on these effects are discussed in later sections.

Since they are easier to analyze and fabricate, two-dimensional photonic crystals have attracted the attention of a large number of researchers and engineers. An example of a fabricated two-dimensional photonic crystal is shown in Fig. **3**. Planar photonic-crystal devices such as splitters [49, 75-78], high-*Q* microcavities [39, 44, 56, 79-82] and channel drop/add filters [45, 46, 83, 84] have been investigated both theoretically [69, 85, 86] and experimentally [52, 55, 58, 87-90]. A selection of such devices is described in later sections of this chapter.

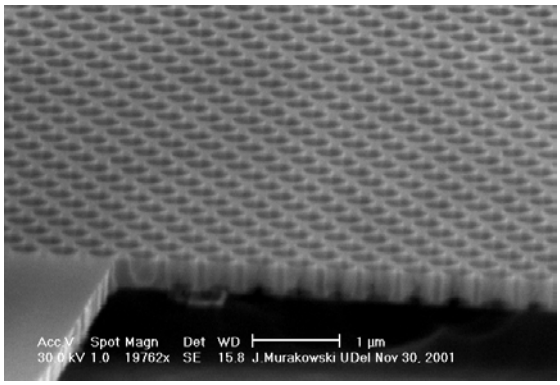

Figure 3: SEM picture of a periodic array of air holes in a suspended Si membrane (slab photonic crystal).

1.3. Analogy Between Photonic and Semiconductor Crystals

The basic Eqs. governing the motion of electrons and photons are, respectively, the Schrödinger Eq. and Maxwell's equations. When applied to the respective problems of electrons in crystalline solids and photons in periodic dielectric media, analogies between these two governing relations become apparent. To make the most of these analogies, we must examine both the similarities and the differences.

In a semiconductor crystal, electron behavior is governed by quantum mechanics [91]. An electron state is described using the Schrödinger equation

$$\underbrace{\left[\frac{-h^2}{8\pi^2 m^*}\nabla^2 + V(\mathbf{r})\right]}_{\text{Hamiltonian operator}}\varphi(\mathbf{r}) = E\varphi(\mathbf{r}) \qquad \textbf{(1)}$$

where h is Planck's constant, m^* is the effective mass [92] of the electron, $V(\mathbf{r})$ is the potential function, $\varphi(\mathbf{r})$ is the wavefunction of the electron, and E is the total energy. The wavefunction $\varphi(\mathbf{r})$ in quantum physics can be interpreted as a *probability amplitude* function, *i.e.,* the probability of a measurement finding the electron within a volume element $d^3\mathbf{r}$, located at a position denoted by $\mathbf{r}$, is given by $|\varphi(\mathbf{r})|^2\, d^3\mathbf{r}$. For a crystal lattice, in the absence of defects, the potential is periodic, *i.e.,* $V(\mathbf{r}) = V(\mathbf{r} + \mathbf{R})$, where $\mathbf{R}$ is a vector representing the displacement between any two lattice sites. In this case, solutions $\varphi(\mathbf{r})$ take the form of propagating waves called *Bloch waves*: plane waves modulated by an amplitude function with the same periodicity as the crystal lattice.

Electromagnetic fields are governed by classical electromagnetic theory [93]. The fields are described using Maxwell's Equations: four coupled Eqs. relating the electric and magnetic fields to one another and to any charges or electric currents present. In non-magnetic media, two of these four Eqs. can be combined to yield

$$\underbrace{\left[\nabla\times\frac{1}{\varepsilon(\mathbf{r})}\nabla\times\right]}_{\text{Maxwell operator}}\mathbf{H}(\mathbf{r}) = (\omega/c)^2\,\mathbf{H}(\mathbf{r}) \qquad \textbf{(2)}$$

where $\mathbf{H}(\mathbf{r})$ is the magnetic field, ω is the angular frequency, c is the speed of light in vacuum, and $\varepsilon(\mathbf{r})$ is the dielectric permittivity. In a photonic crystal, the optical properties of the medium are periodic, *i.e.,* $\varepsilon(\mathbf{r}) = \varepsilon(\mathbf{r} + \mathbf{R})$, and solutions are also Bloch waves.

Eqs. (1) and (2) are eigenvalue Eqs. with similar forms. Inspection of the two Eqs. reveals certain analogous features: each Eq. describes a wavelike function in space, $\varphi(\mathbf{r})$ and $\mathbf{H}(\mathbf{r})$, respectively; each wave exists in a medium characterized by a periodic material function, the periodic potential V and the periodic permittivity ε,

respectively; these periodic functions each appear within second-order space-differential operators, the Hamiltonian and Maxwell operators, respectively; both of these operators are Hermitian, and the corresponding real eigenvalues are the electron energy E and the squared frequency of the electromagnetic wave ω^2, respectively. Additionally, in both cases, due to the coherent superposition of the partial scattering of the wave at each lattice site, there exist certain bands in the eigenvalue spectrum in which propagating modes are forbidden, called bandgaps. Likewise, in both cases there can be defects in the periodic medium, which can support localized states with eigenvalues that would be forbidden in the defect-free lattice. This permits the propagation of states with eigenvalues inside the bandgap of the bulk crystal. This effect is called doping, and is vital to the usefulness of nearly all semiconductor devices like diodes, transistors, LED's, *etc.* Not surprisingly, defects are also essential to the usefulness of many applications of PhCs (see Sections 2 and 3). Because of these analogies, PhC researchers have been able to exploit many of the useful conceptual tools of solid state physics, such as Bloch waves, reciprocal space, Brillouin zones, band structure, conduction and valence bands, and dispersion diagrams [94].

While these analogies are quite useful for understanding and analyzing PhCs, it is imperative to be aware of their limits, *i.e.,* important differences between PhCs and semiconductors. First is the fundamentally different physical nature of the wave: the magnetic field is a vector quantity, while the electronic wavefunction can usually be treated as a scalar (*i.e.,* spin can be ignored). Eq. (2) contains three scalar equations, one for each component of the vector field in 3D. Second, whereas the Schrödinger Eq. contains fundamental physical constants, such as Planck's constant and the electron mass, which conspire to create fundamental scales of length like the Bohr radius, there is no characteristic length scale in Maxwell's equations. Scaling the dimensions of a particular electronic system can profoundly change the behavior. For a photonic system, only the frequencies of the solution will change; the solution is otherwise unchanged. This distinction is of great significance because unlike atoms in semiconductors, the periodically arranged dielectric "atoms" of a PhCs are generally not naturally occurring, and must be designed and fabricated, a challenging process at optical length scales (see Section 4). The scale invariance of the Maxwell eigenvalue Eq. allows PhC structures and devices to be tested at larger (*i.e.,* microwave) scales, with confidence that observed behaviors will be retained if an otherwise identical structure is fabricated on a smaller scale. Third, there is an important distinction between the the two respective eigenvalues: since the photonic eigenvalue is proportional to the squared frequency, there are no negative-energy photonic solutions, *i.e.,* no truly bound states are allowed ($E_{\text{photon}} = h\omega/2\pi$). Nevertheless, photonic microcavities in PhCs can be engineered to possess very high Q values, with correspondingly long lifetimes of confined optical modes. Finally, except in cases where the field amplitudes are very large (*i.e.,* nonlinear optics), the solutions of the photonic eigenvalue problem are uncoupled. Electromagnetic waves obey the principle of superposition; they do not interact. This is in contrast to the often strong interactions between electrons. For this reason, it has been noted by Yablonovitch [95] that band theory, which assumes that the wavefunctions of multiple particles are uncorrelated, actually makes more sense for photons than for electrons.

1.4. Analyzing Photonic Bandgap Structures

For all but the simplest PhC structures and devices, numerical simulations are required to gain insight to the behavior of light interacting with them. One prominent method employed to this end is the plane-wave expansion method (PWEM), which represents normal modes in periodic structures as a superposition of plane waves. In such a representation, Eq. (2) becomes a *matrix* eigenvalue problem, which is solved using standard numerical techniques to obtain the dispersion relation of a PhC [13, 14, 19, 96]. The solutions are eigenfrequencies, plotted as a function of wavevectors tracing the perimeter of an irreducible Brillouin zone, to form a dispersion diagram; two canonical 2D examples are shown in Fig. **4**.

The dispersion diagram is a graphical representation of the frequencies corresponding to propagating modes supported by a PhC lattice. While a standard dispersion diagram, depicting eigenfrequencies only for those wavevectors on the irreducible-Brillouin-zone boundary, is sufficient to determine whether a bandgap exists for a certain PhC structure, it does not conclusively indicate the presence of other interesting and useful dispersive behaviors, such as negative index phenomena, self-collimation, or superprism effects. For such these cases, a three-dimensional plot of the dispersion surface, depicting eigenfrequencies for all wavevectors within the full Brillouin zone, provides a more detailed view of a PhC's supported modes.

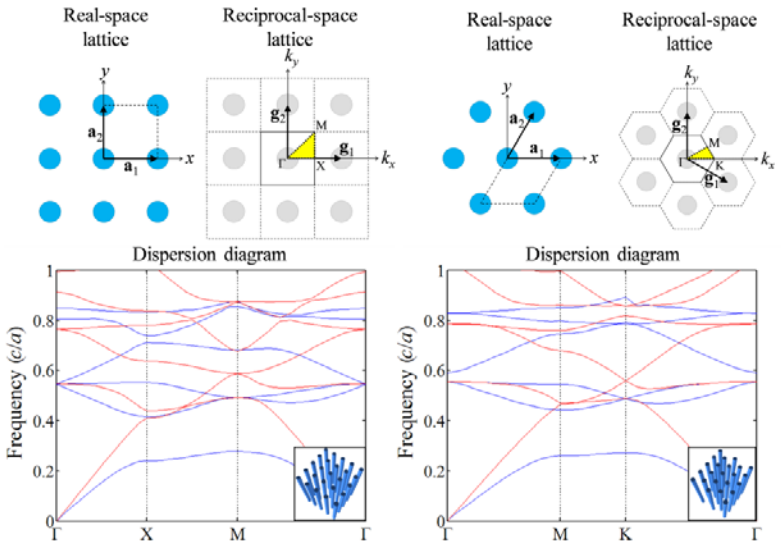

Figure 4: Plane-wave expansion method (PWEM) used to analyze different two-dimensional PhC structures with (a) square or (b) triangular lattices. Eigenfrequencies are determined for Bloch wavevectors around the edge of an irreducible Brillouin zone, indicated by a yellow triangle for each lattice. The result is a dispersion diagram showing the allowed frequencies for different wavevectors within the lattice. The two separable polarization modes, known as transverse-electric (TE) and transverse-magnetic (TM), are indicated by red and blue curves, respectively.

An example is shown in Fig. **5**, where a dispersion surface representing just one of the higher bands is displayed. While the PWEM enables analysis of the dispersion properties of an infinite-size, perfect PhC structure, it is unable to predict transmission spectra, field distributions, and back reflections from finite-size structures. A prominent alternative approach is based on a numerical solution of Maxwell's Eqs. in real space using the finite-difference time-domain (FDTD) method. The FDTD method has been used to analyze multi-channel drop/add filters [83], calculate the transmission through sharp waveguide bends [40], and also in the study of a waveguiding mechanism through localized coupled cavities in three-dimensional photonic crystals [97, 98].

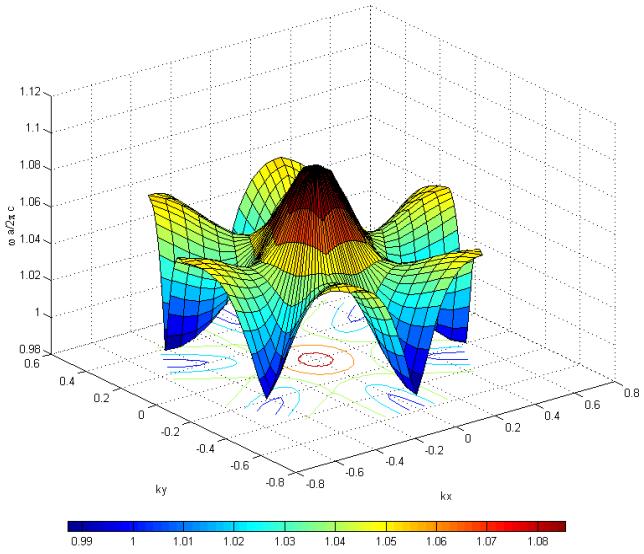

Figure 5: Dispersion surface. The horizontal plane spans both Bloch wavevector components k_x and k_y. The vertical axis gives the normalized frequency $\omega a/2\pi c = a/\lambda$.

To illustrate the use of FDTD on finite-size PhC structures, the transmission and reflection spectra for six layers of a 2D photonic crystal are shown in Fig. **6**. The photonic bandgap possessed by this lattice is manifested in these spectra as a frequency range of low transmission and high reflectivity.

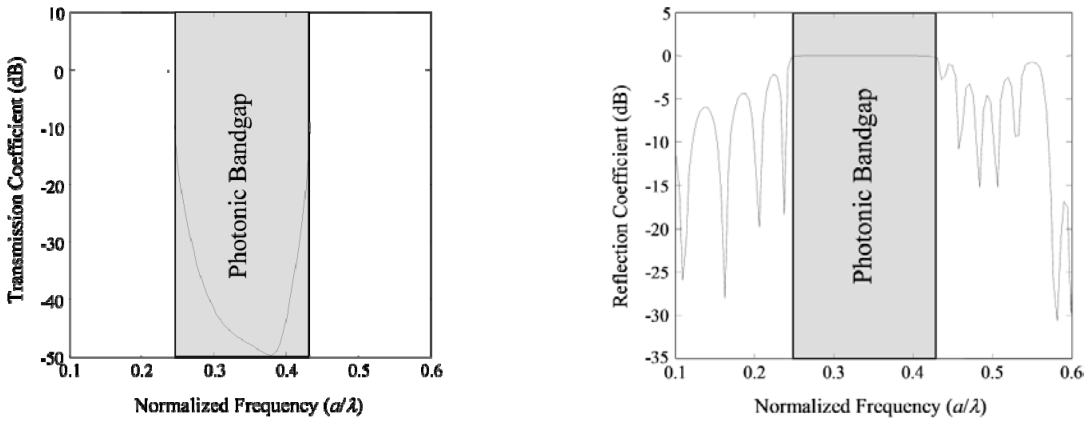

(a) (b)

Figure 6: Transmission (a) and reflection (b) for six layers of a 2D photonic-crystal structure comprised of a square lattice of silicon (ε_r = 11.56) rods in air (ε_r = 1), with r/a = 0.2, obtained using FDTD. Low transmission and near-perfect reflectivity is observed within the bandgap.

2. ENGINEERING CONFINEMENT PROPERTIES OF PHOTONIC CRYSTALS

Semi-conductor materials are engineered by adding donor or an acceptor atoms. This results in a modification of the electrical properties of the atomic crystal by making the material n-type or p-type, respectively. In a similar fashion, the optical properties of a photonic crystal can be altered by introducing defects, which can be of one of two types: a donor type, or an acceptor type [99]. A donor-type defect corresponds to a local increase of the effective refractive index, while an acceptor type defect corresponds to a local decrease of the effective refractive index, by either adding or removing a certain amount of dielectric material [100, 101].

In the presence of a bandgap, such perturbations of the regular photonic-crystal array lead to the localization of light, which becomes confined as a result of coherent scattering and interference of a wave from the surrounding periodic structure.

The defects often take the form of a point, a line, or a plane, where a single lattice site, a row of lattice sites, or a plane of lattice sites are modified, respectively. The efficient confinement of light in the vicinity of defects leads to their use as resonant cavities, in the case of point defects, and waveguides in the case of line defects.

2.1. Photonic Crystal Waveguides

When a line defect is introduced into a photonic crystal that exhibits a bandgap, waveguides may be created. Such waveguides are capable of guiding light at optical wavelengths with minimal propagation losses [102, 103], and are essential elements in any optical integrated circuit. They are used to transmit electromagnetic waves between various devices and components in an interconnected system. Historically, dielectric waveguides have been used to carry light between various components on a single chip, while optical fiber cables were used between systems.

While these architectures were successful in satisfying the bandwidth requirements for an optically interconnected system, the physical size of these links is considerable. However, large lateral dimensions of data pipes are unacceptable for chip-level optical system integration, where the minimum feature size shrinks rapidly with every new generation of chip-manufacturing technology. As a result, nano-scale

optical interconnections are now required to satisfy future interconnect needs in terms of throughput and latency, as well as size. Here, photonic crystals appear to be a good candidate for the miniaturization and large-scale integration of high-density optical interconnects [41]. This is mainly due to their unique ability to control the propagation of light in one, two, and three dimensions at a scale comparable to the wavelength of light.

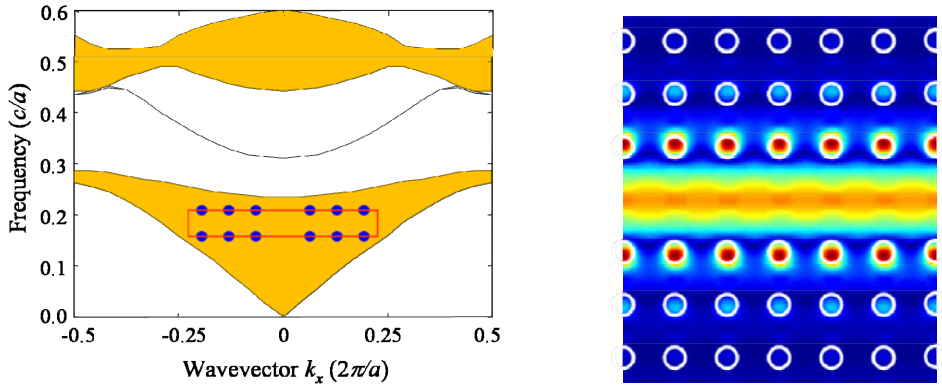

(a) (b)

Figure 7: (a) Dispersion diagram for a two-dimensional square array of dielectric rods with $r = 0.2a$. (b) Electric-field distribution for $k_x = 0.318(2\pi/a)$.

To demonstrate the concept of waveguiding in photonic crystals, consider a two-dimensional system periodic in the *x*-*y* plane and extending infinitely in the *z* direction. For this example, the system consists of an array of high-index dielectric rods arranged on a square lattice embedded in a low-index dielectric background. If the index contrast is high enough, a photonic bandgap may open for TM-polarized waves. A line defect introduced into such a photonic-crystal lattice breaks its symmetry along one of its main crystalline directions, which may result in the appearance of a single or multiple modes in the otherwise vacant bandgap [104, 105]. Depending on their spatial and temporal distribution within the photonic-crystal line-defect structure, these modes can be classified into evanescent, standing or traveling modes. The traveling modes can be used to carry optical signals between components in an integrated system, thereby turning linear defects into bona fide waveguides.

An example of a photonic crystal waveguide structure is shown in Fig. **7**. The dispersion diagram in Fig. **7 (a)** was calculated using the plane-wave expansion method [94]; the electric field distribution for a mode at $k_x = 0.318(2\pi/a)$ is shown in Fig. **7 (b)**.

2.2. Photonic Crystal Resonators

A resonant cavity can be made by introducing a point defect in a photonic crystal [105]. The defect is obtained by locally modifying the shape, size, or dielectric constant of the PhC features. By varying these parameters, the number of modes supported by the cavity and their resonant frequencies can be tuned. Consider, for example, a square lattice of cylindrical rods with a sufficiently high dielectric contrast (*i.e.,* greater than 2.0) [99] between the host and the rod materials. In such a PhC, a point defect can be introduced by changing one of the parameters of a single rod within the crystal. For example, reducing the radius of one dielectric rod results in a point defect supporting a single localized mode. Alternatively, if we increase the radius of one rod, we will introduce multiple modes localized within such cavity. The resonant frequencies supported by such cavities are determined by how much the rod radius is changed.

As an example, consider a point defect in a two-dimensional supercell consisting of a 7 x 7 square array of dielectric rods with one rod missing at the center, Fig. **8**. The dielectric rods are embedded within air background, have a dielectric constant of 12.25, and have a circular cross-section with radius $0.2a$, where a is the lattice constant. The dispersion surfaces of different TM polarized bands, projected onto the ω-k_x

plane, are shown in Fig. **8 (a)**. They are obtained by solving the respective eigenEq. for wavevectors within the first Brillouin zone corresponding to the $7a \times 7a$ supercell. The resonant frequency of the cavity mode within the bandgap is $0.383c/a$. The shaded regions in Fig. **8 (a)** represent the slab band continuum. Once the cavity-mode frequency is known, the field distribution can be obtained from the associated eigenvector. Fig. **8 (b)** shows the amplitude distribution of the electric field for an arbitrarily chosen wavevector $(0.4\hat{x}+0.3\hat{y})2\pi/a$; the electromagnetic wave is well confined within cavity and the intensity drops rapidly in all directions. Similar defect-mode confinement can be observed at other wavevectors.

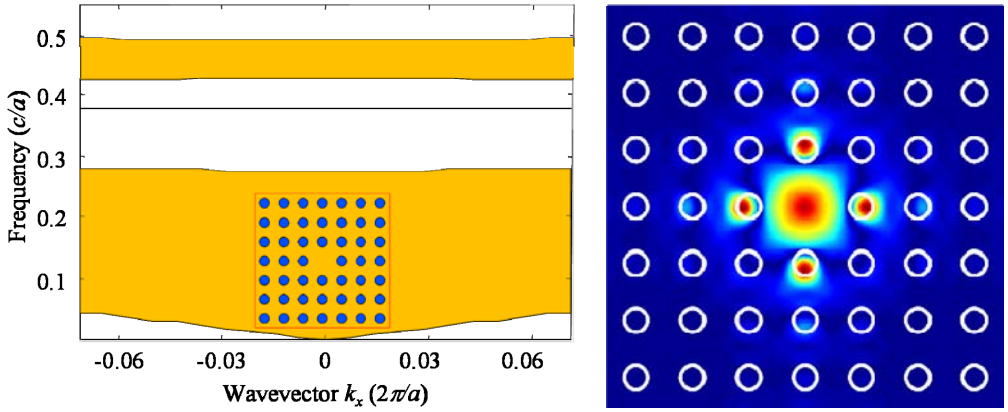

(a) (b)

Figure 8: Supercell analysis of point defect. (a) Dispersion diagram. (b) Electric field distribution for wavevector $(0.4\hat{x}+0.3\hat{y})2\pi/a$.

2.3. Photonic Crystal Filter

A photonic crystal filter is used to spatially separate optical signals based on their respective wavelengths. This characteristic is used in wavelength-division multiplexing (WDM)/demultiplexing (WDD) systems to transmit many optical signals through a single physical communication channel, such as an optical fiber. In such systems, each wavelength represents an optical channel, analogous to a radio or television channel carried by a specific frequency. In dense WDM (DWDM), wavelengths are closely spaced at intervals as small as 0.4 or 0.8 nm in the main telecommunications band near 1550 nm. The International Telecommunications Union (ITU) has specified a grid of standard frequencies separated by increments of 100 GHz (approximately 0.8 nm), referenced to a frequency 193.1 THz, corresponding to a wavelength 1552.52 nm. These wavelengths are in the "conventional" or C band of the erbium-doped fiber amplifier (EDFA) operating between 1530 nm and 1570 nm. Other bands of interest are the "long" or L band (approximately 1570 nm to 1610 nm) and the "short" or S band (approximately 1490 to 1530 nm).

A concept design of a photonic crystal filter is discussed here. Consider first a single-channel version, which is obtained by bringing a point-defect cavity in close proximity to a line defect waveguide, such that the waveguide and the cavity are evanescently coupled. If the frequency of the guided mode overlaps with the resonant frequency of the cavity, energy transfer from the linear defect to the point defect will occur. On the other hand, no such energy transfer will occur when the frequency of the propagating wave differs from the resonant frequency.

The device is illustrated in Fig. **9**, where the photonic crystal, made of dielectric rods 140 nm in diameter, ε_r = 11.56, distributed in a square lattice with pitch a = 350 nm, exhibits an omnidirectional photonic bandgap for λ between 833 nm and 1250 nm. The acceptor-type line-defect waveguide is formed by removing one column of dielectric rods along one of the cardinal directions of the crystal. The point defect cavity is formed by reducing the diameter of a single dielectric rod to $2r$ = 105 nm, and reducing its dielectric constant to ε_r = 7.0.

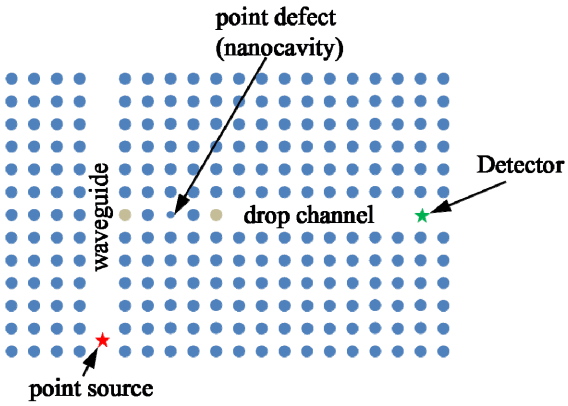

Figure 9: Single-channel optical filter comprising a point defect cavity (r = 52.5 nm, ε_r = 7.0) and an acceptor line defect waveguide created by removing a column of dielectric rods. The photonic-crystal lattice consists of dielectric rods with radius r = 70.0 nm and dielectric constant ε_r = 11.56, distributed on a square lattice with a pitch a = 350 nm. The two rods (r = 70.0 nm) of light gray color have dielectric constant ε_r = 8.0 to enhance coupling between the cavity and the waveguides.

To analyze this structure, a pulse with center wavelength λ_0 = 1.0 μm and width $\Delta\lambda_0$ = 0.6 μm is launched into the waveguide. The pulse propagates along the waveguide channel, confined to the defect region by the virtual walls formed by the photonic-crystal layers. As in a dielectric waveguide, the propagating mode has evanescent tails that extend beyond the defect region. Hence, if the resonant cavity is close enough, the evanescent tail of the propagating mode will excite a single or multiple modes within the cavity. Then, the electromagnetic field in the cavity evanescently couples to a nearby output or "drop" channel, see Fig. **9**. Coupling to and from the point defect cavity is enhanced by lowering the dielectric constant of the two rods, at the cavity/waveguide interface and at the cavity/channel interface, to ε_r = 8.0.

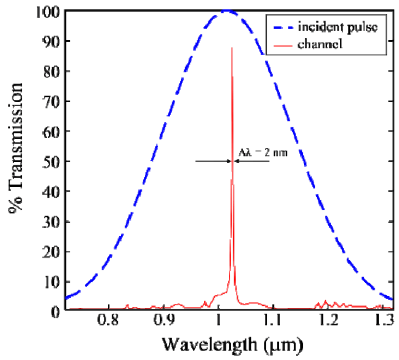

Figure 10: Single-channel optical spectrometer simulation. Wavelength spectrum of an incident broadband pulse and the pulse measured at the detector, placed in the filtered channel, normalized to the input pulse.

A detector placed in the output channel captures the time-variable field, which is then Fourier-transformed to obtain its spectral content. Fig. **10** shows the resulting drop-off spectrum overlaid on the spectrum of the incident pulse. It shows a line-width of the transmitted signal in a 2-nm range with a center wavelength λ = 1025 nm, which is in the ballpark of the 0.8 nm required for DWDM.The single-channel device analyzed above serves as a building block to realize a multi-channel spectrometer. Placing resonator cavities tuned to different wavelengths along a single-line defect, allows extracting individual wavelengths from a broadband optical signal propagating in the waveguide. Fig. **11** shows an example where six cavities are included, each having a different defect size and its own drop channel. The radii of the rods in the point defects are 8.75 nm, 17.5 nm, 26.25 nm, 35 nm and 43.75 nm, in addition to the 52.5 nm analyzed above, and the dielectric constant is maintained at ε_r = 7.0 for all of them. The resonant wavelengths corresponding

to these defects are λ_1 = 1.025 μm, λ_2 = 0.875 μm, λ_3 = 0.895 μm, λ_4 = 0.925 μm, λ_5 = 0.949 μm, and λ_6 = 0.985 μm.

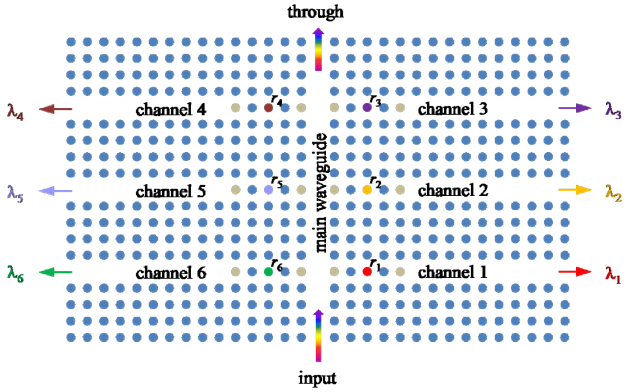

Figure 11: Multi-channel optical spectrometer using cavities with different point defect sizes: r_1 = 8.75 nm, r_2 = 17.5 nm, r_3 = 26.25 nm, r_4 = 35 nm, r_5 = 43.75 nm, and r_6 = 52.5 nm. Each cavity couples to a separate output channel.

The spectral response of this device is shown in Fig. **12**, where the individual peaks color-coded are labeled using the corresponding channel numbers. With the exception of Channel 5, the relative heights of the peaks generally follow the spectral content of the incident pulse shown with a dashed line in Fig. **10**.

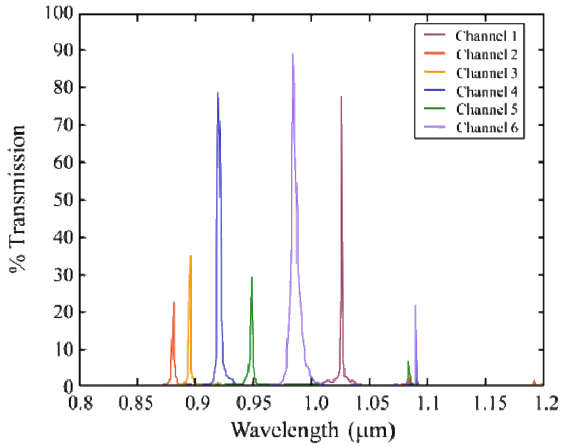

Figure 12: Spectral response of the six-channel device shown in Fig. **5**. Peaks correspond to the resonant wavelengths of the respective cavities.

2.4. Photonic Crystal Switch

A crossbar switch, Fig. **13**, is a four-port device, with two input and two output ports, that can exist in one of two states: the bar state, where the signal from input ports 1 and 3 are sent to ports 2 and 4, respectively, and the cross state, where the signal from the input port 1 is sent to output port 4, whereas the signal from the input port 3 is sent to output port 2.

Suppressing the coupling between the waveguides produces switching in the coupled waveguides system. By sufficiently increasing the conductivity, or loss tangent, of the material in the coupling region between the waveguides, the region acts as a mirror, confining the wave and preventing its transition to the adjacent waveguide. In semiconductors, the change in conductivity can be controlled by (1) carrier injection from forward-biased PN junctions on the rods, (2) depletion of doped rods with MOS gates, (3) generation of electrons and holes by shining light upon the coupling region, where the energy of the photons used is higher than the bandgap of the semiconductor.

In the photonic-crystal structure shown in Fig. **13**, the photonic crystal consists of silicon rods (ε_r = 11.56) arranged in a square lattice with pitch a = 543 nm, and the diameter of the rods is 217 nm. The coupled-waveguides system includes the interaction region of length $L = 28a$, which is approximately equal to the coupling length L_c at the wavelength λ = 1550 nm.

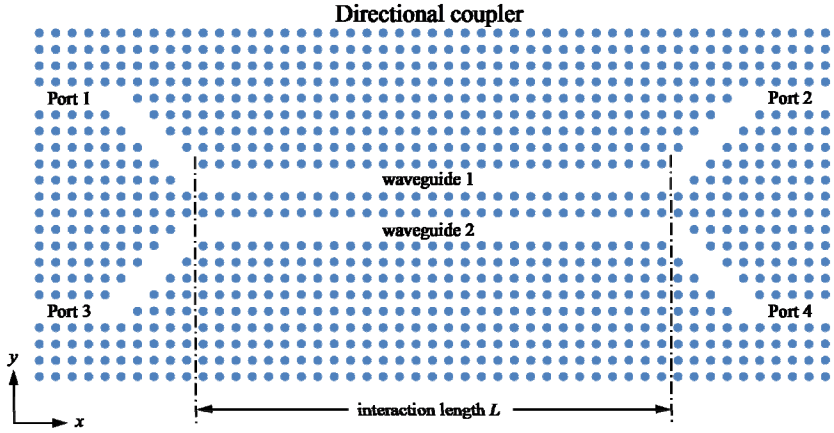

Figure 13: Cross-bar switch in the form of a coupled photonic-crystal waveguide (CPhCW) system, consisting of two closely spaced PhC waveguides of length L separated by two PBG layers.

Four snapshots of the coupled-waveguides system in operation, at different values of conductivity for the rods in the coupling region, are shown in Fig. **14**. At low conductivity, Fig. **14 (a)**, the device behaves like a coupled-waveguides system discussed above, and the optical signal is completely transferred from one waveguide to the other since the interaction length L is approximately equal to the coupling length L_c. At high conductivity, Fig. **14 (d)**, the signal is confined to the waveguide where it was launched. At intermediate values of conductivity, Fig. **14 (b)** and **(c)**, the signal is partially split and largely attenuated due to ohmic losses in the coupling region. The transition from the cross state to the bar state occurs for a conductivity change between 0.001 $(\Omega\ \text{cm})^{-1}$ and 10.0 $(\Omega\ \text{cm})^{-1}$.

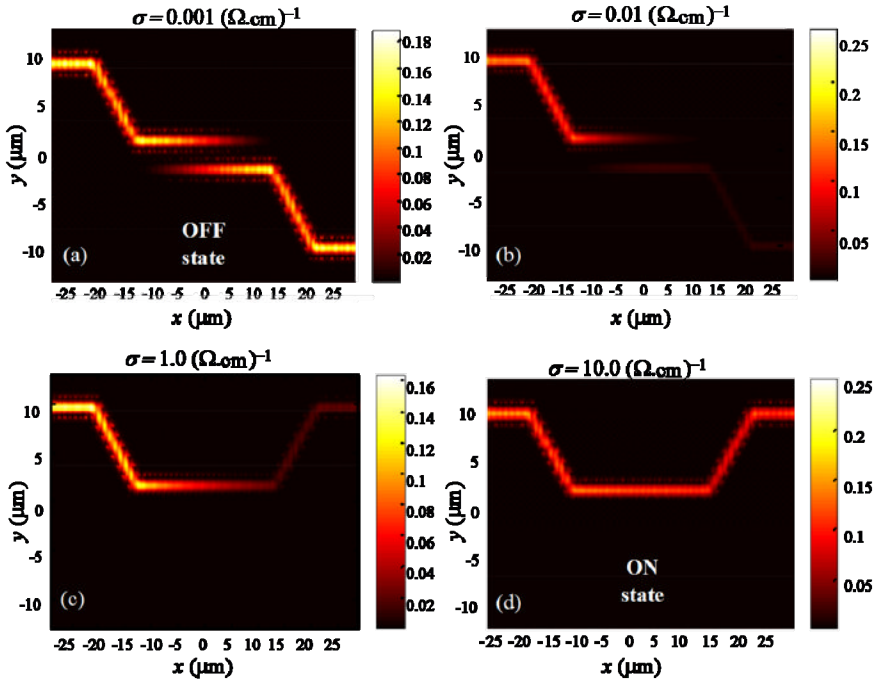

Figure 14: Four snapshots of FDTD simulations of the 2x2 electro-optical switch shown in Fig. **13**.

The operation of the switch is shown in more detail in Fig. **15**, which presents the dependence of the power at the outputs as a function of conductivity of the rods in the interaction region. The switch is characterized by high transmission efficiency of nearly 100% in both cross and bar states, and low cross talk, with the suppression in the range of 20 dB.

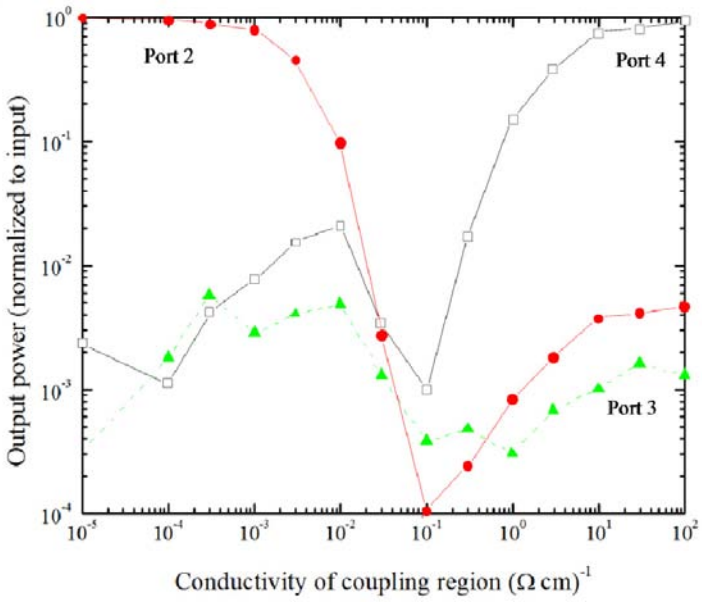

Figure 15: Switching behavior of the crossbar switch shown in Fig. **13**. Light is launched into port 1.

3. ENGINEERING DISPERSION PROPERTIES OF PHOTONIC CRYSTALS

Photonic bandgap provides means for strong confinement of light in photonic crystals. Such confinement was used to realize waveguides, resonators, and other defect-based devices at scales comparable to the wavelength of light. However, photonic crystals can manipulate the behavior of light in a nontrivial manner even in the absence of photonic bandgap, or defects, thanks to a wealth of phenomena ensuing from the coherent interaction of an electromagnetic wave with a periodic structure. To study and understand these interactions, a visualization tool in the form of a dispersion diagram is often employed. Borrowed from the field of solid state theory, which deals with periodic systems on the atomic scale, dispersion diagram shows the functional dependence of the frequency, or energy, of a wave propagating in a crystal on its corresponding wavevector, or (pseudo)momentum. The importance of the dispersion diagram in such investigations stems from the notion of group velocity $\mathbf{v}_g = \nabla_k \omega$, which describes how a wave packet, and the energy it carries, propagates in a medium. The group velocity is a vector pointing in the direction of the steepest ascent of the function $\omega = \omega(\mathbf{k})$, and as such it is perpendicular to the equi-frequency surface (or contour for a 2D system) in the *k*-space. To obtain such a rendering, it is sufficient to compute the eigenfrequencies for wavevectors at all *k*-points within, or on the boundary of, the *irreducible* Brillouin zone. By exploiting the lattice symmetries, dispersion surface for the entire Brillouin zone is found. It will be shown in this section that photonic crystals admit a variety of shapes for equi-frequency contours, as well as dispersion surfaces, and, therefore, correspondingly varied wave-propagation phenomena. This is in contrast to what is known as index ellipsoids admitted by conventional materials. The growing interest in the dispersion characteristics of photonic crystals bore fruit in the discovery of super-prism effect [70], self-collimation [74, 106, 107], negative refractive index [108-110], and left-handed materials [111, 112].

3.1. Self collimation

The dispersion properties of photonic crystals can be exploited to precisely control the propagation of electromagnetic waves. As a result, an alternative exists to conventional defect-based PhC waveguides, self-collimating waveguide, in a form of devices that require no defects for confinement, and yet can

arbitrarily route light. Consider an engineered material exhibiting square EFC for a certain frequency, then for wavevector directions spanning 90°, the group velocity would have the same direction—perpendicular to one side of the square.

To elucidate self-collimation further, consider Fig. **16**, where the EFC of the isotropic material is shown as a blue circle, and the EFC of the self-collimating photonic crystal is indicated with a red dashed curve. At the boundary between the isotropic material and the self-collimating material, the component of the *k*-vector tangential to the boundary, designated in Fig. **16** as the *x*-direction, is preserved. As a result, a wave with a wavevector $\mathbf{k}_0$ in free space assumes $\mathbf{k}_p$ as the wavevector inside the photonic crystal. More importantly, at $\mathbf{k}_p$, the resulting group velocity points in the direction perpendicular to the red dashed contour, which is almost exclusively the *y*-direction for a wide range of incident $\mathbf{k}_0$ angles; this range of angles is indicated in the figure by the range between $\mathbf{k}_0$ and $\mathbf{k}_0'$. In other words, the wave is only allowed to propagate along those directions that are normal to the sides of the square-like contour, and it is possible to vary the incident wavevector $\mathbf{k}_0$ over a wide range of angles and yet maintain a narrow range of propagating directions $\nabla_k \omega$ within the PhC. Fig. **17** shows a comparison of the electromagnetic field distribution produced by a point source placed in a homogeneous slab with the field distribution produced by the same point source placed in a slab perforated by a square lattice of air holes. For the isotropic material, the EFC is a circle, and therefore light waves emanating from the source propagate isotropically within the plane as shown in Fig. **17 (a)**. On the other hand, if the EFC is nearly square, waves originating at a point source located at the center of the PhC lattice, as in Fig. **17 (b)**, are limited to the *x*- and *y*-directions.

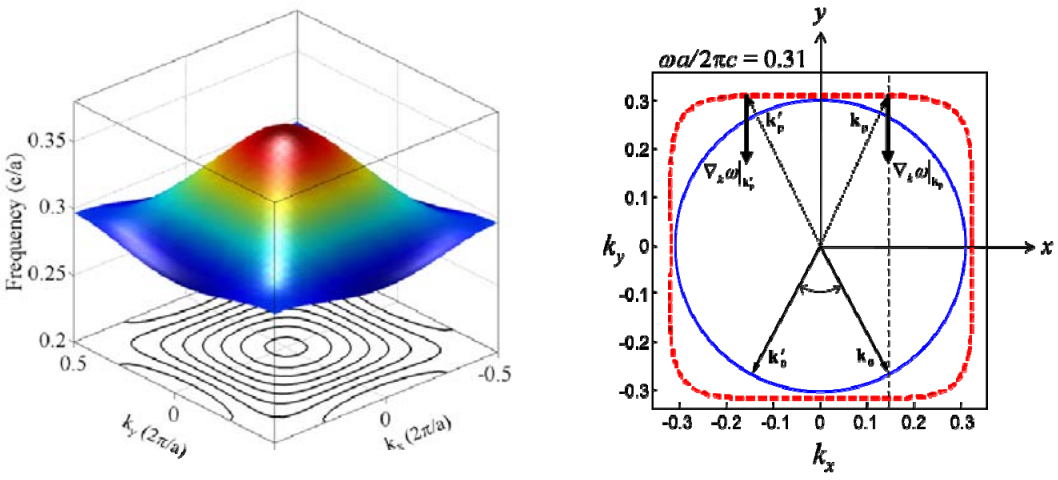

(a) (b)

Figure 16: Dispersion diagram of a PhC designed to have a square EFC for certain frequencies. (a) A dispersion surface. (b) Illustration of self-collimation using a square EFC.

To convincingly demonstrate self-collimation, photonic crystal consisting of circular holes, r = 1.33 nm, arranged in a square grid with pitch a = 442 nm was patterned in a 260-nm-thick layer of silicon in a silicon-on-insulator (SOI) substrate, along with a J-coupler [113] for focusing light with λ = 1480 nm from a wide ridge waveguide to the self-collimating lattice.

The presence of a tightly focused spot at the far end of the PhC lattice demonstrates the lateral confinement and self-collimation of the initially divergent light as it propagates along the length of the PhC. The conspicuous absence of a light trail in Fig. **18** suggests low out-of-plane losses in this guiding structure. In order to quantitatively characterize propagation loss, multiple PhC dispersion waveguides were fabricated with lengths ranging from 23.87 to 62.76μm. These measurements imply propagation loss as low as 1.1 dB/mm, which is a considerable improvement over the propagation loss measured experimentally for PhC line-defect waveguides.

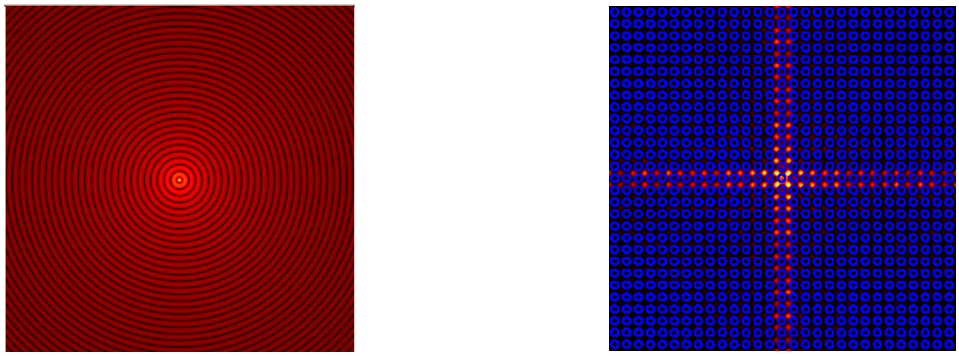

(a) (b)

Figure 17: Propagation of light originating at a point source in (a) homogeneous silicon slab, and (b) PhC consisting of a rectangular lattice of air holes in silicon slab, wherein $r / a = 0.3$.

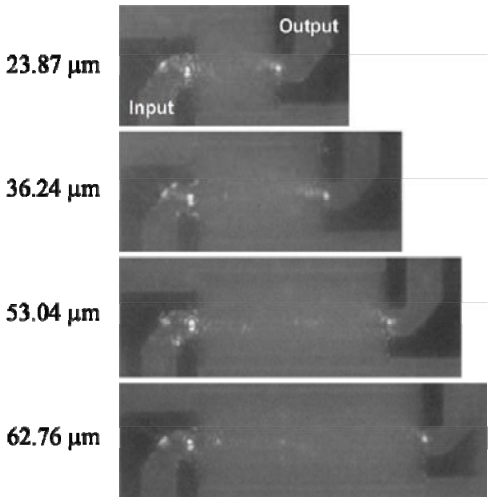

Figure 18: Image captured by a near-IR camera of the scattered light, λ = 1480 nm, at the PhC/silicon boundaries.

(a) (b)

Figure 19: (a) Simple cubic photonic crystal consisting of spherical voids on a cubic grid in a silicon matrix. (b) Equi-frequency surface at normalized frequency $f = 0.34\ c/a$.

Self-collimation in 2D was found for a photonic crystal based on a square-lattice geometry. Since a cube is a three-dimensional analogue of a square, the 3D self-collimation is sought in a simple cubic lattice. To illustrate this, consider a photonic crystal made of silicon with spherical voids with a radius $r = 0.55a$ placed at the nodes of a cubic grid with a lattice constant a, as shown in Fig. **19 (a)**. Fig. **19 (b)** shows an EFS for $f = 0.34\ c/a$. Due to degeneracy, the EFS consists of several disjoint and overlapping surfaces. The dispersion surface of third band, as indicated in blue color, demonstrates a cubic-like shape with a large flat

surface near the direction to crystal axis, which makes it suitable for light guiding and routing applications, whereas band four is devoid of this feature.

3.2. Superprism Effect

Some unique dispersive properties exhibited by photonic crystal, provide spatially and spectrally high sensitivity to the incident plane wave, which is far beyond the limitation of Snell's law. This phenomenon is referred to as a superprism effect.

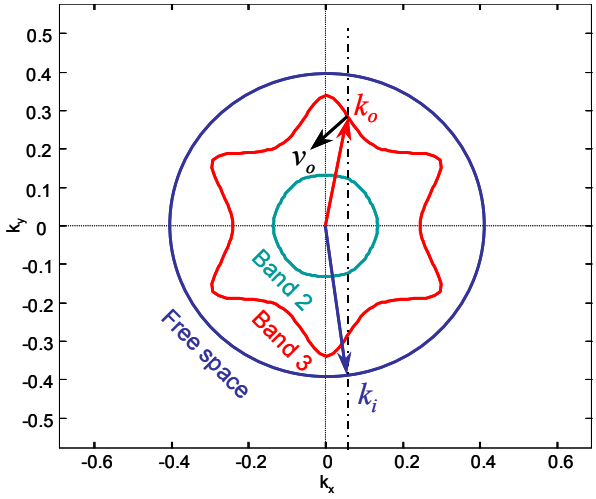

Figure 20: Equi-frequency contours from the 2nd and 3rd bands at normalized frequency 0.4.

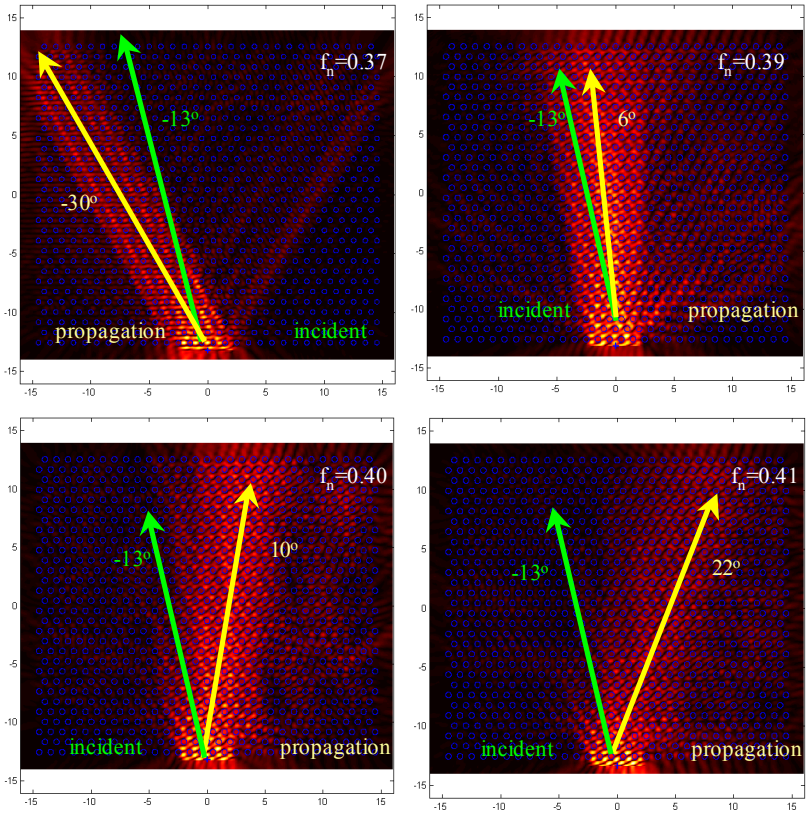

Figure 21: Effect of wavelength change on the direction of the beam propagation inside photonic crystal.

Consider a two-dimensional photonic crystal consists of circular air holes drilled in dielectric with permittivity ε_r = 8 (n = 2.828), arranged in a triangular lattice such that $r/a = 0.24$, where r is the hole radius, and a is the lattice constant. The equi-frequency contour for this structure at normalized frequency 0.4 is shown in Fig. **20**. Assume that the photonic crystal occupies the lower half of the xy-plane ($y < 0$) such that the interface between free space and this photonic crystal is along the x-direction, and that the incident plane wave has wavevector k_i as indicated with an arrow in the same figure. As the wave enters the PhC from free space, the x-component of the incident k-vector is conserved, which means that the k-vector of the wave propagating inside the PhC must lay on the dash-dotted vertical line in Fig. **20**. This line intersects the EFC of the photonic crystal at four points: two for band 2 and two for band 3, so that, potentially, four waves with four different propagation vectors inside the PhC can be created by a single incident wave. However, energy flow considerations eliminate two of these possibilities. For the moment, we will also disregard band 2, and focus on band 3 only. Accordingly, the k-vector in band 3 that satisfies the conservation of the x-component is indicated with a red arrow in Fig. **20**, and labeled as k_o. The group velocity associated with this wave vector is v_o and is shown as a black arrow pointing in the direction of the steepest ascent of ω. Since the group velocity vector is coincident with the energy flow of the optical beam, v_o also shows how the optical beam is 'refracted' as it traverses the free-space/PhC interface. It should be clear now how the high sensitivity of the 'refracted' beam to the incident angle is achieved in a photonic crystal characterized by sharp corners in its equi-frequency contours. As the incident angle moves closer to normal, *i.e.,* the x-component of k_i approaches zero, the wavevector k_o of the wave inside the photonic crystal traces the sharp corner of the EFC, which results in rapid change of the direction of v_o that is always perpendicular to the EFC. In the case described here, the variation of the incident angle in a mere ±4° range produces a whopping ±50°-wide swing of the refracted beam at the normalized frequency 0.4. Such behavior justifies the name 'superprism' given to a structure that exhibits it [72].

In addition to high sensitivity to the incident angle, the PhC described above displays high sensitivity to the wavelength of the incident light as illustrated in Fig. **21**. In this case, the change in frequency by 10% produces a 52° variation of the refracted angle, which further justifies the use of the name 'superprism' for this structure.

3.3. Left-handed Behavior and Negative Refraction

The studies of wave behavior in a Left-handed materials were initiated by Veselago [111] and by Pendry [112]. The left-handed materials have both negative permittivity and permeability. In contrast to right-handed materials, where the direction of the energy flow coincides with the wave propagation vector, for left-handed materials the energy flow is opposite to the phase velocity of the wave. As a result, the refractive index of left-handed materials is negative, and so is the refraction of light at the boundary between left-handed and right-handed material.

Such negative refraction makes an axis-free lens, which is considered as a direct consequence of the fact that the electromagnetic energy moves in opposite direction to the wave vector. In highly structured materials, such as photonic crystals, group velocity points in the direction of energy flow. Thus, left-handedness in this case can be defined as having group and phase velocities point in opposite directions. Furthermore, if an equi-frequency contour (EFC) is circular with a radius k, the effective refractive index for the frequency ω corresponding to such contour can be defined following Snell's law by $\frac{1}{c}(k/\omega)$, where c is the speed of light.

A practical three-dimensional photonic crystal exhibiting negative refraction over a relatively wide bandwidth has been first described by Luo, *et al.* [114]. It consists of air cubes placed in the nodes of a bcc lattice and embedded in high-index dielectric. The sides of the air cubes are parallel to the sides of the conventional bcc unit cell and are ¾ of their length. Since the side of the air cube is more than half of the bcc-cell side, the air cubes overlap to produce a three-dimensional mesh shown in the right inset of Fig. **22 (a)**. The spherical shape of the EFS at $f = 0.36c/a$, as shown in Fig. **22 (b)** allows for determining the effective refractive index of such material. Furthermore, according to the band diagram of Fig. **22 (a)**, for the third band, between points Γ and N as well as between points Γ and H, the slope of the dispersion curve

is negative, which indicates that the group velocity is opposite to phase velocity in for this band. Combined with the spherical shape of the EFS, it makes this photonic crystal suitable for the demonstration of negative refraction, and its utilization as a flat lens. The frequency preferred for this application is 0.35*c*/*a*, where the third-band (red) dispersion curve intersects the light line, shown in Fig. **22 (a)** as straight gray lines originating at the Γ point, thereby producing the effective refractive index of –1, which is important for minimizing aberrations.

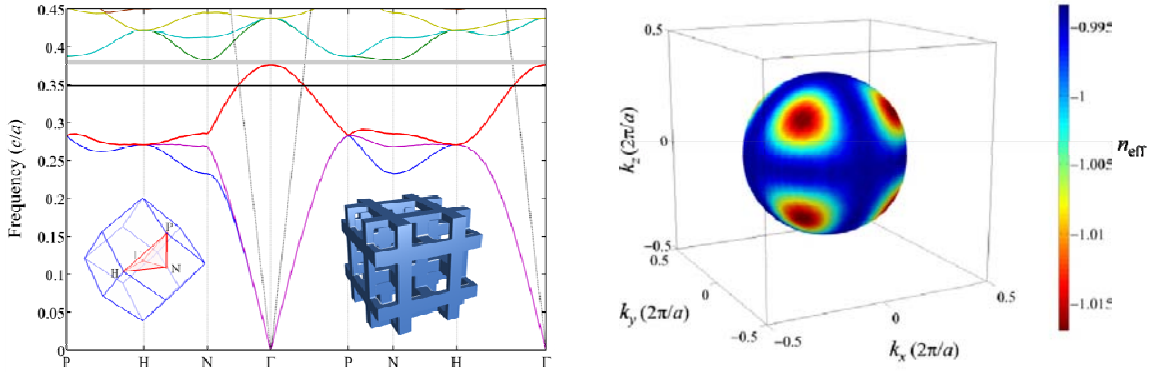

(a) (b)

Figure 22: (a) Band diagram, and (b) equi-frequency surface (EFS) at $f = 0.35c/a$, of a bcc photonic crystal shown in the inset of (a). Dielectric constant of the material is ε_r = 25. The diagonal gray lines originating at the Γ point correspond to the dispersion curves of free space, *i.e.,* light lines. The EFS is colored to indicate the effective index, as indicated by the colorbar.

To demonstrate the flat lens, an entire layer of unit cells can be fabricated by machining both sides of a flat sheet of the dielectric material using a high-precision CNC machine [115]. Stacking such prefabricated sheets produces a three-dimensional photonic crystal as shown in Fig. **23 (a)** where 20 layers were used. Note that the front surface of the slab corresponds to a (101) plane of the photonic crystal since the lattice has been rotated by 45° around the vertical axis. The performance of thus realized photonic crystal flat lens has been tested using a monopole source. Similar monopole configuration was used for a detector, which was placed on an *x*-*y*-*z* computer-controlled scanning stage. The spatial field distribution is obtained by scanning the detector across all three directions, while at each position sweeping the frequency of interest around 17 GHz. Fig. **23 (b)** shows the resulting image of the monopole source produced by the photonic crystal lens at a frequency *f* = 16.4 GHz, in an *x*-*y* plane 12 mm away from the lens surface. The spot size, defined using full-width-at-half-maximum (FWHM) criterion, is about 9 mm by 7 mm, which is considerably smaller than the wavelength of the radiation λ = 18.3 mm, *i.e.,* the lens produced a subwavelength image.

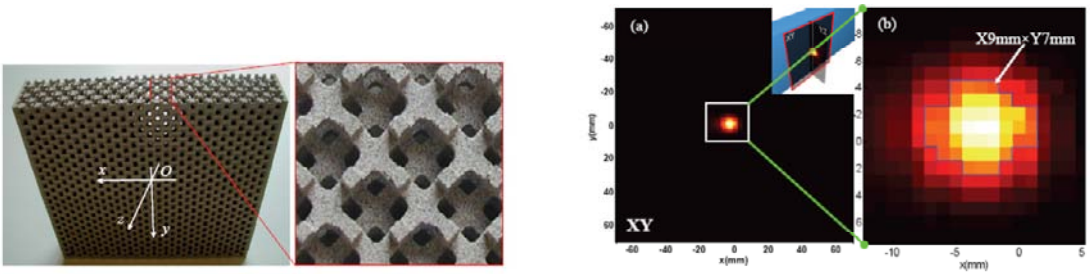

(a) (b)

Figure 23: (a) Three dimensional PhC fabricated following a layer-by-layer process (20 layers in total) with a lattice constant *a* = 6.35 mm (b) Image of a microwave monopole emitting at *f* = 16.4 GHz produced by a photonic crystal flat lens 12 mm from its surface.

4. FABRICATION OF PHOTONIC CRYSTALS

To operate at the near-infrared or visible wavelengths, the minimum feature size of photonic crystals is below 100 nm. To physically realize such features in a controlled way, techniques drawn directly from, or inspired by, approaches used in the microelectronics industry are commonly employed. Here, the experience in patterning electronic circuits at sub-100-nm scale is leveraged to pattern structures for controlling light.

In the sections below, we detail methods that researchers in the field used to realize such patterns. Whether any of the methods find a way to a large-volume production of photonic crystals remains an open issue. However, more likely than not, should the photonic crystals find applications requiring large-volume production, the ultimate method will use elements of the approaches presented below. For more detail on the fabrication process, the reader is referred to [94] and references therein.

4.1. Two-dimensional Photonic Crystals

While a true photonic crystal is periodic in all three spatial dimensions, the difficulty of realizing such structures at the sub-100-nm scales prompted researchers to consider first their two-dimensional analogues. The benefits of stepping back the dimensionality of the system includes the ability to use directly the methods of the semiconductor industry, developed and perfected over the last several decades. At the same time, many of the phenomena predicted to occur in true, *i.e.,* 3D, photonic crystals already exist in two dimensions. Thus, 2D investigations provide valuable insight into the field of photonic crystals.

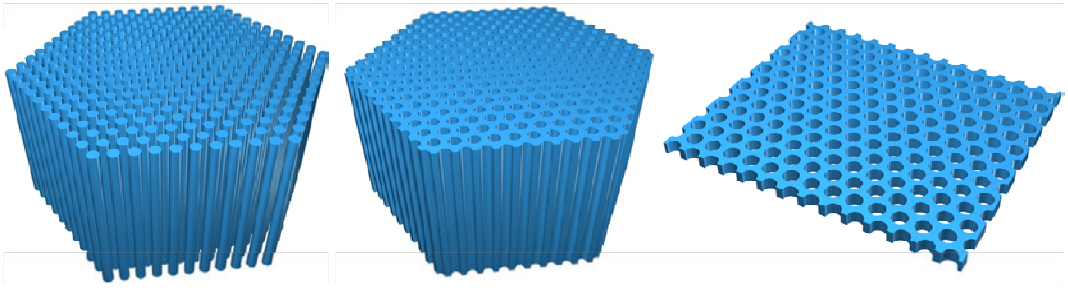

(a) (b) (c)

Figure 24: Two-dimensional photonic crystals. (a) Array of long parallel rods. (b) Array of cylindrical holes in a thick dielectric slab. (c) Perforated dielectric slab.

To be able to ignore the third dimension of our physical space, one of two approaches is generally used.

1. The 2D pattern is extruded along one axis to the size of many wavelengths, Fig. **24 (a)** and **(b)**. If the extrusion were infinite, the system would be truly two-dimensional in the sense that electromagnetic fields variable only in two dimensions, across the patterns, and constant in the extruded dimension, would solve Maxwell's equations. In practice, infinite length is not possible, but the more extended the system is, the more closely it approximates the ideal as the effects of the interaction with the z-boundaries are reduced.

2. The wave is confined to propagate in a thin slab of dielectric material. The confinement is provided by a dielectric-constant contrast between the core slab and the cladding material. In this case the photonic crystal typically takes the form of a perforated slab as in Fig. **24 (c)**. This latter structure is often referred to as planar or slab photonic crystals.

It should be pointed out that the structure of Fig. **25 (a)** is difficult to realize in practice. For sufficiently long rods, so as to reasonably approximate the infinite limit, the rods have a tendency collapse as there is no structural support holding them in place. In contrast, structures of Fig. **25 (b)** and **(c)** provide for mechanical support.

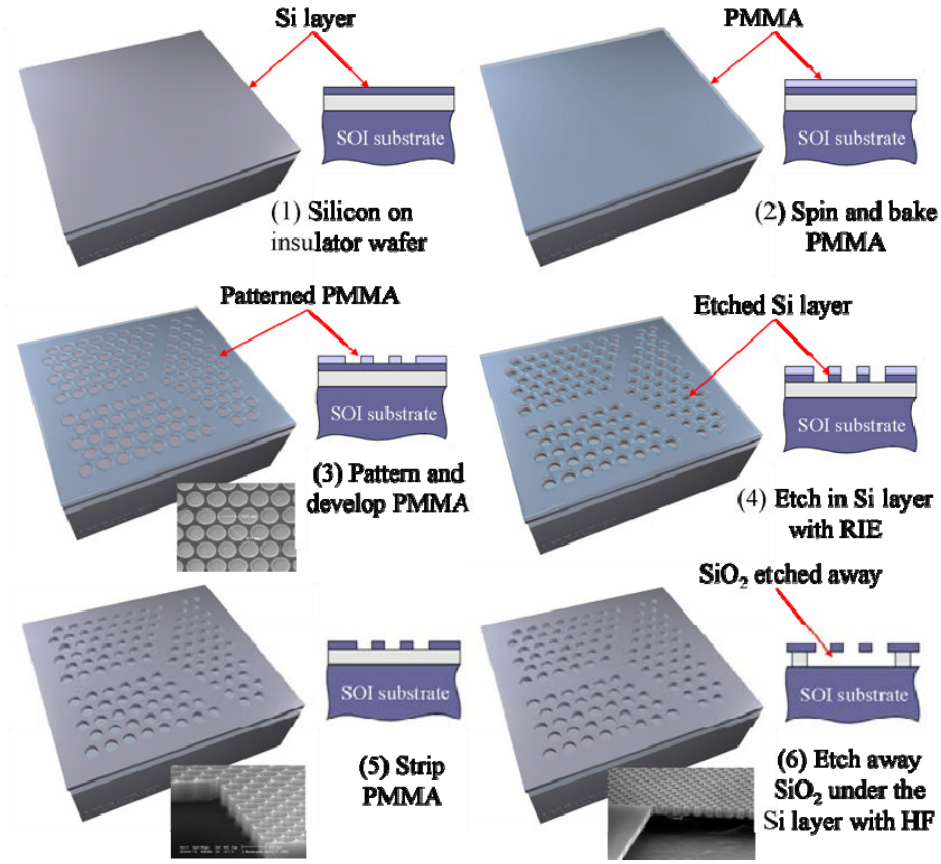

Figure 25: Fabrication of planar photonic crystal.

The fabrication of a planar photonic crystal is shown in Fig. **25** the process starts with a silicon-on-insulator wafer, Fig. **25 (1)**, where a thin silicon device layer, few hundreds of nanometers thick, is isolated from a silicon handle with a layer of oxide. The wafer is coated with resist, Fig. **25 (2)**, which is then exposed in the desired photonic crystal pattern, Fig. **25 (3)**. In research, electron-beam (e-beam) lithography is preferred as it offers high resolution, quick turnaround time, and low overhead thanks to the absence of photolithography masks required in UV projection or contact lithography. For resist, polymethyl methacrylate (PMMA) can be employed. The resist pattern is transferred to the silicon layer by etching, Fig. **25 (4)**. Dry, or plasma, etching offers high directionality and high-fidelity pattern transfer as long as the etch selectivity of silicon over the mask material is sufficiently high. Both can be improved in a time-multiplexed process, also known as Bosch process, where etch and passivation steps are alternated. After stripping the resist, Fig. **25 (5)**, the oxide layer between the silicon device layer and the handle is removed using hydrofluoric acid (HF), Fig. **25 (6)**. The HF etch is timed so as to retain support for the perforated silicon membrane suspended above the substrate. More details on the fabrication process are available in Ref. [94].

The result is a silicon slab photonic crystal few hundreds of nanometers thick clad on both sides with free space. Such an arrangement provides maximum refractive-index contrast and allows for a relatively easy handling of samples thanks to the presence of a handle wafer.

Similar structure can be realized in III-V materials. In this case, a pure GaAs layer is epitaxially grown on top of AlGaAs, as in Fig. **26 (a)**. After patterning photonic crystal, Fig. **26 (b)**, the AlGaAs layer is oxidized in water vapor. The oxidation process is highly selective, and affects only AlGaAS layer while leaving pure GaAs unoxidized, Fig. **26 (c)**. The oxide is removed with HF to leave a suspended photonic crystal membrane, Fig. **26 (d)**.

The use of GaAs as the device layer allows the placement of light sources in the material. This is an advantage over purely silicon-based devices, which require external light sources. On the other hand, the use of silicon facilitates the leveraging of the large investment made in the semiconductor industry over the last several decades thereby providing an avenue for mass production.

To realize structures of the type presented in Fig. **26 (b)**, deep, high-aspect-ratio etch is required. In silicon, this is achieved in electro-photo-chemical process where hole-limited chemical etch of n-type silicon opens deep, uniform-length pores in the material. Adjusting the etch parameters, such as illumination, current density, and electrolyte concentration, yields a range of stable pore growth regimes that have been exploited in the fabrication of high quality 2D photonic crystals operating in the near-infrared regime, [116-125]. In III-V materials, where the elctro-photo-chemical processing has been less investigated than in silicon, deep reactive ion etch is used instead [54]. As a result of material re-deposition and limited mask selectivity, the quality of the photonic crystals thus obtained is typically of lower quality than those realized using electro-photo-chemical etch.

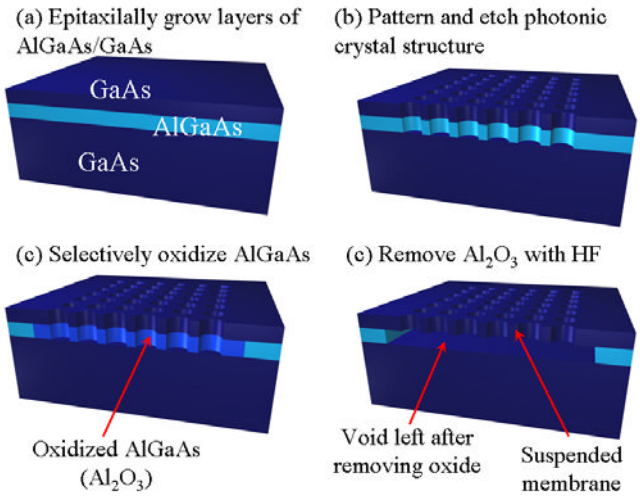

Figure 26: Fabrication of planar photonic crystal in GaAs.

4.2. Micromachining 3D Photonic Crystals

As pointed out above, the main challenge in the fabrication of 3D photonic crystals that operate at near infrared or visible wavelength lies in the scale of features that must be patterned volumetrically. Whereas 2D photonic crystals allow for the direct use methods and tools developed by the semiconductor industry for surface processing, 3D structuring at this scale is still in infancy. As a result, a variety of approaches have been proposed and applied to the realization of 3D photonic crystals.

4.3. Layer-by-Layer Fabrication

The first and, seemingly, most straightforward method is the layer-by-layer approach where the three-dimensional structure is built from individual, finite-thickness layers of materials. The challenge here lies in aligning the consecutive layers so as to obtain the desired three-dimensional pattern. The misalignment must not exceed a small fraction of the photonic crystal period; otherwise the device performance is compromised. Furthermore, given the expense of patterning every layer, the structure has to be designed in such a way as to minimize the numbers of layers required to prepare one period of the photonic crystal. Although any three-dimensional structure can be thought of as consisting of layers, a faithful representation of a sphere may require hundreds whereas a cylinder can be realized with one. Thus, in multilayer fabrication of 3D photonic crystals, major effort is undertaken in designing patterns that would offer interesting optical properties, such as photonic bandgap, at the minimum number of layers per period in the out-of-plane direction. One such pattern has been proposed in Ref. [126] and extensively simulated in [50].

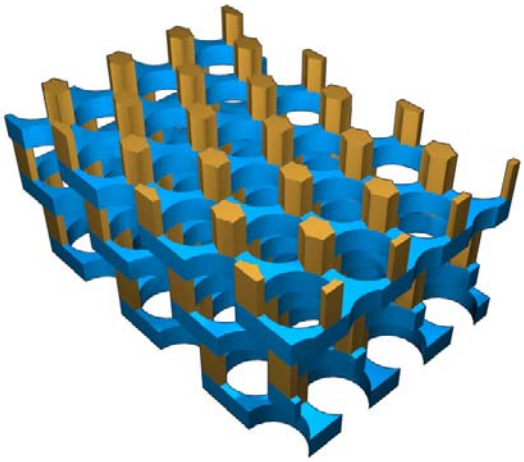

Figure 27: One layer of a three-dimensional photonic crystal proposed in Ref. [126].

It consists of stacked layers that alternate between an array of dielectric pillars, or rods, and cylindrical holes in a dielectric slab as shown in Fig. **27**, which depicts a single vertical period. Although it may seem that six separate etch steps are required to realize one period, the ability to etch both the hole layer, shown in blue, and the two adjacent rod layers, shown in gold, in a single step reduces the number of steps to three per period. The overlapping cylindrical voids form an FCC structure akin to that of closely packed spheres.

The fabrication proceeds in cycles of steps of patterning, etching, back-filling, and polishing. The details are presented in [94] and references therein.

(a) (b)

Figure 28: Woodpile structure. (a) Several layers of logs. (b) Single cell.

Another canonical example of a layered photonic-crystal structure is a woodpile, Fig. **28**. It consists of logs parallel within each layer and perpendicular to adjacent layers. Consecutive parallel layers are offset by half of the spacing between logs within layer. As a result, a single period of such a periodic structure consists of four layers. A single cell is shown in Fig. **28 (b)**. In general, such a structure can be described as face-center-tetragonal lattice. If the distance between the logs in a layer is a factor of $\sqrt{2}$ smaller than the vertical period of the lattice, it becomes an FCC lattice.

Several methods have been developed to fabricate such structures. Here, we describe two that take advantage of the particular geometry in the process.

The first method, known as filleting [127], relies on the fact that a single layer of a woodpile structure consists of separate lines. The fabrication process is shown in Fig. **29**. First, layers of SiN, poly-Si, SiN, and of SiO_2 are deposited on a silicon substrate, Fig. **29 (a)**. Then a pattern of lines in SiO_2 is formed; the dry etch is stopped short, before reaching the nitride layer, Fig. **29 (b)**. Wet etch is used to partly remove the oxide, Fig. **29 (c)**, and polysilicon is conformally deposited as in Fig. **29 (d)**. Anisotropic dry etch

removes silicon to form fillets along the sidewalls of the oxide lines, Fig. **29 (e)**. The sacrificial oxide lines are removed to form a set of free-standing filets, Fig. **29 (f)**, which now act as mask for the wet etch of the nitride layer, Fig. **29 (g)**. The pattern is now transferred with dry etching using the fillets and the nitride lines as an etch mask, Fig. **29 (h)**, and SiO_2 is deposited to fill-in the gaps between the lines, Fig. **29 (i)**. Planarizing the surface, with chemical-mechanical polishing to prevent the propagation of topography, Fig. **29 (j)**, prepares the sample for the next layer, which is processed identically, except for the first nitride layer that acts as an etch stop in step (h). As a result, a woodpile photonic crystal is realized for operation at near infrared wavelengths without upgrading the lithography equipment for higher resolution patterning.

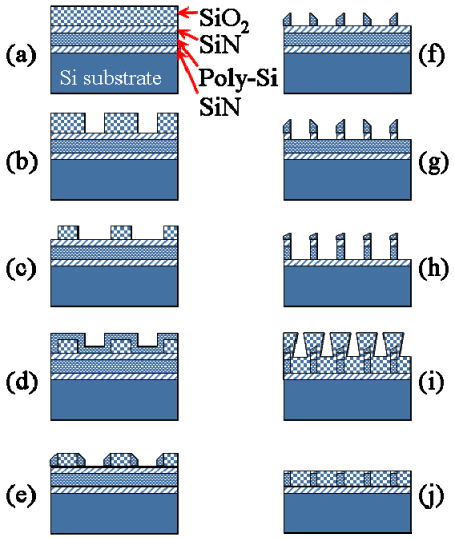

Figure 29: Fabrication of woodpile by filleting.

While high quality photonic crystals have been realized this way, a particular drawback of this method is that the semiconductor material constituting the structure is not crystalline. This limits the applicability of thus fabricated photonic crystals. A method free from this shortcoming described below relies on wafer bonding of patterned substrates to stack the layers made of single crystal semiconductor, [128-138].

First, AlGaAs followed by GaAs layers are grown on GaAs substrate, Fig. **30 (a)**. The thickness of GaAs layer is slightly more than the desired thickness of the resulting PhC layer. A series of parallel rods are patterned and etched using standard lithography techniques, Fig. **30 (b)**. The etch depth is equal to the desired thickness of a single PhC layer and slightly less than the thickness of the top GaAs layer. Two identically patterned wafers are bonded, with rods of the two perpendicular to one another, Fig. **30 (c)**. Then, the handle portion of the top substrate is removed by mechanical polishing followed by wet chemical etch stopping at the AlGaAs boundary, Fig. **30 (d)**, which is followed by the removal of the AlGaAs layer using chemical etch that stops at the GaAs boundary, Fig. **30 (e)**. The remaining thin layer of GaAs is dry-etched using RIE to expose the patterned rods, Fig. **30 (f)**, and the procedure (a)-(f) is repeated with the stacked PhC layers ensuring proper alignment at step (c) to form a structure of Fig. **30 (g)**.

Since the procedure preserves the crystallineity of the material, and the substrate is a III-V material, light sources can be embedded inside the volume of the three-dimensional photonic crystal. Such incorporation of the light source has indeed been demonstrated experimentally [138].

4.4. Autocloning

During plasma assisted etching or deposition, certain shapes can be preserved without getting smoothed out even as thick layers are built up [139]. This is the result of simultaneous removal and deposition of material, which, under certain plasma conditions, lead to the preservation of the slope angle of the surface undergoing processing [94].

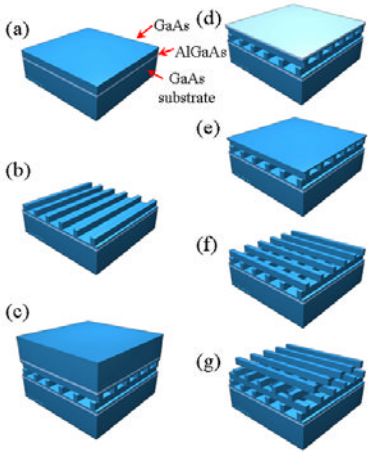

Figure 30: Fabrication of woodpile by wafer bonding of patterned substrate.

This phenomenon can be used to deposit multiple layers of different materials while preserving the original topography of the substrate. By judiciously selecting this original topography, three-dimensional periodic structures such as those shown in Fig. **31** can be realized [140-144] where the lighter and darker shades of blue represent different dielectric materials, such as silicon and silicon dioxide.

Although the structure of Fig. **31** is undeniably periodic in all three dimensions, the photonic crystal that it represents lacks full photonic bandgap, a desirable property of these materials. It is believed that the main reasons for this shortcoming include the continuity of the layers in plane, whereby the effective index modulation is low, and the lack of connectivity in the out-of-plane direction. Both can be remedied by realizing the structure shown in Fig. **32**. In this case, the autocloned pattern is a set of parallel ridges. The sample then undergoes further processing that consists of etching an array of cylindrical holes running across the layers [145]. This structure has a full photonic bandgap and has been successfully fabricated [146-148].

As with other techniques that rely on a single two-dimensional pattern to realize a three-dimensional structure, the placement of arbitrary defects inside the volume of the photonic crystal poses a difficulty.

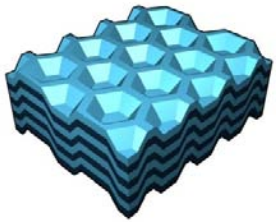

Figure 31: 3D periodic structure obtained by autocloning.

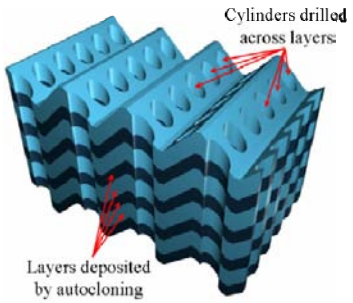

Figure 32: Photonic crystal obtained by the combination of autocloning and directional etching.

4.5. Glancing Angle Deposition

When thin solid films are deposited by evaporation at a grazing angle, they tend to form columnar and highly porous structures. This happens due to shadowing effected by the newly deposited atoms that preclude the incoming atoms from taking arbitrary positions on the substrate. The phenomenon is illustrated in Fig. **33** where the deposited material does not form a uniform film, but rather filaments or columns grow at an angle.

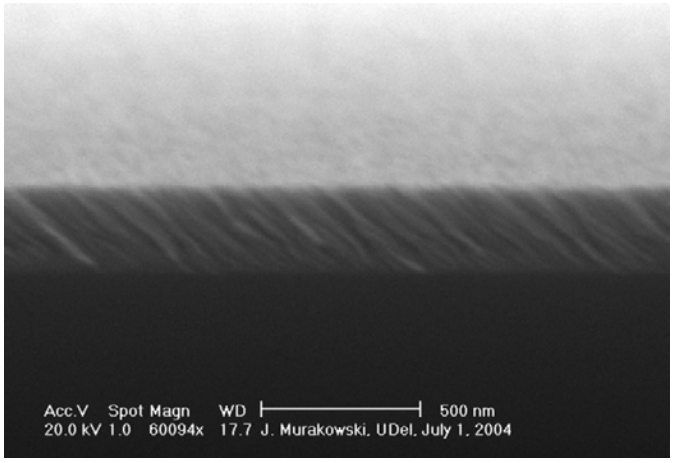

Figure 33: Chromium evaporated at a steep angle forms columnar structure.

(a) (b)

Figure 34: Glancing-angle deposition of periodic spirals. (a) System used for material deposition. Electrons from the glowing orange element in the physical vapor deposition (PVD) source heat material, which evaporates, and condenses on surfaces in line of sight. (b) Resulting photonic crystal.

Such growth has been used to create 3D photonic crystals [149-153]. To this end, first, periodically distributed seeds are pre-patterned on the substrate using standard lithography techniques to ensure the controlled placement features. Then, material is evaporated at an oblique, or glancing, angle α while periodically rotating the substrate, φ, using a system schematically depicted in Fig. **34 (a)**. By properly timing the rotation of the substrate, spirals arranged periodically according to the seed layer are grown as shown in Fig. **34 (b)**.

The structure can be then 'inverted' by back-filling it with a different material, and dissolving the original spirals. As a result, three-dimensional photonic crystal of periodic spiral voids embedded in high-index material is created.

4.6. Macroporous Silicon

Etching of silicon in the solution of hydrofluoric (HF) acid is only possible in the presence of holes; therefore, n-type silicon remains inert in the electrolyte. This situation changes when a source of holes is introduced by positively biasing the substrate with respect to the electrolyte and/or photo-generating

electron-hole pairs, Fig. **35**. If the reaction is hole-supply limited, deep uniform-length pores grow perpendicular to the surface due to the formation of space-charge region (SCR) devoid of holes between the pores.

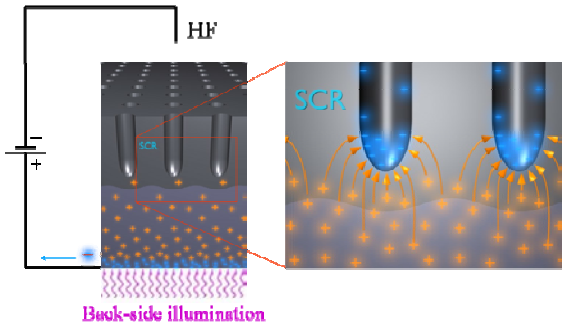

Figure 35: Micro-pore formation during electro-photo-chemical etching of silicon. SCR is devoid of holes, which are swept by the field to the hole tips. This leaves the pore sidewalls impervious to HF attack.

This protects the pore walls from etching, which, as a result, only takes place at the pore tips. Seeding the pore growth by patterning the surface allows the creation of a regular array of openings, whereas modulating the supply of holes, by changing the bias or illumination, enables the variation of the pore cross-section along its depth [154-156]. As a result, a structure periodic in all three dimensions can be created where the initial pattern is a two-dimensional array of seed topography at the substrate.

Following the electrochemical etch, the sample can be further processed using other methods, such as KOH etch, or multiple oxidation-and-etch cycles, to enlarge the pores and thus realize laterally overlapping voids [157]. This method produced some of the largest and most regular 3D photonic crystals for infrared wavelength. However, the types of photonic crystal lattices that can be obtained this way are limited, and the controlled placement of defects is problematic.

4.7. Chemically Assisted Ion Beam Etching

The photonic crystal structure known today as Yablonovite, Fig. **36**, was first created for the microwave region of electromagnetic spectrum in 1991 by mechanically drilling in low-loss dielectric material [11]. The approach has been extended to near infrared by using chemically-assisted ion beam etching (CAIBE) [52, 53, 55] in a process depicted in Fig. **37**. The high anisotropy of the etch allows for drilling high-aspect-ratio holes in the material. The incidence angle of the ion beam determines the angle of the cylindrical voids in the material.

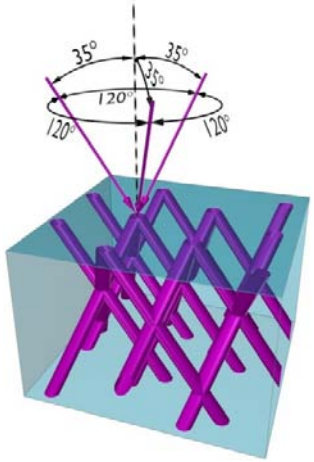

Figure 36: Three-dimensional geometry of Yablonovite.

In the process, one starts with a mask material that is highly resistant to CAIBE, Fig. **37 (1)**, in which a regular array of openings is patterned using standard lithography techniques, Fig. **37 (2)**. Arrows in steps **(3)** through **(5)** indicate the directions of the ion flux incident on the sample during the three consecutive etch steps. The result of the process is the structure of Fig. **37 (6)**, which shows 1.33 periods in the vertical direction that corresponds to the [111]-direction of the crystal.

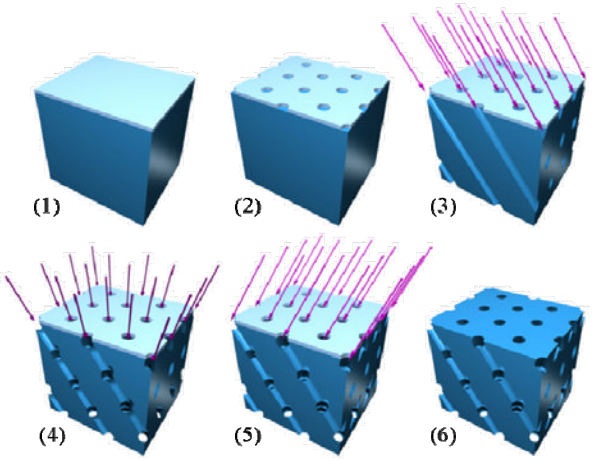

Figure 37: Fabrication of Yablonovite using chemically-assisted ion beam etching.

The main difficulty in this approach has to do with the etch mask. It must be thin, so as to allow line-of-sight access to the substrate for the incident ion flux. The thicker the etch-mask layer, the smaller the resulting cylindrical holes in the material for the same size openings in the mask. On the other hand, to etch deep into the material, the mask must withstand the bombardment of ions for three consecutive etches. This means that very high etch selectivity between the mask and the substrate material is required to achieve even modest size 3D photonic crystals. Although tremendous advances have been made in this regard, [52, 53, 55], the etch selectivity over the mask remains the main limitation of this process. As a result, the size of thus obtained 3D photonic crystals is only a couple of periods [94] in the vertical direction.

4.8. Reactive Plasma for Microsculpting

The development of sophisticated instruments where the generation of plasma and its use for etching are decoupled, enabled contemplating fabrication processes with capabilities to shape matter at the micro- and nano-scale in unprecedented ways. One of the most well-known examples is the Bosch process, whereby deep trenches with vertical sidewalls are realized using a sequence of deposition and etch. In this case, the deposition serves to passivate the sidewalls to protect them from chemical attack by the reactive species generated in the plasma. In general, the use of highly anisotropic and highly isotropic etches, plus the ability to deposit passivation material during a single process opens the possibility to realize a variety of shapes etched as voids in the material [94]. This capability can be used to create a 3D photonic crystal consisting of an array of spherical voids etched in the volume of semiconductor.

The process leading to such a structure is shown in Fig. **38**. It starts with the patterning of a two-dimensional array of openings in a suitable etch mask material as in Fig. **38 (a)**. The sample is subjected to anisotropic etch, which produces cylindrical holes in the underlying substrate, Fig. **38 (b)**. The sidewalls of the cylindrical openings are passivated as part of the Bosch process to inhibit lateral etching of silicon and to ensure that the sidewalls are vertical; the bottoms of the openings are the only exposed regions of silicon for the next step, which is an isotropic etch. The etch proceeds at equal rates in all directions and produces spherical voids as shown in Fig. **38 (c)**. The passivation lining the original cylinder remains intact, as the reaction is highly selective in removing silicon. The isotropic etch is followed by the passivation of the entire silicon surface of the voids, Fig. **38 (d)**. The cycle is then repeated as in Fig. **38 (e)** through **(k)**, and then the passivation layer is stripped to produce a 3D photonic crystal shown in Fig. **38 (l)**.

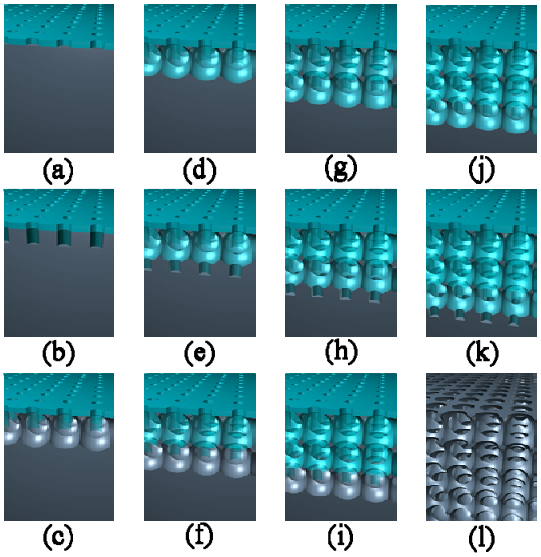

Figure 38: Fabrication of 3D photonic crystal by micro-sculpting of silicon.

CONCLUSIONS

In this chapter we have presented an overview of various computational methods for modeling and simulating PhCs, suitable fabrication processes, and recent developments in efforts to develop and optimize photonic integrated circuits (PICs) using PhC and PBG structures for a broad range of applications. The implication of this research is the ability to incorporate on-chip optical functionality, including confinement and routing, on a scale comparable to, or less than, the wavelength of light.

While we have attempted to present a brief historical overview in the course of this chapter, it is also clear that PhC technology is just beginning to come of age and many applications have yet to be realized. As an example, optical components that can permit the miniaturization of an application-specific photonic integrated circuit (ASPIC) on a subwavelength scale represent good candidates for next-generation high density optical interconnects and integration.

In recent years, there has been extremely rapid growth in efforts toward realization of PhCs for a number of new devices and applications. As a result, we acknowledge that we have included merely a subset of those efforts that have been published, and we regret the unavoidable omission of many interesting and important bodies of work.

We hope and believe that the research summarized herein represents only the beginnings of what will eventually become a mature, important field of study, whose results will be used to realize a new generation of optoelectronic/photonic systems, serving to satisfy the growing demands of next-generation high-technology systems.

ACKNOWLEDGEMENTS

While much of this chapter comprises a review of the work of numerous research groups (Sections 1 and 4 in particular), a signficant proportion of the the results presented were obtained by our research group at the University of Delaware. With respect to these efforts, as is typically the case for sustained research endeavors, there were many students, collaborators, and sponsors who provided key inputs and resources, without which our results could not have been achieved. We would like to acknowledge the entire membership of the Nanophotonic Reserach Group at the University of Delaware (past and present), the software and design teams at EM Photonics, Inc., and the support of Dr. Gernot Pomrenke at the Air Force Office of Scientific Research.

REFERENCES

[1] Sensors. The Freedonia Group, Inc., 2006.

[2] Lambeck PV. Integrated opto-chemical sensors. Sensors Actuat B-Chem 1992; 8(1): 103-16.

[3] Martin R, Sharkawy A, Humphrey J, Kelmelis EJ, Prather DW. Integrated optical chemical sensor using a dispersion-guided photonic crystal structure. Proceedings of SPIE 2006; 6322: 63220I.

[4] Martin R, Sharkawy A, Kelmelis EJ. Photonic crystals reduce the size of optical sensors. SPIE; 2006; Available from: http: //spie.org/x8577.xml?highlight=x2400&ArticleID=x8577.

[5] Bykov V. Spontaneous Emission in a Periodic Structure. Zhurnal Experimentalnoi i Teoreticheskoi Fiziki. 1972; 62(2).

[6] Bykov V. Sponteneous emission in a periodic structure. Soviet Physics JETP 1972; 35: 269-73.

[7] Bykov V. Spontaneous emission from a medium with a band spectrum. Soviet Journal of Quant Electron 1975; 4: 861-71.

[8] Bykov V. Free Oscillations of Elastic Dipole Located in Periodic Structure. Zhurnal Tekhnicheskoi Fiziki. 1978; 48(5).

[9] Yablonovitch E. Inhibited Spontaneous Emission in Solid-State Physics and Electronics. Phys Rev Lett 1987; 58(20): 2059-62.

[10] John S. Strong Localization of Photons in Certain Disordered Dielectric Superlattices. Phys Rev Lett 1987; 58(23): 2486-9.

[11] Yablonovitch E, Gmitter TJ. Photonic band structure: The face-centered-cubic case. Phys Rev Lett 1989; 63(18): 1950-3.

[12] Joannopoulos JD, Villeneuve PR, Fan J. Photonic Crystals. Solid State Commun 1997; 102(165).

[13] Zhang Z, Satpathy S. Electromagnetic Wave Propagation in Periodic Structures: Bloch Wave Solution of Maxwell's Equations. Phys Rev Lett 1990; 65(21): 2650-3.

[14] Leung KM, Liu YF. Photon Band Structures: The Plane-Wave Method. Phys Rev B 1990; 41(14): 10188-90.

[15] John S, Rangarajan R. Optimal Structures for Classical Wave Localization - an Alternative to the Ioffe-Regel Criterion. Phys Rev B 1988; 38(14): 10101-4.

[16] Economou EN, Zdetsis A. Classical wave propagation in periodic structures. Phys Rev B 1989; 40(2): 1334-7.

[17] Datta S, Chan C, Ho K, Soukoulis CM. Photonic bandgaps in periodic dielectric structures-The scalar wave approximation. Phys Rev B 1992; 46(17): 10650-6.

[18] Plihal M, Maradudin AA. Photonic band structure of two-dimensional systems: The triangular lattice. Phys Rev B 1991; 44(16): 8565-71.

[19] Liu L, Liu JT. Photonic Band Structure in the Nearly Plane Wave Approximation. Eur Phys J B 1999; 9: 381-8.

[20] Yablonovitch E, Gmitter TJ, Leung KM. Photonic Band-Structure - the Face-Centered-Cubic Case Employing Nonspherical Atoms. Phys Rev Lett 1991; 67(17): 2295-8.

[21] Ozbay E, Abeyta A, Tuttle G, *et al.* Measuerment of a three-dimensional photonic band gap in a crystal structure made of dielectric rods. Phys Rev B 1994; 50(3): 1945-8.

[22] Ozbay E, Michel E, Tuttle G, *et al.* Terahertz spectroscopy of three-dimensional photonic band-gap crystal. Opt Lett 1994; 19(15): 1155.

[23] Ozbay E, Michel E, Tuttle G, *et al.* Double-etch geometry for millimeter-wave photonic band-gap crystals. Appl Phys Lett 1994; 65(13): 1617-9.

[24] Ozbay E, Michel E, Tuttle G, Biswas R, Sigalas MM, Ho KM. Micromachined millimeter-wave photonic band-gap crystals. Appl Phys Lett 1994; 64(16): 2059-61.

[25] Lin S-Y, Fleming JG. A three-dimensional optical photonic crystal. J Lightwave Technol 1999; 17(11): 1944-7.

[26] John S, Busch K. Photonic band gap formation in certain self-organizing systems. Phys Rev E 1998; 58: 3896-3908.

[27] Tarhan II, Watson G. Photonic band structure of fcc colloidal crystals. Phys Rev Lett 1996; 76: 315-8.

[28] Tarhan II, Zinkin MP, Watson G. An interferometric technique for measurement of photonic band structure in colloidal crystals. Opt Lett 1995; 20: 1571-4.

[29] Tarhan II, Watson G. Optical measurements of photonic band structure in fcc colloidal crystals. In: Soukoulis CM, editor.: Kluwer Academic; 1996. p. 93-106.

[30] Tarhan I, Watson G. Analytical expression for the optimized stop bands of fcc photonic crystals in the scalar-wave approximation. Phys Rev B 1996; 54(11): 7593-7.

[31] Pradhan RD, Tarhan II, Watson G. Impurity modes in the optical stop bands of doped colloidal crystals. Phys Rev B 1996; 54: 13721-4.

[32] Pradhan RD, Bloodgood JA, Watson G. Photonic band structure of bcc colloidal crystals. Phys Rev B 1997; 55: 9503-6.

[33] Rosner BT, Schneider GJ, Watson G. Interferometric investigation of photonic band structure effects in pure and doped colloidal crystals. J Opt Soc Am B. 1998; 15: 2654-8.

[34] Xia Y, Gates B, Park SH. Fabrication of three-dimensional photonic crystals for use in the spectral region from ultraviolet to near-infrared. J Lightwave Technol 1999; 17(11): 1956-62.

[35] Jiang P, Ostojic GN, Narat R, Mittleman DM, Colvin VL. The fabrication and bandgap engineering of photonic multi-layers. Adv Mater 2001; 13(6): 389-93.

[36] Xia Y, Gates B, Li Z-Y. Self-Assembly Approaches to Three-Dimensional Photonic Crystals. Adv Mater 2001; 13(6): 409-13.

[37] Joannopoulos JD, Villeneuve PR, Fan S. Photonic Crystals: Putting a New Twist on Light. Nature 1997; 386: 143.

[38] Chow E, Lin SY, Wendt JR, Johnson SG, Joannopoulos JD. Quantitative analysis of bending efficiency in photonic-crystal waveguide bends at 1.55 um wavelengths. Opt Lett 2001; 26(5): 286-8.

[39] Meade RD, Devenyi A, Joannopoulos JD, Alerhand OL, Smith DA, Kash K. Novel applications of photonic band gap materials : Low-loss bends and high Q cavities. J Appl Phys 1994; 75(9): 4753-5.

[40] Mekis A, Chen JC, Kurland I, Fan S, Villeneuve PR, Joannopoulos JD. High Transmission through sharp bends in photonic crystal waveguides. Phys Rev Lett 1996; 77(18): 3787-90.

[41] Fan S, Winn JN, Devenyi A, Chen JC, Meade RD, Joannopoulos JD. Guided and Defect Modes in Periodic Dielectric Waveguides. J Opt Soc Am B 1995; 12: 1267.

[42] Mekis A, Fan J, Joannopoulos JD. Bound states in photonic crystal waveguides and waveguide bends. Phys Rev B 1998; 58: 4809-917.

[43] Lin SY, Chow E, Hietala V, Villeneuve PR, Joannopoulos JD. Experimental Demonstration of Guiding and Bending of Electromagnetic Waves in Photonic Crystal. Science 1998; 282: 274-6.

[44] Villeneuve PR, Fan S, Joannopoulos JD. Microcavities in Photonic Crystals : Mode Symmetry, Tunability, and Coupling Efficiency. Phys Rev B 1996; 54(11): 7837-42.

[45] Haus HA, Fan S, Villeneuve PR, Joannopoulos JD. Channel Drop Filters in Photonic Crystals. Opt Express 1998; 3(1): 4-11.

[46] Fan R, Villeneuve R, Joannopoulos JD, Haus HA. Channel Drop Tunneling Through Localized States. Phys Rev Lett 1998; 80(5): 960-3.

[47] Centeno E, Guizal B, Felbacq D. Multiplexing and demultiplexing with photonic crystals. J Opt A - Pure Appl Opt 1999; 1: L10-L3.

[48] Zhang C, Qiao F, Wan J, Zi J. Enlargement of nontransmission frequency range in photonic crystals by using multiple heterostructures. J Appl Phys 2000; 87: 3174-6.

[49] Fan S, Johnson SG, Joannopoulos JD. Waveguide branches in photonic crystals. J Opt Soc Am B. 2001; 18(2): 162-5.

[50] Povinelli ML, Johnson SG, Fan J, Joannopoulos JD. Emulation of two-dimensional photonic crystal defect modes in a photonic crystal with a three-dimensional photonic band gap. Phys Rev B 2001; 64: 753131-8.

[51] Johnson SG, Manolatou C, Fan SH, Villeneuve PR, Joannopoulos JD, Haus HA. Elimination of cross talk in waveguide intersections. Opt Lett 1998; 23(23): 1855-7.

[52] Cheng CC, Scherer A. Fabrication of photonic band-gap crystals. J Vac Sci Tech B 1995; 13(6): 2696-700.

[53] Cheng CC, Scherer A, Arbet-Engels V, Yablonovitch E. Lithographic Band gap tuning in photonic band gap crystals. J Vac Sci Tech B 1996; 14(6): 4110-4.

[54] O'Brien J, Painter O, Lee R, Cheng CC, Yariv A, Scherer A. Lasers incorporating 2D photonic bandgap mirrors. Electron Lett 1996; 32(24): 2243-4.

[55] Cheng CC, Scherer A, Tyan R-C, Fainman Y, Witzgall G, Yablonovitch E. New Fabrication Techniques for High Quality Photonic Crystals. J Vac Sci Technol B 1997; 15(6): 2764-7.

[56] D'Urso B, Painter O, O'Brien J, Tombrello T, Yariv A, Scherer A. Modal reflectivity in finite-depth two-dimensional photonic-crystal microcavities. J Opt Soc Am B 1998; 15(3): 1155-9.

[57] Krauss TF, Painter O, Scherer A, Roberts JS, De La Rue RM. Photonic microstructures as laser mirrors. Opt Eng 1998; 37(4): 1143-8.

[58] Painter O, Vuckovic J, Scherer A. Defect modes of a two-dimensional photonic crystal in an optically thick dielectric slab. J Opt Soc Am B 1999; 16(6): 275-85.

[59] Painter O, Husain A, Scherer A, O'Brien J, Kim I, Dapkus PD. Room Temperature photonic crystal defect lasers at near-infrared wavelengths in InGaAsP. J Lightwave Technol 1999; 17(11): 2082-8.

[60] Painter O, Lee RK, Scherer A, *et al.* Two-Dimensional Photonic Band-Gap Defect Mode Laser. Science 1999; 284(11): 1819-21.
[61] Lee RK, Painter OJ, Kitzke B, Scherer A, Yariv A. Photonic bandgap disk laser. Electron Lett 1999; 35(7): 569-70.
[62] Lee RK, Painter OJ, D'Urso B, Scherer A, Yariv A. Measurement of spontaneous emission from a two-dimensional photonic band gap defined microcavity at near-infrared wavelengths. Appl Phys Lett 1999; 74(11): 1522-4.
[63] Xu Y, Vuckovic J, lee RK, Painter OJ, Scherer A, Yariv A. Finite-difference time-domain calculation of spotaneous emission lifetime in a microcavity. J Opt Soc Am B 1999; 16(3): 465-74.
[64] Vuckovic J, Painter O, Xu Y, Yariv A, Scherer A. Finite-Difference Time-Domain Calculation of the spontaneous emission coupling factor in optical microcavities. IEEE J Quantum Elect 1999; 35(8): 1168-75.
[65] Yoshie T, Scherer A, Chen H, Huffaker D, Deppe D. Optical characterization of two-dimensional photonic crystal cavities with indium arsenide quantum dot emitters. Appl Phys Lett 2001; 79(1): 114-6.
[66] Loncar M, Nedeljkovic D, Doll T, Vuckovic J, Scherer A, Pearsall TP. Waveguiding in Planar Photonic Crystals. Appl Phys Lett 2000; 77(13): 1937-9.
[67] Loncar M, Doll T, Vuckovic J, Scherer A. Design and fabrication of silicon photonic crystal optical waveguides. J Lightwave Technol 2000; 18(10): 1402-11.
[68] Adibi A, Xu Y, Lee RK, Yariv A, Scherer A. Properties of the slab modes in photonic crystal optical waveguides. J Lightwave Technol 2000; 18(11): 1554-64.
[69] Adibi A, Lee RK, Xu Y, Yariv A, Scherer A. Design of photonic crystal optical waveguides with single mode propagation in the photonic bandgap. Electron Lett 2000; 36(16): 1376-8.
[70] Kosaka H, Kawashima T, Tomita A, *et al.* Superprism Phenomena in Photonic Crystals. Phys Rev B 1998; 58(16): R10096-R9.
[71] Kosaka H, Kawashima T, Tomita A, *et al.* Photonic Crystals for Micro Lightwave Circuits Using Wavelength-Dependent Angular Beam Steering. Appl Phys Lett 1999; 74(10): 1370-2.
[72] Kosaka H, Kawashima T, Tomita A, *et al.* Superprism Phenomena in Photonic Crystals: Toward Microscale Lightwave Circuits. J Lightwave Technol 1999; 17(11): 2032-4.
[73] Shelby RA, Smith DR, Schultz S. Experimental Verification of a negative index of refraction. Science 2001; 292(6): 77-9.
[74] Kosaka H, Kawashima T, Tomita A, *et al.* Self-collimating phenomena in photonic crystals. Appl Phys Lett 1999; 74(9): 1212-4.
[75] Bayindir M, Temelkuran B, Ozbay E. Photonic Crystal Based Beam Splitters. Appl Phys Lett 2000; 77(24): 3902-4.
[76] Parker G, Charlton M. Photonic Crystals. Physics World. 2000; 13(8).
[77] Sondergaard T, Dridi KH. Energy flow in photonic crystal waveguides. Phys Rev B 2000; 61(23): 15688-96.
[78] Ziolkowski RW. FDTD Analysis of PBG waveguides, power splitters and switches. Opt Quant Electron 1999; 31: 843-55.
[79] Scherer A, Painter O, D'Urso B, Lee R, Yariv A. InGaAsP photonic band gap crystal membrane microresonators. J Vac Sci Tech B 1998; 16(6): 3906-10.
[80] Microcavities and photonic Bandgaps: Physics and Applications. Rarity J, Weisbuch C, editors. Elounda, Crete: Kluwer Academic Publishers; 1995. p. 600
[81] Sun H-B, Mizeikis V, Xu Y, Juodkazis S, Ye J-Y, Matsuo S, *et al.* Microcavities in polymeric photonic crystals. Appl Phys Lett 2001; 79(1): 1-3.
[82] Johnson SG, Shanhui F, Mekis A, Joannopoulos JD. Multipole-cancelation mechanism for high-Q cavities in the absence of a complete photonic band gap. Appl Phys Lett 2001; 78(22): 3388-90.
[83] Sharkawy A, Shi S, Prather DW. Multichannel Wavelength Division Multiplexing Using Photonic Crystals. Appl Optics 2001; 40(14): 2247-52.
[84] Stoffer R, Hoekstra HJWM, Ridder RMD, Groesen EV, Beckum FPHV. Numerical Studies of 2D Photonic Crystals: Waveguides, Coupling Between Waveguides and Filters. Opt Quant Electron 2000; 32: 947-61.
[85] Johnson SG, Fan S, Villeneuve PR, Joannopoulos JD. Guided modes in photonic crystal slabs. Phys Rev B 1999; 60(8): 5751-8.
[86] Johnson SG, Villeneuve PR, Fan S, Joannopoulos JD. Linear Waveguides in Photonic-Crystal Slabs. Phys Rev B 2000; 62(12): 8212-22.
[87] Charlton M, Zoorob ME, Parker G, Netti MC, Baumberg JJ, Cox JA, *et al.* Experimental Investigation of photonic crystal waveguide devices and line-defect waveguide bends. Mater Sci Eng 2000; B74: 17-24.
[88] Gander M, McBride R, Jones J, *et al.* Experimental measurement of group velocity dispersion in photonic crystal fibre. Electron Lett 1999; 35(1): 63-4.

[89] Smith CJM, Rue RMDL, Rattier M, *et al.* Coupled guide and cavity in a two-dimensional photonic crystal. Appl Phys Lett 2001; 78(11): 1487-9.
[90] Hirayama H, Hamano T, Aoyagi Y. Novel surface emitting laser diode using photonic band-gap crystal cavity. Appl Phys Lett 1996; 69: 791-3.
[91] Liboff RL. Introductory quantum mechanics. 4th ed. San Francisco: Addison Wesley; 2003. xvii: 878.
[92] Ashcroft NW, Mermin ND. Solid State Physics. Crane DG, editor. Philadelphia: Saunders College; 1976.
[93] Jackson JD. Classical electrodynamics. 3rd ed. New York: Wiley; 1999. xxi: 808.
[94] Prather DW, Shi S, Sharkawy A, Murakowski J, Schneider GJ. Photonic Crystals: Theory, Applications, and Fabrication. Boreman G, editor. Hoboken, New Jersey: Wiley; 2009.
[95] Yablonovitch E. Photonic Band-Gap Structures. J Opt Soc Am B. 1993; 10(2): 283-95.
[96] Ho KM, Chan CT, Soukoulis CM. Existence of a Photonic Gap in Periodic Dielectric Structures. Phys Rev Lett 1990; 65(25): 3152-5.
[97] Bayindir M, Temmelkuran B, Ozbay E. Propagation of Photons by Hopping: A Waveguiding Mechanism Through Localized Coupled Cavities in Three-Dimensional Photonic Crystals. Phys Rev B 2000; 61(18): R11855-R8.
[98] McGurn AR. Photonic Crystal Circuits: A Theory for Two- and Three Dimensional Networks. Phys Rev B 2000; 61(19): 13235-49.
[99] Yablonovitch E. Photonic Band-Gap Crystals. Journal of Physics-Condensed Matter. 1993; 5(16): 2443-60.
[100] Smith CJM, Benisty H, Olivier S, *et al.* Low-loss channel waveguides with two-dimensional photonic crystal boundaries. Appl Phys Lett 2000; 77(18): 2813-5.
[101] Stanley RP, Houdre R, Oesterle U, Ilegems M. Impurity Modes in One-Dimensional Periodic-Systems - the Transition from Photonic Band-Gaps to Microcavities. Phys Rev A. 1993; 48(3): 2246-50.
[102] Arentoft J, Sondergaard T, Kristensen M, Boltasseva A, Thorhauge M, Frandsen L. Low-loss silicon-on-insulator photonic crystal waveguides. Electron Lett 2002; 38(6): 274-5.
[103] Prather DW, Sharkawy A, Shi S. Design and Applications of Photonic Crystals. Handbook of Nanoscience, Engineering, and Technology. Boca Raton, FL: CRC Press LLC; 2002. p. 211-32.
[104] Foresi JS, Villeneuve PR, Ferrera J, *et al.* Photonic-bandgap microcavities in optical waveguides. Nature 1997; 390(6656): 143-5.
[105] Lin SY, Fleming JG, Sigalas MM, Biswas R, Ho KM. Photonic band-gap microcavities in three dimensions. Phys Rev B 1999; 59(24): R15579-R82.
[106] Witzens J, Loncar M, Scherer A. Self-collimation in planar photonic crystals. IEEE J Sel Top Quant 2002; 8(6): 1246-57.
[107] Prather DW, Shi S, Murakowski J, *et al.* Self-collimation in photonic crystal structures: A new paradigm for applications and device development. J Phys D Appl Phys 2007; 40(9): 2635-51.
[108] Cubukcu E, Aydin K, Ozbay E, Foteinopoulou S, Soukoulis CM. Negative refraction by photonic crystals. Nature 2003; 423(6940): 604-5.
[109] Parimi PV, Lu WTT, Vodo P, Sridhar S. Photonic crystals - Imaging by flat lens using negative refraction. Nature 2003; 426(6965): 404.
[110] Berrier A, Mulot M, Swillo M, *et al.* Negative refraction at infrared wavelengths in a two-dimensional photonic crystal. Phys Rev Lett 2004; 93(7): 073902.
[111] Veselago VG. Properties of Materials Having Simultaneously Negative Values of Dielectric (Xi) and Magnetic (Mu) Susceptibilities. Soviet Physics Solid State, USSR. 1966; 8(12): 3571-3.
[112] Pendry JB. Negative refraction makes a perfect lens. Phys Rev Lett 2000; 85(18): 3966-9.
[113] Prather DW, Murakowski J, Shi SY, Venkataraman S, Sharkawy A, Chen CH, *et al.* High-efficiency coupling structure for a single-line-defect photonic-crystal waveguide. Opt Lett 2002; 27(18): 1601-3.
[114] Luo CY, Johnson SG, Joannopoulos JD. All-angle negative refraction in a three-dimensionally periodic photonic crystal. Appl Phys Lett 2002; 81(13): 2352-4.
[115] Lu ZL, Murakowski JA, Schuetz CA, Shi SY, Schneider GJ, Prather DW. Three-dimensional subwavelength imaging by a photonic-crystal flat lens using negative refraction at microwave frequencies. Phys Rev Lett 2005; 95(15): 153901.
[116] Gruning U, Lehmann V. Two-dimensional infrared photonic crystal based on macroporous silicon. Thin Solid Films 1996; 276(1-2): 151-4.
[117] Gruning U, Lehmann V, Ottow S, Busch K. Macroporous silicon with a complete two-dimensional photonic band gap centered at 5 mu m. Appl Phys Lett 1996; 68(6): 747-9.

[118] Birner A, Gruning U, Ottow S, *et al.* Macroporous silicon: A two-dimensional photonic bandgap material suitable for the near-infrared spectral range. Phys Status Solidi A. 1998; 165(1): 111-7.
[119] Leonard SW, van Driel HM, Busch K, *et al.* Attenuation of optical transmission within the band gap of thin two-dimensional macroporous silicon photonic crystals. Appl Phys Lett 1999; 75(20): 3063-5.
[120] Rowson S, Chelnokov A, Lourtioz J-M. Two-dimensional photonic crystals in Macroporous silicon: from mid-infrared (10um) to telecommunication wavelengths (1.3-1.5um). J Lightwave Technol 1999; 19(11): 1989-95.
[121] Muller F, Birner A, Gosele U, Lehmann V, Ottow S, Foll H. Structuring of macroporous silicon for applications as photonic crystals. J Porous Mat 2000; 7(1-3): 201-4.
[122] Birner A, Wehrspohn RB, Gosele UM, Busch K. Silicon-based photonic crystals. Adv Mater 2001; 13(6): 377-88.
[123] Bettotti P, Dal Negro L, Gaburro Z, *et al.* P-type macroporous silicon for two-dimensional photonic crystals. J Appl Phys 2002; 92(12): 6966-72.
[124] Astrova EV, Borovinskaya TN, Tolmachev VA, Perova TS. Technique for patterning macroporous silicon and the fabrication of bars of 2D photonic crystals with vertical walls. Semiconductors+. 2004; 38(9): 1088-91.
[125] Haurylau M, Shroff AR, Fauchet PM. Optical properties and tunability of macroporous silicon 2-D photonic bandgap structures. Physica Status Solidi a-Applications and Materials Science 2005; 202(8): 1477-81.
[126] Johnson SG, Joannopoulos JD. Three-dimensionally periodic dielectric layered structure with omnidirectional photonic band gap. Appl Phys Lett 2000; 77(22): 3490-2.
[127] Fleming JG, Lin SY. Three-dimensional photonic crystal with a stop band from 1.35 to 1.95μm. Opt Lett 1999; 24(1): 49-51.
[128] Noda S, Yamamoto N, Sasaki A. New realization method for three-dimensional photonic crystal in optical wavelength region. Jpn J Appl Phys Part 2 - Lett. 1996; 35(7B): L909-L12.
[129] Yamamoto N, Noda S. 100-nm-scale alignment using laser beam diffraction pattern observation techniques and wafer fusion for realizing three-dimensional photonic crystal structure. Jpn J Appl Phys 1. 1998; 37(6A): 3334-8.
[130] Yamamoto N, Noda S, Sasaki A. New realization method for three-dimensional photonic crystal in the optical wavelength region: Experimental consideration. Jpn J Appl Phys 1. 1997; 36(3B): 1907-11.
[131] Yamamoto N, Noda S, Chutinan A. Development of one period of a three-dimensional photonic crystal in the 5-10 mu m wavelength region by wafer fusion and laser beam diffraction pattern observation techniques. Jpn J Appl Phys Part 2 - Lett. 1998; 37(12A): L1491-L.
[132] Yamamoto N, Noda S. Fabrication and optical properties of one period of a three-dimensional photonic crystal operating in the 5-10 mu m wavelength region. Jpn J Appl Phys 1. 1999; 38(2B): 1282-5.
[133] Noda S, Yamamoto N, Imada M, Kobayashi H, Okano M. Alignment and stacking of semiconductor photonic bandgaps by wafer-fusion. J Lightwave Technol 1999; 17(11): 1948-55.
[134] Noda S, Yamamoto N, Kobayashi H, Okano M, Tomoda K. Optical properties of three-dimensional photonic crystals based on III-V semiconductors at infrared to near-infrared wavelengths. Appl Phys Lett 1999; 75(7): 905-7.
[135] Imada M, Noda S, Chutinan A, Tokuda T, Murata M, Sasaki G. Coherent two-dimensional lasing action in surface-emitting laser with triangular-lattice photonic crystal structure. Appl Phys Lett 1999; 75(3): 316-8.
[136] Noda S, Tomoda K, Yamamoto N, Chutinan A. Full three-dimensional photonic bandgap crystals at near-infrared wavelengths. Science 2000; 289(5479): 604-6.
[137] Noda S, Imada M, Chutinan A, Yamamoto N. III-V based-semiconductor photonic crystals. Opt Quant Electron. 2002; 34(8): 723-36.
[138] Noda S, Imada M, Okano M, Ogawa S, Mochizuki M, Chutinan A. Semiconductor three-dimensional and two-dimensional photonic crystals and devices. IEEE J Quantum Elect 2002; 38(7): 726-35.
[139] Mogami T, Morimoto M, Okabayashi H, Nagasawa E. Sio2 Planarization by 2-Step Rf Bias-Sputtering. J Vac Sci Technol B 1985; 3(3): 857-61.
[140] Kawakami S. Fabrication of submicrometre 3D periodic structures composed of Si/SiO2. Electron Lett 1997; 33(14): 1260-1.
[141] Kawakami S, Hanaizumi O, Sato T, *et al.* Fabrication of 3D photonic crystals by autocloning and its applications. Electron Comm Jpn 2. 1999; 82(9): 43-52.
[142] Kawakami S, Kawashima T, Sato T. Mechanism of shape formation of three-dimensional periodic nanostructures by bias sputtering. Appl Phys Lett 1999; 74(3): 463-5.
[143] Kawakami S, Sato T, Miura K, Ohtera Y, Kawashima T, Ohkubo H. 3-D photonic-crystal hetero structures: Fabrication and in-line resonator. IEEE Photonic Tech L 2003; 15(6): 816-8.
[144] Hanaizumi O, Ohtera Y, Sato T, Kawakami S. Propagation of light beams along line defects formed in a- Si/SiO2 three-dimensional photonic crystals: Fabrication and observation. Appl Phys Lett 1999; 74(6): 777-9.

[145] Notomi M, Tamamura T, Kawashima T, Kawakami S. Drilled alternating-layer three-dimensional photonic crystals having a full photonic band gap. Appl Phys Lett 2000; 77(26): 4256-8.
[146] Kuramochi E, Notomi M, Tamamura T, *et al.* Drilled alternating-layer structure for three-dimensional photonic crystals with a full band gap. J Vac Sci Technol B 2000; 18(6): 3510-3.
[147] Kuramochi E, Notomi M, Kawashima T, *et al.* A new fabrication technique for photonic crystals: Nanolithography combined with alternating-layer deposition. Opt Quant Electron 2002; 34(1-3): 53-61.
[148] Kuramochi E, Notomi M, Yokohama I, *et al.* Transmission characterization of drilled alternating-layer three-dimensional photonic crystals. J Appl Phys 2003; 93(11): 8848-51.
[149] Azzam RMA. Chiral Thin Solid Films - Method of Deposition and Applications. Appl Phys Lett 1992; 61(26): 3118-20.
[150] Robbie K, Brett MJ. Sculptured thin films and glancing angle deposition: Growth mechanics and applications. J Vac Sci Technol A 1997; 15(3): 1460-5.
[151] Robbie K, Sit JC, Brett MJ. Advanced techniques for glancing angle deposition. J Vac Sci Technol B 1998; 16(3): 1115-22.
[152] Robbie K, Friedrich LJ, Dew SK, Smy T, Brett MJ. Fabrication of Thin-Films with Highly Porous Microstructures. J Vac Sci Technol A. 1995; 13(3): 1032-5.
[153] Toader O, John S. Proposed square spiral microfabrication architecture for large three-dimensional photonic band gap crystals. Science 2001; 2 92(5519): 1133-5.
[154] Lehmann V, Gruning U. The limits of macropore array fabrication. Thin Solid Films 1997; 297(1-2): 13-7.
[155] Matthias S, Muller F, Jamois C, Wehrspohn RB, Gosele U. Large-area three-dimensional structuring by electrochemical etching and lithography. Adv Mater 2004; 16(23-24): 2166.
[156] Matthias S, Muller F, Schilling J, Gosele U. Pushing the limits of macroporous silicon etching. Appl Phys a-Mater. 2005; 80(7): 1391-6.
[157] Matthias S, Muller F, Gosele U. Simple cubic three-dimensional photonic crystals based on macroporous silicon and anisotropic posttreatment. J Appl Phys 2005; 98(2): 023524.

CHAPTER 4

Photonic Crystal Fiber: Theory and Fabrication

Annamaria Cucinotta*

Information Technology Department, University of Parma, I-43124 Parma, Italy

Abstract: Photonic Crystal Fibers (PCFs) have extended the range of capabilities in optical fibers, both by improving well-established properties and introducing new features. PCFs are optical fibers that employ a microstructured arrangement in a background material of different refractive index. The background material is often undoped silica and a low index region is typically provided by air voids running along the length of the fiber.The strong wavelength dependency of the effective refractive index and the inherently large design flexibility of the PCFs allow for a whole new range of novel properties. Such properties include endlessly single-moded fibers, extremely nonlinear fibers and fibers with anomalous dispersion in the visible wavelength region. Fabrication of PCF, like in conventional fiber fabrication, starts with a fiber preform. PCF preforms are formed by stacking a number of capillary silica tubes and rods to form the desired air/silica structure. This way of creating the preform allows a high level of design flexibility as both the core size and shape as well as the index profile throughout the cladding region can be controlled.When the desired preform has been constructed, it is drawn to a fiber in a conventional high-temperature drawing tower and hair-thin photonic crystal fibers are readily produced in kilometer lengths.

Keywords: Photonic crystal fibers, fiber lasers, microstructured fibers.

1. INTRODUCTION

Photonic crystal fibers (PCFs) were first demonstrated in 1996 [1] and have generated much attention since then. PCFs are optical fibers that employ a microstructured arrangement of material in a background material of different refractive index. The background material is often undoped silica and a low index region is typically provided by air voids running along the length of the fiber. PCFs may be divided into two categories, high index guiding fibers and low index guiding fibers [2]. Similar to conventional fibers, high index guiding fibers are guiding light in a solid core by the Modified Total Internal Reflection (M-TIR) principle. The total internal reflection is caused by the lower effective index in the microstructured air-filled region. Low index guiding fibers guide light by the photonic bandgap (PBG) effect. The light is confined to the low index core as the PBG makes propagation in the microstructured cladding region impossible. The strong wavelength dependency of the effective refractive index and the inherently large design flexibility of the PCFs allow for a whole new range of novel properties. Such properties include endlessly single-moded fibers, extremely nonlinear fibers and fibers with anomalous dispersion in the visible wavelength region.

2. HIGH INDEX GUIDING PCFs

PCFs belonging to this category are more similar to conventional optical fibers, because light is confined in a solid core by exploiting the M-TIR. M-TIR is analogous to total internal reflection known from standard optical fibers. It relies on a high index core region, typically pure silica, surrounded by a lower effective index provided by the microstructured region as shown in Fig. **1 (left)**. The guiding mechanism is defined as "modified" because the cladding refractive index is not a constant value, as in standard optical fibers, but it exhibits a wavelength dependency very different from pure silica, an effect which allows PCFs to be designed with a complete new set of properties not possible with standard technology. As an example, the strong wavelength dependence of the refractive index enables thedesign of endlessly single-mode fibers,

***Address correspondence to Annamaria Cucinotta:** Information Technology Department, Università di Parma – Viale G.P: Usberti 181A, 43124 Parma, Italy; Tel: +39-0521-905765; Fax: +39-0521-559; Email: annamaria.cucinotta@unipr.it

Marco Pisco, Andrea Cusano and Antonello Cutolo (Eds)
All rights reserved-© 2012 Bentham Science Publishers

where only a single mode is supported regardless of optical wavelength. Furthermore, it is possible to alter the dispersion properties of the fibers, thereby making it possible to design fibers with an anomalous dispersion at visible wavelengths. By combination of a small core and phase matching dispersion properties close to available pump sources, the PCF technology makes it possible to create very efficient super continuum generation. Due to precise control of the refractive index profile, fibers with extremely large mode field diameters are made possible, supporting high beam quality fiber guidance and amplification/lasing.

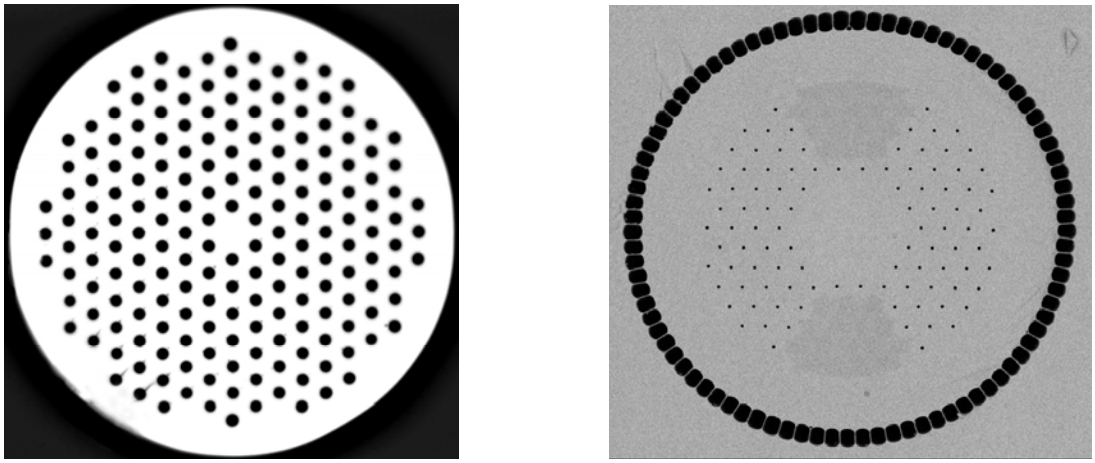

Figure 1: Left: Solid core PCF (SEM image has been kindly provided by NKT Photonics). Right: Polarization maintaining rod-type fiber (SEM picture courtesy of FSU Jena).

2.1. Endlessly Single-Mode

The first fabricated solid-core PCF [3], which consisted of a triangular lattice of air-holes with a diameter d of about 300 nm and a hole-to-hole spacing Λ of 2.3 μm, did not ever seem to become multi-mode in the experiments, even for short wavelengths. In fact, the guided mode always had a single strong central lobe filling the core. This particular endlessly single-mode behaviour can be understood by viewing the air-hole lattice as a modal filter or "sieve" [1]. Since light is evanescent in air, the air-holes act like strong barriers, so they are the "wire mesh" of the sieve. The field of the fundamental mode which fits into the silica core with a single lobe of diameter between zeros slightly equal to 2 Λ, is the "grain of rice" which cannot escape through the wire mesh, being the silica gaps between the air-holes belonging to the first ring around the core too narrow. On the contrary, the lobe dimensions for the higher order modes are smaller, so they can slip between the gaps. When the ratio d/Λ, that is the air-filling fraction of the photonic crystal cladding, increases, successive higher order modes become trapped. More detailed studies of the properties of triangular PCFs have shown that this occurs for d/Λ< 0. 4 [4]. More recently it has been demonstrated that this condition is valid only for 1 or 7-holes core PCF, more accurate evaluations are necessary for 19-holes PCFs [5].

2.2. Large Mode Area PCFs

Optical fibers with large mode areas are necessary for applications requiring high-power delivery, including laser welding and machining and fiber lasers and amplifiers. The nonlinearity of a fiber scales with the fiber length and is inversely proportional to the mode-field area. Therefore, the employment of short large-mode area fibers allows for significant power scaling. Recently PCF technology emerged as an alternative route to large mode areas. In a conventional fiber, one creates large mode area either by increasing the core size or by reducing the numerical aperture. Conventional techniques for reducing the numerical aperture rely on the ability to control the dopant concentration accurately, which ultimate limits the maximum mode size that can be created, especially for short-wavelength operation. In a PCF, large mode areas can be engineered either by increasing the hole-to-hole spacing (Λ) or by decreasing the hole diameter (d). Increasing Λ is analogous to enlarging the core size, while decreasing d allows the field to penetrate farther into the cladding. This effect is particularly striking when d/Λ is small, resulting in a great increase in mode

area for relatively small changes in hole size. The largest mode size that can be tolerated in practice is determined only by the macroscopic bending losses [6]. A further advantage of microstructuring a fiber is the possibility to form an air-cladding region to introduce the double-clad concept with the promising feature of a high numerical aperture of the inner cladding. This is achieved by surrounding the inner cladding with a web of silica bridges which are substantially narrower than the wavelength of the guided radiation, as shown in Fig. **1 (right)**. A solution to bending losses is to avoid bending altogether as provided by the rodlike concept. Rather than a thin and flexible polymer jacket, a rodlike PCF features a rigid glass shall, greater than 1 nm diameter, designed to retain a straight shape, thus avoiding bend loss [7]. This configuration supports high thermal loads, great energy storage and efficient pump absorption even in short practical lengths. Moreover PCF can be made also polarization maintaining by inserting boron-doped regions in the PCF cladding [8, 9], as depicted in Fig. **1 (right)**. The boron regions act as stress applying parts due to their difference in melting point and thermal expansion coefficient compared to the pure silica cladding. It has been demonstrated that the birefringence is enough to split two polarization states of the weakly guided fundamental mode, in a way that the effective index of one polarization is below the cladding index, thus resulting in a single polarization large mode area fiber [8]. Polarizing properties of large mode fibers are particularly attractive for active PCFs [10]. An example of this type of fiber is shown in Fig. **2 (left)**. Three down-doped stress applying parts (showing slightly gray in the picture) are positioned on each side of the core and surrounded by air holes forming an inner cladding. This fiber exhibits abirefringence sufficiently large to give single polarization properties around 1.0 μm. Under active operation, the fiber demonstrated lasing at 150 W with polarized output under free-running conditions without use of additional polarization controlling elements [10].

2.3. Supercontinuum Generation

The possibility to enhance or reduce the Kerr nonlinearity and, at the same time, control the magnitude and wavelength dependence of the group velocity dispersion, makes PCF an excellent medium to observe strong nonlinear effects. A nonlinear PCF is shown in Fig. **2 (right)**. One of the most successful application of nonlinear PCF is the supercontinuum (SC) generation. SC generation, a complex physical phenomenon which causes a significant spectral broadening of laser pulses propagation in a nonlinear medium, has been studied in both bulk media and optical fiber since the 1960s.

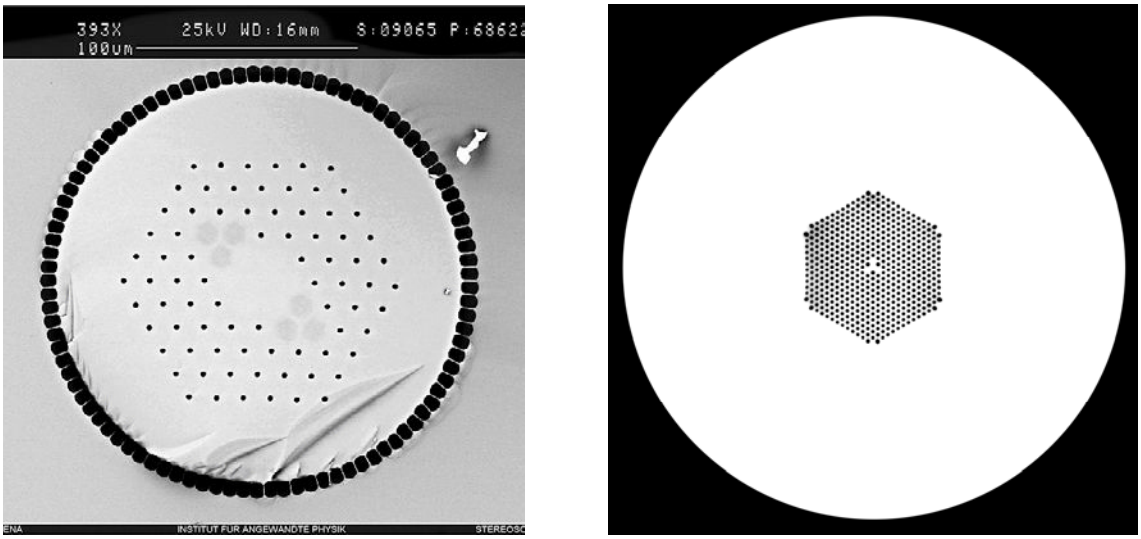

Figure 2: Left: SEM picture of an active (Yb-doped) polarizing PCF (courtesy of FSU Jena). Right: A solid core nonlinear PCF (SEM image has been kindly provided by NKT Photonics).

However the advent of PCF together with development in efficient high power and short pulses fiber lasers, generated a revolution in the generation of ultrabroadband high brightness optical spectra [11]. Moreover, the design freedom of PCF allowed SC generation to be optimized in the wider range of available pump

sources, and experiments reported broadband spectra covering the complete window of transmission of silica based fiber using input pulses with duration ranging from nanoseconds to femtosecond. SC generation in PCF has been applied in many field, including optical coherence tomography, spectroscopy, and optical frequency metrology.

In particular PCFs offer enhanced nonlinear properties, due to their small effective area, thus significantly reducing of about two order of magnitude the peak power necessary to generate the SC. Moreover, by exploiting the dispersion tailoring, it was possible to properly shift the PCF zero-dispersion wavelength in the range of Ti:sapphire femtosecond laser systems operating around 800 nm, thus obtaining SC spectrum in the visible region. The SC spectrum in PCFs is characterized by a complex shape, since a lot of effects, such as group velocity dispersion, self-phase modulation, cross-phase modulation, four wave mixing, stimulated Raman scattering, birefringence, high order soliton formation, third-order dispersion, and self-stepping, participate in the generation process [12]. High nonlinear PCFs are usually characterized by a high air-filling fraction and small hole-to-hole spacing. The choice of the proper PCF in order to generate the SC spectrum strongly depends on the wavelength range of the desired source and on the available pump. In particular, the zero-dispersion wavelength of the high nonlinear PCF should be close to the center wavelength of the pump source.

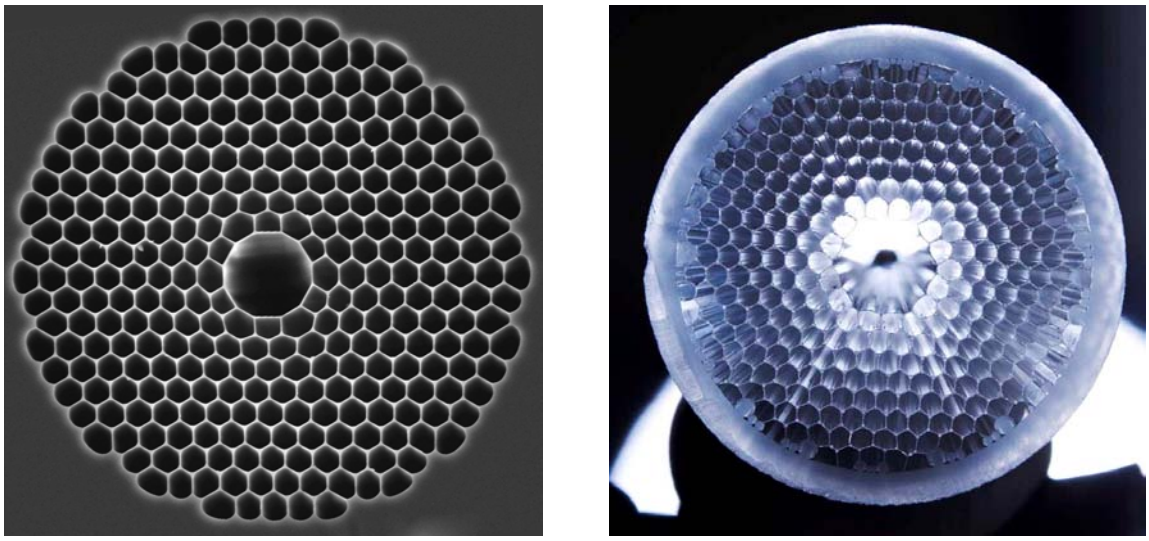

Figure 3: Left: SEM picture of a hollow core PCF. Right: the preform of a hollow core PCF (images have been kindly provided by NKT Photonics).

3. PHOTONIC BAND GAP PCFs

Photonic bandgap fibers are based on physical mechanisms fundamentally different from the M-TIR guiding fibers. The periodic microstructure in the fiber cladding results in a so called photonic band gap, where light in certain wavelength regions cannot propagate. In a PBG fiber, the core is created by introducing a defect in the PBG structure (*e.g.* an extra air hole), thereby creating an area where the light can propagate. As the light can only propagate at the defect region, a low index guiding core has been created. This is not possible in standard fibers, and the low index guiding of PBG fibers therefore opens a whole new set of possibilities. In this way, it is possible to guide light in air, vacuum or any gas compatible with the fiber material.

A special class of PBG guiding fibers is the hollow core fibers, where the field is confined to an air-filled core as shown in Fig. **3**. The first hollow core fiber was reported in [13]. Like other PBG fibers, air-core fibers only guide light in a limited spectral region. For fibers guiding around 1550nm, a typical bandwidth is ~200 nm. Outside this region, the fiber core is anti-guiding.

Guiding light in a hollow core holds many promising applications like high power delivery without the risk of fiber damage, gas sensors or extreme low loss guidance in vacuum. Furthermore, this class of fiber has other spectacular properties not found in any other fiber type. They are almost insensitive to bending (even at very small bending radii) and they have dramatically reduced sensitivity to Kerr effect (>50), temperature transients (~6.5), and Faraday effect (>10). Also, extreme dispersion properties, such as anomalous dispersion values in the thousands of ps/nm/km regime is easily obtained. Due to a negligible contribution from the core material (air), the total dispersion of PBG fibers is to a high degree dominated by waveguide dispersion.

Another special class of PBG guiding fibers is the solid core PBG fibers. Here, the field is confined to a solid core and the cladding region typically consists of an array of high index regions embedded in silica material. Like other PBG fibers, solid core PBG fibers only guide light in a limited spectral region. This filtering effect in combination with a rare earth doped core such as Yb make lasing and amplification possible at new wavelengths with weak fiber gain. The first PBG fiber was a solid core one, and it was reported in 1998 [14].

4. FINITE-ELEMENT ANALYSIS

In high index guiding PCFs as well as PBG ones the guiding mechanism can be attributed, in all cases, to multiple interferences due to the periodic or to therandom set of the air holes and, as a consequence, it strongly depends on the geometry of the cross-section, in particular onshape, dimension, reciprocal distance and arrangementof the holes. For all these reasons a numerical model is able to accurately figure the unusual properties of PCFs, insofar as it is able to accurately describe geometrical characteristics of the cross-section.

The Finite Element Method (FEM) is a powerful tool able to cope with any kind of geometry and to provide a full vectorial analysis [15]. The fiber cross-section representation is very accurate being the domain divided into sub-domains with triangular or quadrilateral shape and step index profiles can be exactly represented. The full vector approach allows to take into account polarization effects and the mode effective indices are directly given as output data. This has allowed to investigate PCF chromatic dispersion and hole-assisted fibers as well as to understand how perturbations on geometrical characteristics can affect transmission properties such as group velocity dispersion and polarization mode dispersion in PCFs [16].

The FEM divides the cross-section of the fiber into a patchwork of triangular elements which can be of different sizes, shapes, refractive indices. In this way any kind of geometry of the holes in PCF and HF cross-sections can be taken into account with high accuracy. Applying the variational finite element procedure to curl-curl equation:

$$\overline{\nabla} \times \left(\overline{\overline{\varepsilon_r}}^{-1} \overline{\nabla} \times \overline{H}\right) - k_0^2 \overline{\overline{\mu}}_r^{-1} \overline{H} = 0 \qquad (1)$$

where $\overline{H}$ is the magnetic field, $\overline{\overline{\varepsilon_r}}$ and $\overline{\overline{\mu_r}}$ are the dielectric permittivity and magnetic permeability tensors respectively and $k_0=2\pi/\lambda$ the wave number in the vacuum, being λ the wavelength, the following eigenvalue algebraic problem:

$$\left([A] - n_{eff}^2 [B]\right)\{h\} = 0 \qquad (2)$$

is obtained.

The eigenvector $\{h\}$ and the eigenvalue n_{eff}^2 provide, respectively, the full vector magnetic field distribution on the cross-section and the effective index of the mode.

Chromatic dispersion of the silica is taken into account by calculating $\overline{\overline{\varepsilon_r}}$ through the Sellmeier equation. Starting from the knowledge of the effective index *vs.* the wavelength, the inverse of the group velocity

$\beta_1 = (1/c)\left[n_{eff} - \lambda\left(dn_{eff}/d\lambda\right)\right]$ and group velocity dispersion parameter $D = -(\lambda/c)\left(d^2 n_{eff}/d\lambda^2\right)$ can be obtained by using finite difference formulas. The matrices $[A]$ and $[B]$ are sparse allowing an efficient resolution on the Eq. by means of high performance algebraic solvers. High order edge elements which avoid spurious modes that pollute the guided mode spectrum, and provide very accurate effective index values are used [15].

In particular the considered formulation employs six tangential unknowns and two facial ones for each triangular element. In order to save computational efforts, structure symmetries can be exploited for the numerical simulations.

Doped PCFs are analyzed to understand how their hole geometry and dopant distribution can be designed in order to improve the amplification properties. The study is performed by the combined use of the full-vector finite element modal solver and the Runge-Kutta algorithm. The first one provides the field distribution of signal and pump on the PCF cross-section; the latter is exploited for the resolution of the conventional propagation and population rate Eqs. to describe the amplification mechanism and to resolve the Amplified Spontaneous Emission (ASE) spectrum. The approach allows an accurate description of the amplification of signals which simultaneously propagate along the fiber. The overlap between the dopant and the field distributions provides a figure of the interaction between the dopant ions and the signals, and, in turn, of the amount of the possible achievable amplification. This overlap can be easily evaluated in conventional doped fiber amplifiers, as both the dopant concentration, often constant all over the core, and the field profile are well known. PCFs, on the contrary, present a very complicate index distribution which make difficult the field evaluation unless proper numerical methods, able to accurately describe the local variation of the field, are adopted. The upper and lower limits of the photonic band gap, within which the core defect allows thefield propagation, are then calculated; the eigenvalue spectrum of the algebraic system is obtained by the FEM applicationby properly translating the research of guided modes within the band gap. The modal solver provides at the given wavelength a very accurate propagation constant and the full vector magnetic field distribution of the PCF guided modes. The electric field $\overline{E}$ is then evaluated through the Maxwell's Eq. $\overline{\nabla} \times \overline{H} = j\omega\varepsilon\bar{\bar{E}}$. Finally the normalized intensity mode distribution *i (x, y)* is derived: $i(x,y) = Re\{(\bar{E}(x,y) \times \bar{H}(x,y))^{*}/P) \cdot \hat{z}\}$ being P the power of the calculated electromagnetic field. By definition, the integral of the normalized intensity over the whole transverse cross-section is equal to one. The FEM is applied to evaluate the pump, the signal and ASE beam intensities defined as $I_k(x,y,z) = i_k(x,y,z)P_k(z)$ with the subscript k referring to the pump, the signal or the ASE spectrum. These intensities are the input data for the population rate Eqs. and the propagationrate equations. These Eqs. are resolved by means of the Runge-Kutta algorithm.

As example the results for a rod-type Yb-doped PCF with a core radius of 30 μm, and a 4 air-hole ring inner cladding, characterized by a hole-to-hole spacing of 12.5 μm and an air-hole diameter of 2.375 μm, are reportedin Fig. **4**. A 5 μm wide ring with a refractive index of 1.4494 has been considered at a distance r_r = 16, 17, 18 μm from the center of the fiber core, whose refractive index is 1.4498 [17]. A spatial and spectral amplifier model [18] has been used to study the mode propagation along the Yb-doped rod-type PCFs, taking into account not only the first higher order mode (HOM), but also the LP_{02}-like mode, whose field distribution is more similar to the fundamental mode (FM) one [19].

The field distribution of the FM; LP_{11} and the LP_{02} like mode was calculated at 1064 nm. The ring is effective in "pushing" the field of the former HOM outwards, while the latter has its peak in the innermost part of the doped area, even if its confinement in the fiber core is quite weak. The field distribution differences among the guided modes are evident looking to the overlap behavior as a function of the doped-area radius r_d, reported in Fig. **4 (a), (b)** and **(c)** for the rod-type PCF with the ring centered at 16, 17 and 18 μm, respectively. The overlap of the FM decreases when r_d becomes lower, as well as the one of the first HOM, for all the rod-type PCFs considered. On the contrary, the LP_{02} like mode overlap becomes lower as r_d decreases from 30 μm to about 22 μm, reaching a constant value until $r_d \approx$ 13 μm and then slightly decreasing again. The rod-type fiber with r_r = 18 μm provides the highest overlap difference between the FM and the most detrimental HOM for all the considered r_d values, thus showing promising properties for an effective single-mode amplification. Simulation results have demonstrated that the LP_{11} like mode is more detrimental than the LP_{02} like one in the

gain competition with the FM. However, it is possible to properly choose the doped-area radius in order to minimize the power of both the HOMs at the amplifier output.

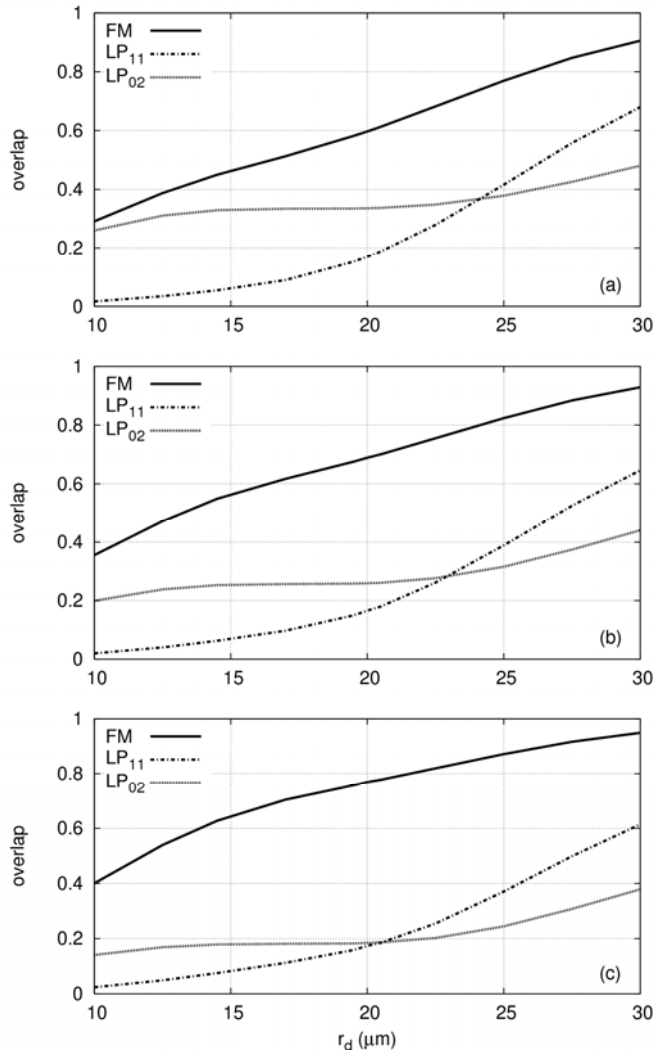

Figure 4: FM and HOM overlap as a function of r_d for the rod-type PCFs with 5 μm wide ring centered at (a) 16 μm (b) 17 μm and (c) 18 μm [18].

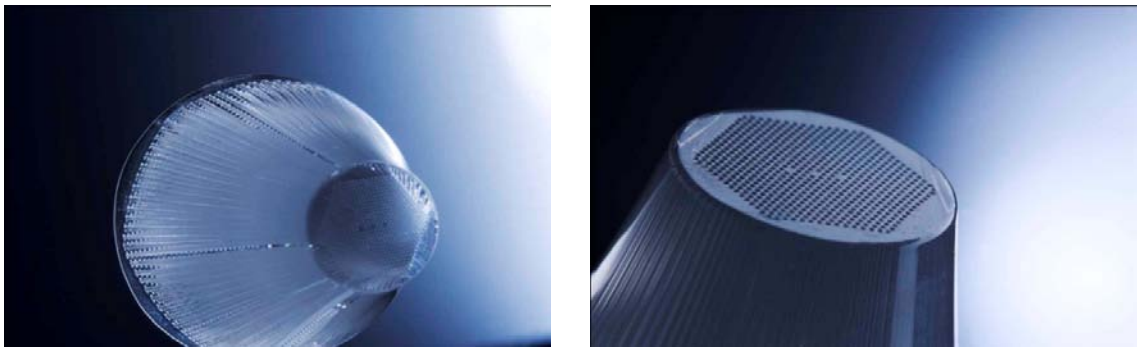

Figure 5: Left**:** Photonic crystal fibers are conventionally fabricated using a stack and draw technique, and accordingly are very flexible both in material and structure. Right: The picture shows a PCF with three cores placed on a straight line each intersected by a single cell. Thereby light will couple between the cores, and the fiber thus has a built-in coupling functionality (images have been kindly provided by NKT Photonics).

5. FABRICATION PROCESS

Fabrication of PCF, like in conventional fiber fabrication, relies on manual assembly of glass capillaries and rods into an appropriate preform stack whose structure corresponds approximately to the desired fiber structure [20]. Microstructured preforms or "canes" are formed by stacking a number of capillary silica tubes and rods to form the desired air/silica structure, fusing the stack into a preform, and then pulling the preform to a fiber at a sufficiently low temperature to avoid collapsing of the hole. The final step in PCF fabrication involves drawing the cane into fiber with the desired dimensions, such as cladding-lattice pitch and the outer fiber diameter as shown in Fig. **5 (left)** and Fig. **5 (right)**. By tuning process parameters such as temperature, preform feed rate and drawing speed, as well as the pressure inside the preform, the size of the air-holes and their regularity can be controlled.

This way of creating the preform allows a high level of design flexibility, as both the core size and shape as well as the index profile throughout the cladding region can be controlled. Through careful process control, the air holes retain their arrangement all through the drawing process and even fibers with complex designs and high airfilling fraction can be produced. Finally, the fibers may be coated to provide a protective standard jacket that prevents micro bending and also allows robust handling of the fibers.

Making of micronsize air-holes uniform along the lengths is the more significant technological challenge. More complex index structures can also be constructed utilizing arrangements of holes of different sizes in various periodic or non-periodic structures. In addition, highly asymmetric core fibers can be fabricated, thereby creating fibers with high level of birefringence.

Doped PCFs can be straightforwardly produced by incorporating a rare-earth-doped cane in the preform stack. Many different design can be realized such as cladding pump geometries.

CONCLUSION

PCFs represent a novel use of optical fibers with applications in many new areas as biophotonics, biochemistry, microfluidics, medical imaging, high power fiber lasers, astronomy. In the next years PCFs will open new possibilities of investigation in different areas of science and technology.

ACKNOWLEDGEMENTS

Author acknowledge Jes Broeng and Lasse Leick of NKT for their useful suggestions and for providing the images.

REFERENCES

[1] Russell PStJ. Photonic Crystal Fibers. Science 2003; 299 (5605): 358-362.
[2] http://www.nktphotonics.com/fiber.
[3] Knight JC, Birks TA, Russell PStJ, Atkin DM. All-silica single-mode fiber with photonic crystal fiber. Opt Lett 1996; 21 (19): 1547-1549.
[4] Mortensen NA. Effective area of photonic crystal fibers. Opt Express 2002; 10 (9): 341-348.
[5] Poli F, Coscelli E, Alkeskjold TT, *et al.* Cut-off analysis of 19-cell Yb-doped double-cladding rod-type photonic crystal fibers. Opt Express 2011; 19 (10): 9896-9907.
[6] Baggett JC, Monro TM, Furusawa K, Richardson DJ. Comparative study of large mode holey and conventional fibers. Opt Lett 2001; 26 (14): 1045-1047.
[7] Limpert J, Deguil-Robin N, Manek-Hönninger I, *et al.* High-power rod-type photonic crystal fiber laser. Opt Express 2005; 13 (4): 1055-1058.
[8] Schreiber T, Röser F, Schmidt O, *et al.* Stress-induced single-polarization single-transverse mode photonic crystal fiber with low nonlinearity. Opt Express 2005; 13 (19): 7621-7630.
[9] Schmidt O, Rothhardt J, Eidam T, *et al.* Single-polarization ultra-large-mode-area Yb-doped photonic crystal fiber. Opt Express 2008; 16 (6): 3918-3923.

[10] Anders P, Jes B, Kim PH, Martin DN, Harald RS, Christian J, *et al.*, editors. Polarization Properties of Photonic Crystal Fibers. 2006: Optical Society of America.

[11] Ranka JK, Windeler RS, Stentz AJ. Visible continuum generation in air-silica microstructure optical fibers with anomalous dispersion at 800 nm. Opt Lett 2000; 25 (1): 25-27.

[12] Apolonski A, Povazay B, Unterhuber A, *et al.* Spectral shaping of supercontinuum in a cobweb photonic-crystal fiber with sub-20-fs pulses. J Opt Soc Am B 2002; 19 (9): 2165-2170.

[13] Cregan RF, Mangan BJ, Knight JC, *et al.* Single-Mode Photonic Band Gap Guidance of Light in Air. Science 1999; 285 (5433): 1537-1539.

[14] Knight JC,Broeng J, Birks TA, Russell PStJ. Photonic Band Gap Guidance in Optical Fibers. Science 1998; 282 (5393): 1476-1478.

[15] Cucinotta A, Selleri S, Vincetti L, Zoboli M. Holey fiber analysis through the finite-element method. IEEE Photonic Tech L 2002; 14 (11): 1530-1532.

[16] Cucinotta A, Selleri S, Vincetti L, Zoboli M. Perturbation analysis of dispersion properties in photonic crystal fibers through the finite element method. J LightwaveTechnol 2002; 20 (8): 1433-1442.

[17] Poli F, Laegsgaard J, Passaro D, Cucinotta A, Selleri S, Broeng J. Suppression of Higher-Order Modes by Segmented Core Doping in Rod-Type Photonic Crystal Fibers. J LightwaveTechnol 2009; 27 (22): 4935-4942.

[18] Poli F, Cucinotta A, Passaro D, Selleri S, J. Laegsgaard, Broeng J. Single-Mode Regime in Large-Mode-Area Rare-Earth-Doped Rod-Type PCFs. IEEE J Sel Top Quant 2009; 15 (1): 54-60.

[19] Poli F, Laegsgaard J, Passaro D, Cucinotta A, Selleri S, Broeng J. Sectioned Core Doping Effect on Higher-Order Mode Amplification in Yb-Doped Rod-Type Photonic Crystal Fibers. European Conference on Optical Communication - ECOC2009:1.15, September 20-24, 2009, Vienna, Austria.

[20] Russell PStJ. Photonic-crystal fibers. J.LightwaveTechnol 2006; 24(12): 4729-4749.

CHAPTER 5

Nanostructured Organic Photonics

Andrea Camposeo[1], Elisa Mele[2], Luana Persano[1] and Dario Pisignano[1,3,*]

[1]NNL, National Nanotechnology Laboratory of Istituto Nanoscienze-CNR, Università del Salento, via Arnesano I-73100 Lecce, Italy; [2]Istituto Italiano di Tecnologia (I.I.T.), Center for Biomolecular Nanotechnologies, via Barsanti 1, I-73010, Arnesano (LE), Italy and [3]Dipartimento di Matematica e Fisica "Ennio De Giorgi", Università del Salento, via Arnesano, I-73100 Lecce, Italy

Abstract: Light emitting organic materials, such as conjugated polymers and low-molar-mass compounds, exhibit appealing characteristics for the realization of active optical devices, including high luminescence efficiency, wide emission tunability, as well as simple and cheap processing. In particular, photonic crystals and their integration in planar and vertical microcavities based on organics provide an effective approach to control the light-matter interaction in solids, and to design and fabricate devices. Examples of applications which are here reviewed include distributed feedback lasers, nanopatterned organic light-emitting diodes and photonic crystal waveguides, and vertical architectures exploited in resonators, photodiodes, and microcavities showing strong exciton-photon coupling.

Keywords: Soft lithography, nanoimprint lithography, organic semiconductors, organic lasers, organic light-emitting diodes, strong coupling.

1. INTRODUCTION

The organic semiconductors combine advantages from their simple processing with novel optoelectronics properties, making them very attractive as active media of photonic crystal (PhC) architectures in lasers, light emitting devices, photodiodes, and waveguides. The great interest in organics (both active and optically inert) for integrated optical elements and circuits is especially due to their fast and ease of manufacturing and cost-effectiveness [1]. In particular, besides conventional nanofabrication methods such as optical and electron-beam lithographies and dry/wet etching, soft lithographies and imprinting are widely used for fabricating PhCs on organics. PhCs provide a way to dramatically alter the optical properties of these materials by quantum electrodynamic effects. The light confinement in PhCs [2] modifies the interaction of photons with matter or, equivalently, the materials absorption and emission properties. Planar and vertical PhC structures can be inserted in organic lasers, light-emitting devices for spectrally selecting and enhancing output, waveguides, filters, and switches, guaranteeing high material flexibility, together with low cost and easy manufacturing.

2. NANOFABRICATION

Current research efforts for developing alternative, non conventional patterning methods on organic materials are especially focused on Soft Lithographies, proposed by Whitesides and coworkers at Harvard University [3], and Nanoimprint Lithography (NIL), proposed by Chou and collaborators at Princeton University [4, 5]. These methods are characterized by the use of elastomeric or rigid molds or stamps to transfer a previously prototyped master pattern onto a target material. They work effectively on very different resolution lengthscales (from tens of nm to many cm), on soft target materials which include polymers, small molecules, and biological compounds. The main advantages of Soft and Nanoimprint Lithographies are the reduced needed capital investment, since these technologies do not require complex and expensive equipments, together with the

***Address Correspondence to Dario Pisignano:** National Nanotechnology Laboratory of Istituto Nanoscienze-CNR and Dipartimento di Matematica e Fisica "Ennio De Giorgi", Università del Salento, *via* Arnesano I-73100 Lecce, Italy; Tel: + 39-0832198104, Fax: +39-0832-298146; Email: Dario.pisignano@unisalento.it

Marco Pisco, Andrea Cusano and Antonello Cutolo (Eds)
All rights reserved-© 2012 Bentham Science Publishers

possibility of producing structures smaller than 100 nm in an easy way, the high flexibility in terms of material and surface chemistry, and consequently of the resulting device applications.

Soft Lithographies include a set of patterning approaches, all of them characterized by the use of elements fabricated by texturing elastomeric polymers: Replica Molding (REM) [3, 6], Microcontact Printing [7], Microtransfer Molding (μTM) [8], Micromolding in Capillaries [9], Soft Molding (SM) [10, 11], and Solvent-Assisted Micromolding [12]. The poly(dimethylsiloxane) (PDMS), or other elastomeric compounds, are employed to replicate the geometry of a starting master by REM. This operation principle offers the possibility to produce faithful copies (replicas) of complex features initially present on the master, and to accomplish high resolution without the drawbacks related to optical diffraction, which affect instead photolithography. Even more important, the chemico-physical properties of the employed elastomers give these technologies an unequalled chemical flexibility. Overall, these characteristics make Soft Lithography an excellent patterning route to produce nanostructures and nanosystems, to realize patterned surfaces for selective proteins and cells attachment [13-17], to assemble micro- and nano-fluidic circuits for basic studies and biological chips [18-20], and to print nanostructured optoelectronic devices [21-23].

The REM process is schematized in Fig. **1a**. The master, containing micro- or nanofeatures in relief, is coated by an elastomeric, liquid prepolymer. After the complete, *in situ* polymerization of the elastomer, generally performed by thermal curing, the replica is peeled off by slightly reversible deformations. The final result is a faithful, negative copy of the master. The elastomers used in REM can prime and propagate a conformal contact over large areas of the target substrates. The resulting, intimate contact between the elastomeric stamp and the substrate, both at macroscopic and microscopic level, is common to all the soft lithographic techniques, and particularly important for favoring the pattern transfer and structuring non-planar surfaces.

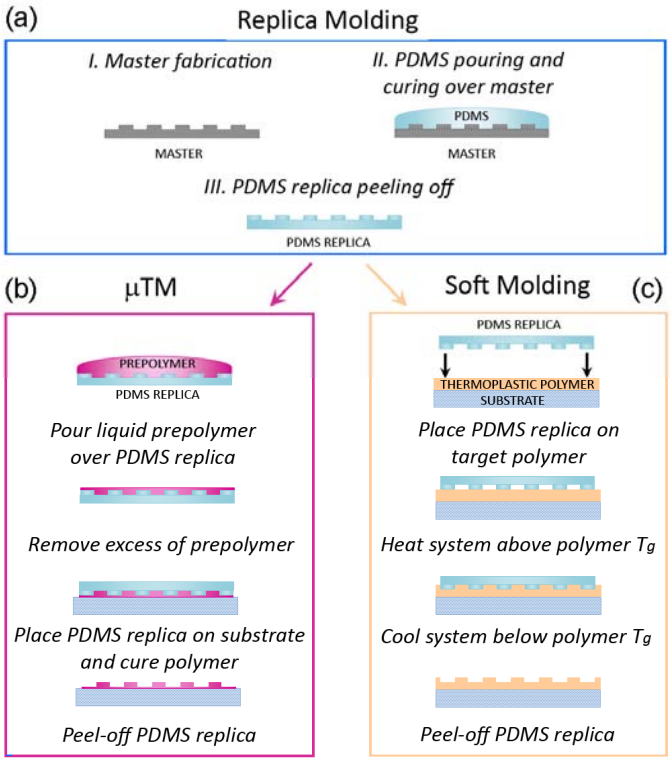

Figure 1: Schematic illustration of procedures of (a) REM. (b) μTM: a drop of prepolymer is poured on the patterned surface of a PDMS replica, which, after removing the excess liquid, is placed in contact with a substrate; the polymer is cured to a solid and the mold is peeled off, leaving structures on the surface of the substrate. (c) SM: the replica is placed in conformal contact with a thermoplastic film; heating the target above Tg activates capillary effects forcing the melt into the void features between the replica and the target film; after subsequent cooling to ambient temperature, the replica is peeled off, and the pattern remains on the target.

Fig. **1b** and **1c** present the schemes of μTM [8] and SM [10, 11], respectively. In particular, the SM combines advantages of replica-assisted techniques and NIL, using elastomeric replicas while exploiting the working principle of embossing technologies, *i.e.,* the molding of a polymer above its glass transition temperature, T_g.

On its turn, the NIL is a high throughput technique for producing features with size down to sub-10 nm onto polymeric layers over large areas [4, 5, 24, 25]. Differently from lithographies based on modifying the chemical structure of a resist by energetic beams, the NIL relies on the deformation of the surface of a thermoplastic film upon applying pressure and temperature. The simple operational procedure, whose resolution is not limited by wave diffraction, and the relatively low cost of the experimental setup, not requiring beam generators, are the main advantages with respect to conventional lithographic approaches. This technique is applied to a wide range of inert [4, 5, 25] and active compounds [26, 27], and for fabricating devices for data storage [28, 29], optical components [30], photonic [31] and biological applications [32].

In NIL, a rigid template with a nanostructured surface is mechanically-pressed onto a thermoplastic film (Fig. **2a**). Upon compression (with pressures of 10^5-10^8 Pa), the polymer is heated above T_g, thus becoming fluid and, hence, flowing into the recessed features of the stamp. Afterwards, the sample is cooled below T_g and the mold is separated from the polymer, a negative copy of the initial template being then transferred to the target. The pattern transfer is regulated by the response of the polymer to the applied external forces, determining deformations driven by elastic and viscous behavior at the initial and at the late stage of imprinting, respectively. Indeed, the immediate deformation is mainly due to the elastic response, and it is reversible and potentially fully recovered after removing the external force. The irreversible deformation is instead consequence of the viscous behavior. Finally, a retarded contribution to the deformation (anelastic) is observed, usually recovered upon unloading [33]. An important aspect to be considered is the temperature dependent timescales of the different conformational changes for amorphous polymers. At low temperature, these variations and relaxations are very slow, with timescales of at least many hours. Upon increasing temperature to glass transition values, first short motions of segments of the polymeric chains, and finally of entire polymeric chains beyond the macromolecular entanglements (terminal flow), take place in experimentally accessible timescales. The deformations induced by the external forces in the organic material are then irreversible.

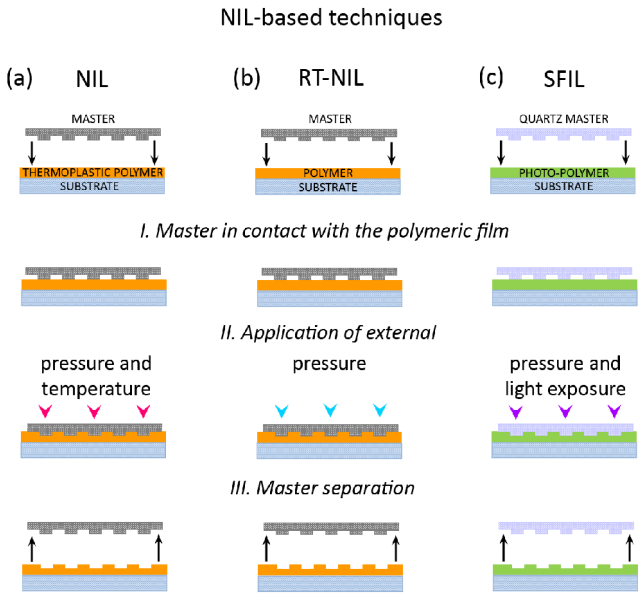

Figure 2: Schematic illustration of (a) NIL, (b) RT-NIL, (c) SFIL. Basic steps are: (I) a rigid master structure (transparent for SFIL) placed in contact with a polymeric layer (thermoplastics for NIL, photopolymerizable materials for SFIL), (II) an external pressure, applied during optional polymer heating (NIL), or light exposure (for SFIL), (III) cooling (NIL) or photopolymer crosslinking (SFIL), mechanical removal of the master.

As alternative, room-temperature NIL (RT-NIL) (Fig. **2b**) is also proposed for patterning polymers avoiding some drawbacks of hot embossing. In particular, since avoiding any thermal cycle, the RT-NIL can be applied directly on light-emitting molecules, in air, without degradation of the emission properties of organics [34-36]. In fact, because of the high temperatures reached during imprinting (up to 200 °C) [4, 5, 24], the application of NIL for the direct patterning of organic active molecules generally requires a setup providing vacuum or nitrogen environments. Indeed, the oxygen incorporation and substitution into conjugated molecules and polymers, that occur at high temperature, can determine the irreversible degradation of the optical and electrical properties of organics [37]. Using chambers with a controlled atmosphere implies reducing the operational simplicity and increasing the overall cost of NIL. RT-NIL also allows one to carry out an easier mold release, and it avoids many distortions of the imprinted structures, which are possible by high temperature imprinting [38]. Importantly, in RT-NIL imprinting processes can be sequentially repeated on the same film, to realize complex patterns by printing the same region of the substrate with the same template for several times [39]. One should point out that the realization of two dimensional (2D) PhCs by electron-beam lithography (EBL) is many times more time-consuming with respect to one dimensional (1D) gratings. Hence the possibility of achieving 2D nanostructures by sequential imprinting, not possible by conventional NIL, is strategic for realizing complex geometries in organic based nanophotonics.

Finally, a different NIL-based method is the Step and Flash Imprint Lithography (SFIL), introduced by Colburn and collaborators [40], using a quartz template to pattern a photopolymerizable layer exposed to ultraviolet (UV) light (Fig. **2c**). Variations of SFIL are developed, exploiting a PDMS template instead of the rigid mold, which retains similar characteristics of quartz in terms of UV-transparency, but with increased cheapness and simplicity [41].

3. PLANAR GEOMETRIES

3.1. Distributed Feedback Lasers

The recent development of organic gain materials [42] and lasers opens new perspectives to portable devices for nanophotonics, chemical and biological sensing and for diagnostic applications.

As well known, a laser device is generally composed by a gain material, amplifying light in a cavity, through stimulated emission (STE). Since photons emitted by STE are in-phase with those incident on the active medium, a distinctive feature of lasing is its coherence, leading to a well-defined wavelength (typical linewidth < 1 nm) and an almost collimated output beam. Lasing is reported in different cavity geometries, embedding organic systems as active layers (a recent review of the field is in Ref. [43]). Among different approaches, the inclusion of a PhC (with wavelength scaled features) in a polymer waveguide is widely studied because of clear advantages in terms of device performances and fabrication. The active medium can be composed by light emitting conjugated oligomers [44], polymers [34, 45-47], or optically inert matrices doped with light-emitting chromophores such as dye molecules [35, 48, 49]. These materials exhibit typical refractive index, n, in the range of 1.5-1.9 [50], namely larger than the usual surrounding media (low-n polymers, quartz, or air), thus constituting a slab waveguide confining and guiding light. The cavity is completed by structuring the waveguide with periodic, wavelength scaled, features. In these devices, originally demonstrated by Kogelnik and Shank [51, 52], the feedback is provided by Bragg diffraction of light in the PhC structure. Part of the energy of waves propagating along the forward or backward direction is continuously reflected in the opposite direction by Bragg diffraction at the corrugations on the active layer/substrate or active layer/air interfaces. The constructive interference of diffracted waves within the waveguide is at the base of the cavity distributed feedback (DFB). The periodic modulation of the structure (*i.e.,* of n as induced by the morphology corrugation and/or of the optical gain) induces a wavelength-dependent feedback, determining the unequalled spectral selectivity of DFB lasers.

The patterns of organic films, enabled by the soft and nanoimprint techniques presented above, generally consist of 1D or 2D gratings, with period (Λ) comparable to the wavelength of the light emitted by the target active material (Fig. **3a** and **3b**). DFB structures are also fabricated by depositing an organic film on a substrate structured by standard lithographies (optical, electron beam, *etc.*) [45-47]. Alternatively, DFB lasers without

morphological features are reported by pumping the devices with optical beams whose intensity is spatially modulated by interference [53, 54] or by exposing a conjugated polymer to electron beams [55].

The coherent sum of the forward and backward components of waves travelling in the waveguide gives rise to lasing if the wavelength, λ_L, roughly matches the condition, $m\lambda_L = 2n_{eff}\Lambda$, where m is the diffraction order and n_{eff} is the effective refractive index of the waveguide. n_{eff} weights the refractive indices of the layers composing the waveguide (substrate/active layer/air or cladding layer) and it can be calculated through a solution of the Helmholtz wave Eq. for a planar multilayer structure, once the optical constants of the used materials and their wavelength dependence are known.

The exact solution of the light propagation into a slab waveguide with a periodic perturbation of n evidences that the Bragg wavelength (λ_B) is, indeed, forbidden and the allowed modes must fulfil the relation [56]:

$$\frac{1}{\lambda_L} = \frac{1}{\lambda_B} \pm \frac{1}{2n_{eff}L}\left(\frac{1}{2} + m'\right) \quad \textbf{(1)}$$

where L is the slab length and m' is an integer.

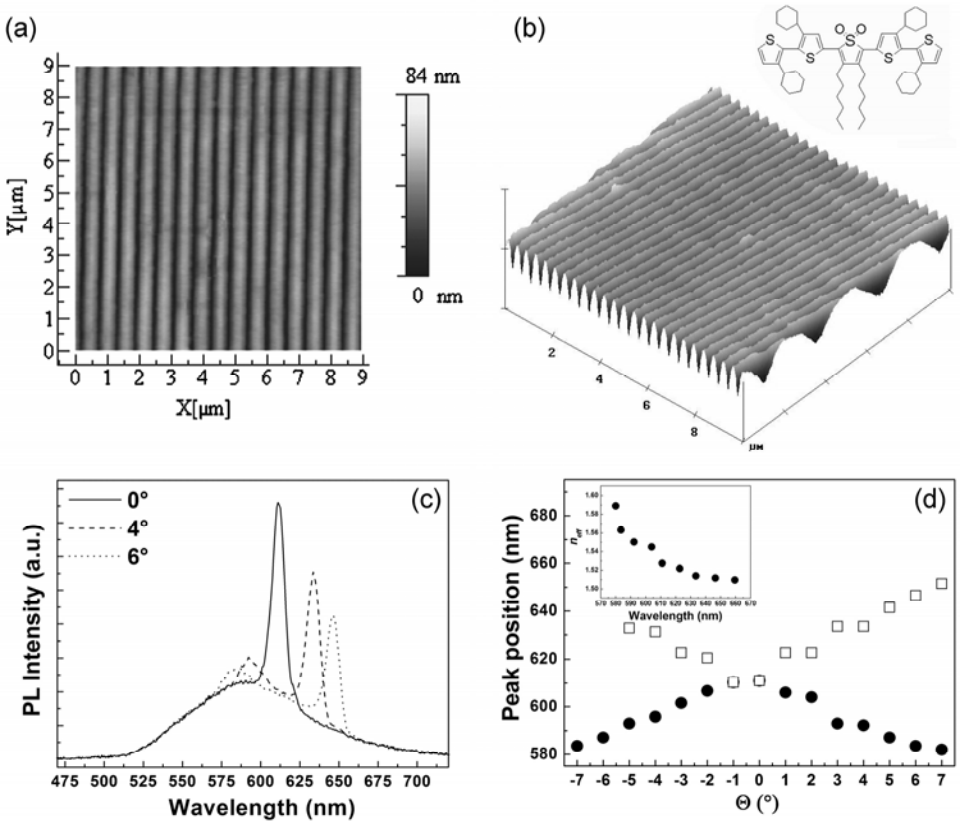

Figure 3: (a) AFM topography of a 600 nm period grating imprinted in MEH-PPV by RT-NIL. Reprinted with permission from [34]. Copyright (2006) by the American Institute of Physics. (b) Topography of a 1D PhC structure (Λ = 400 nm) in a thiophene-based pentamer (molecular structure in the inset). (c) Corresponding normalized angle-resolved PL spectra and (d) angular dependence of the emission peaks. Inset: wavelength dependence of n_{eff}. (b)-(d) Reprinted with permission from [44]. Copyright (2005) by the Optical Society of America.

The operation of DFB lasers can also be analyzed more generally in the framework of PhC theory. Depending on periodicity, symmetry and materials, a stop band for light propagation is associated to the PhC structure. The density of states (DOS) diminishes within the stop band and suppresses spontaneous emission [57]. Near the

band edge, the group velocity approaches zero creating a high DOS and hence, light enhancement [57, 58]. The effective increase of the optical path length of photons at the band edges enables the build-up of a considerable excited-state population in gain media, favouring STE and amplification. Therefore, gain amplification is achieved if the emission spectrum of the active medium falls within the range of the stop band, and lasing occurs at the stop band edges. Laser emission is generally observed at the low-energy edge of the stop band, due to increased self-absorption losses occurring at the high energy edge.

The band dispersion of organic PhCs is easily measured by angle-dependent transmission and/or photoluminescence (PL). Transmission measurements are generally performed by mounting a DFB structure on a rotating stage and measuring the transmission spectrum as a function of the angle formed by the incident light wavevector and the device surface [59]. The band dispersion is obtained by plotting the spectral position of the Bragg dip *vs.* the incident angle. Similar information are obtained by angle-resolved PL spectra (Fig. **3c**), displaying characteristic emission peaks whose spectral position shifts by changing the collection angle, Θ. These peaks are related to the presence of the grating, allowing the light confined in waveguide modes within the organic slab to be scattered out at certain forward directions. By imposing the conservation of the in-plane component of the wave vector of the output light, $|\mathbf{k_0}|=2\pi/\lambda$, and of the guided mode, $|\mathbf{k_g}|=2n_{eff}/\lambda$, by means of the Bragg vector, $|\mathbf{G}|=2\pi/\Lambda$ [59], one has:

$$k_0 \sin\Theta = \pm k_g \pm mG \qquad \textbf{(2)}$$

Plotting the peak wavelength *vs.* Θ (Fig. **3d**) evidences the typical band dispersion of a 1D periodic structure together with the wavelength dispersion of n_{eff} (inset of Fig. **3d**) [60].

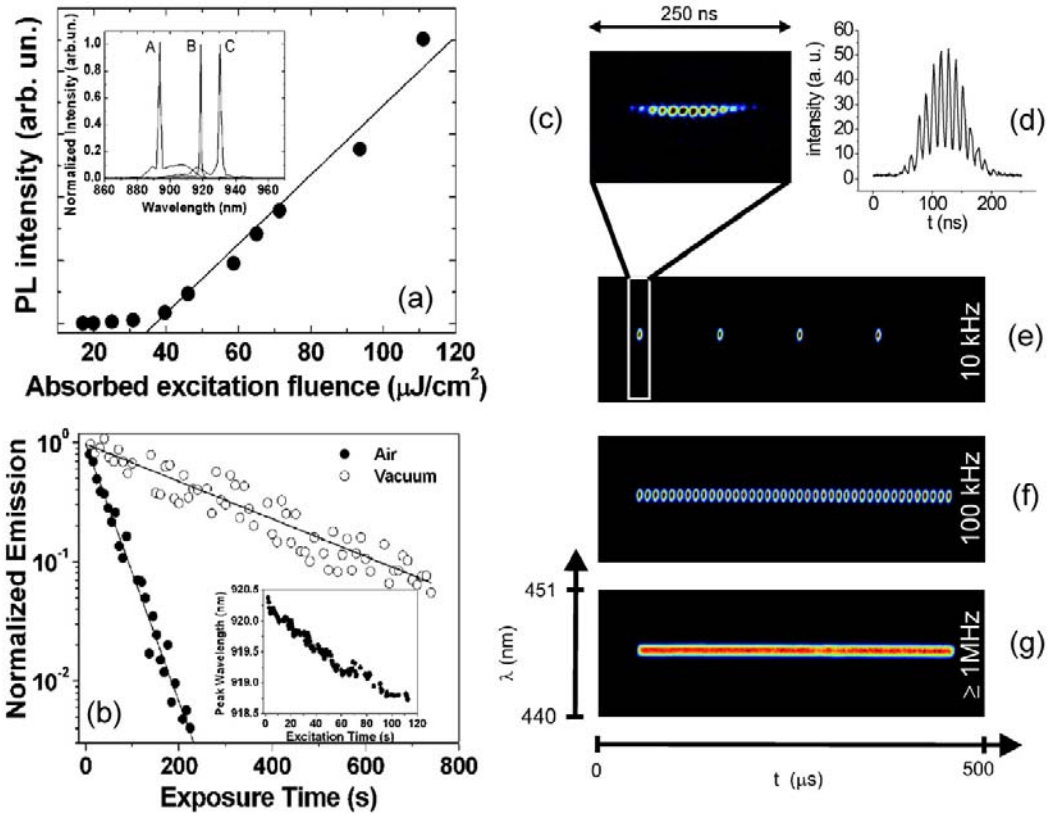

Figure 4: (a) Emission intensity *vs.* absorbed pumping fluence (excitation wavelength=355nm), for a dye-doped poly(methylmethacrylate) film imprinted by RT-NIL. The solid line is a linear fit to the input-output characteristics above threshold. Inset: device tunability. Peaks at 883 nm (A), 918 nm (B) and 930 nm (C) are obtained from structures with Λ=580, 620 and 640 nm, respectively. (b) Temporal evolution of a DFB laser emission when optically pumped in air (full circles) or in vacuum (empty circles). Excitation fluence=63 μJ cm^{-2}. The solid lines are fits by an exponential

function. Inset: DFB wavelength *vs.* exposure time. (a)-(b) Reprinted with permission from [35]. Copyright (2006) by the American Institute of Physics. (c)-(g) Streak camera images of the spectral and temporal emission of a DFB organic laser at different pumping rates. Top: magnified view of a pulse packet. The laser exploits as active layer a thin film of a modified poly(9,9-dioctylfluorene) derivative containing 12% of statistical intrachain 6,6'-(2,2'-octyloxy-1 ,1'-binaphthalene) binaphthyl spacer groups, spin cast on a structured SiO_2 substrate (Λ=270-290 nm). Reprinted with permission from [67]. Copyright (2006) by the American Institute of Physics.

A large number of 1D organic-based DFB lasers are reported [43]. Lasing is generally demonstrated by the collapse of the emission spectrum in a narrow peak (inset of Fig. **4a**) above a pumping threshold fluence, evidence of the increased coherence [35]. Another characteristic feature is the linear dependence of the emission intensity on the pumping fluence above threshold [61] (Fig. **4a**). The slope of the input-output curve in the linear regime provides the differential efficiency, that for 1D DFB devices is, typically, of few percent [43]. DFB lasers are characterized by lower threshold fluences compared to other cavity geometries, with the lowest values in the range 20-400 nJ cm^{-2} [62, 63]. These values depend on a number of factors, including (i) self-absorption losses, that can be minimized by exploiting non-radiative energy transfer processes in host-guest gain systems [62, 64, 65], (ii) diffraction order, affecting the output coupling losses, (iii) quality and uniformity of the slab waveguide and (iv) grating morphology.

Typical operational lifetimes are of 10^2-10^3 pumping pulses in air, increased by an order of magnitude for operation in vacuum (Fig. **4b**) [35]. The diffusion of oxygen in the active layer and its reaction with chromophores is the main cause of emission quenching [37]. A lifetime increase from about 10^3 to 10^7 excitation pulses is reported for poly[2-methoxy-5-(2-ethylhexyl-oxy)-1,4-phenylene-vinylene] (MEH-PPV) devices upon encapsulation [66].

So far, there is a lack of data on continuous wave operation of organic-based devices. Most of the exploited gain materials suffer from the accumulation of triplet excitons through intersystem crossing. These bands overlap with STE spectra, thus increasing losses and generally limiting the operational rate to few kHz. An operational rate up to 5 MHz is reported in a device based on a modified poly(9,9-dioctylfluorene) (Fig. **4c-g**) [67], exhibiting reduced triplet exciton and polaron pairs (also responsible of absorption losses) formation.

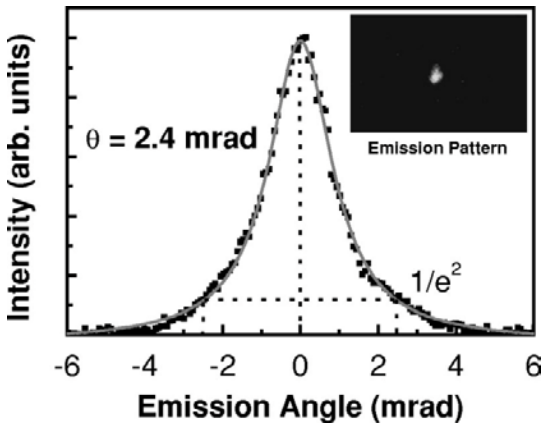

Figure 5: Angular dependence of the transverse profile of the far-field emission pattern of a 2D DFB laser in monomode operation. The shape of the far field emission mode is shown in the inset. Reprinted with permission from [71]. Copyright (2000) by the American Institute of Physics.

2D DFB structures are also studied because of their improved spectral selection, pumping threshold and output efficiency compared to 1D devices. 2D systems are fabricated by imprinting [68, 69] or by depositing a gain medium on patterned substrates with different symmetries (square, hexagonal or honeycomb lattices). A comparison of 1D and 2D DFB structures based on polyfluorene evidences a decrease of the threshold by a factor of 20 with a corresponding increase in the differential slope efficiency by a factor of 3.5 [70]. Furthermore, 2D structures show improved output beam quality. While a surface-emitting 1D DFB laser emits a divergent stripe, parallel to the orientation of the grating grooves, in the 2D

structure the output beam exhibits a typical divergence of only a few milliradiants in any direction, being almost diffraction limited slightly above threshold (Fig. **5**) [70, 71]. More complex far-field patterns are observed well above threshold, generally correlated with spectral broadening and excitation of higher modes. Among different 2D DFB structures, circular resonators [68, 72] composed by periodic concentric rings present feedback in all the directions (in the plane of the active medium) around the center of the grating. Therefore, light experiences a stop band for all the in-plane directions of propagation, and the lasing mode is strongly confined in the center of the structures.

The exploitation of organic DFB structures in applications require controlling the emission, especially for the use as excitation source in laser spectroscopy [73], where the source has to match the absorption band of the investigated systems. Typical organics are characterized by broad STE bands (>100 nm), in principle allowing to widely tune lasing. For instance, a 115 nm tuning range is shown in Fig. **6a** for a DFB device based on Tris-(8-hydroxy-quinoline)aluminum doped with 4-(Dicyanomethylene)-2-methyl-6-(julolidin-4-ylvinyl)-4H-pyran (Alq_3:DCM2) [74]. Tuning is here achieved by varying the grating period, Λ, in the range 370-460 nm. This approach is also demonstrated for holographic DFB structures, where the grating period is easily tuned by adjusting the angle of incidence of the excitation beams, whose interference pattern allows gain modulation and, consequently, lasing [53, 54]. In this method the angle of incidence of the pump can be continuously changed by movable optics, thus allowing a reversible, real-time tuning of laser.

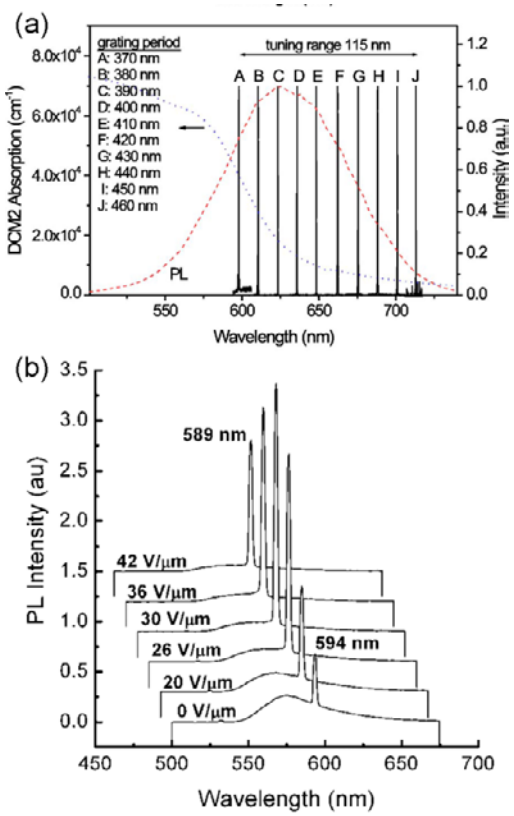

Figure 6: (a) Normalized DFB laser emission varying the grating period, together with PL spectrum (dashed line, right vertical scale) of Alq_3:DCM2, and DCM2 absorption (dotted line, left vertical scale). Reprinted with permission from [74]. Copyright (2004) by the American Institute of Physics. (b) Electrical tunability of an organic, 2D DFB laser optically pumped at 1.3 mJ cm^{-2}. The active layer is pyrromethene 597 in a polymer-dispersed liquid crystal. The 2D structure is realized by holography. Reprinted with permission from [75]. Copyright (2005) by WILEY-VCH Verlag GmbH & Co. KGaA.

Other studies report on tuning by embedded molecules changing their refractive index as a response to an electric field [75-77]. Fig. **6b** displays the emission of a 2D DFB device with polymer-dispersed liquid crystals at different applied electric fields. The tuning is over 5 nm by a field of about 40 V/μm. Larger

tuning ranges (33 nm for an applied voltage of ~300 V) are reported for DFB devices with cholesteric liquid crystals as electro-optically active molecules [76]. DFB lasers on flexible substrates can also be tuned by bending [78] or deformation [79], both approaches affecting the grating period.

The change of the DFB emission wavelength upon varying the effective refractive index and/or grating period is used for sensing applications as well. The presence of external species attaching on the surface of a DFB device can be detected by measuring the emission shift induced by the changed n_{eff}. The resulting sensitivity depends on the emission linewidth (potentially well below the nm, as achieved in passive optical cavity sensors only by fabricating cavities with high quality factors).

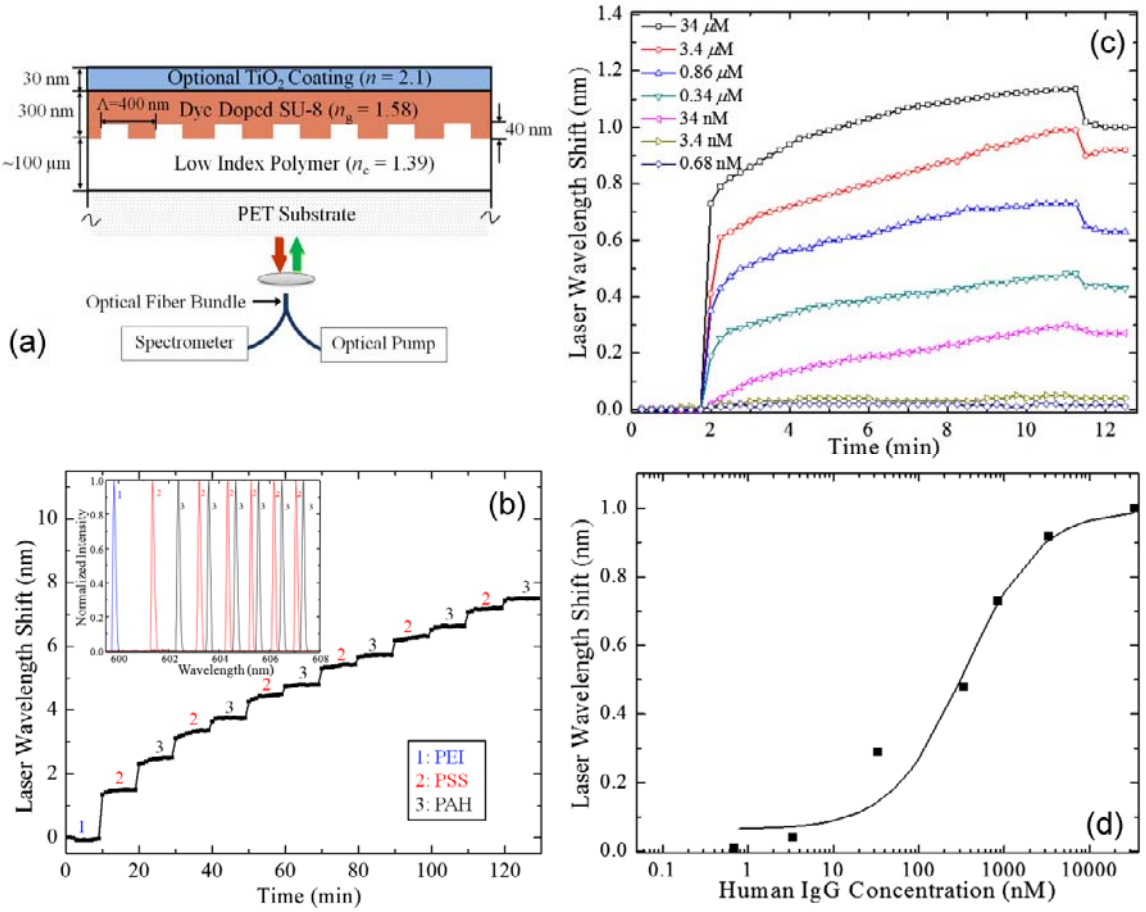

Figure 7: (a) Plastic DFB laser as biosensor. (b) Dynamic detection of alternating layers of positive and negative charged polymer self-limiting monolayers. The used materials are anionic poly(sodium 4-styrenesulfonate) (PSS), cationic poly(allylamine hydrochloride) (PAH) and cationic poly(ethylenimine) (PEI). Inset: normalized laser emission spectrum after each deposition. (c) Binding kinetic response at different concentrations of Human IgG exposed to a surface prepared with immobilized protein A. (d) Wavelength shift *vs.* protein concentration, with superimposed nonlinear curve fitting. Reprinted with permission from [80]. Copyright (2008) by the American Institute of Physics.

A large area DFB-based plastic biosensor is demonstrated, combining a dye-doped plastic gain layer with flexible plastic substrates patterned by a REM process [80]. The biosensor is composed by a polyethyleneterephthalate substrate, on which a low refractive index (n=1.39) UV-curable polymer is deposited and structured (Fig. **7a**). The active layer is made of SU-8 photoresist doped with Rhodamine. A thin layer of titanium dioxide completes the structure, improving the biomolecule immobilization and the sensitivity. The emission shift is first measured after depositing positively and negatively charged stacked polyectrolite layers (Fig. **7b**), evidencing a decrease of the shift by almost a factor 2 for the first two

consecutive layers. The capability of the DFB sensor to detect biomolecules is tested by adsorbing protein A onto the device through non-covalent hydrophobic attachment and subsequently exposing the surface to Human Immunoglobulin G (IgG) (Fig. **7c-d**).

3.2. Nanostructured Organic Light-Emitting Devices

The organic light emitting diodes (OLEDs) are innovating the areas of displays and lighting. They are based on the electroluminescence (EL) from organic materials, first observed in 1960s by Pope *et al.* [81], and by Helfrich and Schneider [82], in anthracene single crystals. Since the first prototypes, presented by Tang *et al.* [83] using Alq_3 and by Burroughes *et al.* by the conjugated polymer poly(*p*-phenylene vinylene) (PPV) [84], a remarkable academic and industrial attention is on the field, yielding green-to-red, blue, and white devices [85]. Many OLEDs features, such as the thin structure, low weight, compatibility with flexible substrates, high brightness, and low energy consumption and cost, are attractive for several high-tech applications, including digital cameras, displays, and portable electronic devices.

The light emission in OLEDs is based on the injection of positive and negative charges into organic layers [86]. The simplest device geometry (single layer architecture) typically consists of one emissive layer sandwiched between a high work-function anode (such as indium tin oxide, ITO) and a low work function cathode (Ca, Mg, Al), deposited onto a transparent substrate (glass or plastic). An electrical voltage applied to the contacts results in the on-set of charge carriers transport. Holes and electrons, injected into the organics, recombine into the emissive materials, forming excitons that can decay radiatively. The device performances are improved by architectures introducing hole-transporting and electron-transporting layers, that make more efficient the emission and the carriers injection and transport.

Though OLEDs are engineered to reach almost unity internal quantum efficiency [87], only a fraction of the generated photons are effectively extracted from the device, whereas most of the emitted light is lost by total internal reflection at the layers interfaces and by guided modes into the electrodes and the organics. Improving methods include microlenses [88], layers of microspheres as scattering medium [89], low-index materials [90], distributed Bragg reflectors [91], photonic band gap structures [92, 93] and DFB gratings [94, 95].

In particular, 1D and 2D PhCs are embedded into OLEDs for effectively controlling the output coupling. As previously mentioned, the insertion of wavelength-scale periodic nanostructures into the light-emitting films or in adjacent layers strongly enhances the forward output from the active compound [92, 93]. The grating enables the light trapped in waveguide modes to be Bragg-scattered out of the device along certain forward direction, thus reducing self-absorption in the organics. The emission angle for an output wavelength is related to the cavity geometry by the usual coupling condition of the guided photons to free radiation, *i.e.,* by the conservation of the in-plane component of the wave vector (Eq. 2).

Several studies highlight the increase of the out-coupling efficiency from OLEDs integrating 1D and 2D PhCs in several positions within the device structures, *i.e.,* between the cathode and the active organics [96], the active region and ITO [97] or the anode and the glass substrate [98-100]. An increment of the external efficiency by a factor of 2 is reported for an OLED based on MEH-PPV [92], embedding a 388 nm periodic grating realized by interference lithography on a photoresist. After evaporating Au as anode onto the pattern, MEH-PPV is spin-cast and capped by Ca/Al [101]. Moreover, an angular dependence of the emission is clearly observed as a consequence of the Bragg scattering [93]. Similar improvements of the light extraction are found in OLEDs using 1D nanogratings [102] and 2D hexagonal structures [103]. Again, the features are first transferred from a stamp to an UV-curable epoxy by NIL and light irradiation, then Au and a three-layers structure consisting of copper phthalocyanine/ N,N'-dephenyl-N,N'-bis(3-methylphenyl)-1,1'-diphenyl-4,4'-diamine / Alq_3 are evaporated, and LiF and Al are used as cathode (Fig. **8a**). The device shows Bragg diffraction upon varying the sample tilting angle, which determines a color change of reflected light, from blue to red (Fig. **8b**).

McGehee and coworkers [104, 105] report on devices constituted by ITO, poly(3,4-ethylene-dioxythiophene)-poly(styrenesulfonate) (PEDOT-PSS), the emissive polymer poly((2-methoxy-5-(3',7'-

dimethyloctloxy)-*para*-phenylenevinylene), and Ag/Ca. They pattern the PEDOT-PSS by μTM to create Bragg gratings with Λ=375-450 nm [104]. The resulting EL spectra exhibit sharp peaks corresponding to the enhanced outcoupling of light (Fig. **8c**). Lee and coworkers [106, 107] fabricate polymeric hexagonal structures with repeated circular holes, with lattice constant (*a*) of 530 nm and diameter and height of 265 nm, by SFIL. The light extraction efficiency increases by more than 50% compared to the non-patterned device (Fig. **8d**). NIL is also used by Ishihara *et al.* for producing square lattice patterns on glass, with periods of 200-300 nm [98]. The OLED consists of indium zinc oxide/(methylphenyl-phenylamino)triphenylamine/ 4,4-bis[N-(1-naphthyl)-N-phenylamino]biphenyl/ Alq_3, and LiF/Al as cathode. Also in this case, the device emission shows narrow peaks due to the diffraction of guided modes to the direction normal to the surface.

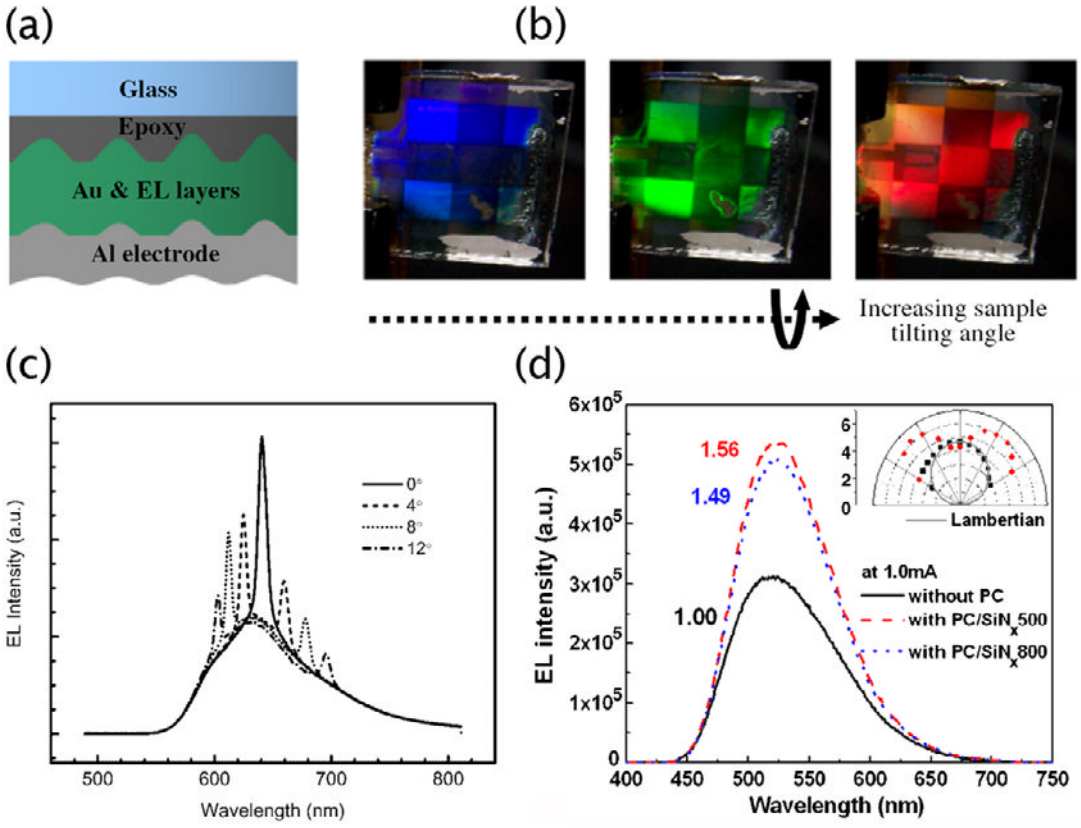

Figure 8: (a) Scheme of an OLED architecture integrating a PhC. (b) Photographs of backside of a device by varying the sample tilting angle. (a)-(b) Reprinted with permission from [103]. Copyright (2008) by the Japan Society of Applied Physics. (c) Angular resolved EL spectra for a device integrating a grating with Λ= 375 nm. Reprinted with permission from [104]. Copyright (2004) by Wiley-VCH Verlag GmbH & Co. KGaA. (d) OLED emission intensity, with and without PhCs. Inset: radiation profile in terms of luminance efficiency. Reprinted with permission from [106]. Copyright (2008) by the American Institute of Physics.

3.3. Waveguides and Other Photonics Devices

Organic PhC structures are advantageously employed in the realization of a large variety of other optical components, including waveguides [108-114], filters [115-121], and optical switches [122-125], together with photovoltaic devices [126, 127]. In particular, in the field of optical waveguides, combining 2D PhCs and a planar slab allows one to exploit both the light confinement in the direction vertical to the slab plane, and the lateral guiding along a PhC-defect structure [108, 109].

Eich and coworkers realize 2D PhCs constituted by holes of 280–300 nm in diameter, embedded into a polymeric layer of benzocyclobutene (Cyclotene 3022, n=1.54 at 1.3 μm, optical losses <1 dB/cm)

deposited on Teflon (n=1.3) [108]. The fabrication is performed by EBL and ion beam etching. The transmission characteristics of the PhC reveal that both TE and TM polarization modes exhibit a stop gap with a minimum of transmission around 1.3 μm and maximum attenuation of 15 and 10 dB, respectively, for propagation lengths of 10a (5 μm). The same authors realize triangular lattices, with a = 650 nm and hole radius of 280 nm, etched into a slab waveguide made by low-index mesoporous silica (n=1.15 at 1.3 μm) and a guiding layer of functionalized poly(methylmethacrylate) [110]. They observe a light transmission suppression of 15 dB between 1170 and 1235 nm over a distance of 40a.

Kee *et al.* produce air-suspended triangular arrays of holes, with diameter of 264 nm and a=775 nm, by NIL on polystyrene [111]. The photonic band structure for TE-like modes exhibits an in-plane gap between 0.49 and 0.51 $\omega a/2\pi c$ (where c is the light speed in vacuum, Fig. **9a**). They also investigate the effect of line defects with width, d =0.9W, where W is the width of line defect created by removing a line of holes in the ΓK direction, clearly finding modes propagating along the defect (Fig. **9b**). The suspended, membrane-like PhCs waveguides are nicely imaged by scanning electron microscopy (SEM, Fig. **9c** and **9d**) [112].

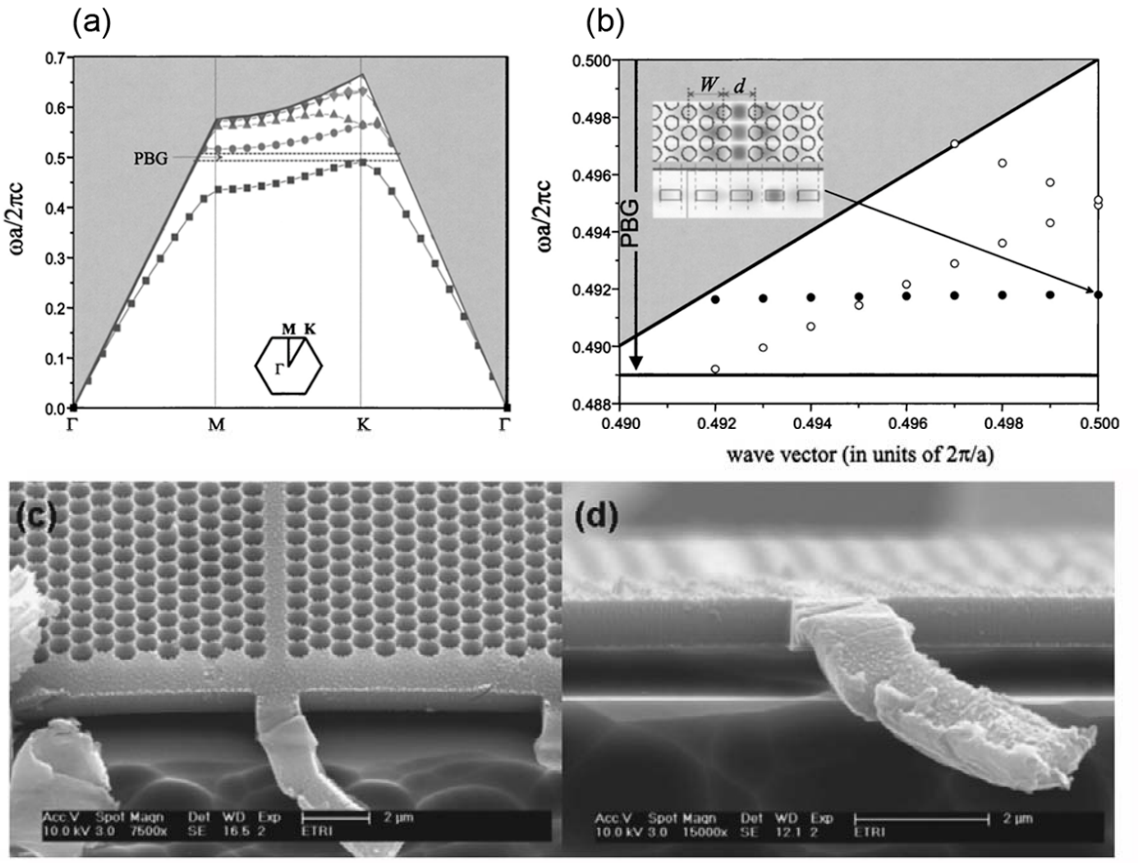

Figure 9: (a) Photonic band structure for TE-like modes of a polystyrene 2D PhC slab in air, with a triangular array of holes with radius 0.34a (frequencies normalized to 2πc/a). The solid line is the light line. The inset indicates the points of high symmetry in the first Brillouin zone. (b) Photonic bands of defect modes for a line defect. The closed (open) circles represent defect modes of even (odd) parity. Inset: field distribution for the even mode at 0.5(2π/a). (a)-(b) Reprinted with permission from [111]. Copyright (2005) by the American Institute of Physics. (c) SEM micrograph of a 2D polystyrene PhCs slabs with a triangular array of air holes and a line defect waveguide fabricated by NIL. (d) Conventional waveguide at the end of the PhCs structure. (c)-(d) Reprinted with permission from [112]. Copyright (2007) by the American Institute of Physics.

Organic PhCs are also developed for producing tunable filters [118, 121]. Oh *et al.* report on a polymeric tunable wavelength Bragg filter based on low-loss fluorinated polymers [115]. They exploit the thermo-optic effect in polymers to obtain a wavelength tuning range over 10 nm when an electrical power of 0.5 W

is applied. Thermo-optic, slightly-tunable polymeric filters are also demonstrated using NIL [116]. The spatial period modulation of a PDMS grating under the mechanical strain, generated by electrostatic actuators, is exploited to achieve a continuous wavelength change from about 557 to 572 nm upon increasing the actuation voltage from 0 to 50 V [117].

Other, all optical, 2D polymer filters are produced with a fast response time (~ 10 ps), and passband shift of 4-6 nm under excitation fluences up to 16 GW/cm^2 [118, 119]. Organics with PhC structures are indeed relevant for all-optical switching in communication networks and ultrahigh speed information processing. An all-optical switch relies on the phase shift of light that interacts with a nonlinear material, and it is characterized by low pump power, high switching efficiency, namely high intensity contrast between two states ("on" and "off"), and fast time response. Hu *et al.* report on 2D PhCs composed of square arrays of cylindrical holes, with a = 220 nm and radius of 90 nm, etched in polystyrene by focused-ion-beam (FIB) [122]. They obtain a time response of the optical switching of about 10 ps and a photonic gap shift of 10 nm under a fluence of 16.7 GW/cm^2. Gong and coworkers employ the MEH-PPV to realize an optical switch based on 2D nonlinear PhCs by FIB. The system operates with a fluence as low as 514 pJ/cm^2, exhibiting switching efficiency and time of 70% and 45 ps, respectively [123]. Moreover, nonlinear PhC microcavities are produced by a nanocomposite made by MEH-PPV doped with Ag nanoparticles [124], and polystyrene hosting the organic chromophores [125], with response time of about 35 ps under fluences of 10^{-1} MW/cm^2, and switching efficiency of 80%.

Finally, approaches based on diffraction gratings [128, 129] and PhCs [130, 131] are proposed for organic solar cells, in order to enhance the optical path length and absorption in the photoactive material [132]. Lopez and coworkers investigate solar cells made of a blend of poly-3-hexylthiophene/[6,6]-phenyl-C61-butyric acid methyl ester and a low-index conducting material, integrating nanostructures into the photoactive layers [127]. They find an optimal nanostructure thickness in the range of 200-300 nm to enhance absorption. They also realize 2D PhCs organic solar cells by soft lithography [126], transferring an hexagonal array of columnar features with period of 400 nm and height of 180 nm into a photoactive blend. In this way, they demonstrate an improvement of the device efficiency by about 70%.

4. VERTICAL GEOMETRIES

Vertical microcavities consist of two mirrors, either metallic layers or distributed Bragg reflectors (DBRs) surrounding an optically-active region of wavelength-scale thickness. Such a structure induces the quantization of the electromagnetic field into a set of discrete, confined photon modes. When the mode energy is resonant with an optical transition, both the emission and the absorption spectra of the active material can be effectively controlled.

4.1. Lasers

Tessler, Denton and Friend [133] report on the first organic microcavity laser, sandwiching PPV between two different mirrors. The laser is fabricated by spin coating the organic layer (with thickness of 100 nm) onto a commercially available DBR made of alternating layers with high and low refractive indices (99% of maximum reflectance). The top mirror, consisting of 60 nm of Al, is thermally evaporated on PPV, thus defining a microcavity which supports a discrete set of longitudinal modes between 520 and 600 nm. Above a pulsed optical pump energy of about 100 nJ, the mode at the PPV gain peak wavelength (545 nm) dominates the spectrum because of STE. Given the reduced distance travelled by light in the amplifying medium, lasing typically needs quite high gain cross sections of the active polymer, together with highly reflecting DBRs enabling the laser oscillation. Peculiar advantages over edge-emitting devices include the inherently high packaging density. Threshold fluences can be as low as a few μJ/cm^2.

Granlund *et al.* report on the attempt to reduce cavity losses, characteristic of asymmetric structures with a metal mirror of relatively low reflectivity (about 98%), and to avoid the intrinsic opacity that forces to collect light in reflection configuration. They excite and collect the output light from the bottom DBR mirror, after assembling a symmetric microcavity by spin-coating polythiophene on two DBRs and manually pressing together the two polymer films on a hot plate (Fig. **10a**) [134, 135]. Building on these ideas, other microcavities

are realized, using liquid-crystalline copolymers to accomplish optical anisotropy [135]. Lasing is obtained for light polarized parallel to the polymer orientation with 0.2 nm linewidth (Fig. **10b**). At 6 μJ/cm^2, the resonance peak polarized perpendicular to the molecular orientation starts also to increase (Fig **10b** and **10c**). Overall, improving the microcavity structure by cladding the organics among DBR mirrors strongly decreases the lasing threshold [136, 137]. However, manually pressing at high temperature (150 °C) the two mirrors can cause an inhomogeneous merging of the cavity layers and possible contamination of the active material. In addition, such sandwiched architectures, although achieving low thresholds, do not allow one to explore the use of matrix-addressable arrays of organic lasers.

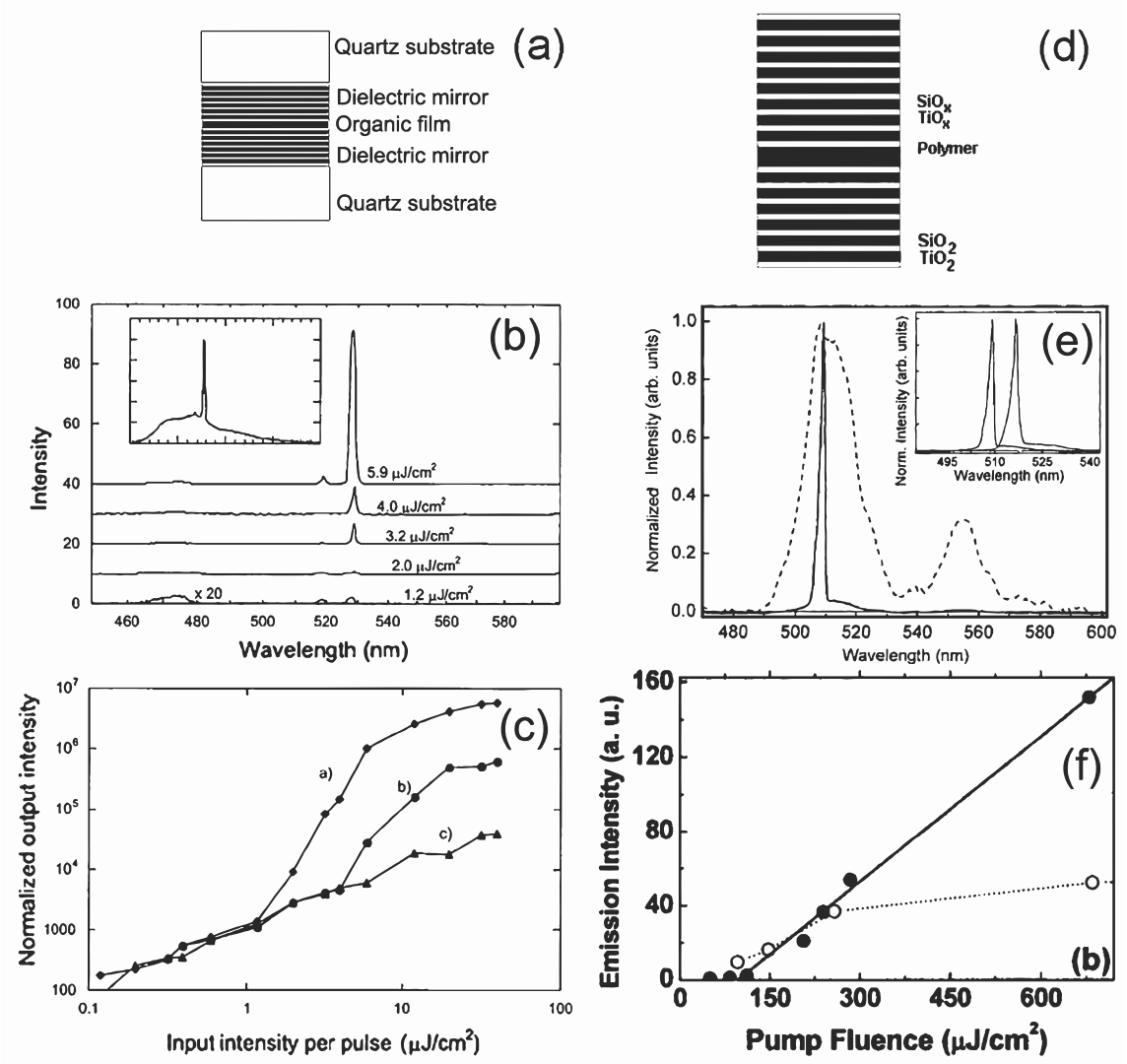

Figure 10: (a) Sandwiched microcavity. (b) Cavity PL varying excitation fluence. Inset: Cavity PL under excitation fluence of 20 μJ/cm^2 in an integrating sphere. (c) Output intensity *vs.* excitation fluence, for detection of the resonance mode in the stop-band polarized parallel -a) and perpendicular -b) to the molecular orientation, and -c) outside the stop-band. (b), (c) Reprinted with permission from [135]. Copyright (2001) by Wiley-VCH Verlag GmbH & Co. KGaA. (d) Monolithic microcavity. (e) Normalized emission spectra at 52 (dashed lines) and 204 μJ/cm^2 (continuous lines) excitation fluences. Inset: Laser spectra obtained by different cavity lengths. (f) Output intensity of a reference film (empty circles) and of the microcavity (full circles) *vs.* pump fluence. The solid line is a linear fit to the laser characteristics. (d)-(f) Reprinted with permission from [139]. Copyright (2006) by the American Institute of Physics.

Monolithic, symmetric architectures, consisting of DBRs cladding the organic layer and deposited in a single evaporation run, represent a solution for fabricating low threshold laser arrays. To avoid loss of adhesion and strong deterioration of the polymer optical properties, induced by the high temperatures and

the oxygen atmosphere required for the stoichiometric deposition of DBR oxides, a specific low-temperature approach is developed [138]. By such technology, lasing is demonstrated in structures in which the top dielectric mirror is directly deposited onto the polymer film (Fig. **10d**) [139, 140]. Persano *et al.* report on a monolithic polymeric microcavity laser with all-dielectric mirrors realized by low-temperature electron-beam evaporation. The vertical heterostructure is realized by 9.5 TiO_x/SiO_x pairs evaporated onto an active conjugated polymer, previously spin-cast onto the bottom DBR. The cavity supports single-mode lasing at 509 nm, with a linewidth of 1.8 nm, and a threshold of 84 $\mu J/cm^2$ (Fig. **10e** and **10f**) [139].

4.2. Light Emitting Diodes

Besides modifying the device structure by surface texturing or by adding scattering layers [90, 141], embedding organics in a vertical microcavity allows one to alter the spatial profiles of the optical modes and to increase the coupling strength of the emissive dipoles to unbound modes in OLEDs. The microcavity modifies the resulting emission through the alteration of the optical transition probabilities. Light intensity enhancement, spectral narrowing, and spatial redistribution of the emitted light are the most effective consequences. In pioneering studies on microcavity-coupled OLEDs, both metallic [142] and dielectric [143] mirrors are added to the EL layer. Dodabalapur *et al.* report on shifting the Fabry-Pérot mode by spacing layers, and exploit the spectral narrowing to overcome the lack of saturated colours needed to realize full-colour displays [144]. By tailoring the spectral position of the cavity modes within the broad band of Alq_3, it is possible to obtain white emission.

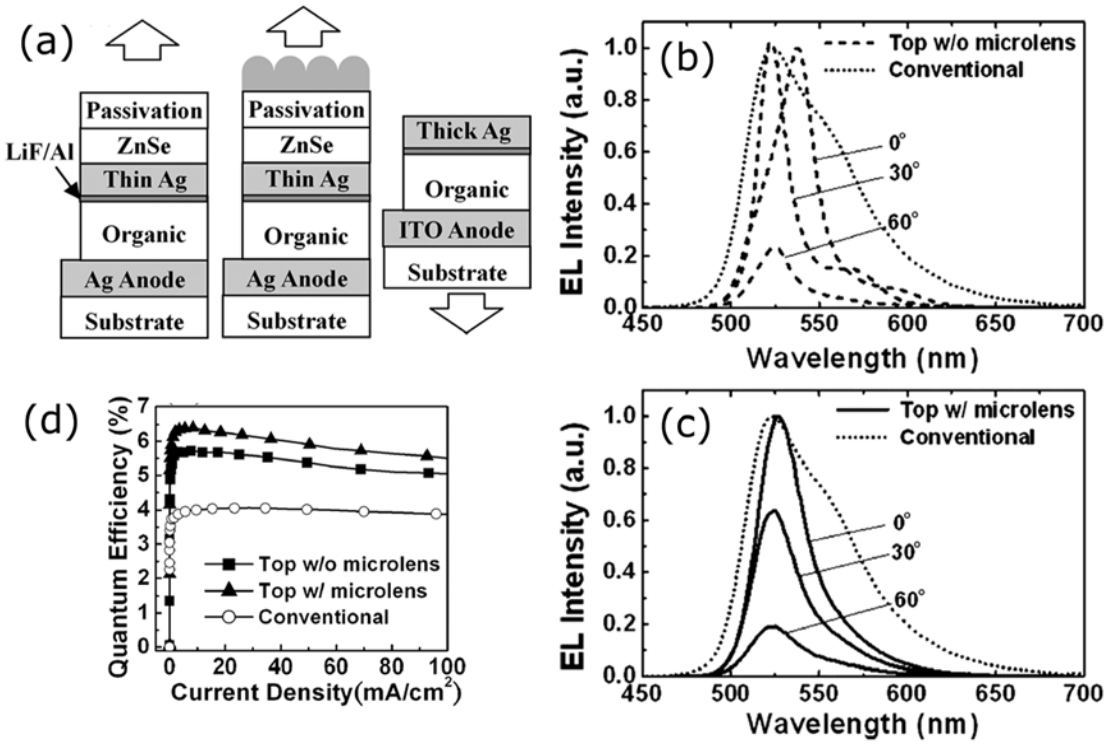

Figure 11: (a) From left to right: top emitting microcavity without and with microlenses, and conventional, bottom-emitting OLED. EL spectra under viewing angles of 0°, 30° and 60° for the top- emitting device (b) without and with (c) microlenses. (d) Quantum efficiency of the three devices. Reprinted with permission from [149]. Copyright (2007) by the American Institute of Physics.

Dirr *et al.* highlight the importance of the active layer positioning on the resulting emission of the microcavity [145]. For instance, placing the active layer at the antinode of the resonant cavity field strongly enhances the emitted light. On the other hand, a suppression of the emission is achieved by positioning the active layer at the node [145].

Research also focuses on reducing the viewing angle dependence of the emission [146, 147] and improving the colour tunability by controlling the bias voltage [148]. The approaches proposed for enhancing the outcoupling efficiency, *i.e.,* substrate micro-structuring and microcavity effects, are combined by microcavity OLEDs integrated with microlens arrays [149]. The microcavity is constituted by sandwiching the emitting layer between two Ag layers. For maximizing the optical output, the top Ag mirror is further capped with a 45 nm high-index layer of thermally evaporated ZnSe. A passivation micrometer-thick parylene film is then deposited on top. Finally, the microcavity is integrated by lamination with a PDMS sheet shaped with microlens by REM (Fig. **11a**). The microlenses are hemispheres with diameter of about 10 μm. The resulting EL spectra (Fig. **11b** and **11c**) demonstrate that the microlenses stabilize the wavelength of output light at different angles and redirect more light to the forward direction. As a consequence, saturated colours are stable over the viewing angles and the emission is slightly more directed with respect to reference microcavity OLEDs without microlenses. In addition, an increase of the external quantum efficiency is achieved (Fig. **11d**). Further optimizing combined vertical/planar approaches is one of the more promising roots for achieving high efficiency with viewing angle stability.

4.3. Photodiodes

The use of organic thin films for light-detecting devices is also receiving increasing interest. A simple architecture to extract a photocurrent is a bilayer device, including organic semiconductor materials with electron-acceptor and electron-donor properties, respectively, sandwiched between anode and cathode. The mechanism leading to charge collection can be schematized by a four-step process. Exciton pairs are generated within one of the organic layer upon light absorption, then excitons diffuse towards the organic-organic interface, where the probability of exciton diffusion is higher. The exciton dissociation, which results in electron transfer to the acceptor material, takes place, and, finally, the generated charges are transported towards the respective electrodes. As for OLEDs, different approaches allow one to increase the device efficiency and to improve the spectral sensitivity. Some methods are based on the optimization of the donor-acceptor layers and interfaces by (i) using organics with high absorption coefficient, and (ii) realizing organic heterojunction spacers comparable with the exciton diffusion length typical of disordered molecular solids (tens of nm) [150-152]. More recent approaches are focused on modifying the electric field of the incident light by microcavities [153-155]. The usual quantization of the light field, only allowing optical modes with resonant wavelengths, results in narrow spectral response and enhanced sensitivity [155] (Fig. **12**). Lupton *et al.* demonstrate that using a Bragg reflector instead of a metallic mirror results in increasing the microcavity quality factor and narrowing the spectral response [155]. By adding optical spacers and positioning a second resonant mode to overlap with the donor–acceptor interface, An *et al.* increase the detector sensitivity by two orders of magnitude with respect to prior works, effectively tuning the response across the visible spectrum [156].

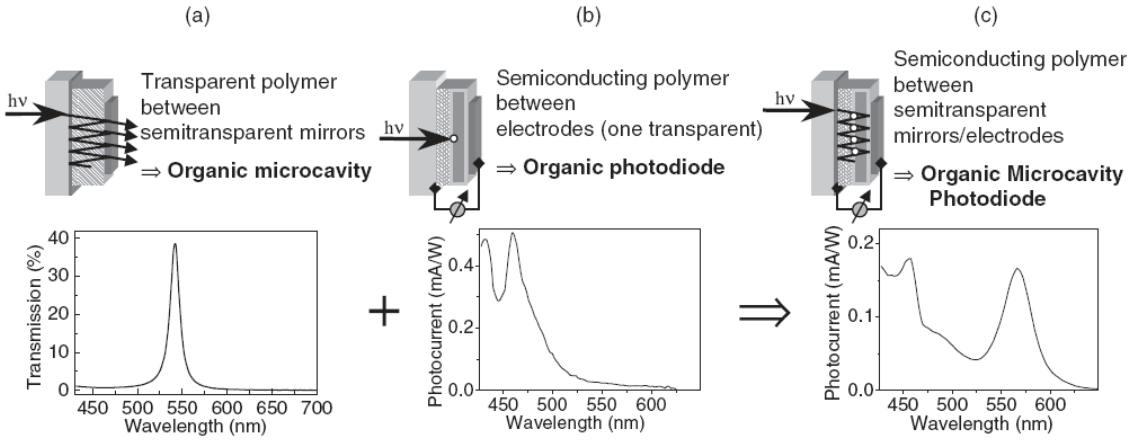

Figure 12: Organic microcavity photodiodes. Organic films into wavelength scale microcavities exhibit distinct peaks in the photonic density of states, corresponding to narrow transmission peaks (a). Conjugated polymers can also be used between electrodes, showing a broad spectral response falling off rapidly to the red of the absorption band (b). A

combination of the two principles gives microcavity photodiodes with narrow spectral response and enhanced sensitivity (c). Reprinted with permission from [155]. Copyright (2003) by Wiley-VCH Verlag GmbH & Co. KGaA.

4.4. Microcavities Operating in the Strong Coupling Regime

Two regimes classify the interactions between a semiconductor in a microcavity and an electromagnetic field, namely the weak and the strong coupling. The weak coupling occurs when the interaction between the cavity mode and the exciton formed in the active layer is weaker than the exciton broadening. In the strong-coupling regime, a cavity photon couples instead strongly to an exciton having the same energy and in-plane momentum, the exciton linewidth being much smaller than the exciton-cavity mode coupling. The coherent, coupled state is termed a cavity polariton, and can be considered as a mixture of the exciton and cavity-photon modes. The interest toward cavity-polaritons relies on their properties to form a Bose-Einstein condensate and to realize a polariton laser [157], both demonstrated in inorganic microcavities [158-160]. Organic microcavities typically operate in the weak coupling regime, because of the large exciton linewidth (few hundreds of meV) due to inhomogeneous broadening and strong interactions with phonons [161]. Typical exciton-cavity mode interaction strength are instead of few tens of meV.

However, a number of organic molecules exhibit narrow exciton transitions (linewidths of few tens of meV) and large oscillator strengths, enabling strong-coupling between exciton and photon modes in vertical microcavities. These materials include porphyrins [162], *J*-aggregated cyanine dyes [163], conjugated polymers [164] and organic single crystals [157]. The large binding energy of exciton in organics (~0.5 eV) allows to observe strong coupling at room temperature, whereas in inorganic systems this regime is generally achieved at low temperature. The strong coupling is identified by an anti-crossing between the cavity photon and exciton modes, that ideally results on resonance in a doublet of cavity polariton states of same linewidth and intensity, separated by the vacuum Rabi-splitting energy ($\hbar\Omega$). The coupling can be described by a 2×2 matrix Hamiltonian [165]:

$$H = \begin{pmatrix} E_{exc} & \frac{\hbar\Omega}{2} \\ \frac{\hbar\Omega}{2} & E_c \end{pmatrix} \quad \textbf{(3)}$$

where E_{exc} and E_c are the energies of the exciton and cavity modes. This Hamiltonian can be diagonalized, giving the following eigenvalues:

$$E_{\pm} = \frac{E_{exc} + E_c}{2} \pm \sqrt{(\hbar\Omega)^2 + (E_{exc} - E_c)^2} \quad \textbf{(4)}$$

The coupled oscillator model can be readily used to calculate microcavity in-plane dispersions [166]. To this aim, the uncoupled exciton and cavity photon energies are made *k*-dependent according to their dispersions. The polariton dispersion is then obtained by solving the coupled oscillator problem for each value of *k*, giving a low energy (LP) and a high energy (UP) polariton branch. The characteristic anticrossing behaviour of the polariton dispersion is obtained by angle-dependent cavity reflectivity (Fig. **13a**) or PL (Fig. **13b**) [163]. In fact, the cavity mode has an angle dependent resonant energy:

$$E_c(\theta) = E_0 \left(1 - \frac{\sin^2(\theta)}{n_{eff}} \right)^{-1/2} \quad \textbf{(5)}$$

E_0 being the photon energy at normal incidence ($E_0 = hc / n_{eff} L_c$) and L_c the cavity thickness. A typical resulting anti-crossing of the polariton dispersion curves is displayed in Fig. **13c**. Vacuum Rabi splitting as large as 430 meV is reported at room temperature, for microcavities embedding a poly-[*bis*(*p*-butylphenyl)silane] [164], a σ-conjugated polymer characterized by a large oscillator strength (absorption

coefficient 129000 cm^{-1}). Polariton emission is also achieved in a microcavity OLED, with a Rabi splitting of 265 meV at room temperature [167].

Finally, microcavity devices can exhibit polarization effects, such as, for example, polarization mode splitting (PMS), as observed in the weak coupling regime in a number of organics [168-170]. In fact, TM and TE polarized fields show different penetration depths into a dielectric mirror and different angular dependence, *i.e.,* the penetration depth increases with the incident (or detection) angle (θ) for TM and decreases for TE polarization. These effects lead to a PMS, that for can be expressed as [168, 171]:

$E_c^{TM}(\theta) - E_c^{TE}(\theta) = A\left[E_s(0) - E_c(0)\right]\sin^2(\theta)$, where A is a constant. The sign of the splitting is determined by the difference between the central energy of the stop band (E_s) and the energy of the cavity mode (E_c). This effect is also found in microcavities with *J*-aggregates of cyanine dye as active layer (Fig. **13d**). The maximum TE-TM polarization splitting is of 35 meV [172], increasing as $\sin^2(\theta)$ for the different polariton branches.

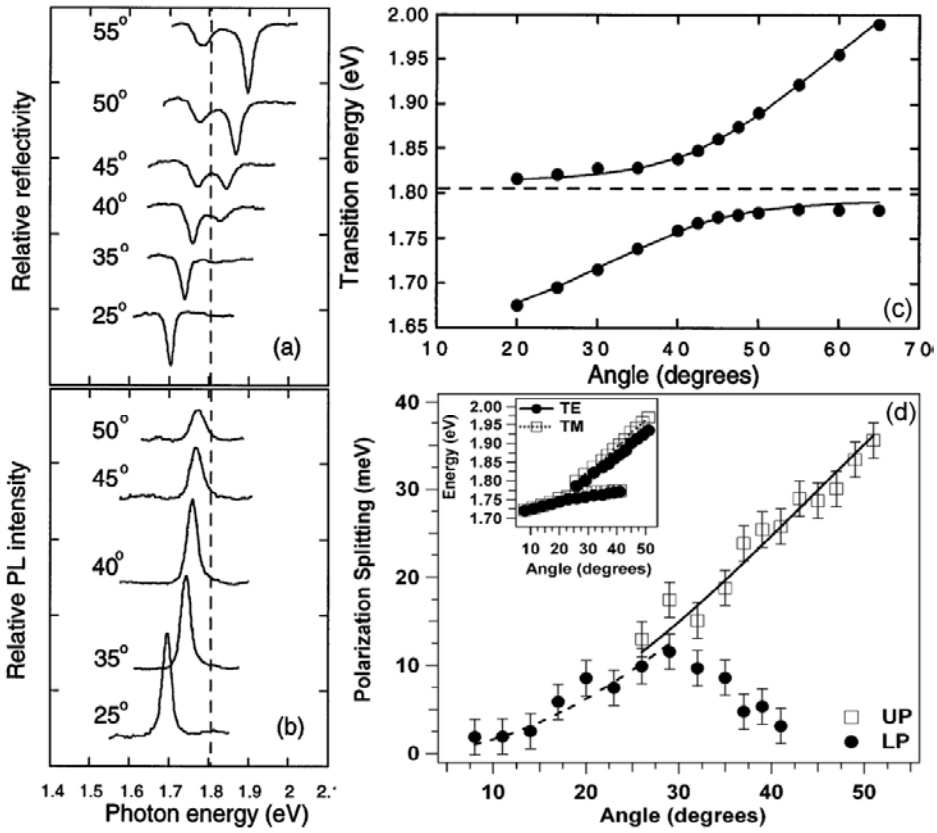

Figure 13: Dependence of the reflectivity (a) and PL (b) spectra on the detection angle for a cyanine dye containing microcavity. The spectra for different collection angles have been shifted vertically for clarity. The exciton energy is denoted by the vertical dashed line. (c) Reflectivity dispersion curves as a function of measurement angle of a cyanine dye containing microcavity. The solid line is a TMR fit (the used exciton energy is marked by the horizontal dashed line). (a)-(c) Reprinted with permission from [163]. Copyright (1999) by the American Physical Society. (d) Angle dependence of the polarization splitting for the LP (filled circles) and UP (empty squares) polariton branches. Data are obtained by reflectivity measurements. The dashed and continuous lines are fits to the data with a $\sin^2(\theta)$ function. The inset shows the experimental TM and TE dispersion curves as a function of the incident angle. Reprinted with permission from [172]. Copyright (2006) by the Elsevier B. V.

CONCLUSIONS

Novel methods such as soft and nanoimprint lithographies, eventually combined with standard exposure or etching technologies, are advantageously employed in the realization of optical components and

nanophotonic devices based on 1D and 2D PhCs. Examples of obtained devices include DFB plastic devices, which can be ultimately integrated with microplates and microarray slides commonly used in automated liquid handling and detection instruments, thus providing a route for the future development of disposable DFB-based biosensors. Nanopatterning PhC extends to a wide variety of other devices such as OLEDs and waveguides, and also to vertical microcavity architectures. Besides lasing, controlled and/or enhanced light-emission, confinement and guiding in polymer materials, organic microcavities can provide the route for demonstrating amplification or condensation of cavity-polaritons in molecular systems.

ACKNOWLEDGEMENTS

This work is partly supported by the Apulia Regional Strategic Project PS_016, and of the Italian Ministry of University and Research through the FIRB projects RBIN045MNB and RBIP06SH3W.

REFERENCES

[1] Ma H, Jen A K-Y, Dalton LR. Polymer-based optical waveguides: materials, processing, and devices. Adv Mater 2002; 14(19): 1339-1365.

[2] Joannopoulos JD, Meade RD, Winn JN, in Photonic crystals: molding the flow of light. Princeton University Press (Cambridge, MA 1995).

[3] Xia Y, Whitesides GM. Soft Lithography. Angew Chem Int Ed Engl 1998; 37(5): 550-575.

[4] Chou SY, Krauss PR, Renstrom PJ. Imprint of sub-25 nm vias and trenches in polymers. Appl Phys Lett 1995; 67(21): 3114-3116.

[5] Chou SY, Krauss PR, Renstrom PJ. Imprint lithography with 25-nanometer resolution. Science 1996; 272(5258): 85-87.

[6] Xia Y, Kim E, Zhao X-M, Rogers JA, Prentiss M, Whitesides GM. Complex optical surfaces formed by replica molding against elastomeric masters. Science 1996; 273(5273): 347-349.

[7] Kumar A, Whitesides GM. Features of gold having micrometer to centimeter dimensions can be formed through a combination of stamping with an elastomeric stamp and an alkanethiol ''ink'' followed by chemical etching. Appl Phys Lett 1993; 63(14): 2002-2004.

[8] Zhao X-M, Xia Y, Whitesides GM. Fabrication of three-dimensional micro-structures: Microtransfer molding. Adv Mater 1996; 8(10): 837-840.

[9] Kim E, Xia Y, Whitesides G. M. Polymer microstructures formed by moulding in capillaries. Nature 1995; 376(6541): 581-584.

[10] Suh KY, Lee HH. Capillary force lithography: large-area patterning, self-organization, and anisotropic dewetting. Adv Funct Mater 2002; 12(6): 405-413.

[11] Pisignano D, Persano L, Cingolani R, Gigli G, Barbudri F, Farinola GM, Naso F. Soft molding lithography of conjugated polymers. Appl Phys Lett 2004; 84(8): 1365-1367.

[12] Kim E, Xia Y, Zhao X-M, Whitesides GM. Solvent-assisted microcontact molding: A convenient method for fabricating three-dimensional structures on surfaces of polymers. Adv Mater 1997; 9(8): 651-654.

[13] Mrksich M, Whitesides GM. Patterning self-assembled monolayers using microcontact printing: a new technology for biosensors? Trends Biotechnol 1995; 13(6): 228- 235.

[14] Singhvi R, Kumar A, Lopez GP, Stehanopoulos GN, Wang DIC, Whitesides GM. Engineering cell shape and function. Science 1994; 264(5159): 696-698.

[15] Mrksich M, Chen CS, Xia Y, Dike LE, Ingber DE, Whitesides GM. Controlling cell attachment on contoured surfaces with self-assembled monolayers of alkanethiolates on gold. Proc Natl Acad Sci USA 1996; 93(20): 10775-10778.

[16] Delamarche E, Bernard A, Schmid H, Michel B, Biebuyck H. Patterned delivery of immunoglobulins to surfaces using microfluidic networks. Science 1997; 276 (5313): 779-781.

[17] Delamarche E, Bernard A, Schmid H, Bietsch A, Michel B, Biebuyck HA. Microfluidic Networks for Chemical Patterning of Substrates: Design and application to bioassays. J Am Chem Soc 1998; 120(3): 500-508.

[18] Whitesides GM. The origins and the future of microfluidics. Nature 2006; 442(7101): 368-373.

[19] Girardo S, Cecchini M, Beltram F, Cingolani R, Pisignano D. Polydimethylsiloxane–$LiNbO_3$ surface acoustic wave micropump devices for fluid control into microchannels. Lab Chip 2008; 8(9): 1557-1563.

[20] Girardo S, Cingolani R, Pisignano D. Microfluidic rheology of non-newtonian liquids. Anal Chem 2007; 79(15): 5856-5861.

[21] Lee T-W, Zaumseil J, Bao Z, Hsu JWP, Rogers JA. Organic light-emitting diodes formed by soft contact lamination. Proc Natl Acad Sci USA 2004; 101(2): 429-433.

[22] De Marco C, Mele E, Camposeo A, Stabile R, Cingolani R, Pisignano D. Organic light-emitting nanofibers by solvent-resistant nanofluidics. Adv Mater 2008; 20(21): 4158-4162.

[23] Mele E, Camposeo A, De Giorgi M, Di Benedetto F, De Marco C, Tasco V, Cingolani R, Pisignano D. Sub-50-nm conjugated polymer dots by nanoprinting. Small 2008; 4(11): 1894-1899.

[24] Chou SY, Krauss PR, Zhang W, Guo L, Zhuang L. Sub-10 nm imprint lithography and applications. J Vac Sci Technol B 1997; 15(6): 2897-2904.

[25] Heidari B, Maximov I, Montelius L. Nanoimprint lithography at the 6 in. wafer scale. J Vac Sci Technol B 2000; 18(6): 3557-3560.

[26] Wang J, Sun X, Chen L, Chou SY. Direct nanoimprint of submicron organic light-emitting structures. Appl Phys Lett 1999; 75(18): 2767-2769.

[27] Kiyohara S, Fujiwara M, Matsubayashi F, Mori K. Organic light-emitting microdevices fabricated by nanoimprinting technology using diamond molds. Jpn J Appl Phys 2005; 44 (6A): 3686-3690.

[28] Krauss PR, Chou SY. Nano-compact disks with 400Gbit/in^2 storage density fabricated using nanoimprint lithography and read with proximal probe. Appl Phys Lett 1997; 71(21): 3174-3176.

[29] McClelland GM, Hart MW, Rettner CT, Best ME, Carter KR, Terris BD. Nanoscale patterning of magnetic islands by imprint lithography using a flexible mold. Appl Phys Lett 2002; 81(8): 1483-1485.

[30] Ahn SW, Lee KD, Kim JS, Kim SH, Park JD, Lee SH, Yoon PW. Fabrication of a 50 nm half-pitch wire grid polarizer using nanoimprint lithography. Nanotechnology 2005; 16(9): 1874-1877.

[31] Cheng X, Hong YT, Kanicki J, Guo LJ. High-resolution organic polymer light-emitting pixels fabricated by imprinting technique. J Vac Sci Technol B 2002; 20(6): 2877-2880.

[32] Guo LJ, Cheng X, Chou CF. Fabrication of size-controllable nanofluidic channels by nanoimprinting and its application for DNA stretching. Nano Lett 2004; 4(1): 69-73.

[33] Strobl G. The Physics of Polymers. 1997, Springer, Berlin.

[34] Mele E, Camposeo A, Stabile R, Del Carro P, Di Benedetto F, Persano L, Cingolani R, Pisignano D. Polymeric distributed feedback lasers by room-temperature nanoimprint lithography. Appl Phys Lett 2006; 89(13): 131109.

[35] Del Carro P, Camposeo A, Stabile R, Mele E, Persano L, Cingolani R, Pisignano D. Near-infrared imprinted distributed feedback lasers. Appl Phys Lett 2006; 89(20): 201105.

[36] Di Benedetto F, Camposeo A, Pagliara S, Mele E, Persano L, Stabile R, Cingolani R, Pisignano D. Patterning of light-emitting conjugated polymer nanofibres. Nat Nanotech 2008; 3(10): 614-619.

[37] Yan M, Rothberg LJ, Papadimitrakopoulos F, Galvin ME, Miller TM. Defect quenching of conjugated polymer luminescence. Phys Rev Lett 1994; 73(5): 744-747.

[38] Khang D-Y, Yoon H, Lee HH. Room-Temperature Imprint Lithography. Adv Mater 2001; 13(10): 749-752.

[39] Mele E, Di Benedetto F, Persano L, Cingolani R, Pisignano D. Multilevel, room-temperature nanoimprint lithography for conjugated polymer-based photonics. Nano Lett 2005; 5(10): 1915-1919.

[40] Colburn M, Johnson S, Stewart M, Damle S, Bailey T, Choi B, Wedlake M, Michaelson T, Sreenivasan SV, Ekerdt JG, Willson CG. Step and flash imprint lithography: a new approach to high-resolution patterning. Proceedings of SPIE 1999; 3676: 379-389.

[41] Mele E, Camposeo A, DeMarco C, Persano L, Cingolani R, Pisignano D. Patterning photo-curable light-emitting organic composites by vertical and horizontal capillarity: a general route to photonic nanostructures. Nanotechn 2008; 19(33): 335301.

[42] Moses D. High quantum efficiency luminescence from a conducting polymer in solution – A novel polymer laser-dye. Appl Phys Lett 1992; 60(26): 3215-3216.

[43] Samuel IDW, Turnbull GA. Organic semiconductor lasers. Chem Rev 2007; 107(4): 1272-1295.

[44] Pisignano D, Persano L, Mele E, Visconti P, Cingolani R, Gigli G, Barbarella G, Favaretto L. Emission properties of printed organic semiconductor lasers. Opt Lett 2005; 30(3): 260-262.

[45] McGehee MD, Diaz-Garcia MA, Hide F, Gupta R, Miller EK, Moses D, Heeger AJ. Semiconducting polymer distributed feedback lasers. Appl Phys Lett 1998; 72(13): 1536-1538.

[46] Heliotis G, Xia R, Bradley DDC, Turnbull GA, Samuel IDW, Andrew P, Barnes WL. Blue, surface-emitting, distributed feedback polyfluorene lasers. Appl Phys Lett 2003; 83(11): 2118-2120.

[47] Kallinger C, Hilmer M, Haugeneder A, Perner M, Spirkl W, Lemmer U, Feldmann J, Scherf U, Mullen K, Gombert A, Wittwer V. A flexible conjugated polymer laser. Adv Mater 1998; 10(12): 920-923.

[48] Spehr T, Siebert A, Fuhrmann-Lieker T, Salbeck J, Rabe T, Riedl T, Johannes HH, Kowalsky W, Wang J, Weimann T, Hinze P. Organic solid-state ultraviolet-laser based on spiro-terphenyl. Appl Phys Lett 2005; 87(16): 161103.

[49] Riechel S, Lemmer U, Feldmann J, Berleb S, Muckl AG, Brutting W, Gombert A, Wittwer V. Very compact tunable solid-state laser utilizing a thin-film organic semiconductor. Opt Lett 2001; 26(9): 593-595.

[50] Campoy-Quiles M, Heliotis G, Xia RD, Ariu M, Pintani M, Etchegoin P, Bradley DDC. Ellipsometric characterization of the optical constants of polyfluorene gain media. Adv Funct Mater 2005; 15(6): 925-933.

[51] Kogelnik H, Shank CV. Stimulated emission in a periodic structure. Appl Phys Lett 1971; 18(4): 152-154.

[52] Kogelnik H, Shank CV. Coupled-wave theory of distributed feedback lasers. J Appl Phys 1972; 43(5): 2327-2335.

[53] Dumarcher V, Rocha L, Denis C, Fiorini C, Nunzi J-M, Sobel F, Sahraoui B, Gindre D. Polymer thin-film distributed feedback tunable lasers. J Opt A: Pure Appl Opt 2000; 2(4): 279–283.

[54] Chen F, Gindre D, Nunzi JM. First-order distributed feedback dye laser effect in reflection pumping geometry. Opt Lett 2007; 32(7): 805-807.

[55] Stabile R, Camposeo A, Persano L, Tavazzi S, Cingolani R, Pisignano D. Organic-based distributed feedback lasers by direct electron-beam lithography on conjugated polymers. Appl Phys Lett 2007; 91(10): 101110.

[56] Yariv A. Quantum Electronics (3rd Ed.). J. Wiley & Son Inc., 1989.

[57] Sakoda K. Optical properties of photonic crystals (2nd Ed.). Springer Verlag Berlin, 2005.

[58] Bulu I, Caglayan H, Ozbay E. Radiation properties of sources inside photonic crystals. Phys Rev B 2003; 67(20): 205103.

[59] Turnbull GA, Andrew P, Jory MJ, Barnes WL, Samuel IDW. Relationship between photonic band structure and emission characteristics of a polymer distributed feedback laser. Phys Rev B 2001; 64(12): 125122.

[60] Ziebarth JM, McGehee MD. Measuring the refractive indices of conjugated polymer films with Bragg grating outcouplers. Appl Phys Lett 2003; 83(24): 5092-5094.

[61] Samuel IDW, Namdas EB, Turnbull GA. How to recognize lasing. Nature Photonics 2009; 3(10): 546-549.

[62] Rose A, Zhu ZG, Madigan CF, Swager TM, Bulovic V. Sensitivity gains in chemosensing by lasing action in organic polymers. Nature 2005; 434(7035): 876-879.

[63] Kozlov VG, Parthasarathy G, Burrows PE, Khalfin VB, Wang J, Chou SY, Forrest SR. Structures for organic diode lasers and optical properties of organic semiconductors under intense optical and electrical excitations. IEEE J Quantum Electron 2000; 36(1): 18-26.

[64] Camposeo A, Mele E, Persano L, Pisignano D, Cingolani R. Low-loss and highly polarized emission from planar polymer waveguides. Opt Lett 2006; 31(10): 1429-1431.

[65] Camposeo A, Mele E, Persano L, Pisignano D, Cingolani R. Role of doping concentration on the competition between amplified spontaneous emission and nonradiative energy transfer in blends of conjugated polymers. Phys Rev B 2006; 73(16): 165201.

[66] Richardson S, Gaudin OPM, Turnbull GA, Samuel IDW. Improved operational lifetime of semiconducting polymer lasers by encapsulation. Appl Phys Lett 2007; 91(26): 261104.

[67] Rabe T, Gerlach K, Riedl T, Johannes H-H, Kowalsky W, Niederhofer J, Gries W, Wang J, Weimann T, Hinze P, Galbrecht F, Scherf U. Quasi-continuous-wave operation of an organic thin-film distributed feedback laser. Appl Phys Lett 2006; 89(8): 081115.

[68] Chen Y, Zhenyu Li Z, Zhaoyu Zhang Z, Psaltis D, and Axel Scherer A. Nanoimprinted circular grating distributed feedback dye laser. Appl Phys Lett 2007; 91(5): 051109.

[69] Reboud V, Lovera P, Kehagias N, Zelsmann M, Schuster C, Reuther F, Gruetzner G, Redmond G, Torres CMS. Two-dimensional polymer photonic crystal band-edge lasers fabricated by nanoimprint lithography. Appl Phys Lett 2007; 91(15): 151101.

[70] Heliotis G, Xia RD, Turnbull GA, Andrew P, Barnes WL, Samuel IDW, Bradley DDC. Emission characteristics and performance comparison of polyfluorene lasers with one- and two-dimensional distributed feedback. Adv Funct Mater 2004; 14(1): 91-97.

[71] Riechel S, Kallinger C, Lemmer U, Feldmann J, Gombert A, Wittwer V, Scherf U. A nearly diffraction limited surface emitting conjugated polymer laser utilizing a two-dimensional photonic band structure. Appl Phys Lett 2000; 77(15): 2310-2312.

[72] Turnbull GA, Carleton A, Tahraouhi A, Krauss TF, Samuel IDW, Barlow GF, Shore KA. Effect of gain localization in circular-grating distributed feedback lasers. Appl Phys Lett 2005; 87(20): 201101.

[73] Schneider D, Rabe T, Riedl T, Dobbertin T, Kroger M, Becker E, Johannes HH, Kowalsky W, Weimann T, Wang J, Hinze P, Gerhard A, Stossel P, Vestweber H. An ultraviolet organic thin-film solid-state laser for biomarker applications. Adv Mater 2005; 17(1): 31-34.

[74] Schneider D, Rabe T, Riedl T, Dobbertin T, Kröger M, Becker E, Johannes H-H, Kowalsky W, Weimann T, Wang J, Hinze P. Ultrawide tuning range in doped in organic solid-state lasers. Appl Phys Lett 2004; 85(11): 1886-1888.

[75] Jakubiak R, Tondiglia VP, Natarajan LV, Sutherland RL, Lloyd P, Bunning TJ, Vaia RA. Dynamic lasing from all-organic two-dimensional photonic crystals. Adv Mater 2005; 17(23): 2807-2811.

[76] Yu H, Tang BY, Li J, Li L. Electrically tunable lasers made from electrooptically active photonics band gap materials. Opt Express 2005; 13(18): 7243-7249.

[77] Jakubiak R, Natarajan LV, Tondiglia V, He GS, Prasad PN, Bunning TJ, Vaia RA. Electrically switchable lasing from pyrromethene 597 embedded holographic-polymer dispersed liquid crystals. Appl Phys Lett 2004; 85(25): 6095-6097.

[78] Berggren M, Dodabalapur A, Slusher RE, Timko A, Nalamasu O. Organic solid-state lasers with imprinted gratings on plastic substrates. Appl Phys Lett 1998; 72(4): 410-411.

[79] Suzuki K, Takahashi K, Seida Y, Shimizu K, Kumagai M, Taniguch Y. A continuously tunable organic solid-state laser based on a flexible distributed-feedback resonator. Jpn J Appl Phys Part 2 2003; 42(3A): L249-L251.

[80] Lu M, Choi SS, Irfan U, Cunningham BT. Plastic distributed feedback laser biosensor. Appl Phys Lett 2008; 93(11): 111113.

[81] Pope M, Kallmann HP, Magnantte P. Electroluminescence in organic crystals. J Chem Phys 1963; 38(8): 2042-2043.

[82] Helfrich WWG, Schneider WG. Recombination radiation in anthracene crystals. Phys Rev Lett 1965; 14(7): 229-231.

[83] Tang CW, Van Slyke SA. Organic electroluminescent diodes. Appl Phys Lett 1987; 51(12): 913-915.

[84] Burroughes JH, Bradley DDC, Brown AR, Marks RN, Mackay K, Friend RH, Burns PL, Holmes AB. Light-emitting diodes based on conjugated polymers. Nature 1990; 347(6293): 539- 541.

[85] Shinar J, Shinar R. Organic light-emitting devices (OLEDs) and OLED-based chemical and biological sensors: an overview. J Phys D: Appl Phys 2008; 41(13): 133001-27.

[86] Müllen K, Scherf U. Organic light emitting devices-synthesis, properties and applications. Wiley VCH Germany 2006.

[87] Adachi C, Baldo MA, Thompson ME, Forrest SR. Nearly 100% internal phosphorescence efficiency in an organic light emitting device. J Appl Phys 2001; 90(10): 5048-5051.

[88] Moller S, Forrest SR Improved light out-coupling in organic light emitting diodes employing ordered microlens arrays. J Appl Phys 2002; 91(5): 3324-3327.

[89] Yamasaki T, Sumioka K, Tsutsui T. Organic light-emitting device with an ordered monolayer of silica microspheres as a scattering medium. Appl Phys Lett 2000; 76(10): 1243-1245.

[90] Tsutsui T, Yahiro M, Yokogawa H, Kawano K, Yokoyama M. Doubling coupling-out efficiency in organic light-emitting devices using a thin silica aerogel layer. Adv Mater 2001; 13(15): 1149-1152.

[91] Jordan RH, Dodabalapur A, Slusher RE. Efficiency enhancement of microcavity organic light emitting diodes. Appl Phys Lett 1996; 69(14): 1997-1999.

[92] Lupton JM, Matterson BJ, Samuel IDW, Jory MJ, Barnes WL. Bragg scattering from periodically microstructured light emitting diodes. Appl Phys Lett 2000; 77(21): 3340-3342.

[93] Matterson BJ, Lupton JM, Safonov AF, Salt MG, Barnes WL, Samuel IDW. Increased efficiency and controlled light output from a microstructured light-emitting diode. Adv Mater 2001; 13(2): 123-127.

[94] Do YR, Kim YC, Song Y-W, Cho C-O, Jeon H, Lee Y-J, Kim S-H, Lee Y-H. Enhanced light extraction from organic light-emitting diodes with 2D SiO_2/SiN_x photonic crystals. Adv Mater 2003; 15(14): 1214-1218.

[95] Fujita M, Ishihara K, Ueno T, Asano T, Noda S, Ohata H, Tsuji T, Nakada H, Shimoj N. Electrical characteristics of organic light-emitting diodes with two-dimensional photonic crystals in organic/electrode layers. Jpn J Appl Phys 2005; 44(6A): 3669-3677.

[96] Liu C, Kamaev V, Vardeny ZV. Efficiency enhancement of an organic light-emitting diode with a cathode forming two-dimensional periodic hole array. Appl Phys Lett 2005; 86(14): 143501.

[97] Fichet G, Corcoran N, Ho PKH, Arias AC, MacKenzie JD, Huck WTS, Friend RH. Self-organized photonic structures in polymer light-emitting diodes. Adv Mater 2004; 16(21): 1908-1912.

[98] Ishihara K, Fujita M, Matsubara I, Asano T, Noda S, Ohata H, Hirasawa A, Nakada H, Shimoji N. Organic light-emitting diodes with photonic crystals on glass substrate fabricated by nanoimprint lithography. Appl Phys Lett 2007; 90(11): 111114.

[99] Adawi AM, Kullock R, Turner JL, Vasilev C, Lidzey DG, Tahraoui A, Fry PW, Gibson D, Smith E, Foden C, Roberts M, Qureshi F, Athanassopoulou N. Improving the light extraction efficiency of polymeric light emitting diodes using two-dimensional photonic crystals. Org Electron 2006; 7(4): 222–228.

[100] Lee Y-J, Kim S-H, Huh J, Kim G-H, Lee Y-H, Cho S-H, Kim Y-C, Do YR. A high-extraction-efficiency nanopatterned organic light-emitting diode. Appl Phys Lett 2003; 82(21): 3779-3781.

[101] Safonova AN, Joryb M, Matterson BJ, Lupton JM, Salt MG, Wasey JAE , Barnes WL, Samuel IDW. Modification of polymer light emission by lateral microstructure. Synth Met 2001; 116(1-3): 145-148.

[102] Jeong SM, Araoka F, Machida Y, Ishikawa K, Takezoe H, Nishimura S, Suzaki G. Enhancement of normally directed light outcoupling from organic light-emitting diodes using nanoimprinted low-refractive-index layer. Appl Phys Lett 2008; 92(8): 083307.

[103] Jeong SM, Araoka F, Machida Y, Takanishi Y, Ishikawa K, Takezoe H, Nishimura S, Suzaki G. Enhancement of Light Extraction from Organic Light-Emitting Diodes with Two-Dimensional Hexagonally Nanoimprinted Periodic Structures Using Sequential Surface Relief Grating. Jpn J Appl Phys 2008; 47(6): 4566-4571.

[104] Ziebarth JM, Saafir AK, Fan S, McGehee MD. Extracting light from polymer light-emitting diodes using stamped bragg gratings. Adv Funct Mat 2004; 14(5): 451-456.

[105] Ziebarth JM, McGehee MD. A theoretical and experimental investigation of light extraction from polymer light-emitting diodes. J Appl Phys 2005; 97(6): 064502.

[106] Jeon S, Kang J-W, Park H-D, Kim J-J, Youn J R, Shim J, Jeong J-H, Choi D-G, Kim K-D, Altun AO, Kim S-H, Lee Y-H. Ultraviolet nanoimprinted polymer nanostructure for organic light emitting diode application. Appl Phys Lett 2008; 92(22): 223307.

[107] Do YR, Kim Y-C, Song Y-W, Lee Y-H. Enhanced light extraction efficiency from organic light emitting diodes by insertion of a two-dimensional photonic crystal structure. J Appl Phys 2004; 96(12): 7629-7636.

[108] Liguda C, Bottger G, Kuligk A, Blum R, Eich M, Roth H, Kunert J, Morgenroth W, Elsner H, Meyer H G. Polymer photonic crystal slab waveguides. Appl Phys Lett 2001; 78(17): 2434-2436.

[109] Bottger G, Schmidt M, Eich M, Boucher R, Hubner U. Photonic crystal all-polymer slab resonators. J Appl Phys 2005; 98(10), 103101.

[110] Wulbern JH, Schmidt M, Eich M, Hubner U, Boucher R, Marlow F. Omnidirectional photonic band gap in polymer photonic crystal slabs. Appl Phys Lett 2007; 91(22): 221104.

[111] Kee C-S, Han S-P, Yoon K B, Choi C-G, Sung HK, Oh SS, Park HY, Park S, Schift H. Photonic band gaps and defect modes of polymer photonic crystal slabs. Appl Phys Lett 2005; 86(5): 051101.

[112] Choi C-G, Han Y-T, Kim J T, Schift H. Air-suspended two-dimensional polymer photonic crystal slab waveguides fabricated by nanoimprint lithography. Appl Phys Lett 2007; 90(22): 221109.

[113] Chuang W-C, Chao C-K, Ho C-T. Fabrication of high-resolution periodical structures on polymer waveguides using a replication process. Opt Expr 2007; 15(14): 8649-8659.

[114] Kehagiasa N, Zankovych S, Goldschmidt A, Kian R, Zelsmann M, Sotomayor Torres C M, Pfeiffer K, Ahrens G, Gruetzner G. Embedded polymer waveguides: design and fabrication approaches. Superlatt Microstruc 2004; 36(1-3): 201–210.

[115] Oh M-C, Lee H-J, Lee M-H, Ahn J-H, Han S G, Kim H-G. Tunable wavelength filters with Bragg gratings in polymer waveguides. Appl Phys Lett 1998; 73(18): 2543-2545.

[116] Kim D-H, Chin W-J, Lee S-S, Ahn S-W, Lee K-D. Tunable polymeric Bragg grating filter using nanoimprint technique. Appl Phys Lett 2006; 88(7): 071120.

[117] Tung Y-C, Kurabayashi K. Nanoimprinted strain-controlled elastomeric gratings for optical wavelength tuning. Appl Phys Lett 2005; 86(16): 161113.

[118] Hu X, Jiang P, Ding C, Gong Q. All-optical tunable narrow-band organic photonic crystal filters. Appl Phys B 2007; 87(2): 255–258.

[119] Hu X, Gong Q, Liu Y, Cheng B, Zhang D. Ultrafast tunable filter in two-dimensional organic photonic crystal. Opt Lett 2006; 31(3): 371-373.

[120] Zhu L, Huang Y, Green WMJ, Yariv A. Polymeric multi-channel bandpass filters in phase-shifted Bragg waveguide gratings by direct electron beam writing. Opt Expr 2004; 12(25): 6372-6376.

[121] Kim K-J, Seo J-K, Oh M-C. Strain induced tunable wavelength filters based on flexible polymer waveguide Bragg reflector. Opt Expr 2008; 16(3): 1423-1430.

[122] Hu X, Liu Y, Tian J, Cheng B, Zhang D. Ultrafast all-optical switching in two-dimensional organic photonic crystal. Appl Phys Lett 2005; 86(12): 121102.

[123] Jiang P, Hu X, Zhang D, Yang H, Gong Q. Ultra-fast all-optical switching in MEH-PPV photonic crystals with resonantly enhanced nonlinearity. Appl Phys B 2010; 99 (1-2): 187-190.
[124] Hu X, Jiang P, Xin C, Yang H, Gong Q. Nano-Ag:polymeric composite material for ultrafast photonic crystal all-optical switching. Appl Phys Lett 2009; 94(3): 031103.
[125] Hu X, Jiang P, Ding C, Yang H, Gong Q. Picosecond and low-power all-optical switching based on an organic photonic-bandgap microcavity. Nat Photonics 2008; 2 (3):185-189.
[126] Ko D-H, Tumbleston JR, Zhang L, Williams S, DeSimone JM, Lopez R, Samulski ET. Photonic crystal geometry for organic solar cells. Nano Lett 2009; 9(7): 2742-2746.
[127] Tumbleston JR, Ko D-H, Samulski ET, Lopez R. Absorption and quasiguided mode analysis of organic solar cells with photonic crystal photoactive layers. Opt Expr 2009; 17(9): 7670-7681.
[128] Roman LS, Inganas O, Granlund T, Nyberg T, Svensson M, Andersson MR, Hummelen JC. Trapping light in polymer photodiodes with soft embossed gratings. Adv Mater 2000; 12(3): 189-195.
[129] Na S-I, Kim S-S, Kwon S-S, Jo J, Kim J, Lee T, Kim D-Y. Surface relief gratings on poly(3-hexylthiophene) and fullerene blends for efficient organic solar cells. Appl Phys Lett 2007; 91(17): 173509.
[130] Zhou D, Biswas R. Photonic crystal enhanced light-trapping in thin film solar cells. J Appl Phys 2008; 103(9): 093102.
[131] Zeng L, Bermel P, Yi Y, Alamariu BA, Broderick KA, Liu J, Hong C, Duan X, Joannopoulos J, Kimerling LC. Demonstration of enhanced absorption in thin film Si solar cells with textured photonic crystal back reflector. Appl Phys Lett 2008; 93(22): 221105.
[132] Duche D, Escoubas L, Simon J-J, Torchio P, Vervisch W, Flory F. Slow Bloch modes for enhancing the absorption of light in thin films for photovoltaic cells. Appl Phys Lett 2008; 92(19): 193310.
[133] Tessler N, Denton GJ, Friend RH. Lasing from conjugated polymer microcavities. Nature 1996; 382(6593): 695-697.
[134] Granlund T, Theander M, Berggren M, Andersson M, Ruzeckas A, Sundstrom V, Bjork G, Granstrom M, Inganas O. A polythiophene microcavity laser. Chem Phys Lett 1998; 288(5-6): 879-884.
[135] Theander M, Granlund T, Johanson DM, Ruseckas A, Sundström V, Andersson MR, Inganäs O Lasing in a Microcavity with an Oriented Liquid-Crystalline Polyfluorene Copolymer as Active Layer. Adv Mater 2001; 13(5): 323-327.
[136] Koschorreck M, Gehlhaar R, Lyssenko VG, Swoboda M, Hoffmann M, Leo K. Dynamics of a high-Q vertical-cavity organic laser. Appl Phys Lett 2005; 87(18): 181108.
[137] Burns SE, Denton G, Tessler N, Stevens MA, Cacialli F, Friend RH. High finesse organic microcavities. Opt Mater 1998; 9(1-4): 18-24.
[138] Persano L, Cingolani R, Pisignano D. Title: Monolithic organic-oxide microcavities fabricated by low-temperature electron-beam evaporation. J Vac Sci Technol B 2005; 23(4): 1654-1658.
[139] Persano L, Del Carro P, Mele E, Cingolani R, Pisignano D, Zavelani-Rossi M, Longhi S, Lanzani G. Monolithic polymer microcavity lasers with on-top evaporated dielectric mirrors. Appl Phys Lett 2006; 88(12): 121110.
[140] Persano L, Camposeo A, Del Carro P, Mele E, Cingolani R, Pisignano D. Title: Low-threshold blue-emitting monolithic polymer vertical cavity surface-emitting lasers. Appl Phys Lett 2006; 89(12): 121111.
[141] Hobson A, Wedge S, Wasey JAE, Sage I, Barnes W L. Surface Plasmon mediated emission from organic light emitting diodes. Adv Mater 2002; 14(19): 1393-1396.
[142] Takada N, Tsutsui T, Saito S. Control of emission characteristics in organic thin-film electroluminescent diodes using an optical-microcavity structure. Appl Phys Lett 1993; 63(15): 2032-2034.
[143] Nakayama T, Itoh Y, Kakuta A. Organic photo- and electroluminescent devices with double mirrors. Appl Phys Lett 1993; 63(5): 594-595.
[144] Dodabalapur A, Rothberg LJ, Miller TM, Color variation with electroluminescent organic semiconductors in multimode resonant cavities. Appl Phys Lett 1994; 65(18): 2308-2310.
[145] Dirr S, Wiese S, Johannes HH, Kowalsky W. Organic electro- and photoluminescent microcavity devices. Adv Mat 1998; 10(2): 167-171.
[146] Djurišić AB, Rakić AD. Asymmetric Bragg mirrors for the reduction of emission wavelength dependence on the viewing angle in organic microcavity light emitting diodes. Opt Com 2004; 236(4-6): 303-311.
[147] Choy WCH, Ho CY. Improving the viewing angle properties of microcavity OLEDs by using dispersive gratings. Opt Express 2007; 15(20): 13288-13294.
[148] Choy WCH, Niu JH, Li WL, Chui PC. Voltage-controlled colour-tunable microcavity OLEDs with enhanced colour purity. J Phys D: Appl Phys 2008; 41(2): 025106.

[149] Yang CJ, Liu SH, Hsieh HH, Liu CC, Cho TY, Wua CC. Microcavity top-emitting organic light-emitting devices integrated with microlens arrays: Simultaneous enhancement of quantum efficiency, cd/A efficiency, color performances, and image resolution. Appl Phys Lett 2007; 91(25): 253508.

[150] Yu G, Gao J, Hummelen JC, Wudl F, Heeger AJ. Polymer photovoltaic cells - enhanced efficiencies *via* a network of internal donor-acceptor heterojunctions. Science 1995; 270(5243): 1789-1791.

[151] Halls JJM, Walsh CA, Greenham NC, Marseglia EA, Friend RH, Moratti SC, Holmes AB. Efficient photodiodes from interpenetrating polymer networks. Nature 1995; 376(6540): 498-500.

[152] Roman LS, Andersson MR, Yohannes T, Inganas O. Photodiode performance and nanostructure of polythiophene/C-60 blends. Adv Mat 1997; 9(15): 1164-1168.

[153] Gattinger P, Rengel H, Neher D. J Photogeneration of charge carriers in anisotropic multilayer structures of phthalocyaninato-polysiloxane. Appl Phys. 1998; 84(7): 3731-3740.

[154] Singh TB, Waghmare UV, Narayan KS. Photocurrent studies of an active polymer layer in a resonant microcavity. App Phys Lett. 2002; 80(7): 1213-1215.

[155] Lupton JM, Koeppe R, Müller JG, Feldmann J, Scherf U, Lemmer U. Organic Microcavity Photodiodes. Adv Mater 2003; 15 (17): 1471- 1474.

[156] An KH, O'Connor B, Pipe KP, Shtein M. Organic photodetector with spectral response tunable across the visible spectrum by means of internal optical microcavity. Org Electr 2009; 10 (6): 1152–1157.

[157] Kéna-Cohen S, Davanço M, Forrest SR. Strong exciton-photon coupling in an organic single crystal microcavity. Phys Rev Lett 2008; 101(11): 116401.

[158] Kasprzak J, Richard M, Kundermann S, Baas A, Jeambrun P, Keeling JMJ, Marchetti FM, Szymanska MH, Andre R, Staehli JL, Savona V, Littlewood PB, Deveaud B, Dang LS. Bose–Einstein condensation of exciton polaritons. Nature 2006; 443(7110): 409-414.

[159] Christopoulos S, Baldassarri G, von Högersthal H, Grundy AJD, Lagoudakis PG, Kavokin AV, Baumberg JJ, Christmann G, Butté R, Feltin E, Carlin JF, Grandjean N. Room-temperature polariton lasing in semiconductor microcavities. Phys Rev Lett 2007; 98(12): 126405.

[160] Balili R, Hartwell V, Snoke D, Pfeiffer L, West K. Bose-Einstein condensation of microcavity polaritons in a trap. Science 2007; 316(5827): 1007-1010.

[161] Farchioni R, Grosso G (Eds.). Organic Electronic Materials. Springer, Heidelberg , 2001.

[162] Lidzey DG, Bradley DDC, Skolnick MS, Virgili T, Walker S, Whittaker DM. Strong exciton-photon coupling in an organic semiconductor microcavity. Nature 1998; 395(6697): 53-55.

[163] Lidzey DG, Bradley DDC, Virgili T, Armitage A, Skolnick MS, Walker S. Room temperature polariton emission from strongly coupled organic semiconductor microcavities. Phys Rev Lett 1999; 82(16): 3316-3319.

[164] Takada N, Kamata T, Bradley DDC. Polariton emission from polysilane-based organic microcavities. Appl Phys Lett 2003; 82(12): 1812-1814.

[165] Skolnick MS, Fisher TA, Whittaker DM. Strong coupling phenomena in quantum microcavity structures. Semicond Sci Technol 1998; 13(7): 64-669.

[166] Houdré R, Weisbuch C, Stanley RP, Oesterle U, Pellandini P, Ilegems M. Measurement of cavity-polariton dispersion curve from angle-resolved photoluminescence experiments. Phys Rev Lett 1994; 73(15): 2043-2046.

[167] Tischler JR, Bradley MS, Bulovic V, Song JH, Nurmikko A. Strong coupling in a microcavity LED. Phys Rev Lett 2005; 95(3): 036401.

[168] Virgili T, Lidzey DG, Bradley DDC, Walker S. Cavity mode polarisation splitting in organic semiconductor microcavities. Synth. Met. 2001; 116(1-3): 497-500.

[169] Persano L, Mele E, Cingolani R, Pisignano D. Polarization mode splitting in monolithic polymer microcavities. Appl Phys Lett 2005; 87(3): 031103.

[170] Stelitano S, De Luca G, Savasta S, Patane S. Polarized emission from high quality microcavity based on active organic layered domains. Appl Phys Lett 2008; 93(19): 193302.

[171] Panzarini G, Andreani LC, Armitage A, Baxter D, Skolnick MS, Astratov VN, Roberts JS, Kavokin AV, Vladimirova MR, Kaliteevsky MA. Exciton-light coupling in single and coupled semiconductor microcavities: polariton dispersion and polarization splitting. Phys Rev B 1999; 59(7): 5082-5089.

[172] Camposeo A, Persano L, Del Carro P, Virgili T, Cingolani R, Pisignano D. Polarization splitting in organic-based microcavities working in the strong coupling regime. Org. Electron. 2007; 8(2-3): 114-119.

CHAPTER 6

Slow Light for Sensing

Michael A. Fiddy*

Center for Optoelectronics and Optical Communications, University of North Carolina at Charlotte, Charlotte, NC 28223, USA

Abstract: Both patterned periodic or random structures can exhibit large slow down factors associated with large field enhancements. These properties can be exploited to good effect for a variety of sensing functions. We describe here some basic mechanisms responsible for these effects and discuss their use. Some experimental results are reported using porous form-birefringent super-lattice structures which can be scaled in size for use from microwave to optical frequencies.

Keywords: Periodic structures, field enhancement, slow light.

1. INTRODUCTION

Periodic structures can exhibit unique properties based on their patterning and the scale of their features with respect to the wavelength. For example, photonic-crystal (PC) structures offer an important platform for optofluidic devices, photonic circuits, and dispersion-engineered metamaterials. These devices promise lab-on-a-chip sensing capabilities with considerable flexibility for managing light. PC circuits have primarily been defined by their periodicity and the architecture of the holes or columns fabricated in the transparent material. This has encouraged the development of stamping and printing technologies that can produce prototypes quickly and make large quantities of sensors inexpensively. In addition to being manufacturable, PC platforms have two attractive attributes for sensing applications. First, a gas or liquid analyte can flow directly through the nanoscopic holes within the photonic structure. Second, 'slow light' can boost the device's sensitivity. Optical sensors that exploit spectroscopic analysis, such as surface-enhanced Raman phenomena, are already theoretically capable of molecular sensitivity: PC sensors using slow light can increase even this sensitivity. We limit ourselves here to describing a mechanism for slowing light and generating large field enhancements that can be exploited for sensing.

Controlling the speed of light has a host of important applications, engineers have learned to manage the dispersion characteristics of a material to control it or, more specifically, to control the group velocity of light. In an isotropic linear medium, the velocity of light is the same in all directions and is defined by the angular frequency (ω) divided by the wavenumber (k). The plot of ω *versus* k provides the phase velocity of the light. An optical pulse—which one can consider as the envelope or constructive interference arising from a number of frequencies—has a group velocity that is the derivative of ω with respect to k. If this derivative is zero, then at that frequency and for the small band of frequencies in its neighborhood, a pulse has a group velocity that is close to zero. This important because slow-light pulse propagation can enhance the energy density of the electromagnetic field within the structure. Such an effect can lower the threshold for exploiting nonlinear optical effects. These enhanced local fields also have the potential to increase the overall sensitivity of chemical and biological sensors.

There are several approaches to slowing group velocity, such as electromagnetically induced transparency. The structure we describe here is a 1D anisotropic periodic PC or superlattice, which can be engineered to have a very low group velocity over a specific bandwidth. The structure requires two anisotropic layers and one isotropic layer per period. Using the theory presented by Alex Figotin and Ilya Vitebskiy in [1]. The

***Address correspondence to Michael A. Fiddy:** Center for Optoelectronics and Optical Communications, University of North Carolina at Charlotte, Charlotte, NC 28223, USA; Tel: 704-687-8594; E-mail: mafiddy@uncc.edu

Marco Pisco, Andrea Cusano and Antonello Cutolo (Eds)
All rights reserved-© 2012 Bentham Science Publishers

band-edge resonant effect of a PC structure in which a unit cell has just two misaligned in-plane anisotropic layers with a small air gap between them, can exhibit extraordinarily large field enhancements associated with very low group velocities. These structures can be understood in terms of use the transfer-matrix method: a single plane wave incident on a parallel layer of an anisotropic medium will, in general, initiate four plane waves in the medium. We can represent the relation between the input and output parameters for anisotropic multiple-layered structures using a 4×4 transfer matrix. Using this method, we can calculate most of the characteristics of light traveling through the structure, including the dispersion relation, transmission, reflection, and the field distribution inside the structure. For any given frequency and wavevector components (k_x, k_y), we can always find the 4×4 transmission matrix and four eigenvalues for k_z, *i.e.*, $\{k_1, k_2, k_3, k_4.\}$. When these eigenvalues are real, based on the order of their degeneracy, three types of special points can be defined at which the group velocity is zero. A special case, known as a degenerate band edge (DBE), occurs when $k_1 = k_2 = k_3 = k_4$. In this situation, the transverse electric and transverse magnetic modes of light couple to each other. This structure's resonant effect slows light. Theory predicts that in the vicinity of the DBE, the resonant field intensity increases as N^4, where N is the total number of periods in the PC. This is in contrast to a regular band edge, at which the field intensity is proportional only to N^2. The higher field intensity could be exploited to make more sensitive sensors.

Slow light in photonic crystals and other periodic structures is thus associated with stationary points of the photonic dispersion relation, where the group velocity of light vanishes. In some cases, the vanishing group velocity is accompanied by a so-called frozen mode regime, when the incident light can be completely converted into a slow mode with huge diverging amplitude. The frozen mode regime is regarded as a qualitatively new wave phenomenon [2] and it does not reduce to any known electromagnetic resonance. Formally, this frozen mode regime is not a resonance, in that it is not particularly sensitive to the size and shape of the photonic crystal, and it has much higher tolerance to absorption and structural imperfections. A very important point to make is that the approach pursued here to engineer the velocity of light in materials is new. It is based on periodic stacks of anisotropic dielectric layers with the electromagnetic dispersion relation $\omega(k)$ exhibiting a stationary inflection point well away from a band-edge, thereby permitting a slowing down of light with little or no reflections from the slab boundary and no losses. This has tremendous implications for optical systems used in communications, lasing and sensing platforms. It permits lower power implementation, longer interaction times and higher intensity interactions for sensors.

We also consider structures that are aperiodic or random in nature. Wave propagation in disordered media is a rich field and it has become clear that the interference of multiply scattered fields has dramatic effects such as strong localization of fields in weakly-disordered random media. Following Anderson's original paper [3], many publications have appeared on this topic [4-8]. Of importance here, is that even a small amount of disorder, which can arise from a change in the structure's environment, could affect its properties dramatically. Consequently, disordered systems possess properties that make them potentially useful as an alternative to the pure periodic (PC) sensor configurations.

One-dimensional strong localization has received the most attention and localization of eigenstates in closed 1D disordered systems and exponentially small (with respect to the length) transparency of open systems with 1D disorder have been rigorously studied [4, 8]. The most common physical manifestation of these effects is the fact that a thick stack of transparencies reflects light just like a rather good mirror but less obvious is that for sufficiently long disordered 1D samples, there exists a quasi-discrete set of frequencies that travel through the sample unreflected, *i.e.,* with a transmission coefficient close to one [9-11]. Values of these frequencies are random and are determined by the fine structure of the disorder. One can regard the set of transmitted frequencies as a fingerprint defining any given sample. Of importance is that high transparency is typically accompanied by a large concentration (localization) of energy at randomly located points inside the system. Therefore, an open random 1D sample can be considered as an open resonator with a set of quasi-modes (resonances) with very high quality factors. Consequently, in

contrast to a regular resonator, each frequency is localized inside its own effective resonant cavity, whose position is random and whose size is much smaller than the size of the sample.

Obviously, a small perturbation to even one region or layer in such a random structure will totally alter its fingerprints, serving as a very sensitive sensor. The resonances are sharp and well defined not only for sensing, but also for creating a random laser [12-14].

2. SLOW-WAVE ANISOTROPIC PERIODIC STRUCTURES

1D anisotropic photonic crystal structures have attracted attention in recent years due to their potential use in polarization elements [15], for slow-light applications [16, 17] and nonlinear devices. Compared with 1D isotropic photonic crystal structures, the theoretical analysis, fabrication and characterization of 1D anisotropic photonic structures is much more complicated. This is due to the anisotropy, and other unique characteristics 1D isotropic photonic crystal structures do not possess. As stated previously, a one-dimensional isotropic photonic crystal structure has a field intensity resonance at the band edge proportional to N^2 where N is the total number of periods [18]. This band-edge resonance slows down light and nonlinear effects near the band edge have been investigated by Scalora *et al.* [19, 20]. However, less is known about the band edge resonant effect for anisotropic one-dimensional structures. Recently, Figotin and Vitebskiy [1, 2, 21] proposed that for a transmission resonance near a degenerate band edge (DBE), the resonant field intensity enhancement is proportional to N^4 in contrast to N^2 for the regular band-edge. Based on their predictions, we have investigated this band edge enhancement with various anisotropic materials [22, 23].

From Snell's law, when a single plane wave propagates through the multiple layer structure, the tangential components of the wave vectors remain the same throughout the layered medium, and all the wave vectors lie in the same plane (the incident plane). Without loss of generality, the light propagation can be assumed to be in the x-y plane, as a consequence, the z-component of the wave vector is zero, and the electric field has an exp $i(k_0\alpha x + k_0\beta y - \omega t)$ dependence in each layer, where $\alpha = n\cos\theta$, $k_0 = 2\pi/\lambda = \omega/c$ and $\beta = n\sin\theta$. A plane wave propagating in the x-y plane and incident on a single parallel-sided layer of biaxial material leads to four plane waves in the biaxial layer, two forward-traveling waves and two backward-traveling waves in the same x-y plane. The four waves are linearly polarized, and share the same value of the Snell's law quantity β with the incident wave.

We can specify the field transfer matrix M and associated Bloch waves $E_K(x)$ that are the eigenvectors of M. The Bloch wave numbers K are related to the eigenvalues of M, L_i by $L_i = \exp(-iK_iL)$. Since M depends on ω and the Snell's law quantity β, M is a 4×4 matrix, and at any one frequency there are four wave numbers K_i. Real K_i correspond to propagating Bloch waves and imaginary K_i correspond to evanescent modes. Based on the degeneracy of the Bloch wave numbers K_i at a specific frequency, say $\omega = \omega_0$, one can find four special types points in the dispersion curve. The first is an inflection point corresponding to a regular band edge point (RBE), which is the degenerate point of order 2 at which one ω corresponds to two equal real K's. The second type is an inflection point called stationary inflection point (SIP), which has degeneracy of order 3 and one ω corresponds to three equal real K's. The third type is inflection point is called degenerate band edge point (DBE), which has fourth order degeneracy and one ω corresponds to four equal real K's. Finally one can realize a so-called split band-edge (SBE).

The first step in searching for an SBE or DBE point is to calculate the field transfer matrix for the unit cell. This depends on several parameters such as the misalignment angle between the two anisotropic layers φ, the dielectric permittivity and thickness of each layer, incident beam frequency ω, and incident direction θ ($\beta=n\sin\theta$, $\beta = 0$ for the normal incident situation). After the field transfer matrix of the unit cell is known one can calculate the dispersion curves in chosen frequency ranges. Adjusting the misalignment angle between two anisotropic layers, and the thickness of the isotropic layer DB, one can find a possible

parameter range for the SBE or DBE point by checking the corresponding dispersion curves. For the exact DBE point, we fix one parameter such as making φ equal to π/4, and adjust another parameter such as DB, until the desired band edge is found. This is illustrated in Fig. **1**.

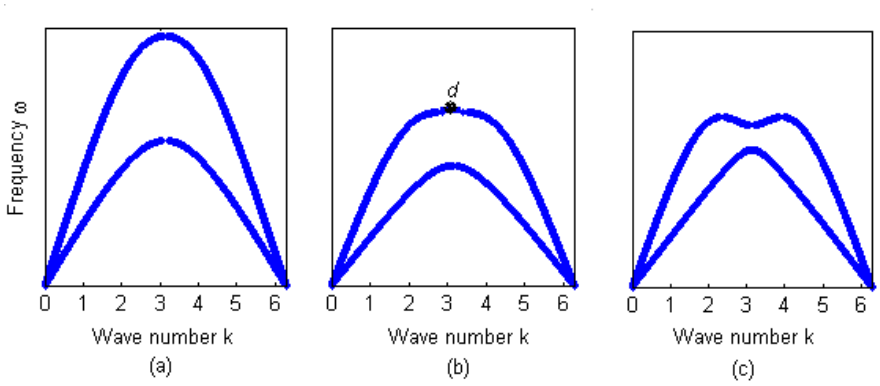

Figure 1: (a) DB = 0.4L, regular band edge. (b) DB = 0.26L, degenerate band edge. (c) DB = 0.1L, split band edge; where DB is the width of the isotropic layer within each period L.

At the inflection points, the group velocities are all equal to zero and there is a strong field resonant effect connected with these points. However, because of their different degenerate orders, these resonant effects will differ from one to another.

Chabanov [26] recently presented experimental results showing a strongly resonant transmission associated with a split band edge phenomenon which also has near perfect impedance matching at the boundaries and polarization independence. Rotation of the angle ϕ between the anisotropic layers guaranteed a resonance for a given number of periods, N, even when N is small. He shows the superiority of SBE over DBE as a resonator and over a defect localized state in the bandgap. By an SBE resonance, he refers to a resonance at the frequency at which the two counterpropagating slow (Bloch) modes, indicated below, can co-exist. Microwave experiments were conducted with two horns and teflon rods attached to a thin ring and spectra were obtained using an HP N5230A VNA. Figotin and Vitebskiy [22] since showed that the DBE point would not be perfectly impedance matched for any polarization state, it being the result of a coupling with only one elliptic polarization state of the incident field. This paper shows that the "giant enhancement" predicted with the DBE point can still be achieved with an SBE resonance by changing ϕ. Our simulations can study an SBE-like dispersion diagram as shown below, at which we might have a single frequency at the band edge for two counter propagating k vectors, k+ and k- , but we might also have four k vectors close to this frequency, or two frequencies at Fabry-Perot resonances, which are inevitably closer in frequency near the band edge.

It is interesting to note that increasing the index contrast of the anisotropic material widens the bandgap. For example, a birefringent index contrast of 1.2:1.35 has a common TE and TM bandgap of width 0.6GHz, while 1.2:1.5 has common bandgap of 1GHz and 1.2:1.6 has a bandwidth of ~ 1.3GHz. By comparison, fixing the index contrast but reducing (increasing) the absolute index values shifts the bandgaps to higher (lower) frequencies but otherwise leaves the shape of the transmission spectrum the same. This is obvious since only path length differences are being changed. Thus constant contrast ratios produce the same bandgap and for example 1.2:1.35 has a band edge at 10GHz, while 1.1:1.23 shifts the edge to 10.85GHz.

The necessary condition for the existence of the DBE or SBE is that TE and TM modes should be coupled each other inside the structure so that 4x4 matrix has to be always involved to solve the dispersion relation. If TE and TM modes are decoupled, the field transfer matrix will be reduced to the block-diagonal form, the dispersion relation will exist for TE and TM modes separately, and there is no DBE point. Even if anisotropic layers are present, but the anisotropy axis in all anisotropic layers are either aligned, or

perpendicular to each other, TE and TM modes remain decoupled. The only way to satisfy the DBE or SBE condition with normal incidence is to have at least two misaligned anisotropic layers in a unit cell with the misalignment angle being different from 0 and $\pi/2$. We chose $\pi/4$ in the example illustrated below in Fig. **2**.

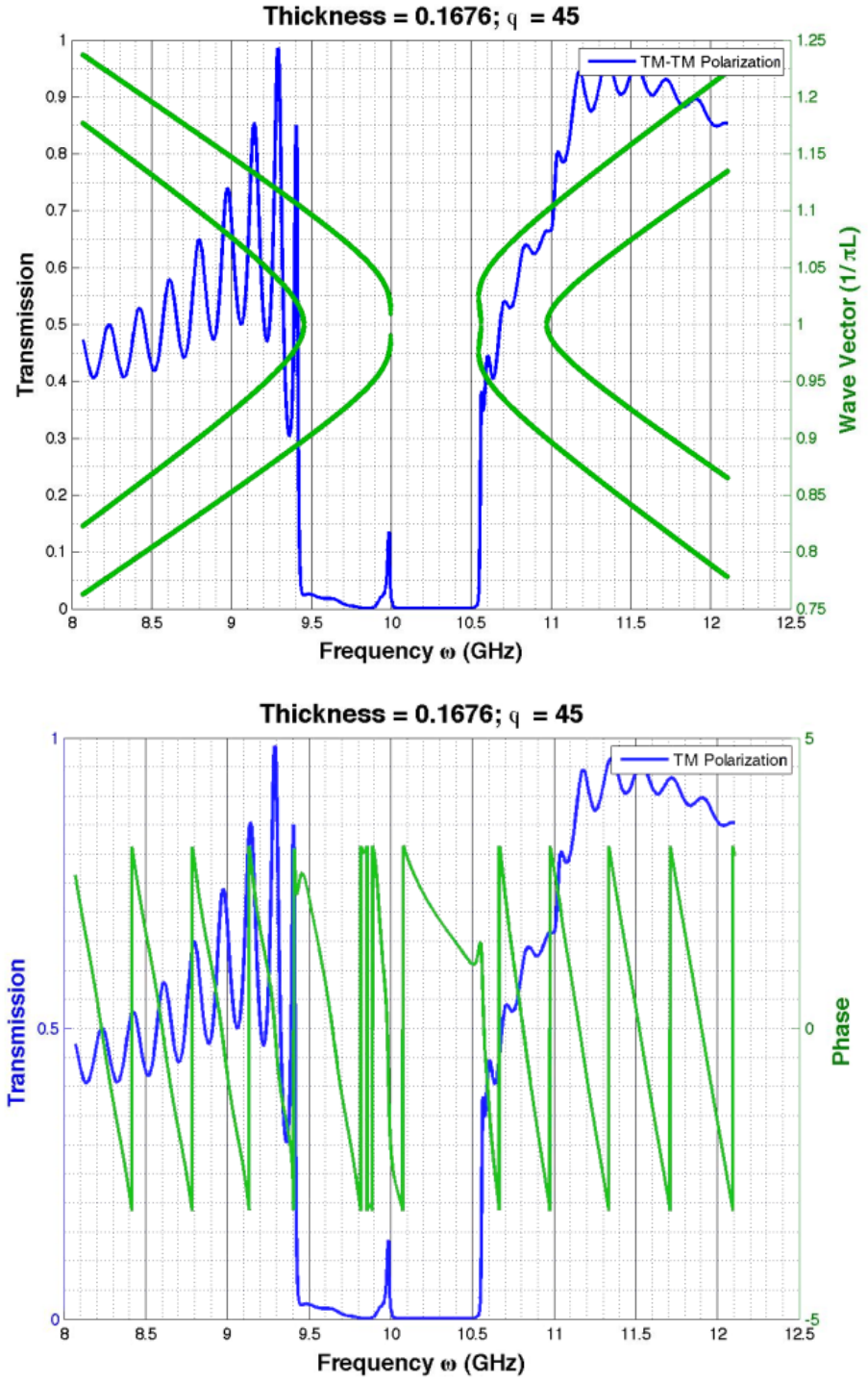

Figure 2: (left) shows an example of the transmission spectrum for our structure with TM input and TM measured at the output. The misalignment angle between the anisotropic layers is 45 degrees, and we expect to be close to satisfying DBE conditions. Superimposed are the associated dispersion curves (green). The curves on the right show the spectral phase (green) indicating regions of rapid phase fluctuation and positive phase slope (negative phase delay) are seen.

3. PRACTICAL REALIZATION OF SENSOR STRUCTURES

As noted previously, the simplest choice to realize frozen electromagnetic modes in a plane-parallel periodic stack of two materials (A and B) requires that their respective permittivities be:

$$\varepsilon_A = \begin{bmatrix} \varepsilon_{xx} & 0 & \varepsilon_{xz} \\ 0 & \varepsilon_{yy} & 0 \\ \varepsilon_{xz} & 0 & \varepsilon_{zz} \end{bmatrix}, \quad \varepsilon_B = \begin{bmatrix} \varepsilon_B & 0 & 0 \\ 0 & \varepsilon_B & 0 \\ 0 & 0 & \varepsilon_B \end{bmatrix} \tag{1}$$

The more general requirement is as follows:

$$\varepsilon_A = \begin{bmatrix} \varepsilon_{xx} & \varepsilon_{xy} & \varepsilon_{xz} \\ \varepsilon_{xy} & \varepsilon_{yy} & \varepsilon_{yz} \\ \varepsilon_{xz} & \varepsilon_{yz} & \varepsilon_{zz} \end{bmatrix}, \quad \varepsilon_B = \begin{bmatrix} \varepsilon_B & 0 & 0 \\ 0 & \varepsilon_B & 0 \\ 0 & 0 & \varepsilon_B \end{bmatrix} \tag{2}$$

Therefore, to develop practical slow light or frozen mode sensors, one needs to fabricate a crystalline superlattice of two materials alternating between zero and non-zero off-diagonal permittivities. It was mentioned earlier that one requires a layered structure in which the A- layers are birefringent. There are three approaches to meeting this need, i) cutting and assembling crystal layers from bulk crystals (the least attractive), ii) monolithic growth of anisotropic superlattice structures using epitaxial as well as non epitaxial methods and iii) exploiting sub-wavelength diffractive layers which exhibit inherent birefringence. It is difficult to cut crystals at oblique angles, and if one confines the cuts to the simpler case of two Euler angles the situation is somewhat simpler. Even simpler is the situation where only one Euler angle is used (like the AT-cut of quartz). Therefore, one can use almost any material provided one has the appropriate cut.

Consider the following example, if one works with green light and refractive index of the material is about 2.3, then the typical layer thicknesses must be below 150 nm, the lower the better, for example 50 -100 nm would meet the requirement. A slab comprised of at least 30 double layers is needed, each double layer consisting of two different uniform layers. However, to prove the concept, one would start with a stack of ten double layers. The optimal number of layers essentially depends on their quality:

a) They must be plane-parallel;

b) Their thicknesses must be uniform and the same for identical layers;

c) The dielectric tensor must be uniform within each layer and its value must be the same in all identical layers.

Knowledge of the exact values of the permittivity parameters is not that important, because one can always offset them by adjusting the direction of the incident light. There is no remedy, of course, for the lack of uniformity of the layers. For example, if the dispersion of any of the above parameters in one stack is about 5%, this roughly means that there is no point in having more than 20 double layers in the slab. For epitaxial growth, this difficulty can be alleviated due to accurate control over the layer thickness and composition.

Specific examples of systems that could exhibit frozen electromagnetic modes (*i.e.*, satisfy the conditions given above) include GaN/glass and $BaTiO_3$/glass. MOCVD techniques have been used to grow (polycrystalline) C-axis oriented GaN films on glass substrates. The permittivities for GaN (Class VI; point group 6mm) and glass (isotropic) are, respectively: $\varepsilon_{11}^S = 9.5$ nF/m, $\varepsilon_{33}^S = 11.0$ nF/m and $\varepsilon_{11} = \varepsilon_{22} = \varepsilon_{33} = 0.018$ nF/m. For a superlattice of such C-axis oriented GaN and isotropic glass film layers and a 45° angle of incidence such that the $\psi = 45$ degree condition is met. GaN obviously is piezoelectric and also has been shown to exhibit electroluminescence (either intrinsically or doped). Intriguing possibilities arise from active axially frozen mode structures that are either light emissive or acousto-optic.

A parallel approach is the successive fabrication of strongly birefringent layers, sandwiched between isotropic layers, based on the properties of sub-wavelength diffracting structures. Photonic crystal dichroism and birefringence can produce new ways to provide polarization control, leading to photonic crystal polarizing beam splitters and anisotropic phase effects in transparent regions, providing quarter and half waveplates. Taking this approach immediately suggest the fabrication of 2D photonic crystals in suitable materials that could then provide structures with the desired properties for each A - layer. More generally, it is possible to engineer controlled polarization dependent effects through sub-wavelength micro-structuring of material surfaces. The example we gave of engineered form-birefringence is ideal for sensor applications. The radiation "sees" a film with an effective refractive index somewhere between the index of the surrounding medium and the index of the substrate material. A subwavelength profile is used to create an artificial index of refraction that can be tailored to an optimum value by changing the fill factor of the grating structure. A subwavelength structure can be used to artificially create two different indices of refraction in orthogonal directions by fabricating different grating fill factors in the orthogonal directions.

We have exploited sub-wavelength or form-birefringence to realize the anisotropic layers; this is important for optical sensors since few materials exhibit the required relatively large birefringent index differences demanded. It is also important for sensing devices, since the porous nature of form-birefringent elements provides a natural route for gases or liquids whose properties are to be sensed, assuming air is present where material has been removed.

Fully exploiting this phenomenon for sensors will require the evaluation of different fabrication techniques which in turn will depend upon the suitability and availability of appropriate materials.

In order to decide the grating period and duty cycle of the grating layer, we calculate both zero-order and second-order effective index by using the following formula, when grating-period-wavelength ratio is small enough that the zero-order and second results are consistent within the tolerance level, the grating period will be decided, and the optimum duty cycle is chosen to maximize the anisotropy (n_0 / n_e) of the effective uniaxial layer.

The zero-order effective index

$$n_o^{(0)} = \sqrt{f_1 n_1^2 + f_2 n_2^2} \tag{3}$$

$$n_e^{(0)} = \sqrt{1/(f_1 / n_1^2 + f_2 / n_2^2)} \tag{4}$$

The second-order effective index

$$n_o^{(2)} = \sqrt{n_o^{(0)2} + (1/3)(\Lambda/\lambda)^2 \pi^2 f_1^2 f_2^2 (n_2^2 - n_1^2)} \tag{5}$$

$$n_e^{(2)} = \sqrt{n_e^{(0)2} + (1/3)(\Lambda/\lambda)^2 \pi^2 f_1^2 f_2^2 (1/n_2^2 - 1/n_1^2)^2 n_o^{(0)2} n_e^{(0)6}} \tag{6}$$

Here, $f_2 = W/\Lambda$, $f_1 = 1 - f_2$.

For the three-layer unit cell structure, shown in Fig. **3**, various combinations of anisotropic and isotropic layers within each period are possible, as shown. The anisotropic layer has a subwavelength-scale grating patterned through it, as shown in Fig. **4**, to impart the magnitude of the birefringence required. Once the anisotropic material and isotropic material are chosen, the parameters to be decided are the misalignment angle between adjacent A-layers φ and the thickness of the B-layer D_B. The thickness of two A layers can be calculated using formula $D_{A1} = D_{A2} = (L\text{-}D_B)/2$. In the first step of searching for the DBE point, we calculate the field transfer matrix for the unit cell. This depends on parameters such as the misaligned angle

between two anisotropic layers φ, the dielectric permittivity and thickness of each layer, incident beam frequency ω, and incident direction θ ($\beta=n\sin\theta$, β = 0 for the normal incident situation). After the field transfer matrix of the unit cell is found, we can get the dispersion curves in our specified frequency ranges. When we adjust the misalignment angle between two anisotropic layers, and the thickness of the air layer $D_{B,}$ we can find a possible parameter range for the DBE by checking the corresponding dispersion curves. For the exact DBE point, we fix one parameter such as making φ equal to π/4, and adjust another parameter until the DBE is found.

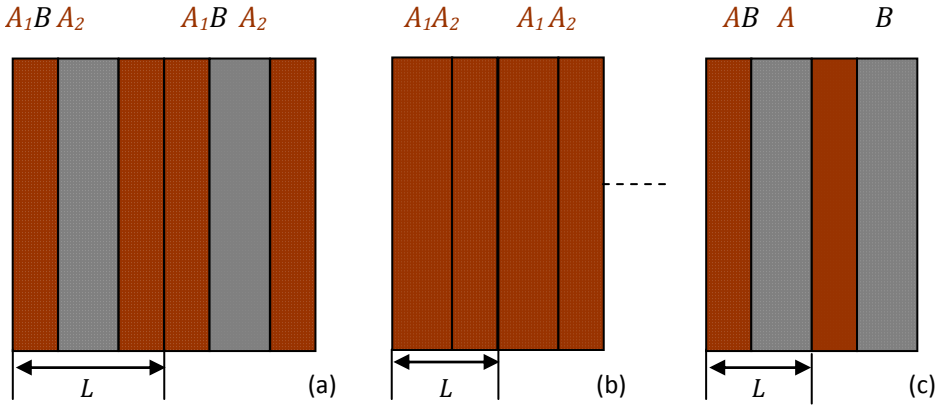

Figure 3: (a) Periodic stack of N elementary cells L, A1 and A2 are equal-thickness misaligned anisotropic layers with in-plane anisotropy, B are isotropic layers. (b) Periodic stack of N elementary cells L, two misaligned in-plane anisotropic layers A1 and A2 with different thicknesses or different anisotropic materials. (c) Periodic stack of N elementary cells L, A layers have in-plane anisotropy, B are isotropic layers, DBE can exist under oblique incidence.

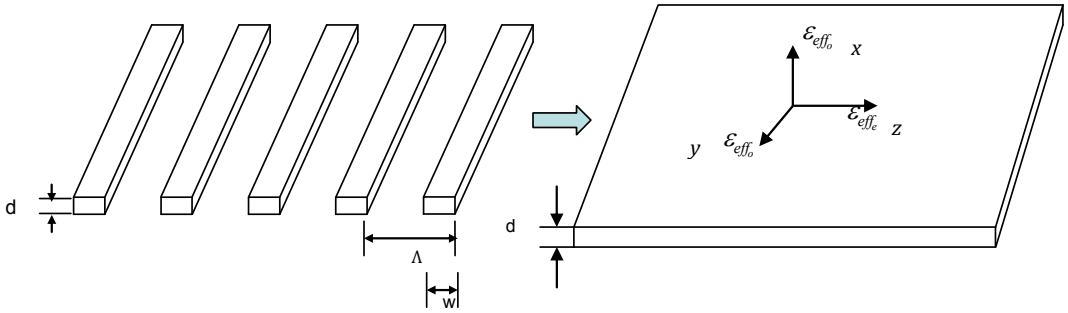

Figure 4: The subwavelength grating structure and its equivalent anisotropic layer.

In order to verify the DBE effect, we fabricated our microwave frequency (X band 8~12 GHz) degenerate band edge structure on a rapid prototype machine (Eden 333) using uv curable Fullcure 720 material, and built a simple microwave setup to characterize the structure such as S_{21} parameters and the electric field intensity distribution inside the structure.

The index of refraction of the bulk material used for our DBE sample is 1.64. The entire structure consisted of between 30 to 55 unit cells. One unit cell is made up of three layers A1, A2 and B, in which A1 and A2 are identical subwavelength 1-D grating layer with 45 degree grating vector orientation with each other, and B layer is the isotropic layer which is air here. The total thickness for one unit cell L is 1.2265 cm, the thickness for two anisotropic layer $D_{A1} = D_{A2} = 0.4020$ L= 0.4931cm, and the thickness for the air layer D_B = 0.1959L= 0.2403 cm. The period of the grating Λ is 1.75 mm, which is about 1/17 of the incident wave wavelength, and close to the quasi-static limit and the duty cycle of the grating layer is 0.58.

By using the effective medium equations, we get n_o= 1.4071, n_e= 1.2543 and n_{o2} = 1.4078, n_{e2}= 1.2546, which means the dielectric tensor of the effective uniaxial thin film is represented by the following matrix, when the 1-D grating vector is along *z* direction, the grating line and spacing are along y direction as shown in Fig. **4**.

$$\varepsilon = \begin{pmatrix} 1.4078^2 & 0 & 0 \\ 0 & 1.4078^2 & 0 \\ 0 & 0 & 1.2546^2 \end{pmatrix} \tag{7}$$

In order to verify the "gigantic" field enhancement associated with the DBE, we used X band (8~12 GHz) and degenerate band edge structure built using a rapid prototype machine. We expect to see a narrowing of the transmission spectra close to the band edge (see Fig. **5**(**a**)) and with very low material absorption, a field enhancement that is a maximum in the center of the structure (see Fig. **5** (**b**)).

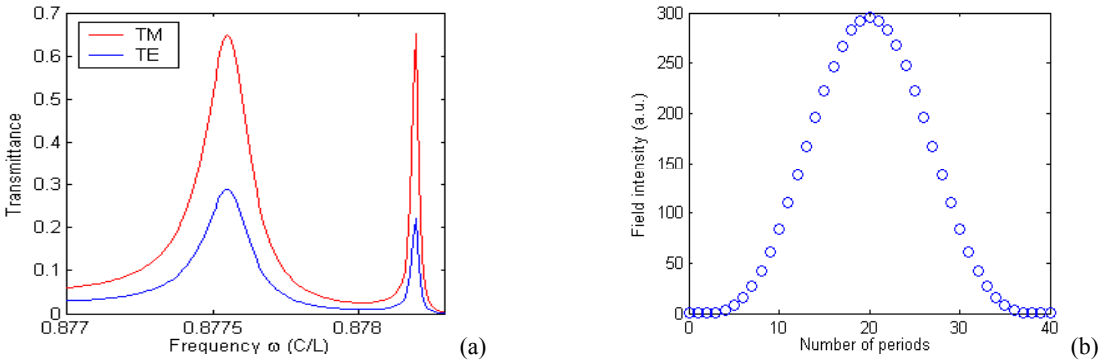

Figure 5: (a) The transmission curves around the DBE frequency (at right edge of frequency axis); (b) the field intensity distribution inside the structure at a frequency close to the DBE.

In our setup, the field intensity distribution inside the structure was measured by using a probe. The index of refraction of the bulk material used for our DBE sample is 1.64 and effective medium calculations give n_o= 1.36, n_e= 1.21, which defines the dielectric tensor of the effective uniaxial layer.

Fairly sharp Fabry-Perot resonances can be seen, as expected, despite the fact that we have only an approximation to an incident plane wave. Measured data are presented in Fig. **6**(**a**) for the TE input and TE measured case. There are some noticeable differences between the measured data and the idea cross- and co-polarization transmission spectra shown in Fig. **6**(**b**) in which there was zero absorption assumed. More importantly, the input cross-sectional area of the fabricated structures is always finite and has supporting structures around the perimeter, which while being relatively small in size, will obviously affect the ideal assumption a plane wave being incident. Also, it is well known that disorder or defects in the photonic crystalline structure can have a significant effect on the transmission properties especially near a band edge. Mookherjea and Oh [40] argue that the strongest effects are at the band edge and conclude that, at least for the case of resonator coupling, variations in coupling coefficients of 1% to 10% can lead to reduced slow down factors (X10 to X30) because of band tail effects. Also, Freilikher *et al.* [41], when modeling 1D "periodic-on-average" structures show that localized states (resonances) can occur in pass and stop bands. Furthermore, it has been reported that anomalously high transmission combined with small losses improve conditions for detection of resonances in reflection [42].

More needs to be done to fully understand the observed results but nevertheless, these data are in good qualitative agreement with the Figotin model and measurements of the associated field intensity enhancement were made. Large enhancements are seen up to factors of 80 at frequencies close to the DBE point. The spatial position of the maximum field is observed near hole 15, the structure having small openings in each period for a probe, hole 1 being closest to the source.

Our experiments demonstrated field enhancements of the order of X80 but with a non-uniform spatial distribution along the length of the structure [24]. These observations are in agreement with predictions for the materials being used, given their intrinsic absorption losses and the degree of anisotropy. Of great relevance for potential sensing applications is the positive phase delay in the transmitted field that is observed at frequencies close to the band edges at which at large field enhancement occurs. At these frequencies, we have also observed substantial external field emission and an effective negative refractive index at these frequencies provides a plausible explanation for this.

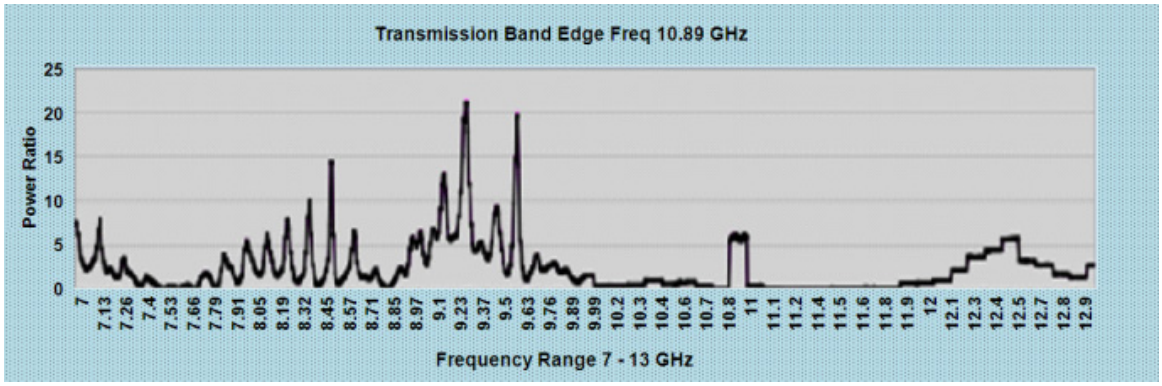

(a)

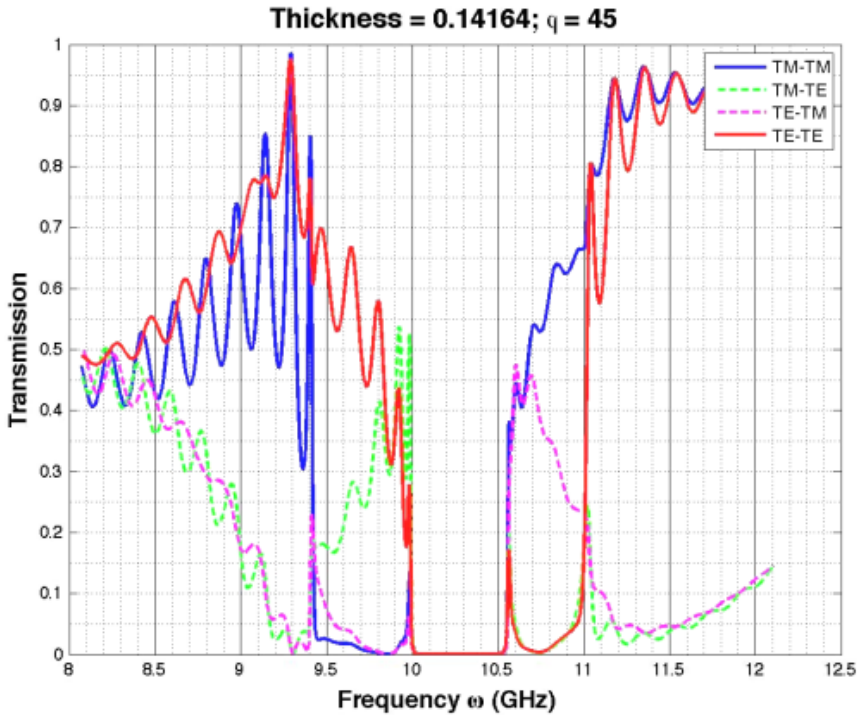

(b)

Figure 6: Top graph (a) shows the measured TE-TE transmission spectrum for a finite cross section structure designed to have the response shown in the lower graph. The lower graph, (b), shows an example simulation of predicted TE-TE and TE-TM transmission spectra; there is a discrepancy between the expected transmission characteristics and the measured spectrum. Note that simply changing the index values aligns this plot with the measured data as a function of frequency.

There are other slow-wave mechanisms which can be exploited for sensing which we do not detail here. For example, tuning of functional PC devices has been reported by selectively modifying the refractive index of certain lattice sites. Pustai *et al.* [24] proposed to tune the resonance frequency of a PC defect in a

2D silicon slab by locally filling a defect with liquid crystals but inserting anything that alters the local refractive index would serve the same purpose. Sharkawy *et al.* [25] proposed a 2 x 2 switch based on a PC coupled directional coupler. A change in the properties in the coupling region between the waveguides modulates the coupling coefficient and modulates the switching.

4. SLOW LIGHT AND NONLINEARITIES

The guided wave's group velocity is given by $v_g = d\omega/dk = c/[n + \omega dn/d\omega] = c / n_g$. Consequently increasing $dn/d\omega$ can slow light. From the Kramers-Kronig relationship, or more generally, a Hilbert transform relationship, the absorption spectrum determines $dn/d\omega$. This quantity will be large if the absorption profile varies rapidly. To a first approximation, one can think of a Hilbert transform as in some ways similar to the derivative of the function whose transform is being taken (see. *e.g.* [27]). Note that the group delay, $t_g = L/v_g$ and that $n_g = c\ t_g / L$. Hence increasing the physical length L for increased delay implies some kind of resonant enhancement, comes at the expense of bandwidth [28] since $t_g \Delta\omega \sim$ constant. In nonlinear cavities, the effective length is increased due to the increased number of roundtrips in the cavity. It is also known that the nonlinear phase shift produced by a ring resonator constructed from a given nonlinear material, can be greater than the phase shift produced by the a single pass through an infinite length of that material [29]. Thus the fabrication or insertion of a ring resonator into the PC substrate with evanescent or nonlinear coupling into one or more ring resonators will provide delays. Many PC delay lines based on one-dimensional coupled defects have been reported [30].

It has been established that there is a significant enhancement in the optical nonlinearity near photonic band edges [31]. Indeed, SHG has been achieved in PCs at the edges of photonic bands and in PCs with defects [32]. Use of MEMs probes to effect changes due to their material properties, or, for example due to high fields at a probe tip, provide a mechanism for inducing local index changes. A recent example of a PC fabricated from high index rods in air, each made from an instantaneous Kerr material (see [33]), has been demonstrated to make an optical isolator which provides another highly sensitive sensing structure. Another benefit of locating specific materials into a strongly confining PC waveguide is the possibility of saturating the absorption locally and inducing a narrow spectral hole burn in that inserted medium. Over a sufficiently narrow bandwidth (*e.g.* [34]) we can expect considerable slowing of light.

The slow light structure described above has a unit cell with two misaligned in-plane anisotropic layers and one isotropic layer. The field intensity enhancement strongly depends on the anisotropy of the material, and a larger anisotropy usually leads to a stronger resonant effect. We investigated the effect of a χ_3 nonlinearity at the DBE resonant frequency and our numerical results show several interesting effects.

The giant field intensity enhancement for the DBE structure can induce a strong nonlinear effect to the structure, we further numerically simulated band edge effect of our DBE device caused by the nonlinear refractive index. We use the formula $n = n_o + n_2 I$ to represent the nonlinear refractive index of the material, here n_o is the linear refractive index 1.64, n_2 is the nonlinear refraction coefficient of the material. Since the nonlinear index of air is several orders of magnitude smaller than that of the ABS material, the refractive index of the air was simply assumed to be 1 in our simulation.

The simulation method is as follows [35]. We first calculate the linear transmission curve T_0 and linear field intensity distribution D_{FI0} inside the structure at the DBE transmission resonance frequency. We use the formula $n = no + n_2 I = no + n_2 I_{input} D_{FI0}$ to get the new index distribution of the structure D_{n1}. The corresponding transmission curve T_1 and field intensity distribution D_{FI1} are thus defined. We use the formula $n = no + n_2 I = no + n_2 I_{input} D_{FI1}$ to get the second order index distribution D_{n2}, and the second order transmission T_2. We use the intensity distribution D_{FI2} to calculate the third order index D_{n3}, transmission T_3, and field intensity distribution D_{FI3}. We continue calculating the higher order index distribution, the corresponding transmission and intensity distribution, until we get stable results. For simplicity, we show the results for TM input polarization; the results are similar for TE input polarization. In the linear regime, the TM and TE co-polarization transmission spectra are illustrated in Fig. **7**(**a**) and the associated field enhancement inside the structure at the DBE frequency, is shown in Fig. **7**(**b**).

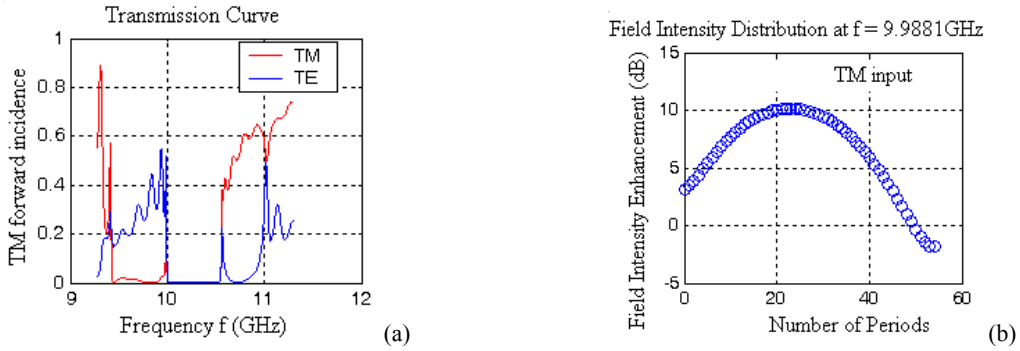

Figure 7: Transmission curve (a) and field distribution (b) for linear refractive index structure.

When $n_2 I_{input} = 10^{-4}$, both the transmission curve and the intensity are almost the same as the linear case, but when $n_2 I_{input} = 10^{-3}$, after several transmission and intensity calculations, we see two stable situations. When $n_2 I_{input} = 10^{-2}$, after several transmission and intensity calculations, we find two possible solutions. At the original DBE transmission resonance frequency, the input wave is clearly switching between two states, transmitted or blocked. We also simulated the transmission and field distribution results when $n_2 I_{input} = 5\times10^{-2}$ and 10^{-1} *etc.* In this case, we see oscillation between two states similar to Figs. **8** and **9**. When $n_2 I_{input} = 10^{-2}$, the signals at the original DBE transmission resonance frequency are modulated at two well-defined states, namely transmitted or blocked.

Thus by optimizing the optical field incident on the DBE structure, one has a dynamic limiter or switch at frequencies close to the degenerate band-edge. We also considered the case when the ABS material had a negative nonlinear refractive index coefficient n_2. Here the signal switches between two states but at the high frequency rather than low frequency side of the DBE.

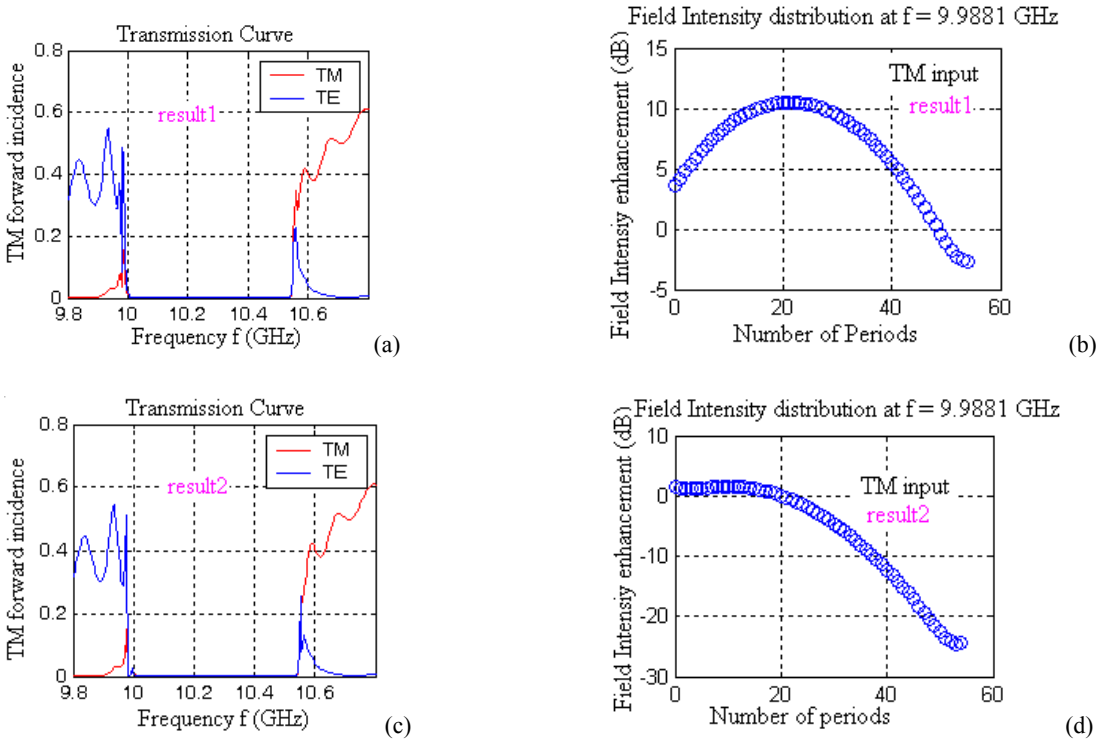

Figure 8: The transmission curve and field distribution when $n_2 I_{input} = 10^{-3}$ (a-b) similar to the linear effect (c-d) here the transmission at the original DBE transmission resonance frequency goes to zero.

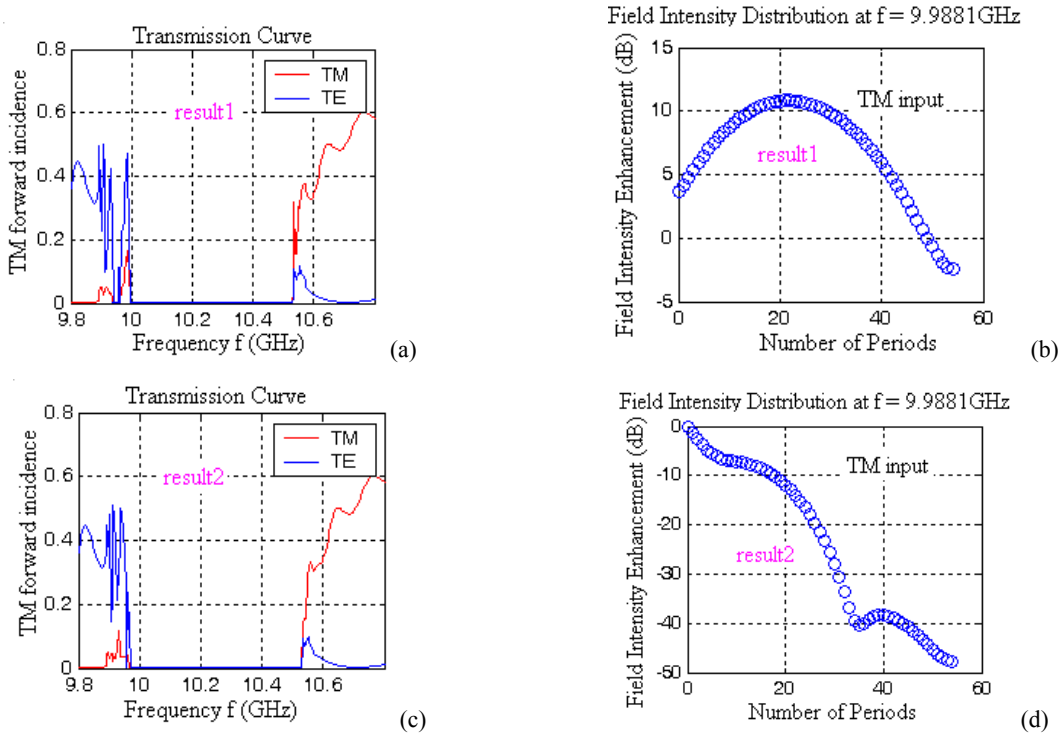

Figure 9: The transmission curve and field distribution when $n_2 I_{input} = 10^{-2}$ (a) similar to the linear effect, (b) the original DBE transmission resonance frequency has become part of the forbidden gap.

Finally, the very large internal field enhancements do suggest that we can design materials (*i.e.,* doped polymers) that exhibit large electromagnetic nonlinearities. The high intensities can be expected to induce changes in the band diagram either to further enhance the effect through a self-focusing behavior, or conversely shift the bandgap and suppress the enhancement. The latter could be exploited as an optical limiter. Some suggestions along these lines have been made n the past but without success; the DBE point was unknown at that time [36] but some more recent work has observed nonlinear changes in the bandgap using liquid crystals at visible wavelengths [37].

We have simulated the effect of nonlinearities on the DBE structure's properties. Assuming a simple model for the refractive index of $n = n_o + n_2 I$ and choosing $n_2 = 2.6 \text{ X } 10^{-4}$ cm^2/W at microwave frequencies [38], bandgap shifts and oscillation between two transmission states are predicted. This is consistent with some earlier numerical simulations by Wang *et al.* [39] near the band edge in a 2D medium.

5. EXAMPLE GAS SENSOR

There are two designs to be considered. The first makes use of the simplest axially frozen mode phenomenon, which results in a very high tangential flux near the surface of the structure. Such a surface will allow significantly enhanced coupling into chemicals on that surface allowing, for example enhanced Raman spectroscopy. A frozen mode stack will also permit increased sensitivity in observing fluorescence phenomena and wavelength selectivity when a bank of such slow light stacks is employed.

One could fabricate a set of slow light regions with an array of DBE structures as illustrated in the sketch shown in Fig. **10**. The resonant wavelength strongly depends on the geometry, *i.e.,* shape, periodicity, and air-filling fraction etc of the structures. This can provide highly selective sensors. If voids in the form birefringent layers are air, then gas can freely diffuse in and out of the sensing structure. As light is slowed down, energy accumulates in the structure, as do the electric fields. This enhanced electric field will increase the light-matter interaction, linearly or nonlinearly. If there are molecules in the gas with resonances interactions will be substantially enhanced by the slow light.

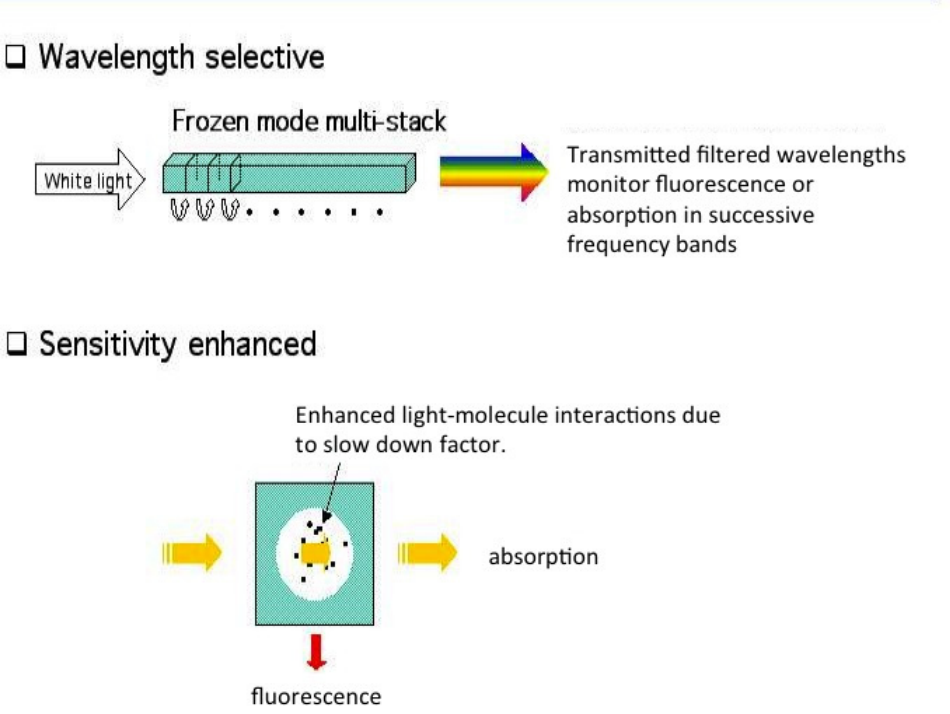

Figure 10: An enhanced multispectral gas sensor design is shown above; the voids in the photonic crystal are interconnected and gas can diffuse and fill in the voids freely.

6. THE POTENTIAL OF RANDOM STRUCTURES FOR SENSORS

The unique spectral properties of one-dimensional random systems suggests a different approach for sensor design. Rather than combat the imperfections in periodicity, if one fabricated highly disordered samples they could be equally well harnessed as high-Q resonant cavities in optical and microwave devices, including highly sensitive sensors [43, 44]. Since the resonances are sharp and very sensitive to small changes in parameters (such as optical path length), one can switch a sample from reflection to transmission by exploiting small changes the dielectric constant of the material arising from ambient environmental changes.

A practical disadvantage of this approach is that such samples have parameters that are random and hard to predict. An approach developed recently in [45, 46] opens ways for overcoming this obstacle. In makes possible the retrieval of information about the resonances inside a particular sample from standard "outside" measurements of the transmitted and reflected fields. The algorithm is based on the analogy of the problem with the quantum mechanical problem of tunneling and resonant transmission through an effective regular potential. By means of this algorithm one can effectively solve a kind of inverse problem, and find a set of parameters representing the sample using the data of the external transmission and reflection measurements, and then to calculate the field distribution inside the sample. Moreover, in [47] a method was presented for tuning the frequency of the disorder-induced resonances and creating coupled resonant cavities. The analytical results deduced from the associated quantum-mechanical analogy are in close agreement with numerical simulations and with preliminary experimental results [48].

In [49], the transport through one-dimensional systems with correlated disorder has been studied theoretically. It was found that arbitrary transmission patterns can be produced, including bands and mobility edges which usually are present only in periodic arrangements, just by an appropriate choice of the correlation. The predictions have been experimentally verified in a one-dimensional microwave guide with inserted scatterers [49]. In addition it has been possible to produce extremely short localization lengths (of

the order of the distance between the scatterers) within given frequency windows [50].The theory has been extended to quasi-one-dimensional wave guides with surface disorder [51].

CONCLUSIONS

There is a strong overlap between the topic here of slow light for sensing and the much larger field of photonic crystal structures for sensing, (*e.g.* [52-54]). We have described two slow wave structures that can be used for sensing. Both provide a longer interaction times of the passing wave combined with an associated field enhancement. We first described the properties of a highly anisotropic 1D photonic crystal structure that was designed to exhibit large field enhancements close to a DBE or SBE point. The structure was designed by exploiting form birefringence for a number of reasons. Initially it was done because there are no naturally occurring materials that could easily be used to realize this phenomenon at optical frequencies and producing large anisotropies using form birefringence addresses this in principle. However efforts to fabricate a highly anisotropic periodic structure for use at optical wavelengths remains challenging and relies on e-beam and nanoimprint capabilities. Additional advantages of form birefringence, for both optical and microwave applications are that the sensing structures will be low cost and easy to manufacture and they can be porous. The large predicted internal field enhancement was measured to be close to that expected from the theoretical model and can be increased further with lower loss dielectrics. A significant external field was measured but not predicted. Closer inspection of the simulations and the measured spectral phase revealed that a negative phase velocity is possible close to a band edge which is the likely mechanism.

The second class of slow wave structures were random in nature. For these, large slowdowns and high field enhancements are also observed but one cannot control the frequencies at which these effects occur. Nevertheless, such structures are in some ways easier to fabricate and once made have a unique spectral behavior, which is easily modified by small permittivity changes to any one region or layer in the structure. This provides the opportunity for multiplexing several sensing modes into one structure if a number of possible sensing needs can be parallelized.

The dramatic field enhancements lend themselves to a number of applications such as increased antenna sensitivity as well as increased sensor sensitivity where large intensities are required, such as for Raman spectroscopy. Because of the very large group index, objects inside or possibly inset on the surface of the structure, will be probed by much shorter wavelengths allowing higher resolution imaging or probing of those objects. One can also imagine this slow wave structure to be somewhat similar to a very high index immersion lens. Ideas of this kind have been reported [55, 56].

Finally, for the structures described here, our ability to tune the DBE and SBE to find strong resonances provides an important degree of freedom to maximize the field enhancement internally at a desired frequency. We also described a DBE structure, designed using the transfer matrix method, and investigated the effects of a third order nonlinearity. This leads to dynamic limiting and switching at frequencies near the DBE transmission resonance frequency. Because of a DBE's large resonant field, a third order material nonlinear effect will change the dispersion diagram and hence the transmission characteristics. This can be exploited for optical limiting and switching applications involving specific frequencies and input intensities. A long term goal of studying slow light is to better understand and exploit how structured materials, such as 1D, 2D or 3D PCs can be engineered to manage light locally. Local changes in structural features define functionality and also lend themselves to high density integration. Moreover, this approach to realizing extensive and varied sensing functionality is achieved simply by patterning the host material, of which form-birefringence is just a special case. This in turn allows low cost manufacturing at the wafer level using techniques such as nano-imprinting.

ACKNOWLEDGEMENTS

The author is grateful to his colleagues and collaborators for their contributions over the last few years to the material presented in this chapter. Special thanks got to Weiguo (Bill) Yang, Yang Cao, Alex Figotin, IlyaVitebskiy, Robert Ingel and John Schenk.

REFERENCES

[1] Figotin A, Vitebsky I. Oblique frozen modes in periodic layered media. Phys Rev B 2003; 68: 036609.

[2] Figotin A, Vitebsky I. Gigantic transmission band-edge resonance in periodic stacks of anisotropic layers. Phys Rev E; 72, 036619 (2005).

[3] Anderson PW. Absence of Diffusion in certain Random Lattices. Phys Rev 1958; 109: 1492.

[4] Lifshits IM, Gredeskul SA, Pastur LA. Introduction to the Theory of Disordered Systems, Wiley, 1988.

[5] Freilikher V, Gredeskul S. Localization of waves in media with one-dimensional disorder. Prog Optics 1992; 30: 37.

[6] Cheng P. Introduction to Wave Scattering, Localization and Mesoscopic Phenomena. Springer-Verlag, Heidelberg, 2006.

[7] Akkermans E, Montambaux G. Mesoscopic physics of electrons and photons, Cambridge University Press, 2007.

[8] Fouque J-P, Garnier J, Papanicolaou G, Solna K. Wave propagation and time reversal in randomly layered media, Springer, 2007.

[9] Frisch U, Froeschle C, Scheidecker J-P, Sulem P-L. Stochastic resonance in one-dimensional random media. Phys Rev A: 1973; 8: 1416.

[10] Ya. Azbel M, Soven P. Transmission resonances and the localization length in one-dimensional disordered systems. Phys Rev B 1983; 27(2): 831.

[11] Azbel MY. Eigenstates and properties of random systems in one dimension at zero temperature. Phys Rev B 1983; 28(8): 4106.

[12] Wiersma DS, Cavalieri S. A temperature-tunable random laser. Nature 2001; 414: 708.

[13] Jiang X, Soukoulis CM. Time Dependent Theory for Random Lasers. Phys Rev Lett 2000; 85: 70.

[14] Milner V, Genack A, Photon Localization Laser: Low-Threshold Lasing in a Random Amplifying Layered Medium *via* Wave Localization. Phys Rev Lett 2005; 94: 073901.

[15] Hodgkinson IJ, Wu Q-H. Birefringent Thin Films and Polarizing Elements, World Scientific, New Jersey, 1998.

[16] Ballato J, Ballato A. Materials for freezing light. Waves in Random and Complex Media. 2005;15(1):113-8.

[17] Kanaev A, Cao Y, Fiddy MA. Axially frozen modes in finite anisotropic photonic crystals. Opt Eng 2005; 44 (9): 095201.

[18] Bendickson LM, Dowling JP, Scalora M. Analytic expressions for the electromagnetic mode density in finite, one-dimensional, photonic band-gap structures. Phys Rev E 1996; 53: 4107.

[19] Scalora M, Flynn RJ, Reinhardt SB, *et al.* Ultrashort pulse propagation at the photonic band edge: large tunable group delay with minimal distortion and loss. Phys Rev E 1996; 54: R1078-R1081.

[20] Scalora M, Dowling JP, Bowden CM, Bloemer MJ. Optical limiting and switching of ultrashort pulses in nonlinear photonic band gap materials. Phys Rev Lett 1994; 73: 1368-1371.

[21] Figotin A, Vitebskiy I. Slow-wave resonance in periodic stacks of anisotropic layers. Phys Rev A 2007; 76: 053839.

[22] Cao Y, Fiddy MA. Resonant effect analysis at finite one-dimensional anisotropic photonic crystal band edges. Proceedings of SPIE 2006; 6128: 345-356.

[23] Schenk JO, Ingel RP, Cao Y, Fiddy MA. Anisotropic periodic structure exhibiting gigantic field enhancements. Proceedings of SPIE 2008; 6992: 69920P.

[24] Pustai D, Sharkawy A, Shi S, Prather DW. Tunable photonic crystal microcavities. Appl Optics 2002; 41: 5574.

[25] Sharkawy A, Shi S, Prather DW, Soref RA. Electro-optical switching using coupled photonic crystal waveguides. Opt Express 2002; 10: 1048.

[26] Chabanov AA. Strongly resonant transmission of electromagnetic radiationin periodic anisotropic layered media. Phys Rev A 2008; 77: 033811.

[27] Fiddy MA. The Role of Analyticity in Image Recovery. In: Stark H, Eds. Image Recovery: Theory and Applications. Florida: Academic Press 1987; pp. 499-529.

[28] Lenz G, Eggleton BJ, Madsen CK, Slusher RE. Optical delay lines based on optical filters. IEEE J Quantum Elect 2001; 37(4): 525-32.

[29] Blair S, Heebner JE, Boyd RW. Beyond the absorption-limited nonlinear phase shift with microring resonators. Opt Lett 2002; 27(5): 357-9.

[30] Nishikawa S, Lan S, Ikeda N, Sugimoto Y, Ishikawa H, Asakawa K. Optical characterization of photonic crystal delay lines based on one-dimensional coupled defects. Opt Lett 2002; 27(23): 2079-81.

[31] Scalora M, Bloemer MJ, Manka AS, *et al.* Pulsed second-harmonic generation in nonlinear, one-dimensional, periodic structures. Phys Rev A 1997; 56(4): 3166.

[32] Babin A, Figotin A. Nonlinear photonic crystals: II. Interaction classification for quadratic nonlinearities. Wave Random Media 2002; 12(4): R25-R52.
[33] Soljacic M, Luo C, Joannopoulos JD, Fan S. Nonlinear photonic crystal microdevices for optical integration. Opt Lett 2003; 28(8): 637-9.
[34] Bigelow MS, Lepeshkin NN, Boyd RW. Observation of ultraslow light propagation in a ruby crystal at room temperature. Phys Rev Lett 2003; 90(11): 113903.
[35] Cao Y, Schenk J, Fiddy MA. Third order nonlinear effect near a degenerate bandedge. Optics and Photonics Letters 2008; 1: 1-7.
[36] Herbert CJ, Capinski WS, Malcuit MS. Optical power limiting with nonlinear periodic structures. Opt Lett 1992; 17(15): 1037-9.
[37] Hwang J, Ha NY, Chang HJ, Park B, Wu JW. Enhanced optical nonlinearity near the photonic bandgap edges of a cholesteric liquid crystal. Opt Lett 2004; 29(22): 2644-6.
[38] Bobbs B, Shih R, Fetterman HR, Ho WW. Nonlinear microwave susceptibility measurement of an artificial Kerr medium. Appl Phys Lett 1988; 52 (1): 4.
[39] Wang Z, Wu J, Liu X, Zhu Y, Ming N. Nonlinear transmission resonance in a two-dimensional periodic structure with photonic band gap. Phys Rev B. 1997; 56(15): 9185.
[40] Mookherjea S, Oh A. Effect of disorder on slow light velocity in optical slow-wave structures. Opt Lett 2007; 32(3): 289-91.
[41] Freilikher VD, Liansky BA, Yurkevich IV, Maradudin AA, McGurn AR. Enhanced transmission due to disorder. Phys Rev E 1995; 51(6): 6301.
[42] Bliokh KY, Bliokh YP, Freilikher VD. Resonances in one-dimensional disordered systems: localization of energy and resonant transmission. J Opt Soc Am B 2004; 21(1): 113-20.
[43] Xu Y, Li Y, Lee RK, Yariv A. Scattering-theory analysis of waveguide-resonator coupling. Phys Rev E 2000; 62(5): 7389.
[44] Yariv A. Universal relations for coupling of optical power between microresonators and dielectric waveguides. Electron Lett 2000; 36: 321.
[45] Bliokh KY, Bliokh YP, Freilikher VD. Resonances in one-dimensional disordered systems: localization of energy and resonant transmission. J Opt Soc Am B 2004; 21(1): 113-20.
[46] Bliokh KY, Bliokh YP, Freilikher V, Genack AZ, Hu B, Sebbah P. Localized Modes in Open One-Dimensional Dissipative Random Systems. Phys Rev Lett 2006; 97(24): 243904.
[47] Bliokh KY, Bliokh YP, Freilikher V, Genack AZ, Sebbah P. Coupling and Level Repulsion in the Localized Regime: From Isolated to Quasiextended Modes. Phys Rev Lett 2008; 101(13): 133901.
[48] Izrailev FM, Krokhin AA. Localization and the Mobility Edge in One-Dimensional Potentials with Correlated Disorder. Phys Rev Lett 1999; 82 (20): 4062.
[49] Kuhl U, Izrailev FM, Krokhin AA, Stöckmann HJ. Experimental observation of the mobility edge in a waveguide with correlated disorder. Appl Phys Lett 2000; 77: 633.
[50] Kuhl U, Izrailev FM, Krokhin AA. Enhancement of Localization in One-Dimensional Random Potentials with Long-Range Correlations. Phys Rev Lett 2008; 100(12): 126402.
[51] Izrailev FM, Makarov NM. Controlled transparency of many-mode waveguides with rough surface. Phys Status Solidi C 2003; 0(8): 3037-41.
[52] Cooper J, Glidle A, De La Rue R. Photonic Crystal Structures in Molecular Biosensing. Opt Photon News 2010; 21(9): 26-31.
[53] El Beheiry M, Liu V, Fan S, Levi O. Sensitivity enhancement in photonic crystal slab biosensors. Opt Express 2010; 18(22): 22702-14.
[54] Glushko EY. Pneumatic photonic crystals. Opt Express 2010; 18(3): 3071-8.
[55] Le Coarer E, Blaize S, Benech P, *et al.* Wavelength-scale stationary-wave integrated Fourier-transform spectrometry. Nat Photon. 2007;1(8):473-8.
[56] Mookherjea S, Park JS, Yang S-H, Bandaru PR. Localization in silicon nanophotonic slow-light waveguides. Nat Photon 2008; 2(2): 90-3.

CHAPTER 7

Circular Bragg and Photonic Crystal Resonators

Jacob Scheuer*, Eyal Benisty and Ori Weiss

School of Electrical Engineering, Department of Physical Electronics, Tel-Aviv University, 69978 Tel-Aviv, Israel

Abstract: Circular resonators are key components for diverse applications, ranging from optical telecommunication systems through basic research involving highly confined fields and strong photon-atom interactions to biochemical and rotation sensing. The important properties of circular resonators are the Q factor, the free spectral range (FSR) and the modal volume, where the last two are determined by the resonator radius and the index contrast. The total-internal-reflection (TIR) mechanism employed in "conventional" resonators links these attributes and limits the ability to construct small footprint devices exhibiting large FSR and small modal volume on one hand, and high Q on the other. Recently, a new class of circular resonator, based on a single defect surrounded by radial Bragg reflectors, has been proposed and demonstrated. The radial Bragg confinement breaks the link between the modal volume and the Q, and paves the way for the realization of compact, high-Q resonators. These characteristics as well as the unique mode profile and polarization properties of these resonators and lasers make them attractive tools for nanometer scale semiconductor lasers, ultrasensitive detectors, as well as to study nonlinear optics, light tweezers and cavity QED.

Keywords: Radial bragg lasers, sagnac effect, rotation sensing, biochemical sensing.

1. INTRODUCTION

Disk and ring shaped resonators, are key elements needed for the realization of various basic components used in advanced optical communication systems, sensing applications and basic research. During the last decade, numerous circular resonator based applications such as lasers, filters [1], add/drop multiplexers [2], modulators [3] and delay lines [4] have been proposed and demonstrated. Moreover, the applicability of circular resonators extends beyond telecommunication to additional fields such as sensing [5], spectroscopy and biophotonics [6], and to basic research in QED, nonlinear optics and other related fields [7].

For many of these applications, circular resonator exhibiting low losses or, equivalently, a high quality factor (Q) and small dimensions are also desirable. For telecommunications, for example, small resonator dimensions provide large free spectral range (FSR). Unfortunately, for conventional resonators, employing total internal reflection (TIR) as the radial confinement mechanism, these requirements are linked and contradictory. To reduce the cavity dimensions, a circular resonator is required to have a small bending radius. As a result the efficiency of the TIR confinement mechanism is significantly impaired, leading to larger power dissipation and lower Q factor through bending losses [8].

Recently, we have proposed utilizing distributed feedback Bragg reflection instead of TIR in circular resonators as the radial confinement mechanism in order to break the connection between the dimensions and loss and thus facilitate low-loss, yet compact circular resonators [9–11]. This concept is illustrated in Fig **1**. A pillar (Fig. **1(a)**) or an annular defect (Fig. **1(b)**) is surrounded by radial Bragg layers. The confinement of the modal field in the disk (Fig. **1(a)**) or within the defect (Fig. **1(b)**) is accomplished by Bragg reflection. Unlike conventional resonators, the reflectivity of the Bragg mirror can be increased simply by adding more layers to the external reflector. As a result, the radius of the disk (or the annular defect) can be reduced almost arbitrarily without inducing larger bending losses. Such microcavities,

Address correspondence to Jacob Scheuer: School of Electrical Engineering, Department of Physical Electronics, Tel-Aviv University, 69978 Tel-Aviv, Israel; Tel: +972-3-6407559; Fax: +972-3-6423508; Email: kobys@eng.tau.ac.il

Marco Pisco, Andrea Cusano and Antonello Cutolo (Eds)
All rights reserved-© 2012 Bentham Science Publishers

employing distributed Bragg reflection as the transverse confinement mechanism, *e.g.* photonic crystal (PC) defect cavities [12, 13] and annular Bragg resonators [9–11] exhibit unique characteristics (*e.g.* mode profile, dispersion relation, *etc.*) which are advantageous for numerous applications as discussed in the following sections.

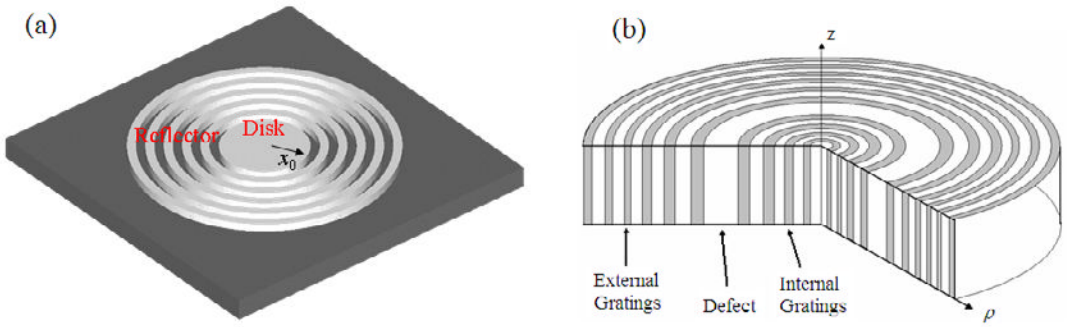

Figure 1: (a)"Disk"-like and (b)"ring"-like circular Bragg cavities.

2. BASIC THEORY – COUPLED-WAVES EQUATIONS

Consider a radially symmetric photonic structure, consisting of an annular defect surrounded by concentric rings (serving as radial Bragg reflectors) as illustrated in Fig. **1**. The guiding defect consists of a material of refractive index n_{defect}, and the reflectors' layers are of refractive indices n_1 and n_2. Fig **1(a)** illustrates a "disk"-like resonator where light is confined in a central pillar while Fig. **1(b)** shows a "ring"-like resonator in which light is confined in an annular defect. All electromagnetic field components can be expressed in terms of the vertical (z) component of the electric and magnetic fields [14]. These components satisfy the scalar Helmholtz Eq. which in cylindrical coordinates is given by:

$$\left[\rho^2\frac{\partial^2}{\partial\rho^2}+\rho\frac{\partial}{\partial\rho}\left(k^2(\rho)-\beta^2\right)\rho^2+\frac{\partial^2}{\partial\theta^2}\right]\begin{pmatrix}E_z\\H_z\end{pmatrix}=0, \tag{1}$$

where ρ and θ are respectively the radial and angular coordinates, β is the z component of the wave-vector, $k(\rho) = k_0 \cdot n(\rho)$, and k_0 is the wavenumber in vacuum.

We look for a modal solution of the Helmholtz Eq. in radial coordinates which is resonant in the structure shown in Fig. **1**, with the following functional form:

$$E_z = E(\rho)\cdot\exp(im\theta) \tag{2}$$

where m is an integer and the radial part of the field, $E(\rho)$ satisfies the Bessel equation. Eq. (1) can be solved by either assuming that the refractive index $n(\rho)$ is weakly perturbed [15] or by assuming it is piece-wise constant [9]. We assume that the dielectric coefficient $\varepsilon(\rho)$ is given by $\varepsilon=n_0^2$ in the unperturbed area and by $\varepsilon=n_0^2+\Delta\varepsilon(\rho)$ within the perturbed region. Introducing the normalized radius $x=k_0n_0\rho$ yields the dimensionless wave equation:

$$\begin{aligned} &x^2E_{xx}+xE_x+\left[x^2-m^2\right]E=0 && x\le x_0\\ &x^2E_{xx}+xE_x+\left[x^2\left(1+\frac{\Delta\varepsilon(x)}{n_0^2}\right)-m^2\right]E=0 && x>x_0 \end{aligned} \tag{3}$$

where $x_0=k_0n_0\rho$ is the dimensionless radius of the disk. The solution of (3) in the disk region is given by a superposition of the m^{th} order Hankel function of the first and second kind. When the perturbation $\Delta\varepsilon(\rho)$ is

small compared to n_0^2, the solution of (3) in the perturbed region can be written as slowly varying envelopes multiplying the Hankel functions:

$$E(x)=\begin{cases}\bar{A}H_m^{(1)}(x)+\bar{B}H_m^{(2)}(x) & x\le x_0\\ A(x)H_m^{(1)}(x)+B(x)H_m^{(2)}(x) & x>x_0\end{cases} \tag{4}$$

Introducing (4) into (3) and neglecting the second derivatives of $A(x)$ and $B(x)$ leads to:

$$\frac{dA}{dx}\cdot\left(2\frac{dH_m^{(1)}}{dx}+\frac{H_m^{(1)}}{x}\right)+\frac{dB}{dx}\cdot\left(2\frac{dH_m^{(2)}}{dx}+\frac{H_m^{(2)}}{x}\right)+ +\frac{\Delta\varepsilon}{n_0^2}\left(AH_m^{(1)}+BH_m^{(2)}\right)=0 \tag{5}$$

where the specific x dependence of the amplitudes and the Hankel functions was dropped for clarity. It is common to use the asymptotic approximation for the Hankel functions in order to derive a simplified equation, yielding complex exponentials in x as the required perturbation profile. Here we introduce the following approximation for large x: $H_m^{(1,2)}/x<<dH_m^{(1,2)}/dx$ and $dH_m^{(1,2)}/dx\approx\pm iH_m^{(1,2)}$ [15]. Apparently, this approximation for the derivatives of the Hankel functions is more accurate than the derivative of the "conventional" asymptotic approximation (see [15] for more details). Under these approximations, Eq. (5) can be rewritten as:

$$2i\left[H_m^{(1)}(x)\cdot A_x(x)-H_m^{(2)}(x)\cdot B_x(x)\right]+ \frac{\Delta\varepsilon(x)}{n_0^2}\left[A(x)H_m^{(1)}(x)+B(x)H_m^{(2)}(x)\right]=0 \tag{6}$$

$H_m^{(1)}$ and $H_m^{(2)}$ represent radially incoming and outgoing cylindrical waves. Therefore, it is clear that the perturbation $\Delta\varepsilon$ which is required to efficiently couple power between the incoming and outgoing waves, should have the following form:

$$\Delta\varepsilon(x)=\alpha\frac{H_m^{(2)}(x)}{H_m^{(1)}(x)}+\alpha^*\frac{H_m^{(1)}(x)}{H_m^{(2)}(x)} \tag{7}$$

where a is a complex amplitude of the perturbation. Introducing (7) into (6) and keeping only the first order in $H_m^{(1)}$ and $H_m^{(2)}$ yields a set of coupled Eqs. for the wave amplitudes A and B:

$$\begin{aligned}&2i\frac{dA(x)}{dx}+\frac{\alpha^*}{n_0^2}B(x)=0\\ &-2i\frac{dB(x)}{dx}+\frac{\alpha}{n_0^2}A(x)=0\end{aligned} \tag{8}$$

Eq. (8) describe the evolution of the amplitudes of the cylindrical waves in ρ, can be readily solved to yield:

$$\begin{aligned}&A(x)=A_1\exp(kx)+A_2\exp(-kx)\\ &B(x)=-i\frac{k}{k^*}\left[A_1\exp(kx)-A_2\exp(-kx)\right]\end{aligned} \tag{9}$$

where $k=\alpha/2n_0^2$ is the coupling coefficient between the outgoing and incoming waves. Knowing the perturbation profile needed to attain radial confinement (7) and the modal field profile (9), it is possible to design and analyze a circular DFB resonator.

3. DESIGN RULES FOR CIRCULAR DFB CAVITIES

In order to design a circular Bragg or PhC resonator one must first decide of the resonance wavelength and the desired angular modal number m. Therefore, given the perturbation profile (7) the only parameters left to be determined are the internal disk radius (x_0 in Fig. **1**) or, equivalently, the defect radius for a ring-like resonator, and the perturbation strength α. We focus on the design rules for a disk-like resonator because it is the simpler geometry.

Inside the disk ($x<x_0$), the modal field is given by (4). For the field to be finite at $x=0$ it is required that the amplitudes of the incoming and outgoing waves are equal, *i.e.,* $\bar{A} = \bar{B}$. As a result, the field at $x<x_0$ is given by $J_m(x)$ where J_m is the m^{th} order Bessel function of the first kind. In the grating region ($x>x_0$) the field profile is given by (7). For simplicity, we assume that the gratings extend to very large radius so that the exponentially increasing term in (7) vanishes, *i.e.,* $A_1=0$. At the interface between the disk and the grating ($x=x_0$), both the field and its derivative must be continuous (for TE polarization). The phase of the coupling coefficient $k=|k|\exp(i\varphi_k)$ (or α) can be, in principal, selected arbitrarily (as for Cartesian Bragg reflectors) – it merely introduces a spatial shift of the gratings. However, this phase affects the required disk radius, x_0, which satisfies the boundary conditions. For the specific case of $i\varphi_k=\pi/2$, the characteristic Eq. for x_0 is simple - $J_m(x)=0$. In this case, the required perturbation and field profiles are given by:

$$\Delta\varepsilon(x) = \begin{cases} 0 & x < x_0 \\ -2|\alpha| \cdot \sin\left[2 \cdot \text{phase}\left(H_m^{(1)}(x)\right)\right] & x \geq x_0 \end{cases} \tag{10a}$$

$$E(x) = \begin{cases} J_m(x) & x < x_0 \\ J_m(x)\exp\left[-|k|\left(x - x_0\right)\right] & x \geq x_0 \end{cases} \tag{10b}$$

Eq. (10) yields both the pertinent perturbation term and the field profile. In order to radially confine the mode, the perturbation profile must include a term with the functional form of (10a). To realize a PhC reflector, we suggest the following index profile:

$$\varepsilon(x,\theta) = \begin{cases} n_0^2 - (n_0^2 - n_p^2) \cdot \Im\left[2 \cdot \text{phase}\left(H_m^{(1)}(x)\right), \alpha_1\right] \cdot \Im\left[l\theta, \alpha_2\right] & x > x_0 \\ n_0^2 & x \leq x_0 \end{cases}$$
$$\Im\left(y, \alpha\right) = \begin{cases} 0, & \sin(y) < \alpha \\ 1, & \sin(y) \geq \alpha \end{cases} \tag{11}$$

where $-1<\alpha_1,\alpha_2<1$, n_0 is the material index of refraction and l is the azimuthal number of the index profile. The structure consists of dielectric material of refractive index n_0 perforated by holes with refractive index n_p.

This index profile is the radial equivalent of a rectangular PC with rectangular holes. The perforation function $\Im\left(y,\alpha\right)$ can be interpreted as a generalized rectifier of $\sin(y)$, generating square "pulses" only where $\sin(y)>\alpha$. The larger the value of α, the narrower the "pulses". The index profile (12) includes two $\Im$ functions – the first generates annular slits centered at the maxima of $\sin[2\cdot\text{phase}(H^1_m(x))]$ with widths that are determined by α_1. The second $\Im$ function modulates these slits as a function of the angle θ with angular frequency l and "duty-cycle" determined by α_2. If, for example, $\alpha_2<-1$ then there is no angular modulation of the refractive index and the index profile is radially symmetric as in Fig. **1**. Introducing angular modulation results in a circular photonic-crystal like structure as depicted in Fig. **2** For $n_p=1$ (air holes), the Fourier expansion of the perforation function $\Im\left(y,\alpha\right)$ is given by:

$$\Im\left(y,\alpha\right) = \cos^{-1}\left(\alpha\right)/\pi - \sum_{m=1}^{\infty} \frac{(-1)^m - 1}{m\pi} \cos\left[m \cdot \sin^{-1}\left(\alpha\right)\right] \cdot \sin\left(my\right)$$
$$- \sum_{m=1}^{\infty} \frac{(-1)^m + 1}{m\pi} \sin\left[m \cdot \sin^{-1}\left(\alpha\right)\right] \cdot \cos\left(my\right) \tag{12}$$

The term which is responsible for the radial confinement of the modal field is the first order in the radial expansion and zero order in the azimuthal expansion, which is given by:

$$\Delta\varepsilon_{1,0} = -2\cdot\left(n_0^2-1\right)\cos\left[\sin^{-1}\left(\alpha_1\right)\right]\cdot\cos^{-1}\left(\alpha_2\right)\Big/\pi^2 \qquad \textbf{(13)}$$

The fact that $\Delta\varepsilon_{1,0}$ is independent of the azimuthal number of the perturbation, l, indicates that the azimuthal details of the index profile are of less significance. The azimuthal modulation is averaged over the device circumference and its only influence on the coupling coefficient is through the "filling factor" $\cos^{-1}(\alpha_2)$. A similar conclusion was also deduced for micro-structured fibers [16]. It should be clear, however, that this result stems directly from neglecting all the terms in (11) except $\Delta\varepsilon_{1,0}$, which is accurate only if $l>>m$. Nevertheless, in this limit the conclusion holds and the azimuthal dependence of (11) can be modified without deteriorating the performances of the device.

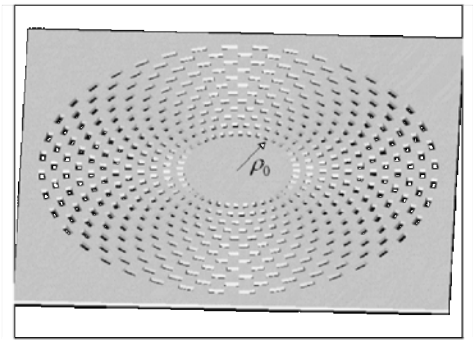

Figure 2: Schematic index profile of a PC disk resonator. Gray – material; black- air holes.

4. MODAL FIELD PROFILE AND PROPERTIES

The basic properties of the modal field solutions in the CBRs are the field profile, resonance wavelength, emitted beam profile and quality factor. In addition, it should be noted that there are many ways to achieve a perturbation profile as given in 10(a), where of the perturbation (11) is just one of them. Specifically, (11) generates a "square-lattice"- like profile, which is the cylindrical equivalent to the well-known rectangular PhC. Fig. **3(a)** illustrates this index profile. Fig. **3(b)** depicts a "triangular"-type lattice PC reflector, in which every other "necklace" of holes is rotated by π/l (l is the azimuthal periodicity of the perturbation). Not surprisingly, if the radial duty-cycle of the triangular lattice is kept identical to that of a rectangular lattice, the resulting leading term (indicating the strength of the perturbation) remains the same as in (13).

Fig. **3(c)** depicts a reflector which does not consist of a single azimuthal modulation frequency. This type of reflector was constructed with an attempt to keep the holes shape as close as possible to an ideal square. As a result, the number of holes per "necklace" increases for larger radii. We designate this type of reflector as a "varying–l" lattice. This type of reflector does not have an equivalent Cartesian PhC because it does not form a genuine crystal. Nevertheless, in the small perturbation regime we expect the characteristics of such resonator to be similar to those of the resonators shown in Fig. **3(a)** and **3(b)**.

Fig. **4** compares between the numerically calculated radial mode profiles of various resonator types which have the same α_1 and α_2 parameters and the analytically calculated profile (10b). The wavelength is 1.52μm and the parameters of the structures are defined in the figure caption. The numerical solutions indicate that, as expected, the mode profiles of the different structures are practically identical. In addition, the good agreement with the approximated analytical solution is clear, even though the index contrast in the reflector region is relatively high.

Fig. **5** depicts the resonance frequencies calculated by two-dimensional FDTD for several PhC reflector structures (α_1 and α_2 are the same for all structures). The spatial resolution was 0.01 μm. The resonances

were calculated by exciting the structure with a very short pulse (20fs) and letting it circulate in the resonator for a long period while monitoring the field amplitude at the peak of the mode. Taking the Fourier transform of the field yields the spectral response of the resonator. The spectral responses of all the structures are almost identical, with resonances at λ=1.52 μm for *m*=8 (the target mode) and at 1.455 μm for m=9. The inset of Fig. **5** shows the modal field profiles at the resonance frequencies and the corresponding field profiles, which are also identical for all structures. It is evident that the field profile of *m*=8 is more confined in the resonator than the field profile of *m*=9. This is because the radial part of the gratings is designed for m=8 and, as a result, the *m*=9 mode has a smaller decay coefficient in the gratings. This is in contrast to conventional (TIR based) disk resonators for which higher *m* numbers are generally associated with more grazing incidence angles of the field at the interface. These modes are confined more strongly to the disk and, therefore, experience lower bending losses.

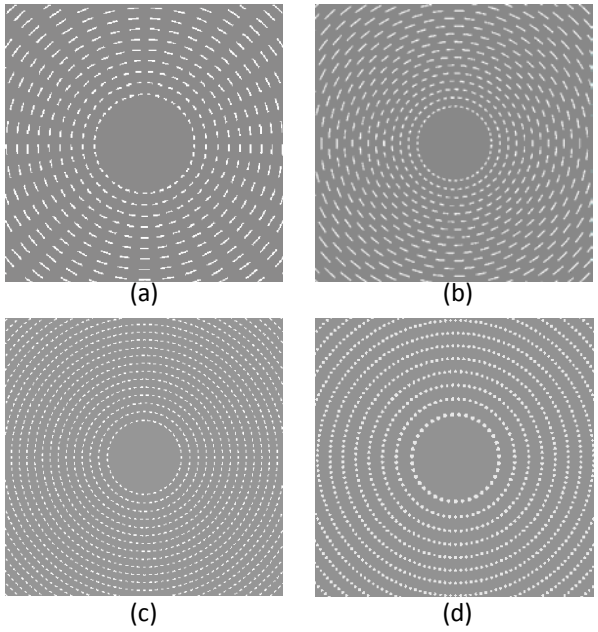

Figure 3: Schematic index profile of a The different reflector types: (a)"Rectangular" lattice, (b)"Triangular" lattice, (c)"varying–*l*" lattice with rectangular holes, (d)"varying–*l*" lattice with circular holes.

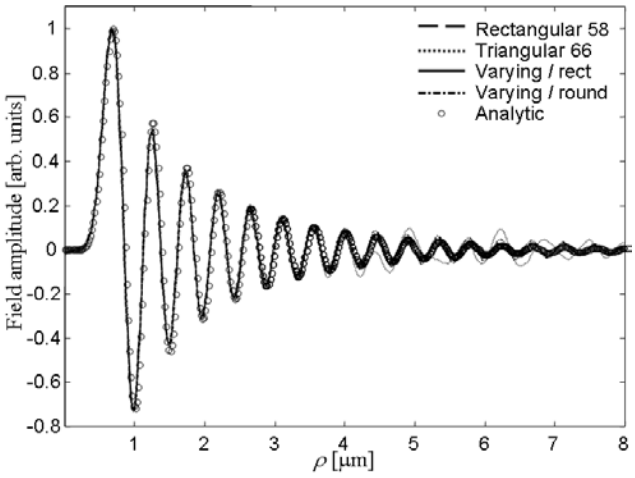

Figure 4: Comparison between the modal field profiles of the different resonator structures: "Rectangular" lattice with *l*=58 (dashed), "Triangular" lattice with *l*=66 (dotted), "varying–*l*" lattice with rectangular holes (solid), "varying–*l*" lattice with circular holes (dash-dot), Analytical solution (circles). The other parameters of the structure are n_0=3.5, *m*=8, α_1=0.9, α_2=0.

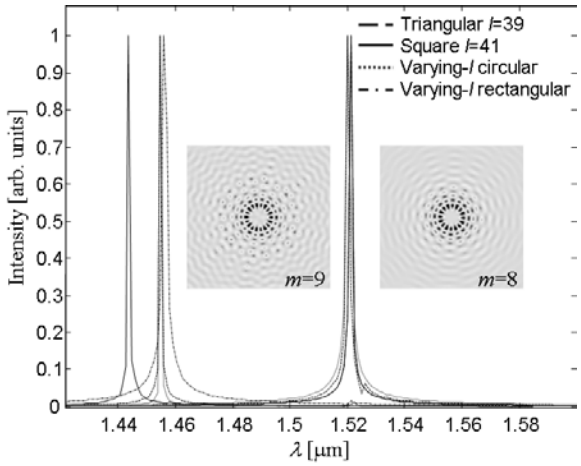

Figure 5: Resonance frequencies of the various structures: "Triangular" lattice with l=39 (dashed), "Rectangular" lattice with l=41 (solid), "varying–l" lattice with circular holes (dotted), "varying–l" lattice with rectangular holes (dash-dot). The Inset shows the corresponding field profiles.

According to (13), the modal field profile of the resonator is independent of the azimuthal frequency of the perturbation, l. Fig. **4**, which depicts the field profile for various structures, indicates that this is indeed correct. Moreover, as shown in Fig. **5**, the spectral response (*i.e.,* the resonance wavelengths) of the resonators is almost independent of the lattice type and the azimuthal perforation frequency. It is, therefore, interesting to examine whether the quality factor is also independent of the reflector architecture. Fig. **6** shows the dependence of the ringdown time constant (and, hence, the Q) on the azimuthal perforation frequency l. The ringdown time constant is a measure for the photon lifetime in the cavity and it is related to the Q according to $Q=\omega_0\tau_0$ where ω_0 is the resonance (angular) frequency of the resonator.

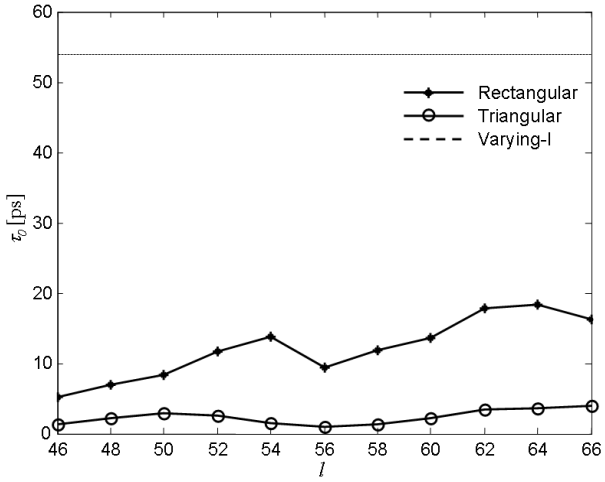

Figure 6: The cavity ringdown time constant as function of the azimuthal perturbation frequency l: "Rectangular" lattice (solid), "Triangular" lattice (dashed). The dash-dot line indicates the ringdown time constant of the "varying–l" lattice with rectangular holes.

It seems that the general trend is that higher Q factors are attained for larger values of l for both the triangular and the rectangular lattices. However, there is a clear decrease in the Q for l=56, most probably due to grating assisted phase matching to a radiating mode. The simulations also indicate that a rectangular lattice reflector exhibits lower losses compared to a triangular lattice reflector with the same angular perturbation frequency. Nevertheless, as seen in Fig. **6**, a reflector consisting of higher angular perturbation frequency for larger radii ("varying-l") is significantly superior (from the quality factor point of view) to a reflector with constant angular perturbation frequency. This result can be understood as stemming from the

dependence of the Q on l. At larger radii, the angular frequency of the "varying-l" reflector increases and, as a result, the reflectivity of the gratings is improved.

In a three dimensional CBR, the Q factor is determined by two independent loss mechanisms: radial loss through the Bragg reflector, and vertical loss, caused by out-of-plane scattering from the CBR surface. On the other hand, the later loss mechanism can also be used as an output coupling mechanism. By using a photonic crystal which period matches the resonant wavelength, the vertical emission (*i.e.,* the output coupling) can be enhanced by realizing a radial structure where the low-index radial layers are "quarter-wavelength" wide while the high-index layers are three "quarter-wavelength" wide. This is, however, in the sense of the quasi-periodicity of the Bessel function, *i.e.*, each quarter-wavelength section stretches from a local extremum to a zero of the field. This method creates coherent scattering in the vertical directions which lowers the Q factor, but provides an output coupling port.

As for any laser, the properties of the emitted beam are of much interest. In order to study these properties, we simulated the CBR structure using 3D finite difference time domain (FDTD). The simulated structure consisted an InGaAsP (n_1=3.4) suspended in air, with structure thickness of 800nm. Two CBR prototypes were studied: A TM optimized structure with a 180nm wide central disk, and a TE optimized CBR where the central disk radius is 270nm. Both structures where designed for a target resonance wavelength of 1535nm at the 0^{th} order azimuthal mode (m=0). The CBRs were excited using a short pulse (0.066 psec) after which the field decayed to the resonant mode. A snapshot of the field emitted from a TM CBR is shown in Fig. **7**.

Note that at the center of the beam there is a zero-intensity spot. The null in the intensity pattern stems from polarization singularity at ρ=0. The polarization patterns of the beam emitted from a TM (A) and TE (B) optimized structures are shown in Fig. **8**.

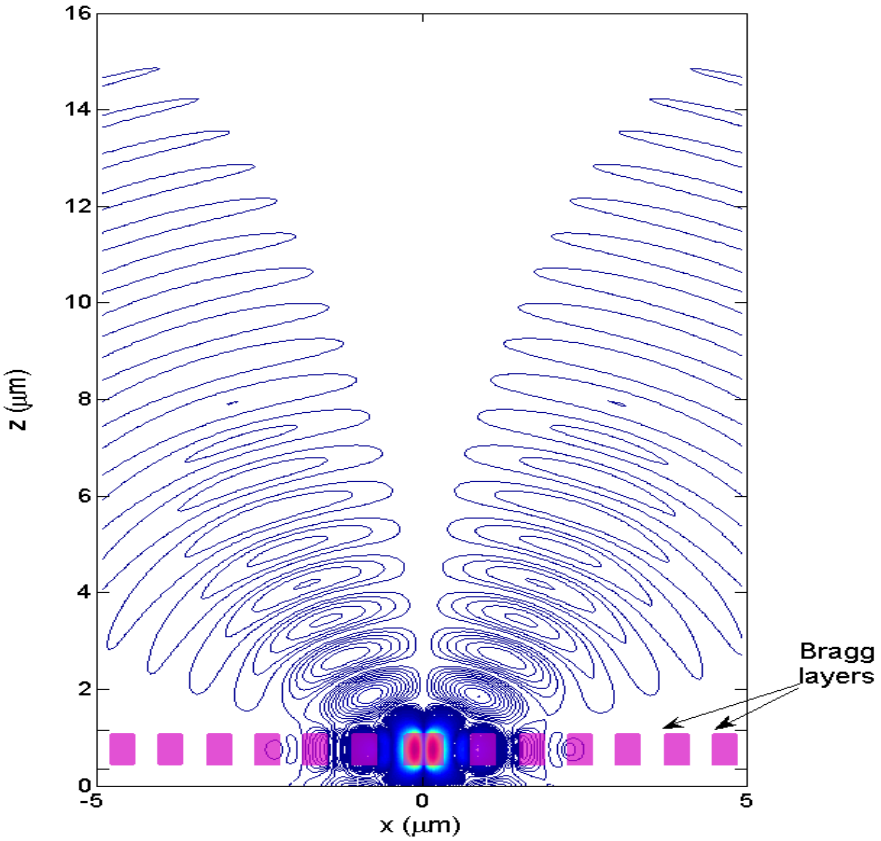

Figure 7: Electric field in a vertical cross-section of a TM polarized mode. The Bragg layers are at the bottom.

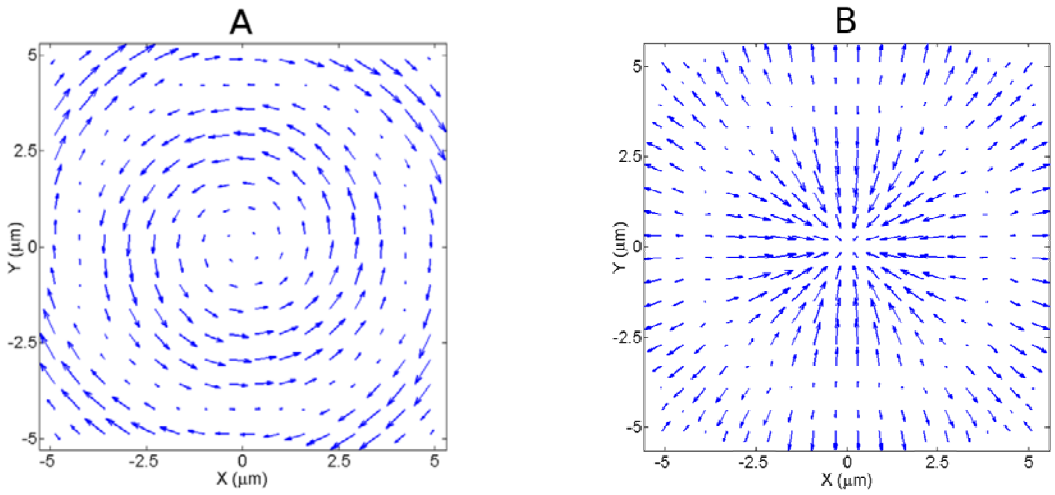

Figure 8: (a)Azimuthal polarization radiated from a TM polarized mode and (b)radial polarization radiated from a TE polarized mode in a plane 16µm above the CBR.

It is clearly seen that the TE optimized CBR emits a radially polarized beam, while the TM optimized CBR exhibits an azimuthal polarization, that is the electric field is perpendicular to the radial direction. As a result, at the center of this beam the polarization state is not well-defined thus necessitating the field to completely vanish, as shown in Fig. **7**. In real structures the fabrication of perfectly circular CBRs is nearly impossible and small deformations in structure can be expected. Such deformation could result in slightly elliptic structure. The deformation of the structure was modeled by introducing a straight section of length ΔL in the y axis of a TM optimized CBR, as depicted in Fig. **9**.

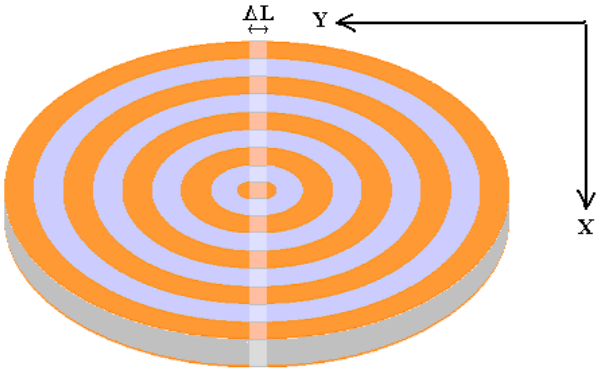

Figure 9: An elliptic CBR is formed by the straight deformation factor ΔL.

In order to check the effects of the deformation on the emission characteristics similar simulations were run on CBRs with different deformation factors ranging for 0 to 100nm. The polarization of the emitted beam did no change dramatically, still exhibiting its clear azimuthal tendency. The properties which did change significantly are the Q-factor and the resonance wavelength, which are shown in the Fig. **10**.

As ΔL is increased, the resonance wavelength red-shifts. Surprisingly, the Q-factor of the structure also increases with ΔL although the perfectly symmetric CBR is designed for maximal confinement of the field in the central disk. This increase in the Q stems from the coherent vertical Bragg reflection induced by the structure. One of the loss mechanisms in the structure is the vertical emission which is responsible to the formation of the output beam depicted in Fig. **7**. Apparently, the impact of the deformation on this scattering is substantially larger than its impact of the lateral Bragg confinement, resulting in a substantial lower vertical emission which, consequently, increases the over-all Q-factor of the cavity.

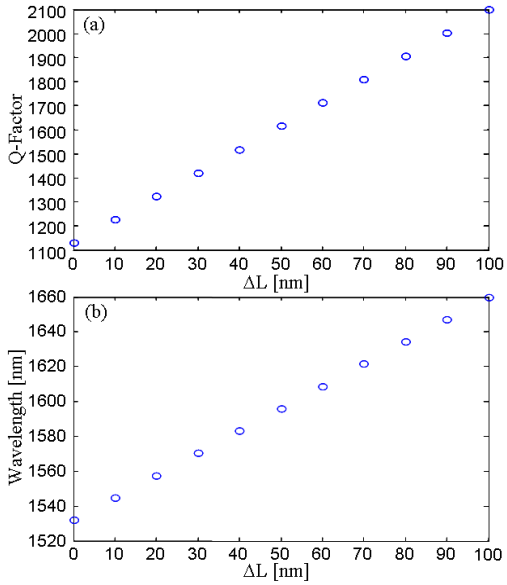

Figure 10: Q factor (a) and resonance wavelength (b) as a function of the deformation factor ΔL.

5. APPLICATIONS: BIOCHEMICAL AND ROTATION SENSING

Among the most straightforward approaches for optoelectronic (bio)chemical sensing is to detect the change in the refractive index or the absorption caused by the presence of a (bio)chemical agent. Several schemes have been suggested to detect these types of changes, employing directional couplers [17], Mach-Zehnder interferometers (MZI) [18] or high-Q optical resonators [19].

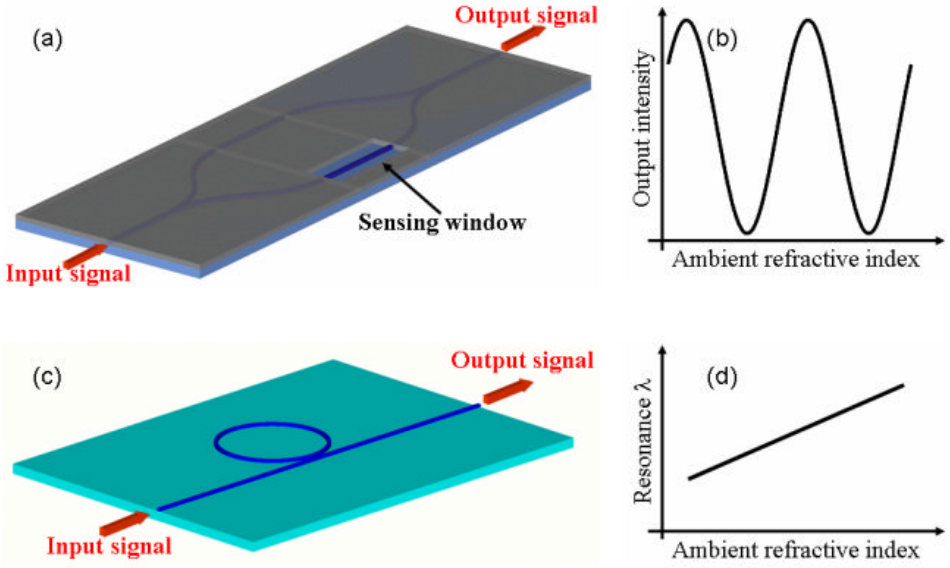

Figure 11: (a)MZI-based biochemical sensor; (b)Output signal dependence on the ambient refractive index for the MZI sensor; (c)Micro-ring based sensor; (d)Resonance wavelength dependence on the ambient refractive index for the micro-ring sensor.

The two later concepts are illustrated in Fig. **11**. The detection mechanism underlying these sensors is the modification of the phase accumulation rate (*i.e.*, the propagation coefficient) of the field due to the interaction of the evanescent tail of the field with the analyte. In the MZI-based senor, one of the channels is exposed to the surrounding while the other is not. The existence of the biochemical agent modifies the

phase shift accumulated by the signal traveling through the exposed channel, thus modulating the intensity of the signal at the MZI output port. In the microring based sensor, the existence of the biochemical agent modifies the phase accumulated by the electromagnetic wave circulating in the cavity, thus modifying the resonance wavelength of the micro-ring. The detection of this shift (*e.g.* by monitoring the output intensity of light launched in the original resonance wavelength) indicates the existence of the biochemical reagent.

The primary disadvantage of these detection methods is that the interaction of the field with the surrounding environment is weak, and therefore, the influence of the analyte on the propagation coefficient is small. As a result, achieving high sensitivity requires large interaction length leading to the requirement of long interferometers and very high-Q resonators. In addition, the MZI-type sensors might have difficulties detecting small numbers (or single) molecules, regardless of their length. On the other hand, the CBR structure and mode profile allow for the interaction of the non-evanescent part of the field, especially when the device is designed to include an air defect. As a result, CBR-based sensors are expected to offer significantly enhanced sensitivity compared to sensors that are based on conventional resonators of similar dimensions and materials [20].

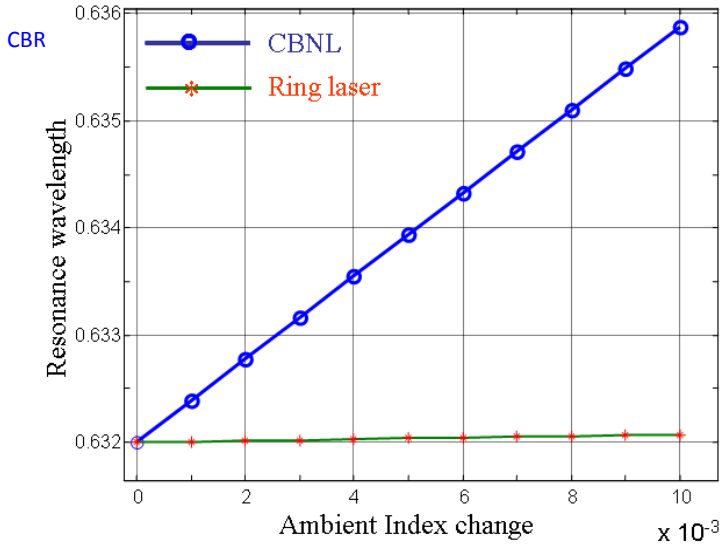

Figure 12: Comparison of the sensitivity of an CBNL and a conventional ring resonator to changes in the refractive index of the surroundings.

Fig. **12** shows a comparison between the shifts of the resonance frequency of a CBR and a conventional ring resonator due to changes in the refractive index of the surroundings. The CBR structure consists of alternating layers with refractive indices of 1.545 and 1.0 and an air defect. The conventional resonator consists of n=1.545 core surrounded by air cladding. Both resonators are approximately 16μm in diameter and designed to resonate in the visible wavelength regime. The sensitivity of each device is indicated by the slope of the curves shown in Fig. **11**. The resonance wavelength of the conventional ring resonator shifts by approximately 0.007 nm for an increase of 10^{-3} in the refractive index. For the same index change, the Bragg resonator's resonance wavelength shifts by 0.4nm, *i.e.*, the CBR exhibits higher sensitivity by a factor of 60.

In addition to sensitivity, an important feature for any biochemical sensor is selectivity, *i.e.,* the ability to response to a specific chemical or agent. In additional to the obvious significance (reducing the "false alarm" rate, *etc.*), this ability is important because it provides a mean of identifying biochemical materials and not only detecting their presence. The combination of compact yet sensitive sensors with biochemical selectivity allows constructing an array of sensors where each one is dedicated to a specific agent. Such an array is literally a complete biochemical lab implemented on a single chip, in particular, if combined with an efficient delivery system such as a micro-fluidic channels network [21].

In order to achieve selectivity, the resonator surface must be coated with specific binder with high affinity to the analyte [22]. This is the most commonly used method for realizing selectivity in optical sensors. For bacterial sensing, for instance, the sensor's surface is usually coated with a layer of specific antibodies, which are capable of binding specific types of bacteria to the sensor surface (see Fig. **13**). This coating ensures that only specific kind of bacteria, which matches the antibodies, can bind and influence the resonator optical properties. Unlike conventional resonators, for which the evanescent part probes only a small part of the cell (~200 nm), the Bragg resonator modal field can interact with the whole cell – attaining higher sensitivity without sacrificing the selectivity properties.

Another interesting and important application of the CBR structure is rotation sensing. Rotation sensors and Gyroscopes have numerous applications ranging from inertial navigation systems in aircrafts and vessels to control, stabilization and positioning systems for robotics, virtual reality applications and more. While rotation sensing can be based on both mechanical and optical effects, it is the optical Gyros which provide both higher sensitivity and lower drift rates.

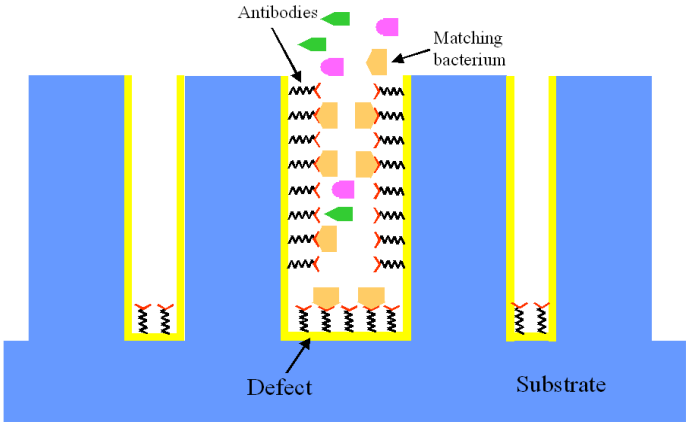

Figure 13: Antibodies coated Bragg resonator for enhanced selectivity.

Although the details may vary according to the specific implementation, all optical rotation sensors exploit the Sagnac effect [23] – the different phase shifts accumulated by waves propagating in a circular path along or against the rotation direction. This phase shift is then converted to measurable optical power using interferometry. The Sagnac phase shift exhibits some interesting characteristics, in particular, it is determined solely by the angular velocity, the optical frequency and the area circumvented by the closed-loop optical path while completely independent of the medium index of refraction and dispersion properties [24, 25]. This surprising property of the Sagnac effect has been the subject of ongoing debates for several decades [24] not only because to its fundamentality but also because it inherently limits the possibilities to attain highly-sensitive miniaturized rotation sensors.

Recently, we have proposed a novel approach for rotation sensing based on the rotation induced modification of radial Bragg reflection [26]. This effect, which is as fundamental as the Sangac effect, exists also in conventional optical rotation sensors but it is negligible compared to the Sagnac phase shift in such gyros. In CBR, on the other hand, this effect could be substantially larger than the Sagnac phase shift, thus providing a completely new approach for rotation sensing which can potentially achieve sensitivities which are order of magnitude larger that those of conventional optical rotation sensors.

To demonstrate that increase of sensitivity in CBR, we reconsider how Eq. (1) is modified once the device is exposed to rotation. For simplicity, we assume the CBR is rotated around the symmetry axis z in an angular velocity Ω_r, which is relatively slow compared to the transient time of light across the device, *i.e.,* $\Omega_r << c/L$ where c is the velocity of light in vacuum and L is the maximal dimension of the CBR. Under these circumstances, mechanical relativistic effects can be neglected and the impact of rotation is introduced as [26]:

$$\begin{bmatrix} \rho^2\frac{\partial^2}{\partial\rho^2}+\rho\frac{\partial}{\partial\rho}+\left(k^2(\rho)-\beta^2\right)\rho^2+\frac{\partial^2}{\partial\varphi^2} \\ +2ik\frac{\Omega_r}{c}\rho^2\frac{\partial}{\partial\varphi} \end{bmatrix}\begin{pmatrix} E_z \\ H_z \end{pmatrix}=0, \tag{14}$$

where the last term is the leading term due to rotation subjected to Maxwell Eqs. in a non-inertial frame of reference. Introducing (2) into (14) suggests that the rotation of a CBR basically modifies the index of refraction, such that (14) regains the form of (1), with the replacement $n_0 \rightarrow n_{eff}$, and n_{eff} is given by:

$$n_{eff}^2 = n_0^{\,2} + 2m\frac{\Omega_r}{\omega} \tag{15}$$

where n_0 is the refractive index profile of the (stationary) CBR, m is the azimuthal number and ω is the optical angular frequency. The solutions of (14) are now dictated by the angular velocity, which splits the counter-propagating degenerate wavenumbers k ($k_0=k\cdot n_{eff}$) into two different wavenumbers according to (15). This splitting shifts the resonance frequency of the resonator relatively to its stationary value by $\Delta\omega$, where

$$\left|\Delta\omega\right| = m\frac{\Omega_r}{n_0^{\,2}} \tag{16}$$

As shown in [26, 27], in a stationary CBR, the photon lifetime τ, which as previously mentioned is linked to the Q factor by the relation $Q=\omega_0\tau$, exhibits an exponential dependence on the overall length of the Bragg reflector and the perturbation strength:

$$\tau \propto \exp\left[2\frac{\Delta\varepsilon\cdot\omega_0}{\pi n_0 c}\left(\rho_R-\rho_0\right)\right] \tag{17}$$

Once the CBR is rotated in a non-vanishing angular velocity, the average refractive index, n_0, and the perturbation, $\Delta\varepsilon$, are modified according to (15). Nevertheless, $\Delta\varepsilon$ remains virtually identical, as the entire structure experiences a uniform rotation, *i.e.,* the dielectric coefficient increases or decreases entirely in the same manner such that no additional perturbation is formed. Assuming that the rotation rate is relatively small compared the optical resonance frequency, we find that:

$$\tau\left(\Omega_r\right)=\tau\left(\Omega_r=0\right)\exp\left[-\frac{4m\Delta\varepsilon\cdot\left(\rho_R-\rho_0\right)}{\pi n_0^{\,3} c}\Omega_r\right] \tag{18}$$

Eq. (18) holds the key to the great potential of employing the CBR for rotation sensing: the exponential dependence of the Q factor on the rotation rate (compared to the linear dependence of the Sagnac phase shift in conventional optical Gyros), allows for substantial increase in the sensitivity of the device.

Eq. (18) provides the static dependence of the photon lifetime of the CBR on the rotation rate. However, in a laser the dynamic properties of the field and the population inversion introduce substantial complexity when the device is pumped above lasing threshold. Thus, it is essential to analyze the dynamics of the CBR laser using the rate Eqs. for the counter-propagating waves and the population inversion. The rate Eqs. of the fields are coupled with a Bloch Eq. for the excess carrier charge density. Together they complete a set which its solution defines the temporal evolution of the electrical and magnetic fields in the CBR.

Eq. (19) describes the conventional rate Eq. model for a dual mode laser which was modified in order to incorporate the impact of rotation. The first two Eqs. describe the temporal evolution of the amplitudes of the clockwise and counterclockwise waves. The third Eq. describes the dynamic behavior of the carrier density.

$$\begin{aligned}
\frac{dE_{cw}}{dt} &= \frac{1}{2}(1+i\alpha)\cdot\left(G_{cw}-\frac{1}{\tau_p^{cw}}\right)\cdot E_{cw}-\kappa_{cw}E_{ccw}+ \\
&\quad +i\cdot\Delta\omega\cdot E_{cw} \\
\frac{dE_{ccw}}{dt} &= \frac{1}{2}(1+i\alpha)\cdot\left(G_{ccw}-\frac{1}{\tau_p^{ccw}}\right)\cdot E_{ccw}-\kappa_{ccw}E_{cw}+ \\
&\quad -i\cdot\Delta\omega\cdot E_{ccw} \\
\frac{dN}{dt} &= \frac{J}{e\cdot 2\Delta\rho}-\frac{N}{\tau_s}-G_{cw}\cdot|E_{cw}|^2-G_{ccw}\cdot|E_{ccw}|^2
\end{aligned} \tag{19}$$

G is the overall gain, τ is the cavity lifetime and α is the phase-amplitude coupling, also known as the linewidth enhancement factor. Coupling between the counter-propagating waves due to backscattering is manifested through $k=k_c+ik_d$, which consists of a dissipative and conservative components. The last term, $\Delta\omega$, represents the rotation induced frequency change of the resonance given by (16). The third Eq. describes the carrier density, and its dynamics is affected by the charge density of the pump J/e (normalized to the laser active thickness $\Delta\rho$), the carriers' lifetime τ_s, and the depletion associated with the modal fields gain. The gain coefficient G is given by

$$G_{cw/ccw}=G_n\cdot(N-N_0)\cdot\left(1-\gamma_s\left|E_{cw/ccw}{}^2\right|-\gamma_c\left|E_{ccw/cw}{}^2\right|\right) \tag{20}$$

where G_n is a small signal gain, N_0 is the carrier density at transparency and γ_s, γ_c are respectively the self- and cross- saturation coefficients.

It is useful to normalize (19) to form a dimensionless set of equations. We introduce the definitions of reference [28], rescaling the time with respect to the stationary-CW-photon-lifetime at rest τ^p_{cw}, and define the pump factor μ which is normalized with respect to the lasing threshold:

$$\begin{cases}
E_{1/2}=\sqrt{G_n\tau_s}\cdot E_{cw/ccw};\quad n=G_n\left(N-N_0\right)\tau_p{}^{CW} \\
\tau=\dfrac{t}{2\tau_p{}^{CW}};\quad \mu=\dfrac{J-J_0}{J_{th}-J_0} \\
\gamma=\dfrac{\tau_p^{CW}}{\tau_s};\quad \gamma_p=\dfrac{\tau_p^{CW}}{\tau_p^{CCW}};\quad \Delta=m\cdot\Omega_{rot}\cdot 2\tau_p{}^{CW} \\
s=\gamma_s\big/G_n\tau_s;\quad c=\gamma_c\big/G_n\tau_s; \\
\xi_{1/2}=1-s|E_{1/2}|^2-c|E_{2/1}|^2
\end{cases} \tag{21}$$

Introducing (20) and (21) into (19), yields:

$$\begin{aligned}
\frac{dE_1}{dt} &= (1+i\alpha)\cdot(\xi_1 n-1)\cdot E_1-\left(k_d^{cw}+ik_c^{cw}\right)E_2+ \\
&\quad +i\cdot\Delta\cdot E_1 \\
\frac{dE_2}{dt} &= (1+i\alpha)\cdot(\xi_2 n-\gamma_p)\cdot E_2-\gamma_p\left(k_d^{ccw}+ik_c^{ccw}\right)E_1+ \\
&\quad -i\cdot\Delta\cdot E_2 \\
\frac{dn}{dt} &= 2\gamma\cdot\left[\mu-n\cdot\left(1+\xi_1\cdot|E_1|^2+\xi_2\cdot|E_2|^2\right)\right]
\end{aligned} \tag{22}$$

Eqs. (22) are solved numerically to obtain the evolution of the modal fields in time and examine the impact of the various parameters. Fig. **14** depicts the temporal evolution of the amplitudes of the fields and the carrier density for a specific choice of parameters (see figure caption). Because of the rotation induced difference in the photon lifetime experienced by the CW and CCW propagating waves, the amplitudes of the counter-propagating split where the mode experiencing lower loss dominates. To understand the impact of the various parameters on the response of the CBR laser to rotation we solved (22) for several sets of parameters. The cross and self gain modulation coefficients are $c=2s=0.006$ [29], α=3.5, m=9, $\tau_p^{cw/ccw}(\Omega_r=0)$=10ps, τ_s=1ns, $G_n=10^{-6}\text{cm}^{-3}/\text{s}$, $N_0=3.5\cdot10^{16}\text{cm}^{-3}$, $k_d^{cw/ccw}=-10^{-4}$, and $k_c^{cw/ccw}=10^{-3}$.

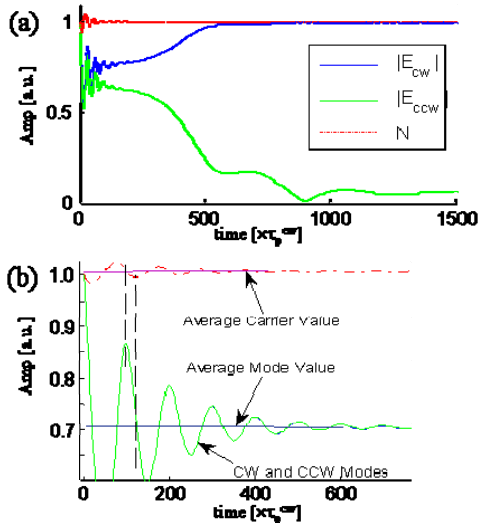

Figure 14: Counter-propagating modes splitting (a) and relaxation oscillations between the excess carrier charge and the modal field (b). $\Omega_r=10^6$; τ_p^{cw}=10ps; τ_p^{ccw}=9.98ps; τ_s=1ns; μ=2.

Fig. **15** depicts the evolution of the modal fields and the carrier density for various pump levels. As can be intuitively expected, higher pump levels yield faster convergence to steady state and a larger contrast between the amplitudes of the lasing modes at steady state. In order to quantify these effects, we define the splitting time as the period elapsed from turn on at which the difference between the amplitudes of the CW and CCW waves exceeds 1%. We can then investigate the dependence of the splitting time on the rotation rate, pump level and the other parameters.

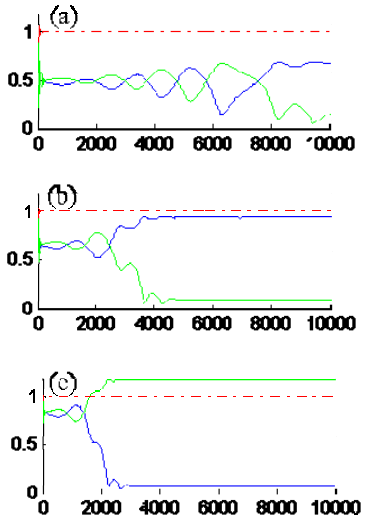

Figure 15: Rotating CBR dynamics for different pump powers: (a)μ=1.5; (b)μ=1.9; (c)μ=2.4.

Fig. **16** shows the dependence of the splitting time on the rotation rate for μ=2, m=9. Three different zones are found: extremely low rates (less than 0.02 degrees per hour), midrange and high rotation rates.

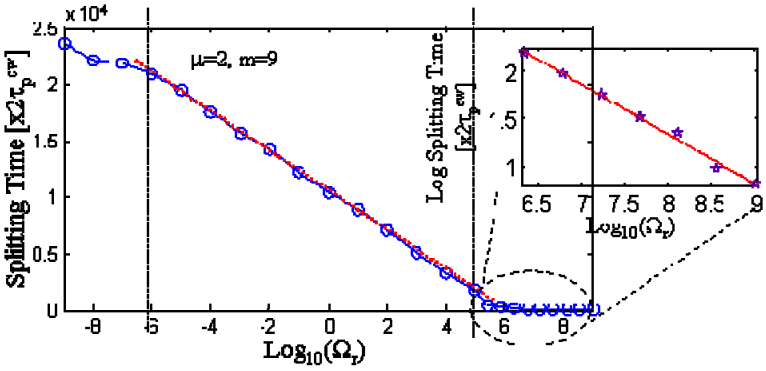

Figure 16: 1% Splitting time *vs.* rotation rate. Inset: high rotation rates (notice logarithmic scale to reveal a linear dependence of the splitting time in the rotation rate).

As can be seen in Fig. **16**, the splitting time decreases monotonically as the rotation rate is increased. The dependence on the rotation rate is logarithmic for the midrange, and linear for high rotation rates. Similar dynamics is found for other sets of pump parameters and azimuthal modal numbers. Fig. **17** shows the dependence of the splitting time on the pump level for various rotation rates. To good agreement, the splitting time dependence on the pump factor can be modeled as:

$$T_{split}\left(\kappa,\mu,\Omega_r,m\right)=\frac{p_1\left(\kappa,m\right)\log\left(\Omega_r\right)+p_2\left(\kappa,m\right)}{\log\left(\mu\right)} \qquad \textbf{(23)}$$

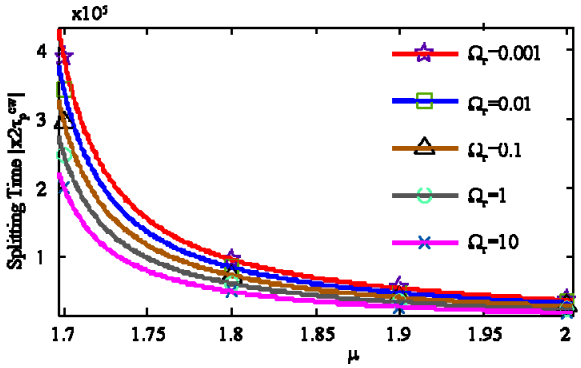

Figure 17: Splitting time fittings to the pump factor and rotation rate.

Clearly, as the rotation rate is increased, the bifurcation becomes more significant. Higher angular rotation rates generate larger rotation-induced changes in the refractive indices of the Bragg reflectors, resulting in stronger impact on the splitting of the degenerate mode. This dynamics is mainly evidential through the decrease in the splitting time itself and the increase of the contrast of the modes' amplitudes (referred to as 'visibility'), as shown above. The logarithmic correlation between the splitting time and the rotation rate suggests that the sensitivity of a rotating-CBR based device practically increases as the rotation rate decreases. Although this is true only for a certain range of angular velocities, this unique observation renders the employment of such a device for slow rotation sensing applications highly attractive.

6. CBR FABRICATION AND CHARACTERIZATION

Circular Bragg resonators based nanolasers of several geometries and Bragg reflector orders were fabricated within a thin membrane of InGaAsP semiconductor material [30]. A cross-section of the

semiconductor epitaxial structure used is illustrated in Fig. **18**. The layers were grown by MOCVD on a (100) oriented InP substrate. This structure consists of a 500 nm thick InP buffer layer, followed by a 50 nm InGaAsP (λ_g = 1.3 μm) stop etch, and a 250nm InP sacrificial layer. A 250nm membrane composed of 605 Å InGaAsP (λ_g = 1.1 μm) layers sandwiching six 75Å quantum wells (1% compressive strain) separated by 120 Å InGaAsP barriers (λ_g = 1.2 μm, 0.5% tensile strain) completes the structure. Photoluminescence from the quantum wells peaks at a wavelength λ = 1559 nm. Annular Bragg resonators were designed to have resonant wavelengths between 1.5-1.6μm, for large overlap with the gain spectrum of the multi-quantum-well material.

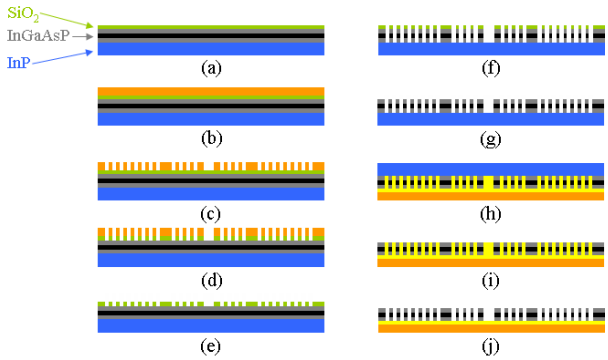

Figure 18: InGaAsP/InP multi-quantum-well semiconductor structure process (a) SiO_2 etch mask deposition; (b) PMMA spin coating; (c) E-beam lithography & develop; (d) SiO_2 etch; (e) PMMA stripping; (f) InGaAsP membrane etch; (g) SiO_2 stripping; (h) Chip flipping and bonding to sapphire; (i) InP substrate etch; (j) Adhesive etch.

The optical gain of the semiconductor epitaxial structure used favors the TE polarization (H_z), because of the optical properties of compressively strained quantum wells [31]. Therefore, the design of the fabricated devices is optimized for this polarization. In order to simplify the design calculations, we employ the effective index approximation in the vertical dimension. An effective index n_{eff} = 2.8 is found by solving for the TE-polarized mode of the transferred InGaAsP slab. To facilitate the fabrication of the device, a mixed Bragg order scheme is used, with second-order (3 λ/4 ~ 430 nm) high-index layers and first-order (λ/4 ~ 400 nm) low-index layers.

In addition to relaxing the fabrication tolerances, the mixed Bragg order implementation induces a coherent diffraction component in the vertical direction [26]. Although this mechanism reduces the overall Q of the cavity, it facilitates the observation and measurement of the resonator emission.

The procedure followed to fabricate the annular Bragg resonators is as follows. First, an etch mask consisting of 120 nm of PECVD SiO_2 was deposited on the semiconductor substrate. A 550 nm thick layer of PMMA electron-sensitive resist was spin-coated onto the substrate, and electron beam lithography was used to define the resonator patterns in the PMMA. The patterns were then transferred to the SiO_2 layer with a reactive ion etching (RIE) step in after which the remaining PMMA was stripped using O_2 plasma. Then, a second RIE step was used to transfer the SiO_2 pattern through the 250 nm thick InGaAsP membrane. Finally, the remaining SiO_2 etch mask was removed with a wet chemical etch.

The high refractive index of the InP substrate ($n \approx 3.17$ at λ = 1.55 μm) reduces the vertical confinement of the guided optical mode within the membrane. Therefore, in order to achieve strong vertical optical confinement and improve the quality factor Q of the resonators, the patterned InGaAsP membrane must be surrounded by low index material. One method for achieving this is to generate an air-suspended membrane by selective removal of the InP beneath the device, as is commonly done with photonic crystal devices [31, 32]. However, this technique is not applicable to the resonators studied here, because the concentric ring structure would collapse if the solid substrate were removed. Therefore, the resonators were flip-bonded to a double-side polished sapphire substrate with a thin layer of UV curable optical adhesive (Norland NOA 73, $n \approx 1.54$ at λ = 1.55 μm). After fully curing the adhesive under a UV lamp, the InP substrate was

removed using a combination of mechanical lapping and selective chemical etching. Note that the excellent thermal properties of sapphire can improve the conduction of heat generated during optical pumping away from the membrane. In addition, the large bandgap energy of sapphire, and associated transparency at visible and infrared wavelengths, permits optical pumping and imaging of the resonator luminescence from either the top or bottom of the device. Transfer of the semiconductor membrane to a transparent substrate also facilitates use of annular Bragg resonators for sensing applications. For instance, a solution containing an analyte whose concentration is to be monitored by the resonator could be introduced *via* the exposed topside of the device, while optical pumping of the resonator and imaging of the sensor signal could be accomplished through the transparent substrate.

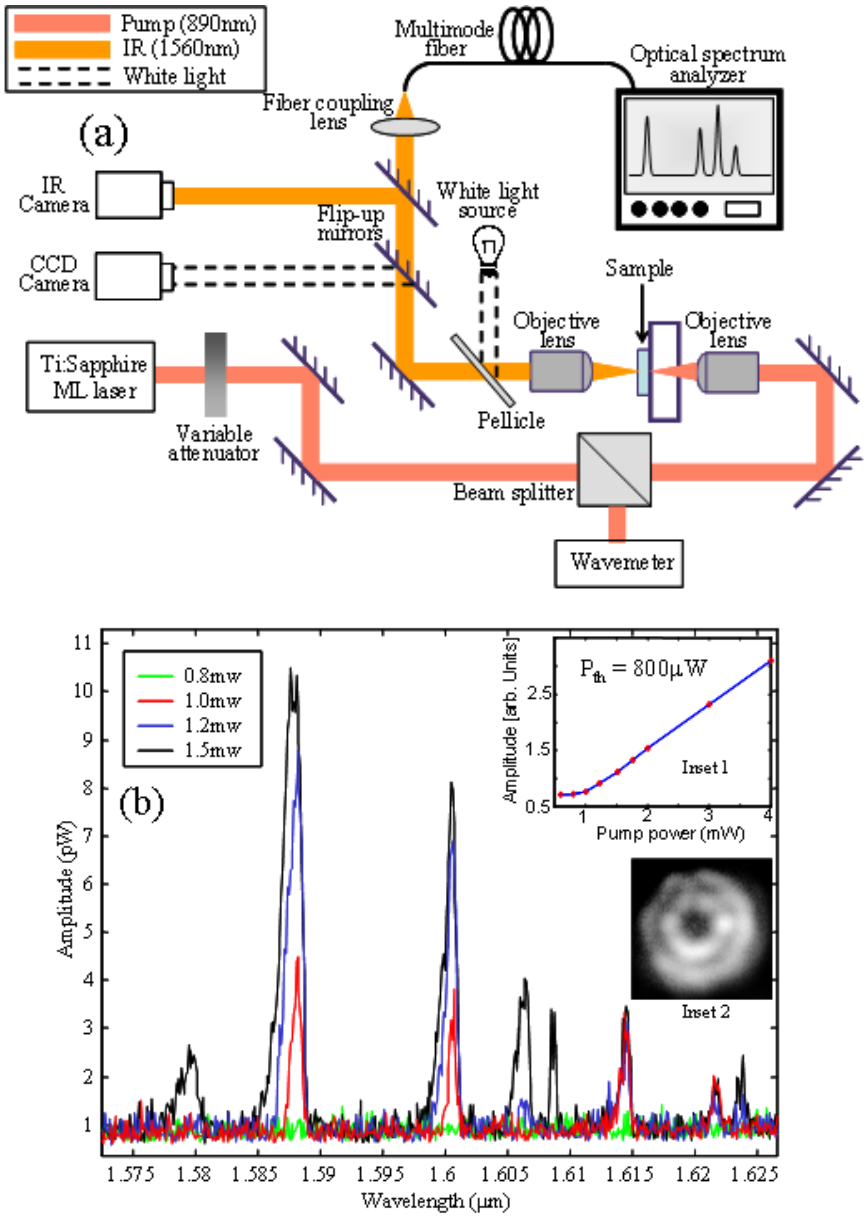

Figure 19: (a)The experimental setup. (b)Optical spectra emitted from a CBNL under different pump levels. Inset: Integrated emitted power *vs.* pump power, showing laser threshold at ~ 800 mW. Inset2 – Lasing pattern.

We measured and analyzed the vertical emission from the resonators under pulsed optical pumping. The experimental setup is illustrated in Fig. **19(a)**: A Ti:sapphire mode-locked laser was used to optically pump

the devices at a center wavelength of 980 nm, repetition rate of 76.6 MHz and pulse duration of approximately 150 fs. A variable attenuator was used to control the pump power. The average pump power and center wavelength were monitored by a wavemeter, through a 50/50 beamsplitter. The pump beam is focused on the back side of the sample with a 50X objective lens. A 20X objective lens is used to collect the vertical emission from the sample and to focus it on an IR camera to obtain the NF intensity pattern and to couple the light into a multi-mode fiber to obtain the emitted spectrum. A CCD camera is used to image the resonators and the pump spot, for alignment purposes, using a white light source.

When the un-patterned QW layer structure is pumped, the emitted spectrum consists of a wide peak centered at 1559 nm. As the pumping power is increased from 1 mw to 20 mW, the FWHM of the luminescence broadens from approximately 70 nm to 110 nm, and the peak of the photoluminescence shifts towards longer wavelength due to heating. No significant shift is observed when the pump power is below 5 mW, indicating that heating is of less significance at these pump levels. When a laser is pumped, the emission characteristics change significantly. While the specific details (threshold levels, emitted wavelengths, *etc.*) vary from device to device, the overall behavior is similar. Once a certain pump intensity threshold is exceeded, clear and narrow (~0.5 nm FWHM) emission lines appear in the spectrum (see Fig. **19(b)**). As the pump intensity is increased, the intensity of the emission lines increase as well and they broaden towards shorter wavelengths. Increasing the pump power further results in the appearance of additional emission lines.

Depending on the defect width and design, the CBR based laser can emit patterns with very small angular modal number (see Fig. **20**). These modes correspond to effective index which is lower than 1 and, thus, cannot evolve in conventional, TIR based, micro-ring lasers. The ability to support such lasing modes provides substantial flexibility and control over the properties of the modal field, allowing for the engineering of field profiles that are highly susceptible to changes in the ambient refractive index.

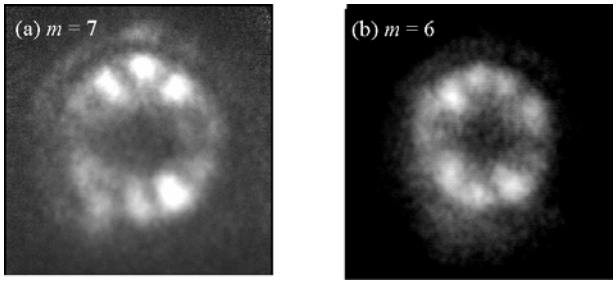

Figure 20: IR images of emitted patterns with small angular modal number (a) m=7 and (b) m=6.

Fig. **21(a)** and **21(b)** show respectively an SEM micrograph of a CBR based laser and conventional ring based sensors realized within a thin membrane of InGaAsP active material. Fig. **21(c)** and **21(d)** depict a cross-section of the mode profile of the CBNL and the conventional ring. The index structure is superimposed on the calculated mode profiles. The field profile of the CBNL peaks in the defect and decays while oscillating in the reflector regions. Fig. **21(c)** and **21(d)** also illustrate the advantages of the CBNL structure for sensing applications. Even though the main lobe of the mode profile does not interact with the device surroundings, significant part of the field within the trenches between the semiconductor rings are exposed to the surroundings, thus yielding large interaction volume (compared to a conventional resonator). Thus, a CBR based sensor is expected to exhibit enhanced sensitivity compared to a conventional resonator of similar dimensions.

To demonstrate the advantages of CBR-sensors in terms of sensitivity and resolution, we compare the performance of our device to that of a conventional ring resonator with 5 μm radius consisting of the same material [33]. The conventional ring was tested under the same conditions (pump power, spot-size, *etc.*) that were used to characterize the CBR sensor. Fig. **22** depicts the relative shifts in the resonance wavelengths of the CBR and the conventional microrings as a function of the ambient refractive index. The sensitivity of the conventional resonator is approximately $d\lambda/dn \sim 33$ nm (dashed) and the resonance

FWHM is ~1.4 nm wide, while the sensitivity of the CBR is $d\lambda/dn$ ~ 130 nm (solid) and the resonance FWHM is ~1 nm wide. As a result, the advantage of the CBR as a sensor is two-fold: 1) The sensitivity of the CBR is 4 times larger than that of the conventional device because of the larger interaction volume and 2) the conventional resonator has wider linewidth because of its lower Q, which reduces the ability to resolve the resonance wavelength.

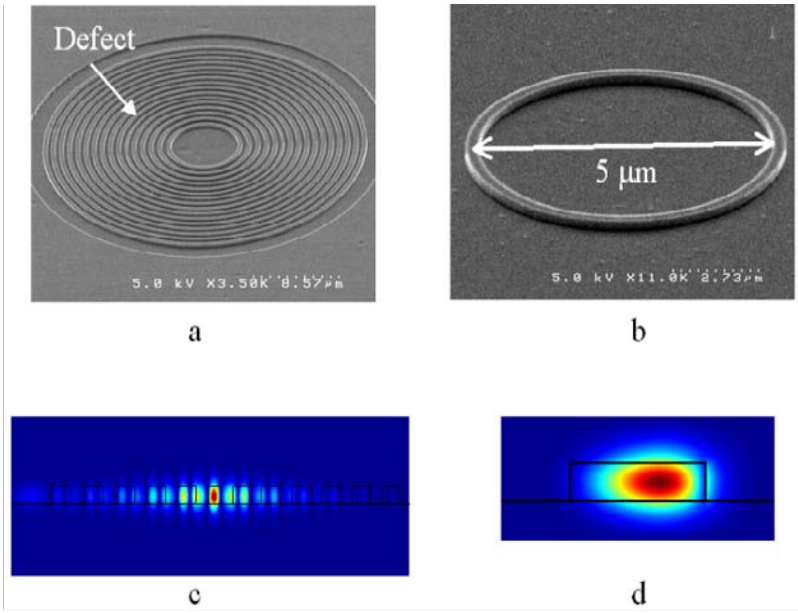

Figure 21: SEM images of the CBNL (a) and the conventional ring (b) sensors, and their corresponding modal field profiles (c, d).

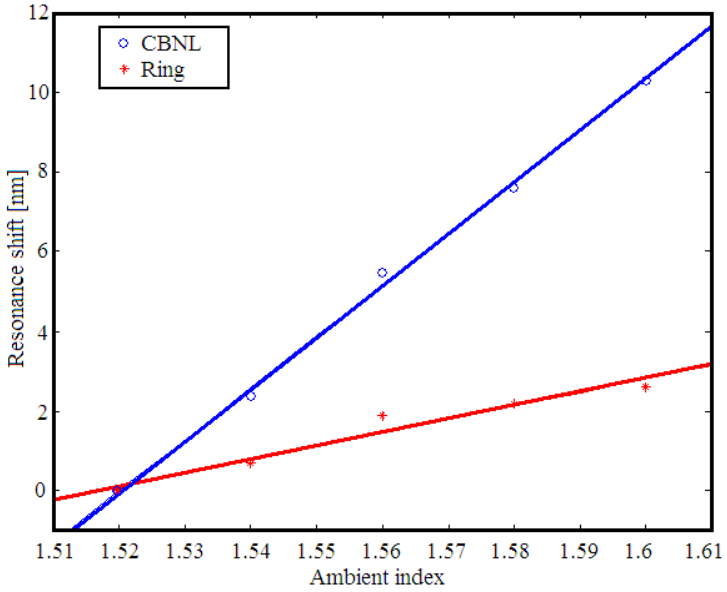

Figure 22: Comparison between the shifts in the emitted wavelength of a CBNL (blue) and a conventional ring laser (red) for changes in the ambient refractive index.

For the 1nm linewidth of the CBR, shifts in the resonance wavelength of 0.1nm can be easily resolved, thus allowing the detection of ambient index changes of Δn~5×10^{-4}, which to our knowledge is the one of the best resolutions ever demonstrated using integrated optical nano-sensors [13]. As a comparison, for 1.4 nm

FWHM of the conventional ring, the ability to resolve the resonance wavelength is limited to ~0.14 nm, which when combined with the lower sensitivity of the conventional device, yield a minimum detectable index change of $\Delta n \sim 4 \times 10^{-3}$ – approximately an order of magnitude less than that of the CBR sensor.

CONCLUSIONS

We have studied, theoretically and experimentally, the characteristics of a novel class of lasers that are based on radial Bragg reflectors. Lasing action with low threshold levels are demonstrated at room temperature under pulsed optical pumping. The observed *Q* factors are in the order of several thousands. The unique characteristics on these lasers make them promising candidates for numerous applications in telecommunications, sensing and basic research.

Circular Bragg resonators offer significant enhancement of the ability to detect small changes in the ambient refractive index, compared to conventional micro-rings, because of their lager interaction volume and *Q*. Sensitivity enhancement of an order of magnitude in a CBR compared to conventional resonators has been demonstrated experimentally. Further enhancement of the CBR sensor sensitivity can be achieved by employing an air-defect design. The lasers' highly compact dimensions and enhanced resolution make them excellent candidates for becoming key components for the realization of compact, integrated biochemical sensor arrays.

In addition to biochemical sensing, CBR are highly attractive for ultra-sensitive rotation sensing. We have shown that in such devices the *Q*-factor of the cavity exhibits exponential dependence on the rotation rate which increases for stronger perturbation and larger Bragg reflectors. In addition, it was shown that, in contrast to conventional micro-cavities, the rotation-induced relative change in the threshold gain level (or equivalently the cavity *Q*-factor) can be significantly larger than the shift in the resonance wavelength (the Sagnac effect). In particular, for the CBR structures, the relative change in the threshold gain level is larger by more than an order of magnitude than the corresponding shift in the resonance frequency. The reason for this profound difference between conventional microcavities and CBRs stems from the employment of a different radial confinement mechanism (TIR in conventional microcavities *vs.* Bragg reflection in CBR). The TIR mechanism is barely affected by the minuscule shifts in the effective index of refraction induced by the rotation (unless extremely close to cutoff conditions) while the Bragg confinement mechanism is highly susceptible to such changes. The dependence of the rotation-induced change in the *Q*-factor, and hence in the threshold gain level, on the parameters of the device differ significantly than the dependence of the Sagnac effect on these parameters. In particular, the response to rotation depends on the *diameter* and not the area of the resonator, and it is substantially affected by the average refractive index of the medium.

The dynamical behavior of a CBR laser subjected to rotation offer a simple approach for evaluating the rotation rate according to the split time. As the rotation rate is increased the split time decreases logarithmically. Higher pump levels, μ decrease the split time for a given rotation rate, thus allowing further increase in the sensitivity of the CBR rotation sensor.

The CBR offers a new approach to detect and measure mechanical rotation which relies on completely different mechanism than those underlying conventional optical gyros. Such approach can, potentially, increase the sensitivity of micro-rotation-sensors by order of magnitudes.

ACKNOWLEDGEMENTS

The partial support of the Israeli MOD and the Israeli Science foundation in this project is gratefully acknowledged.

REFERENCES

[1] Madsen CK, Zhao JH. Optical Filter Design and Analysis: A Signal Processing Approach. Wiley-Interscience, New York, NY 1999.

[2] Little BE, Chu ST, Haus HA, Foresi J, Laine J-P. Microring resonator channel dropping filters. J Lightwave Technol 1997; 15: 998-1005.
[3] Yariv A. Critical coupling and its control in optical waveguide-ring resonator systems. IEEE Photon Technol Lett 2002; 14: 483-485.
[4] Heebner JE, Boyd RW. 'Slow' and 'fast' light in resonator-coupled waveguides. J Mod Opt 2002; 49: 2629-2636.
[5] Chao CY, Guo LJ. Biochemical sensors based on polymer microrings with sharp asymmetrical resonance. Appl Phys Lett 2003; 83: 1527-1529.
[6] Boyd RW, Heebner JE, Lepeshkin NN, *et al.* Nanofabrication of optical structures and devices for photonics and biophotonics. J Mod Opt 2003; 50(15-17): 2543-50.
[7] Vahala KJ. Optical microcavities. Nature 2003; 424: 839-846.
[8] Marcatili EAJ. Bends in optical dielectric guides. Bell Syst Tech J 1969; 48: 2103-2132.
[9] Scheuer J, Yariv A. Annular Bragg defect mode resonators. J Opt Soc Am B 2003; 20: 2285-2291.
[10] Scheuer J, Green WMJ, DeRose G, Yariv A. Low-threshold two-dimensional annular Bragg lasers. Opt Lett 2004; 29(22): 2641-3.
[11] Scheuer J, Green WMJ, DeRose GA, Yariv A. Lasing from a circular Bragg nanocavity with an ultrasmall modal volume. Appl Phys Lett 2005; 86(25): 251101--3.
[12] Loncar M, Scherer A, Qiu Y. Photonic crystal laser sources for chemical detection. Appl Phys Lett 2003; 82(26): 4648-50.
[13] Chow E, Grot A, Mirkarimi LW, Sigalas M, and Girolami G. Ultracompact biochemical sensor built with two-dimensional photonic crystal microcavity. Opt Lett 2004; 29: 1093-1095.
[14] Yeh P, Yariv A, Marom E. Theory of Bragg fiber. J Opt Soc Am. 1978; 68(9): 1196-201.
[15] Scheuer J, Yariv A. Coupled-waves approach to the design and analysis of Bragg and photonic crystal annular resonators. IEEE J Quantum Elect 2003;39(12): 1555-62.
[16] Golowich SE, Weinstein MI. Homogenization expansion for resonances of microstructured photonic waveguides. J Opt Soc Am B 2003; 20(4): 633-47.
[17] Luff BJ, Harris RD, Wilkinson JS, Wilson R, Schiffrin DJ. Integrated-optical directional coupler biosensor. Opt Lett 1996; 21(8): 618-20.
[18] Luff BJ, Wilkinson JS, Piehler J, Hollenbach U, Ingenhoff J, Fabricius N. Integrated Optical Mach-Zehnder Biosensor. J Lightwave Technol 1998; 16(4): 583.
[19] Boyd RW, Heebner JE. Sensitive Disk Resonator Photonic Biosensor. Appl Opt 2001; 40(31): 5742-7.
[20] Scheuer J, Sun X. Radial Bragg Resonators. Photonic Microresonator Research and Applications. In: Chremmos I, Schwelb O, Uzunoglu N, editors.: Springer Berlin / Heidelberg; 2010. p. 361-91.
[21] Levy U, Shamai R. Tunable optofluidic devices. Microfluid Nanofluid 2008; 4: 97-105.
[22] Luff BJ, Harris RD, Wilkinson JS, Wilson R, Schiffrin DJ. Integrated-optical directional coupler biosensor. Opt Lett 1996; 21(8): 618-20.
[23] Post EJ. Sagnac Effect. Rev Mod Phys 1967; 39: 475-493.
[24] Arditty HJ, Leèfovre HC. Sagnac effect in fiber gyroscopes. Opt Lett 1981; 6(8): 401-3.
[25] Ezekiel S, Smith SP, Zarinetchi F. Basic Principles of Fiberoptic Gyroscopes. In Optical Fiber Rotation Sensors; Burns WK, Eds, Academic Press Inc., Boston, 1994.
[26] Scheuer J. Direct rotation-induced intensity modulation in circular Bragg micro-lasers. Opt Express 2007; 15: 15053.
[27] Scheuer J, Green WMJ, DeRose G, Yariv A. InGaAsP annular Bragg lasers: theory, applications and modal properties. IEEE J Sel Top Quant 2005; 11: 476-484.
[28] Sorel M, Giuliani G, Scirè A, Miglierina R, Donati S, Laybourn PJR. Operating Regimes of GaAs-AlGaAs Semiconductor Ring Lasers: Experiment and Model. IEEE J Quantum Elect 2003; 39: 1187-1195.
[29] Coldren LA, Corzine SW. Diode Lasers and Photonic Integrated Circuits, Wiley-Interscience Publications, New York, NY, 1995.
[30] Yoshie T, Shchekin OB, Chen H, Deppe DG, Scherer A. Planar photonic crystal nanolasers (II): Low-threshold quantum dot lasers. IEICE T Electron 2004; E87-C: 300-3007.
[31] Painter O, Lee RK, Scherer A, Yariv A, O'Brien JD, Dapkus PD, *et al.* Two-Dimensional Photonic Band-Gap Defect Mode Laser. Science. 1999; 284(5421): 1819-21.
[32] Kim S, Ryu H, Park H, *et al.* Two-dimensional photonic crystal hexagonal waveguide ring laser. Appl Phys Lett 2002; 81: 2499-2501.
[33] Green W, Scheuer J, DeRose G, Yariv A. Ultra-Sensitive Biochemical Sensor Based on Circular Bragg Micro-Cavities. CLEO/QELS 2005, Baltimore, Maryland, paper CPDA7.

CHAPTER 8

Photonic Crystal Fiber for Chemical Sensing Using Surface-Enhanced Raman Scattering

Yun Han and Henry Du*

Department of Chemical Engineering and Materials Science, Stevens Institute of Technology, Hoboken, NJ 07030, USA

Abstract: The unique feature of photonic crystal fiber (PCF) both as a light guide and a gas/liquid transmission cell allows synergistic integration of optics and microfluidics. There is a growing interest in PCF as a platform for spectroscopy-based chemical and biological sensing. In this chapter, we focus on PCF for sensing and detection using surface-enhanced Raman scattering (SERS). We examine the state-of-the-art, challenges and opportunities in the development of SERS-active PCF sensors.

Keywords: Photonic crystal fiber, surface-enhanced raman scattering, chemical sensing.

1. INTRODUCTION

Two-dimensional silica-based photonic crystal fibers (PCF, also known as microstructured or holey fibers) are glass fibers with a periodic array of air channels (sub-micron to tens of microns in diameter) running axially along the fiber length. They can be classified into two general categories: [1] solid-core PCF with light guiding in the silica core *via* total internal reflection due to index contrast between the core and the air cladding and [2] hollow-core PCF with light guiding in the air core *via* bandgap confinement by carefully configured periodic air cladding [1-5].

The design versatility of the air-silica cladding structure affords PCF many unique properties such as endlessly single mode, large mode area with high power transmission, high non-linearity, and broadly controllable dispersion [6-9]. As a new fiber optic research frontier, PCF are being increasingly explored for a multitude of scientific and technological applications that range from novel optical devices to multi-modality sensors [10-16]. The combination of waveguide characteristics and unique microstructure feature in the form of axial air channels over the entire fiber makes PCF a potentially robust and versatile chemical and biological sensing platform. Indeed, PCF have been increasingly explored utilizing spectroscopic sensing schemes based principally on absorption [17, 18], fluorescence [16], and Raman scattering [14, 15, 19].

Raman scattering provides a high degree of molecular structure information but the extremely small cross section of the event, typically 10^{-30} cm^2 to 10^{-25} cm^2, with the larger values occurring only under favorable resonance Raman conditions, precludes the use of Raman spectroscopy as a method for trace detection. Surface-enhanced Raman spectroscopy (SERS), first reported in 1970s [20-22], combining molecular fingerprinting capability with ultrahigh sensitivity, has tremendous potential for label-free molecular identification at trace or even single-molecule levels due to up to 10^{14} increase in the Raman scattering cross section of a molecule in the presence of nanostructured noble metals (mainly silver or gold) [23-25]. Another advantage of SERS, in contrast to other analytical techniques such as IR, is the ability to obtain high-quality spectra in water because Raman scattering from water molecules is inherently weak. This technique has been successfully used for monitoring of environmental pollutants in water [26, 27], food analysis [28, 29], detection of explosives and pathogens [30, 31].

The accessibility to the air channels of PCF has opened up endless possibility for functionalization of the channel surfaces (silica in nature) at the molecular and the nano scales. In particular, there has been a

***Address correspondence to Henry Du:** Department of Chemical Engineering and Materials Science, Stevens Institute of Technology, Hoboken, NJ 07030, USA; Fax: +01-201-216-5262; Email: hdu@stevens.edu

Marco Pisco, Andrea Cusano and Antonello Cutolo (Eds)
All rights reserved-© 2012 Bentham Science Publishers

growing interest in imparting the functionality of SERS in PCF for sensing and detection. We will discuss the current progress in the development of SERS-base PCF sensors, different sensing schemes, advantages and challenges of using two different types of PCF (*i.e.*, solid-core and hollow-core PCF) for SERS detection and measurements.

2. SOLID-CORE PCF FOR SERS SENSING

2.1. Raman Detection with Silica Core as an Internal Reference

Solid-core PCF as a spectroscopic sensing platform can be realized *via* interaction of evanescent field excitation of the analyte in the air channels immediately surrounding the light-guide solid core. For example, a solid-core PCF allowed absorption spectroscopic measurement of 6 parts per million (ppm) acetylene gas present in the air holes of the PCF *via* the evanescent field of the waveguiding core [32]. By filling analyte solution into the air channels of solid-core PCF, Raman scattering of analyte solution can be generated by interacting with evanescent field in the cladding air channels. These Raman signals can be then coupled into the fiber core and be detected from the fiber end.

Pristinski *et al.* [15] demonstrated Raman detection of acetonitrile solution using a solid-core PCF. The intrinsic Raman background signals from silica core were effectively utilized as an internal reference that alleviates otherwise difficult problems associated with light-coupling losses. Shown in Fig. **1(a)** are Raman spectra of bare PCF with laser attenuation as a parameter. The bands centered at 802 cm^{-1} (Si–O–Si bending) and 1048 cm^{-1} (Si–O stretching) were found to provide reproducible values after the dark noise subtraction and thus could serve as a useful internal reference. The reference silica Raman peak intensities have a linear power dependence, as illustrated in Fig. **1(b)**. A cutback experiment with bare PCF showed that short bare PCF (~50 cm) had negligible power loss, and the silica Raman peak intensities decreased linearly with the fiber length. A cutback experiment with an acetonitrile-filled PCF indicated that the overall losses in the optical system did not increase after the filling of the PCF air holes (Fig. **1(c)**). The normalized Raman peak intensities from silica core (802 and 1048 cm^{-1}) and from acetonitrile (2252 cm^{-1}, associated with C≡N stretching vibrations in acentonitrile) had nearly identical values and trends when plotted as a function of fiber length (Fig. **1(c)**). These results again suggested that silica Raman peaks from the fiber could be used as an internal reference for Raman spectroscopy when using solid-core PCF as a detection platform, alleviating problems arising from laser power variation and alignment irregularity. The increase in Raman intensities of acetonitrile with fiber length resulted from increased interaction path between excitation light and acetonitrile solution.

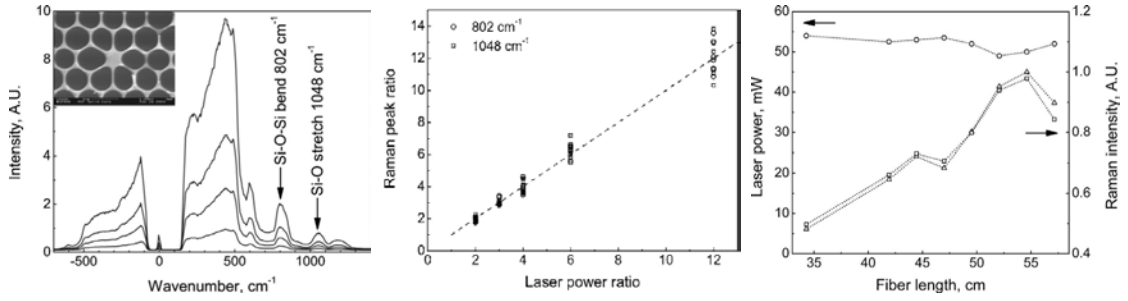

(a) (b) (c)

Figure 1: (a) Raman spectra of bare PCF. Fiber length 26.67 cm; laser power 8 mW exiting the fiber; laser attenuation 0, 3, 6, and 10.8 dB in descending order. Inset, scanning electron micrograph of the PCF structure. (b) Power dependence of two Raman peak intensities of bare PCF. Fiber length from 11.43 to 26.67 cm. (c) Length dependence of the laser power exiting the fiber (circles) and of Raman peak intensities of silica (triangles) and acetonitrile (squares). Reproduced with permission (ref. [15]).

2.2. SERS Detection with Analyte-Containing Colloidal Solution

Gold and silver nanoparticles have been extensively used for SERS because they provide very large Raman enhancement and can be easily synthesized in solution. One straightforward way of using solid-core PCF as

SERS platform is to fill a mixed solution of SERS- active gold or silver nanoparticles and analyte into cladding air channels. A solid-core PCF with a silica core surrounded by four large air holes (~20 μm in diameter) inside a periodical array of cladding air holes (cross section shown in Fig. **2(a)**) was utilized to detect a solution mixture of gold nanoparticles with Rhodamine B (RhB) at low concentration [33]. The gold nanoparticles for SERS enhancement were mixed with analyte in aqueous solution. The resultant solution mixture was then filled into cladding air channels up to ~1 cm in length *via* capillary force. During SERS measurements, the excitation light was coupled into one end of the fiber (measuring tip) while the other end of the fiber (probing tip) was filled with SERS-active solution. The excitation light propagated in the silica core and interacted with the gold nanoparticles and the analyte through the evanescent wave in the air holes, leading to a large interaction volume between the excitation light and the mixture of nanoparticles and analyte. The SERS signal generated from the sample partly propagated through the silica core and back to the measuring tip and was subsequently collected into the Raman spectrometer. Fig. **2(b)** shows the measured SERS spectra of RhB at different concentrations with a limit of detection of 10^{-7} M (curve A and C in Fig. **2(b)**). This solution mixture was also measured directly with the same excitation power and integration time, but no RhB SERS signal could be obtained. These results indicated that SERS detection sensitivity could be increased substantially using PCF as SERS sensing platform.

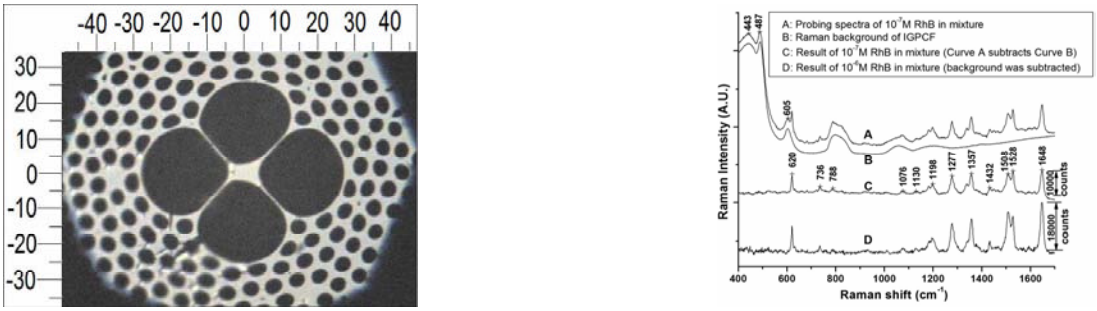

(a) (b)

Figure 2: (a) Cross section of photonic crystal fiber (scale: μm). (b) SERS spectra of Rhodamine B (RhB) mixed with gold nanoparticles (excitation power 4.7 mW; scan time 10 s; accumulation times 3). Reproduced with permission (ref. [33]).

2.3. SERS Detection with Metal Nanostructures Coated within Cladding Air Channels

SERS functionality can be imparted to solid-core PCF by directly depositing SERS-active metal nanostructures inside of their cladding air channels. For example, a high-pressure chemical deposition technique was used for this purpose [34]. An organic solvent was employed to deliver a silver precursor complex into the fiber air channels by a high pressure differential. The high-pressure flow overcame mass-transport constraints within the small fiber air channels. A simple thermal reduction method was utilized to reduce the precursor and hence to deposit silver nanoparticles within the PCF air channels. As shown in Fig. **3**, deposited silver nanostructures could be tuned by varying the experimental parameters such as the deposition time, temperature, precursor concentration and flow rate. The size of the deposited silver nanoparticles could be well controlled from tens of nanometers to hundreds of nanometers, and the thickness of the silver layers could be up to a few microns. A uniform silver coating in the air channels across the fiber structure was achieved, as illustrated in the inset of Fig. **3C**. The longitudinal deposition profile was determined by several factors including heater cartridge hot zone profile as a function of length as well as the precursor concentration, flow rate and deposition time.

The silver coated fibers (~15 mm long) with a monolayer of benzenethiol adsorbed on silver surface were used for SERS measurements through a back propagating mode (laser excitation and Raman detection from the same fiber end). As shown in Fig. **4B**, the measured SERS intensity from the positions closer to the core of the fiber (shown in Fig. **4A**) was always higher, due the higher energy of the evanescent field in the air channels closer to fiber core.

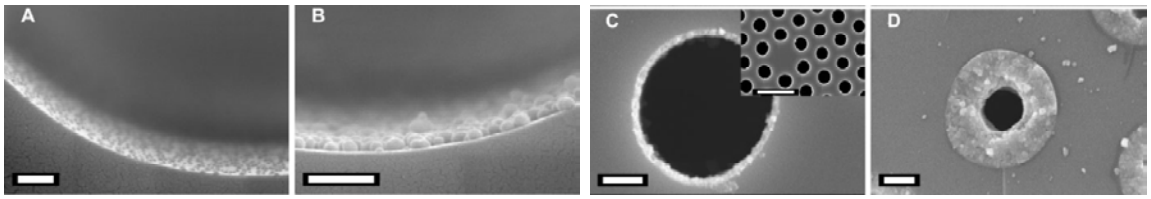

Figure 3: Different silver deposition profiles obtained by tuning the experimental parameters. (A) deposition time of 0.5 h, precursor concentration of 5 mg/mL, 1 μm of scale bar. (B) deposition time of 0.5 h, precursor concentration of 10 mg/mL, 1 μm of scale bar. (C) deposition time of 2 h, precursor concentration of 10 mg/mL, 2 μm of scale bar and 20 μm of scale bar in the inset. (D) deposition time of 3 h, precursor concentration of 15 mg/mL, 2 μm of scale bar. Copyright Wiley-VCH Verlag GmbH & Co. KGaA. Reproduced with permission (ref. [34]).

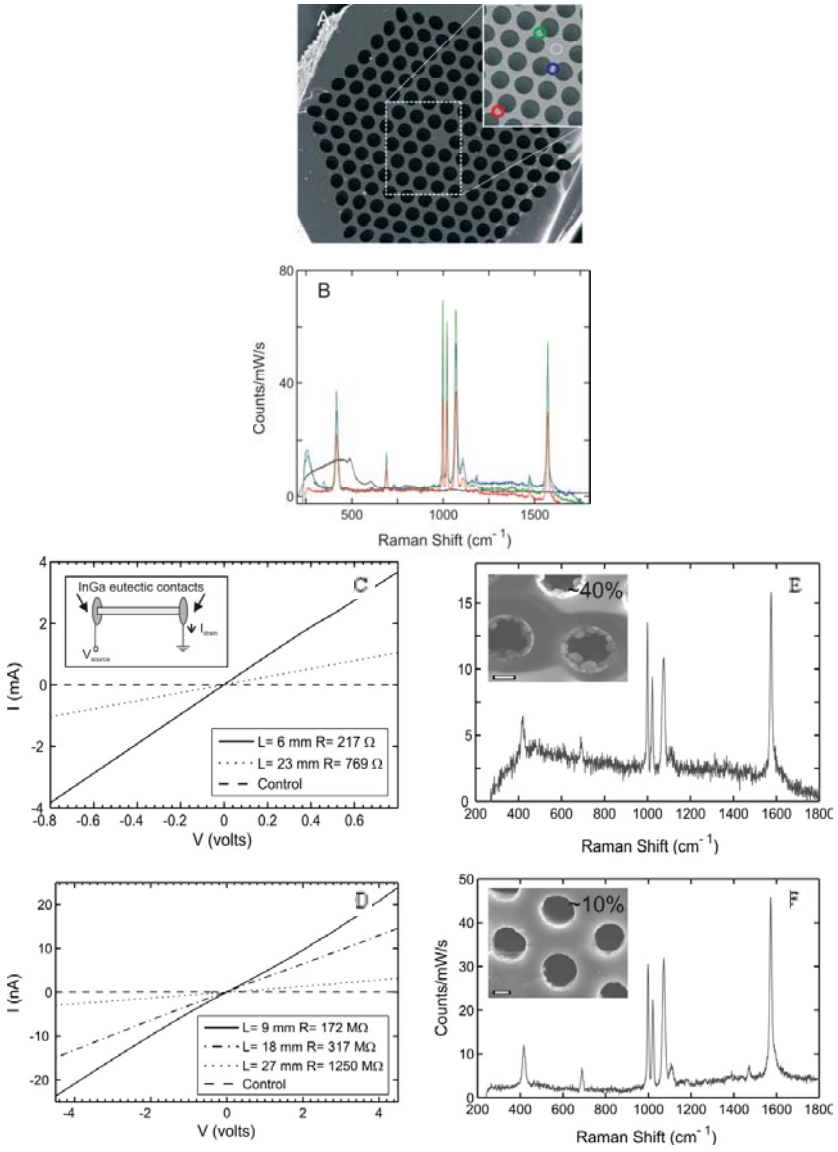

Figure 4: (A) Cross sectional SEM image of the 168-hole solid-core PCF with a low filling fraction (inset: a fractional area of the fiber cross section at higher magnification). (B) Color coded SERS spectra across the cleaved face of the PCF corresponding to the colored positions marked on the micrograph inset of (A). (C) and (D): Current *vs.* voltage measured from the silver nanostructure coated PCFs at filling fractions of 40% (C) and 10% (D) with various fiber lengths. (E) and (F): the corresponding SERS spectra from 15 mm fibers with the different filling fractions shown in the micrograph insets. Scale bars are 2 μm. Copyright Wiley-VCH Verlag GmbH & Co. KGaA. Reproduced with permission (ref. [34]).

Electrical resistivity measurements on the PCF coated with silver nanostructures at different filling fractions were carried out to get important information on the homogeneity and quantity of silver deposition. The filling fraction was defined as filled cross-sectional area of each pore. Before measurements, Indium-Gallium eutectic was placed onto cleaved ends of the fiber with the polymer coating removed to provide a low resistance contact between the fiber and the probe station, as illustrated in the inset of Fig. **4C**. Fig. **4C** and **4D** show the curves of current *versus* voltage with silver filling fractions of approximately 40% (C) and 10% (D) for different fiber lengths. For the fiber with a higher silver filling fraction, the measured resistance per millimeter of a 23 mm long sample increased slightly compared with that measured from the 6 mm long fiber (Fig. **4C**), whereas for the fiber with the lower silver filling fraction, the resistance per millimeter decreased dramatically when fiber length was reduced from 27 mm to 9 mm (Fig. **4D**). Drastic increase in resistance with fiber length suggested that the deposited silver coating was not homogeneous and the particle density was sparse for the low filling fraction sample. There was a strong correlation between the electrical resistance of the fibers and the corresponding SERS intensities, as shown in Fig. **4E** and **4F** where the signal from the low filling fraction fiber (high resistance) was three times higher than the sample (low resistance) with a high filling fraction. This might be associated in part with the higher loss in the high filling fraction fiber and in part increased scattering from the larger silver particles as well as plasmon resonance shifting and broadening.

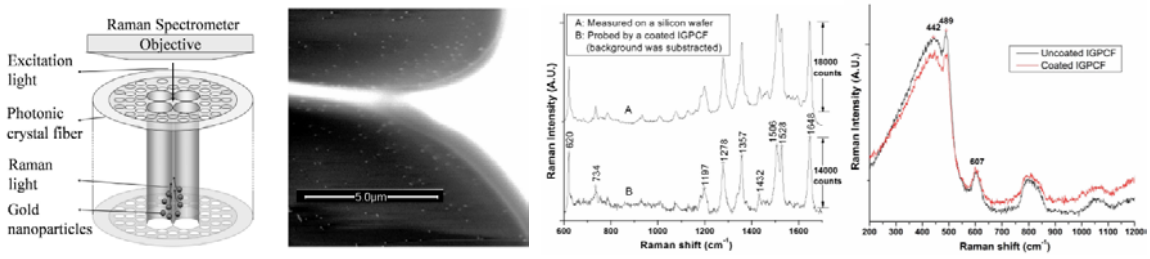

(A) (B) (C) (D)

Figure 5: (A) Scheme of SERS measurements. (B) SEM image of attached gold nanoparticles taken from the side surface of the silica core. (C) SERS spectra of 10^{-5} M RhB obtained from a SERS substrate on Si wafer (Curve A, excitation power 0.47 mW, scan time 20 s, and accumulation times 1) and from a SERS active PCF geometry(Curve B, 4.7 mW; scan time 10s; accumulation times 3). (D) Raman backgrounds of uncoated and coated PCF. Reproduced with permission (ref. [33]).

Solid-core PCF can also be functionalized by means of immobilization of SERS active metal nanoparticles which were pre-synthesized in solution. Unlike the high-pressure chemical deposition technique, this method does not require sophisticated process control nor high pressure and high temperature.

For example, Yan *et al.* [33] reported a SERS-active solid-core PCF by coating pre-synthesized gold nanoparticles on the inner surface of the fiber air channels. The experiment was carried out as shown in Fig. **5A**. The solid-core PCF (cross section shown in Fig. **2A**) of ~5 cm in length was cleaved carefully at both fiber ends. The produced gold nanoparticles (~80 nm in diameter) with a positive surface charge due to an adsorbed layer of hexadecyl trimethyl ammonium bromide (CTAB) were directly attached to the inner surface of the fiber by electrostatic interaction. The probing end of the fiber was dipped into the gold colloidal solution for about 5 minutes to allow the solution to fill in ~2 cm air holes of the PCF by capillary force. The gold nanoparticles were deposited on the inner surface of the air holes upon drying the solution at a temperature of 60ºC for ~2 h. Shown in Fig. **5B** is the SEM image of attached gold nanoparticles in the large air holes surrounding silica core of the fiber piece cut at a location of 15 mm above the probing end. These gold nanoparticles served as SERS-active area around the silica core. The SERS-active probing tip was dipped into the RhB solution for 5 seconds to fill in ~ 1 cm long air channels *via* capillary effect. Curve B in Fig. **5C** shows the measured SERS signal of RhB (the fiber Raman background has been subtracted) which was in agreement with the result obtained from the planar SERS substrate (curve A in Fig. **3(a)**, the same gold nanoparticles were coated on the silicon wafer). The Raman background from the fiber is a result of the interaction between the excitation light and the silica core, Raman background spectra were similar

before and after the coating process as shown in Fig. **5D**, indicating that the nanoparticles coated on the air channel surface did not enhance the fiber background.

2.4. Full Length SERS-Active Solid-Core PCF

As discussed in previous sections, different attempts have been made to integrate SERS with solid-core PCF platform by incorporating Ag or Au nanostructures, revealing the versatile and promising attributes of PCF for SERS. However, those studies focused on a very limited segment (typically a few centimeters) of the fiber air channels for SERS functionalization and their SERS measurements were carried out by back propagating data acquisition mode, leaving a question on the relative contribution of the waveguide core and the cladding to measured Raman intensity. Therefore, it is of critical importance to building uniform SERS functionality throughout the length of the PCF while preserving its light guide characteristics. This way, the entire length of the PCF can be utilized for SERS detection in forward propagating mode to unambiguously assess the SERS-active nature of PCF.

To realize full-length SERS-active PCF, an important step is uniform incorporation of Ag or Au nanostructures inside the air channels along the entire fiber length. Recently, our group [35] demonstrated polyelectrolyte-mediated surface immobilization of silver nanoparticles in air channels of PCF with controlled surface coverage density, as shown in Fig. **6A**. This strategy was based on the electrostatic interaction and Ag-N bonding between positively charged polyelectrolyte and negatively charged silver nanoparticles. As a solution-based approach, polyelectrolyte-mediated self-assembly has shown to be efficient, versatile and environmentally benign for immobilization of noble nanoparticles for SERS detection [36-38].

In contrast to previous work where gold nanoparticles were attached to 60-μm-long nanocanal walls of porous alumina [39, 40], we focused on controlling nanoparticle density in a wide range, and achieving low and uniform coverage density of silver nanoparticles inside much longer air channels of PCF. To mediate nanoparticle attachment, polyallylamine hydrochloride (PAH) was first allowed to adsorb at the surface of the air channels, served as anchoring site for silver nanoparticles. Silver nanoparticles used in this work were synthesized using a modified Lee and Meisel method with the nanoparticle size of 35 nm ± 5 nm and the zeta potential of approximately -35 mV [41].

Surface functionalization of the fiber air channels and immobilization of silver nanoparticles were carried out in a custom-built pressure cell at a 200 psi pressure differential between the entrance end (submerged in a solution) and the exit end (exposed to the laboratory ambient) of the PCF. PCF typically 25-30 cm in length were first filled with PAH solutions at pH 4-7 for polymer self-assembly on the air channels, then with silver colloidal solution at pH 5.6. Intense rinsing with Milli-Q water was applied after each deposition step to remove unbound PAH or silver nanoparticles from the channels. The negative surface charge of silica, whose charge density increases with pH >3, afforded control over the amount of adsorbed polycation [42] and thus the availability of binding sites for silver nanoparticles. Silver nanoparticle coverage density strongly correlated with the solution pH used during PAH adsorption step, with more nanoparticles immobilized in the air channels at higher pH values of the PAH assembly, as shown in Fig. **6B**. SEM images of various segments of the solid-core PCF showed similar coverage of discrete silver nanoparticles (Fig. **6C**-**6D**), indicating that our experimental approach allowed a high degree of control in immobilization of silver nanoparticles inside the microscopic air channels along the entire PCF length.

We carried out measurements of forward-propagating Raman spectra as well as hyperspectral imaging using the full length SERS-active solid-core PCF with the Raman setup shown in Fig. **6E** [43]. In Fig. **7A**, curves (a)-(f) compared and contrasted the Raman spectrum of 2 μM Rhodamine 6G (R6G) solution using a SERS-active PCF with immobilized silver nanoparticles (1 particle/μm^2) and those of others as control and reference all in the forward propagating geometry. The solid-core PCF used here was supplied by OFS Laboratories (Somerset, NJ, USA) with a microstructure consisting of a silica core (~2.5 μm in diameter) surrounded by six rings with 126 air channels (~3.5 μm in diameter) in the cladding. All spectra except in Fig. **7A** (a) resembled the Raman spectrum of silica with characteristic vibrational peaks between 0 and

1300 cm^{-1} and a main peak corresponding to Si–O bending at 485 cm^{-1}. While silica Raman bands were also present in Fig. **7A** (a), the additional Raman peaks between 1300 cm^{-1} and 1700 cm^{-1}, notably at 1307 cm^{-1}, 1351 cm^{-1}, 1509 cm^{-1}, 1570 cm^{-1}, and 1645 cm^{-1} are characteristic of various vibrational modes in R6G [44, 45]. The R6G Raman intensity in Fig. **7A** (a) clearly results from SERS, solid evidence of forward-propagating Raman scattering in a 30 cm long SERS-active PCF.

Shown in Fig. **7B** (a) and (b) are the forward propagating Raman image and mode-field profile of the silica peak at 485 cm^{-1} for bare PCF, respectively. The Raman intensity of silica was strongly confined to the solid-core region, propagating *via* total internal reflection, with a minor contribution from the cladding region. The core mode diameter, defined as the width of the intensity profile at $1/e^2$ of its peak value per International Organization for Standardization (ISO) 11146 standard, is calculated to be 4.32 μm, indicating an evanescent field extending beyond the waveguide core. The signal contribution by the cladding region, while weak, resulted from finite confinement loss of the PCF structure.

Depicted in Fig. **7B** (c) and (d) are the respective hyperspectral forward propagating Raman image and mode-field profile of the silica band at 485 cm^{-1} using the PCF with immobilized silver nanoparticles and containing the R6G aqueous solution.

The Raman intensity as well as the mode-field diameter, 2.86 μm, in the core region notably decreased with essentially no cladding mode contribution compared with the results for bare PCF (see Fig. **7B** (a) and (b)), a strong indication of the scattering/absorption loss induced by immobilized silver nanoparticles. Presented in Fig. **7B** (e) and (f) are the hyperspectral forward-propagating Raman image and mode-field profile, respectively, of the band at 1509 cm^{-1} associated with an aromatic C–C vibration of an R6G molecule. Contrary to the features in Fig. **7B** (a)-(d), R6G SERS intensity was coupled to and guided by the waveguide core with a core mode diameter of 2.52 μm. The analyte solution filled in the cladding air channels contributed little to Raman signal gain in the SERS-active platform. Note that our 30 cm PCF, as received, with adsorbed polymer or filled with water but in the absence of silver nanoparticles, showed an insertion loss-dominated attenuation of ~-3 dB. However, with immobilized silver nanoparticles ($1/\mu m^2$), a loss of ~-20 dB was observed, apparently induced by nanoparticle scattering and absorption. The contrast in attenuation between bare PCF and PCF with immobilized silver nanoparticles both filled with analyte solutions was self-consistent with the variation in the corresponding mode diameter. Clearly, while silver nanoparticles impart SERS functionality, their presence significantly modifies the optical properties of the PCF, including loss and mode-field profile.

Losses due to the absorption and radiative scattering of electromagnetic energy by nanoparticles were examined by numerical analysis. SERS signal from the solid-core PCF with immobilized silver nanoparticles in cladding air channels was a result of strong interaction between the evanescent field of the guided light and the analyte adsorbed on metal nanoparticles along the fiber length. The evanescent field allowed controlling optical power propagation direction of probing and Raman-shifted signal as well as the further coupling of both signals with signal processing optics. Moreover, it allowed realizing a non-coherent gain of the Raman signal with the fiber length. This is explained in Fig. **8A** where the Raman-shifted power radiated to the fiber at the total internal reflection critical angle by the electric dipoles of each Raman-active molecule was captured by the wave-guide and travels to the optical spectrometer [46]. The Raman-active molecules are induced by the evanescent field to the probing mode. This integral Raman effect can be described with only two exact Eqs. listed below,

$$\frac{dP_{probing}}{dz} = -\alpha_{losses} P_{probing} - \frac{dP_{Raman}}{dz} \quad \textbf{(1)}$$

$$\frac{dP_{Raman}}{dz} = \alpha_{losses}^{Raman} P_{Raman} + \left[\alpha_{Gain}^{Raman} (P_{probing}^2) + \alpha_{chemical-Gain}^{Raman} \right] P_{Raman} \quad \textbf{(2)}$$

where $P_{probing}(z)$ and $P_{Raman}(z)$ were the powers of probing optical signal and Raman-shifted signals propagating through the arbitrary fiber cross section z, α_{losses} was the loss coefficient due to the fiber

losses, and, in particular, due to the electromagnetic energy absorption and radiative scattering by nanoparticles in PCF. α_{losses}^{Raman} was the attenuation coefficient for Raman-shifted signal, which was very close to α_{losses} since the signal frequency shift was small. $\alpha_{Gain}^{Raman}(P_{probing}^2)$ was the non-coherent electromagnetic gain of Raman-shifted signal due to the Proper Integral effect, which must be proportional to $P_{probing}^2$ at $P_{probing} \to 0$. $\alpha_{chemical-Gain}^{Raman}$ was the non-coherent Raman-shifted signal gain due to the chemically induced SERS on nanoparticles independent of probing power. In order to find the optimal nanoparticle coverage that provides the complete transformation of the probing optical signal into the Raman-shifted one, the power losses coefficient α_{losses} and $\alpha(P_{probing}^2)$ should be derived depending on the nanoparticle size and surface coverage, PCF geometry and chosen probing optical frequency. The difference of the two loss coefficients was directly determined by the absorption and scattering loss from the interactions with the silver nanoparticles.

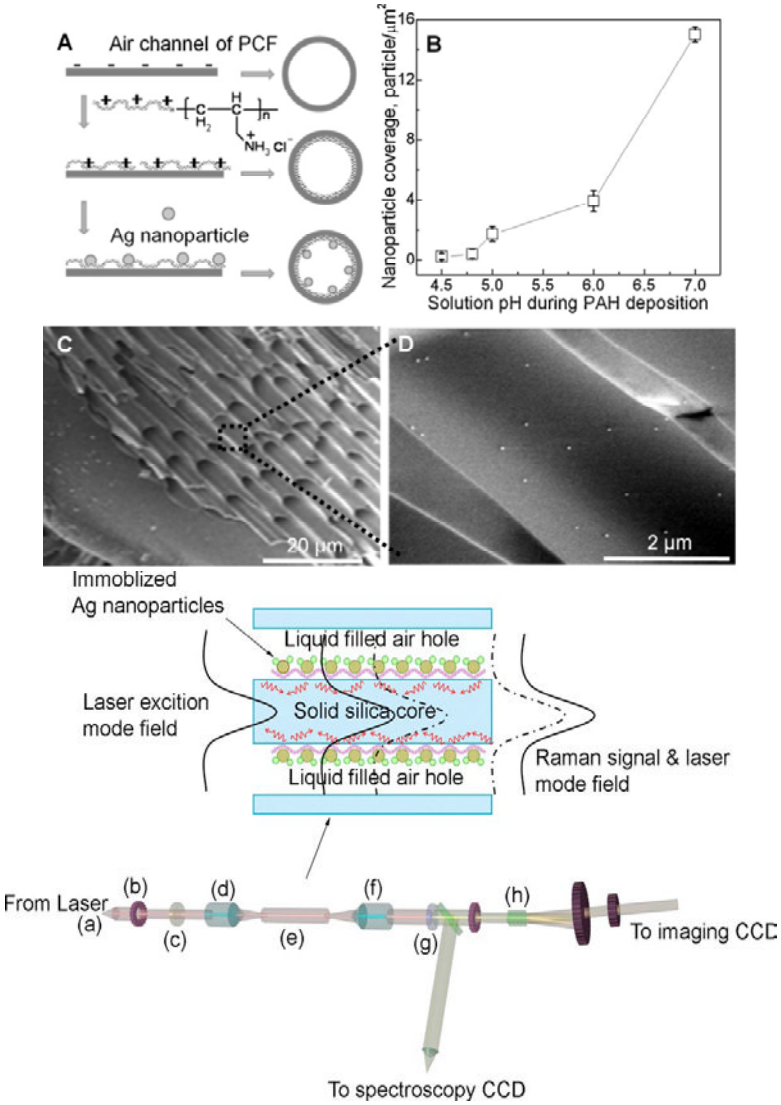

Figure 6: (A) Schematic illustration of the procedure for immobilization of silver nanoparticles in the PCF air channels. (B) Effect of the deposition pH of PAH solution on nanoparticle coverage density. (C) and (D) SEMs of immobilized Ag nanoparticles in the cladding air channels of solid-core PCF. Copyright Wiley-VCH Verlag GmbH & Co. KGaA. Reproduced with permission (ref. [35]). (E) (top) Depiction of light propagation and evanescent-field interaction with analyte solution in a PCF with immobilized silver nanoparticles and (bottom) optical train of the high-resolution hyperspectral Raman imaging and spectroscopy system. (a) He–Ne laser; (b) spatial filter; (c) spectral filter; (d) aspheric lens; (e) PCF; (f) objective; (g) notch filter; (h) acousto-optic tunable filter. Reproduced with permission (ref. [43]).

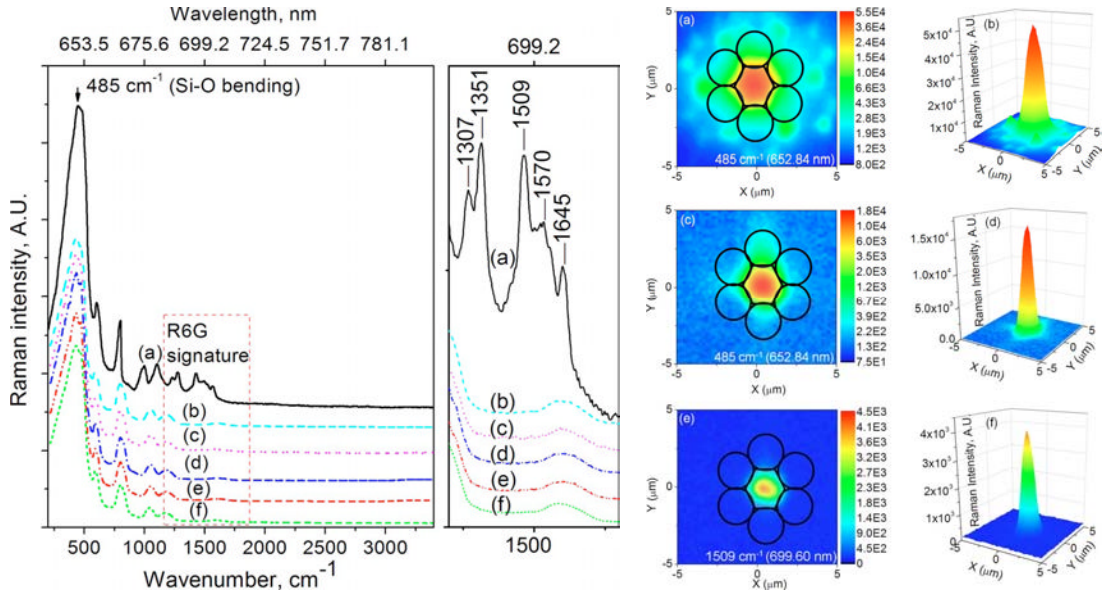

(A) (B)

Figure 7: (A) Raman spectra from (a) SERS-active PCF filled with 2 μm R6G solution, (b) SERS-active PCF filled with water, (c) PCF with adsorbed gelatin and filled with R6G solution, (d) PCF with adsorbed gelatin and filled with water, (e) PCF filled with water, and (f) bare PCF. The right panel corresponds to spectral enlargement in the region of characteristic peaks of R6G. The forward Raman measurements were done at 632.8 nm, ~5 mW laser power, and acquisition time of 10 s. (B) (a) Hyperspectral image and (b) mode-field profile of the silica peak at 485 cm^{-1} using a bare PCF; (c) hyperspectral image and (d) mode-field profile of the 485 cm^{-1} peak using a 30 cm SERS-active PCF; (e) hyperspectral image and (f) mode-field profile of the R6G peak at 1509 cm^{-1} using a 30 cm SERS-active PCF. These data were collected in forward scattering geometry at 632.8 nm, ~5 mW laser power, and acquisition time of 0.2 s for bare PCF and 20 s for SERS-active PCF. Reproduced with permission (ref. [43]).

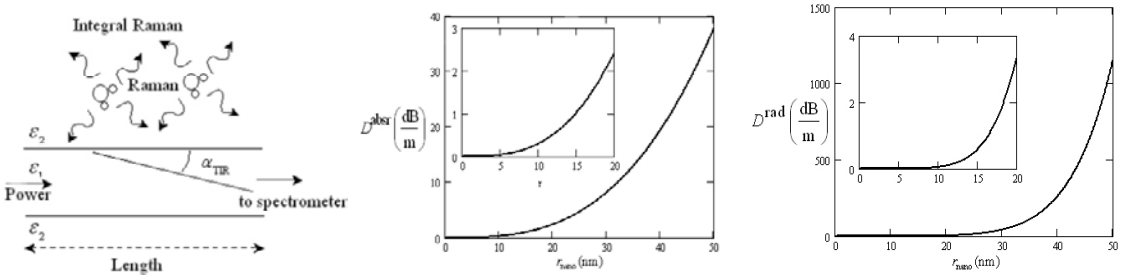

(A) (B) (C)

Figure 8: (A) Illustration of integral Raman effect. (B) and (C) The power-damping coefficients due to the electromagnetic energy (B) absorption in Ag nanoparticles and (C) scattering by nanoparticles as a function of nanoparticle radius. Reproduced with permission (ref. [46]).

Fig. **8B** and **8C** present the dependencies of the electromagnetic power-damping coefficient (in dB/m) due to the absorption (Fig. **8B**) and scattering (Fig. **8C**) on "average" silver nanoparticle radius for TM01 (E01) mode propagating in SiO_2 dielectric probe with a PCF core radius 2 μm at λ = 785 nm [46]. As seen in the figure, both losses were rapidly increasing with the size of the nanoparticles. The nanoparticle coverage used here was 1 particle/μm^2. Due to the coverage randomness, both losses were strictly proportional to the nanoparticle coverage, and one could easily estimate the optical power losses at different coverage values. A positive difference between $\alpha(P^2_{probing})$ and α_{losses} was required to obtain the gain of Raman signal with PCF length, which could be achieved by decreasing the nanoparticle coverage density. These calculation results were used as a key guidance in our modification steps to obtain SERS-active PCF with proper nanoparticle density that could realize a non-coherent gain of the Raman signal with the fiber length.

Fig. **9A** are SERS spectra of R6G solutions using a 20-cm-long solid-core PCF containing immobilized silver nanoparticles at a coverage density of ~0.1 particle/μm^2. The R6G vibrational features were evident even at 10^{-7} M and became more distinct and intense at higher R6G concentrations. Importantly, for planar substrates with the same silver nanoparticle coverage density, no SERS could be observed for a much higher R6G concentration of 10^{-5} M. The dependence of SERS intensity on PCF length was evaluated in fiber cut-back experiments. PCF with silver nanoparticles immobilized to various particle coverage densities were filled with 10^{-6} M R6G. The dependence of the measured SERS R6G peak intensity at 1351 cm^{-1} on the fiber length of solid-core PCF is shown in Fig. **9B**. SERS intensity increased with the fiber length at the lower end of the silver nanoparticle coverage (below 0.5 particle/μm^2), indicating a net signal accumulation along the optical path thus the benefit of long interaction length. Note that the Raman signal declined with the fiber length at higher nanoparticle coverage densities. The pattern was a result of the interplay between accumulative Raman signal gain and the progressive scattering and absorption losses of both the excitation light intensity and the Raman signal intensity as the path length increased. The Raman gain prevailed at lower nanoparticle coverage densities where light attenuation was low, whereas at higher nanoparticle coverage densities the loss overwhelmed the Raman gain over the fiber length. Importantly, substantial gain in Raman sensitivity could be achieved using longer PCF with very low nanoparticle densities such as 0.1 particle/μm^2).

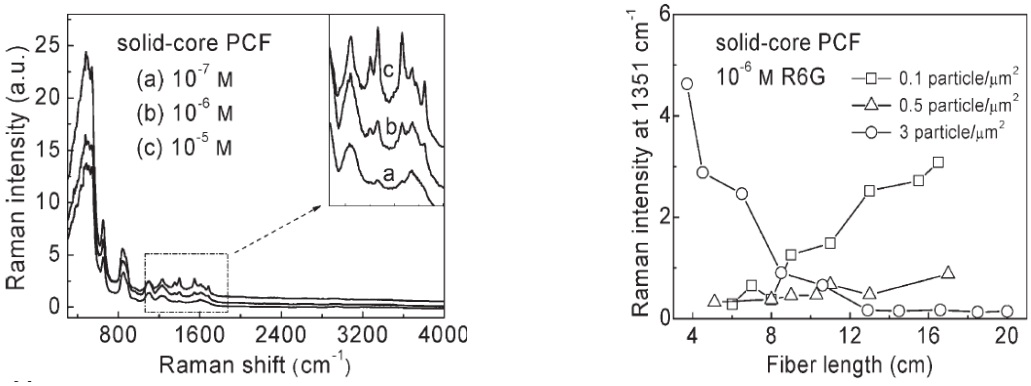

(A) (B)

Figure 9: (A) SERS spectra of various R6G solutions using 20 cm long solid-core PCF coated with silver nanoparticles of 0.1 particle/μmm^2. (B) SERS intensity of 10^{-6} M R6G as a function of fiber length. Raman excitation wavelength was 632.8 nm; the laser power 5 mW; and acquisition time 60 s. Copyright Wiley-VCH Verlag GmbH & Co. KGaA. Reproduced with permission (ref. [35]).

2.5. Effect of the Cladding Microstructure of Solid-Core PCF on SERS

For evanescent-field sensing using solid-core PCF, an important selection criterion is maximum mode-field overlap in the air channels and minimum confinement loss of the guided modes. This actually can be realized by proper design of cladding microstructure. It has been numerically demonstrated that the confinement loss can be reduced and the mode-field overlap increased by increasing the number of rings of air channels around the solid core, increasing the diameter of air channels, and decreasing the web thickness in the cladding air channels [47].

For example, Fini presented numerical results on design of PCF microstructure for sensing applications [48]. Fig. **10A** shows mode-field overlap and confinement loss with varying ratio of cladding hole diameter and spacing (d/Λ) in solid-core PCF. Generally, mode-filed overlap increased with the diameter of cladding air holes. Longer wavelengths and larger d/Λ led to better penetration into the holes, however large λ/Λ came along with higher confinement losses. The loss plotted in Fig. **10A** was for the solid-core PCF with a structure of the three-ring cladding holes, and it could be reduced by adding more cladding holes. However, adding more cladding holes caused weaker confinement at long wavelengths. Simulation results in Fig. **10B** confirmed that the mode-field overlap from the modified solid-core PCF structure could be dramatically higher than the corresponding solid-core structure with $d_{core} = 0$ at a given wavelength,

however it also caused a higher confinement loss, leading to the complex results. Shown in Fig. **10C** were the results of overlap *versus* loss. Clearly, the modified PCF structure design was able to improve the mode-filed overlap for a fixed loss as well as a fixed wavelength.

Recently, our group [49] studied the design of a solid-core PCF with steering-wheel pattern of three large cladding air holes as platform for evanescent-field sensing. Both geometry and optical properties of the fiber were numerical computed and analyzed by evaluating a triangular lattice of holes with three rings in the design structure. Less than 0.7 dB/m confinement loss at 850 nm, 29%, 13.7%, and 7.2% of light intensity overlap in air holes at 1500 nm, 1000 nm, and 850 nm wavelength were predicted with such a solid-core PCF. It was suggested that the low loss and high mode-field overlap made the steering-wheel structured fiber well suited for evanescent-field sensing and detection.

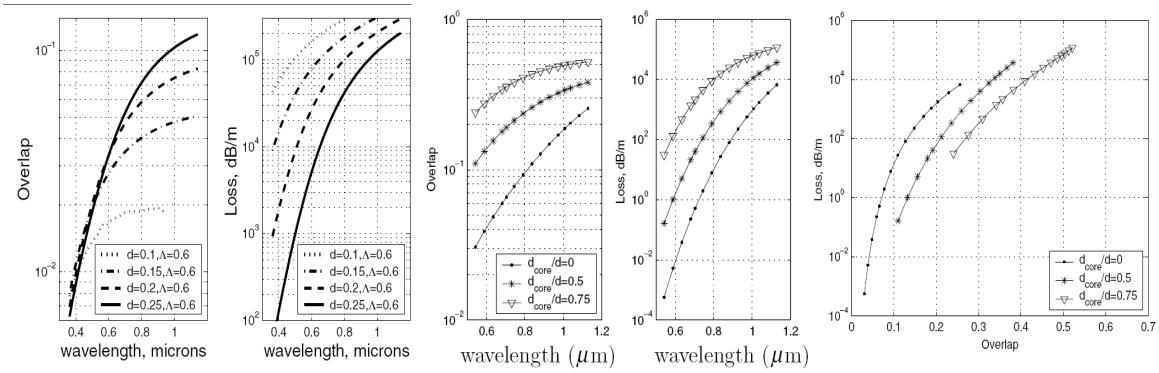

Figure 10: (A) Mode-field overlap and confinement loss with varying ratios of hole diameter and spacing in solid-core PCF. (B) Mode-field overlap and confinement loss with varying ratios of silica core diameter and air hole diameter. (C) Mode-field overlap plotted *versus* confinement loss by varying ratios of silica core diameter and air hole diameter. Copyright IOP Publishing Ltd. Reproduced with permission (ref. [48]).

Yan *et al.* [33] calculated the light distribution in the solid-core PCF with a microstructure consisting of four large air holes inserted between the solid silica core and the photonic crystal cladding holes (shown in Fig. **2A**). Numerical calculations were performed with the MIT photonic-bands (MPB) code. The parameters were defined as: air hole diameter d, pitch Λ, and the diameter of the four air holes d1. Mode profile and energy overlap factor (the percentage of energy propagating in the four air holes with respect to total mode energy) were calculated. It was shown that the calculated energy overlap factor increased with $d1/\Lambda$, but was not sensitive to d/Λ. When the fiber core diameter was much larger than the excitation wavelength, the index guiding was dominant. On the other hand, higher energy overlap could be obtained by increasing $d1/\Lambda$ and decreasing the fiber core to be equal to or even smaller than the excitation wavelength. In this case, the majority of energy spread to the glass bridges surrounding the silica core, leading to confinement loss. Therefore, the outer cladding holes made it possible to confine the light in the fiber core by both total internal reflection and photonic band gap, in cases both with and without liquid in the air channels. The calculated energy overlap factor with the fiber parameters: $d/\Lambda = 0.8$, $d1/\Lambda = 2.6$, $\Lambda = 1\ \mu$ m and $\lambda = 632.8$ nm was 0.0042 for air holes and 0.0203 for liquid filled holes. When d/Λ and $d1/\Lambda$ increased to 0.9 and 3, the energy overlap factor reached 0.0939 without liquid and 0.2145 with liquid, suggesting a highly efficient usage of the excitation light.

Using a full vectorial finite element method (FEM), Peacock *et al.* [50] calculated the guided modes of the two different types of solid-core PCF for the visible excitation wavelength of 633 nm. Shown in Fig. **11(a)** and **11(b)** are SEM images of the two PCF: a large core fiber $\Lambda = 15$ μm and d = 11 μm, and a small core fiber $\Lambda = 1.4$ μm and d = 1 μm. Fig. **11(c)** and **11(d)** show the fundamental guided modes for the two fibers. It was clear that there was significantly more of the field (> 4000X the optical power) in the inner air holes of the small core fiber which could interact with the coated SERS nanostructures.

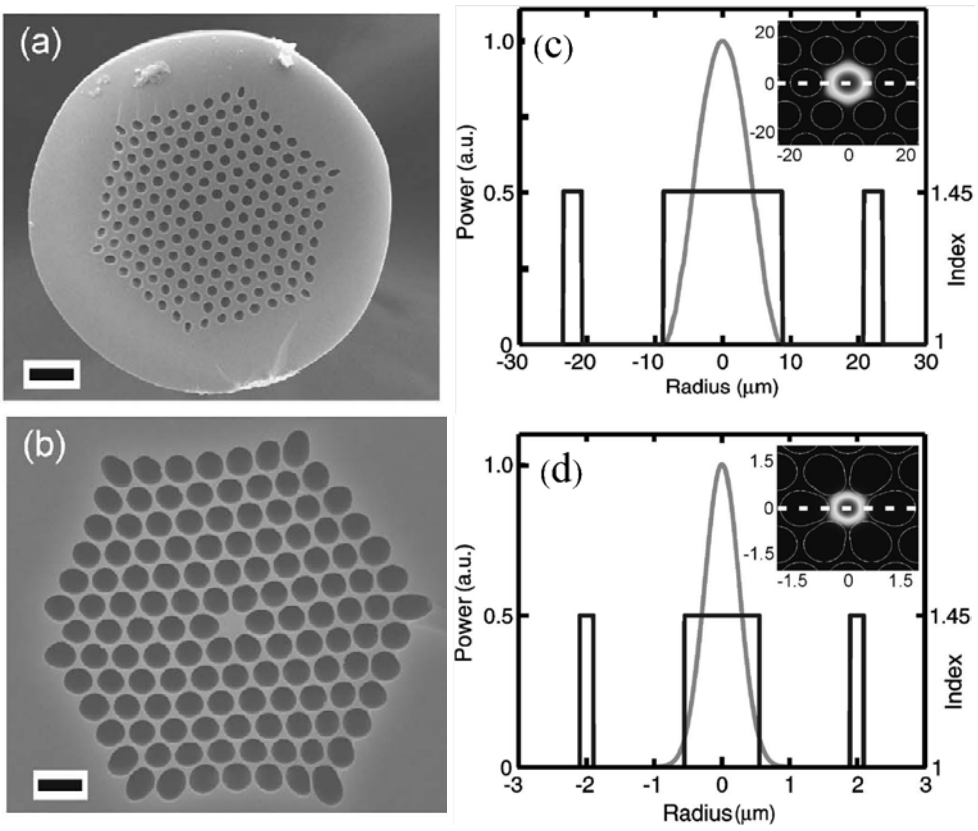

Figure 11: SEM micrographs of solid-core PCFs with large (a) and small (b) silica cores and normalized power distribution of the fundamental guided modes as a function of the radial position for PCF with large (c) and small (d) silica cores. Insets are 2D intensity profiles. Copyright American Institute of Physics. Reproduced with permission (ref. [50]).

To study how the cladding microstructures of solid-core PCF affect SERS performance of the fibers, we used three different solid-core PCF to impart SERS functionality over the full fiber length [51]: nonlinearity PCF (NL PCF) as shown in Fig. **12(a)** with the core surrounded by six rings of air channels, steering-wheel PCF (SW PCF) as shown in Fig. **12(b)**, and suspended-core PCF (SC PCF) as shown in Fig. **12(c)** with the core surrounded by three large air channels separated by thick silica wall and by thin silica web. The robustness of these three solid-core PCF as full-length SERS-active platforms were compared and contrasted by means of numerical simulation, SERS spectroscopy, and hyperspectral SERS imaging using R6G solution as a model analyte.

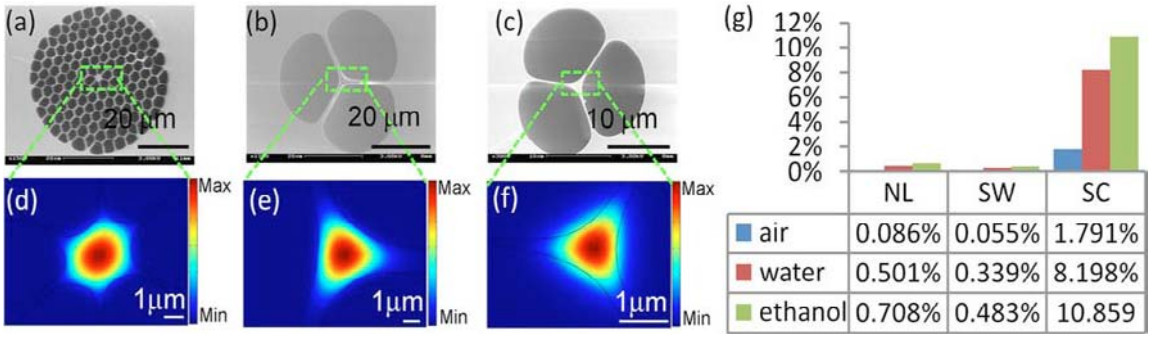

Figure 12: Cross-sectional scanning-electron micrographs of (a) NL PCF, (b) SW PCF, and (c) SC PCF; simulated electric field distribution of the fundamental mode in (d) NL PCF, (e) SW PCF, and (f) SC PCF all filled with ethanol at an excitation wavelength of 632.8 nm; (g) calculated power fraction (PF) in the cladding air channels for NL PCF, SW PCF, and SC PCF filled with air, water, and ethanol at 632.8 nm. Reproduced with permission (ref. [51]).

Finite-element modeling was first performed using commercially available COMSOL 3.5 package with anisotropic perfectly matched layers [52] to assess the field distribution of the fundamental guided modes in air-, water-, and ethanol-filled PCF. The method of calculating the modal power fraction (PF), and effective modal area (A_{eff}) of PCFs has been described elsewhere [53]. Shown in Fig. **12(d) - 12(f)** are respective fundamental mode-field diameters (MFDs) in NL PCF, SW PCF, and SC PCF filled with ethanol at an excitation wavelength of 632.8 nm. According to Fig. **12(g)**, for a given medium, PF increased in order of SW PCF, NL PCF, and SC PCF (SW PCF:NL PCF:SC PCF ~1:2:23 for ethanol). For a chosen PCF platform, the medium (*i.e.*, ethanol) with its index value closest to that of silica experienced the strongest evanescent field of the guided light (air:water:ethnol ~1:5:6 for SC PCF).

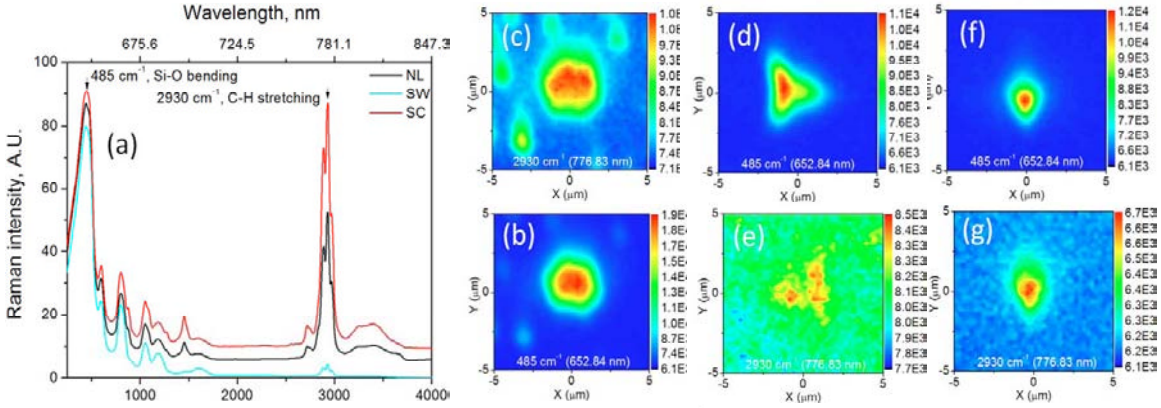

Figure 13: (Color online) (a) Raman spectra from NL PCF, SW PCF, and SC PCF filled with ethanol; hyperspectral Raman images of (b) silica (485 cm^{-1}) and (c) ethanol (2930 cm^{-1}) in ethanol-filled NL PCF; (d) silica and (e) ethanol in ethanol-filled SW PCF; (f) silica and (g) ethanol in ethanolfilled SC PCF. The Raman measurements were carried out at 632.8 nm and 5 mW power, with an acquisition time of 20 s and 10 s for spectral analysis and imaging, respectively. Reproduced with permission (ref. [51]).

Table 1. Theoretical and Experimental MFDs in NL PCF, SW PCF, and SC PCF Filled with Ethanol for Propagating Silica (485 cm^{-1}, 652.84 nm) and Ethanol (2930 cm^{-1}, 776.83 nm) Raman Signals

	Core Diameter (μm)	Calculated MFD (μm) at 652.84 nm	Calculated MFD (μm) at 776.83 nm	Experimental MFD (μm) at 652.84 nm	Experimental MFD (μm) at 776.83 nm
NL PCF	2.60	2.68	2.75	4.36	5.31
SW PCF	3.10	3.23	3.31	4.39	N.A.[a]
SC PCF	1.10	1.28	1.41	3.13	4.19

[a]Signal intensity too weak to experimentally determine MFD.

Reproduced with permission (ref. [51]).

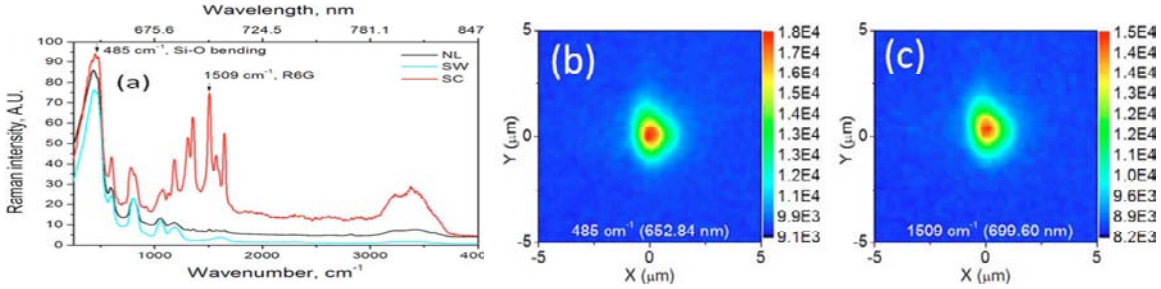

Figure 14: (a) SERS spectra from NL PCF, SW PCF, and SC PCF containing immobilized Ag nanoparticles (0.2 particle/μm^2) and filled with 1×10^{-10} M R6G aqueous solution; corresponding hyperspectral Raman images of (b) silica (485 cm^{-1}) and (c) R6G (1509 cm^{-1}). The Raman measurements were carried out at 632.8 nm and 5 mW power, with an acquisition time of 20 s and 10 s for spectral analysis and imaging, respectively. Reproduced with permission (ref. [51]).

Raman measurements were conducted using the three solid-core PCF each 24 cm in length completely filled with ethanol (99.5% ethyl alcohol). The experiments were carried out by laser excitation at one end of the PCF and signal collection at the other end, as described in Fig. **6E**. The integrated peak intensity at 2930 cm^{-1} in Fig. **13(a)**, characteristic of C-H stretching vibration from ethanol, increased in order of SW PCF, NL PCF, and SC PCF (SW PCF:NL PCF:SC PCF ~ 1:14:28 in Raman intensity ratio), in qualitative agreement with the numerical results. The propagating core mode contributed principally to the measured Raman intensity of both silica (by direct excitation) and ethanol (through evanescent field interaction) in all three PCFs, according to hyperspectral images taken at 485 cm^{-1} (Fig. **13(b)**, **13(d)**, and **13(f)**) and 2930 cm^{-1} (Fig. **13(c)**, **13(e)**, and **13(g)**). In the NL PCF, however, there was notable contribution from the cladding region (Fig. **13(b)** and **13(c)**). This result could be attributed to the fact that silica at the triple-air-channel junctions in the cladding could guide light to a limited extent.

The theoretical MFD was calculated using relation $A_{eff} = \pi\omega_{eff}^2$, where ω_{eff} was the effective modal spot size, one half of MFD [54] The experimental MFD was obtained from the Raman intensity distributions in Fig. **13(b)-13(g)** following the International Organization for Standardization 11146 standard. As seen in Table **1**, for a given PCF, the longer the wavelength, the larger the theoretical or experimental MFD owing to wavelength-dependent beam divergence in solid-core PCF. The ratio of the experimental MFD to the physical diameter of the waveguide core increased in order of SW PCF (1.42), NL PCF (1.68), and SC PCF (2.85) at 652.84 nm, indicating increasing mode field overlap in the cladding air channels [55]. The ratio of the theoretical MFD to the physical diameter of the waveguide core also followed the experimental trend but with significantly smaller values, because high order mode profile was not counted in the simulation. The MFD results were consistent with the Raman intensity measurements, both of which suggested the robustness of the SC PCF as attractive evanescent field sensing platform. The SERS functionality of the NL PCF, SW PCF, and SC PCF was achieved by controlled and reproducible immobilization of negatively charged silver nanoparticles (35 nm ± 5 nm in diameter) on the silica surface of the cladding air channels. A uniform silver nanoparticle density of 0.2 nanoparticle/μm^2 was maintained to ensure prevailing SERS gain *versus* signal attenuation along the fiber length. Common to all the spectra in Fig. **14(a)** are the silica bands in 0-1300 cm^{-1} inherent to silica-based PCFs. The spectrum from SC PCF was strikingly different from those from NL PCF and SW PCF: strong peaks between 1300-1700 cm^{-1} associated with molecular vibrations in R6G. The characteristic water band around 3400 cm^{-1} was prominently revealed in the spectrum from SC PCF. In comparison, little or no R6G spectral features were observed using SERS-active NL PCF and SW PCF at 1×10^{-10} M concentration. Note that R6G could readily be measured at 1×10^{-6} M using these two platforms, suggesting their SERS-active nature. As shown in Fig. **14(b)** and **14(c)**, the forward-propagating Raman signals for both silica and R6G were from the fundamental core mode, well confined within the waveguide core in SC PCF.

Fig. **14(c)** also demonstrated the effectiveness of the coupling of the SERS of R6G to the light-guide core. The close resemblance in the distribution of silica Raman intensity in SC PCF without (Fig. **13(f)**) and with (Fig. **14(b)**) immobilized nanoparticles suggested little, if any, adverse effect of the presence Ag nanoparticles at low coverage density on the MFD of the propagating Raman signals.

These theoretical and experimental studies have consistently indicated that the solid-core PCF microstructure played a critical role in the evanescent field-based sensing and measurements. For the development of SERS-active solid-core PCF platform, the SC PCF had an overwhelming advantage over the other two types investigated in terms of the ultimate limit of detection of an analyte of interest. The large size of the air channels in SC PCFs compared with that of NL PCF, also substantially eased the challenge for gas or liquid transmission through the fiber length, from the standpoint of fiber modification and sensing implementation.

3. HOLLOW-CORE PCF FOR SERS SENSING

Different from solid-core PCF, hollow-core PCF as a spectroscopic sensing platform can be realized *via* direct interaction of light excitation with the analyte in the hollow core. For example, Smolka *et al.* [16] demonstrated the potential of hollow-core PCF for highly sensitive fluorescence detection by selectively

coating the central hole of the PCF with fluorophores. Detection of dye concentrations down to 10^{-9} M was achieved using only nanoliter sample volume. In the following sections, we focus on the use of hollow-core PCF as Raman and SERS sensing platform.

3.1. Selective Sealing of Hollow-Core PCF

The ability to selectively seal the cladding air channels at the distal ends of hollow-core PCF while leaving the hollow core open affords the opportunity for liquid filling or surface functionalization in the core, facilitating practical exploration of the hollow-core PCF sensing scheme. One way to realizing this selective sealing is through selectively filling the air holes with liquid phase materials, as shown in Fig. **15(a)** [56]. It utilized different infusion speed inside the holes resulting from the difference in hole size from core to cladding when an overhead pressure was applied to the fluid. After a certain time, different infusion lengths were generated. If the fluids were UV curable polymers, by cleaving between the two hardened fluid surfaces that have propagated away from each other, either the small cladding air holes or the central hole could be selectively sealed. Fig. **15(b)** and **15(c)** show cross section of the hollow-core PCF with all the holes filled with polymer and only the bigger holes filled with polymer. Nielsen *et al.* [57] elaborated a quantitative description of the time needed for this spatial separation as well as considerations of only using capillary forces for this infusion. They developed a model to qualitatively predict the infusion time of a specific liquid into micro-sized holes and conducted the experiments to verify the accuracy of the model. In addition, the time needed to achieve a given spatial difference between the liquid-filled holes, as a function of pressure, is also specified.

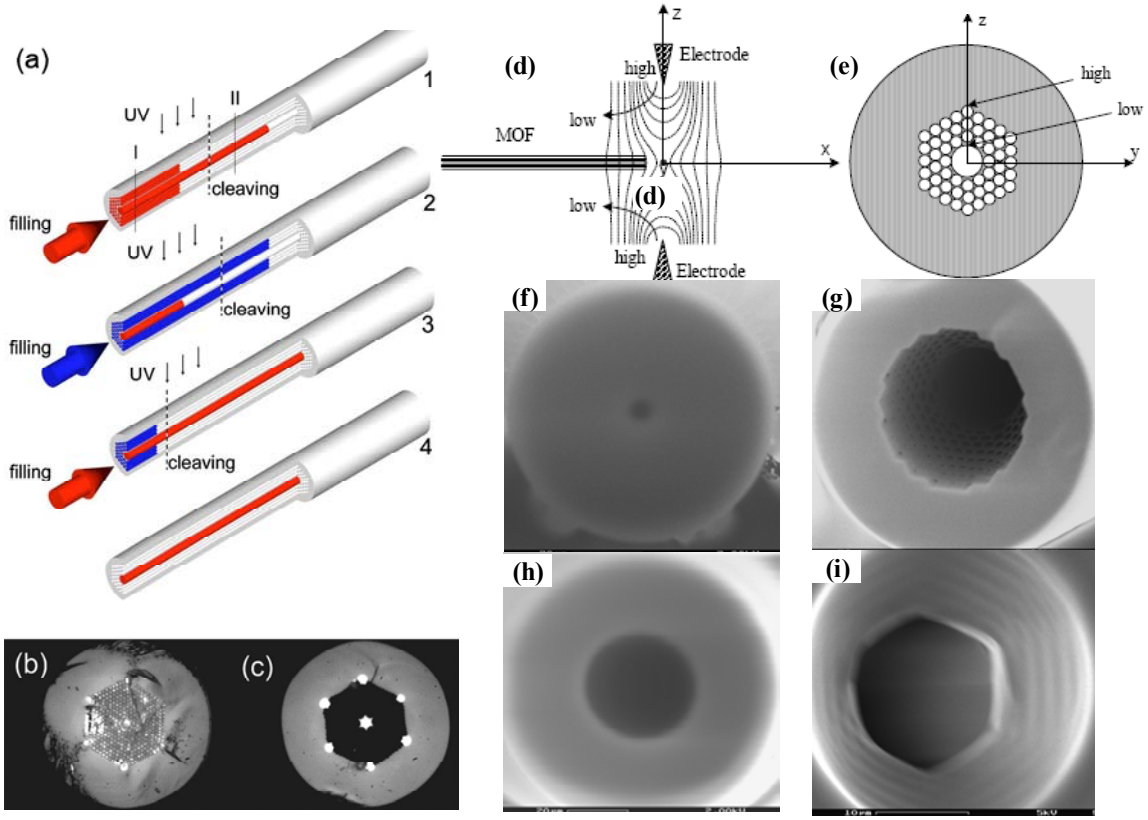

Figure 15: Schematic flowchart on selective filling of PCF (a) and optical microscope images of the fiber cross sections at the cleave positions I (b) and II (c). The light regions correspond to the holes filled with polymer. Copyright American Institute of Physics. Reproduced with permission (ref. [56]). The current and energy density distribution in an arc fusion with the end part of the PCF (d) and illustration of the transverse temperature distribution in the PCF. Reproduced with permission (ref. [58]). Cross-sectional SEM micrographs of the distal end of hollow-core PCF after splice fusion with varying parameters: (f) overly collapsed; (g) under collapsed; (h) well collapsed; (i) central hole shown in (h) at high magnification. Reproduced with permission (ref. [59]).

Another strategy to selectively collapse cladding air holes of the hollow-core PCF was realized by utilizing a conventional fusion splicer [57, 58] This method appeared to be the most promising one due to its simplicity, good reproducibility and low cost. Briefly, one end of the carefully cleaved hollow-core PCF was placed in a fusion splicer with certain "offset" (the distance between the tip of the PCF and the electrode axis of the fusion splicer). An arc discharge from the fusion splicer heated the end face of the hollow-core PCF. Fig. **15(c)** shows the current density or energy density distribution in the fusion splicer. The energy density changed with the square of the current density and the temperature of the discharge was proportional to the energy density. The arc discharge was hottest at the electrode tips and the temperature at the midpoint between the electrode tips decreased along the electrode's axis. Therefore, at the end face of PCF the inner cladding temperature was lower than the outer cladding temperature (Fig. **15(d)** and **15(e)**) when the offset was small. Due to the presence of the air holes and the relative slower heat transfer in the air than in solid silica, the heat transfer from the outer solid silica web to the inner holey region was very slow. Therefore, temperature in the inner cladding air channels was lower than that in the outer cladding holes during a very short discharge period. When the temperature of heated fiber exceeded the softening point of silica (~1670° C), the surface tension overcame the viscosity in the silica, resulting in the collapse of the air channels in the hollow-core PCF. Lower temperature in the center of the fiber, compared to the cladding area, enabled selective sealing of the cladding air channels only. Several parameters including fusion current, fusion duration and fusion offset affected collapse of the air holes in the hollow-core PCF. Shown in Fig. **15(f)-15(i)** are typical cross-sectional SEM images of hollow-core PCF after splice-fusing treatment with different parameters [59]. Fig. **15(h)** and **(i)** correspond to a well-sealed distal end of a hollow-core PCF, the type of which was suitable for selective fill of liquid in the hollow core.

3.2. Raman Measurements using Hollow-core PCF

Our group demonstrated Raman measurements of solutions using a hollow-core PCF filled with analyte solution in the core [59]. As the first step, the cladding air channels at both ends of the fiber were selectively sealed while leaving the central core open using a conventional fusion splicer. The open core of the resultant fiber was then filled with solutions of interest using a custom-made pressure chamber. Raman measurements were carried out with a similar setup shown in Fig. **6E**. Shown in Fig. **16(a)** are Raman spectra of water and ethanol obtained from the hollow-core PCF with the core filled with water and ethanol, respectively. The spectra, from just ~0.1 μL of sample volume, are clearly representative of water (spectrum A) and ethanol (spectrum B), indicating the robustness of the hollow-core PCF platform for Raman measurements of minute volume of solution phase. Note that Raman signal from silica in the spectral range of 500-1500 cm^{-1} (inset in Fig. **16(a)**) constitutes only a weak background, suggesting strongly that Raman scattering from the PCF is a result of direct interaction of the excitation light within the liquid core. The weak silica signal most likely originates from evanescent field interaction with the thin silica web of the air cladding surrounding the liquid core as well as from the propagating surface modes in the silica part of the air cladding structure coupled with the core mode. For comparison, control experiments were carried out using 30 cm long solid-core PCF with cladding air channels filled with water, ethanol, or water and ethanol mixture. The microstructure of the solid-core PCF is illustrated in the inset in Fig. **16 (b)**. Raman spectra of water and ethanol from the measurement scheme are shown in Fig. **16 (b)**. As seen in this figure, while spectral features of the solution of interest are clearly present, silica intensity is very strong in the spectral range of 500-1500 cm^{-1} as expected. In contrast, Raman signal from silica in the hollow-core PCF platform is fairly weak, opening up a broader spectral window for sensing and measurements of analytes.

The robust nature of the hollow-core PCF for Raman spectroscopy was also demonstrated in our measurement of 1 vol.% ethanol in Milli-Q water, as revealed by the distinct spectral features of ethanol at 2925 and 2975 cm^{-1} originating from C-H vibrations shown in the spectrum A in Fig. **16 (c)**. For comparison, conventional Raman measurement was also attempted using the same ethanol-Milli-Q water solution contained in a glass vial under a similar condition of laser excitation and acquisition time. As depicted in spectrum B in Fig. **16 (c)**, not only is the overall Raman intensity dramatically reduced for the water band around 3400 cm^{-1}, no features corresponding to ethanol can be observed (see enlargement in inset). These results indicate that the strong light-field overlap with the solution phase over a long path length attributes to powerful normal Raman capability using the hollow-core PCF as a measurement platform.

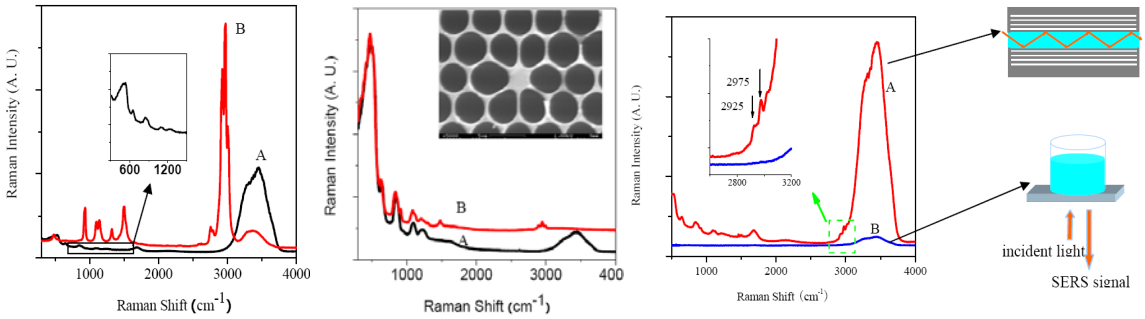

Figure 16: Raman spectra acquired using hollow-core PCF (a) and solid-core PCF (b) filled with Milli-Q water (spectrum A) and pure ethanol (spectrum B). Inset of (b) is a cross-sectional SEM micrograph of solid-core PCF. Raman spectra (c) of 1 vol.% ethanol in Milli-Q water acquired from hollow-core PCF (spectrum A) and conventional Raman measurement (spectrum B). The Raman spectra were all taken using an excitation wavelength of 632.8 nm, 2.1 mW, acquisition time of 20 seconds. Reproduced with permission (ref. [59]).

3.3. SERS Measurements in a Back Propagating Mode

Yan *et al.* [60] presented a hollow-core PCF SERS probe with a layer of gold nanoparticles coated on the inner surface of the air holes at one end of the fiber. In the experiments, the probing tip of the fiber was dipped into the gold nanoparticle solution for about 5 min. The solution entered the air holes for about 1-3 cm due to the capillary effect. After drying the solution at 60°C for about 2 h, the gold nanoparticles were attached on the inner surface of the air holes. After drying analyte solution of 10^{-5} M RhB in the SERS active air holes of the probing fiber tip, SERS measurements were conducted by collecting SERS signals from another fiber tip in a backscattering mode. It was shown that this fiber geometry could increase the number of nanoparticles involved in SERS activity because of larger area of interaction of light and analyte/nanoparticles, thus potentially increasing SERS sensitivity.

By selectively filling the sample solution containing analyte and silver nanoparticles in the hollow core up to 1 cm of one fiber end, Zhang *et al.* [61] demonstrated a liquid-core PCF SERS probe with SERS measurements in a backscattering mode. Using the same type of hollow-core PCF but with all air holes filled with sample solution, SERS measurements from the backscattering mode showed less sensitivity than that when liquid core PCF was used. When only the hollow core was filled with sample solution, better SERS enhancement was achieved due to the confinement of both light and sample in the liquid-core of the PCF. Cox *et al.* [62] demonstrated the feasibility of surface- enhanced resonance Raman scattering (SERRS) in hollow-core PCF.

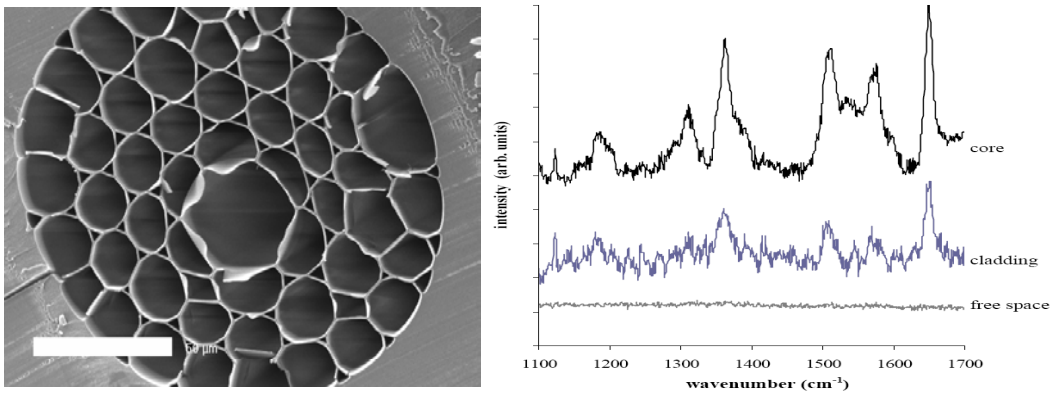

Figure 17: Cross sectional SEM image of PMMA hollow-core PCF with a kagome lattice cladding (a) and SERRS spectra (b) obtained from the fiber core (top), fiber cladding (middle) and free space (bottom) geometries. The Raman spectra were all taken using an excitation wavelength of 514.5 nm, 0.13 mW, acquisition time of 500 s. Reproduced with permission (ref. [62]).

The fiber used in this experiment is a PMMA hollow-core PCF with a kagome lattice cladding as shown in Fig. **17 (a)** and a broad transmission window desirable for in-fiber spectroscopy applications. This fiber when filled with mili-Q water in air holes exhibited transmission wavelengths in a range of 480 nm to 840 nm. In SERRS measurement, a laser excitation at 514.5 nm was used to generate SERRS from the solution filled PCF in that this wavelength is in resonance with both the silver nanoparticle plasmon and analyte molecule excitation of R6G themselves.

The sample solution containing R6G of 210 nM, silver nanoparticles of 5.1 x 10^{-11} M, NaCl of 2.19 nM was first filled into the fiber. SERRS signals were collected in a back propagating mode with an effective fiber length of 5 cm. SERRS spectra obtained from the fiber core, fiber cladding and cuvette measurements were shown in Fig. **18 (b)**. The SERRS signal from the core of the fiber displayed the best Raman peaks. Whereas, the SERRS signal was barely distinguishable from the noise from the cladding measurement and no signal could be observed from the cuvette measurement. The enhanced signal from the core of the fiber resulted from the guidance and accumulation of back propagating Raman signals to the spectrometer through the fiber core. The spectrum obtained from the fiber cladding displayed weak Raman peaks, due probably to a weak guidance in a hollow capillary as well as antiguiding. It was suggested that the higher SERRS signal could be achieved by tuning the several parameters of the hollow-core PCF. The first was the use of a material with the higher refractive index than that of PMMA to fabricate the PCF. The resultant fiber could collect the larger portion of light propagated in the transverse direction, therefore guide more light to the detector. An improved uniformity of microstructure in the PCF and an increased number of cladding hole rings could reduce the loss of guided modes and increase the measured SERS signal. Finally, increase in fiber length could lead to higher SERS enhancement due to the increased interaction path.

3.4. Full Length SERS Active Liquid-core PCF

The above mentioned liquid-core approach explored for SERS by using hollow-core PCF is a novel one but the very short liquid filling length (1-5 cm) for SERS, particularly the utilization of the remaining hollow-core PCF for transmission of back-scattered SERS unnecessarily restricts the window of transmitted Raman spectrum due to the relatively narrow transmission band of the bandgap fiber. Our group recently realized full-length liquid-core PCF for SERS detection in a forward propagating mode with the fiber length up to 30 cm. Two approaches were explored to use liquid-core PCF as SERS platform. In the first scheme, a sample solution containing analyte and SERS active nanoparticles were filled into the central core of the hollow-core PCF, a forward propagating measuring geometry took advantage of full fiber length for the interaction of light excitation and analyte solution [59]. Shown in Fig. **18 (a)** A is the SERS spectrum obtained from 30 cm long liquid-core PCF filled with a solution mixture of NaSCN-silver nanoparticle aggregates (~2.4x10^{9} particles/mL in water) with 1.7x10^{-7} M SCN^{-}. The Raman spectrum B from the same mixture contained in a glass vial using conventional Raman measurements was also plotted for comparison. The characteristic peak at 2100 cm^{-1} associated with SCN^{-} stretching vibration was very pronounced in the spectrum obtained from liquid-core PCF platform. In contrast, such vibrational feature was not detectable using the conventional measurement geometry. Raman intensity of water band at ~ 3400 cm^{-1} from liquid-core PCF was significantly higher than that obtained from the conventional approach. These results further illustrated the excellent prospect of liquid-core PCF for SERS sensing. The effect of the loss of the solution in fiber core is an important consideration in the assessment of liquid-core PCF for SERS. If the liquid in the core of the fiber is highly absorbing, then the forward propagating intensity through the fiber will be small and little or no advantage is gained by using the fiber geometry. However, to detect trace quantities in dilute aqueous solution the liquid-core PCF with tens of centimeters is certainly useful because the transparency of the solution allows for confinement over longer path lengths than in free space with little loss.

In the second scheme, SERS-active metal nanostructures were first incorporated and then analyte solution was filled into the central hole of hollow-core PCF for SERS detection. The key to realize full-length SERS-active liquid-core PCF while preserve the light guide property of the fiber is uniform incorporation of SERS active nanostructures inside the hollow-core along the entire fiber length with controlled surface coverage density, as

in the case of solid-core PCF. We achieved uniform immobilization of silver nanoparticles inside of the hollow core of the PCF with tunable particle density using a polymer-mediated approach (see section 2.4). Fig. **18 (b)** shows SERS spectra of R6G solutions using a 20 cm long hollow-core PCF containing immobilized silver nanoparticles at a coverage density of 0.2 particle/μm^2. Raman spectra were dominated by intense water peak around ~ 3400 cm^{-1} caused by laser excitation of the liquid core.

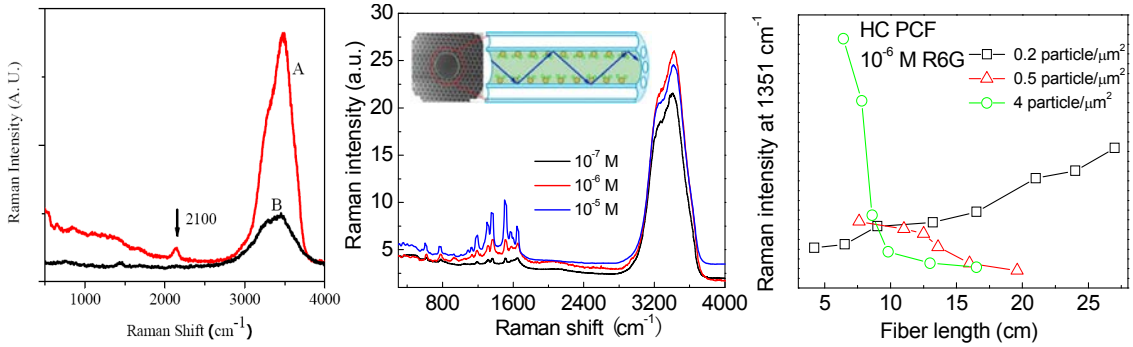

(a) (b) (c)

Figure 18: (a) SERS spectra obtained using liquid-core PCF filled with an analyte solution of 1.7x10^{-7} M SCN$^-$ containing colloidal silver nanoparticles (spectrum A) and using a glass vial filled with the same analyte solution (spectrum B). (b) SERS spectra of various R6G solutions using 20 cm long hollow-core PCF coated with silver nanoparticles of 0.2 particle/μm^2. (c) SERS intensity of 10^{-6} M R6G as a function of fiber length. Reproduced with permission (ref. [35, 59]).

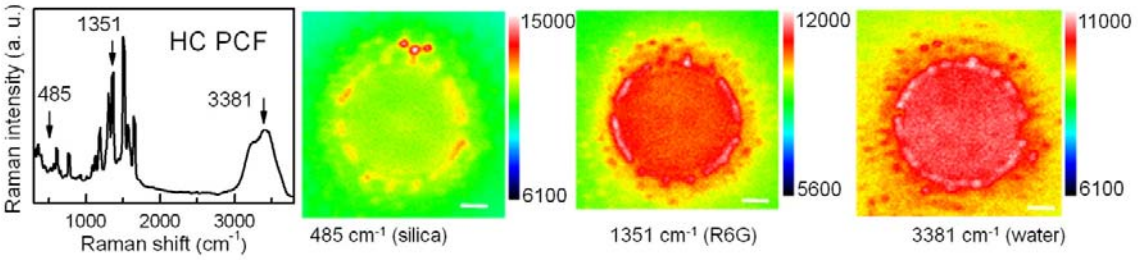

(a) (b) (c) (d)

Figure 19: SERS spectra of 10^{-5} M R6G (a) and hyperspectral Raman images of silica (b), R6G (c), and water (d) from hollow-core PCF with immobilized silver nanoparticles of ~ 0.5 particle/μm^2 in coverage density. The measurements were done using forward-propagating geometry at an excitation wavelength of 632.8 nm. Copyright Wiley-VCH Verlag GmbH & Co. KGaA. Reproduced with permission (ref. [35]).

The silica bands present were weak as expected. The R6G vibrational features were evident even at 10^{-7} M and became more distinct and intense at higher R6G concentrations. The effect of PCF length on SERS intensity was evaluated in fiber cut-back experiments. As shown in Fig. **18(c)**, SERS intensity increased with the fiber length at the lower end of the silver nanoparticle coverage, indicating a net signal accumulation along the optical path. Raman signal declined with the fiber length at higher nanoparticle densities. As discussed in Section 2.4, this pattern was a result of the interplay between accumulative Raman signal gain and the progressive scattering and absorption loss of both the excitation light intensity and the Raman signal intensity as the path length increased. To assess how the waveguide core (fundamental core mode) and the cladding structure (cladding mode) contribute to the overall Raman intensity, hyperspectral imaging at the distal end of the PCF was carried out to map the intensity distribution of a specific Raman line when overlaying with the cross-sectional microstructure of the PCF. The hyperspectral Raman imaging was performed using forward-propagating Raman signal at the distal end of the PCF. Shown in Fig. **19** is Raman spectrum obtained from hollow-core PCF with the core filled with 10^{-5} M R6G solution as well as three hyperspectral Raman images corresponding to silica (485 cm^{-1}), R6G

(1351 cm^{-1}), and water (3381 cm^{-1}) in liquid-core PCF. Raman imaging yielded dashed ring-like Raman intensity distribution of silica surrounding the liquid core as shown in Fig. **19(b)**, a clear evidence that the triple air channel junctions between the core and two adjacent air channels allowed light guiding, *i.e.*, forward propagating of silica signal. The Raman distributions of R6G and water (in Fig. **19(c)**) were also confined in the liquid core, suggesting dominant core mode contribution to the measured Raman intensities. These results provided strong evidence that the liquid core was a robust waveguide, and that the SERS signal of R6G could be effectively coupled and forward-propagated along the liquid core.

CONCLUSIONS

In summary, work to date by many researchers has demonstrated the great potential of PCF as a robust Raman and SERS sensing platform. Unique microstructure of PCF and their functionality both as a light guide and a gas/liquid transmission cell allows unusually large interaction path length between light and analyte, leading to unparallel detection sensitivity using a minute analyte volume. The accessibility to the PCF air channels offers infinite possibilities for fiber functinalization. The evanescent-field sensing scheme of using solid-core PCF takes advantage of the inherently low transmission loss over long fiber length so as to allow accumulation of Raman signal intensity over a long fiber length. An air-guided hollow-core PCF *via* bandgap confinement can be turned to a liquid-guided hollow-core PCF *via* total internal reflectance by selectively filling the hollow core with a solution of interest, making hollow-core PCF an excellent platform for Raman sensing and measurements of a solution phase *via* direct laser excitation (*vs.* evanescent-field excitation) with little or no spectral interference from silica. By proper incorporation of silver or gold nanostructures inside of the PCF air channels, fiber-based SERS-active optofluidic sensing and detection scheme can be realized.

However, challenges remain in integrating SERS with PCF. In the evanescent-field sensing scheme, Raman scattering of the silica core is an intrinsic and predominant part of the data acquisition process. Although it can be used as a reliable internal reference for Raman measurements, it potentially leads to spectral interference in the wavenumber region of 500-1500 cm^{-1}. Using hollow-core PCF with the core filled by a liquid, light transmission loss in the liquid phase is much higher than in silica, thus potentially limiting the light-analyte interaction length in a liquid-guided hollow-core PCF platform. Therefore, future study on optimization of fiber length is very important to improve the sensing performance of liquid-core PCF. Incorporation of SERS-active nanostructure in the PCF air channels results in inevitable light attenuation and total loss of the waveguiding characteristics of the fiber. There is a competitive interplay between SERS gain and scattering/absorption-induced loss by the nanostructure inside of the fiber air channels. Low coverage density of nanostructures proves to be essential for a net accumulative Raman gain along the fiber length. Key to achieving the full-length SERS-active PCF thus lies in the high degree of control of nanostructure coverage density. It is known that SERS hot spots (like dimers and trimers of nanoparticles) contribute to much larger SERS enhancement compared to individual nanoparticles. A future direction would be the introduction of sparsely distributed nanoparticle clusters as SERS hot spots inside of the PCF air channels for further increase of detection sensitivity. Since the presence of SERS-active nanostructure significantly complicates light propagation and light/analyte interactions, in-depth theoretical analysis of related issues should provide much needed insights for design optimization of SERS-based PCF sensors.

We believe that imparting SERS in PCF will allow further exploitation of the rapidly advancing PCF specialty fiber. In particular, SERS-active PCF optofluidic platform is inherently easy for system integration, robust in light coupling and harvesting, and unparalleled in optical path length for label-free and sensitive identification. Its potential applications include fundamental studies of chemical, biological, and catalytic interactions in geometrically confined systems; chemical and biological sensing and detection; and *in situ* process monitoring. Specific examples include detection of contaminants in water for environmental protection, diagnosis of body fluids for disease screening and diagnosis, and in-line measurements of trace chemicals for quality control.

ACKNOWLEDGEMENTS

Dr. Jiri Kanka, Dr. Maung kyaw Khaing Oo, Dr. Denis Pristinski, Dr. Alexander Raspopin, Prof. Svetlana Sukhishvili, Dr. Siliu Tan, and Dr. Yinian Zhu have all contributed significantly to some of the work

presented in this chapter. Funding by NSF under ECS-0404002 and by the US Army ARDEC under W15QKN-05-D-0011 is greatly acknowledged. YH and HD thank the publishers for their permission to include many referenced studies in the chapter.

REFERENCES

[1] Knight JC, Broeng J, Birks TA, Russell PSJ. Photonic band gap guidance in optical fibers. Science 1998; 282(5393): 1476-78.

[2] Knight JC. Photonic crystal fibres. Nature 2003; 424(6950): 847-51.

[3] Russell P. Applied physics: Photonic crystal fibers. Science 2003; 299(5605): 358-62.

[4] Cregan RF, Mangan BJ, Knight JC, Birks TA, Russell PSJ, Roberts PJ, Allan DC. Single-mode photonic band gap guidance of light in air. Science 1999; 285(5433): 1537-39.

[5] Broeng J, Mogilevstev D, Barkou SE, Bjarklev A. Photonic Crystal Fibers: A New Class of Optical Waveguides. Opt. Fiber Technol. 1999; 5(3): 305-30.

[6] Dong L, McKay HA, Fu L. All-glass endless single-mode photonic crystal fibers. Opt Lett 2008; 33(21): 2440-42.

[7] Limpert J, Schreiber T, Nolte S, Zellmer H, Tunnermann T, Iliew R, Lederer F, Broeng J, Vienne G, Petersson A, Jakobsen C. High-power air-clad large-mode-area photonic crystal fiber laser. Opt Express 2003; 11(7): 818-23.

[8] Dudley JM, Genty G, Coen S. Supercontinuum generation in photonic crystal fiber. Rev. Mod. Phys. 2006; 78(4): 1135-84.

[9] Benabid F, Couny F, Knight JC, Birks TA, Russell PSJ. Compact, stable and efficient all-fibre gas cells using hollow-core photonic crystal fibres. Nature 2005; 434(7032): 488-91.

[10] Sazio PJA, Amezcua-Correa A, Finlayson CE, *et al.* Microstructured optical fibers as high-pressure microfluidic reactors. Science 2006; 311(5767): 1583-86.

[11] Couny F, Benabid F, Light PS. Subwatt threshold cw Raman fiber-gas laser based on H2-filled hollow-core photonic crystal fiber. Phys Rev Lett 2007; 99(14): 143903-06.

[12] Monro TM, Belardi W, Furusawa K, Baggett JC, Broderick NGR, Richardson DJ. Sensing with microstructured optical fibres. Meas. Sci. Technol. 2001; 12: 854-58.

[13] Villatoro J, Finazzi V, Minkovich VP, Pruneri V, Badenes G. Temperature-insensitive photonic crystal fiber interferometer for absolute strain sensing. Appl Phys Lett 2007; 91(9): 091109.

[14] Konorov SO, Addison CJ, Schulze HG, Turner RFB, Blades MW. Hollow-core photonic crystal fiber-optic probes for Raman spectroscopy. Opt Lett 2006; 31(12): 1911-13.

[15] Pristinski D, Du H. Solid-core photonic crystal fiber as a Raman spectroscopy platform with a silica core as an internal reference. Opt Lett 2006; 31(22): 3246-48.

[16] Smolka S, Barth M, Benson O. Selectively coated photonic crystal fiber for highly sensitive fluorescence detection. Appl Phys Lett 2007; 90(11): 111101.

[17] Pickrell G, Peng W, Wang A. Random-hole optical fiber evanescent-wave gas sensing. Opt Lett 2004; 29(13): 1476-78.

[18] Jensen JB, Pedersen LH, Hoiby PE, *et al.* Photonic crystal fiber based evanescent-wave sensor for detection of biomolecules in aqueous solutions. Opt Lett 2004; 29(17): 1974-76.

[19] Benabid F, Knight JC, Antonopoulos G, Russell PSJ. Stimulated Raman scattering in hydrogen-filled hollow-core photonic crystal fiber. Science 2002; 298(5592): 399-402.

[20] Fleischmann M, Hendra PJ, McQuillan AJ. Raman spectra of pyridine adsorbed at a silver electrode. Chem. Phys. Lett. 1974; 26 163-66

[21] Albrecht MG, Creighton JA. Anomalously intense Raman spectra of pyridine at a silver electrode. J Am Chem Soc 1977; 99: 5215-17.

[22] Jeanmaire DL, Van Duyne RP. Surface Raman Spectroelectrochemistry Part I. Heterocyclic, Aromatic, and Aliphatic Amines Adsorbed on the Anodized Silver Electrode. J. ElectroAnal Chem1977; 84: 1-20.

[23] Kneipp K, Wang Y, Kneipp H, Perelman LT, Itzkan I, Dasari RR, Feld MS. Single molecule detection using surface-enhanced Raman scattering (SERS). Phys Rev Lett 1997; 78(9): 1667-70.

[24] Nie S, Emory SR. Probing single molecules and single nanoparticles by surface-enhanced Raman scattering. Science 1997; 275(5303): 1102-06.

[25] Campion A, Kambhampati P. Surface-enhanced Raman scattering. Chem. Soc. Rev. 1998; 27(4): 241-50.

[26] De Jesus MA, Giesfeldt KS, Sepaniak MJ. Improving the analytical figures of merit of SERS for the analysis of model environmental pollutants. J. Raman Spectrosc. 2004; 35(10): 895-904.

[27] Peron O, Rinnert E, Lehaitre M, Crassous P, Compere C. Detection of polycyclic aromatic hydrocarbon (PAH) compounds in artificial sea-water using surface-enhanced Raman scattering (SERS). Talanta 2009; 79(2): 199-204.

[28] Peica N, Pavel I, Cîntă Pînzaru S, Rastogi VK, Kiefer W. Vibrational characterization of E102 food additive by Raman and surface-enhanced Raman spectroscopy and theoretical studies. J. Raman Spectrosc. 2005; 36(6-7): 657-66.

[29] He L, Kim NJ, Li H, Hu Z, Lin M. Use of a fractal-like gold nanostructure in surface-enhanced Raman spectroscopy for detection of selected food contaminants. J. Agri. Food Chem. 2008; 56(21): 9843-47.

[30] Kneipp K, Wang Y, Dasari RR, Feld MS, Gilbert BD, Janni J, Steinfeld JI. Near-infrared surface-enhanced Raman scattering of trinitrotoluene on colloidal gold and silver. Spectrochim. Acta, Part A 1995; 51(12): 2171-75.

[31] Sylvia JM, Janni JA, Klein JD, Spencer KM. Surface-enhanced Raman detection of 2,4-dinitrotoluene impurity vapor as a marker to locate landmines. Anal Chem 2000; 72(23): 5834-40.

[32] Hoo YL, Jin W, Shi C, Ho HL, Wang DN, Ruan SC. Design and modeling of a photonic crystal fiber gas sensor. Appl. Opt. 2003; 42(18): 3509-15.

[33] Yan H, Liu J, Yang C, Jin G, Gu C, Hou L. Novel index-guided photonic crystal fiber surface-enhanced Raman scattering probe. Opt Express 2008; 16(11): 8300-05.

[34] Amezcua-Correa A, Yang J, Finlayson CE, *et al.* Surface-enhanced Raman scattering using microstructured optical fiber substrates. Adv Funct Mater 2007; 17(13): 2024-30.

[35] Han Y, Tan S, Khaing Oo MK, Pristinski D, Sukhishvili S, Du H. Towards Full-Length Accumulative SERS-active Photonic Crystal Fiber. Adv. Mater. 2010; 22: 2647-51

[36] Freeman RG, Grabar KC, Allison KJ, *et al.* Self-assembled metal colloid monolayers: An approach to SERS substrates. Science 1995; 267(5204): 1629-32.

[37] Han Y, Sukhishvili S, Du H, Cefaloni J, Smolinski B. Layer-by-layer self-assembly of oppositely charged Ag nanoparticles on silica microspheres for trace analysis of aqueous solutions using surface-enhanced Raman scattering. J. Nanosci. Nanotechnol. 2008; 8(11): 5791-800.

[38] Erol M, Han Y, Stanley SK, Stafford CM, Du H, Sukhishvili S. SERS not to be taken for granted in the presence of oxygen. J Am Chem Soc 2009; 131(22): 7480-81.

[39] Ko H, Tsukruk VV. Nanoparticle-decorated nanocanals for surface-enhanced Raman scattering. Small 2008; 4(11): 1980-84.

[40] Ko H, Chang S, Tsukruk VV. Porous substrates for label-free molecular level detection of nonresonant organic molecules. ACS Nano 2009; 3(1): 181-88.

[41] Lee PC, Meisel D. Adsorption and Surface-Enhanced Raman of Dyes on Silver and Gold Sols. J Phys Chem 1982; 86(17): 3391-95.

[42] Sukhishvili SA, Granick S. Polyelectrolyte adsorption onto an initially-bare solid surface of opposite electrical charge. J. Chem. Phys. 1998; 109(16): 6861-68.

[43] Khaing Oo MK, Han Y, Martini R, Sukhishvili S, Du H. Forward-propagating surface-enhanced Raman scattering and intensity distribution in photonic crystal fiber with immobilized Ag nanoparticles. Opt Lett 2009; 34(7): 968-70.

[44] Hildebrandt P, Stockhurger M. Surface-Enhanced Resonance Raman Spectroscopy of Rhodamine 6G adsorbed on colloidal silver. J. Phys. Chemi. 1984; 88(24): 5935-44.

[45] Michaels AM, Jiang J, Brus L. Ag Nanocrystal Junctions as the Site for Surface-Enhanced Raman Scattering of Single Rhodamine 6G Molecules. J Phys Chem B 2000; 104(50): 11965-71.

[46] Raspopin A, Cui HL, Du H. Calculation of evanescent field interaction with metallic nanoparticles immobilized on the air holes of solid-core photonic crystal fiber. Proceedings of SPIE Int. Soc. Opt Eng 2005; 6005: 60050F

[47] White TP, McPhedran RC, De Sterke CM, Botten L C, Steel MJ. Confinement losses in microstructured optical fibers. Opt Lett 2001; 26(21): 1660-62.

[48] Fini JM. Microstructure fibres for optical sensing in gases and liquids. Meas. Sci. Technol. 2004; 15(6): 1120-28.

[49] Zhu Y, Du H, Bise R. Design of solid-core microstructured optical fiber with steering-wheel air cladding for optimal evanescent-field sensing. Opt Express 2006; 14(8): 3541-46.

[50] Peacock AC, Amezcua-Correa A, Yang J, Sazio PJA, Howdle SM. Highly efficient surface enhanced Raman scattering using microstructured optical fibers with enhanced plasmonic interactions. Appl Phys Lett 2008; 92: 141113.

[51] Khaing Oo MK, Han Y, Kanka J, Sukhishvili S, Du H. Structure fits the purpose: Photonic crystal fibers for evanescent-field surface-enhanced Raman spectroscopy. Opt Lett 2010; 35(4): 466-68.

[52] Saitoh K, Koshiba M, Hasegawa T, Sasaoka E. Chromatic dispersion control in photonic crystal fibers: Application to ultra-flattened dispersion. Opt Express 2003; 11(8): 843-52.

[53] Warren-Smith SC, Afshar VS, Monro TM. Theoretical study of liquid-immersed exposed-core microstructured optical fibers for sensing. Opt Express 2008; 16(12): 9034-45.

[54] Koshiba M, Saitoh K. Structural dependence of effective area and mode field diameter for holey fibers. Opt Express 2003; 11(15): 1746-56.

[55] Gander MJ, McBride R, Jones JDC, Birks TA, Knight JC, Russell PSJ, Blanchard PM, Burnett JG, Greenaway AH. Measurement of the wavelength dependence of beam divergence for photonic crystal fiber. Opt Lett 1999; 24(15): 1017-19.

[56] Huang Y, Xu Y, Yariv A. Fabrication of functional microstructured optical fibers through a selective-filling technique. Appl Phys Lett 2004; 85(22): 5182-84.

[57] Nielsen K, Noordefraaf D, Sørensen T, Bjarklev, A, Hansen, TP. Selective filling of photonic crystal fibres. J Optics A-Pure And Appl Optics 2005; 7(8): L13-L20.

[58] Xiao L, Jin W, Demokan MS, Ho HL, Hoo YL, Zhao C. Fabrication of selective injection microstructured optical fibers with a conventional fusion splicer. Opt Express 2005; 13(22): 9014-22.

[59] Han Y, Khaing Oo MK, *et al.* Liquid-core photonic crystal fiber platform for Raman scattering measurements of microliter analyte solutions. Proceedings of SPIE Int. Soc. Opt Eng 2007; 6767: 67670G

[60] Yan H, Gu C, Yang C, *et al.* Hollow core photonic crystal fiber surface-enhanced Raman probe. Appl Phys Lett 2006; 89: 204101.

[61] Zhang Y, Shi C, Gu C, Seballos L, Zhang JZ. Liquid core photonic crystal fiber sensor based on surface enhanced Raman scattering. Appl Phys Lett 2007; 90: 193504.

[62] Cox FM, Argyros A, Large MCJ, Kalluri S. Surface enhanced Raman scattering in a hollow core microstructured optical fiber. Opt Express 2007; 15(21): 13675-81.

CHAPTER 9

Guided Resonances in Photonic Crystal Slabs for Sensing Applications

Armando Ricciardi[1], Marco Pisco[1], Giuseppe Castaldi[2], Vincenzo Galdi[2,*], Stefania Campopiano[3], Antonello Cutolo[1] and Andrea Cusano[1,*]

[1]Optoelectronic Division, Department of Engineering, University of Sannio, I-82100 Benevento, Italy; [2]CNR-SPIN and Waves Group, Department of Engineering, University of Sannio, I-82100 Benevento, Italy and [3]Department for Technologies, University of Naples "Parthenope," I-80143, Naples, Italy

Abstract: In this Chapter, we provide a compact overview of possible applications of the "guided resonance" phenomenon in photonic crystal slabs to sensing scenarios. More specifically, starting from the outline of the basic aspects, we review a number of selected results from the recent topical literature dealing with applications to displacement, chemical, and biological sensing. Besides theoretical and physical issues, emphasis is also placed on experimental and technological aspects.

Keywords: Photonic crystals, guided resonances, sensors.

1. INTRODUCTION

During the last decade, photonic crystals (PCs) have elicited a great attention in the scientific community, and many research efforts have been devoted to their possible applications to communications and information scenarios, mainly motivated by their unprecedented capabilities of efficiently manipulating the light flow on wavelength and sub-wavelength scales. The reader is referred, *e.g.* to [1] for a recent comprehensive review. Especially intriguing appear those applications to *sensing* scenarios. In such framework, the strong influence of the physical and geometrical parameters in the PC optical response has paved the way to the development of novel and intriguing transduction principles.

Particular attention has been focused on the exploitation of the fascinating properties of PC slabs (PCS) consisting of one-dimensional (1-D) or 2-D periodically patterned dielectric layers. In a PCS, light can be confined either to guided modes (with no coupling to externally incident optical beams), or to the so called "guided resonance" (GR) modes in the slab, for which coupling to externally incident optical beams is allowed [2]. The GR mechanism, which is of interest for what follows, relying on standing electromagnetic (EM) waves strongly confined within the slab and yet capable of coupling to the external radiation, provides an effective and appealing way to sense the external environment.

The sensitivity and selectivity performances of PCS-based chemical and biological sensing devices may be improved by functionalizing the slab surface with sensitive materials. For instance, by filling the PCS air holes with a sensitive material, the light-matter interaction can be strongly improved and optimized. Alternatively, holey PCS may exploited to directly detect target molecules by infiltrating analytes solutions or gas mixtures into the holes.

PCSs may thus offer new perspectives for realizing effective and compact sensors and developing "lab-on-chip" portable devices which allow several chemical and biological analyses to be performed in parallel onto the same platform, by taking advantage of the large scale integration and wavelength multiplexing capabilities. In this context, a significant advance is represented by the integration of PC structures with

***Adddress correspondence to Vincenzo Galdi:** Waves Group, Department of Engineering, University of Sannio, Corso Garibaldi 107, I-82100 Benevento, Italy; Tel: +39-0824-30.58.09; Fax: +39-0824-30.58.40; E-mail: vgaldi@unisannio.it and **Andrea Cusano:** Department of Engineering, University of Sannio, Corso Garibaldi 107, I-82100 Benevento, Italy; Tel: +39-0824-30.58.35; Fax: +39-0824-30.58.46; E-mail: a.cusano@unisannio.it

Marco Pisco, Andrea Cusano and Antonello Cutolo (Eds)
All rights reserved-© 2012 Bentham Science Publishers

micro- or nano-fluidic circuits, so as to provide compact and multifunctional systems to be employed as valuable technological platforms for modern chemical and biological applications.

Furthermore, by placing two PCSs together, and suitably choosing the spacing, it is possible to develop a displacement sensor, for which the transmission is sensitively dependent upon the distance between the slabs. Unlike standard Fabry-Perot sensors, in which photons propagate between the mirrors, with this configuration the photons can also *tunnel* between them, thereby providing high displacement sensitivity combined with low sensitivity to wavelength and to structural disorder.

The rest of this Chapter is structured as follows. In Section 2, we review the basic aspects pertaining to GRs in a PCS. In Section 3, *via* a number of selected examples from the literature, we illustrate their sensitivity to refractive index (RI) variations. In Section 4, we focus on GR-based experimental platforms for biosensing. In Section 5, we deal with biological and displacement sensors based on broadband mirrors in PCS optical cavities. Finally, in Section 6, we provide some compact conclusions.

2. GUIDED RESONANCES IN PHOTONIC CRYSTAL SLABS: BASICS

Starting from the pioneering works by Yablonovitch [3] and John [4] in 1987, the research activity in the PC field has strongly advanced, and nowadays constitutes one of the key fields in optics and photonics [2]. A PC can be defined as a spatially periodic arrangement of a basic building block ("unit cell") made of materials with various constitutive properties.

The dimensionality of a PC is determined by the number of independent axes along which the lattice or variation of the RI is periodic (*e.g.* 1-D, 2-D, or 3-D). The simplest conceivable 1-D PC is formed by a multi-layer of two alternating materials (Bragg reflector), exhibiting *stop-band* regions characterized by high reflectivity [5]. 2-D PCs represent a good compromise in terms of fabrication technology complexity and potential applications in integrated photonic circuits, compared to the 1-D and 3-D counterparts. Prominent among 2-D PC structures, are PC slabs (PCSs), *i.e.*, 2-D, generally periodic, arrangements of air holes in a host dielectric substrate (see, *e.g.* Fig. **1**). In such structures, the light confinement occurs *via* two mechanisms — namely, 2-D band-gap confinement in the periodicity plane, and total internal reflection (along the vertical axis) due to the RI contrast between the patterned slab and the surrounding media. Thus, light propagation through the crystal is explained by the interference of light, which is reflected, refracted and diffracted in the plane of the lattice due to the periodic index variations.

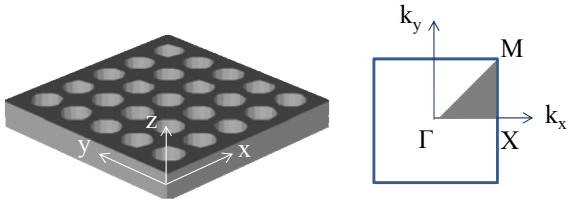

Figure 1: Left: Schematic example of 2D PC slab in which a square pattern of air holes has been introduced into a high RI material (*e.g.* silicon) where the light is restricted to the x and y directions by waveguiding in the z-direction. Right: Part of the corresponding reciprocal lattice and its first Brillouin zone (square area) with the irreducible Brillouin zone (shaded) limited by the high-symmetry points Γ, X and M.

Light traveling through the structure shows a dispersion that depends on the propagation direction. Capitalizing on the formal analogy between solid-state physics and EM, the concept of a "Brillouin zone" (BZ), used to describe crystalline lattices, is also useful in the PC counterpart. Since PCSs possess discrete translational symmetry, the calculations can be reduced by considering all the photonic modes in the BZ, which is the unit cell of the reciprocal lattice (or *k*-space). Accordingly, in order to find *all* the EM field distributions admitted in a 2-D PC slab, only wavevectors within the BZ need to be considered. Within this zone, a number of *high-symmetry* points can be defined, which lie on the corners of the irreducible BZ, and are usually termed as Γ, X and M (see Fig. **1**, **right**). The in-plane wavevector of the crystal varies along the

edge of the irreducible BZ. The dispersion relation $\omega(\boldsymbol{k})$ in the infinitely extended momentum space can be "folded" back onto the first BZ, by introducing a discrete mode or band index n. Mathematically, this means that for all possible values of $\boldsymbol{k}$ inside the irreducible BZ, the Helmholtz Eq. admits solutions of the form $\omega_{k,n}$, labeled by the band-number n in order of increasing frequency. If the wavevector is varied over all possible k-vectors along the symmetry points, the set of solutions $\omega_{k,n}$ for a fixed integer n constitute a "band." The collection of all these bands constitutes the band diagram of the crystal, which can be considered as its "fingerprints." A typical example of a numerically-calculated band diagram for a PC slab is shown in Fig. **2**. If adjacent bands (n and n+1) do not intersect in the wavevector k space, then a "bandgap" appears. The so-called "light cone" is formed by a continuous of states corresponding to all possible frequencies in the superstrate and in the substrate that can radiate in the vertical direction. As a consequence, guides modes (*i.e.*, localized within the slab plane) are allowed to exist only in the regions of the band diagram that are outside the light cone. In fact, the states lying below the light cone cannot radiate and, thus, are guided in the plane of the slab and decay exponentially in the regions surrounding the slab. Such guided modes are typically used for applications that require the light-flow control at a wavelength scale inside the PC slab.

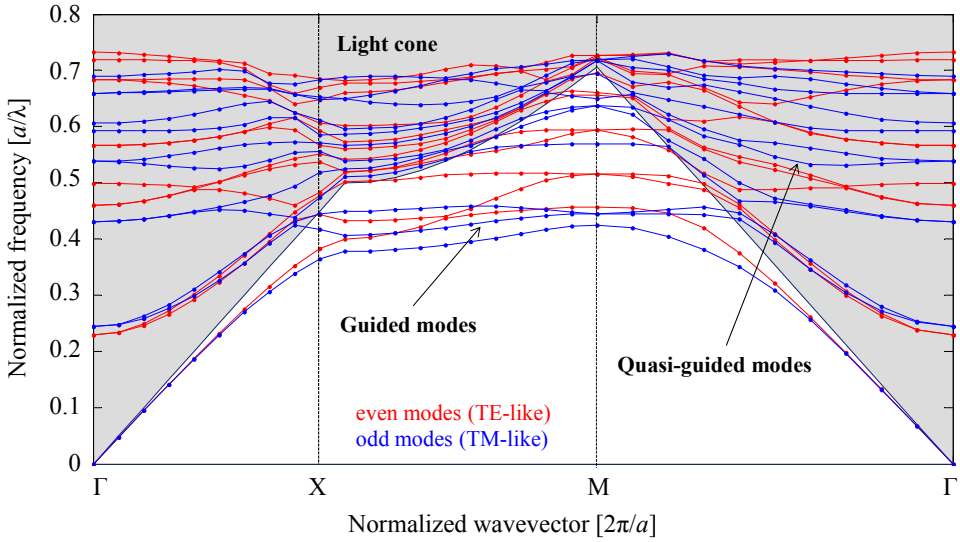

Figure 2: A calculated band diagram for a 2-D silicon (RI = 3.4) PC slab, with thickness of 0.75a, and a square lattice of round air holes of radius 0.25a, with a denoting the "pitch" (or lattice constant).

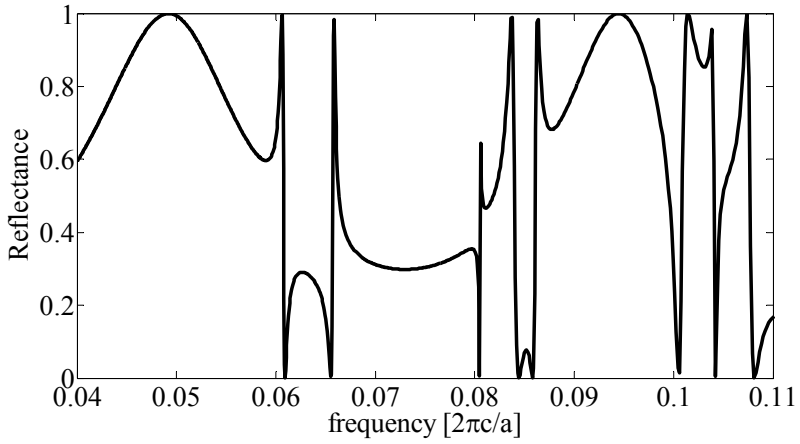

Figure 3: Transmittance spectrum pertaining to a free-standing (in air) silicon PC slab with hole radius r=0.2a and thickness h=0.5a, under normally-incident plane-wave illumination.

In addition to the guided modes above, PCSs also support "leaky" modes, with finite lifetimes inside the slab, that may also couple to the continuum of radiative modes in the surrounding environment. Such modes are represented above the light line in the band diagram, and are known as "quasi-guided" modes, since their EM power is strongly confined within the slab but, at the same time, they can also couple to the external radiation. Quasi-guided modes may be excited under normally-incident (with respect to the crystal-periodicity plane) plane-wave illumination. For instance, Fig. **3** shows the reflectance of a self-standing silicon slab of thickness 0.5*a* patterned with a square lattice of holes with radius 0.2*a* (with *a* denoting the lattice period). It is possible to notice a smoothly varying background (with two maxima at 0.049 and 0.094 ($2\pi c/a$)) due to the Fabry-Peròt effect broken by a set of sharp and asymmetrical Fano-like resonances [6]. In the theory of gratings, such transmission/reflection features may be understood as a particular case of the so-called Wood's anomalies (see, *e.g.* [7]). Fan and Joannopoulos [8], who first analyzed the quasi-guided modes in PCs, defined them as GRs. Basically, the sharp and asymmetrical resonant features in the transmission/reflection spectra of a PCS under out-of-plane excitation are due to the interference between the directly transmitted/reflected wave and those originating from the excited GRs. The resonance frequencies and lifetimes depend on the geometrical and physical parameters of the PC structure, as well as on the direction and polarization of the incident wave.

3. REFRACTIVE-INDEX SENSITIVITY OF GUIDED RESONANCES

In this Section, we summarize the main results of a selected studies on the RI sensitivity of GRs in PCSs.

3.1. Bulk Spectral Sensitivity in Symmetric and Asymmetric Photonic Crystal Slabs

A comprensive study on the bulk sensitivity of symmetric and asymmetric PC slab with respect to the slab surrounding refractive index was performed and presented by El Beheiry *et al.* [9].

As a case of study, they considered PCS structures made of a high-index material, silicon nitride (SiN_x, with RI=2.00), immersed in a low-index fluid, such as water (RI=1.33). Both symmetric and asymmetric PCSs were analyzed: In the symmetric case shown in Fig. **4(a)**, the SiN_x PCS is surrounded by water from above and below.

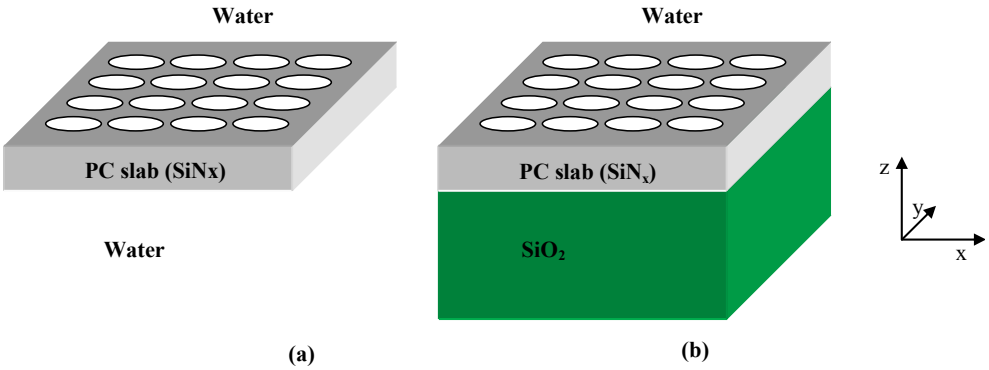

Figure 4: Schematic illustrations of symmetric (a) and asymmetric (b) PC slab designs, respectively.

In the asymmetric case shown in Fig. **4(b)**, it is instead resting on a silicon dioxide (SiO_2, RI = 1.46) substrate. Excitation is a normally-incident plane wave (along the *z*-direction) with a *y*-polarized electric field, although the effects described are general, and apply to *x*-polarized fields as well. As previously discussed, the transmission spectra for a typical PCS design include sharp Fano resonances superimposed on a smoothly varying background similar to the transmission response obtained from a Fabry-Pérot etalon [8].

The sensing mechanism in PCS sensors relies on the detection of the shifts in the GR spectral location. This shift comes from changes in the RI of the medium surrounding the PCS. As a method of biosensing, the

PCS surface may be coated with a thin layer of biorecognition molecules that bind specifically to an analyte (*e.g.* antibodies with affinity to a specific protein, or streptavidin with an affinity to biotin). When excited at a GR frequency, the PCS will have significant EM energy concentrated in the biorecognition layer. In an aqueous environment, such as in a flow channel, analytes binding to the biorecognition layer will induce a change in the local RI of that region [10], which, in turn, will induce a detectable spectral shift of the GRs.

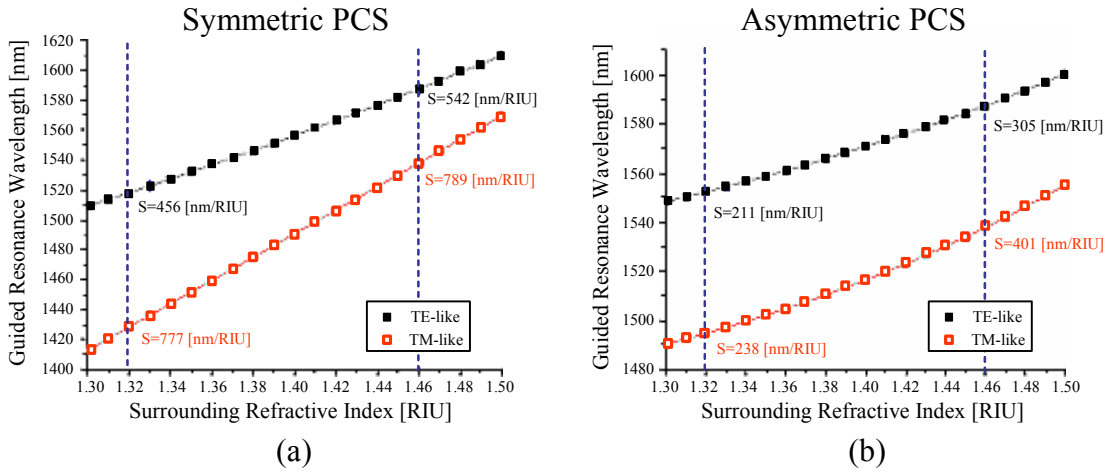

Figure 5: GR wavelength as a function of surrounding RI for (a) symmetric and (b) asymmetric sensor design (r = 300 nm, h = 250 nm). Specific sensitivity values are explicitly indicated for surrounding RI values of 1.33 and 1.46. (Reprinted with permission from El Beheiry M, Liu V, Fan S, Levi O. Sensitivity enhancement in photonic crystal slab biosensors. Opt Express 2010; 18(22): 22702-14. Copyright 2010, Optical Society of America).

A normally-incident plane wave may excite both transverse-electric- (TE) or transverse-magnetic- (TM) like GR modes, characterized by even or odd symmetry (with respect to the mirror plane parallel to the slab), respectively, in their electric field distribution [11]. Generally, TE-like GRs exhibit an electric field mostly co-polarized with the excitation and a short lifetime (*i.e.*, low quality factor Q), as most of the EM energy is concentrated within the slab. Increasing the hole radius-to-period ratio (r/a) yields a reduction in the Q value, and increases the energy concentration in the holes. On the other hand, the EM energy associated with TM-like GRs is more extended in the regions surrounding the slab, with the electric field mostly polarized in the direction normal to the slab surface, which results in long lifetimes (higher Q values). Moreover, compared to the TE-like counterparts, TM-like GRs tend to exhibit narrower linewidths, which implies that smaller spectral shifts are required in order to detect analytes bound to the PC slab surface.

In the TE-like case, when the hole diameter is increased, the effective RI of the PCS is reduced, yielding a stronger interaction between the EM energy and the immersing fluid and, hence, increasing the sensitivity. However, this effect is moderate. The large increase in sensitivity for the TM-like case, compared to the TE-like counterpart, is due to the significant EM energy penetration in water. The spectral sensitivities observed in the TM-like case are largely invariant to the hole diameter as the EM energy is primarily located outside the slab region. When the hole diameter is increased, the scattering within the slab is effectively increased and the resonance lifetime is decreased, resulting in a lower Q value. Moreover, decreasing the PCS slab thickness results in slightly higher penetration of the EM energy into the water, increasing the sensitivity.

The same authors focused their analysis on the nature of GR modes also in asymmetric PCS designs. Indeed, the PCS architecture (symmetric or asymmetric, as shown in Fig. **4**) is an important aspect for the optimization of a PCS biosensor. Many of the recent experimental studies concerning PC-based sensing structures rely on asymmetric configurations, where the PC layer rests on a dielectric substrate, such as SiO_2, since this significantly reduces the fabrication challenges, by comparison with the symmetric,

suspended PCS designs. In order to fabricate a symmetric device, with water above and below the PCS, the underlying SiO_2 substrate can be etched away. However, creating such a suspended slab membrane represents a significant complication in the sensor fabrication [12], and introduces stress-related issues which may hinder the sensing properties.

The mode profiles in an asymmetric PCS design correspond closely to those pertaining to the symmetric design. The asymmetric design does, however, introduce a RI contrast with the substrate that is smaller than that of the (water) superstrate. The result is that most of the evanescent field energy exists in the substrate, strongly affecting the sensing characteristics. Notably, for the same TM-like GR, the spectral sensitivity for the symmetric design (cf. Fig. **5(a)**) is three times higher than that for the asymmetric design (cf. Fig. **5(b)**). The effects of the substrate are further pronounced when considering asymmetric designs with a thin PCS.

An additional practical consideration is related to the *linearity* of the relationship between changes in the GR spectral location and the surrounding RI. Clearly, such behavior may be assumed valid only as a first-order approximation. For larger values of the surrounding RI, a *non-linear* behavior is observed, as shown in Fig. **5**.

3.2. Surface Spectral Sensitivity in Photonic Crystal Slabs

The analysis presented above is concerned with monitoring changes in the GR spectral location when the RI of the whole surrounding fluid is changed. Although the previous study describes and explains the GR modes behavior with respect to the surrounding RI, the resulting sensitivity is a meaningful figure of merit when GR mechanism would be exploited to realize a refractometer. Refractometers find application in chemical and biological sensing where refractive index sensors are able to provide information on chemical species as well as biological targets concentrations. In addition, refractometers often offer transduction principles employed in more complex chemical and biological sensing configurations in which a sensitive material undergoes a refractive index change *via* target molecules absorption. For these reasons, the "bulk" sensitivity is a valuable figure of merit in practical situations such as the sensing of large analytes (*e.g.* cells and bacteria), which may be represented *via* a bulk RI [13].

Another important metric, for chemical and biological sensing applications, is the resonance sensitivity with respect to RI changes in a layer located in close proximity to the surface of the PCS, otherwise known as the "detection zone." In an ideal scenario, the resonant mode will overlap with the active binding region for analytes within the detection zone. This metric, referred to as the "surface spectral sensitivity," represents the change of RI that occurs due to analytes binding to a functionalized PCS biosensor.

The depth of the detection zone depends on the analyte, and may vary from ~25 nm (large proteins [14]), to ~100 nm (for a textured surface, such as nano-rods or permeable organic or inorganic nano-cavities), up to few microns (for detecting changes inside cells [15]). In view of their field penetration properties, TM-like GRs tend to be better suited for detection of bacteria and cells, and may also be exploited for detection of proteins and enzymes with the addition of hydrogel matrices above the PC slab (as in surface-plasmon-resonance sensors [16]). On the other hand, the modal profile of TE-like GRs is less extended in the external regions, and may be better optimized for protein and enzyme detection assays.

3.3. Spectral Sensitivity in Photonic Crystals and Quasi-Crystals

Concerning the pattern geometry of the PCS, most results in the literature are based on *periodic* (*e.g.* square, hexagonal) lattices. Recently, the possibility of exciting GRs in "photonic quasi-crystal" (PQC) slabs based on *aperiodically-ordered* lattices has been numerically [17] and experimentally [18] investigated, opening up new attractive perspectives for high-performance photonic devices and components [19].

Both in PCs and in PQCs, besides the dependence on the direction and polarization of the incident wave, the structural parameters of the slab also play a key role in determining the GR spectral features, as already discussed above.

In a recent paper [20], we presented a comparative study of the tuning efficiency of GRs in PCSs (based on both periodic and aperiodically-ordered unit cells), aimed at assessing the applicability of these important technology platforms to ultra-compact optical sensors and active devices. In connection with PQCs, we considered an aperiodic lattice based on the octagonal Ammann-Beenker tiling made of square and rhombus tiles, and a square lattice as a periodic PC counterpart. We carried out a comprehensive parametric study of the tuning efficiency and sensitivity characteristics, as a function of the slab RI, thickness, and filling fraction. More specifically, for both the PQC and the PC case, we computed the GR wavelength shift induced by variations of the hole RI within the range (1, 1.5), focusing the attention on the GRs corresponding to the lowest-order TE-like and TM-like modes exhibiting an in-plane even symmetry in the electric and magnetic fields, respectively. Such study was repeated for different parameter configurations, by varying the hole radius *r*, the slab thickness *t*, and the slab RI. The comparisons, concerning the PC *vs.* PQC case, were performed by choosing the geometrical parameters in order to equalize the hole/dielectric volumetric fraction.

The GR wavelength shifts have been evaluated with respect to variations of the refractive index of the holes (arranged in periodic or aperiodic fashion), and maintaining the refractive index of the surrounding environment unchanged. This configuration is suitable for biological and chemical sensing applications, where the GR sensitivity with respect to variations of the hole refractive index represents the transduction principle of a PC- or PQC-based sensor featuring a sensitive material integrated within the slab holes. The presence of a specific sensitive material in the slab holes, undergoing a RI change *via* specific target molecules adsorption, improves the overall sensing performance since it allows detection of low target analyte concentrations (which would be unable to change the bulk refractive index).

Our results confirm that, in both the PQC and PC case, the GR sensitivity increases with increasing the hole radius *r* and the slab thickness *t.* In the high-index case (n_{slab}=3.41), the sensitivity of the GRs associated to TE-like modes tend to be higher than those associated to TM-like modes. More specifically, for TE-like modes, the GR sensitivities observed in the PQC case tend to be higher than their PC counterparts, while the sensitivities related to TM-like modes are basically comparable. In the low-index case (n_{slab}=1.58), the efficiencies in the PQC case tend to be higher than their PC counterpart for TE-like modes, whereas they tend to be lower for TM-like modes. By comparing the overall results obtained with high- and low-index slabs, for PQCs and PCs, counterintuitive differences in the behavior of the GR wavelength-shift as a function of the hole RI can be noted. As matter of fact, the GRs associated to TE-like modes in PQCs tend to be more sensitive in the high-index slab case than in low-index slab case, while the contrary (*i.e.*, GRs associated to even modes more sensitive in the low-index slab case) happens in the PC case.

In view of the above illustrated complex dependence of the GR sensitivity on the slab refractive index, mode type (*z*-even or *z*-odd), and lattice geometry (PC or PQC), in what follows, we try to gain further insight in the relationship between the wavelength shift and the modal field distribution of the unperturbed (n_{holes}=1) structures. In particular, we apply the perturbation theory, originally developed in connection with microwave cavity tuning [21], to model the dependence of GRs wavelength shift on the hole RI (*i.e.*, $n_{holes}\neq1$). Such shift can be related to the unperturbed $(\boldsymbol{E}_0, \boldsymbol{H}_0)$ and perturbed $(\boldsymbol{E}, \boldsymbol{H})$ electric and magnetic modal field distributions as follows:

$$\Delta\lambda \approx \lambda_0 \frac{\left(n_{holes}^2 - 1\right) \iiint_{holes} \left|\boldsymbol{E}_0(\boldsymbol{r})\right|^2 d\boldsymbol{r}}{2 \iiint_{cavity} n^2(\boldsymbol{r}) \left|\boldsymbol{E}_0(\boldsymbol{r})\right|^2 d\boldsymbol{r}}, \quad \textbf{(1)}$$

where $n(\boldsymbol{r})=n_{slab}$ within the slab region and $n(\boldsymbol{r})=1$ in the holes and background region, and λ_0 indicates the unperturbed GR wavelength. Note that the previous Eq. is valid in the limit of *small perturbations* ($n_{holes}\approx1$), where one can assume $\boldsymbol{E} \approx \boldsymbol{E}_0$, $\boldsymbol{H} \approx \boldsymbol{H}_0$.

From the physical viewpoint, Eq. (1) states that the GR wavelength response to variations of the holes RI strongly depends on the electric field concentration in the slab holes. In Fig. **6**, the GR wavelength shifts

resulting from a full-wave modal analysis are compared with those predicted from the numerical implementation of the perturbative model in Eq. (1), for the PCS parameters specified in the figure caption. A substantial agreement in the trends can be observed, thereby confirming that the previously highlighted differences between PCs and PQCs in terms of sensitivity-tuning efficiency are actually captured by the simple perturbative model in Eq. (1). This essentially confirms that the GR sensitivity to variations in the hole RI is basically dictated by the electric field concentration in the holes. The above analysis, besides offering a physical insight in the observed differences, also suggests that the spatial arrangement of the holes (and, in particular, the *aperiodic* arrangement in PQC-type supercells) represents an important degree of freedom to increase the interaction with the material infiltrated in the holes.

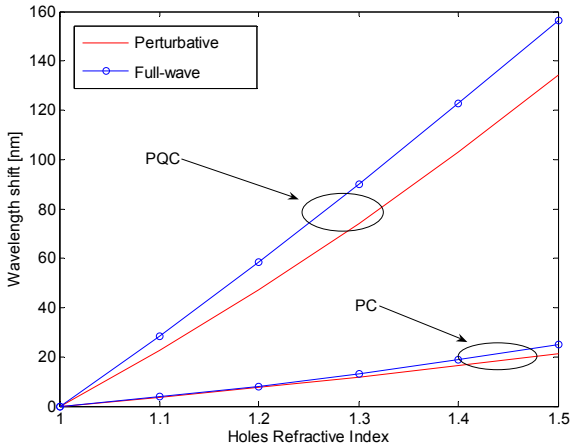

Figure 6: GR wavelength shift calculated *via* full-wave modal analysis and perturbative model [cf. (1)], pertaining to the lowest-order TE-like mode, for a square PC with r =0.275a and PQC with same filling factor, assuming a high-index (n_{slab}=3.418) slab of thickness t=0.75a (Reprinted with permission from Pisco M, Ricciardi A, Gallina I, Castaldi G, Campopiano S, Cutolo A, Cusano V, Galdi V. Tuning efficiency and sensitivity of guided resonances in photonic crystals and quasi-crystals: A comparative study. Opt Express 2010; 18(16): 17280-93. Copyright 2010, Optical Society of America).

3.4. Peculiar Configurations

Another interesting numerical study on PCS sensor designs for sensing changes in the analyte RI has been conducted by Shi *et al.* [22]. In their work, by using the finite-difference time-domain method, they explored several sensor designs based on PCS consisting of either a monolayer of a triangular lattice of silica beads embedded into a dielectric slab placed on top of a substrate (see Fig. **7(a)**), or, alternatively, spherical voids embedded into a dielectric suspended on one side in air (see Fig. **7(b)**). For such configurations, the authors characterized the GR sensitivity with respect to changes in the RI of analyte covering the PCS, and studied the dependence of the spectral position of GRs on the RI of the slab material.

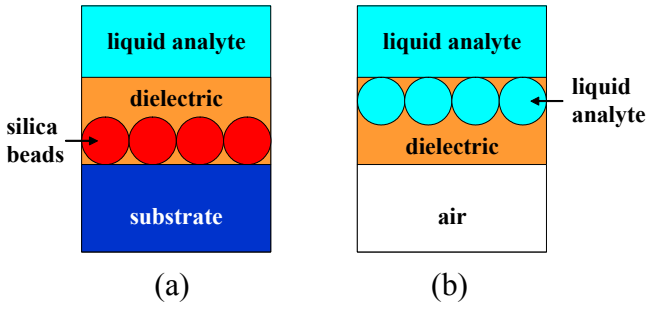

Figure 7: Schematics of GR-based sensors in [22]. (a) Monolayer silica beads (red) inside a dielectric slab (orange) on substrate (blue). The cyan denotes liquid analyte. (b) Monolayer of analyte-filled spherical voids (cyan) inside a dielectric slab (blue).

In the first case, PCs featuring silica beads (Fig. **7(a)**) embedded into a dielectric slab sensor were found to yield a sensitivity of $\Delta\lambda / \Delta n$ = 63 nm/RI-units (RIU) at the operation wavelength of 820 nm. It is typically a safe assumption that a 0.1 nm change in the position of a resonance peak can be detected reliably, which leads to a sensor resolution of 1.5×10^{-3} RIU. Such value is, however, quite standard for many medium-resolution RI sensors. Such relatively low sensitivity may be attributed to the strong localization of the EM field of a GR inside the PCS, with only a small overlap with the analyte. Consequently, changes in the analyte RI have only little effect on the GR electric field and, therefore, do not sensibly affect the reflection spectrum.

On the other hand, PCSs featuring analyte-filled spherical holes turn out to exhibit much higher sensitivities, due to improved overlap between the GR field and the analyte. In such sensors, some GRs have a substantial fraction of their EM energy localized in the analyte, thereby enabling designs with spectral sensitivities as high as 327 nm/RIU at a 600 nm operation wavelength.

Song *et al.* [23] investigated the GR behavior in PCSs made of both isotropic and anisotropic materials, by using an extension of the Scattering Matrix Method. As discussed before, the GR wavelength shift can be obtained by acting on the slab RI. For instance, assuming an asymmetric Si/SiO_2 isotropic PCS, the RI of Si can be changed by electron injection. When the GR wavelength shift occurs, transmission and reflection spectra shift occur too. The authors found that appreciable wavelength variations are possible also for small RI changes (Δn=-0.01). For anisotropic materials, they considered the case of a Potassium Titanium Oxide Phosphate (KTP) crystal, since its RI is temperature sensitive. The showed numerically that the GRs shift to longer wavelengths by increasing the temperature. Because of its sensitivity, KTP can be utilized for applications where high-definition temperature control is an issue.

4. EXPERIMENTAL PLATFORMS FOR BIOSENSING

In spite of their very promising potentials for chemical and biological sensing applications, the technological challenges in the fabrication processes still prevent full exploitation of PC-based platforms. Nevertheless, several examples of experimental biosensing platforms are available.

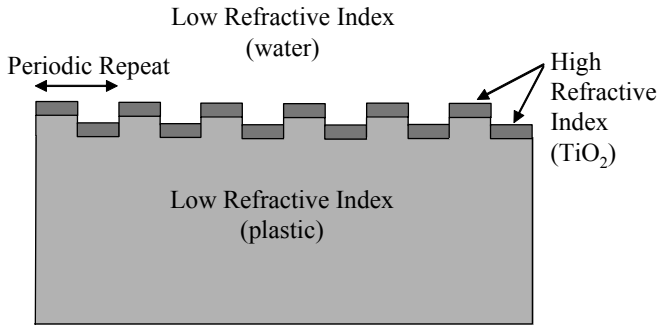

Figure 8: Cross sectional schematic structure of a PC-based biosensor fabricated from replica molded plastic material. (Reprinted with permission from Cunningham, B. T.; Block, I. D.; Chan, L.; Ganesh, N.; Lu, M.; Mathias, P. C. Photonic crystals for biosensing. In Selected Topics in Photonic Crystals and Metamaterials; Andreone, A., Cusano, A., Cutolo, A., Galdi, V., Eds.; World Scientific: Singapore, 2011; pp. 329-358. Copyright 2011, World Scientific).

For instance, in [24], Ganesh *et al.* proposed a platform basically consisting of a periodic grating surface structure made of a low RI material overcoated with a high RI material (see Fig. **8**), fabricated *via* a nanoreplica molding process in which a silicon wafer was used as a mold template for producing the PC. From the reflection spectrum shown in Fig. **9(A)**, pertaining to normal-incidence illumination with polarization oriented perpendicular to the 1-D grating, it can be observed that the PC is nearly transparent within most of the range, and behaves as a nearly perfect mirror around a resonant wavelength. The spectral location of the resonance is given by the second-order Bragg condition

$$\lambda_R = n_{eff}\Lambda, \quad \textbf{(2)}$$

where λ_R is the resonant wavelength, n_{eff} is the effective RI, and Λ is the modulation period [25]. The effective RI of the resonant mode is affected by the presence of a material deposited upon the PC surface. For instance, incorporation of biological analytes (*e.g.* proteins), which exhibit a higher RI than that of water, will increase the effective RI of the resonant mode, and thus shift the resonance. Moreover, as evident from Fig. **9(B)**, at the resonant wavelength, the electric field intensity at the PC surface is stronger than the incident one. Therefore, molecules in close proximity with the interface will experience a much stronger field intensity, compared, *e.g.* to what they would experience on an ordinary glass surface. The above illustrated wavelength-shift and field-enhancement mechanisms of interactions between molecules and a resonant PC surface can be exploited for the development of PC-based biosensor platforms for both label-free and fluorescence-based (labeled) detection.

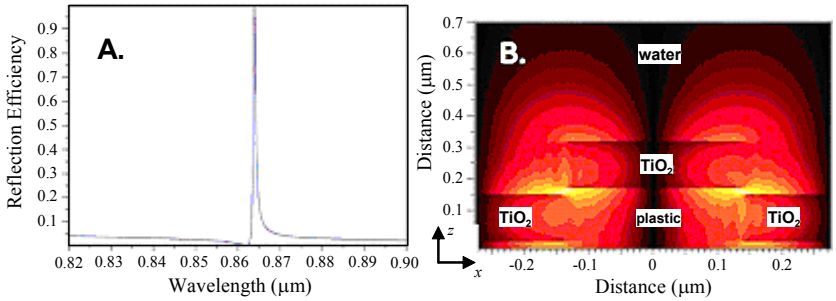

Figure 9: (A) Reflection spectrum for the PC surface, showing nearly perfect reflection for a narrow band of wavelengths. (B) Electric field intensity distribution at the PC surface at the resonant wavelength, which shows the resonantly enhanced field extending into the surrounding water media. . (Reprinted with permission from Cunningham, B. T.; Block, I. D.; Chan, L.; Ganesh, N.; Lu, M.; Mathias, P. C. Photonic crystals for biosensing. In Selected Topics in Photonic Crystals and Metamaterials; Andreone, A., Cusano, A., Cutolo, A., Galdi, V., Eds.; World Scientific: Singapore, 2011; pp. 329-358. Copyright 2011, World Scientific).

Most bioassays currently utilized in biological research exploit some sort of "labels" in order detect proteins, DNA, small molecules, or cells [26]. Label-free detection eliminates a series of artifacts and uncertainties by the effect of the label, and significantly simplifies the assay development [27].

Several other examples of PC-based biosensing platforms for label-free and labeled (fluorescence-based) detection have been proposed by Cunningham *et al.* (see, *e.g.* [25, 28-33]). For label-free detection, the underlying mechanism relies on the above illustrated wavelength shift. For instance, an attachment of DNA to one location on the PC sensor surface was able to provide a wavelength shift of about 2.5 nm. For labeled fluorescence detection, the sensor structure is designed so as to enhance the intensity of emission of fluorescent samples that are placed within the regions where GR field distribution is concentrated. Fluorescence amplification factors of nearly 500 have been experimentally demonstrated. Moreover, when the radiation from fluorescent species placed on the PC surface can couple to the photonic dispersion, the emitted light can be redirected to certain preferred directions, where it can be efficiently detected [33]. Such scheme may be effectively applied to the development of fluorescence biosensors.

The capability to combine enhanced-fluorescence images with label-free adsorption detection on a single PC would provide significant benefits for a wide range of assays of practical interest. For instance, the measurement of immobilized DNA microarray spots for spot density and spatial uniformity may be performed in a label-free mode (for calibration and quality control) during the detection of fluorescent-labeled DNA. The label-free mode may also be used for detection of species that cannot be labeled, as well as for integrated independent verification. In this framework, two different approaches have been proposed. The first approach utilizes a 2-D PC surface designed with different periods along orthogonal directions, so as to achieve the resonant coupling of two independent wavelengths for separate polarizations of the

illumination. For instance, in [31], the enhanced-fluorescence resonant coupling was designed so as to coincide with the 635 nm excitation wavelength of the fluorophore Cyanine-5, while the label-free resonant coupling was designed to occur near 850 nm (typical for most label-free PC biosensors). The second approach relies on an imaging instrument with both label-free and enhanced-florescence detection capabilities [32]. Unlike the first approach, this instrument is based on a standard 1-D PC structure, and measures the angle of minimum transmission (AMT) for each pixel of a charge-coupled device (CCD) camera to generate the label-free image. For enhanced-fluorescence imaging, the 1-D PC sensor is illuminated at the resonance angle pre-determined from the AMT image. The instrument sensitivity was characterized by depositing microspots of strepavidin-cyanine-5 (SA-Cy5) on the PC surface. Fig. **10(a)** and **10(b)** show two representative enhanced-fluorescence and label-free images. Overall, enhancements up to 328× were observed by comparison to a standard glass slide.

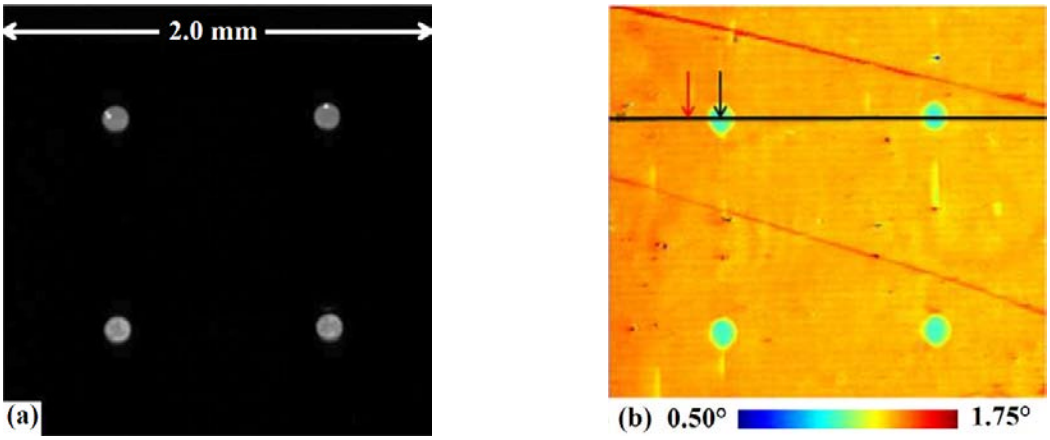

Figure 10: (a) Enhanced fluorescence and (b) label-free images pertaining to 50 μg/ml SA-Cy5 spots deposited on the PC surface (Reprinted with permission from Block, I. D.; Mathias P. C.; Ganesh, N.; Jones, I. D.; Dorvel, B. R.; Chaudhery, V.; Vodkin, L.; Bashir, R.; Cunningham, B. T. A detection instrument for enhanced fluorescence and label-free imaging on photonic crystal surfaces. Opt Express 2009, 17, 13222-13235. Copyright 2009, Optical Society of America).

In [34], Huang *et al.* introduced another interesting experimental design of a PC-based sensor which combines nano-photonics and nano-fluidics on a single free-standing (symmetric) PC slab. They also proposed a novel fluidic channel capable of actively steering the convective flow through the nanoholes for a more effective delivery of the analytes. As schematically illustrated in the rightmost inset of Fig. **11(a)**, the free-standing PC slab is sealed in a chamber in such a way that the flow between the top and bottom channels can only occur through the nanoholes. In such a configuration, particularly critical is the mechanical strength of the membrane, in view of the relatively high pressures generated by the perpendicular convective flow. In this framework, low pressure chemical vapor deposition (LPCVD) silicon nitride (SiNx) films are an excellent choice from both the mechanical and optical viewpoints. In particular, the experiments were carried out on free-standing SiNx membranes of area ~200×200 μm^2 fabricated by *via* electron beam lithography (EBL) and dry-etching, characterized by a square lattice of period a=605 nm, hole radius r=0.45a, and thickness h=0.15a.

Fig. **11(a)** compares the transmitted spectra in different operational conditions. In particular, the transmission spectrum in air clearly shows the excitation of the two resonant modes at 667 nm and 610 nm. From the red and the green curves, which represent the responses in the solution (deionized-water) for both flow schemes, it is observed that the actively-controlled scheme yields a higher sensitivity (over 40nm additional wavelength shift) and a narrower line-width. The experimental results were found to be in very good agreement with the numerical simulations (cf. Fig. **11(b)** and **11(c)**). Overall, *via* a comprehensive series of experiments (with RI ranging in the interval (1.330, 1.424)), a sensitivity of ~510 nm/RIU (around 850 nm, and with a line-width of about 10 nm) was experimentally estimated.

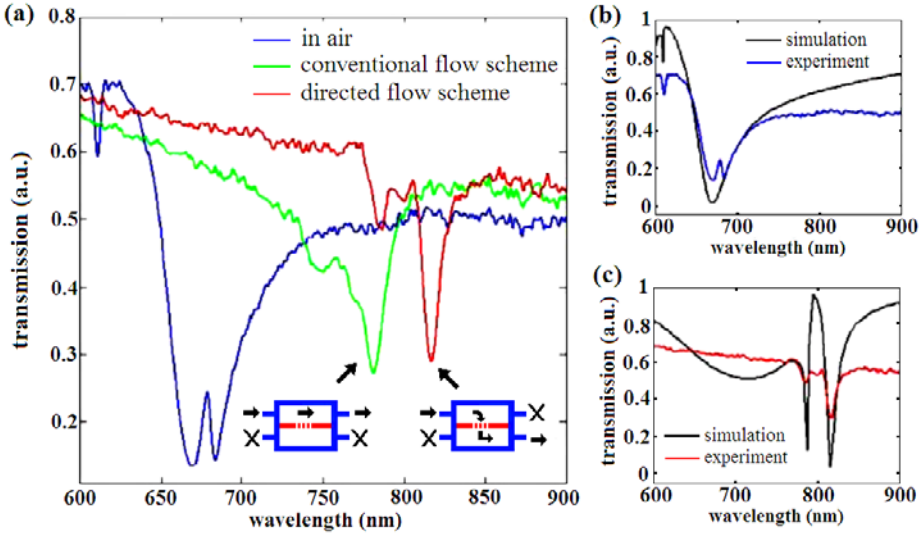

Figure 11: (a) Measured transmission spectra of a PC slab (with lattice of period a=605 nm, hole radius r=0.45a, and thickness h=0.15a) for both flow schemes (schematically illustrated in the insets). (b), (c) Comparison between simulations and measurement in air and water, respectively. (Reprinted with permission from Huang M, Yanik AA, Chang TY, Altug H. Sub-wavelength nanofluidics in photonic crystal sensors. Opt Express 2009; 17(26), 24224-33. Copyright 2009, Optical Society of America).

Another interesting GR-based configuration for detecting RI changes in aqueous solutions was proposed in [35] by Levi *et al.* The GR sensor was fabricated in SiO_2/SiNx dielectric materials by using EBL to pattern a square array of holes to a resist and subsequently Fluorine-based dry etching to transfer the structure from the resist to the SiNx layer. The sensor consisted of a silica (n=1.46) slab of thickness d=250 nm perforated by a square array of air holes of radius r=100 nm with lattice constant a=500 nm. The entire slab was immersed in different liquid solution (Iso-propanol/Water mixtures) of refractive indices varying in the 1.33-1.338 range. The excitation of the photonic crystal slab guided resonances occurs perpendicular to the sample. The local refractive index change results in a variation in the guided resonance condition and consequently generates a shift in the resonance peak location. They were able to measure a transmission peak shift of 2 nm corresponding to a detectable refractive index change of 1.5×10^{-3}.

5. COUPLED PCS: BIOLOGICAL AND DISPLACEMENT SENSORS

In PC slabs with large air holes, the GR is not a narrow-band phenomenon, and may give rise to high reflectivity over a fairly wide bandwidth [36]. By pairing two such PC slabs acting as mirrors in close proximity, it is possible to obtain an optical cavity which exhibits a narrow Fabry-Pérot-type transmission peak corresponding to the excitation of a resonant mode. In such regime, nanoscale variations of the spacing between the slabs may induce strong variations of the transmission/reflection coefficients. The width of the peak depends critically on the reflectivity of the single PC slab, and it is possible to reconfigure arbitrarily the sensitivity of the structure by varying the slab spacing. In practice, the achievable sensitivity is limited by optical losses, especially from absorption and scattering by fabrication-related disorder. In this framework, structures characterized by strong in-plane scattering strength, such as PC slabs with large air holes, may be useful to reduce the GR lifetime, and thus mitigate the optical losses.

As an illustrative example, we review the case of study considered by Suh *et al.* [37], which features two coupled PC slabs (see Fig. **12(a)**) with RI=3.46 and a square lattice (with period a) of air holes of radius r=0.4a, and thickness of 0.55a. Fig. **12(b)** shows the theoretical transmittance spectrum of a single PC slab, from which it can be observed a strongly reflective behavior within a neighborhood of the GR normalized frequency 0.53 (c/a). For the two-slab configuration, as shown in Fig. **12(c)**, superimposed onto a low-transmittance broadband background, sharp high-transmittance resonant peaks may appear, with spectral position dependent on the slab spacing, thereby enabling for *longitudinal* displacement sensing.

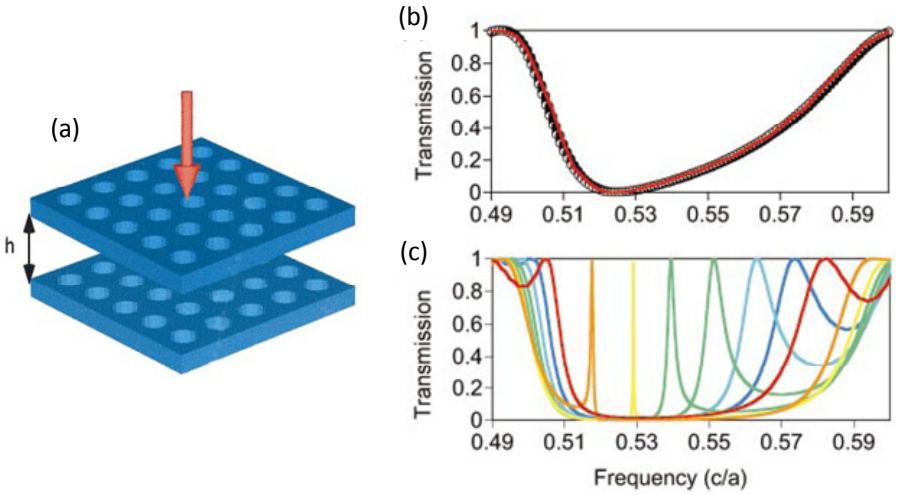

Figure 12: (a) Schematic of a PC-based displacement sensor. (b) Theoretical transmittance spectrum, for normally-incident illumination, pertaining to a single PC slab with square lattice (of period a) of air holes of radius r=0.4a, thickness of 0.55a, and RI=3.46. (c) Transmittance spectra for a two-slab configuration (with parameters as in (b)), for spacing h of 1.35a, 1.1a, 0.95a, 0.85a, 0.75a, 0.65a, and 0.55a (solid curves with colors varying from red to blue). (Reprinted with permission from Suh W, Yanik MF, Solgaard O, Fan S. Displacement-sensitive photonic crystal structures based on guided resonance in photonic crystal slabs. Appl Phys Lett 2003; 82(13): 1999-2001. Copyright 2003, American Institute of Physics).

Moreover, the GR characteristics also allow for *lateral* displacement sensing. While for slab spacing larger than 0.5a, the coupling relies primarily on propagating waves and the transmission is essentially independent of the lateral alignment, for smaller spacing, evanescent tunneling and near-field coupling play a major role [38]. Fig. **13** shows the transmittance spectra pertaining to a two-slab structure with spacing 0.1a, in the presence and absence of lateral displacement. As it can be observed, in the absence of lateral displacement, the GR supported by the single PC slab (cf. **Fig. 12(b)**) is split by the near-field coupling, resulting in strong reflections at 0.524 (c/a) and 0.555 (c/a). More interestingly, a lateral shift (along the symmetry plane direction) as small as 0.05a breaks the 90° rotational symmetry of the structure, and introduces extra resonances at 0.540 (c/a) and 0.566 (c/a), corresponding to the (otherwise uncoupled) singly degenerate states. Therefore, in the near-field coupling regime, the structure allows for lateral displacement sensing. It is worth emphasizing that, in this regime, the operating characteristics differ substantially from conventional resonant optical sensors, and high sensitivity may be obtained without the use of highly-reflective mirrors [36], with the consequent robustness with respect to wavelength and structural disorder.

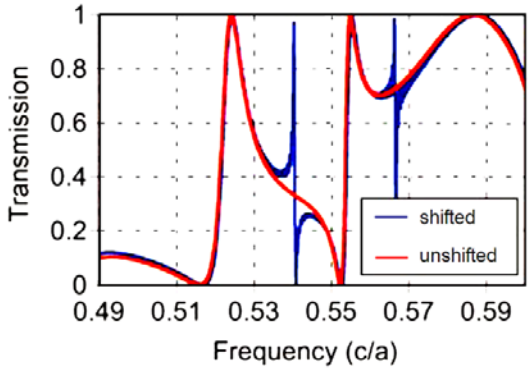

Figure 13: Transmission spectra pertaining to two-slab structures (as in Fig. **12(c)**) with spacing h=0.1a, for perfectly aligned holes in two slabs aligned (red curve), and for the hole lattice in the top slab shifted by 0.05a along the periodicity plane direction with respect to the bottom slab. (Reprinted with permission from Suh W, Yanik MF, Solgaard O, Fan S. Displacement-sensitive photonic crystal structures based on guided resonance in photonic crystal slabs. Appl Phys Lett 2003; 82(13): 1999-2001. Copyright 2003, American Institute of Physics).

Another interesting application of two-PC-slab optical cavities was proposed by Shi *et al.* [39], in connection with fluorescence enhancement and multi-analyte detection. As for the previous example, the mechanism relies on a narrow band Fabry-Pérot resonant mode supported by the cavity, which may be tuned by adjusting the slab spacing, *e.g. via* a micro electro-mechanical (MEMS) actuator. For instance, with specific reference to a configuration featuring two silicon nitride (RI=2.05) PC slabs (with triangular lattice of period a, hole radius r=0.35a, and thickness of 0.4a), they obtained a tunable range of 75 nm for a 4 nm wide transmission peak within the spectral range 511-586 nm. *Via* numerical simulations, they showed that, at the peak wavelengths, the structure may provide electric field enhancement up to a factor 32 at the outer surface, which may be used for fluorescence enhancement. Within this framework, the resonance tunability may be particularly useful in multi-analyte detection of different pathogens, where different fluorescent labels (with different emission wavelengths) need to be utilized.

CONCLUSIONS

In this paper, we have attempted a compact survey of the salient results on GR-based sensing devices. Starting with the outline of the basic physical aspects of GRs in PC slabs, we have illustrated their sensitivity with respect to variations of the RI in the surrounding environment, also highlighting the role of the various parameters and degrees of freedom available (*e.g.* field polarization, pattern geometry, *etc.*). Subsequently, we have presented a number of selected examples from the recent topical literature, illustrating theoretical/numerical and experimental aspects, as well as realistic applications to displacement, chemical, and biological sensing scenarios.

Overall, GR-based devices constitute very promising technological platforms for the development of novel compact, multi-functional sensing devices. Of particular interest appear the application perspectives of PC functionalization as well as the integration with micro- or nano-fluidic circuits.

REFERENCES

[1] Prather DW, Shi SY, Murakowski J, Schneider GJ, Sharkawy A, Chen CH, Miao BL. Photonic crystal structures and applications: Perspective, overview, and development. IEEE J Sel Top Quantum Electron 2006; 12(6): 1416-37.

[2] Joannopoulos JD, Johnson SG, Meade RD, Winn JN, Photonic Crystals: Molding the Flow of Light, second edition, Princeton University Press, New Jersey, 2008.

[3] Yablonovitch E. Inhibited spontaneous emission in solid-state physics and electronics. Phys Rev Lett 1987; 58(20): 2059-62.

[4] John S. Strong localization of photons in certain disordered dielectric superlattices. Phys Rev Lett 1987; 58(23): 2486-89.

[5] Yariv A, Nakamura M. Periodic structures for integrated optics. IEEE J Quantum Electron 1977; 13(4): 233-53.

[6] Rosenblatt D, Sharon A, Friesem AA. Resonant grating waveguide structures. IEEE J Quantum Electron 1997; 33(11): 2038-59.

[7] Nevière M. The homogeneous problem. In Electromagnetic Theory of Gratings. Petit R (Ed), Springer-Verlag, Berlin, 1980, p 123-57.

[8] Fan S, Joannopoulos JD. Analysis of guided resonances in photonic crystal slabs. Phys Rev B 2002; 65(23): 235112.

[9] El Beheiry M, Liu V, Fan S, Levi O. Sensitivity enhancement in photonic crystal slab biosensors. Opt Express 2010; 18(22): 22702-14.

[10] Erickson D, Mandal S, Yang AHJ, Cordovez B. Nanobiosensors: optofluidic, electrical and mechanical approaches to biomolecular detection at the nanoscale. Microfluid Nanofluidics 2008; 4(1-2): 33–52.

[11] Johnson SG, Fan SH, Villeneuve PR, Joannopoulos JD, Kolodziejski LA. Guided modes in photonic crystal slabs. Phys Rev B 1999; 60(8): 5751–58.

[12] Kilic O, Kim S, Suh W, Peter YA, Sudbø AS, Yanik MF, Fan SH, Solgaard O. Photonic crystal slabs demonstrating strong broadband suppression of transmission in the presence of disorders. Opt Lett 2004; 29(23): 2782–84.

[13] Fang Y, Ferrie AM, Fontaine NH, Mauro J, Balakrishnan J. Resonant waveguide grating biosensor for living cell sensing. Biophys J 2006; 91(5): 1925–40.

[14] Block ID, Ganesh N, Lu M, Cunningham BT. Sensitivity model for predicting photonic crystal biosensor performance. IEEE Sens J 2008; 8(3): 274–80.

[15] Ziblat R, Lirtsman V, Davidov D, Aroeti B. Infrared surface plasmon resonance: A novel tool for real time sensing of variations in living cells. Biophys J 2006; 90(7): 2592–99.
[16] Andersson O, Larsson A, Ekblad T, Liedberg B- Gradient hydrogel matrix for microarray and biosensor applications: An imaging SPR study. Biomacromolecules 2009; 10(1): 142–48.
[17] Ricciardi A, Gallina I, Campopiano S, Castaldi G, Pisco M, Galdi V, Cusano A. Guided resonances in photonic quasicrystals. Opt Express 2009; 17(8): 6335-46.
[18] Ricciardi A, Pisco M, Gallina I, Campopiano S, Galdi V, O' Faolain L, Krauss TF, Cusano A. Experimental evidence of guided resonances in photonic crystals with aperiodically-ordered supercells. Opt Lett 2010; 35(23): 3946-48.
[19] Gallina I, Pisco M, Ricciardi A, Campopiano S, Castaldi G, Cusano A, Galdi V. Guided resonances in photonic crystals with point-defected aperiodically-ordered supercells. Opt Express 2009; 17(22): 19586-98.
[20] Pisco M, Ricciardi A, Gallina I, Castaldi G, Campopiano S, Cutolo A, Cusano V, Galdi V. Tuning efficiency and sensitivity of guided resonances in photonic crystals and quasi-crystals: A comparative study. Opt Express 2010; 18(16): 17280-93.
[21] Harrington RF. Time-Harmonic Electromagnetic Fields, McGraw-Hill, New York, 1961.
[22] Shi L, Pottier P, Peter YA, Skorobogatiy M. Guided-mode resonance photonic crystal slab sensors based on bead monolayer geometry. Opt Express 2008; 16(22): 17962-71.
[23] Song J, Proietti Zaccaria R, Yu MB, Sun XW. Tunable Fano resonance in photonic crystal slabs. Opt Express 2006; 14(19): 8812-26.
[24] Ganesh N, Zhang W, Mathias PC, Chow E, Sooares JANT, Malyarchuk V, Smith AD, Cunningham BT. Enhanced fluorescence emission from quantum dots on a photonic crystal surface. Nature Nanotechnology 2007; 2(8): 515-20.
[25] Cunningham, B. T.; Block, I. D.; Chan, L.; Ganesh, N.; Lu, M.; Mathias: C. Photonic crystals for biosensing. In Selected Topics in Photonic Crystals and Metamaterials; Andreone, A., Cusano, A., Cutolo, A., Galdi, V., Eds.; World Scientific: Singapore, 2011; p. 329-58.
[26] Cunningham AJ. Introduction to Bioanaytical Sensors. John Wiley & Sons, New York, 1998.
[27] Brecht A, Gauglitz G. Optical probes and transducers. Biosensors Bioelectronics 1995; 10(9-10): 923-36.
[28] Li:; Lin, B.; Gerstenmaier, J.; Cunningham, B. T. A new method for label-free imaging of biomolecular interactions. Sens Actuat B 2004, 99(1): 6-13.
[29] Cunningham, B. T.; Li:; Schulz, S.; Lin, B.; Baird, C.; Gerstenmaier, J.; Genick, C.; Wang, F.; Fine, E.; Laing, L. Label-free assays on the BIND system. J Biomol Screen 2004; 9(6): 481-490.
[30] Block, I. D.; Chan, L. L.; Cunningham, B. T. Photonic crystal optical biosensor incorporating structured low-index porous dielectric. Sens Actuat B 2006; 120(1): 187-93.
[31] Mathias: C.; Ganesh, N.; Chan, L. L.; Cunningham, B. T. Combined enhanced fluorescence and label-free biomolecular detection with a photonic crystal surface. Appl Opt 2007; 46(12): 2351-60.
[32] Block, I. D.; Mathias P. C.; Ganesh, N.; Jones, I. D.; Dorvel, B. R.; Chaudhery, V.; Vodkin, L.; Bashir, R.; Cunningham, B. T. A detection instrument for enhanced fluorescence and label-free imaging on photonic crystal surfaces. Opt Express 2009; 17(15): 13222-35.
[33] Yu, H. Y.; Zhang, W.; Mathias: C.; Cunningham, B. T. Magnification of photonic crystal fluorescence enhancement *via* TM resonance excitation and TE resonance extraction on a dielectric nanorod surface. Nanotechnology 2010; 21(12): 125203-10.
[34] Huang M, Yanik AA, Chang TY, Altug H. Sub-wavelength nanofluidics in photonic crystal sensors. Opt Express 2009; 17(26): 24224-33.
[35] Levi O, Lee MM, Zhang J, Lousse V, Brueck SRJ, Fan S, Harris JS. Sensitivity analysis of a photonic crystal structure for index-of-refraction sensing Proceedings of SPIE 2007; 6447: 2–9.
[36] Ricciardi A, Campopiano S, Cusano A, Krauss TS, O'Faolain L. Broadband mirrors in the near-infrared based on sub-wavelength gratings in SOI. IEEE Photonics 2010; 2(5): 696-702.
[37] Suh W, Yanik MF, Solgaard O, Fan S. Displacement-sensitive photonic crystal structures based on guided resonance in photonic crystal slabs. Appl Phys Lett 2003; 82(13): 1999-2001.
[38] Suh W, Solgaard O, Fan S. Displacement sensing using evanescent tunneling between guided resonances in photonic crystal slabs. J Appl Phys 2005; 98(3): 033102.
[39] Shi L, Pottier P, Skorobogatiy M, Peter YA. Tunable structures comprising two photonic crystal slabs – optical study in view of multi-analyte enhanced detection. Opt Express 2009; 17(13): 10623-32.

CHAPTER 10

Physical, Chemical and Biological Sensors Based on Photonic Crystals

Sanja Zlatanovic[1,*] and Annette Grot[2]

[1]Department of Electrical and Computer Engineering, University of California San Diego, 9500 Gilman Drive, La Jolla, CA 92093, USA and [2]Pacific Biosciences, Inc., 1505 Adams Drive, Menlo Park, California 94025-1451, USA

Abstract: Photonic crystal sensors have recently drawn much attention due to their inherent compactness and high sensitivity. Different types of photonic crystal sensors rely on one main transduction mechanism: perturbations in environmental conditions alter index of refraction or periodicity of the structure which is transferred to a detectable change in optical power or spectrum. This transduction mechanism facilitates utilization of photonic crystal for sensor applications ranging from pressure and displacement measurements to detection of chemical composition change and binding events. In this chapter, we give a summary of different types of photonic crystal sensors such as waveguides, microcavities and self-assembled 3D structures and review their application to physical, chemical and biological sensing. We discuss advantages and limitations of the technology.

Keywords: Optical sensing, photonic crystals, compact sensors.

1. INTRODUCTION

Photonic crystal sensors are a class of devices based on photonic bandgap materials. The optical properties of these periodic structures are determined by interference of multiply diffracted waves and are sensitive to material parameters such as refractive index and lattice spacing. Consequently, any environmental phenomenon that can alter periodicity and refractive index of the structure of the photonic crystal can be sensed by measuring optical properties such as spectral signature, reflected and transmitted optical power or angular deviation of light. Sensing *via* the photonics crystal structures is an emerging field, attractive due to the inherent compactness and high sensitivity of devices. In addition, they have well-defined physical properties and can be designed to operate at virtually any wavelength range. Especially attractive are those working in the visible range in which detected ambient changes can even be monitored visually. Potential applications of the photonic crystal sensors span wide range of disciplines including environmental monitoring for hazardous chemicals, biosensing, drug discovery, as well as monitoring of physical properties such as pressure, stress, strain, temperature or humidity. In addition to high sensitivity, applications such as hazardous chemical sensing require fast and continuous operation. Portable, low cost and low-power sensors for chemical and biological warfare agents are currently of great interest. For biosensing, development of compact sensor devices capable of detecting ultrasmall sample volumes is an important goal toward realization of efficient "lab on a chip" systems. "Lab on a chip" devices are envisioned as tools that can combine biosensing and other analytical functionalities with microfluidic delivery of small sample volumes. The photonic crystal sensors can provide all that functionality since they can be integrated with electronic circuits as well as microfluidic flow cells.

2. TYPES OF PHOTONIC CRYSTAL SENSORS

Beside by different physical, chemical or biological properties that they can measure, the photonic crystal sensors can be classified into different types according to their topologies. Numerous structures have been proposed and demonstrated so far. We will overview three major groups: porous silicon based photonic crystal

***Address correspondence to Sanja Zlatanovic:** Department of Electrical and Computer Engineering, University of California San Diego, 9500 Gilman Drive, La Jolla, CA 92093, USA; Tel: +1-858-822-7897; E-mail: szlatanovic@ucsd.edu

Marco Pisco, Andrea Cusano and Antonello Cutolo (Eds)
All rights reserved-© 2012 Bentham Science Publishers

sensors, arrays of holes and pillars, and three-dimensional self assembled structures. Porous silicon sensors include subgroups such as bulk sensors, multilayered structures and microcavities. The photonic crystals based on two-dimensional pillars and holes arrays are proposed and demonstrated in the waveguide and microcavity configurations. Three-dimensional self-assembled photonic crystals are based on the bulk topology.

The principle of operation of all photonic crystal sensors is similar. The spectral signature of photonic crystal devices is determined by the periodicity of the photonic lattice structure, introduced defects and material and ambient index of refraction. These properties determine the conditions for resonant Bragg reflection, and consequently structural color of the photonic crystal device. Photonic crystal color is therefore inherently sensitive to environmental conditions. Ambient perturbations can cause dimensional variations in the photonic crystal lattice and change in effective index of refraction.

These changes can be monitored either visually or by spectroscopic methods involving the measurement of reflectance and transmittance spectra. The high sensitivity to refractive index change of the photonic crystal sensors is mainly due to their capability to localize the light to very small volume, such that even minute average changes in the environment produce significant spectral response. In addition, the high degree of light confinement implies very small sensing volumes. Porous silicon photonic crystals are fabricated using anodic etching of monocrystaline silicon in the presence of hydrofluoric acid. The result is material comprised of unidirectionally aligned pores whose size can be precisely controlled and varied using different current densities. By applying a periodic current-time waveform, structures that act as one dimensional photonic crystal can be generated. Alternating current densities in a stepwise manner can result in multilayered structures corresponding to discrete variation in porosity (Fig. **1a**, Fig. **2a**) [2]. If the current density is varied in a sinusoidal manner, a rugate filter is formed (Fig. **2b**) [3]. Such devices provide a single sharp feature in the optical reflectivity spectrum. Sailor and colleagues showed that rugate filters can be released from the support wafer, broken into fragments and used in solution-phase sensing. These sensors are referred to in the literature as "smart dust" [4, 5]. Bragg condition determines the light wavelength that will be reflected from the structure. The rugate filters offer cleaner reflection spectra than multilayer structures due to suppression of sidelobes. In similar manner, by varying current density, one-dimensional microcavities can be formed in porous silicon (Fig. **1b**). In these structures a narrow resonance appears as a dip in reflectance spectrum. This resonance is extremely sensitive to the changes in refractive index that arise from environmental factors. Freshly etched porous silicon is unstable in aqueous solutions and for purpose of biosensing has to be stabilized usually by means of oxidation.

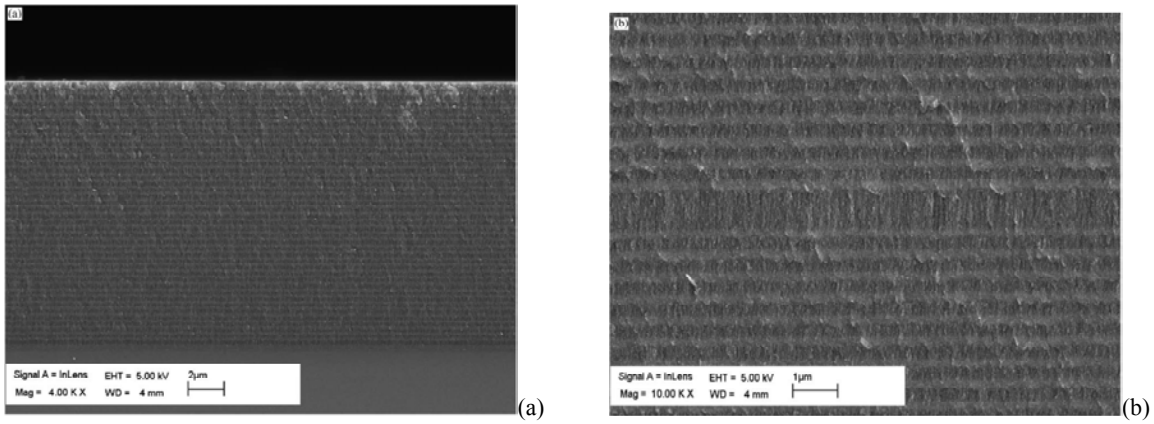

Figure 1: (a) Cross-section SEM image of multilayer porous silicon structure (b) Cross-section SEM image of porous silicon microcavity structure [1]. Reproduced with permission from Elsevier.

Photonic crystals based on pillars and holes arrays have been demonstrated in different materials. Active photonic crystal sensors in laser configurations are made in InGaAsP membranes with quantum wells inside the slab material that serve as gain medium [7]. The laser microcavity in such medium is created using a point defect. While the sensitivity of the device improves with larger defect diameter due to

increase in interaction volume between light and analyte, the decrease in the light enhancement factor also raises lasing threshold. In such a structure, the linewidth of emission is very narrow due to very high Q-factors and position of the emission line is highly dependent on the index of refraction of the material that fills the sensors holes. The photonic crystal sensors in passive configuration are usually made from silicon on insulator wafers using combination of wet and dry etching on photonic crystal lattice predefined by either deep UV or e-beam lithography. In waveguide configurations (Fig. **3**), the photonic crystal bandgap serves to confine light to the guiding region, while in vertical dimension light is confined by total internal reflection arising from the large index differences. In these types of sensors the changes in environmental factor are based on measuring the spectral shifts in bandgap edge. In contrast, in the case of microcavity structures (Fig. **4**), analogous to active laser devices, the spectral shifts in narrow resonance introduced by defect are monitored.

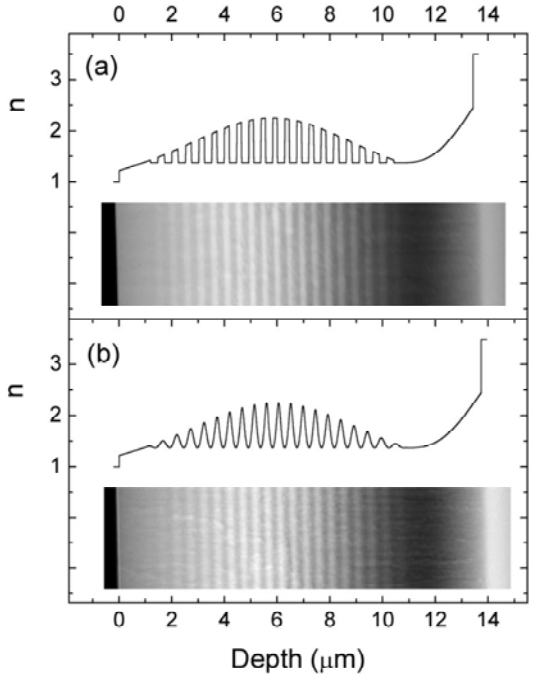

Figure 2: Comparison of (a) an apodized distributed Bragg grating and (b) a rugate filter, both upon silicon substrates. The nominal index profiles of the designs are shown, and a cross-sectional scanning-electron micrograph is shown below each curve [6]. Reproduced with permission from Optical Society of America.

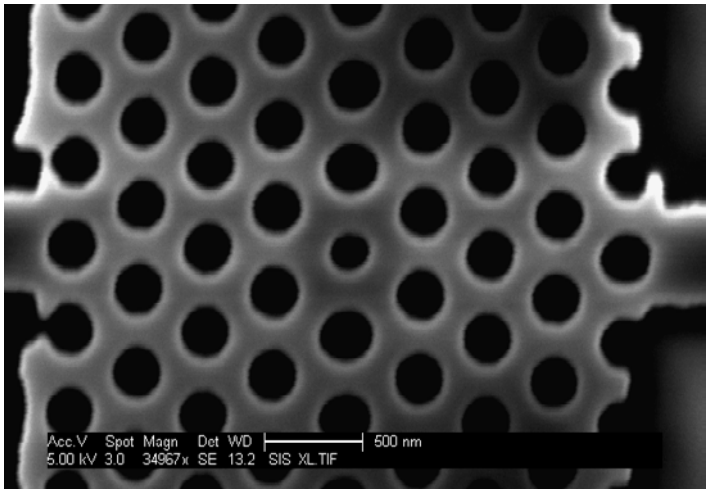

Figure 3: SEM of photonic crystal microcavity [8]. Reproduced with permission from Elsevier.

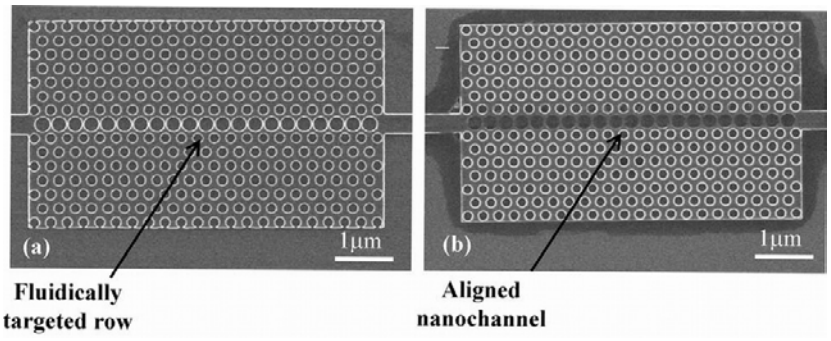

Figure 4: SEM of photonic crystal waveguide SEM images showing the photonic crystal (a) prior to integration with nanofluidics and (b) after removal of the fluidics. The darkened regions show deposited CTAB after allowing the solvent to evaporate within the nanochannels, illustrating precise nanofluidic confinement within the targeted region of the photonic crystal [9]. Reproduced with permission from Optical Society of America.

Three-dimensional photonic crystals are formed by self-assembly of colloidal particles in hydrogels or other polymers. The periodic lattice results from electrostatic repulsion between monodisperse, highly charged colloidal particles, which form cubic array inside the polymer (Fig. **5**). They are also referred to as polymerized crystalline colloidal array (PCCA). The principle of detection is based on reversible swelling of the hydrogel or flexibility of the polymer that changes the condition for Bragg reflection. Another type of the three-dimensional photonic crystals is the inverse opal. Instead of consisting of a regular arrangement of uniform colloidal particles, inverse opals consist of a regular arrangement of spherical void spaces surrounded by solid walls. The inverse opals are made by self-assembly of colloidal particles that serve as a template, injection and solidification of polymer and subsequent removal of the template. This procedure leaves a three-dimensionally ordered porous solid (Fig. **6**).

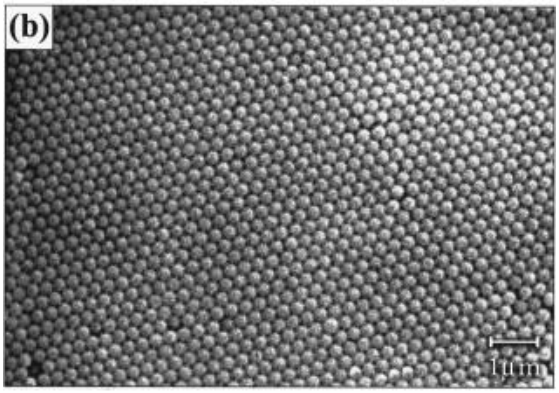

Figure 5: Self-assembled three-dimensional photonic crystal [10]. Reproduced with permission from American Institute of Physics.

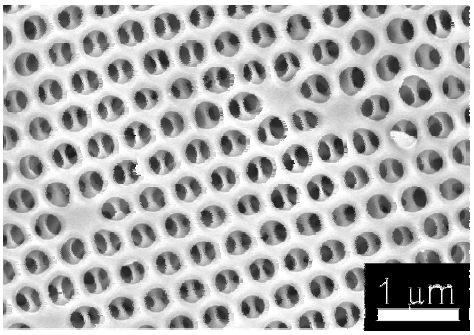

Figure 6: Inverse opal [11]. Reproduced with permission from American Chemical Society.

3. SENSING OF PHYSICAL PROPERTIES

While sensing of physical properties is of importance for numerous applications, the photonic crystals have not found major application in this field. The reason probably lies in the fact that other structures, less complicated from a fabrication point of view, can provide similar performance. In particular because physical properties affect large scales in terms of area and volume, compact sensors are not of major importance except in the case where such physical properties have to be measured locally. Three-dimensional self-assembled photonic crystals therefore present the most cost-effective topology for physical sensors. Here, we will overview existing application of PCCA self-assembled photonic crystals for strain and temperature sensing, application of two-dimensional photonic crystal with holes for measurements of film thickness, refractive index, pressure and humidity measurements.

3.1. Strain Sensor

In 1994, Asher *et al.* [12] proposed a novel type of sensor based on polymerization of crystalline colloidal array. They have demonstrated that diffraction maximum in the spectrum shifts when the uniaxial strain is applied in the plane of the film and returns back to initial value after the stress is relieved. The shift in the peak wavelength corresponded to increase and decrease in the interplanar distances of the sensor initiated by applied force.

3.2. Displacement Sensor

The physical sensing using photonic crystals relies on displacements or deformations introduced by physical force that change periodicity of the photonic crystal structure. In principle, due to miniature size the photonic crystal sensors are expected to be sensitive to smaller displacements and forces. It has been shown through simulations that high sensitivity can be achieved for nanoscale displacements [13]. However, while such structures have been proposed, designed and analyzed numerically, no experimental demonstration has been shown to date.

In such a displacement sensor, a two-slab photonic crystal structure is used [13]. A strong variation of transmission and reflection can be induced by nanoscale changes of separation between the slabs. A sensitivity of such sensor is estimated to be 1% of the operating guided resonance wavelength in structures with the radius of the holes is 40% of the lattice period,corresponding to approximately 10nm.

3.3. Film Thickness Measurements

Burr *et al.* have demonstrated application of photonic crystal microcavity to film-thickness sensing [14]. In the experiment, the monlayer polyelectrolyte films were deposited on the photonic crystal microcavity by sequentially adsorbing layers of oppositely charged polymers. Initially a nucleation layer of poly(ethyleneimide) PEI (+) was deposited onto the sample surface to establish a uniform surface charge. A multilayer composite film was then formed by repeating the sequential electrostatic adsorption of poly(styrene sulfonate) PSS(-) and polylysine PLS (+). Authors used ellipsometry measurements on flat Si substrate to measure both the refractive index of composite polyelectrolyte film (n=1.49), as well as the dependence of film thickness on the number of layers (inset of Fig. **7**). While the thickness increased non-linearly for the initial layers, a linear deposition regime was reached after 10 layers. The non-linear deposition was attributed to the low negative charge density on the bare substrate, which lead to incomplete coverage in the initial electrostatic adsorption process. Once a uniform charge was established across the entire surface, a consistent deposition rate is observed from layer to layer. Fig. **7** shows the resonant wavelength shift as a function of the number of polyelectrolyte layers. Consistency between photonic crystal wavelength shift measurements and ellipsometry measurements was demonstrated (figure inset). A linear increase is observed from 10–20 layers with thickness responsivity of 1.5 nm/nm. It was also demonstrated that responsivity saturates when more than 50 layer are deposited due to the fact that the holes of the photonic crystal have been completely filled.

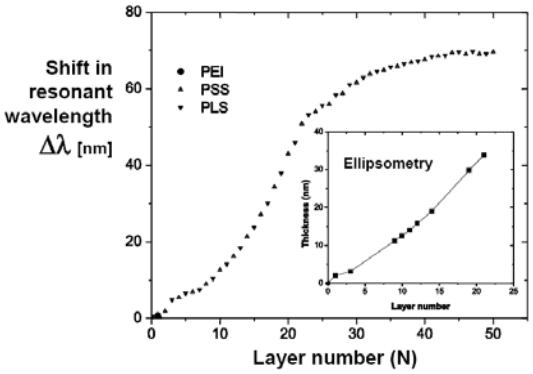

Figure 7: Measured wavelength shift as a function of the number of polyelectrolyte layers. The variation from linearity over the first ten layers is attributed to incomplete coverage by the first adsorbed layer due to the weak initial surface charge on the bare substrate [14]. Reproduced with permission from Optical Society of America.

3.4. Temperature Sensor

Takeoka and Watanabe showed a temperature sensor, fabricated as an inverse opal from colloidal crystal array of SiO_2 that was immersed with temperature-sensitive poly(N-isopropylacrylamide) (NIPA), and subsequently polymerized [15]. The authors used solvent evaporation technique for making finely-ordered colloidal crystal arrays. The samples were then immersed in HF to remove SiO_2 colloids. By doing so, they were able to produce a single crystalline inverse opal with sharp diffraction peak.

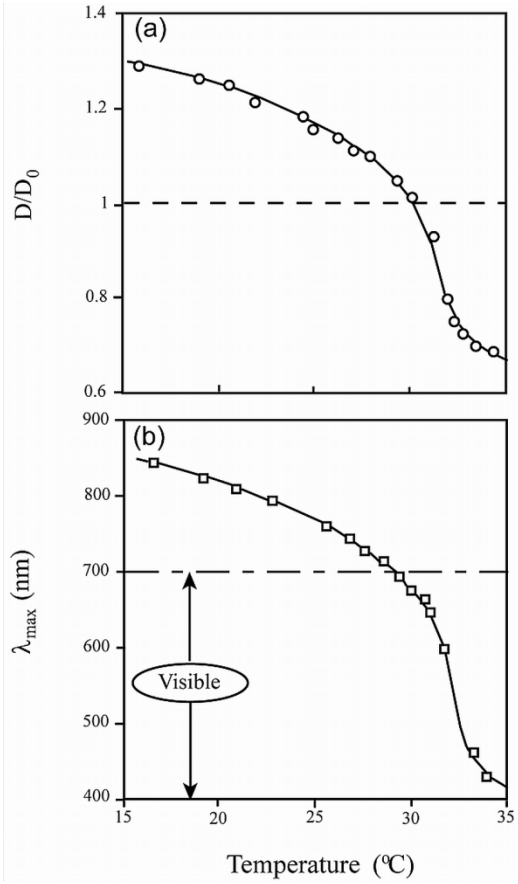

Figure 8: (a) Equilibrium swelling degree of the NIPA gel as a function of temperature, (b) Peak wavelength of reflection spectra from porous gel as a function of temperature [15] Reproduced with permission from John Wiley and Sons.

Due to Bragg diffraction the observable color depends on direction of incident light, index of refraction of porous gel that consists of a polymer part and water-filled voids and the size of the voids when temperature is changed. In Fig. **8**, the equilibrium degree of swelling of the gel was given where D and D_0 are diameters of the gel at investigated and reference temperature, respectively. Reversible diffraction shift from 400nm to 850nm corresponding to temperature change from 15^o-35^o were demonstrated.

3.5. Humidity Sensor

Among other applications, hydrogel-based photonic crystal can be used for sensing humidity variations in the environment by their direct exposure to the ambient atmosphere. A polyacrylamide inverse opal hydrogel structure was created from a colloidal crystal template and tested under various humidity conditions [11]. When the ambient humidity is increased, the hydrophilic acrylamide hydrogel absorbs water from the air and reaches a new equilibrium. The structure deforms from its previous equilibrium as it absorbs water. While the swelling should happen in all directions, due to the surface attachment or the hydrogel, the most considerable swelling occurs primarily in the direction perpendicular to the surface. The swelling causes a spacing increase between the layers of pores and hydrogel and results in the shift of the reflectance spectrum peak. In addition when this hydrogel is absorbing water from the air, the water brought into the polymer structure will change that structure's refractive index, bringing the average index of the water-hydrogel composite down with more water added. The dry, collapsed hydrogel has a refractive index of about 1.49, while water has a value of 1.33. Therefore, the response to the humidity changes is noticeably shifting of optical reflection peak within the visible wavelength range when relative humidity is changed from 20% to 80% (Fig. **9**). By observing the kinetics of the peak shifts a rapid response to ambient humidity changes was verified.

Humidity sensors have also been demonstrated using one-dimensional photonic crystals in TiO_2. These sensors were fabricated using glanced angle deposition technique (GLAD) that allows columnar microarchitectures with nanometer scale precision, similar to those of multilayer porous silicon structures. The mesoporous nature of this photonic crystal sensor allows water vapor to condense inside and change the effective refractive index of sensor volume. This condensation shifts the photonic crystal stopband from 548.1 nm, at 3% relative humidity to 586.3 nm at 90% relative humidity. The shift is reversible and repeatable over many cycles. This spectral shift corresponds to an easily visible color change of the sample, allowing visual monitoring of the sensor. This simple visual feedback system is desirable to minimize the cost and power consumption of the sensor device [16].

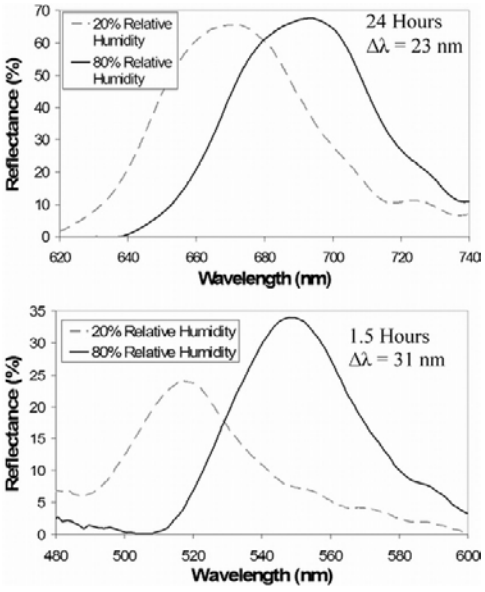

Figure 9: Spectra shift of IOH for sample with (a) 24-h infiltration time and (b) 1.5-h infiltration time. The shift occurred in both cases by changing the relative humidity from 20% to 80% [11]. Reproduced with permission from American Chemical Society.

In addition, unlike other sensors, the humidity sensors do not require specific functional groups to be incorporated to hydrogels. It is a hydrophilic nature of the polymer that is sufficient to sense the photonic crystal structural changes in presence of different levels of humidity.

3.6. Refractive Index Measurements

As previously discussed, the spectral peak of the photonic crystal inherently depends on index of refraction of the ambient. Several groups have reported highly sensitive measurements of refractive index using photonic crystal microcavities.

Loncar *et al.* were the first to demonstrate photonic crystal laser structure in InGaAsP membranes for refractive index measurements and chemical sensing [7]. The geometry of their device was based on single-defect triangular lattice, with additional fractional dislocation introduces by extending the length of one of the rows of holes. This served to break the symmetry of optical cavity, thereby increasing the quality factor of the cavity beyond 6000. In addition to high Q-factors such cavities also possess small modal volume. The authors reported measurements of wavelength shifts in the laser spectrum when the laser was immersed into a solution of methanol and isopropanol and when it was exposed to air. They demonstrated the lasing wavelength dependence on index of refraction of ambient material. The reported sensitivity, *i.e.,* dependence of the resonant wavelength shift on the change in refractive index of the analyte was 266 nm per refractive index unit (RIU). The authors also reported that when ambient index is around 1.4, wavelength shifts that can still be observable from the cavity (Q~1000) are approximately 1.55 nm, which corresponds to measurable refractive index change of 0.0056. In addition to detection of refractive index changes within the samples of femtoliter volumes, the authors have also demonstrated that their devices can be integrated into arrays to permit analysis of many reagents at the same time.

Chow *et al.* employed passive photonic crystal microcavities with moderate Q-factors of ~400 to demonstrate improvement in measurements of change in ambient refractive index down to 0.002 [17]. Their device was a triangular lattice photonic crystal with defect hole fabricated in a silicon slab waveguide. In addition, the authors reported the first time-resolved measurement in passive microcavity configuration by monitoring evaporation of water in 5% glycerol mixture. The sensitivity of the sensor was ~200 nm/RIU. Authors have also demonstrated excellent stability of the sensor over time when ambient conditions were constant.

A refractive index sensing scheme based on superprism effect that utilizes photonic crystal opal has been proposed by Prasad *et al.* [18]. Their refractometric method exploits the sensitivity of the diffraction angle to the material properties, such as refractive index contrast, for frequencies near the photonic band edge. The device has not been demonstrated experimentally, but authors claim potential three-orders of magnitude improvement in sensitivity to small changes in index contrast compared to other optical sensing methods.

Three-dimensional inverse opals made in silica [19] have also shown to have a good response to index of refraction. The estimated refractive index sensitivity is ~0.001. The authors have demonstrated that sensitivity increases with particle size for both direct and inverse opals, while overall sensitivity of inverse opals was better. They also showed, that besides spectral measurements, optical sensing can be realized by simple reflection or transmission measurements that register only the powers.

Dorfner *et al.* demonstrated the use of photonic crystal drop filters that are microcavities with evanescently coupled light [20] for refractive index measurements. Two types of microcavities, one with defect introduced as single hole of larger size (H1), and the other one created by removing three holes from the photonic crystal (L3) were investigated. The demonstrated sensitivity for H1 type of cavity was 155 nm/RIU, while for L3 it was 63 nm/RIU. The L3 cavity had q-factor of ~3000, while the H1 has 400. The lower sensitivity in L3 waveguide can be attributed to poor overlap of the mode with analyte, since majority of the field is located inside the silicon. On the other hand, in an H1 cavity, the analytes penetrate the defect hole where most of the modal field is confined resulting in higher sensitivity. Assuming a minimal detectable shift on the order of resonance linewidth, they estimated limit of detection to be 0.0018 for H1 and 0.006 for L3. However, it should be pointed out that the minimum detectable shifts can indeed be smaller than a resonance linewidth. With excellent signal

to noise ratio, the shifts that are nearly three orders of magnitude smaller can be detected using narrow linewidth tunable laser sources in combination with high speed photodetectors. However, the better the quality factors are the easier it is to detect small spectral shifts.

Another type of refractometer based on photonic crystal slotted waveguides has recently been demonstrated [21]. As mentioned before the two most important factors for achieving high sensitivity and better detection limits are good overlap between analyte and modal volume and high q-factors. In slotted waveguide geometry, a narrow slot is introduced into the photonic crystal waveguide, which enables both high q cavity and excellent overlap between the modal volume and analyte (Fig. **10**). Dry q-factor of 50 000 was demonstrated in such a structure. The infiltrated waveguide had q of ~4000. The sensitivity measurements were performed using different concentration of caster sugar, with corresponding refractive indices of the solution obtained with refractometer at sensor operating wavelength. The obtained sensitivity value was very high compared to other studies 1538nm/RIU. Reported estimated detection limits are 7.8×10^{-6}.

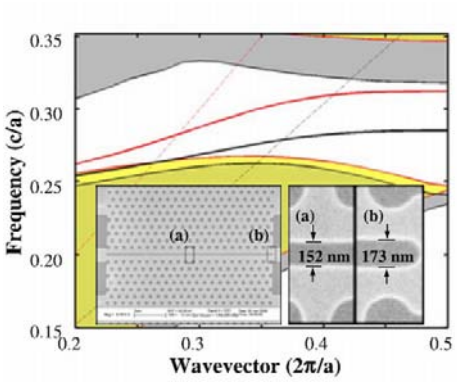

Figure 10: Dispersion properties of slotted photonic crystal (SPhC) waveguide with different background refractive indices yellow shade and red lines n=1, gray shade and black lines n=1.315. Inset: SEM image of a SPhC cavity, with zoomed view of the (a) central and (b) external part of the slot [21]. Reproduced with permission from American Institute of Physics.

3.7. Pressure Sensor

Sunner *et al.* demonstrated a gas and pressure sensor using high quality factor cavities in GaAs [22]. The device was mounted on a temperature controlled stage inside an airtight chamber which allowed measurements in vacuum and in different gaseous environments. Keeping the temperature constant in such an experiment is imperative, because temperature variation of even 1K produce wavelength shift comparable to the shift caused by ambient gas or pressure changes. Typical measured quality factors for cavity were 40000. The refractive index variation was caused by changing the ambient pressure of SF_6 atmosphere. This gas was chosen because it offers the largest refractive index of 1.0007. The measurements were performed for pressures ranging from 5×10^4 down to 0.1×10^4Pa in steps of 0.5×10^4 Pa (Fig. **11**).

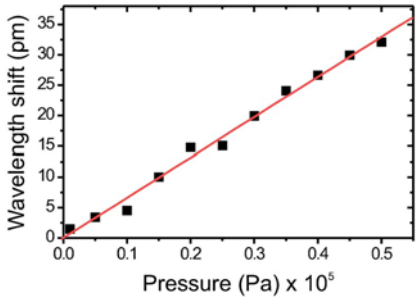

Figure 11: Resonance wavelength behavior for different SF6 pressures. The pressure was lowered from 5×10^4 to approximately 0.1×10^4 Pa. The solid line is a linear fit to the data [22]. Reproduced with permission from American Institute of Physics.

4. CHEMICAL SENSORS

While we are going to list here gas and fluid sensors, we need to stress out that they are based on index of refraction measurements and have no specificity. While different gases and liquids posses different indices of refraction, the values of refractive index is not sufficient to specifically determine which chemical or gas is present in the sensor. Specificity has to be provided by other means, such as chemical reactions or recognition mechanisms. On the other hand, ionic sensors that are presented are specific to certain ions and can be used for their detection in mixture of different chemicals.

4.1. Gas Sensors

Sunner *et al.* also studied response of the cavity to changes of the ambient refractive index. Transmission measurements of the cavity under different gaseous environments showed a linear dependence of the resonance wavelength on the refractive index of the ambient gas. Reported sensitivity was 78 nm/RIU. A change of refractive index by 10^{-4}, therefore shifts the resonance by 8 pm, which can be readily detected due to high quality factor of the cavity (Fig. **12**). The measurements were performed for helium, nitrogen, argon and SF_6.

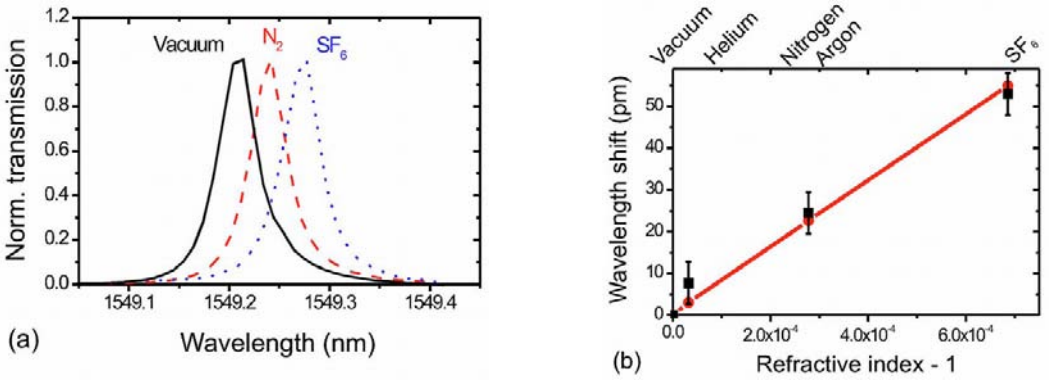

Figure 12: (a) Transmission of a PhC resonator in vacuum, (solid black line), nitrogen (dashed red line), and SF6 (blue dotted line). (b) Shift of resonance wavelength for different gaseous environments H2, N2, Ar, and SF6. Black squares: measured values; red dots/red line: calculated values and linear interpolation. The refractive indices of N2 and Ar and the corresponding wavelength shifts are identical within the error bars [22]. Reproduced with permission from American Institute of Physics.

4.2. Fluid Detection

While similar in principle to refractive index detection, Topol'ancik *et al.* demonstrated application of photonic crystal waveguides to fluid detection [23]. They designed a structure consisting of three photonic crystal waveguides with different transmission properties at excitation wavelength. The device consisted of a common photonic crystal waveguide after which the light was branched to photonic crystal waveguide 1 and 2 that had different design. This structure was employed in a fluid detection based on transmission scheme. The design of the structure ensured that in presence of liquid of certain index of refraction light was coupled into only one of the two output photonic crystal waveguides. Introducing isopropyl alcohol caused the change in index of refraction and effect on defect modes in both output waveguides, but light coming from common branch waveguide was only transmitted through waveguide 2. On the other hand, introduction of xylene enabled transmission through the waveguide 2 only. In refractive index measurement schemes [7, 17], the photonic crystal waveguides were also shown to be able to detect different chemicals.

4.3. pH and Ionic Strength Sensor

Three-dimensional photonic crystal hydrogels have been applied to the measurements of pH factor and ionic strength. Lee and Asher [24] demonstrated sensitivity of the acrylamide hydrogel with 100nm polystyrene colloids to pH and ionic strength. The principle of operation is based on swelling of hydrogel

due to ionization of carboxyl groups. This ionization is dependent on solution pH and causes immobilization of counterions inside the gel that result in an osmotic pressure and swelling of the hydrogel against the restoring force. Swelling of the hydrogel changes the periodicity of the colloidal particle lattice that can be detected optically by Bragg diffraction. The authors reported 250nm diffraction wavelength shift from 550 nm to 800 nm when pH changed from 4 to nearly 10. However, the sensor response to pH is not monotonic and it drops as pH increases beyond 9.6, because ionization is complete and only ionic strength increases, which in turn decreases the osmotic pressure and shrinks the gel.

Detection of pH with inverse opal hydrogels formed through photo-polymerization of 2-hydroxyl-ethylmethacrylate and various functional monomers was reported by Braun *et al.* [25]. They demonstrated higher sensitivity where the resonant wavelength changed from 544 to 850 nm for a pH change from 4 to 7.

4.4. Ion Detection

In 1997 Holtz and Asher [26, 27] proposed a novel PCCA structure based on acrylamide gel and demonstrated Pb^{2+} detection. They showed that when a crown ether that selectively complexes with Pb^{2+} ions is incorporated into acrylamide gel the sensor responds to Pb^{2+} most strongly, and much weaker to K^{+} that bind more weakly, and Li^{+} that binds negligibly. The diffraction peak maximum redshifts when binding of cations occurs. At very high concentrations of complexed ion, the PCCA contracts slightly, causing a small diffraction blueshift. The detectable concentration range for Pb^{2+} is between 0.1 μM and 20 mM.

The same group has reported application of PCCA for sensing of metal cations such as Cu^{2+}, Co^{2+}, Ni^{2+} and Zn^{2+} [28]. In this case, metal cations binding to 8-hydroxyquinoline was monitored by diffraction peak changes. It was demonstrated that the concentration of cations on the order of μM can be determined visually from the color of the diffracted light or can be determined by reflectance measurements using a spectrophotometer. This particular sensor can find application in quality control of drinking water.

4.5. Explosive Detection

Trinitrotoluene (TNT) detection has been reported in porous silicon using displacement assay in combination with signal processing techniques that increase sensitivity of the measurement [29]. The displacement assay is a strategy in which a small molecule displaces a larger molecule. In this case authors used TNBS molecule as a large molecule and attached it on the single layer film of conjugate immobilized on the surface of porous silicon. Shift in diffracted wavelength was detected upon binding of TNT that replaces TNBS molecules. Using this scheme the authors reported detection limit of 1 μg/ml TNT in solution.

5. PHOTONIC CRYSTAL BIOSENSORS

Photonic crystal biosensors are especially attractive since they belong to a group of label-free optical sensing platforms, such as surface plasmon sensors. Surface plasmon resonance has demonstrated effectiveness in drug research, paving the road for label-free optical biosensors to replace more conventional methods used nowadays. In addtion to surface plasmon resonance, a number of optical label-free sensors have been demonstrated to date, including microring [30] and microtoroid resonators [31], fiber optic and waveguide sensors, porous silicon and resonant mirrors. Some of them have been used over the past decade in many areas of drug discovery, including target identification, ligand fishing, assay development, and manufacturing quality control [32].

They allow the determination of the affinity and kinetics of a wide variety of molecular interactions in real time, without the need for a molecular tag or label, because they are based on refractive index measurements. At present, most screens that are used in drug discovery require some type of fluorescent labeling or radio-labeling to report the binding of a ligand to its receptor. This labeling step imposes extra time and cost demands, and can in some cases interfere with the molecular interaction by occluding a binding site, which leads to false negatives. Fluorescent compounds are invariably hydrophobic, and in many tests, background binding is a significant problem, leading to false positives. Label-free detection can avoid those problems.

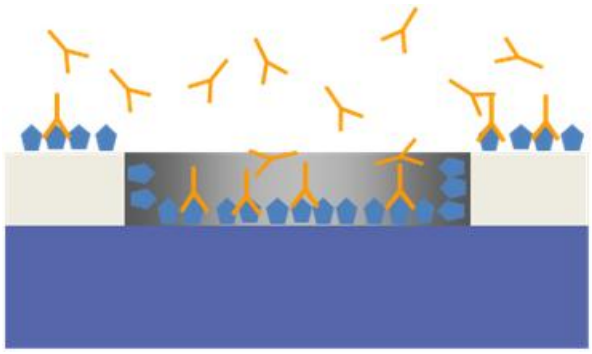

Figure 13: Binding of molecules to the hole of the photonic crystal sensors. Blue polygons presents target molecules to which anti-bodies presented as orange Y-shapes bind specifically.

In optical biosensors, the molecules that bind to the surface usually interact with the tail of an evanescent field. Since evanescent fields are weak and exponentially decay with distance, this interaction is very weak and has low sensitivity. The exception is in the case of surface plasmon resonance in which a very strong evanescent field is generated by conductive electrons in metal films. The highest sensitivity being reported so far are 7120 nm per refractive index unit [33] given as a shift in resonant wavelength per unit change of refractive index. However, in this technique the size of readout beam requires large sensing volumes and the resolution with which the binding can be measured is low because of very wide resonant peaks.

Compared to the surface plasmon resonance sensors the photonic crystal biosensors possess advantage in size that follows from their capability to localize and guide light through narrow regions. This allows for effective testing of minute amounts of analytes, which is at the same time more cost-effective. In addition, though in general photonic crystal sensors demonstrate lower sensitivity values, usually their ultra-narrow resonance linewidth allows for high sensitivity measurements.

A variety of photonic crystal biosensors have been proposed and demonstrated so far. Their principle is based on measurement of changes in refractive index of the environment or lattice periodicity that occur when biomolecules bind to the sensor surface (Fig. **13**)

We will give a review of some of the photonic crystal biosensor topologies and applications.

5.1. Glucose Sensing (Small Molecule Detection)

There is a growing demand for continuous, noninvasive glucose monitoring due to the increasing number of people diagnosed with type-1 diabetes. The need for minimally invasive glucose sensing has also increased due to the recognition that the long term health of diabetes patients is dramatically improved by careful glucose monitoring and control [34]. The development of accurate, reliable, real-time, and noninvasive glucose sensors is imperative to improve lives of diabetic patients and decrease their risk of hypoglycemia. Requirement for glucose sensors are rigorous since they have to operate reliably at the physiological pH values and ionic strengths and have to be immune to interference by other species present in bodily fluids.

Holtz and Aher [26] fabricated a PCCA glucose sensor by attaching the enzyme glucose oxidase (GOx) to a PCCA of polystyrene colloids. They demonstrated sensor response to different concentrations of glucose, as well as impact of concentration of oxygen in aqueous solution to glucose concentration measurements. The glucose sensor using inverse opal has also been demonstrated for measurements of glucose from 0 to 100 mM concentration which corresponded to wavelength shift from 599 to 719 nm [25]. The performance of this sensor was, however, limited because it did not function at high ionic strength and its response depended upon the oxygen concentration. In addition, as a result of chemical reaction, hydrogen peroxide was produced which was problematic for many applications. The same group developed a new class of glucose sensing materials by attaching phenylboronic acid to our PCCA photonic crystal hydrogels [36]. This was the first report on use of boronic acid derivatives as molecular recognition elements in PCCA to sense glucose. Such PCCA photonic

crystal sensors can be utilized in the form of contact lenses for *in vivo* monitoring of glucose concentration in tear fluid or in the form of subcutaneous inserts to report glucose concentration in an interstitial fluid. However, this carbohydrate sensor responded only in low ionic strength solutions. In subsequent papers, the authors reported on a more sophisticated boronic acid complexation motif, which showed selectivity for glucose and was responsive at physiological pH values and ionic strengths [35, 37]. The color change of such a sensor with change in glucose concentration is show in Fig. **14**. As can be seen the color changes from red to blue as the concentration of glucose varies from 0 to 40mM.

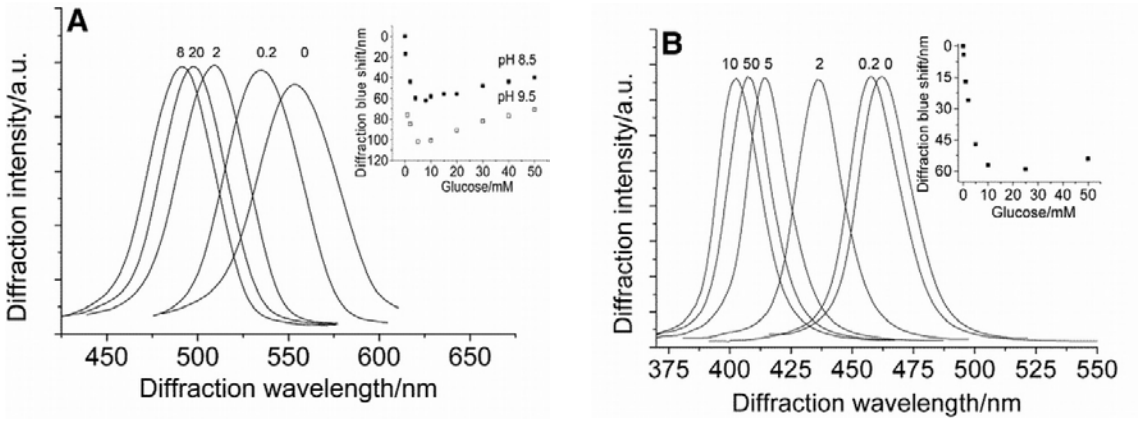

Figure 14: Effect of glucose concentration on diffraction of the sensor in aqueous solution containing 2mM tris-HCl (pH 8.5) and 150 mM NaCl. Concentration of glucose (in mM) is shown above the diffraction peaks. Inset:Diffraction peak shift dependence on glucose concentration of the sensor in 2 mM tris-HCl (pH 8.5) and 150 mM NaCl and in a solution containing 100 mM sodium carbonate-bicarbonate buffer (pH 9.5) and 150 mM NaCl. (B) Glucose concentration dependence of diffraction in the 4-amino-3-fluorophenylboronic acid in 2 mM tris-HCl (pH 7.4) and 150 mM NaCl. Inset: Dependence of diffraction peak shift on glucose concentration [35]. Reproduced with permission from American Chemical Society.

5.2. Protein Detection

Silicon-based photonic crystal structures are attractive from point of view of fabrication since they are compatible with silicon microelectronics technology. In the porous silicon photonic bandgap biosensors present the size of the pores can be well controlled and is of extreme importance for biosensing, both in terms of the size of molecules that can penetrate the pores and be detected and in terms of determining sensitivity. In general, the responsivity of this type of biosensors decreases as pore size increase [38].

Dancil *et al.* demonstrated the application of porous silicon to detection of reversible binding of antibody IgG to a protein A-modified surface [39]. Antibody IgG was added and removed from the sensor surface by changing solution pH in s flow cell, and the system was found to be reversible through several cycles. The sensor had a pore diameter of the sensor were between 100-300 nm and 5 μm deep. The sensor surface was modified to incorporate bovine serum albumin (BSA) linker. An increase of 100nm in the effective optical thickness (EOT), which is defined as a product ΔnL and detected as a shift in Fabry-Perot fringes, was observed in response to binding of biotinylated-BSA. The increase is due to replacement of aqueous phase (n_W=1.33) with protein of higher refractive index (n_p=1.42), that changes the average refractive index. In addition the increase can be ascribed to better wetting of the porous silicon layer upon binding of hydrophilic BSA linker, when presumably trapped air bubbles in the film are replaced with aqueous phase. After binding of BSA linker the wetting is complete and consequently binding of any additional biomolecules will lead to a change in EOT that directly scales with the mass of analyte. Subsequent binding of streptavidin, biotinylated-protein A and IgG showed that increase in EOT is directly proportional to molecular weight of the molecules (Fig. **15**).

The responsivity was shown to be 0.25 nm/kDa. In this experiment reliable data could be obtained for analyte masses above 20 kDa. In addition the binding kinetics could be monitored, because the sensor is integrated with flow cell.

Ouyang *et al.* demonstrated micromolecule detection using macroporous silicon microcavities [38, 40]. They fabricated macroporous silicon microcavities using highly doped n-type silicon. The pore diameter was well-controlled to 120 nm. They showed infiltration of 60nm diameter latex spheres inside the pores. The sensing capability of the device was demonstrated using biotin/streptavidin couple. The response of the sensor was numerically studied in terms of the dependence on the pores size. It was shown that for a given thickness of the coating the larger spectral shifts were produced in the sensors with smaller pore size. The sensor sensitivity on biomolecule concentration was also demonstrated. The sensor was able to detect protein concentrations down to 1-2 μM, which is equivalent to 0.3ng/mm^2.

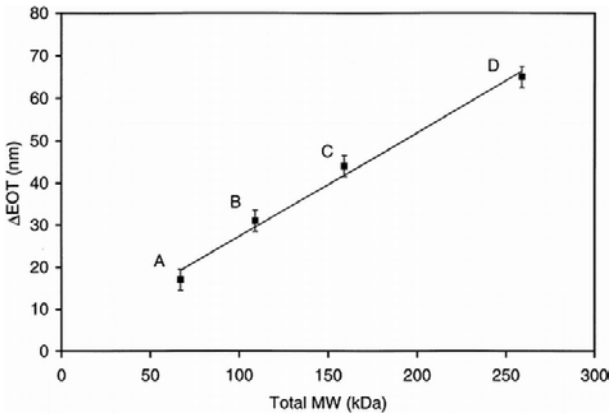

Figure 15: Overall change in EOT of the porous Si sensor as a function of total MW of protein complex bound to the inner pore walls: A, streptavidin (67 kDa); B, streptavidin/b-Prot A (109 kDa); C, streptavidin/ b-Prot A/Fc fragment (159 kDa); and D, streptavidin/b-Prot A/Human IgG (259 kDa) [39]. Reproduced with permission from American Chemical Society.

Silicon-based two-dimensional (2D) periodic structures of both holes and pillars have been demonstrated by number of groups in different topologies. The photonic crystal microcavities owe their high responsivity to light confinement to very small volume and excellent overlap between that volume analyte. In their paper Mortensen *et al.* theoretically analyzed response of the photonic crystal sensors pointing out that the dispersive photonic crystal environment can be used to enhance light matter interaction [41]. One of the most important factors determining sensor sensitivity is the fraction of the resonant cavity modal volume that interacts with the sample. Because the sensor works by measuring the change in refractive index, the sensitivity can be expressed as:

$$\Delta\lambda = \eta\lambda\frac{\Delta n}{n_{eff}} \quad \textbf{(1)}$$

In the equation, η represents a fraction of modal volume that overlaps with the sensing volume, in this case with volume of the physiological buffer, Δn is the change in refractive index and n_{eff} is effective refractive index experienced by the resonant mode.

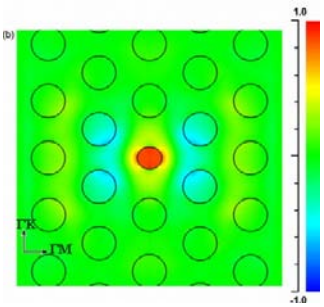

Figure 16: Mode profile of the electric field parallel to the ΓK direction as calculated by FDTD showing strong field localization inside the intentionally smaller "defect" hole [8]. Reproduced with permission from Elsevier.

The modal fraction that overlaps with analyte volume in photonic crystal microcavity sensor is calculated using

$$\eta = \frac{\int_{water} \varepsilon E^2 dV}{\int_{total} \varepsilon E^2 dV} \tag{2}$$

where E represents the electric field and ε dielectric constant of the medium.

From the distribution of the optical field (Fig. **16**), it can be seen that optical field is concentrated inside the central hole and the first layer of surrounding holes. Therefore, the presence of molecules in this region produces the strongest signal, which can be monitored as the spectral shift of the resonant wavelength of the photonic crystal microcavity. An FDTD investigation of sensor response has shown that 70% of the response of the sensor comes from the binding inside the defect hole and the first layer of surrounding holes.

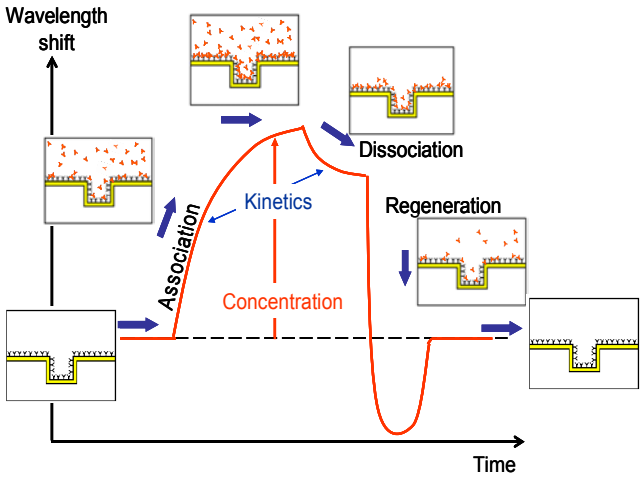

Figure 17: Schematics of protein binding, explaining different kinetic processes.

Mirkarimi *et al.* reported a demonstration of molecular binding detection using 2D photonic crystal microcavities [42]. The detection is based on measuring the change in position of photonic crystal resonance as biomolecules such as anti-biotin specifically bind to targets located on the surface of the sensor. The protein concentrations down to 1 μg/ml were measured. In later work the same group demonstrated ability of the sensor to monitor binding process in real time by integrating the sensor with fluidic channel. The authors have also demonstrated measurements of protein binding kinetics [8]. This is of great importance for investigation of biomolecular interactions, specifically for drug discovery where binding kinetics can provide information on effectiveness of potential drug compounds (Fig. **17**).

Binding curves (Fig. **18**) were obtained for range of frequencies and the experimental data were fitted with the Langmuir equation that describes the relationship between the concentrations of the analyte and binding site occupancy (Fig. **19**).

For the photonic crystal microcavity sensor the occupancy of binding sites is proportional to the spectral shift ($\Delta\lambda$). Therefore the Langmuir curve can be written in the form of

$$\frac{\Delta\lambda}{\Delta\lambda_{\max}} = \frac{K_{aff} c}{1 + K_{aff} c} \tag{3}$$

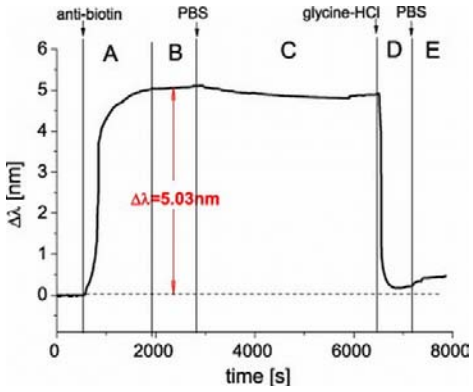

Figure 18: Experimental binding curve of anti-biotin to biotinylated-BSA layer showing: (A) association, (B) saturation (binding equilibrium), (C) dissociation and (D) regeneration using acidic solution [8]. Reproduced with permission from Elsevier.

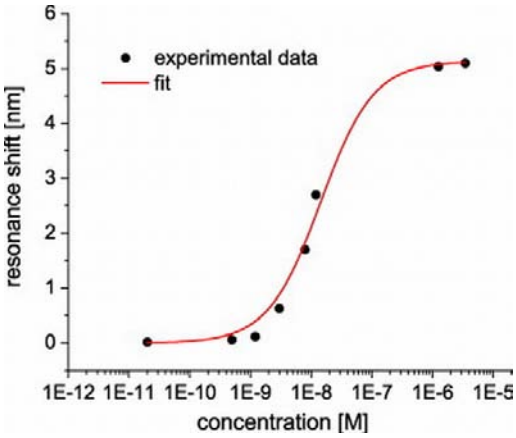

Figure 19: Concentration response curve for anti-biotin measured with photonic crystal microcavity sensor [8]. Reproduced with permission from Elsevier.

where $\Delta\lambda_{max}$ is sensor response corresponding to a full monolayer and c is the concentration. Affinity constant K_{aff} for the system of an antibody- antigen pair was obtained by fitting experimental data with this equation.

The detection limit of 20 pM were reported equivalent to less than 4.5 fg of mass on the total sensor surface and corresponding to 21 attogram of mass in the detection volume. Based on noise figure, the limit of detection of such sensor is estimated to be fewer than 10 molecules in the detection volume.

Lee and Fauchet [43] demonstrated detection of streptavidin binding in dehydrated solution using photonic crystal microcavity sensor. Their sensor is an array that has an internal pore wall surface area of ~ 50. Using Finite-Different Time Domain (FDTD) simulations (Fig. **20**) they have demonstrated that the redshift is much larger when the molecules are attached on the pore walls compared to the contribution of material bound in mesa on top of the device and at the bottom of the pores that have nearly an order of magnitude smaller shift. This is expected because vertically the light is confined within the photonic crystal slab.

With the device presented in the paper, authors were able to detect a minimum shift of ~ 0.1 nm. This shift corresponded to the minimum amount of analyte that can be measured of 2.5 fg, assuming that the biomolecules form a uniform monolayer on the internal surface of all the pores. They have also demonstrated the capability of detecting the dehydrated molecular layer of 1 Å in thickness. In general, due to the fact that proteins replace air in this case, the average local index changes more than when senor is in aqueous solution.

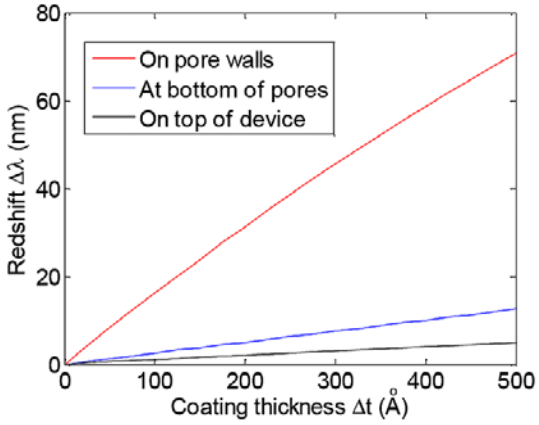

Figure 20: Calculated resonance redshift *versus* the monolayer coating thickness on the pore wall, bottom, and top of the device [43]. Reproduced with permission from Optical Society of America.

The same group later reported an interesting variant of photonic crystal microcavity in which defect hole is larger than other holes [44]. This type of sensor can be used to selectively target binding of the larger particles (200 nm-625 nm) to the defect hole. This particle size range corresponds to size of various viruses of interests, including influenza A (~100 nm in diameter) and Vaccinia virus (300–450 nm by 170–260 nm). The performance of the sensor was demonstrated using latex sphere (~360 nm in diameter) that produced a 4.2 nm-shift upon binding to the defect hole (Fig. **21**). With an active sensing volume of 0.15 μm^3, the device was capable of detecting ~1 fg of matter.

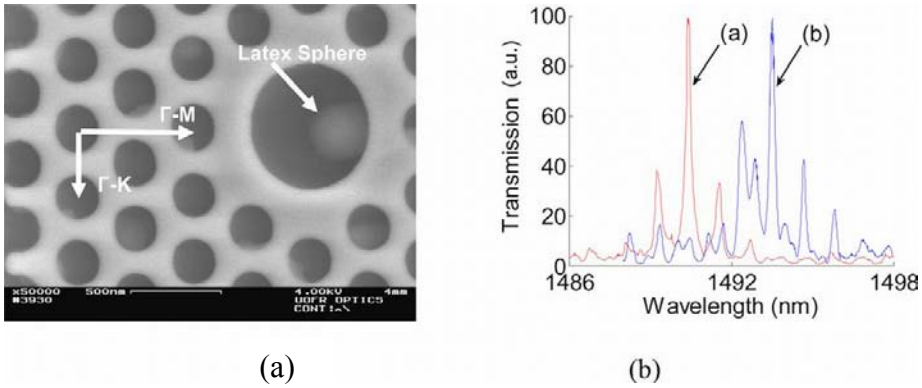

Figure 21: Top view of our device with one latex sphere (~370 nm in diameter) captured inside the central defect of the microcavity. (b) Normalized transmission spectra of the PhC microcavity. Curve (a) is measured before capture, and curve (b) is measured after one latex sphere is infiltrated inside the defect [44]. Reproduced with permission from Optical Society of America.

An optical biosensor based on light propagation through a photonic crystal waveguide was presented by Skivesen *et al.* [45]. In this type of sensor, the cutoff wavelength of the photonic crystal waveguide was used as an indicator of molecular binding and refractive index change. The authors demonstrated capability of monitoring protein binding. They measured concentrations of 0.15 μM and 1.5 μM of BSA-solution with excellent signal to noise ratio. This kind of sensor possesses larger sensing area compared to photonic crystal microcavity sensors. The authors have also shown that it is possible to distinguish between different surface coverage densities. The photonic crystal waveguide sensor showed a logarithmic response to changes in cutoff wavelength *vs.* protein-concentrations. A surface coverage of 6 ng/mm^2 was easily detected.

While providing high sensitivity and small detection volume, previously described photonic crystal biosensors can be employed for characterization of only one sample at the time. For biomedical sensing especially in

clinical laboratories, it is of great importance that measurements be performed in highly parallelized manner. One type of photonic crystal microcavity sensor that provides such a capability was proposed by Mandal *et al.* [46, 47]. This opto-fluidic sensor array is based on the use of arrays of 1D photonic crystal resonators in which light was evanescently coupled using a single bus waveguide. The parallelism is enabled by having resonators designed for different operating resonant wavelength. The authors have demonstrated binding and recorded dose-response curve for streptavidin and anti-streptavidin pair. They have also demonstrated that instead of continuously tuning the laser to obtain spectral shifts, it is also possible to monitor the output power at a fixed wavelength along the slope of the resonance. However, this type of detection limits the concentrations that can be measured to those for which the spectral shift is smaller than the sensor linewidth. The authors predict that the detection limit of such a sensor is on the order of tens of attograms. They have experimentally demonstrated detection of refractive index change of 7×10^{-5} RIU.

Another type of photonic crystal sensors that can accomplish high parallelism was developed by Cunningham *et al.* This unique type of photonic crystal biosensors is a narrowband wavelength reflectance filter that can reflect nearly 100% of light at resonant wavelength [48]. Such a sensor can be inexpensively manufactured on plastic film or sol-gel derived nanoporous silica film using replication from silicon master wafer [49]. The sensor operates by measuring changes in the wavelength of reflected light as biochemical or cellular binding events take place on the surface. The sensor has demonstrated a relatively good sensitivity as well as a large dynamic range with ability to detect surface density of 0.4 pg mm^{-2} in dehydrated solution [50]. The authors have demonstrated its applications to monitoring biomolecular interactions [51, 52] as well as for characterization of surface molecules on live cells [53]. The authors also showed that when the photonic crystal sensor is operated in the near ultraviolet wavelength range, the surface-sensitivity to bulk-sensitivity ratio will be enhanced over 4.5 times compared to the infrared range, which enables enhanced detection resolution and low concentrations of biomolecules [54]. The sensor can be operated in "single point mode" or "imaging mode", which greatly increases the throughput of the system. The structure of the sensor is compatible with standard microtiter plate-based and microarrays that are most widely used for high throughput biomolecular interaction analysis.

Recently, nanonporous silicon photonic crystal based sensors has been demonstrated [55] for *in vitro* monitoring of cellular metabolism. Such a device can serve as a complementary technology to patch clamp technique. If cells could be aligned to an array of such sensors, they can be utilized as multiple parallel patch clamps.

The photonic crystal biosensors are still in their early phase of development and require further consideration such as development of surface chemistry, compatible microfluidics for efficient sample delivery, and detection procedures, such as rinsing to minimize non-specific binding.

CONCLUSIONS

Photonic crystal sensors are an emerging class of sensing devices that have been developed in past couple of decades. The transduction mechanism relies on a change in refractive index or lattice periodicity that is initiated by physical phenomena, presence of chemicals or molecular binding events. Different types of structures have been employed for sensing starting from 3D self-assembled structures, porous silicon structures to 2D ordered lattices. In terms of sensing of physical phenomena and chemical compounds, 3D polymer hydrogels have found widest application, while 2D structures have not been used for such purpose, likely due to their complexity, but have found application in biosensing.

In terms of sensing physical properties, photonic crystal sensors have been used for measurements of temperature, humidity, pressure and index of refraction. They have also found application in measurements of thin film thickness. For chemical sensing, it was shown that photonic crystal sensors can be used to specifically detect ions. However, detection of different gases and liquids is based solely on index of refraction measurements and as such do not possess specificity. Specificity is usually provided by chemical reactions or recognition mechanisms. Therefore, these mechanisms present an important aspect of every sensing platform and require development of reliable chemistries to accompany transduction principle. For

detection of biomolecules, numerous interactions that have been developed and are employed in every day clinical laboratories need to be transferred to existing sensors. Using some of these interactions, it was demonstrated that photonic crystals with an ultra-compact footprint can be utilized for specific detection of low concentration of analytes.

The instrumentation required to obtain signal from the photonic crystal sensors can vary from simple, that detect only power changes, to complex spectroscopic equipment. In general, 2D photonic crystal sensors require expensive equipment, such as tunable lasers, sensitive detectors and optics to efficiently couple light into the sensor. However, they provide high sensitivity and excellent limits of detection that can potentially go down to single molecules. On the other hand, signals from porous silicon sensors and hydrogel sensors require broadband light sources and spectrographs or even visual detection, but these sensors have lower sensitivity when compared to 2D microcavities, for example.

For purpose of biosensing, it was demonstrated that photonic crystal sensors can be integrated with microfluidic platforms for efficient delivery of analytes. Due to the corrugated sensor surfaces, transport of the analytes to sensing area is governed mainly by diffusion. This can affect kinetics of detection process. However, this impairment can be minimized by careful design of microfluidic system. In addition, in photonic crystal sensors light can be concentrated in a very small volume, thus achieving a large light-matter interaction with a volumes as low as femtoliters, which presents a significant advantage in comparison with other existing technologies.

In summary, photonic crystals have been successfully demonstrated for physical, chemical and biological sensing. While their development is still in its initial stage, based on the experimental demonstrations achieved to date, photonic crystal structures are a very promising platform. However, further investigations are still needed to improve the overall performance.

REFERENCES

[1] Qian M, Bao XQ, Wang LW, Lu X, Shao J, Chen XS. Structural tailoring of multilayer porous silicon for photonic crystal application. Journal of Crystal Growth 2006; 292 (2): 347-350.

[2] Snow PA, Squire EK, Russell PSt J, Canham L T. Vapor sensing using the optical properties of porous silicon Bragg mirrors. J Appl Phys 1999; 86 (4):1781-1784.

[3] Beger MG, Arens-Fischer R, Thoenissen M, Krueger M, Billat S, Lueth H, Hilbrich S, Theiss W, Grosse P. Dielectric filters made of PS: advanced performance by oxidation and new. Thin Solid Films 1997; 297: 237–240.

[4] Lin VS-Y, Motesharei K, Dancil K-PS, Sailor MJ, Ghadiri MR. A porous silicon-based optical interferometric biosensor. Science 1997; 278: 840-843.

[5] Schmedake TA, Cunin F, Link JR, Sailor MJ. Standoff detection of chemicals using porous silicon “smart dust” particles. Adv Mater 2002; 14: 1270-1272.

[6] Lorenzo E, Oton CJ, Capuj NE, Ghulinyan M. Porous silicon-based rugate filters. Appl Optics 2005; 44: 5415-5421.

[7] Lončar M, Scherer A, and Qiu Y. Photonic crystal laser sources for chemical detection. Appl Phys Lett 2003; 82: 4648.

[8] Zlatanovic S, Mirkarimi LW, Sigalas MM, Bynum MA, Chow E, Robotti KM, Burr GW, Esener S, Grot A. Photonic crystal microcavity sensor for ultracompact monitoring of reaction kinetics and protein concentration. Sensor Actuat B-Chem 2009; 141 (1): 13-19.

[9] Erickson D, Rockwood T, Emery T, Scherer A, and Psaltis D. Nanofluidic tuning of photonic crystal circuits. Opt Lett 2006; 31: 59-61.

[10] Ye Y-H, LeBlanc F, Hache A, Truong V-V. Self-assembling three-dimensional colloidal photonic crystal structure with high crystalline quality. Appl Phys Lett 2001; 78: 52.

[11] Barry RA and Wiltzius P. Humidity-Sensing Inverse Opal Hydrogels. Langmuir 2006; 22 (3): 1369-1374.

[12] Asher SA, Holtz J, Liu L, and Wu Z. Self-Assembly Motif for Creating Submicron Periodic Materials. Polymerized Crystalline Colloidal Arrays. J Am Chem Soc 1994; 116: 4997-4998.

[13] Suh W, Yanik MF, Solgaard O, and Fan S. Displacement-sensitive photonic crystal structures based on guided resonance in photonic crystal slabs. Appl Phys Lett 2003; 82: 1999-2001.

[14] Burr GW, Chow E, Mirkarimi LW, Sigalas M, and Grot A. Photonic crystal microcavities as ultracompact film–thickness monitors for biosensing. Integrated Photonics Research and Applications/ Nanophotonics for Information Systems, Technical Digest (Optical Society of America), 2005; p. paper NThC4.

[15] Takeoka Y, Watanabe M. Template Synthesis and Optical Properties of Chameleonic Poly(N-isopropylacrylamide) Gels Using Closest-Packed Self-Assembled Colloidal Silica Crystals. Adv Mater 2002; 15: 199-201.

[16] Hawkeye MM, Krause KM, and Brett MJ. Ambient humidity monitoring using a 1D photonic crystal sensor fabricated with glancing angle deposition. Proceedings of SPIE 2009; 7356.

[17] Chow E, Grot A, Mirkarimi LW, Sigalas M, and Girolami G. Ultracompact biochemical sensor built with two-dimensional photonic crystal microcavity. Opt Lett 2004; 29: 1093-1095.

[18] Prasad T, Mittleman DM, Colvin VL. A photonic crystal sensor based on the superprism effect. Opt Mater 2006; 29: 56–59.

[19] Nishijima Y, Ueno K, Juodkazis S, Mizeikis V, Misawa H, Tanimura T, and Maeda K. Inverse silica opal photonic crystals for optical sensing applications. Opt Express 2007; 15: 12979-12988

[20] Dorfner DF, Hürlimann T, Zabel T, Frandsen LH, Abstreiter G, and Finley JJ. Silicon photonic crystal nanostructures for refractive index sensing. Appl Phys Lett 2008; 93: 181103.

[21] Di Falco A, O'Faolain L and Krauss TF. Chemical sensing in slotted photonic crystal heterostructure cavities. Appl Phys Lett 2009; 94: 063503.

[22] Sünner T, Stichel T, Kwon S-H, Schlereth TW, Höfling S, Kamp M, and Forchel A. Photonic crystal cavity based gas sensor. Appl Phys Lett 2008; 92: 261112.

[23] Topol'anc˘ik J, Bhattacharya P, Sabarinathan J and P Yu P-C. Fluid detection with photonic crystal-based multichannel waveguides. Appl Phys Lett 2003; 82 (8): 1143.

[24] Asher SA, Lee K. Photonic Crystal Chemical Sensors: pH and Ionic Strength. J Am Chem Soc 2000; 122: 9534-9537.

[25] Braun PV, Lee Y-J. Three-dimensional photonic crystal sensors. Proceedings of SPIE 2003; 5224: 86-93.

[26] Asher SA, Holtz JH. Polymerized colloidal crystal. Nature 1997; 389: 829-832.

[27] Holtz JH, Holtz JSW, Munro CH and Asher SA. Intelligent Polymerized Crystalline Colloidal Arrays: Novel Chemical Sensor Materials. Anal Chem 1998; 70: 780-791.

[28] Asher SA, Sharma AC, Goponenko AV and Ward MM. Photonic Crystal Aqueous Metal Cation Sensing Materials. Anal Chem 2003; 75 (7): 1676-1683.

[29] Tinsley-Bown A, Smith RG, Hayward S, *et al.* Immunoassays in a porous silicon interferometric biosensor combined with sensitive signal processing. Phys Stat Sol A 2005; 202(8): 1347–1356.

[30] Yalçin A, Popat KC, Aldridge JC, *et al.* Optical Sensing of Biomolecules Using Microring Resonators. IEEE J Sel Top Quant 2006; 12(1).

[31] Armani AM, Kulkarni RP. Fraser SE, Flagan RC, Vahala KJ. Label-Free, Single-Molecule Detection with Optical Microcavities. Science 2007; 317 (5839): 783-787

[32] Cooper MA. Optical biosensors in drug discovery. Nat Rev Drug Discov 2002; 7: 515-528.

[33] Pfeifer P, Aldinger U, Schwotzera G, Diekmann S, Steinrücke P. Real time sensing of specific molecular binding using surface plasmon resonance spectroscopy. Sensor Actuat B-Chem 1999; 54: 166-175.

[34] Pickup J, McCartney L, Rolinski O, Birch D. *In vivo* glucose sensing for diabetes management: progress towards non-invasive monitoring. BMJ 1999; 319(7220): 1289.

[35] Alexeev VL, Sharma AC, Goponenko AV, *et al.* High Ionic Strength Glucose-Sensing Photonic Crystal. Anal Chem 2003; 75: 2316-2323.

[36] Asher sA, Alexeev VL, Goponenko AV. Photonic Crystal Carbohydrate Sensors: Low Ionic Strength Sugar Sensing. J Am Chem Soc 2003; 125: 3322-3329.

[37] Alexeev VL, Das S, Finegold DN, and Asher SA. Photonic Crystal Glucose-Sensing Material for Noninvasive Monitoring of Glucose in Tear Fluid. Clin Chem 2004; 50: 2353–2360.

[38] Ouyang, H, DeLouise LA, Miller BL, Fauchet PM. Label-free quantitative detection of protein using macroporous silicon photonic bangap biosensors. Anal Chem 2007; 79: 1502-1506.

[39] Dancil KS, Greiner DP, Sailor MJ. A porous silicon optical biosensor: Detection of reversible binding of IgG to a Protein A-modified surface. J Am Chem Soc 1999; 121: 7925-7930.

[40] Ouyang H, Christophersen M , Viard R, Miller BL, Fauchet PM. Macroporous silicon microcavities for macromolecules detection. Adv Funct Mater 2005;. 15: 1851-1859.

[41] Mortensen NA, Xiao S, Pedersen J. Liquid-infiltrated photonic crystals: enhancef light-matter interaction for lab-on-a-chip applications. Microfluid Nanofluid 2008; 4: 117-127.

[42] Mirkarimi LW, Zlatanovic S, Sigalas MS, Bynum MA, Robotti K, Chow E and Grot A. Toward Single Molecule Detection with Photonic Crystal Microcavity Biosensors. Digest of the LEOS Summer Topical Meetings 2006; 29 - 30.

[43] Lee MR and Fauchet PM. Two-dimensional silicon photonic crystal based biosensing platform for protein detection. Opt Express 2007; 15: 4530-4535.

[44] Lee MR and Fauchet PM. Nanoscale microcavity sensor for single particle detection. Opt Lett 2007; 32: 3284-3286,

[45] Skivesen N, Têtu A, Kristensen M, Kjems J,. Frandsen LH, and Borel PI. Photonic-crystal waveguide biosensor. Opt Express 2007; 15: 3169-3176.

[46] Mandal S, Erickson D. Nanoscale Optofluidic Sensor Arrays. Opt Express 2008; 16: 1623.

[47] Mandal S, Goddard JM, Erickson D. A multipexed optofluidic biomolecular sensor for low mass detection. Lab Chip 2009; 9: 2924-2932.

[48] Cunningham B, Li P, Lin B, Pepper J. 1Colorimetric Resonant Reflection as a Direct Biochemical Assay Technique Sensor Actuat B-Chem 2002; 81: 316.

[49] Block ID, Chan LL, Cunningham BT. Photonic crystal optical biosensor incorporating structure lox-index porous dielectric. Sensor Actuat B-Chem 2006; 120: 187-193.

[50] Li PY, Lin B, Gerstenmeier J, Cunningham BT. A New Method for Label-Free Imaging of Biomolecular Interactions. Sensor Actuat B-Chem 2004; 99: p. 6.

[51] Lin B, Qiu J, Gesrtenmeier J, Li P, Pien H, Pepper J, Cunningham B. A Label-Free High Throughput Optical Technique for Detecting Small Molecule Interactions. Biosens Bioelectron 2002; 17: 827.

[52] Cunningham BT, Liang L. Label-free Detection of Biomolecular Interactions: Applications in Proteomics and Drug Discovery Expert Rev. Proteomics 2006; 3: 271.

[53] Lin B, Li P, Cunningham BT.A label-free biosensor-based cell attachment assay for characterization of cell surface molecules. Sensor Actuat B-Chem 2006; 114: 559–564.

[54] Ganesh N, Block ID, Cunningham BT. Near ultraviolet-wavelength photonic-crystal biosensor with enhanced surface-to-bulk sensitivity ratio. Appl Phys Lett 2006; 89 (2): 023901-023904

[55] Killian KA, Lai LMH, Magenau A, *et al.* Smart Tissue Culture: *In situ* Monitoring of teh Activiry od Pretease Anzymes Secreted from Live Cells Using Nanostructured photonic Crystals. Nano Letters 2009; 9: 2021-2025.

CHAPTER 11

Photonic Crystal Fibers for Physical, Chemical and Biological Sensing

Roberto Corradini[1] and Stefano Selleri[2,*]

[1]Department of Organic and Industrial Chemistry, University of Parma, I-43124, Italy and [2]Department Information Engineering, University of Parma, I-43124, Italy

Abstract: Remarkable developments and improvement have been observed in the field of optical fiber-based sensors in the last decade, for physical, chemical and biological applications. Many new sensors for specific analytes have been reported, novel sensing chemistries or transduction principles have been introduced, and applications in various fields have been realized. This boost has been pushed also by the mature fabrication technology of photonic crystal fibers whose peculiar properties well fit requirement for efficient sensing systems. Discussions on the main issues related to the use of photonic crystal fibers in biosensing applications is reported. Specific description of fiber functionalization for the detection of biologically relevant analytes is described highlighting deposition procedures of selective probes.

Keywords: Biosensing, optical fibers, photonic crystal fibers, DNA, PNA probe, silanization.

1. INTRODUCTION

Photonic Crystal Fibers (PCFs) are also known as microstructured optical fibers or holey fibers and have been deeply studied in recent years because of a number of unique features [1, 2]. The cross-section of such fibers is defined by an array of air-holes, running throughout the whole length, in a matrix of dielectric material. The air holes can be randomly [3, 4] as well as regularly, often periodically, displaced in the fiber cross-section. The light-guiding properties can be tailored with unprecedented degrees of freedom with a proper design of air-holes relative position, size and shape, thus making PCFs suitable for a wide range of applications, spanning from telecommunications systems, spectroscopy, microscopy, high-power devices, sensing.

PCFs can be divided into two main categories: hollow-core fibers and solid-core ones, based on the different guiding mechanism which they rely on. Hollow-core PCFs provide light confinement in a low refractive index core exploiting the photonic band-gap mechanism, which is due to the presence of a periodic lattice of holes in the cladding. Solid-core PCFs can guide light either in a high refractive index core, through modified total internal reflection, or in a low refractive index one, exploiting again the photonic band-gap provided by the microstructured region [5, 6]. Both kinds of PCFs have undergone extensive research, with the aim of exploiting their unique characteristics to produce highly sensitive physical, chemical and biological sensors [7-10]. Fiber based and optical sensors have been widely developed for years [11-14] and a considerable expertise level has been achieved all over the world developing sensor systems based on optical fiber and optical technology. However PCFs have opened up a new fascinating branch in fiber-based sensor field as their air-holes can be easily infiltrated with gases or liquids [15-18] without compromising the fiber robustness, thus obtaining a very long interaction length, even in presence of very limited quantity of sample. In fact, because of the micrometric dimensions of the holes, PCFs are able to sense ultra small volume samples with typical volumes of hundred of nl usually required to fill one metre long PCF. In addition, the probing light can be confined to a small area, which means that high intensities can be achieved, facilitating optical nonlinearity-based sensing techniques [19]. In this perspective, optical biosensors based on the use of PCFs can be classified as true intrinsic sensors, where interaction with the analyte occurs within the fiber itself, differently from extrinsic sensors, in which the optical fiber is used as signal transmission medium to couple light, usually to and from the region where

***Address correspondence to Stefano Selleri:** Department of Information Engineering – Viale G.P. Usberti 181/A, 43124 Parma, Italy; Tel: +39-0521-905763; Fax: +39-0521-905758; E-mail: stefano.selleri@unipr.it

Marco Pisco, Andrea Cusano and Antonello Cutolo (Eds)
All rights reserved-© 2012 Bentham Science Publishers

the light beam is influenced by the liquid solution under test, often outside the fiber itself. Finally, the fact that optical fiber technology is used, provides the usual advantage to perform remote sensing.

In the following, the main issues related to the use of photonic crystal fibers in sensing applications will be discussed. Being aware of the immense number of different configurations and working principles of physical, chemical and biological sensors, which can be based for example on absorbance, reflectance, fluorescence, luminescence, refractive index variation and other measurement techniques [14], the authors will provide a brief overview on some basic aspects of optical sensing mechanisms, focusing on selected structures and applications, in particular for the detection in bio-samples. Fiber based sensors for physical parameters like temperature [20] or strain, will not be considered here.

2. EVANESCENT WAVE SENSING

Sensing performed in solid-core fibers, exploits the evanescent tails of the guided mode field. The light propagating through a fiber is usually mostly confined into the core, but due to the evanescent component of the electromagnetic wave, the exponential tail of the optical field will penetrate into the holes of the microstructured cladding and thereby probe any sample placed there [21-25]. Therefore, the system can be seen as a highly advanced capillary tube with strong sample–light interaction. The efficiency of this approach is given by a proper fiber cross section design to allow an high fraction of the optical field intensity to penetrate into the holes which have been infiltrated with the sample under test [26, 27]. The larger the fraction of the field that propagates as evanescent wave, the stronger the interaction between the optical field and samples placed in the air holes. Solid-core fibers provide a lower field-sample interaction with respect to the hollow-core ones, however their confinement losses can be very low on a broader wavelength range. Different solid-core PCF structures have been considered for sensing, primarily fibers with a triangular lattice, air-suspended core and hole assisted ones, all shown in Fig. **1**. In the following the first two types will be discussed.

Triangular lattice fibers presents a microstructured patterns of air holes, running along the length of a glass fiber, forming the fiber cladding [28, 29]. A common cross-section geometry is created by omitting one hole or multiple holes in the center of the triangular-lattice as shown in Fig. **1** (**left**). The typical fabrication method for this fibers is based on mature techniques, such as the stack-and-draw one [30], which guarantees high accuracy and control of the fiber parameters. The detection mechanism relies on the spectral analysis of signals obtained from light measured in transmission and/or reflection, from loss behavior analysis as well as from the fluorescence provided by proper markers of the sample.

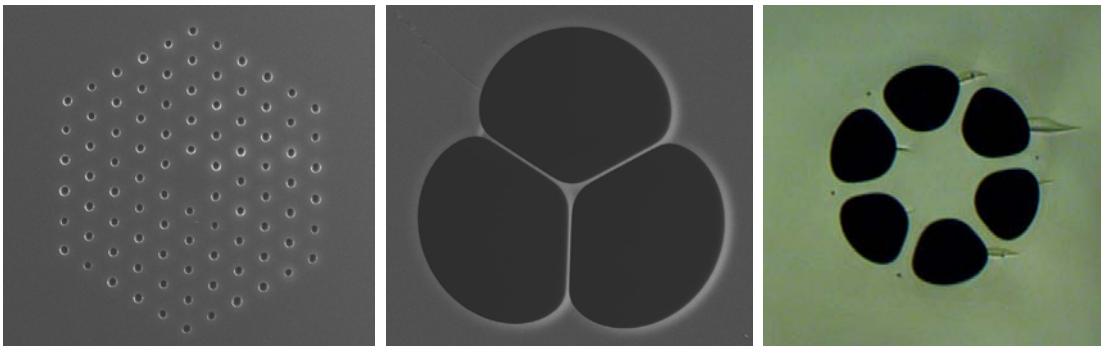

Figure 1: Photonic crystal fiber with a triangular pattern of air holes forming the microstructured cladding (left), air-suspended core fiber (center) and hole assisted fiber (right) (images kindly provided by Institute of Photonic Technology (IPHT Jena)).

Air-suspended core fibers are based on the idea of a cross section made of a solid rod suspended in air by three thin webs, which separate as many large non-circular air holes as shown in Fig. **1** (**center**). Very long spools of fiber can be drawn without any relevant variation of structural parameters. Any fabrication method can be used, such as stack-and-draw [31], sol-cast [32] or ultrasonic drilling of the perform [33].

This structure has many advantages for biosensing [34, 35] as the large air holes can be filled easily and more quickly with liquids or infiltrated with gas. Most important, air-suspended core fibers show very low confinement losses on a broad band and provide a modal overlap significantly higher than many other index guiding structure. Power fraction belonging to evanescent tails, increases reducing core diameter, similarly to triangular-lattice PCFs. Lastly, as will be discussed in the following, the filling process can be controlled and the filling time can be decreased through side access of the fiber. A number of air-suspended core fiber-based sensors have been reported recently. They can be parted into two main categories, depending on the sensing mechanism they rely on: absorption based and fluorescence based. In absorption-based sensors the detection of a particular analyte is carried out by measuring the attenuation spectrum of a sample-filled fiber. Absorption at a certain wavelength λ, $A(\lambda)$, is correlated with the sample molar concentration C through Beer-Lambert law [30]:

$$A(\lambda)[\mathrm{dB}] = 10\, \varepsilon(\lambda)\, C\, \Phi(\lambda)\, L \qquad \textbf{(1)}$$

where $\varepsilon(\lambda)$ is the molar absorbance of the specie, $\Phi(\lambda)$ is the light power fraction overlapping with the sample and L is the length of the sample-filled fiber. For a given substance, *i.e.,* a certain $\varepsilon(\lambda)$, and the given minimum measurable $A(\lambda)$, the smallest concentration of analyte which can be detected depends on fiber length and the overlapping field fraction. Notice that the attenuation limits the maximum fiber length, so that maximizing the light-sample overlap impacts directly on the sensitivity of the device. Also, the existence of higher order modes can define the precision of the derived concentration, because of the unpredictability of the power exchanged between them and the different $\Phi(\lambda)$ which characterizes each of them. A proper fiber design can overcome this problem, through single-mode propagation [36].

3. GUIDED WAVE SENSING

Another possibility to exploit photonic crystal fiber for sensing is based on the field propagation in hollow core fibers, as those shown in Fig. **2**, thus yielding to the possibility to realize sample-filled core-sensors [10, 36]. In this way the fluid under test is infiltrated into the fiber core and the interaction directly undergoes with the guided field rather than with the evanescent one.

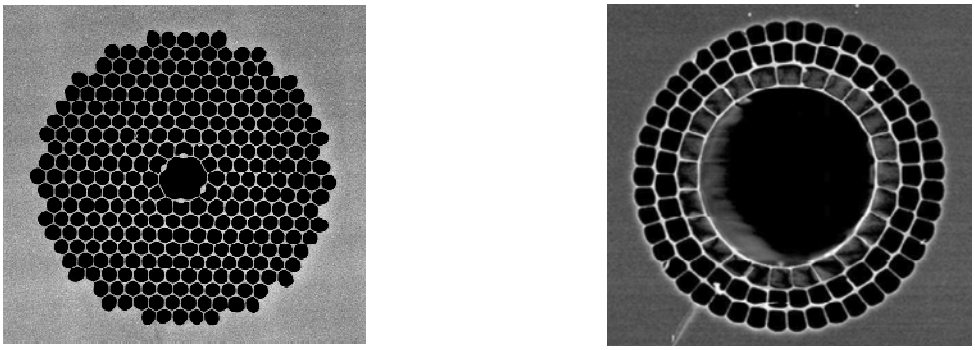

Figure 2: Cross section of hollow-core fibers. The right image reports a Bragg fiber realized using the concentric rings of air holes separated by thin silica bridges (images kindly provided by NKT Photonics A/S).

One of the most intriguing structure for air-guiding is provided by hollow-core Bragg fibers. Bragg fibers, firstly theoretically proposed in 1978 [37], have been fabricated with a hollow core by combining solid base materials of widely different refractive indexes [38] and light is guided by concentric multilayer dielectric mirrors [39]. Due to the finite number of cladding layers, the guided modes in the Bragg fibers are affected by leakage. In order to reduce this leakage loss and to enhance the reflections from the cladding layers, the Bragg fibers proposed in literature usually show cladding structures with a large index contrast between the alternating layers. This kind of fibers provides interesting characteristics, but the fabrication is still an active research field, being quite complex. Different methods have been proposed in the literature to manufacture both solid- and hollow-core Bragg fibers with alternating material layers in the cladding, using silica or polymers [40-45].

PCF technology provides an efficient approach for the fabrication of these fibers. Bragg fibers, simply made by silica and air, with a cladding characterized by thin silica rings, surrounded by air and connected by nanoscale silica bridges, have been recently fabricated [46, 47]. In order to realize this kind of fibers, silica can be used as the high refractive index material, and the stack-and-draw approach employed. In particular, an outer silica tube can be filled with tubes of decreasing sizes. Within the annular gap, thin capillaries can be introduced and evenly distributed. The stack of tubes and capillaries is then drawn to a preform cane, which is subsequently pulled to fibers of different outer diameters. The sensing mechanism, in this case, usually relies on the variation of the transmission spectral properties given by the interaction of the analyte infiltrated into the hollow core with the hole surface [10].

4. CALCULATION OF MODE OPTICAL PROPERTIES

As can be derived from the previous discussion, the design of an effective optical fiber-based sensor includes many aspects and depends on different details. The calculation and design of the relevant PCF optical properties, in particular the loss and the optical power fraction in air which is available for interaction with the sample, are of primarily importance. Is it clear, for example, that a greater power fraction turns into a higher sensitivity, which means a more accurate response for a given quantity of sample. Moreover, single-mode or multi-mode operation may be required in some systems, particularly if interferometric detection is being used.

One of the most powerful approach to accurately compute the mode properties, is a full-vector modal solver based on the finite element method (FEM) [48, 49]. In particular the FEM magnetic field formulation assures the absence of discontinuities of the unknown field in correspondence of the interface between materials with different refractive index. The FEM approach starts by decoupling the Maxwell Eqs. to obtain the magnetic field curl-curl:

$$\overline{\nabla} \times \left(\varepsilon^{-1} \overline{\nabla} \times \overline{h} \right) - k_0^2 \mu \overline{h} = 0 \qquad \textbf{(2)}$$

being h the magnetic field, ε and μ, respectively, the complex relative dielectric permittivity and magnetic permeability, and $k_0 = 2\pi/\lambda$ the wave number in the vacuum. The expression of the modal solution magnetic field is

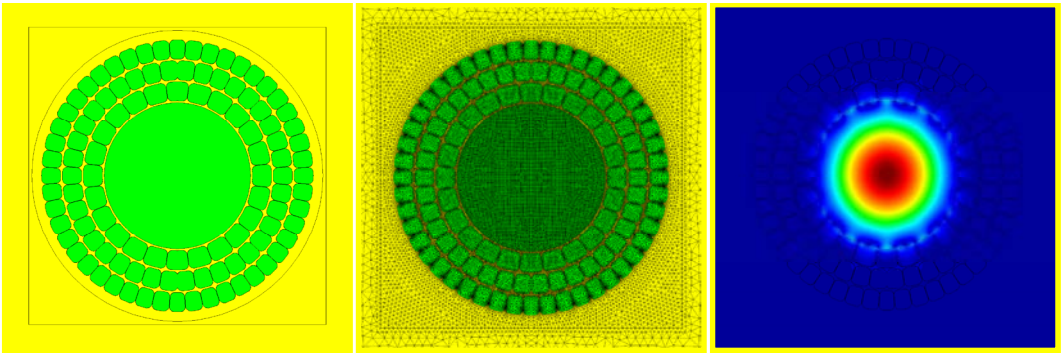

Figure 3: The model of the Bragg fiber cross-section (left), the discretized mesh realized with triangular second order elements (center) and the computed fundamental mode magnetic field distribution (right).

$$\overline{h} = \overline{H} e^{-\gamma z} \qquad \textbf{(3)}$$

where H is the field distribution on the transverse plane and $\gamma = \alpha + j\beta$ is the complex propagation constant, being α the attenuation constant and β the phase one, related to the effective index of the guided mode as $n_{eff} = \beta/k_0$. The variational finite element procedure applied to the full vector curl-curl Eq. yields an algebraic problem whose eigenvector is the discretized magnetic field vector, which provides the guided

mode field distribution on the fiber cross-section. In order to enclose the computational domain without affecting the numerical solution, and to allow the loss computation, the so called perfectly matched layers are usually applied and placed before the outer boundary [50, 51].

The important parameters for what concerns a fiber based design are the loss and the field distribution on the fiber cross section. In particular γ is related with the confinement losses (CL) as:

$$\text{CL [dB/m]} = 20\,\alpha\,\log_{10} e \cong 8.686\,\alpha\,, \qquad \textbf{(4)}$$

while the field distribution *H* allows the power fraction in air to be computed. The numerical method can of course compute all different modes, in case of multimode regime. As an example Fig. **3** reports, on the left, the model of the Bragg fiber cross-section, the discretized mesh realized with triangular second order elements, in the center, and the computed fundamental mode magnetic field distribution, on the right. Multiple analysis at different wavelengths provides spectral dependence of the various computed parameters thus allowing, for example, to derive the transmission, reflection and loss spectra.

5. COUPLING LIGHT AND INFILTRATING FLUIDS

Getting light and fluids into the fiber at the same time is crucial to a practical design and different approaches have been already suggested [52, 53]. The usual procedure is to fill the holes through one of the fiber ends. This increases the complexity of using such structures when compared with conventional fibers, as light in- and out-coupling requires to manage the patterned fiber ends. A two-stage preparation may be applied, in which the fiber ends have to be cleaned and optically prepared after the sample insertion. Usually the outer surface of the PCF needs to be coated with an index matching material, to avoid liquid coming out, or to strip any fluorescent emission eventually coupled to the cladding modes. In microstructured fibers, where a large number of channels are present in the fiber cross-section, selective infiltration of analytes or reagents within a definite number of channels can also be obtained by obtruding the terminal holes of a selected number of channels. This can be achieved by arc fusion collapsing air-holes [54], by injection-cure-cleaving [55] and by laser micromachining [56]. Another potential and intriguing solution to this issue is to generate a lateral access to the PCF holes, through which the sample can be inserted. This approach cannot be applied to triangular lattice PCFs where too many holes should be taken into account, while can be effective, for example, in air-suspended core fibers, where few and relative large holes are easily accessible. In order to open a lateral access, a technique that is based on simultaneously increasing the pressure in the PCF holes and locally melting the fiber by applying an electric arc with a commercial arc fusion splicer has been successfully developed [16, 57]. This approach, which doesn't interfere with light guidance, has the great advantage to separately manage light coupling into the core and sample insertion into the fiber holes. However, the simplest way to infiltrate liquid solutions into the fiber holes is using the capillary effect [24] which, however, cannot allow a fine control of the considered volumes. In this case, for example, the position of the liquid in the holes can be recorded by observing the fluorescent emission at the liquid interface, in case fluorescent markers are employed. Procedures for selective filling of hollow core fibers have been studied in detail using this method [58]. Tapered tips can also be considered as alternative approach to access liquids, still through capillary effect, once properly designed and realized [59]. As an alternative to the capillary effect, proper microfluidic pumps can be used which allow a very precise control of the infiltrated solution. Fig. **4** shows an example of a laboratory set-up.

6. GRATING-BASED AND LABEL FREE SENSORS

As already mentioned in the previous sections, there is an immense number of different working principles of fiber optical biosensors which focus on procedures exploiting fluorescent markers, or the change in the refractive index achieved when target analytes bind to the biorecognition molecules, or the spectral response in transmission or reflection, or even that one given by Bragg, long period and relief gratings which can be inscribed into the fiber core or capillary surfaces [13]. However, detection configurations can be generally classified into two main categories: fluorescence-based detection [24, 33, 60] and label-free detection [8, 12]. In fluorescence-based detection, target molecules are labeled with fluorescent tags, such

as dyes; the intensity of the fluorescence indicates the presence of the target molecules. Fluorescence-based detection is extremely sensitive, with the detection limit down to a single molecule, but it suffers from laborious labeling processes that may also interfere with the function of a biomolecule. In contrast, in label-free detection, target molecules are not labeled or altered, and are detected in their natural forms. Typical fiber-optical label-free biosensors measure the change of a resonance given by grating [61], surface plasmon, or Fabry-Perot etalon, introduced by the presence of a biological agent. Such sensors are truly label-free because they require no labeled molecules at all, thereby greatly simplifying the sample treatment. Moreover, label-free detection mechanisms measure refractive index change induced by molecular interactions, which is related to the sample concentration instead of to the total sample mass. As a result, the detection signal does not scale down with the sample volume.

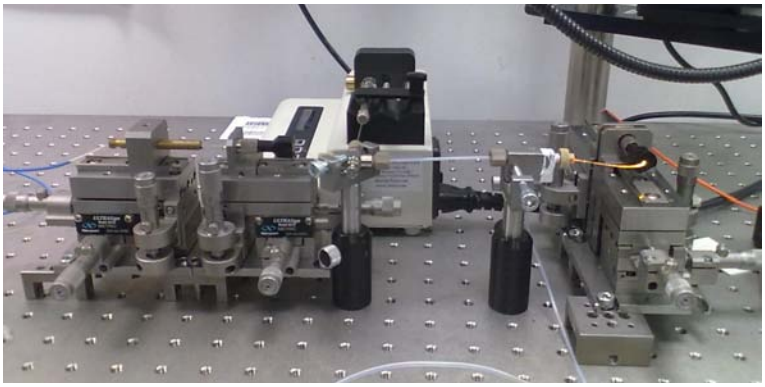

Figure 4: A possible experimental set-up showing the microfluidic pump, on the background, which can be used to flow small volumes of liquid around a fiber or to infiltrate reagents and samples into the holes of a microstructured fiber hung between the two vertical holders. On the right is clearly visible the light coupled into the fiber.

The main disadvantage of grating based sensor is that processing of the fiber must be performed, such as grating writing, cladding etching to expose the core, femtosecond laser direct writing and so on [62]. In addition, it must be noticed that, even though the grating inscription in standard optical fibers constitutes a mature technology, the progress achieved in such grating inscription in photonic crystal and microstructured fibers is still limited and challenging due to the presence of effects such as the side-illumination scattering induced by the capillary structure, the complex geometry core and the absence of significant photosensitivity for the case of all-silica fibers [63, 64].

7. PCF BIOSENSING APPLICATIONS

The great interest in using photonic crystal fibers for biosensing purposes is reflected by many research groups active in this field and in a large numbers of papers on optical fiber sensors with both solid and hollow cores. The simultaneously confinement of the liquid phase materials and the optical guided modes on the surface or within the holes of PCFs allows strong light-sample interaction over an extended length and may be useful for the development of highly sensitive chemical and biological sensing in liquids. Among numerous recent investigations into applications of fiber optic sensing, some of the most intriguing possible applications include the detection of DNA [60, 65]. Well established DNA analysis techniques are usually performed immobilizing a single strand of DNA on the glass and checking the hybridization of this strand to its complementary. Particular developments in this field will be described in the following sections. Many other applications can be found in the cited papers and reference therein.

Differently from sensing of physical properties such as temperature and strain where the changes in intrinsic characteristic of the fibers can be exploited [66], chemical and biological sensing normally require modification of the outer or inner surfaces of the fibers with layers of sensing molecules. Generally, this treatment, the so-called functionalization of the surfaces, is required in order to allow the binding of biological species to the glass surface [67]. Hybridization can be proved and tested through the measurement of the fluorescence signal produced by the labeled sample or the change in the guiding

properties of the fiber. Two approaches are possible in this process: adsorption or covalent linking, with the latter being preferable in terms of stability and durability. They are shown in Fig. **5**. Although still not able to provide performances as other type of sensors, *e.g.* those based on Raman effect or plasmonics, fiber-optical biosensors have been increasingly gaining importance due to their simpler construction and use. For example, the portable multi-analyte RAPTOR is present on the market, with only 10 min. processing time for detection of a bio-agent. On the other hand, optical fiber sensors are more readily used in clinical context, as demonstrated by specific applications in cancer diagnostics or in small volume measurements of bioanalytes in diagnosis and food safety.

8. SENSING FORMATS

Several different formats can be used for the detection of analytes in photonic crystal fibers. A simple version of sensor is that of infiltrating a solution of a given analyte and measuring the changes in the guidance characteristics of the fiber itself. Different liquids showing different refractive index can change the spectrum of transmitted or backscattered light and change the position of the bandgap in a very sensitive way [53]. Fluorescent analytes can be detected by their emission properties using interaction of the fluorophore with the guided light or with evanenscent field. Hollow core PCF can perform very efficiently in these applications, more than solid-core PCFs allowing the detection of fluorescent molecules such as rhodamine at very low concentration, as low as 10^{-10} M [68]. However, in most biosensing processes a molecular recognition procedure is necessary to distinguish between analytes, and this is very important in view of applications of sensors in complex biological fluids or even directly in tissues, where many substances having similar optical properties but very different biological effects have to be distinguished. In this case a recognition element, for example a receptor, able to selectively capture the target analyte must be incorporated onto the surfaces of the fiber. The capturing element, the probe coupled with the fiber, constitute a selective biosensor, provided that appropriate changes in refractive index or guiding properties can be generated upon capture of the analyte. Deposition of the selective probe component onto the outer or inner surface of PCF can be achieved by adsorption or by covalent linking to the fiber material, again shown in Fig. **5**.

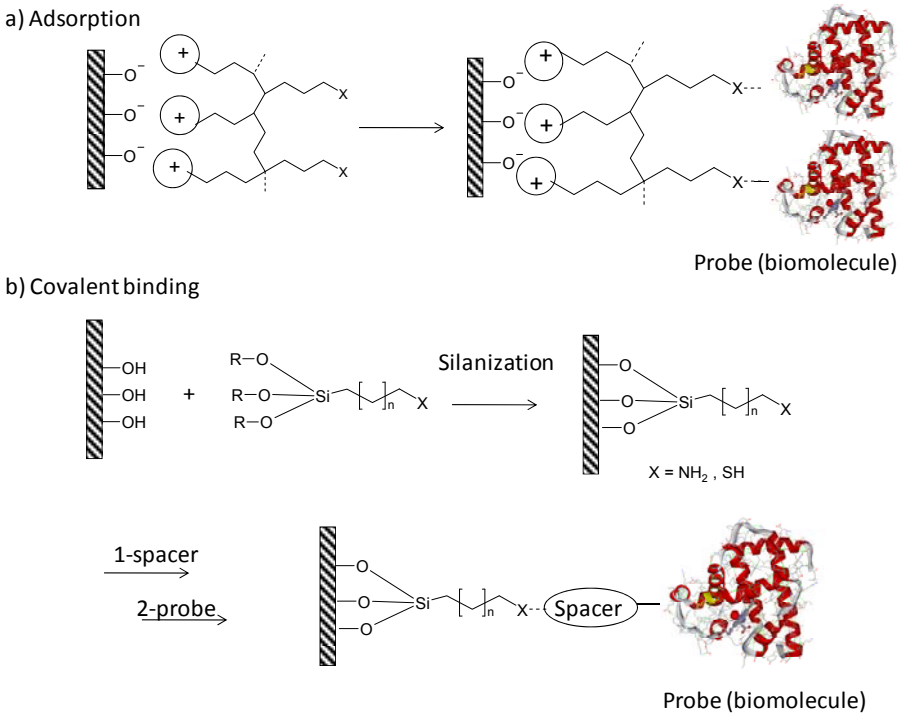

Figure 5: Different strategies for the generation of functionalized PCF using either (a) adsoption or (b) covalent binding of a specific probe.

9. ADSORPTION PROCEDURES

Adsorption of capture probes or of analytes is readily performed by infiltrating a solution into the holes of a PCF, followed by drying or by washing with an appropriate solvent. Polycations such as the polypeptide poly-Lys are strongly adsorbed onto the negatively charged silica surface, at appropriate pH, as shown in Fig. **5** (**a**). This can then be used as functional layer for further derivatization. This approach has been used for the fabrication of DNA sensing components of a microchip device bases on PCFs [7]. Frequently used biorecognition elements are streptavidin, avidin or neutravidin, all having very strong affinity for molecules marked with a terminal biotin. This allows to further link a layer of bioactive molecules to the surface through this very strong non-covalent bonding [8]. Procedures for coating of the inner surface of PCF with metal nanoparticles have also been described as a tool for increasing sensitivity of surface enhanced Raman scattering [68].

10. COVALENT BINDING

Derivatization procedures based on covalent binding, shown in Fig. **5** (**b**)**,** make use of liquid solutions which are brought in contact with the outer or inner surfaces of the fibers. External surfaces can be modified, as depicted in Fig. **6** (**a**), by immersion of the fiber in an appropriate solution of the reactant, followed by washings and air drying. After modification, the surface of the fiber should be exposed to the analyte by immersion. Inner surfaces modification, illustrated in Fig. **6** (**b**), requires infiltration of liquids inside the holes of the fibers for both modification reactions and then for analysis, Fig. **6** (**c**). Different techniques have been described for infiltration, using dipping the end into a solution, which is indeed a long and less reproducible process and can take several tenth of minutes to complete [24] or pumping with moderate pressure using liquid handling devices or microfluidics, as illustrated for example in Fig. **4**. Inner derivatization of the microstructure of fibers let optical processes to more confined and a more regular distribution of the probes, as shown in Fig. **6** (**d**) from our own experiments. Silica based surfaces have been largely used as support for covalently linking molecules able to perform recognition and sensing processes. Silica-based materials with covalent modification of the surface are used in liquid chromatography and in the production of supported catalysts. Glass supports are largely used in the production of DNA and protein microarrays; several examples of end-modified optical fibers have been described in the last decades for the production of specific sensors. The derivatization procedures are normally carried out in three steps: a) cleaning of the glass surface, b) silanization with an appropriate silicon-based reagent bearing a functional group; c) linking of the sensing molecule to the functional group as shown in Fig. **5**.

Cleaning procedures make use of acidic solutions of either sulphuric or hydrochloric acid, and in some cases of oxidizing reagents such as hydrogen peroxide [69]. A good comparison of cleaning procedures was reported for glass slides, with the aim of obtaining regular surfaces to be used for subsequent silanization [70]. The best combination was found to be the use of 1:1 mixture of HCl and methanol, followed by washings.

Silanization is carried out using trialkoxysilanes as illustrated in Fig. **5 b**) in which the alkyl chain linked to silicon have either an amino or a sulphide group at its end [71], thus allowing reaction with electrophilic reagents. Other approaches are also possible, such as the use of epoxy or carboxylic functional groups, allowing the silica surface to be linked to nucleophilic reagents. The silanization reaction takes place at high temperatures in apolar solvents such as toluene [72] or at room temperature with either basic [73] or acid catalysis [74].

The functional group at the end of the silane group is then normally reacted with a spacer group. Glutaraldehyde, dimethyl suberimidate, and dicarboxylic acids can be used for this purpose. The spacers allow to join functional groups which cannot be normally made to react with each other, and provide sufficient space to avoid hindrance of the recognition process by the surface. Chemistry of reactions developed for covalent linking biomolecules, such as proteins and DNA, to solid supports is more and more transferred from microsensing technology, *e.g.* microarray fabrication, to fiber optics for creating specific biosensors [75]. For example, long period grating fibers were functionalized either with a green fluorescent

protein or a DNA probe using silanization, linking of a suberimidate spacer and then reaction with amino groups of the biomolecule [76]. Glutaraldehyde is normally used to react with amino function creating a Schiff base [74], although this type of linkage is reversible and reaction time are rather long, but faster and irreversible reactions are to be preferred, such as reductive amination [77] or amide bond formation by an activated ester of a carboxylic moiety are more suitable for good fabrication. Other type of chemistry, such as isothiocyanate-amine reaction to generate thiourea or the so called "click chemistry" reactions, chemical ligation or Staudinger ligation are also possible, though yet not largely applied to PCF modification [78].

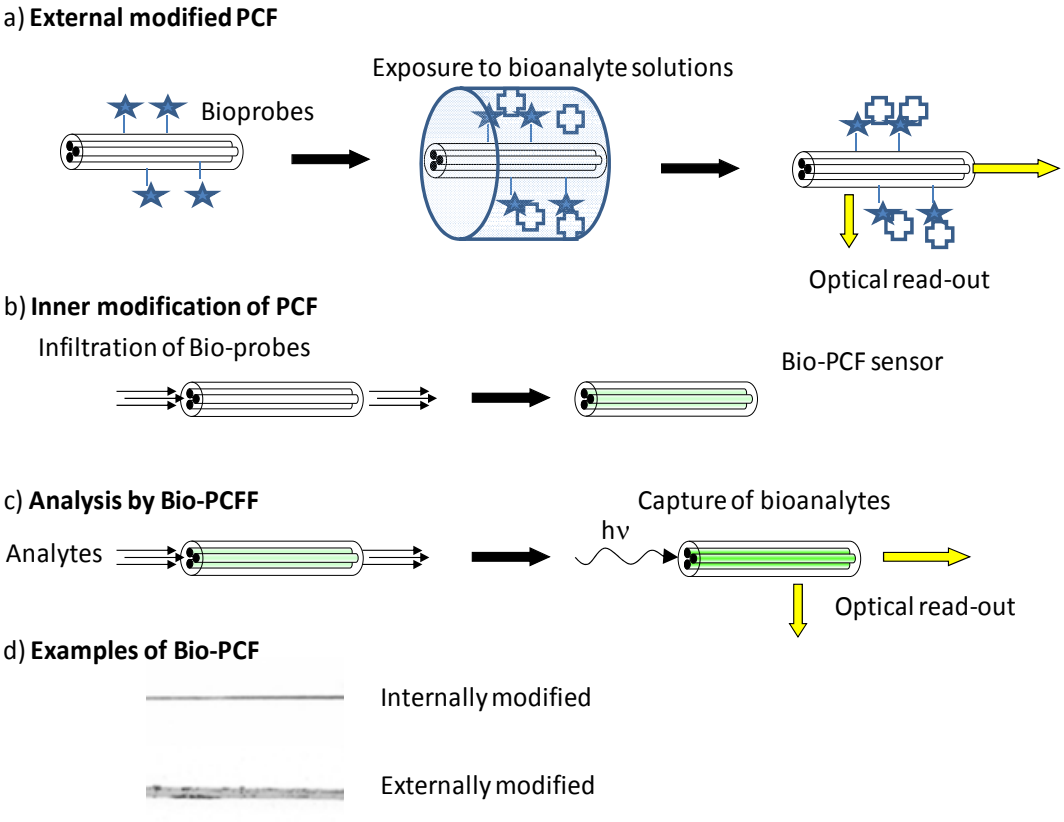

Figure 6: Different format for PCF-based biosensors. a) Use of externally modified fibers; b) fabrication of modified PCF sensor with inner biosensing surfaces; c) bioanalysis by PCF described in b), which requires filling the PCF with the sample solution; d) examples of fluorescent analyte capture by a solid core PCF internally or externally modified, as measured by fluorescence scanning, showing the higher homogeneity of the former.

Mild derivatization procedures are needed when the probe to be attached is sensitive to environment and can be denaturated or degraded under derivatizing conditions. This is the case of proteins, *i.e.,* of most small molecules receptors and antibodies, which can be denatured and of DNA, which can be degraded under acidic conditions, or fluorophores which are chemically or photochemically labile. Using a silanization protocol as that described in Fig. **5**, suspended-core PCF could be externally modified with a fluorescent molecule such as tetramethyrhodamine TAMRA achieving fluorescence properties, as detected by laser scanning [27].

Optical fibers made of polymeric materials such as poly(methyl methacrylate) (PMMA) can also be modified by exploiting the intrinsic functional groups present in the polymer (esters) as electrophiles [79].

11. ANALISYS OF SAMPLES OF BIOLOGICAL INTEREST

Numerous recent investigations report the usefulness of fiber optic sensing, with examples of detection of pH, oxygen, copper [80], anthrax [81], protein C [82], the pathogenic bacterium *Listeria monocytogenes*

[83], and single nucleotide polymorphism in DNA. Detection of analytes by fiber optics sensors either in small volume biological samples or directly in tissues has been one of the major effort in this field, with specific projects dedicated to instrumental implementation of this methods [84]. Photonic crystal fibers offer the possibility to be infiltrated with only few nanoliter sample size, with the analyte confined in the guiding or in the cladding parts. Hollow core PCFs have been shown to have different spectral features in the presence of ascorbate solutions [85]. Several examples report the use of PCFs in the detection of fluorophores tipically used for labeling biomolecules, such as rhodamine [78]. Using this approach, a multi-core PCFs was used for the detection of fluorophore-labeled DNA molecules in aqueous solutions [17]. The effect on spectral properties of hollow core PCF as a function of filling of either the core or the cladding holes has been studied both theoretically and experimentally [86]: the latter was tested using 1 μL of Alexa Fluor 700-labeled DNA solution, with detection of concentrations as low as 50 nM, due to high propagation of light through the sample in this type of PCF [87]. Highly efficient immobilization of fluorescently labeled DNA was demonstrated using hydrogel-filled hollow-core PCF. The hydrogel matrix, which is 3-dimensional, has a higher loading of the probes, thus allowing to detect as low as 260 nM DNA concentration [88].

Recently, selective functionalization of PCFs has been demonstrated by using very specific probes based on peptide nucleic acids (PNA) [89]. Fig. **7** (**a**) shows the two different structures of DNA and PNA. These molecules are DNA analogs in which the backbone has been replaced by a polyamide composed of monomeric repeating units of N-(2-aminoethyl)glycine covalently linked to nucleobases, and are able to interact with complementary DNA sequences with high affinity and specificity [90]. Furthermore, they are very stable chemically and resist to enzymatic degradation, which can cause severe problems to biosensors based on proteins or on DNA; thus they are ideal probes for DNA detection in sensing devices used clinically [91] or for food analysis [92], especially in ultrasensititve techniques [93, 94].

As a first example, a recognition of complementary DNA labelled with Cy5 fluorophore in the presence of a mismatched DNA (*i.e.,* with the same sequence except for one nucleobase) labelled with Cy3 has been performed. The results showed that the full-match was much more efficiently captured by the modified fiber [60]. Inner derivatization led to more defined signals and more regular distribution of captured full match DNA, as shown in Fig. **7** (**b**), (**c**), with a 53 fold increase in the signal compared with an unmodified fiber infiltrated with the same DNA and a 3:1 signal ratio compared to the same modified fiber infiltrated with a mismatched DNA corresponding to single nucleotide polymorphisms [95]. Moreover, instead of using synthetic short oligonucleotides, the same capture has been performed using, a real DNA sample. This real DNA sample has been obtained from extraction of the genetic material from olive leaves, followed by amplification by polymerase chain reaction (PCR) to a final size of 150 bp, as shown in Fig. **7** (**d**), which was shown to captured by the PNA-PCF and not by an unmodified PCF, as illustrated in Fig. **7** (**e**). Thus the entire detection process from tissue to PCF capture was demonstrated in this example.

The inner channels of the microstructured fibers can also be used as microfluidics components [96], and capillary electrophoresis able to separate fluorescently labelled DNA samples was demonstrated using solid-core PCF, which was shown to be superior to normal capillaries in terms of resolution [97].

Metal nanoparticle filled PCFs have been reported as very sensitive devices exploiting Surface Enhaced Raman Scattering (SERS), allowing to detect rhodamine 6G [98, 99], 4-aminothiophenol [100], human insulin, and tryptophan [101] in considerably sensitive assays.

Finally, combination of PCF with quantum dots has also been reported, mainly aimed to obtain fiber lasers, but the techniques can be applied in sensing devices [102]. In one of the few examples reported, a fiber sensor was obtained by infiltrating PCF with micromolar solutions of quatum dots; radical species were detected by quenching of quantum dot fluorescence, as demonstrated by injection of a solution of 2, 2, 6, 6-tetramethylpiperidine-N-oxide free radical (TEMPO) [103].

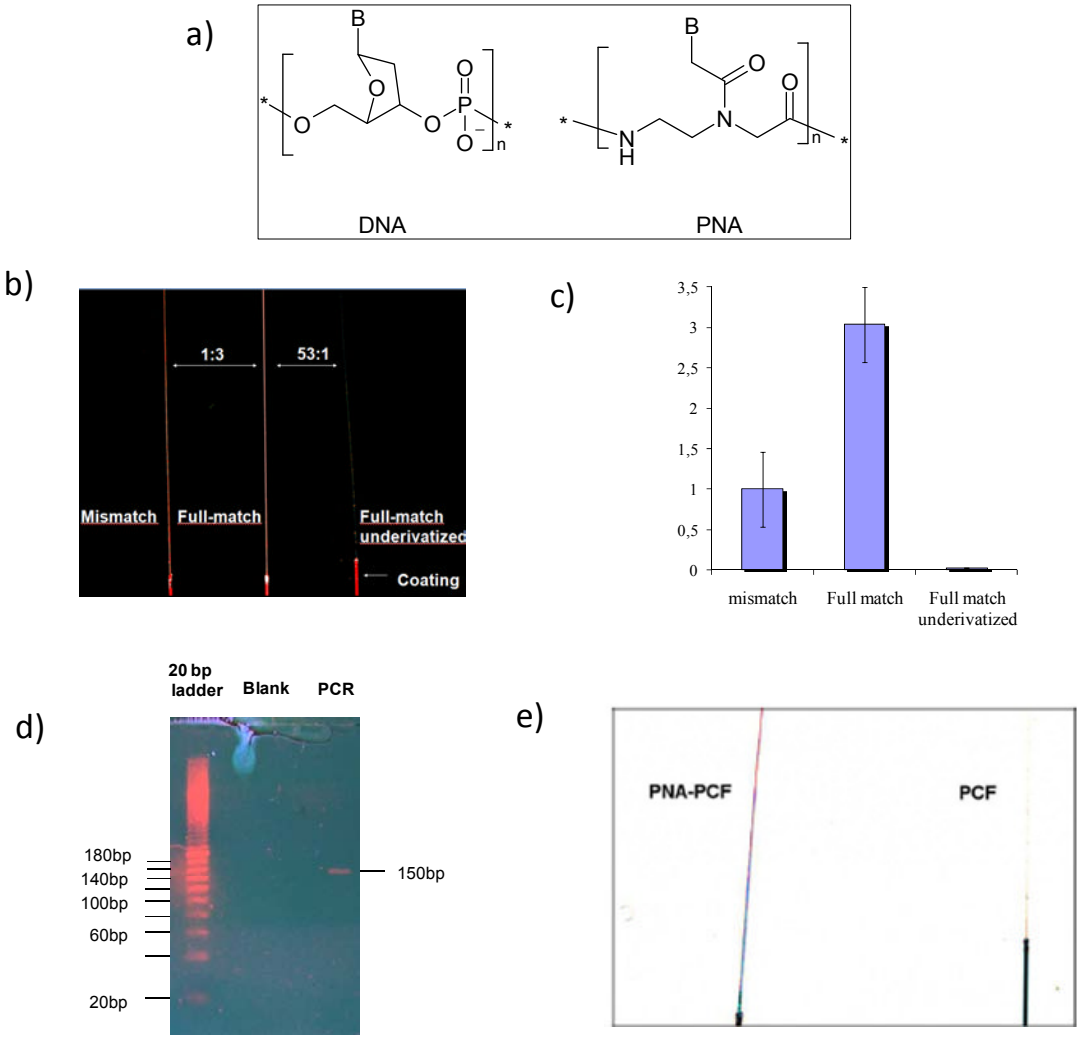

Figure 7: a) Structure of PNA compared to DNA; b) Fluorimetric detection of Cy3 labelled DNA oligonucleotides using suspended core PCF modified with PNA: middle full-match DNA with modified fiber, left: mismatched DNA with modified fiber, right: full-match DNA with unmodified fiber; c) quantitative comparison of signals obtained in b); d) agarose gel electrophoresis showing the size of the Cy3-labelled PCR product amplified from olive leaves and subsequently used in e); e) Fluorimetric detection (negative image) of the signal obtained by capturing the 150bp PCR product by either a PNA modified PCF (left) or an unmodified PCF (Right). From reference [90].

CONCLUSIONS

Photonic crystal fibers will play a significant role in the development of physical, chemical and biological sensors because of their unique features of direct and strong interaction with the analytes under test. These sensor types have been the objective of a large number of investigations in the last years and they provide numerous ways of performing a rapid, remote, in-line and *in situ* determination of many types of analytes in a wide range of application fields. They are under continuous development and research in this area places increasing emphasis on the works concerning the sensor performances, such as micro-structural stability, leaching, reversibility, response time, repeatability, sensitivity and selectivity, instead of simply demonstrating the sensing potential. Also, rapid advances have been made in improving immobilization protocols. In the next future, photonic crystal fiber biosensors, specifically treated for selected biological targets, must be able to demonstrate devices flexible and simple in use, miniaturized in diameter and packaging size, with enhanced optical read-out and able to be in line with the increasing need of fast-response instrumentation to perform real-time and on-site analysis. Rapid real-time analysis will also help

to diagnose severe illness at an early stage with crucial beneficial effect on healthcare system and on the society. Photonic crystal fibers based sensors for physical, chemical and biological agents have the potentiality to face these challenges.

ACKNOWLEDGEMENTS

The authors want to thank Federica Poli, Enrico Coscelli, Michele Sozzi, Claudia Lantano and Alessandro Candiani for support and useful discussions. This work was carried out in the context of Eurobiotech project.

REFERENCES

[1] Russell PStJ. Photonic-crystal fibers. J Lightwave Technol 2006; 24(12): 4729-4749.

[2] Poli F, Cucinotta A, Selleri S. Photonic Crystal Fibers, Properties and Applications. Material Science Springer-Verlag, Dordrecht, The Netherlands, 2007.

[3] Pickrell G, Peng W, Wang A. Random-hole optical fiber evanescent-wave gas sensing. Opt Lett 2004; 29(13): 1476-1478.

[4] Apetrei AM, Moison JM, Levenson JA, Foroni M, Poli F, Cucinotta A, Selleri S, Legré M, Wegmuller M, Gisin N, Dukel'skii KV, Khokhlov AV, Shevandin VS, Kondrat'ev YN, Sibilia C, Serebryannikov EE, Zheltikov AM. Electromagnetic field confined and tailored with a few air holes in a photonic-crystal fiber. Applied Physics B 2005; 81: 409-414.

[5] Larsen T, Bjarklev A, Hermann D, Broeng J. Optical devices based on liquid crystal photonic bandgap fibres. Opt Express 2003; 11: 2589-2596.

[6] Luan F, George AK, Hedley TD, Pearce GJ, Bird DM, Knight JC, Russell PStJ. All-solid photonic bandgap fiber. Opt Lett 2004; 29: 2369-2371.

[7] Rindorf L, Høiby PE, Jensen JB, Pedersen LH, Bang O, Geschke O. Towards biochips using microstructured optical fiber sensors. Anal Bioanal Chem 2006; 385(8): 1370-1375.

[8] Ott JR, Heuck M, Agger C, Rasmussen PD, Bang O. Label-free and selective nonlinear fiber-optical biosensing. Opt Express 2008; 16(25): 20834-47.

[9] Petrovich MN, van Brakel A, Poletti F, Mukasa K, Austin E, Finazzi V, Petropoulos P, O'Driscoll E, Watson M, Del Monte T, Monro TM, Dakin JP, Richardson DJ. Microstructured fibres for sensing applications. SPIE Opt East Conf 2005; Boston, MA, October 23-26, 2005.

[10] Passaro D, Foroni M, Poli F, Cucinotta A, Selleri S, Lægsgaard J, Bjarklev A. All-Silica Hollow-Core Microstructured Bragg Fibers for Biosensor Application. IEEE Sensors J 2008; 8(7): 1280-1286.

[11] Lee B. Review of the present status of optical fiber sensors. Optical Fiber Technology 2003; 9: 57-79.

[12] Fan X, White IM, Shopova SI, Zhu H, Suter JD, Sun Y. Sensitive optical biosensors for unlabeled targets: a review. Analytica Chimica Acta 2008; 620: 2-26.

[13] Narayanaswamy R, Wolfbeis OS. Optical Sensors. Springer, New York, 2004.

[14] Bosch ME, Sánchez AJR, Rojas FS, Ojeda CB. Recent Development in Optical Fiber Biosensors. Sensors 2007; 7: 797-859.

[15] Fini J., Microstructure fibres for optical sensing in gases and liquids, Meas. Sci. Technology 2004; 15: 1120-1128.

[16] Cordeiro CMB, de Matos CJS, dos Santos EM, Bozolan A, Ong JSK, Facincani T, Chesini G, Vaz AR, Cruz CHB. Towards practical liquid and gas sensing with photonic crystal fibres: side access to the fibre microstructure and single-mode liquid-core fibre. Meas. Sci. Technol. 2007; 18: 3075-3081.

[17] Jensen JB, Pedersen LH, Hoiby PE, Nielsen LB, Hansen TP, Folkenberg JR, Riishede J, Noordegraaf D, Nielsen K, Carlsen A, Bjarklev A. Photonic crystal fiber based evanescent-wave sensor for detection of biomolecules in aqueous solutions Optics Lett 2004; 29(17): 1974-1976.

[18] Ritari T, Tuominen J, Ludvigsen H, Petersen JC, Sørensen T, Hansen TP, Simonsen HR. Gas sensing using air-guiding photonic bandgap fibers. Opt Express 2004; 12(17): 4080-4087.

[19] Frosz MH, Stefani A, Bang O. Highly sensitive and simple method for refractive index sensing of liquids in microstructured optical fibers using four-wave mixing. Opt Express 2011; 19(11): 1471-10484.

[20] Soto MA, Sahu PK, Bolognini G, Di Pasquale F. Brillouin-based distributed temperature sensor employing pulse coding. IEEE Sensor Letters 2008; 8(3): 225-226.

[21] Yinian Z, Du H, Bise R. Design of solid-core microstructured optical fiber with steering-wheel air cladding for optimal evanescent-field sensing. Opt Express 2006; 14(8): 3541-3546.

[22] Cordeiro CMB, Franco MAR, Chesini G, Barretto ECS, Lwin R, Cruz CHB, Large MCJ. Microstructured-core optical fibre for evanescent sensing applications. Opt Express 2006; 14(26): 13057-13066.

[23] Stewart G, Culshawb. Optical Waveguide Modeling and Design for Evanescent Field Chemical Sensors. Optical Quantum Electron 1994; 26: 249.

[24] Shahraam AV, Warren-Smith SC, Monro TM. Enhancement of fluorescence-based sensing using microstructured optical fibres. Opt Express 2007; 15(26) 17891-17901.

[25] Jensen JB, Pedersen LH, Hoiby PE, Nielsen LB, Hansen TP, Folkenberg JR, Riishede J, Noordegraaf D, Nielsen K, Carlsen A, Bjarklev A. Photonic crystal fiber based evanescent-wave sensor for detection of biomolecules in aqueous solutions. Opt Lett 2004; 29: 1974-1976.

[26] Coscelli E, Poli F, Passaro D, Cucinotta A, Selleri S, Corradini R, Marchelli R. DNA-recognition by pepetide nucleic acid-modified PCFs: from models to real samples. SPIE Photonics Europe 2010, April 12-16, 2010, Bruxelles, Belgium.

[27] Coscelli E, Sozzi M, Poli F, Passaro D, Cucinotta A, Selleri S, Corradini R, Marchelli R. Towards biosensing with suspended core photonic crystal fiber. 3rd EOS Topical Meeting on Optical Microsystems (OμS'09), 27-30 September 2009, Capri, Italy.

[28] Knight JC. Photonic crystal fibres. Nature 2003; 424: 847-851.

[29] Russell PStJ. Photonic crystal fibres. Science 2003; 299: 358-362.

[30] Birks TA, Atkin DM, Wylangowski G, Russell PStJ, Roberts PJ. 2D Photonic Band Gap Structures in Fibre Form. Photonic Band Gap Materials, Soukoulis CM, Ed. Kluwer, 1996; 437-444.

[31] Euser TG, Chen JSY, Scharrer M, Russell PStJ. Farrer NJ, Sadler PJ. Quantitative broadband chemical sensing in air-suspened solid-core fibers. J Applied Physics 2008; 103(10): 103108-103108.

[32] Zhu Y, Bise RT, Kanka J, Peterka P, Du H. Fabrication and characterization of solid-core photonic crystal fiber with steering-wheel air-cladding for strong evanescent field overlap. Opt Commun 2008; 281(1): 55-60.

[33] Webb AS, Poletti F, Richardson DJ, Sahu J. Suspended-core holey fiber for evanescent-field sensing. Opt Eng Letters 2007; 46(10): 10503-10503.

[34] Ruan Y, Schartner EP, Ebendorff-Heidepriem H, Hoffmann P, Monro TM. Detection of quantum-dot labeled proteins using soft glass microstructured optical fibers. Opt Express 2007; 15: 17819-17826.

[35] Monro TM, Richardson DJ, Bennett PJ. Developing holey fibers for evanescent field devices. Electron Lett 1999; 35(14): 1188-1189.

[36] Cregan RF, Mangan JB, Knight JC, Birks TA, Russell PStJ, Roberts PJ, Allan DC. Single-mode photonic bandgap guidance of light in air. Science 1999; 285: 1537-1539.

[37] NYeh P, Yariv A, Marom E. Theory of Bragg fiber. J Opt Soc Amer 1978; 68: 1196-1201.

[38] Fink Y, Ripin DJ, Fan S, Chen C, Joannopoulos JD, Thomas EL. Guiding optical light in air using an all-dielectric structure. J Lightwave Technol 1999; 17: 2039-2041.

[39] Johnson SG, Ibanescu M, Skorobogatiy M, Weisberg O, Engeness TD, Soljacic M, Jacobs SA, Joannopoulos DJ, Fink Y. Low-loss asymptotically single-mode propagation in large-core OmniGuide fibers. Opt Express 2001; 9: 748-779.

[40] Likhachev ME, Semjonov SL, Bubnov MM, Dianov EM, Khopin VF, Yu M, Salganskii, Gurjanov MA, Gurjanov AN, Jamier R, Viale P, Février S, Blondy JM. Development and study of Bragg fibres with a large mode field and low optical losses. Quantum Electron 2006; 36: 581-586.

[41] Viale P, Février S, Leproux P, Jaouën Y, Obaton AF. Modal properties of solid-core photonic bandgap fibers. Photon Nanostruct Fund Applicat 2006; 4: 116-122.

[42] Pone E, Dubois C, Gu N, Gao Y, Dupuis A, Boismenu F, Lacroix S, Skorobogatiy M. Drawing of the hollow all-polymer Bragg fibers. Opt Express 2006; 14: 5838-5852.

[43] Mignanelli M, Wani K, Ballato J, Foulger S, Brown P. Polymer microstructured fibers by one-step extrusion. Opt Express 2007; 15: 6183-6189.

[44] Dupuis A, Guo N, Gauvreau B, Hassani A, Pone E, Boismenu F, Skorobogatiy M. Guiding in the visible with colorful solid-core Bragg fibers. Opt Lett 2007; 32: 2882-2884.

[45] Skorobogatiy M, Dupuis A. Ferroelectric all-polymer hollow Bragg fibers for terahertz guidance. Appl Phys Lett 2007; 90: 113514-1-113514-3.

[46] Vienne G, Xu Y, Jakobsen C, Deyerl HJ, Hansen TP, Larsen BH, Jensen JB, Sørensen T, Terrel M, Huang Y, Lee RK, Mortensen NA, Broeng J, Simonsen H, Bjarklev A, Yariv A. First demonstration of air-silica Bragg fiber. OFC 2004, PDP25.

[47] Vienne G, Xu Y, Jakobsen C, Deyerl HJ, Jensen JB, Søhrensen T, Hansen TP, Huang Y, Terrel M, Lee RK, Mortensen NA, Broeng J, Simonsen H, Bjarklev A, Yariv A. Ultra-large bandwidth hollow-core guiding in all-silica Bragg fibers with nano-supports. Opt Express 2004; 12: 3500-3508.

[48] Selleri S, Cucinotta A. Analysis and design of photonic crystal fibers: Solid and hollow core fibers through the finite element method. International Journal for Computation and Mathematics in Electrical and Electronic Engineering 2008; 27(6): 1227-1235.

[49] Cucinotta A, Selleri S, Vincetti L, Zoboli M. Perturbation Analysis of Dispersion Properties in Photonic Crystal Fibers through the Finite Element Method. IEEE/OSA J Lightwave Technol 2002; 20(8): 1433-1442.

[50] Selleri S, Vincetti L, Cucinotta A, Zoboli M. Complex FEM Modal Solver of Optical Waveguides with PML Boundary Conditions. Optical Quantum Electronics 2001; 33(4/5): 359-371.

[51] Vincetti L, Poli F, Selleri S. Confinement loss and nonlinearity analysis of air-guiding modified honeycomb photonic bandgap fibers. IEEE Photonic Tech L 2006; 18: 508-510.

[52] Lehmann H, Bruckner S, Kobelke J, Schwotzer G, Schuster K, Willsch R. Toward photonic crystal fiber based distributed chemosensors. 17th Int. Conf. on Optical Fibre Sensors 2005, Proceedings of SPIE 5855 419.

[53] Kuhlmey BT, Eggleton BJ. Fluid-Filled Solid-Core Photonic Bandgap Fibers. J Lightwave Technol, 2009; 27(11): 1617-1630.

[54] Xiao L, Jin W, Demokan MS, Ho HL, Hoo YL, Zhao C. Fabrication of selective injection microstructured optical fibers with a conventional fusion splicer. Opt Express 2005; 13(22): 9014-9022.

[55] Huang Y, Xu Y, Yariv A. Fabrication of functional microstructured optical fibers through a selective filling technique. Appl Phys Lett 2004; 85(22): 5182-5184.

[56] Wang Y, Liao CR, Wang DN. Femtosecond laser-assisted selective infiltration of microstructured optical fibers. Opt Express 2010; 18(17): 18056-18060.

[57] Cordeiro CMB, dos Santos EM, Brito Cruz CH. Lateral access to the holes of photonic crystal fibers - selective filling and sensing applications. Opt Express 2006;14(18): 8403-8412.

[58] Nielsen K, Noordegraaf D, Sorensen T, Bjarklev A, Hansen TP. Selective filling of photonic crystal fibres. J Optics A-Pure And Appl Optics 2005; 7(8): L13-L20.

[59] Broderick NGR, Vukovic NT, Brambilla G, Horak P, Richardson DJ, Poletti F. Novel applications of fibre tapers. WSOF 2010 Oaxaca, Mexico 13-15 Oct 2010.

[60] Coscelli E, Sozzi M, Poli F, Passaro D, Cucinotta A, Selleri S, Corradini R, Marchelli R. Toward Highly Specific DNA Biosensor: PNA-Modified Suspended Core Photonic Crystal Fiber. IEEE J Sel Top Quant 2010*;* 16(4): 967 - 972.

[61] Zhu Y, Shum P, Chong JH, Rao MK, Lu C. Deep-notch, ultracompact long-period grating in a largemode-area photonic crystal fiber. Opt Lett 2003; 28: 2467-2469.

[62] Cusano A, Paladino D, Iadicicco A. Microstructured Fibre Bragg Gratings. J Lightwave Technol 2009; 27: 1663-1697.

[63] Pissadakis S, Livitziis M, Tsibidis GD. Investigations on the Bragg grating recording in all-silica, standard and microstructured optical fibres using 248 nm 5 ps, laser radiation. J. Europ Opt Soc Rap Public 2009; 4: 09049.

[64] Rindorf L, Jensen JB, Dufva M, Pedersen LH, Hoiby PE, Bang O. Photonic crystal long-period gratings for biochemical sensing. Opt Express 2006; 14(18): 8224-8231.

[65] Jensen JB, Emiliyanov G, Bang O, Hoiby PE, Pedersen LH, Hansen TP, Nielsen K, Bjarklev A. Microstructured polymer optical fiber biosensor for detection of DNA and antibodies. Opt Fiber Sens 2006, ThA2, October 23-27, Cancun, Mexico.

[66] Rindorf L, Bang O. Sensitivity of photonic crystal fiber grating sensors: biosensing, refractive index, strain, and temperature sensing. J Opt Soc Am B 2008; 25(3): 310-324.

[67] Smolka S, Bart, Benson O. Highly efficient fluorescence sensing with hollow core photonic crystal fibers. Opt Express 2007; 15(20): 12783-12791.

[68] Shi C, Lu C, Gu C, Tian L, Newhouse R, Chen S, Zhang JZ. Inner wall coated hollow core waveguide sensor based on double substrate surface enhanced Raman scattering. Appl Phys Lett 2008; 93(15) 153101.

[69] Konopsky VN, Alieva EV. Photonic Crystal Surface Waves for Optical Biosensors Anal Chem 2007**;** 79(12): 4729-4735.

[70] Han Y, Mayer D, Offenhaüsser A, Ingebrandt S. Surface activation of thin silicon oxides by wet cleaning and silanization Thin Solid Films 2006; 510 (1-2):175-180.

[71] Tazawa H, Kanie T, Katayama M. Fiber-optic coupler based refractive index sensor and its application to biosensing. Appl Phys Lett 2007; 91(11): 113901.

[72] Evstrapov A, Esikova N, Rudnitskaya G, Antropova TV. Porous glasses as a substrate for sensor elements. Optica Applicata 2010; 15(2): 333-340.

[73] Lundgren JS, Bright FV. Biosensor for the Nonspecific Determination of Ionic Surfactants. Anal Chem 1996; 68(19): 3377-3381.

[74] Cordek J, Wang X, Tan W. Direct Immobilization of Glutamate Dehydrogenase on Optical Fiber Probes for Ultrasensitive Glutamate Detection. Anal Chem 1999; 71(8):1529-1533.

[75] Borisov SM, Wolfbeis OS. Optical Biosensors. Chem Rev 2008; 108(2): 423-461.

[76] Chen X, Zhang L, Zhou K, Davies E, Sugden K, Bennion I, Hughes M, Hine A. Real-time detection of DNA interactions with long period fiber-grating-based biosensor. Opt Lett 2007; 32(17): 2541-2543.

[77] Calabretta A, Wasserberg D, Posthuma-Trumpie GA, Subramaniam V, van Amerongen A, Corradini R, Tedeschi T, Sforza S, Reinhoudt DN, Marchelli R, Huskens J, Jonkheijm P. Patterning of Peptide Nucleic Acids Using Reactive Microcontact Printing. Langmuir, *asap*, DOI: 10.1021/la102756k.

[78] Rusmini F, Zhong Z, Feijen J. Protein Immobilization Strategies for Protein Biochips. Biomacromolecules 2007**;** 8(6): 1775-1789.

[79] Kulkarnia A, Leeb J-H, Namb J-D, Kima T. Thin film-coated plastic optical fiber probe for aerosol chemical sensing applications. Sensors and Actuators B 2010; 150(1) 154-159.

[80] Zeng H-H, Thompson RB, Maliwal BP, Fones GR, Moffett JW, Fierke CA Real-Time Determination of Picomolar Free Cu(II) in Seawater Using a Fluorescence-Based Fiber Optic Biosensor Anal Chem 2003; 75(24):6807-6812.

[81] Tims TB, Lim DV. Rapid detection of Bacillus anthracis spores directly from powders with an evanescent wave fiber-optic biosensor. J Microbial Methods 2004; 59(1):127-130.

[82] Tang L, Kwon HJ, Kang KA Theoretical and experimental analysis of analyte transport in a fiber-optic, Protein C immuno-biosensor Biotechnol Bioeng 2004; 30(7); 869-879.

[83] Geng T, Morgan MT, Bhunia AK. Detection of low levels of Listeria monocytogenes cells by using a fiber-optic immunosensor. Appl Environ Microbiol 2004; 70(10):6138-6146.

[84] Gorris HH, Walt DR. Anal Chem on the Femtoliter Scale. Angew Chem Int Ed. 2010; 49(23): 3880-3895.

[85] Tuchin VV, Skibina Yu S, Beloglazov VI, Chainikov M V, Skibina NB, Mikhailova NA, Zhestkov P M, Silokhin I Yu. Sensor Properties of Hollow-Core Photonic Crystal Fibers. Technical Physics Letters 2008; 34(8): 663-665.

[86] Sun J, Chan CC, Dong XY, Shum P. High-resolution photonic bandgap fiber-based biochemical sensor. J Biomed Opt 2007; 12(4): 044022.

[87] Sun J, Chan CC, Zhang YF, Shum P. Analysis of hollow-core photonic bandgap fibers for evanescent wave biosensing. J Biomed Opt 2008; 13(5): 054048.

[88] Gorris HH, Walt DR, Kivlehan F, Moore E, Brennan D, Galvin P, Ellis AD. Integration of a 3D hydrogel matrix within a hollow core photonic crystal fibre for DNA probe immobilization. Meas Sci Technol 2010; 21.

[89] Nielsen PE (Ed.). Peptide Nucleic Acids: Protocols and Applications, Horizon Bioscience, Norfolk, UK, 2004.

[90] Nielsen PE. Peptide nucleic acid: a versatile tool in genetic diagnostics and molecular biology. Curr Opin Biotech 2001; 12(1): 16-20.

[91] Corradini R, Feriotto G, Sforza S, Marchelli R, Gambari R. Enhanced Recognition of Cystic Fibrosis W1282X DNA Point Mutation by Chiral Peptide Nucleic Acids Probes by a Surface Plasmon Resonance Biosensor. J Mol Rec 2004; 17(1): 76-84.

[92] Sforza S, Corradini R, Tedeschi T, Marchelli R. Food analysis and food authentication by peptide nucleic acid (PNA)-based technologies. Chem Soc Rev 2010; DOI: 10.1039/b907695f.

[93] D'Agata R, Corradini R, Grasso G, Marchelli R, Spoto G. Ultrasensitive Detection of DNA by PNA and Nanoparticle-Enhanced Surface Plasmon Resonance Imaging. Chem Biochem 2008; 9(13): 2067-2070.

[94] D'Agata R, Corradini R, Ferretti C, Zanoli L, Gatti M, Marchelli R, Spoto G. Ultrasensitive detection of non-amplified genomic DNA by nanoparticle-enhanced surface plasmon resonance imaging. Biosens Bioelectron 2010; 25(9): 2095-2100.

[95] Selleri S, Coscelli E, Poli F, Passaro D, Cucinotta A, Lantano C, Corradini R, Marchelli R. DNA-recognition by peptide nucleic acid-modified PCFs: from models to real samples. SPIE Photonics Europe 2010; Conference 7715, April 12-16, Bruxelles, Belgium.

[96] Borecki M, Korwin-Pawlowski ML, Beblowska M, Szmidt J, Jakubowski A. Optoelectronic Capillary Sensors in Microfluidic and Point-of-Care Instrumentation. Sensors 2010; 10(4): 3771-3797.

[97] Sun Y, Nguyen N-T, Kwok YC. Enhanced electrophoretic DNA separation in photonic crystal fiber. Anal Bioanal Chem 2009; 394(6): 1707-1710.

[98] Yan H, Liu J, Yang C, Jin G, Gu C, Hou L. Novel index-guided photonic crystal fiber surface-enhanced Raman scattering probe. Opt Express 2008; 16(11): 8300-8305.

[99] Cox FM, Argyros A, Large MCJ, Kalluri S. Surface enhanced Raman scattering in a hollow core microstructured optical fiber. Opt Express 2007; 15 (21): 13675-13681.

[100] Peacock AC, Amezcua-Correa A, Yang J, Sazio PJA, Howdle SM. Highly efficient surface enhanced Raman scattering using microstructured optical fibers with enhanced plasmonic interactions Appl Phys Lett 2008; 92(14): 141113.

[101] Zhang Y, Shi C, Gu C, Seballos L, Zhang JZ. Liquid core photonic crystal fiber sensor based on surface enhanced Raman scattering. Appl Phys Lett 2007; 90(19): 193504.

[102] Jorge P, Martins MA, Trindade T, Santos JL, Farahi F. Optical Fiber Sensing Using Quantum Dots. Sensors 2007; 7(12): 3489-3534.

[103] Galian RE, Laferriere M, Scaiano JC. Doping of photonic crystal fibers with fluorescent probes: possible functional materials for optrode sensors. J Mater Chem 2006; 16(18): 1697-1701.

Subject Index

B

Bragg
- condition; 11; 188
- diffraction; 96; 102; 201; 205
- fiber; 218-219
- grating; 11; 102; 196-197
- reflector; 4; 13; 105; 181
- resonators; 135-155

D

Dispersion Properties; 18-20; 62-67; 98; 109; 118-130

E

Endlessy Single mode; 85

F

Filter; 58-60; 103-105; 196-197; 202; 212

G

Guided Resonances; 180-193

H

Hollow core Optical Fibers; 87-88; 170-175; 217-219

L

Large Mode Area; 87
Light-Emitters; 17-18; 96-103; 105-108; 150-155

N

Nano-imprinting Lithography; 93-96
Nano-Lithography; 68; 151; 190; 197

O

Organic Photonics; 93-111

P

Photonic Crystal Fiber Sensors; 157-176; 216-227
Photodiodes; 108
Photonic Quasi-Crystals; 185-187

S

Simulation methods
- Block Floquet Method; 9
- Finite Difference Time Domain; 10; 44-47; 55-56

Marco Pisco, Andrea Cusano and Antonello Cutolo (Eds)
All rights reserved-© 2012 Bentham Science Publishers

Finite Element Method; 10; 24; 29; 88-91
Plane Wave Method; 9; 29-40; 54-55
Scattering Matrix Method; 10
Transfer Matrix Method; 10-23
Slow Light; 118-132
Soft Lithography; 94
Solid core Photonic Crystal Fibers; 84-91; 158; 170
Stack and Draw; 91
Supercontinuum generation; 86
Surface Enhanced Raman Scattering; 157-179; 225
Surface Plasmon Resonance; 205-206
Switch; 60-62; 105; 128-131